

Anchorage Detailing Effects on
Lateral Deformation Components of R/C Shear Walls

Section	Page
Chapter 1: Introduction	1
Chapter 2: Review of Related Literature	13
Chapter 3: Test Specimen Description	24
Chapter 4: Instrumentation and Behaviors of Interest	39
Chapter 5: Test Setup & Procedures	63
Chapter 6: Load v. Deflection Relationships	75
Chapter 7: Axial Strain from Flexure	85
Chapter 8: Moment v. Curvature Relationships	104
Chapter 9: Flexural Component of Lateral Deformation	121
Chapter 10: Steel to Concrete Bond Slip	145
Chapter 11: Shear Component of Lateral Deformation	160
Chapter 12: Total Calculated v. Measured Deformations	181
Chapter 13: Instability & Bar Fracture	201
Chapter 14: Conclusions & Recommendations	222
Appendix 1: Calculation of Axial Strain	242
Appendix 2: Calculation of Curvatures and Rotations	257
Appendix 3: Calculation of Flexural Deformation	274
Appendix 4: Calculation of Shear Deformation	284
Appendix 5: Calculation of Strains With Krypton Data	299
Appendix 6: Data Management & Reduction	303
Appendix 7: Photographs	324

Chapter 1: Introduction

1.0: Background

Structural walls, or shear walls, are elements used to resist lateral loads, such as those generated by wind and earthquakes. Structural walls are considerably deeper than typical beams or columns. This attribute gives structural walls considerable in-plane stiffness which makes structural walls a natural choice for resisting lateral loads. In addition to considerable strength, structural walls can dissipate a great deal of energy if detailed properly. Walls are an invaluable structural element when protecting buildings from seismic events.

Buildings often rely on structural walls as the main lateral force resisting system. Shear walls are required to perform in multiple ways. Walls must be able to prevent damage to non-structural elements during seismic loading events that are small in magnitude, but more frequent during the buildings design life. In addition, walls must be able to prevent the collapse of the building during ultimate seismic loading events that are very infrequent. Determining the necessary level of building protection and acceptable damage through structural design for any loading event is the core of performance based design. Performance based design allows engineers and stakeholders to determine the necessary and desired level of protection to the building under the possible loading conditions. Shear walls can then be designed to limit building damage to the specified degree. The load-deformation response of the structural walls must be accurately predicted and related to structural damage in order to achieve these performance goals under loading events of various magnitudes. Relating the strength and stiffness of shear walls to lateral displacement and damage is one of the main goals of this thesis.

In order to relate strength and stiffness to displacement and damage, each individual deflection mode, or component of total lateral deformation, must be able to be predicted. Predicting each component of lateral deformation individually is necessary, as not all

components exhibit the same change in stiffness from elastic to plastic behavior. Understanding each individual deformation component relationship with load allows a much more precise estimate of total wall deformation and deflected shape. The three modes that account for almost the entirety of lateral deformation are flexural in-plane rotation, shear distortion, and axial strain in the longitudinal reinforcement penetrating into the foundation and causing rotation of the wall at the foundation/wall interface (strain penetration). Refer to Figures 1.1 through 1.3 for illustrations of these three deformation modes. Flexural deformation is covered in Chapter 9, deformation from strain penetration is covered in Chapter 10, and shear deformation is discussed in Chapter 11. Other displacements can arise from foundation rotation/rocking and sliding at the wall foundation/interface. The deformation of the wall itself, not foundation rotation and sliding, is the focus of the lateral deformation study in this thesis.

The predictions of the components of lateral deformation are contingent on the type of damage and degree of damage to the structure. Specifically, yielding of longitudinal reinforcement affects the flexural mode of lateral deformation & wearing of concrete along existing shear cracks affects the shear mode of deformation. Determining the relationships between lateral deflection components, drift, and damage of structural walls is one of the main objectives of this thesis.

1.1: Motivation for Experimental Testing

Constructability of concrete members is greatly improved by splicing reinforcement. Splicing can be achieved in several ways. Reinforcement can be spliced with mechanical couplers or through lap splices (i.e. overlapping straight bars). Lap splices may include end welds connecting the two bars in the splice. This study focuses on lap splices that are not welded at any point in the splice and mechanically spliced reinforcement with threaded couplers. Splices are typically located to facilitate constructability. The structural concrete building code, ACI committee 318, restricts the locations of splices in some circumstances to avoid potential problems with behavior of the structural element.

Such restrictions are usually imposed in locations of structural members where large strain demands and a plastic response could occur. Other restrictions are placed on the strength and ductility of splicing mechanisms that may compromise the ultimate strength of the reinforcement being spliced. These restrictions are covered in greater depth in the review of related literature, Chapter 2.

Construction of structural walls can be very cumbersome. This is due to the fact that walls must be constructed vertically, requiring support of longitudinal reinforcement and formwork in the air prior to casting. Splicing longitudinal reinforcement close to the foundation allows less vertical support to be in place prior to casting the foundation. This improves constructability for structural walls, decreasing the time to construct the member and overall cost of the building. The base of structural walls is the easiest location to splice and the most effective location to increase construction productivity. However, this location is also the most critical location of the member where moments and shear demands are the largest. Splices can possibly interfere with the performance of this critical section in the wall. The possibility of performance interference from splices changes when considering different types of shear walls.

Shear wall behavior is closely tied to the aspect ratio of element. Aspect ratio is defined as the ratio of wall height (vertical dimension) to wall length (in-plane horizontal dimension). Walls with an aspect ratio of 1 or less are typically called 'squat walls'. These walls have small lever arms, a smaller distance from the applied lateral loads to the support boundary condition. Smaller lever arms from less height generate less moment in the section, requiring smaller flexural resistances. In addition, these walls are typically very deep to resist shear demands, in return increasing the sections ability to resist moment from a large internal moment arm. For these reasons, flexure does not control wall behavior and performance. Squat wall behavior is dominated by the effects of shear. Conversely, walls with larger aspect ratios have a structural response that is dominated by flexure from the increased applied moment arm caused by the increased wall height. Walls with aspect ratios of approximately three or greater can be classified as 'slender'

walls that are controlled by flexural demands. These walls typically undergo plastic flexural deformation and development of a plastic hinge at the base of the wall. The shear wall specimens researched in this thesis have a height of 240 inches, a length of 90", and an aspect ratio of 2.67. The shear wall specimens discussed in this thesis can be considered "slender". Wall dimensions are covered further in the test specimen description, Chapter 3.

The base of the wall, the critical section, is expected to undergo plastic deformation from yielding of longitudinal reinforcement in slender walls under extreme loading event. This occurs at the base of the wall from the largest lever arm in the section, creating the largest moments that must be resisted by the wall. This plastic deformation, or formation of a plastic hinge, is especially important when dissipating energy in the system and achieving large lateral deformations and drift ductility in the ultimate considered seismic event. These requirements of energy dissipation and drift ductility are important when considering the ultimate loading performance of the very infrequent seismic events in the performance based design approach (drift is defined as the ratio of lateral displacement of the shear wall to the height of the wall). These aspects are key when considering the performance requirement of building collapse prevention. The ability to achieve such drift ductility may not be possible when splices are present in this region of plastic hinging. Behavior can be modified from the different cross sectional reinforcement properties of the wall through the length of the splice. In addition, strength of the shear wall may be compromised from embrittlement of bars when welded for mechanical couplers or end welded lapped splices. Longitudinal reinforcement splices can have a significant impact on the performance of shear walls under ultimate loading conditions.

Required ductility may not be achieved from a termination of the plastic hinge at the location of the splice. Plastic hinge termination is defined as a sudden reduction in axial tensile strains in the longitudinal reinforcement to the point where longitudinal reinforcement is no longer undergoing plastic deformations. Such a termination can occur through the length of a splice. The drop in axial strain happens as a result of the

increasing cross-sectional area of steel or stiffness through the splice length (increased bar stiffness from the presence of a coupler, or the extra area of an entire bar when considering lapped splices). The necessary force in the reinforcement does not change through the length of the splice, but the area of steel does. Increased steel area decreases the stress in the bar, in turn decreasing the strain in the reinforcement through the lapped splice. The required plastic rotations that the walls must undergo at the base to achieve the needed drift ductility may not be met in the length of the splice, the section of wall height where splices are present. This is more of a concern for lapped splices, where the length that yield strain cannot be achieved is far larger than any decrease that could occur over the length of a mechanical coupler.

Possible wall behavior problems associated with splicing longitudinal reinforcement in critical sections have been acknowledged by many sources, including the building requirements put forth by ACI (ACI Committee 318-05). Restrictions have been placed on the locations at which splices can be placed and the necessary proven strength of splices. However, the provisions in place are mostly for splices in columns of moment frames and not structural walls. The demands of longitudinal reinforcement in structural walls are not that dissimilar from the demands of reinforcement in columns and cantilevered beams. Longitudinal reinforcement in both cases must undergo yielding to achieve ductility and energy dissipation from the structural element. These similarities in reinforcement demands of different types of structural elements would suggest that similar restrictions on splicing longitudinal reinforcement exist for each type of element. This is not necessarily the case for shear walls. The differences in the code requirements for shear walls are discussed in great detail in Chapter 2. The effect of anchorage detailing, splicing longitudinal reinforcement at the base of the wall to longitudinal reinforcement in the foundation, is investigated in this report to determine if any additional provisions on splices in structural walls should be included in the building codes for structural concrete. This is the primary goal of this thesis.

1.2: Experimental Testing and Analysis

Anchorage detailing effects on the components of lateral deformation (flexural deformation, shear deformation, and deformation from strain penetration) and performance of structural walls were investigated by experimental tests of three wall specimens. These specimens were approximately 1/2-scale, 6" thick, 90" long, 240" tall, and had a rectangular cross section. Test specimens contained specially confined boundary elements (concentrated longitudinal reinforcement with transverse reinforcement providing confinement of concrete) at each end of the rectangular cross section. The test specimens were cantilevered walls without openings. The term "cantilevered" refers to a fully constrained boundary condition at the bottom of the wall and a fully free boundary condition at the top of the wall. The only variation between wall specimens was the connection of the longitudinal reinforcement in the wall section to the longitudinal reinforcement in the foundation below the wall. The connection of these two sections of reinforcement is referred to as an anchorage detail in this thesis. A total of three anchorage details were investigated.

The first wall was the control specimen. This wall featured an anchorage detail of longitudinal reinforcement that was continuous throughout the wall section and foundation block. No discontinuities were present in the longitudinal reinforcement. This test specimen was named "rectangular wall, with normal reinforcement", or "RWN" for short. The second structural wall specimen had mechanically spliced couplers that connected the longitudinal reinforcement in the wall section to the anchored reinforcement in the foundation. These mechanical splices had two threaded devices friction welded to the ends of the reinforcement. These two ends could be simply screwed together, much like a nut and bolt. This test specimen is named "rectangular wall, with mechanically coupled reinforcement", or "RWC". Lapped splices were used in the final test specimen. These splices began at the wall/foundation interface and terminated at the height equal to the required lapped splice development length from ACI Committee 318-02. The height of the termination varied for the longitudinal bars, as different bar

diameters were used for the boundary elements and distributed web reinforcement. This test specimen is named “rectangular wall, with lapped splices at the base of the wall”, or “RWS”. Specimen dimensions, material strengths, and reinforcement details are discussed in greater detail in Chapter 3.

Testing of the rectangular wall specimens involved a single lateral load applied to the top of the wall, no axial load was present during the experimental test. The lateral load was distributed across the length of the wall, by means of steel channels clamping the two side faces of the specimen. Displacement normal to the plane of the wall was constrained at the top of the wall with effectively rigid bracing attached to a strong wall. The foundation of the wall was anchored to a strong floor. The test setup was found to not contribute or hinder the behavior of the test specimens. Refer to Chapter 5 for a more detailed discussion of the test setup.

Load was applied to the structure to achieve targets of lateral displacements. Target displacements were achieved for both the positive and negative displacement directions, placing one boundary element side in tension each direction, loading in reversed cyclic fashion. That is, the wall was displaced to the North and then to the South, always displacing in the opposite direction from the previous displacement. The boundary element in tension alternates for each time load is applied to the test specimen.

Achieving a target displacement is referred to as a “loading event”. A total of six loading events were performed for a single target displacement, three loading events for each displacement direction, returning to the target displacement each time. This was done to determine if the structural response was stable at the displacement in question. A stable structural response is defined in this thesis as the structural element being able to achieve the same load as the previous loading event upon returning to the same target displacement many times. An unstable structural response would correspond to a shear wall specimen returning to the same target displacement, while the load required to achieve that displacement continually decreases upon each return. Many target

displacements were chosen that would allow researchers to collect ample data for the test specimen in the relatively undamaged state, elastic range, inelastic range, and the ultimate strength and ductility of the test specimens. Refer to Chapter 5 for a more detailed discussion on the testing procedures and loading protocol of the test specimens.

Behavior of the test specimens was determined with several types of sensors attached to the test specimens in multiple configurations. Differences in sensor configurations existed between different types of sensors within the same test specimens, instrumentation schemes were not changed a great deal between test specimens (some additional instrumentation was added as researchers noticed additional behaviors during the test that were of interest). The same components of lateral deformation were then determined with multiple sensors, using various analysis techniques. Instruments were also installed to measure the total lateral deformation of the wall. This was done to compare the total deformation along the wall height of the specimens, the deflected shape of the test specimens. Global displacement measurements were also taken in order to verify that all calculated components of lateral deformation have been accounted for and that no additional deformation modes were overlooked. Lastly, instruments were used to determine and monitor any movement or rotation of the test setup structures that would contribute to the measured displacement of the test structures. The test setup was found to not contribute to the total measured deformation for the shear wall specimens. Refer to Chapter 4 for a complete description of the instrumentation models used to determine wall behavior.

Qualitative data was also collected during the experimental tests. Photographs were taken of cracking and other types of damage, such as concrete spalling off, occurring to the test specimens throughout the experimental tests. Cracking patterns were also recorded for the specimens on scale drawings of the walls. The widths of the cracks, observed spalling, widening of existing cracks, and offsets of undeformed gridlines drawn on the specimen from shear sliding were also documented at loading event peak pauses. This information is contained in Appendix 7. This information was used to help quantify damage levels,

such as those used to set goals in performance based design. Relationships were then formed between these quantified damage levels and the various deflection components of the specimens for performance based design information. The performance based design information of these specimens can then be used to guide designs of similar structural elements for various performances under specified loads.

1.3: Report Organization

This report is divided into many different chapters and appendices. Each chapter or appendix begins with the text of the chapter or appendix. All figures that are referenced in the chapter follow the text, followed by tables of information and references to other publications, respectively. All reported dimensions and quantities in this report are in standard English units (inches, kips, etc.).

This thesis contains a great deal of terminology when referring to behaviors of interest, instrumentation, testing procedures, and other terms. Uncommon terms and commonly used abbreviations in this thesis are listed with the introductory material at the beginning of the thesis, under the heading of “Definition of Terms”, following the list of figures. The page number referenced for each term corresponds to the first time the term is introduced in the thesis.

The chapters immediately following are in place to further explain the motives for the tests performed and how the experimental tests were performed. These materials are contained in Chapters 1 through 5. These chapters include a review of related literature; full descriptions of the test specimens, including the design and construction; instrumentation schemes used to determine the behaviors of interest discussed in this chapter; and the testing procedures and loading protocol used in the experimental testing of the three shear wall specimens.

The second group of chapters covers the results of the experimental tests. Data that was collected during the tests of the shear wall specimens is used to determine the behaviors of interest for the specimens. Behaviors of interest include the load-total deformation response, the individual components of lateral deformation, and wall instability that was observed during the experimental tests. These topics are covered in Chapters 6 through 13. The analysis techniques used to calculate the behaviors of interest from the experimental test data and the possible errors associated with the analysis techniques used are discussed further in Appendices 1 through 5. Appendices that accompany specific chapters are referred to in the beginning of the accompanying chapter.

Lastly, the ramifications from using various anchorage detailing are presented in Chapter 14. The test data and results are summarized, along with the performance based design information discussed in this chapter. Recommendations are made about the future use of mechanical and lapped splices at the base of shear walls, as well as future research that is needed to further verify the results of this thesis.

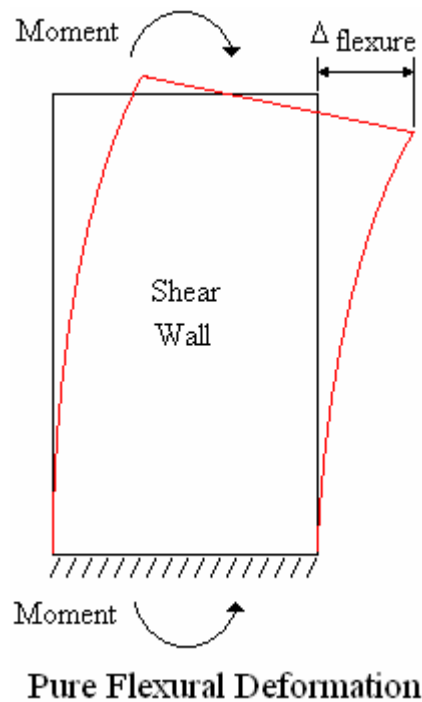
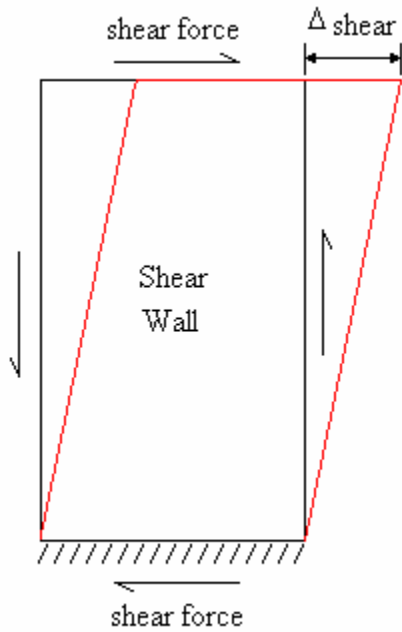
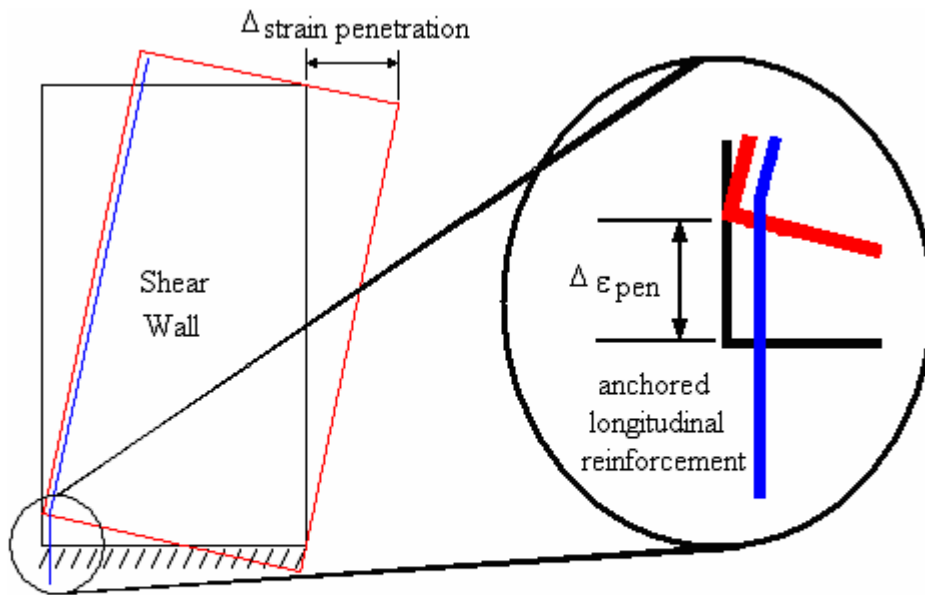


Figure 1.1: Condition of pure flexural deformation



Pure Shear Deformation

Figure 1.2: Condition of pure shear deformation



$$\Delta \epsilon_{pen} = \text{Elongation of longitudinal reinforcement from axial strain in anchored longitudinal reinforcement}$$

Strain Penetration Deformation

Figure 1.3: Illustration of deformation from strain penetration

ACI Committee 318, 2005, "Building Code Requirements for Structural Concrete (ACI 318-05) and Commentary (ACI 318R-05)," American Concrete Institute, Farmington Hills, Michigan, pp. 305-342.

Chapter 2: Review of Related Literature

2.0: Introduction

This chapter covers the literature used to help guide the experimental tests, data analysis, and conclusions documented in this report. Literature used in this report includes previous experimental test results and theory published in engineering journals and text books, as well as current provisions in the structural concrete building code. The general findings of these resources are discussed in the following sections, focusing on the information used specifically in the production of this document.

2.1: Components of Lateral Deformation

One of the main goals of this report was to determine the individual components of lateral deformation and relate them to the damage state of the test specimen. These goals are very similar to tests discussed in the technical paper: “Load-Deformation Responses of Slender Reinforced Concrete Walls”, published by Massone and Wallace (2004). This article covers methods used to determine the lateral deformation components of flexure and shear at any damage state of concrete shear walls. These methods were applied to experimental test data of concrete walls of various cross-sectional geometries. Test specimens included 1/4 scale slender concrete walls of rectangular, ‘barbell’, and ‘T’ shaped cross sections. A total of three walls with rectangular cross sections were tested. The longitudinal reinforcement for these specimens was continuous throughout the wall section and foundation. Two of these specimens were continuous walls while the other had a perforated opening. These walls were cantilevered walls, the same type discussed in Chapter 1. Specimens were subjected to reversed cyclic lateral loads of increasing amplitude and an axial load equal to ten percent of the nominal concrete strength, multiplied by the gross concrete area.

The results of the three rectangular wall tests presented in this paper suggest that the contribution of shear to the total lateral deformation at one third of the wall height is approximately 20% at the flexural elastic limit and 30% at inelastic flexural displacements. These contributions of shear and flexural deformation were observed before and at drift levels of 2.5%. These results were from the two walls that were continuous, without perforations. Similar flexural and shear deformation contribution results can be expected from the test specimens used in the experiments for this thesis from the similar aspect ratios as the specimens used by Massone and Wallace (2004).

The shear deformation was observed to increase in a non-linear fashion at the larger drift levels achieved by the test specimens. The contribution of shear increased as the wall became more damaged. A non-linearly increasing shear deformation from increased damage is referred to as inelastic coupling, increased inelastic shear deformation from inelastic flexural damage. The shear stiffness of the test specimens had been decreased by the damage to the walls from flexural effects. Decreased shear stiffness was the reason for shear deformation to increase disproportionately to load at inelastic drift levels. Inelastic coupling of the flexural and shear response was observed in the lower one third of the wall height was observed for multiple test specimens. This occurred even though the nominal shear strength of the specimens was twice the magnitude of the applied shear load during the experimental tests.

The effects of strain penetration of longitudinal reinforcement into the foundation of the test specimen were found to contribute a negligible amount of lateral deformation to the total response of the test specimen. For this reason, the lateral deformation from shear and flexure was assumed to be the sole contributing modes of lateral deformation. Lateral deformation of the test specimen at the top of the wall was reported to be dominated by flexural deformation.

2.2: Instrumentation Models

The instrumentation schemes used to determine components of lateral deformation for this report were also influenced by Massone and Wallace (2004). String/wire potentiometers are the focus of the instrumentation discussion section in the beginning of the technical paper by Massone and Wallace (2004). This was done because string/wire potentiometers are used to determine the contribution of flexural and shear deformation along the entire wall height. The results of the tests are dependant mostly on this type of sensor. Improving the accuracy of instrumentation models using string/wire potentiometers greatly improves the accuracy of the experimental results.

Various methods for determining shear and flexural deformation with string potentiometers have been proposed for experimental wall tests. Each of the different methods discussed by Massone and Wallace (2004) include an 'x' configuration, discussed in Appendix 5. This instrumentation model consists of two string/wire potentiometers that span a segment/section of the wall height diagonally, forming an 'x' over the height segment. The basis of the 'x' configuration is the use of the undeformed wall geometry and diagonal displacement readings to determine the lateral deformation of the section of wall height the 'x' configuration spans. Previous methods using the 'x' configuration varied in the assumptions used to determine the amount of shear deformation. Massone and Wallace (2004) discuss the limitations of this configuration in great detail. Studying the traditional 'x' configuration of string pots revealed that shear deformation was being overestimated from the effects of axial elongation and shortening of the test specimens when using previous 'x' configuration assumptions. The axial elongation and shortening of the test specimen is from flexural deformation effects through the segment of wall height spanned by the 'x' configuration. This overestimation is corrected with vertical string potentiometers that measure the axial elongation and shortening at the opposite ends of the 'x' configurations.

The methods used for determining the flexural contribution to total lateral deformation were also examined at the end of the technical paper by Massone and Wallace (2004). Flexural deformation is the deformation mode where the wall undergoes bending and rotations in the plane of the wall from applied moment. The wall displaces laterally from the cumulative effect of the changing angle of the vertical wall axis from bending. Flexural deformation is illustrated in Chapter 1 and explored fully in Chapter 9. Flexural deformation is typically estimated from measuring the flexural rotation over a segment of wall height and multiplying the rotation by the estimated distance to the center of rotation. The center of rotation is defined as the wall height point at which half of the total rotation at the point of interest occurs (point of interest is the height at which the flexural deformation is being computed). The sources of error with this method of flexural deformation calculation are largely due to the estimation of the distance to the center of rotation. Distance to the center of rotation is typically estimated with the assumption of an ideal curvature distribution (curvature is the first derivative of rotation), where the center of rotation is the centroid of the curvature distribution over wall height. An ideal distribution of curvature over wall height refers to a predicted curvature distribution from elastic beam theory. The center of rotation for any segment of wall height can then be assumed by calculating the ideal, theoretical curvature distribution.

Assumptions of an elastic curvature distribution to determine the center of rotation may lead to good results when the wall is behaving elastically, but could underestimate the flexural deformation in the inelastic range from an inelastic curvature distribution. This is due to the curvature at the base of the wall increasing non-linearly from plastic action. The curvature will be larger at the base of the wall, shifting the center of rotation downward, increasing the distance to the center of rotation and consequent flexural deformation. Failure to account for this change in curvature distribution will lead to under predictions of plastic flexural deformation. Massone and Wallace (2004) confront this issue by including an additional study on the number of vertical string potentiometers required over a certain span of height to accurately estimate the center of rotation from actual recorded test data and limit the possible error.

The center of rotation is determined by calculating the centroid of the curvature distribution. The curvature distribution from experimental data becomes a step function over the wall height, where each step in curvature is defined by the gage length of the string/wire potentiometers. The magnitude of each step in curvature over the wall height is the average curvature calculated over the gage length of the string/wire potentiometers from the axial elongation and shortening measured. The calculation of curvature from string/wire potentiometers and other instruments is covered in Chapter 8 and Appendix 2. Increasing the number of sensors between the height span in question increases the resolution of the curvature step function distribution. The study concludes that between 4 and 6 sensors between height segments spanned by the 'x' configuration of string potentiometers give reliable results for flexural deformation. Center of rotation estimation error can be expected to be less than 5% when using at least 4 sensors. This approach is discussed in greater detail in Appendix 3, where the methods used to calculate flexural deformation from the test data are covered. Additional quantification of center of rotation error is discussed in Appendix 3. It was found that the possible error was less than 1% when estimating the height of the center of rotation from the actual string potentiometer configurations used in the experimental tests for this thesis.

2.3: Plastic Hinge Region Splices

Mechanical and lapped splices require more attention than continuous reinforcement when detailing reinforced concrete members. Additional attention is needed due to the possibility mechanical and lapped splices changing the behavior of the structural element in a negative way. Mechanical and lapped splices can have a large impact on the strength, toughness, and ductility of a structure. The main concerns when considering mechanical and lapped splices in sections of large strain and material demands are brittle failures from discontinuities and welds, inability to develop required strength from concrete bond demands, and interference with mechanisms that provide necessary curvature ductility (ability to develop large plastic curvatures and drift ductility in an ultimate loading

condition). Literature chosen to illustrate these possible negative effects of longitudinal splices is the textbook by Paulay & Priestley (1992) and the structural concrete building code from ACI Committee 318 (2005).

The first concern when using any type of longitudinal bar splice is that the strength of the longitudinal reinforcement is not compromised. ACI Committee 318-05 requires that mechanical splices be able to develop 125% of the specified yield strength of the bars. Note that this applies to a “type 2” mechanical splice that can be used in regions where stresses that approach yield stress are possible or expected. The other type of mechanical splice, “type 1”, is not required to develop 125% of the yield strength, and is also not allowed to be used in regions of the structure where stresses approaching yield stresses are expected. This helps ensure that the mechanical splice will not fail locally before yielding will occur in the bar as a whole. ACI Committee 318-05 also requires that mechanical splices be placed at a distance at least twice that of the member depth from joints, unless the mechanical splice has been shown to be able to develop the full strength of the bar being spliced (type 2 mechanical splice). These restrictions apply only to columns in lateral load resistant moment frames where stresses may approach the yield stress in the reinforcement of the members. No specific restrictions are given for structural/shear walls, even though the same possibility of large strain demands also exists for reinforcement at the base of cantilevered shear walls.

Requiring mechanical splices to be placed at the code required distance from joints further decreases the possible demand of the splice, reducing the chances of localized brittle failure. Similar guidelines are given by Paulay & Priestley (1992), where it is stated that mechanical splices could be allowed in regions of potential plastic hinging if validated by experimental tests with similar conditions. It is stated specifically that the effects of reversed cyclic loads need to be considered if possible in the proposed field structure, simple tension tests may not capture the behavior of the detail when previous damage and hysteresis is considered.

The second concern when using splices is the possibility of concrete bond failure, preventing the necessary strength of the bars being spliced to be developed. This aspect is especially important when considering ordinary lapped splices, which rely completely on concrete bond to transfer force through the connection. Failure of the lapped splice can occur from bond degradation under cyclic loading or the inability to resist the forces required to develop the full strength of the bars being spliced. These types of failures can be mitigated by the presence of transverse reinforcement. ACI Committee 318-05 addresses this issue by placing additional requirements on transverse reinforcement in the presence of lapped splices. Note that these requirements help ensure strength development of the reinforcement, but do not address the possibility of changes occurring to the behavior of the member containing splices. Changes to structural behavior, including the load-displacement relationship and deflected shape of the member, can arise from the difference in cross-section reinforcement properties of the member through the length of the splice. These possible changes to the structural behavior from splices are not addressed by ACI Committee 318-05.

The final concern is that of wall behavior and ductility. Changes in localized axial stiffness can affect how the overall structure responds to load or moment. Refer to Figure 2.1 for an illustration of a change in axial stiffness from addition material. The increased stiffness will decrease the axial strain in the reinforcement through the length of the splice. Additional axial stiffness of the longitudinal reinforcement through a splice from either a mechanical coupler or additional longitudinal bar from a lapped splice may prevent yielding to occur at the location of the additional material from the decreased axial strains. This may terminate a plastic hinge that has begun to develop outside the splice, decreasing the amount of plastic deformation and energy dissipation of the wall.

A plastic hinge is defined as an area in a structural member in bending that undergoes large plastic rotations. This occurs at the critical section of the member, where the moments that must be resisted are the largest. The rotational stiffness of the critical section, the ability to resist moments, effectively decreases to zero when considering an

elastic-perfectly plastic stress-strain relationship (this assumption can be made for steel reinforcement). Such a large decrease in rotational stiffness makes the critical section behaves much like a hinge, where the member is free to rotate and achieve large displacements. Termination of this plastic hinge occurs at points where rotational stiffness still exists, and the member is no longer free to rotate as a hinge. Instead, the section begins resisting rotation again, preventing large deformations. An increase in axial stiffness of the longitudinal reinforcement can provide an increased rotational stiffness that will terminate a plastic hinge.

Plastic hinge termination can be expected over the length of the splice where the increased rotational stiffness exists. This suggests that lapped splices will have a significant impact on wall behavior, as splices can span a significant portion of the wall height (as much as one third of the wall height for the longest splices in the specimens researched in this thesis). A termination of the plastic hinge at the base of the wall will force the wall to deform differently than a wall with continuous reinforcement that can develop a full plastic hinge. One of the expected differences comes from the additional strain demands that are created at the terminations of the splice in order for the wall to achieve plastic deformations. These increased demands are documented in Chapters 7 and 8. Larger demands at the splice terminations may then lead to possible fracture of the longitudinal reinforcement. ACI Committee 318 addresses this problem by specifying that splices may only be placed at the mid height of columns in moment frames where the lowest stress demands of the member exist. This placement would limit the impact of the lapped splices on wall behavior and decrease the demand on the splice connection itself. No limitations are specified by ACI Committee 318 for structural walls, even though there is a large possibility of plastic hinging for this type of member during ultimate loading events. Good engineering judgment should lead to the guidelines from Paulay & Priestley (1992), where it is suggested that no splices should be in plastic hinge regions for the impact they have on the ductility of the member.

2.4: Instability of Boundary Elements

Instability of structural walls can occur through different mechanisms. Walls which are particularly slender and unbraced in the direction normal to the plane of the wall may experience typical elastic instability consistent with Euler buckling. Another mode of buckling may arise also from large ductility demands of a structural wall. Such a buckling mode is discussed in the technical paper “Stability of Ductile Structural Wall” by Paulay and Priestley (1993). The principles of this paper were applied to the test specimens researched in this thesis.

This reference discusses the type of instability that can arise from a localized unbraced condition that is created from large cracks that open during large lateral drifts. Load reversals cause the cracks from tension in the previous loading direction to close before the concrete can participate in resisting compressive forces from the applied moment. The reinforcement in the boundary elements must resist the entire compressive force until cracks close. As stated by Paulay and Priestley (1993), eccentricities in the locations of reinforcement from random variations during construction in the plane of the applied moment can cause a single curtain of reinforcement to yield before the other. Refer to Figure 2.2 for a hypothetical example of reinforcement eccentricity in a boundary element. When considering two curtains of reinforcement, the curtain of reinforcement that is closer to the centroid of the applied compressive load must resist a larger portion of the compressive load when compared to the opposing curtain of reinforcement. The larger applied load on one curtain of reinforcement will cause one side to yield before the other. This causes a change in rotational stiffness in the plane normal to the plane of the wall, causing out-of-plane rotation to occur. These out-of-plane rotations increases until the previous tensile cracks close and concrete participates in resistance the out-of-plane moments and rotations. Out-of-plane displacements and wall stability are closely related to previous axial tension strains and crack widths. This concept and the observed instability of the test specimens for this thesis are discussed further in Chapter 13.

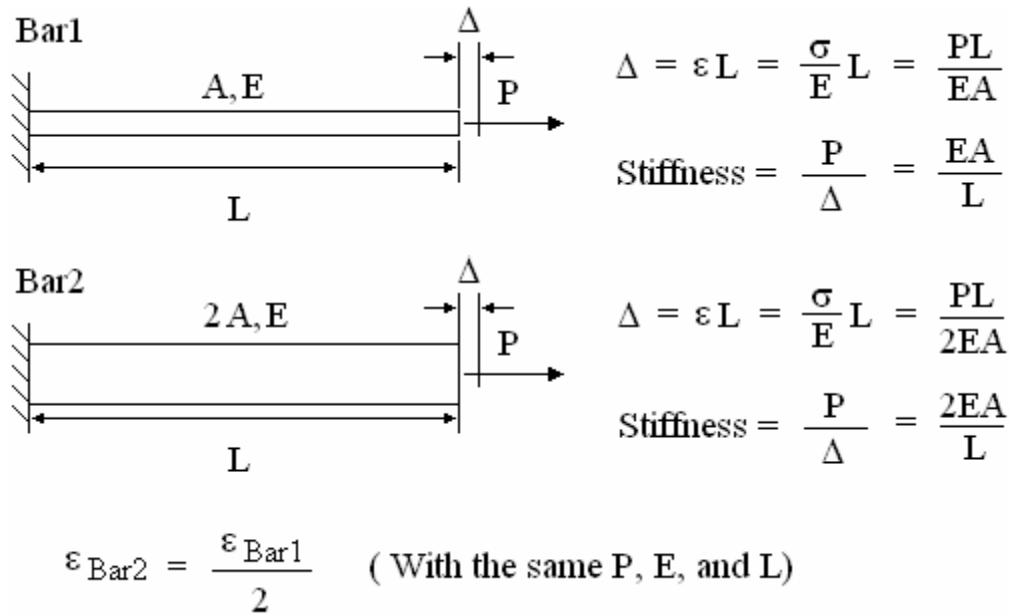


Figure 2.1: Example of stiffness change from additional material

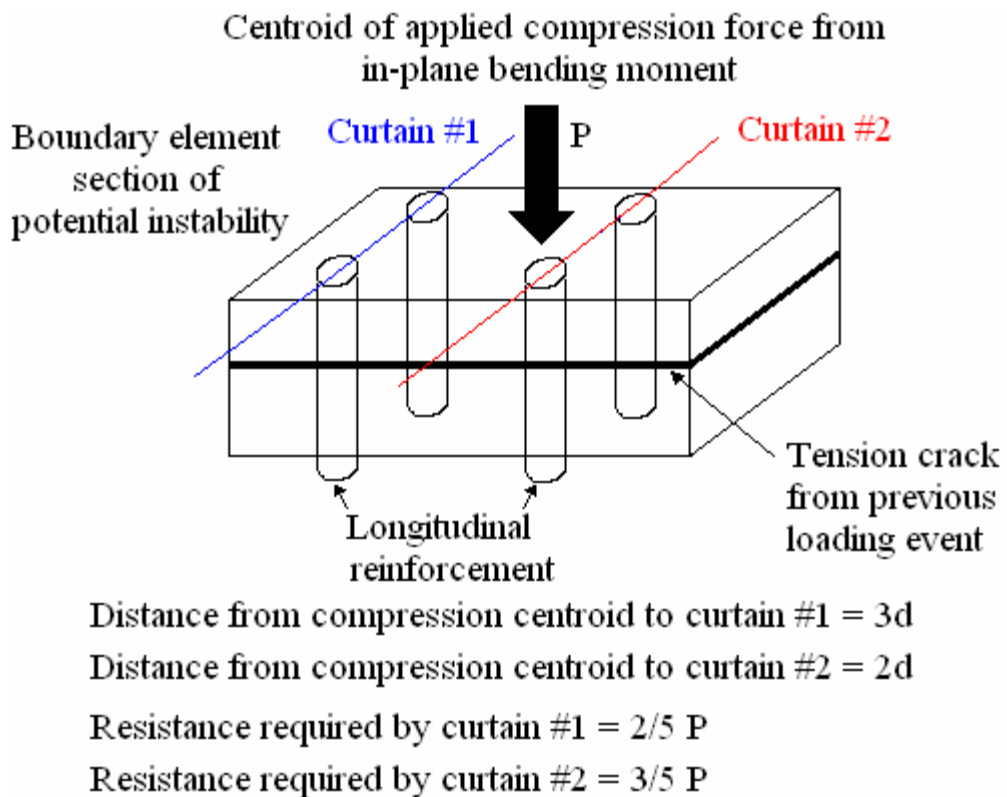


Figure 2.2: Hypothetical boundary element eccentricity

Massone, L. M., and Wallace, J. W., 2004, "Load-Deformation Responses of Slender Reinforced Concrete Walls," *ACI Structural Journal*, V.101, No.1, January-February, pp. 103-113.

Paulay, T., Priestley, M. J. N., 1992, "Seismic Design of Reinforced Concrete and Masonry Buildings," John Wiley & Sons, USA, pp. 151-153, 213, 232-233.

ACI Committee 318, 2005, "Building Code Requirements for Structural Concrete (ACI 318-05) and Commentary (ACI 318R-05)," American Concrete Institute, Farmington Hills, Michigan, pp. 305-342.

Paulay, T., Priestley, M. J. N., 1993, "Stability of Ductile Structural Walls," *ACI Structural Journal*, V.90, No.4, July-August, pp. 385-392.

Chapter 3: Test Specimen Description:

3.0 Introduction:

Three shear walls of a rectangular cross section were used in this project to determine the effects of anchorage details on wall behavior and give guidance for performance based design. These walls were part of a larger investigation regarding the behavior of a 1/2-scale T-shaped shear wall. The reinforcement details of the rectangular walls were chosen to mimic the behavior of the T-shaped wall. Reinforcement was detailed in this manner to help predict the effects of the anchorage details in question on the behavior of T-shaped walls without testing additional T-shaped shear walls. This section covers the reasons for the geometry and reinforcement of the three rectangular wall specimens. In addition, this chapter covers the general construction techniques used to build the specimens and their resulting as-built dimensions and reinforcement geometry.

3.1: Specimen Description:

The walls used in this project had a single variable among them, the anchorage detailing of the longitudinal reinforcement. The shear wall designated RWN, the control specimen, had continuous longitudinal reinforcement throughout the wall section and foundation. The wall designated RWC incorporated mechanical coupling devices to connect the reinforcement in the wall section to the reinforcement in the foundation. The wall designated RWS incorporated lapped splices which initiated at the wall/foundation interface and extended vertically to the required lap splice lengths. A generalized, conceptual drawing of these variables is given in Figure 3.1. Each wall was rectangular in cross section with special boundary elements at each extreme fiber in the plane of the wall. The detailing of such boundary elements and reinforcement is discussed in the following section.

3.2: Specimen Design:

The reinforcement distribution in the rectangular walls was intended to emulate the behavior of a shear wall with a T-shaped cross section that was part of the larger investigation. The T-wall was built with continuous longitudinal reinforcement throughout the wall section and foundation, but the benefits of using mechanically spliced couplers and lapped splices were also of interest. For this reason, the three rectangular walls were built to mimic the behavior of the T-wall web being loaded in plane with different anchorage details (i.e. mechanical couplers and lap splices at the base of the wall). These tests provided an opportunity to investigate the behavior of these anchorage details with simplified test specimens. The results of the tests were used to determine anchorage details used in the construction of a subsequent T-wall specimen.

The boundary elements and reinforcement of the rectangular walls were detailed to create a similar flexural strain gradient along the wall cross section as the T-wall would experience when loaded in the plane of its web. The first step in achieving this was to examine the requirements and behavior of the T-wall and its design. The T-wall was designed for a prototype building. This building was a typical, 6-story, rectangular office building with a floor plan of 22,500 square feet. The prototype building was designed for seismic use group D. The prototype building is shown in Figure 3.2:

The walls in the prototype building were designed according to ACI 318-02, IBC-2003, and FEMA 450 provisions. The design computations for the T-wall can be found in the University of Minnesota Masters of Science thesis by Jung, Narina (yet to be published as of June, 2007). In general, the design procedure was a typical iterative design. Base shear and load demands for the building were determined according to the International Building Code (2003). Following the determination of loads, wall sizes were estimated and loads distributed according to relative stiffness. Finally, critical biaxial demands were computed and flexural, shear, and confinement reinforcement were detailed.

Once the T-wall had been designed, the rectangular wall dimensions and reinforcement were chosen. Again, this was done to mimic the behavior of the T-wall when loaded in the direction of its web. The effect of the large reinforcement contribution of the flange causes a non-symmetric flexural strain gradient along the web when load is applied toward the web tip compared to load applied toward the flange. When loaded towards the web tip, the large amount of tension reinforcement in the flange requires a significant portion of the web cross section to be in compression for internal force equilibrium. Whereas when loading toward the flange, the smaller amount of tension reinforcement in the web in combination with the large effective area of the flange available to resist compression results in a very shallow depth of the cross section to be in compression. See Figure 3.3 for a conceptual drawing of the resulting strain gradients.

The reinforcement in the boundary elements of the rectangular walls was chosen to be nonsymmetric to achieve the same differential strain gradients as those in the T-wall. This reinforcement, as compared to the 1/2-scale T-shaped wall reinforcement is shown Figure 3.4. Only one side of the 1/2-scale T-wall flange is shown in the figure because of symmetry. The No.6-No.5-No.6 reinforcement pattern of the T-wall web tip was simulated with three pairs of bars in one of the tips of the rectangular wall specimens. This simulated web tip boundary element is called the “No. 5&6 boundary element” and is often abbreviated as the “No. 5&6 BE”. It was important in this investigation to model the effects of lap splice lengths and mechanical couplers on bar sizes used in the T-wall structure. The flange was emulated using a concentration of No.9 bars in the second boundary element of the rectangular wall. The simulated flange of the T-wall is called the “No. 9 boundary element” and is often abbreviated as the “No. 9 BE”. The resulting strain gradients in the rectangular walls are compared to those of the T-shaped wall in Figure 3.3. It should be noted that No.4 bars were used in the web section of the rectangular walls instead of No.3 bars as was done for the T-wall. This was because No.4 bars were the smallest bars to which a mechanically spliced coupler could be attached. In order to limit the variables among the three rectangular walls to just the anchorage details,

No.4 bars were used within the web section of all three rectangular walls. For this reason, the bar sizes in the webs of the rectangular walls were increased along with the spacing.

Once the general details of the rectangular walls were chosen to emulate the 1/2-scale T-wall, the rectangular walls were further detailed for their specific demands. Further detailing specific to the rectangular walls included the spacing of the confinement reinforcement in the boundary elements, the height at which the confinement reinforcement was no longer required, and the spacing of the horizontal shear reinforcement. Figure 3.5 shows the cross sections of the three rectangular walls (RWN, RWC, and RWS), as well as the numerical bar naming scheme for identification.

Each wall was initially designed with the same spacing of longitudinal reinforcement. This was changed slightly for the lapped spliced wall, as the bottom and top splices could not occupy the same location. The bottom and top splice locations were placed as close to their nominal locations as possible and are documented later in this section. The boundary elements were designed with confinement consisting of No.2 deformed wire. The transverse reinforcement was anchored within the confined core on the No.5&6 boundary element and outside the confined core on the No.9 boundary element. This was done again to match the T-wall, which did not have transverse reinforcement anchored in a confined core opposite to the web tip. Transverse reinforcement was spaced at a nominal 7.5 inches along the entire wall height. Figure 3.6 shows a more detailed view of the boundary elements for the rectangular walls.

The length of the lapped splices was determined from the necessary development length and bar cut-off requirements. This length was determined from the minimum requirements given in ACI 318-02 for straight bar development. The splice lengths for each bar, as well as an elevation view of each wall can be seen in Figure 3.7. Required splice lengths are dependant in part on the diameters of the bars being spliced. The difference in splice lengths for the two boundary elements and web reinforcement is the product of this requirement. The height of the confinement is also shown in this view.

The height of the confinement was set equal to the length of the wall, 90 inches, as required by ACI 318-02 section 21.7.6.

3.3: Specimen Construction:

Each specimen was constructed at the University of Minnesota MAST laboratory by researchers and laboratory staff. Construction of the test specimens varied with the type of anchorage detail being used in the construction process. The construction methods of the three rectangular specimens helps show the advantages of using mechanical and lap splices at the base of shear walls.

The foundation block was the first section of the test specimens to be cast in concrete. Longitudinal reinforcement that was anchored in the foundation block was required to be in place before the foundation block could be cast. This required the erection of longitudinal reinforcement through the entire wall height for RWN before casting. Longitudinal reinforcement for RWN had to be supported by temporary shoring until the wall section of the specimen was cast. More construction time was required for RWN when compared to RWC and RWS due to the required support of the longitudinal reinforcement prior to foundation block casting and the cumbersome nature of a bar as long as the entire wall height in constructing the foundation block. The dimensions and weight of the longitudinal bars in RWN made placement more difficult than those for RWC and RWS. These problems are partially alleviated by using longitudinal reinforcement at the base of the wall.

Anchored longitudinal reinforcement in the foundation block of RWC and RWS was required to be in place prior to casting of the foundation block, the same requirement as RWN. Construction time of the foundation blocks for RWC and RWS was shorter than RWN because the longitudinal reinforcement of the entire wall was not needed to be in place at the time of foundation casting. The anchored portion of the longitudinal reinforcement was the only length of longitudinal reinforcement that needed to be

supported. This removed the need for temporary shoring to be in place prior to casting the foundation of the test specimens. In addition, the shorter longitudinal bar lengths for RWC and RWS were easier for researchers to handle during construction (positioning bars at the nominal cross section location and placing confining reinforcement), further improving the construction time for these two specimens.

The wall section of the test specimens was constructed after the foundation block. Longitudinal reinforcement was in place following the casting of the foundation block for RWN, requiring only the placement of horizontal reinforcement and confinement reinforcement before casting of the wall section. Longitudinal reinforcement had to be erected for RWC and RWS before the same construction steps as RWN could be taken. The top portion of the longitudinal bars were connected to the anchored portion for RWC by connecting the threaded mechanical couplers. The weight of the top portion was supported by the foundation. Lateral support of the bar was provided by the shoring constructed to support the concrete formwork. The construction step of using shoring to support the longitudinal bars only for RWN was still avoided for RWC. The same construction steps were taken for RWS as were for RWC, except that the lap splice connection of the longitudinal bars required only the placement of the top portion of the longitudinal bar next to the longitudinal bars already cast in the foundation.

The wall section of the test specimens were cast in two sections. The first concrete pour reached a height of ten feet above the top of the foundation block. The second pour for the wall section went to the top of the wall, the remaining eleven feet. This is shown in Table 3.4, where the concrete material properties are not the same for the top and bottom of the test specimens. Note that the foundation block properties are the same for RWC and RWS, as these sections of the test specimens were cast with the same batch of concrete.

3.4: Specimen As-Built:

Researchers tried to achieve the nominal locations for each type of reinforcement and the nominal wall cross section dimensions during construction of the test specimens. This section documents the actual as-built locations of reinforcement as well as changes that had to be made which deviated from the initial plan.

The coordinates for each bar in the plan view of figure 3.5 are given with respect to the origin shown in the inset to Table 3.1. The origin is located at the corner of the wall closest to the bar identified as '1'. Refer to Table 3.1 for the coordinates of longitudinal reinforcement in the 'X' direction, along the wall length. An 'X' coordinate of zero refers to the extreme concrete face of the No.5&6 boundary element. Positive 'X' coordinates denote a location in the direction into the web of the wall. The coordinates of the longitudinal bars were measured with a tape measure from the concrete formwork that was in place that corresponded to the tip of the No.5&6 boundary element, the outside face of the test specimens. The locations given for the longitudinal reinforcement are for the bottom of the wall/foundation interface. Measurements were taken after casting of the foundation block, prior to casting of the first wall section.

The last two columns of Table 3.1 denote the two components of the lapped splice for RWS. Note that the distances for the top bars are closer to the extreme fiber than the bottom splice bar. This was done to facilitate the construction process. Constructing the top bar of the splice to be the most extreme bar allowed the location of the bar to remain the same following termination of the splice. Longitudinal bars in RWS did not have to then be bent following splice termination to achieve the nominal bar locations. In addition, the location of the bars was affected by the confining reinforcement of the boundary elements. Irregularities in the dimensions of the confining reinforcement and the rounded corners forced researcher to place the longitudinal bars of RWS at the location given in Table 3.1. The 'Y' coordinates of the bars for each test specimen were close to nominal from the use of chairs on the transverse reinforcement.

Table 3.2 lists the as-built dimensions for the confinement spacing in the boundary elements. The confinement spacing for RWC was slightly different than that for RWN and RWS. This happened as a result of the maximum coupler dimensions and vertical locations of the couplers. The company supplying the couplers attached the male end of the coupler to the foundation segment of the bar and the female end to the bar segment in the wall section. This forced the location of the coupler to be placed immediately above the wall/foundation interface. This was done to for several reasons. Namely, this was done to for the attachment of the top bar (threads of the male end of the coupler had to be exposed above the foundation to be connected). The location of the coupler was also chosen to preserve the location of the ‘zero’ height strain gages (these gages had to be placed above or below the coupler) and to leave space for the strain penetration studs on the bars (strain penetration studs discussed further in Chapter 4). The increased coupler size just above the interface made placement of confinement hoops around them too difficult. This lead to a large gap in confinement hoops at the location of the couplers, the bottom 6 inches of the specimen wall height. The spacing in the confinement reinforcement for RWC at the coupler location is shown in Figure 3.8.

Confinement spacing for the test specimens is reported in Table 3.2. Confinement reinforcement spacing was calculated by dividing the distance between two confinement hoops by the number of spaces between the hoops over that distance. Columns labeled “Hoop #” in Table 3.2 refer to the number of confinement hoops at and bellow the height given in the next column to the right. The confinement reinforcement spacing for RWC was computed by measuring the height of the third confinement hoop from the interface. This does not reflect the actual gap in the confinement at the location of the coupler. The height of the first hoop was initially at 0.5 inches above the interface, followed by the second hoop at approximately 6 inches above the wall/foundation interface. This spacing was almost three times the nominally specified spacing.

3.5: Specimen Material Strengths:

The materials used in this experiment were in accordance with ACI provisions for seismic use. Grade 60 reinforcing steel was used for all bars in the wall. ASTM A706 steel was chosen from ACI 318-02 requirement 21.2.5. Rebar tensile coupons were pulled for each bar size, as well as additional rebar tensile coupons to check the effects of the capacitor discharge welded studs and bars ground to remove mill scale for strain gage application. Capacitor discharge welded studs for measuring strain penetration are defined in Chapter 4, along with the discussion of other instrumentation used in this experiment. The average steel strengths from the coupon tests for each bar size are shown in Table 3.4. These averages were calculated from three coupon tests for each bar size. Variation between coupon tests was within +/- 1ksi. Reported bar strengths are from rebar tensile coupons that did not have capacitor discharge welded studs attached or that were ground for application of strain gages. No detriment to bar strength was found for coupons with either capacitor discharge welded studs attached or that were ground for strain gage application. The strength results of coupons with capacitor discharge welds and attached strain gages had even exceeded the average bar strength in some cases, suggesting that random variation in bar strength is larger than the effects of the capacitor discharge welding. Tensile coupons with capacitor discharge welded studs broke at the point of the weld. However, this location is the center of the coupon that was expected to fracture.

The concrete used for these walls was specified to have a 28-day compressive strength of 5,000psi. The cylinder tests conducted by researchers at 28 days after casting and at the time of the wall test showed a considerable difference. Table 3.3 contains the tabulated compressive strengths of the concrete used for each test, along with the rupture strength and elastic modulus of the concrete for each specimen at the time the experimental tests were conducted. Reported material properties are an average of 10, 4 inch by 8 inch cylinders for compressive strength; 2 four point bending beams for tensile rupture strength; 3 split cylinder tests for tensile rupture strength; and 3, 6 inch by 12 inch

cylinders for determining the elastic modulus. Reported tensile concrete strengths are an average of the tensile strength results from the four point beam tests and split cylinder tests. Results of the material property tests used to compute the average values were typically within +/- 100psi of the average value. Problems with the elastic modulus testing apparatus lead to poor results for RWN. These values are erroneous and excluded from Table 3.3.

Bar#	Nominal	RWN	RWC	RWS-Bot	RWS-Top
1	1.50	1.81	2.25	2.13	1.88
2	1.50	1.63	2.38	2.25	1.88
3	5.00	4.56	5.19	4.94	4.38
4	5.00	4.56	5.50	4.94	4.31
5	8.50	7.31	8.25	7.56	8.44
6	8.50	7.44	8.19	7.69	8.56
7	17.00	15.69	15.88	15.88	16.69
8	17.00	15.56	15.50	15.81	16.63
9	35.00	32.56	33.63	33.81	34.38
10	35.00	32.56	33.50	33.94	34.50
11	53.00	49.69	51.50	51.50	51.94
12	53.00	49.75	51.50	51.81	51.31
13	71.00	67.31	69.00	67.56	68.81
14	71.00	67.75	69.00	67.82	68.50
15	76.25	76.81	78.25	77.44	76.31
16	76.25	77.25	78.25	77.38	76.25
17	80.25	80.88	81.83	80.94	79.81
18	80.25	81.13	81.83	80.94	79.81
19	84.25	85.00	85.25	84.75	82.63
20	84.25	85.38	85.25	84.75	82.69
21	88.25	88.25	88.00	87.94	86.69
22	88.25	88.19	88.00	87.94	87.06

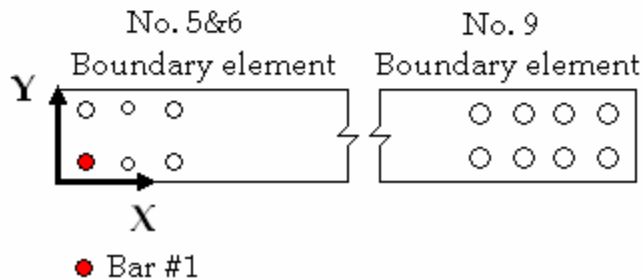


Table 3.1: Longitudinal bar locations

No.5&6 Boundary Element

RWN			RWC			RWS		
Hoop#	Height [in]	Spacing [in]	Hoop#	Height [in]	Spacing [in]	Hoop#	Height [in]	Spacing [in]
6	12	2.00	5	11	2.75	6	12	2.00
12	23	1.83	12	24.25	1.89	12	25	2.17
18	34	1.83	18	36	1.96	18	37	2.00
24	46	2.00	24	47.5	1.92	24	49	2.00
31	59.5	1.93	30	59.5	2.00	30	59.5	1.75
38	72	1.79	36	71.75	2.04	36	72	2.08
44	84.5	2.08	42	84	2.04	42	84	2.00
46	88.75	2.13	45	89.5	1.83	45	89.75	1.92

No.9 Boundary Element

RWN			RWC			RWS		
Hoop#	Height [in]	Spacing [in]	Hoop#	Height [in]	Spacing [in]	Hoop#	Height [in]	Spacing [in]
6	11.25	1.88	3	11	3.67	5	10	2.00
12	24	2.13	9	24	2.17	12	23.75	1.96
18	36	2.00	15	35.25	1.88	18	36	2.04
24	47	1.83	21	47.25	2.00	24	47.25	1.88
30	60	2.17	28	61	1.96	30	59	1.96
36	70.5	1.75	33	71	2.00	36	71.5	2.08
42	83	2.08	38	83.75	2.55	42	84	2.08
45	87	1.33	43	89.25	1.10	45	89.5	1.83

Table 3.2: As-built confinement spacing

Specimen Section	f_c [psi]	f_t [psi]	E [ksi]
RWN-Foundation	8,980	930	-
RWN-Wall bottom	7,870	860	-
RWN-Wall top	6,880	770	-
RWC-Foundation	8,330	860	5,450
RWC-Wall bottom	7,500	950	5,960
RWC-Wall top	9,100	840	6,400
RWS-Foundation	8,330	860	5,450
RWS-Wall bottom	8,110	910	5,770
RWS-Wall top	6,580	810	5,610

Table 3.3: Concrete material properties

Bar Size	A_s [in ²]	Diam [in]	F_y [ksi]	F_u [ksi]
4	0.20	0.500	64.0	100.9
5	0.31	0.625	72.1	98.2
6	0.44	0.750	71.2	97.0
9	1.00	1.128	67.4	92.0

Table 3.4: Longitudinal reinforcement strengths

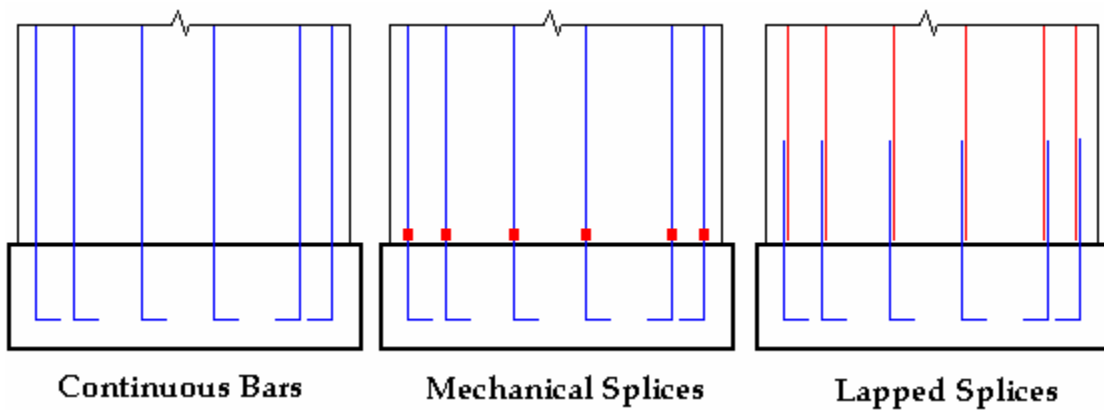


Figure 3.1: Conceptual anchorage variables

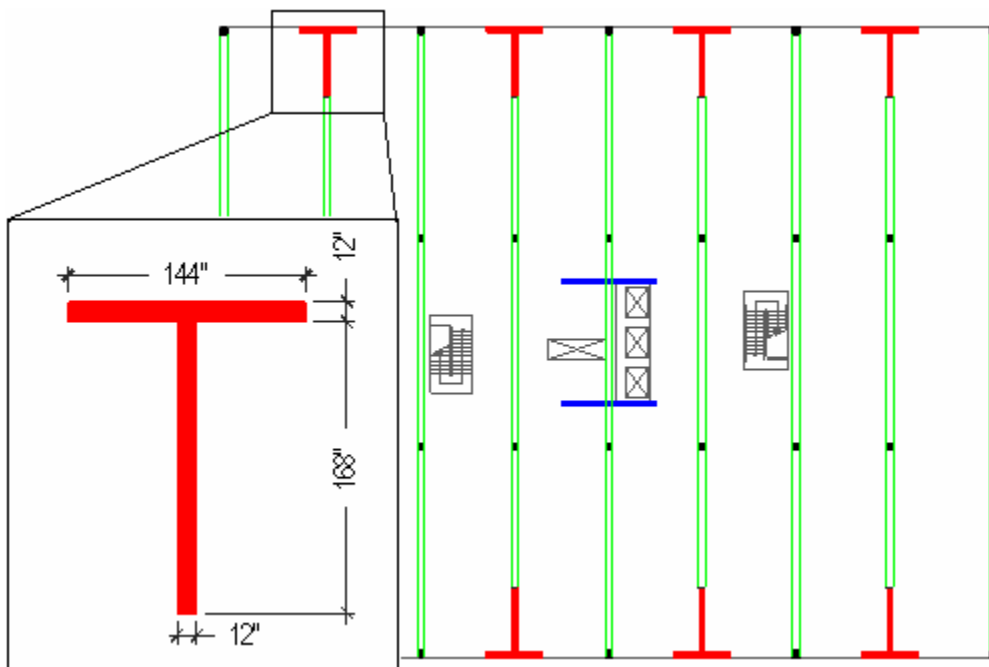
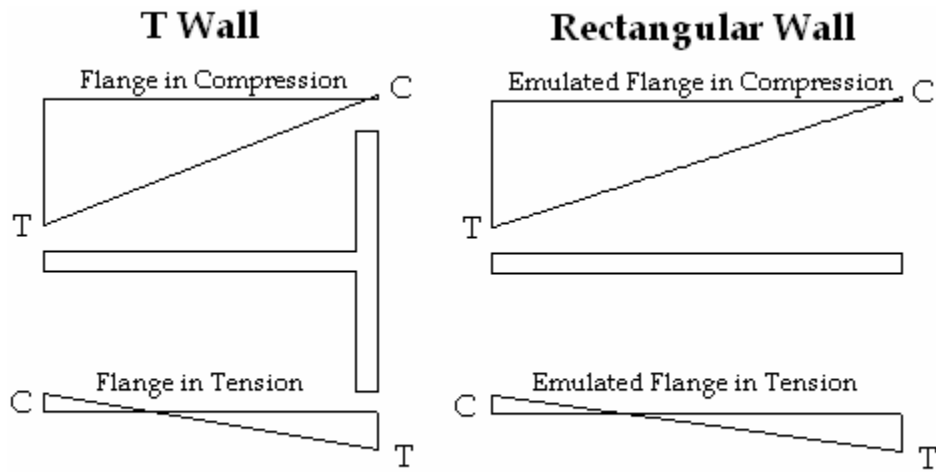


Figure 3.2: Prototype building, highlighting T-shaped shear walls



Plan view, flexural strain gradients

Figure 3.3: Plan view and flexural strain gradients of T-wall and rectangular wall

Twall v. Rectangular Wall Reinforcement

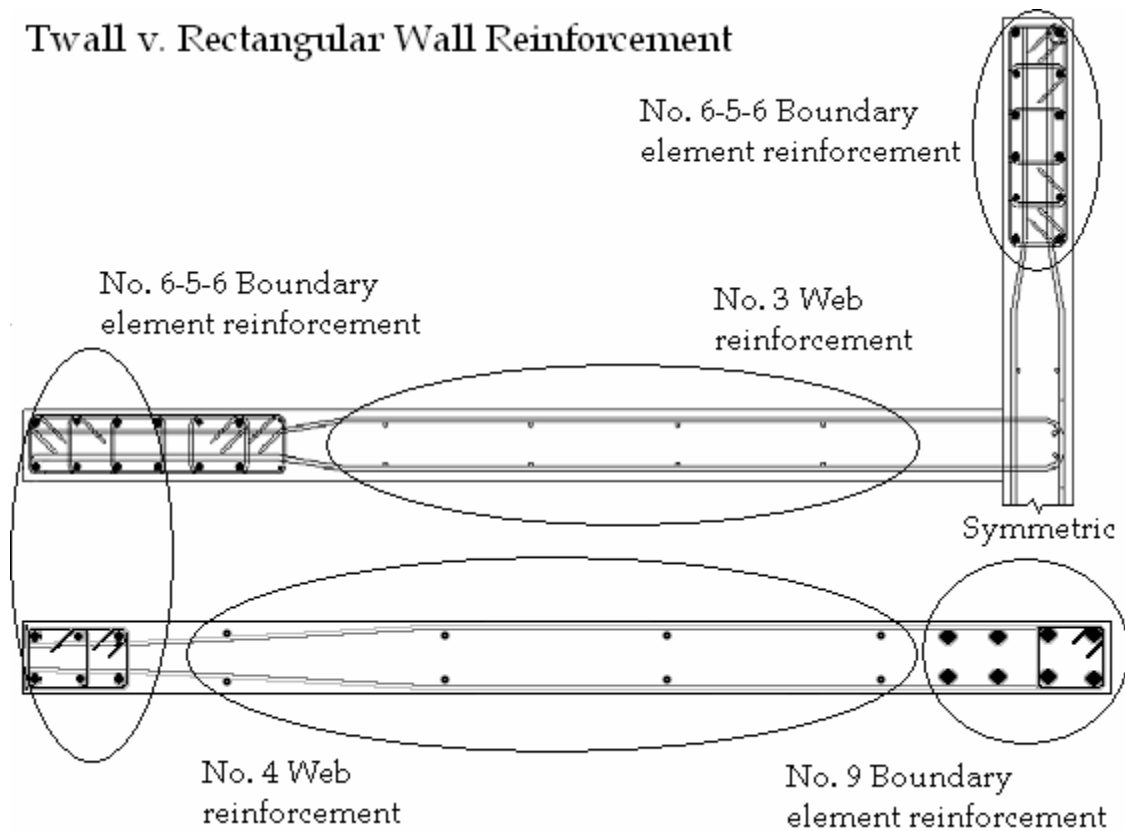
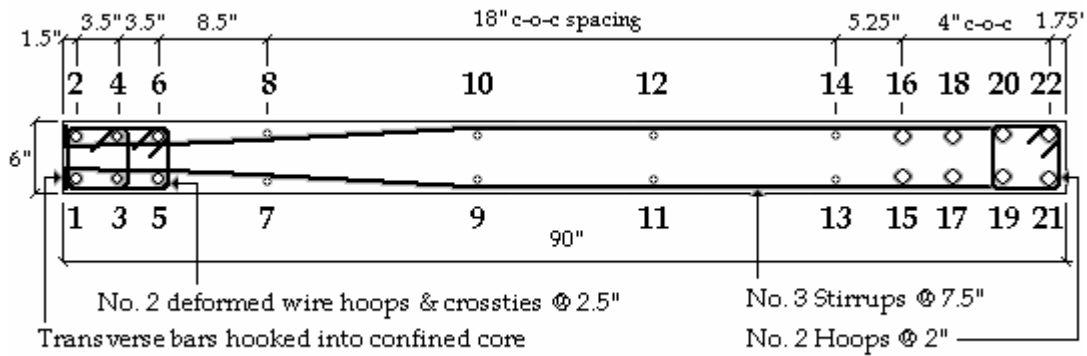


Figure 3.4: T-wall and rectangular wall reinforcement

RWN - Continuous Bars



RWC - Mechanical Splices



⊙ Shaded area - maximum coupler dimensions

RWS - Lapped Splices



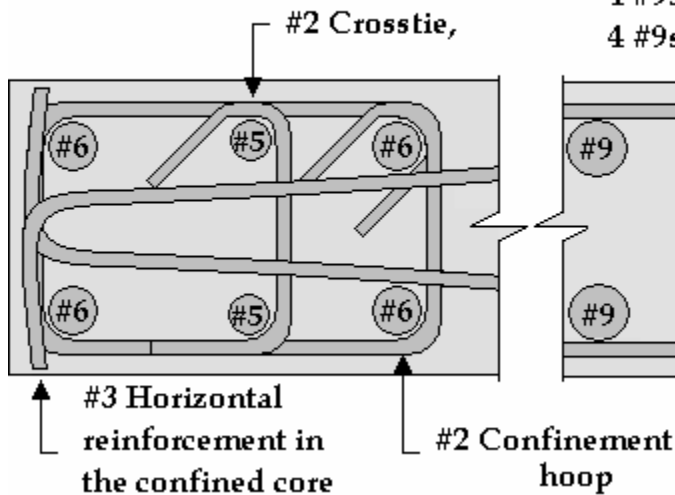
○ Bar anchored in foundation

● Lap splice bar initiating in wall section

Nominal Cover of 3/4"

Figure 3.5: Rectangular wall reinforcement at the base of the wall

No. 5 & 6 Boundary Element



No. 9 Boundary Element

4 #9s in the confined core,
4 #9s outside the confined core.

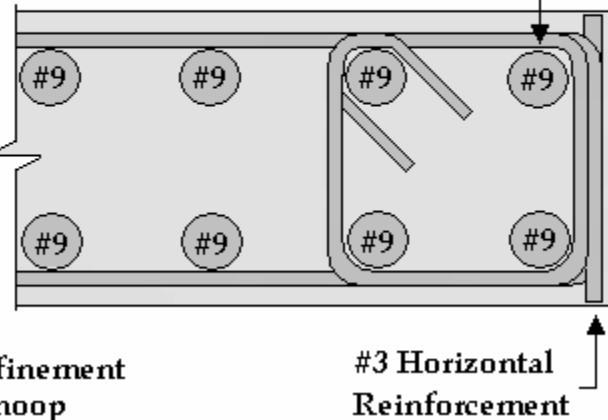


Figure 3.6: Boundary element reinforcement

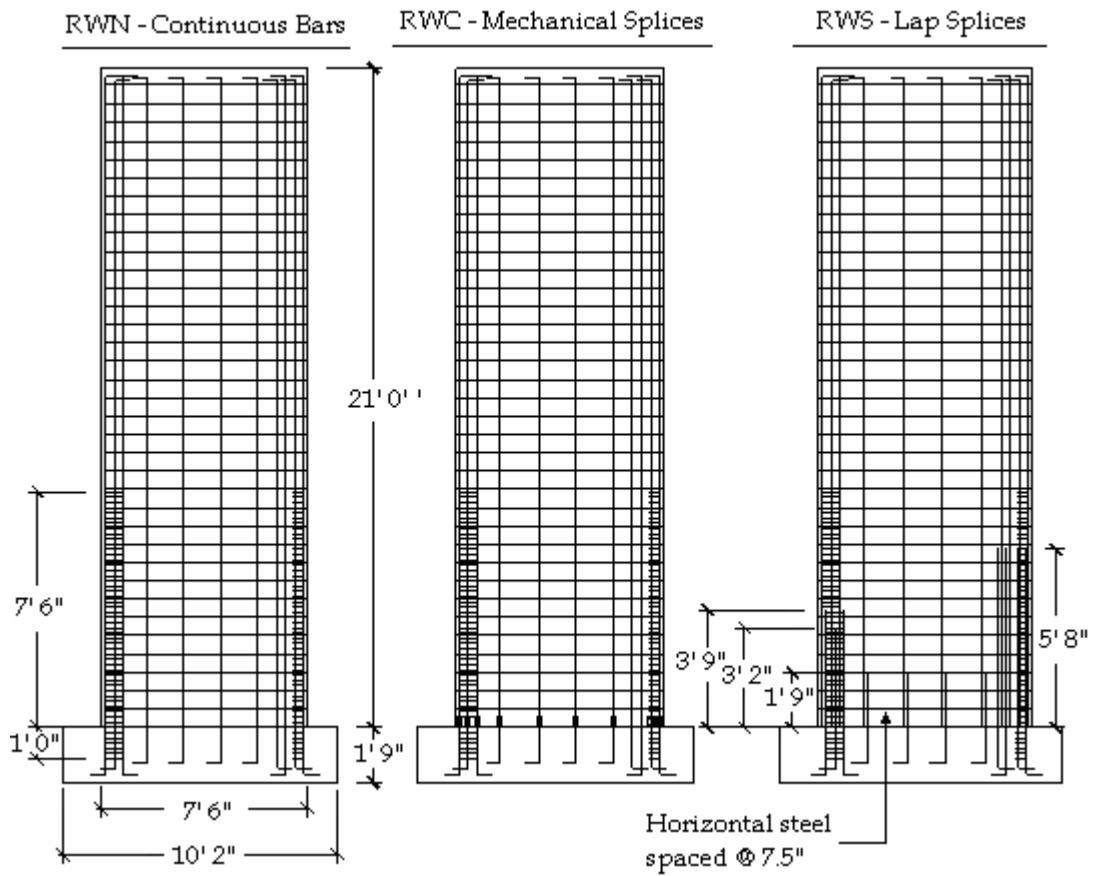


Figure 3.7: Elevation view of rectangular wall reinforcement



Figure 3.8: Spacing changes to confinement from coupler dimensions

Chapter 4: Instrumentation and Behaviors of Interest

4.0: Introduction

This chapter covers the instrumentation setup and the behaviors of interest that were to be measured from the instrumentation setup. Several types of instruments were used including linear variable differential transformers (LVDTs), string potentiometers (string pots), Krypton-6000 3D coordinate measuring machine (CMM), and various strain gages. These instruments were used to determine the components of lateral deformation from effects of flexure, shear, and strain penetration. In addition to these behaviors, instruments were used to verify that the test setup did not affect the response of test specimens. Refer to Figures 4.1 through 4.4 for schematics of the instrumentation layouts. Tables 4.1 through 4.4 provide as-built wall attachment locations of the instrumentation. The orientation of the test specimens in the test frame is covered in Section 4.2.4. The orientation of test specimens on the test floor affected the attachment location of some instrumentation. Differences in instrumentation attachment location for each test specimen from wall orientation is addressed in each section of this chapter.

4.1.0: Linear Variable Differential Transducers (LVDTs)

LVDTs were used to measure displacements between two points of the test structures. The nominal locations of the LVDT attachments are shown in Figures 4.2 and 4.3. The as-built attachment locations of these instruments are provided in Table 4.1. All attachment location for LVDTs are given as the distance from the exterior face of the No.5&6 boundary element. This convention is the same for each specimen, regardless of orientation on the test floor.

4.1.1: Interface LVDTs

LVDTs were installed at the wall/foundation interface at two heights. The LVDTs were attached to the top of the foundation block and the test structures at heights of 6” and 12” above the wall/foundation interface. The displacements recorded by these instruments included the displacements from flexural elongation and compression, as well as elongation and compression from the effects of strain penetration. These sensors were used to help estimate the neutral axial of the walls at the foundation interface.

The naming convention for the interface LVDTs is as follows: LV(nominal distance from the extreme face of the No.5&6 boundary element)(L for LVDTs attached at 12” above the foundation/wall interface or S for LVDTs attached at 6” above the wall/foundation interface). For example, LV21S denotes an LVDT anchored at 6” above the foundation block, 21” from the exterior face of the No.5&6 boundary element.

4.1.2: Bar LVDTs

LVDTs were also used to determine the elongation of longitudinal reinforcement at the foundation interface from the effects of strain penetration. These sensors were attached to the foundation block top face and the longitudinal reinforcement by means of a capacitor discharge welded stud (capacitor discharge welded studs are also discussed in Chapter 3, Section 3.5). The locations of the studs were approximately one half inch above the wall/foundation interface. The number of available Bar LVDTs was different for each wall, due to interference with string pots spanning the bottom 3” of the wall. The attachment locations of these instruments are shown in Figure 4.3b for RWN. Note that the naming convention changed among the test specimens.

The naming convention for BAR LVDTs was as follows:

- RWN: BAR1 was attached to longitudinal bar #1, BAR2 was attached to longitudinal bar #3, BAR3 was attached to longitudinal bar #22, and BAR4 was attached to longitudinal bar #12.
- RWC and RWS: BAR(identification number of the longitudinal bar to which the instrument is attached).

Longitudinal bar identification numbers are covered in Chapter 3. Figure 4.3c shows a schematic of how the BAR LVDTs were attached to the longitudinal reinforcement and foundation block of the test specimens. Calculation of strain penetration from the measurements of these instruments is covered in Chapter 10.

4.1.3: Test Setup LVDTs

Several additional LVDTs were used to verify the effectiveness of the test setup. The first group of these sensors were attached to the foundation block and strong floor at each end of the foundation block to measure any rotation of the foundation block. These LVDTs were called LVBRN (north end of the wall) and LVBRs (south end of the wall). The second type of test setup LVDT used to measure any shear sliding at the wall/foundation interface. The LVDT was attached horizontally between the foundation block and test floor at the No.5&6 boundary element end of the wall. This LVDT was called LVBS. The final test setup LVDT was attached between the loading channels (refer to Chapter 5 for an explanation of the loading channels) and test wall face to measure any loading channel slip. These sensors were not installed until loading channel slip was visually noticed during the loading of the first wall, RWN. Relative slip was observed to be on the order of 10% of the displacement applied to the test structures. Slip occurred when loading the test structures in both the north and south directions. For this reason, the global external displacements of the string pots are used instead to report the global displacement of the test specimens, rather than the measured actuator displacement.

4.2.0: String Potentiometers (String Pots)

String/wire potentiometers, or string pots, were another type of sensor used to measure the relative displacement between two points of attachment. String pots were used to investigate several important behaviors discussed in the following sections and were attached to the test specimen in several different orientations. The layout of all string potentiometers is shown in Figures 4.1 and 4.2. The locations of the wall attachments for these sensors are given in Table 4.2. The string pot sensor names and the attachments they spanned are reported in Table 4.3. The naming convention for the string pot wall attachments is shown in Figure 4.5. The naming convention and attachment locations for the string pot sensors was the same for each test specimen, with the exception of the global displacement string pots discussed in Section 4.2.4 and the test setup string pots discussed in Section 4.2.5 from test specimen orientation on the test floor.

4.2.1: Vertical String Potentiometers

String pots oriented vertically (along the axis of the test specimen height) were placed at three locations across the length of the test walls. These three locations were the No.5&6 boundary element, the centerline of the test wall, and the No.9 boundary element. String pots that were attached to the No.5&6 boundary element are named SPL(identifier for the locations spanned by the instrument). String pots that were attached at the centerline of the test specimens had the same naming convention at string pot at the No.5&6 boundary element but begin with SPM. String pots at the No.9 boundary element follow the same naming convention as the other two locations, beginning with SPR. String pot span naming conventions are shown in Figure 4.1. The vertical string pots in the boundary elements were approximately three inches from the outside faces of the walls. The vertical string pots were used to determine axial strain, curvature, rotation, and flexural deformation. The measurements of these instruments was used in Chapters 7, 8, and 9.

4.2.2: Horizontal String Potentiometers

The lateral expansion of the walls from cracking was measured with string pots that were oriented horizontally at wall heights of 3", 36", 69", 122", 176", and 230". Splitting cracks developed at the top of the test specimens at large load levels. These cracks propagated from holes in the specimen used to attach the loading channels. Splitting cracks were observed to be as large as 0.25" wide. These cracks created a different lateral deformation between the boundary elements in tension and compression due to the wall expansion. String pots that measured the lateral expansion from splitting cracks were named SPH(height of the test specimen the instrument spanned horizontally). For example, SPH230 measured the lateral expansion of the walls at a height of 230" above the wall/foundation interface.

4.2.3: Diagonal String Potentiometers

String pots oriented diagonally over the wall height were used to determine the shear component of deformation. Additional diagonal string pots were used toward the bottom of the structure, where a greater variability in shear deformation occurred from the increased flexural damage. The naming convention of these instruments is shown in Figure 4.1. The measurements of these instruments is used to calculate shear deformation in Chapter 11.

Each diagonal string pot name began with the letters "SP". The following characters referred to the diagonal span of the string pot. "LB" referred to a span from the No.5&6 boundary element to the centerline of the test structure from a height of 3" to 36". "LT" referred to a span from the No.5&6 boundary element to the centerline of the test structure from a height of 36" to 69". The same convention was used for string pots spanning from the centerline of the structure to the No.9 boundary element. These string pots were referred to as "RB" and "RT", with the same height spans as those specified for "LB" and "LT". String pots at the bottom 69" of the wall that span from the No.5&6

boundary element to the No.9 boundary element begin their names with “SPB”, for a height span from 3” to 36” and “SPT” for a height span from 36” to 69”. All diagonal string pots above a height of 69” span from the No.5&6 boundary element to the No.9 boundary element. The characters following “SP” for these instruments was “2T” for a height span from 69” to 122”, “3T” for a height span from 122” to 176”, and “4T” for a height span from 176” to 230”. The numbers that followed the span location indication characters referred to the counter clockwise angle the diagonal string pots formed with the test floor. For example, “SP2T45” designate a string pot that spans diagonally from the No.5&6 boundary element to the No.9 boundary element, from a height of 69” to 122”, and forming a 45 degree counter clockwise angle with the test floor. The naming convention and string pot wall attachment locations for the diagonal string pots were the same for each wall, regardless of the wall orientation on the test floor.

4.2.4: External Global Displacement String Pots

String pots were used to determine the global, total deformation of the test specimens. These string pots were connected to the test specimen at various heights, correlating with the attachments of the vertical and diagonal string pots. Wall heights where global displacement was measured was 36”, 69”, 122”, 176”, and 230”. Additional string pots were connected near the top of the wall at the same approximate height of the load being applied to the wall. The second ends of these global string pots were connected to a rigid external reference frame constructed from EFCO shoring. The connection to the reference frame was approximately 15 feet away from the connection to the wall. This was done to ensure that the vertical displacement of the wall would not contribute significantly to the measurement of lateral deformation of the test specimens. The global displacement string pots were always attached to the south end of the test structures. The orientation of RWC was opposite of that of RWN and RWS (i.e., when the specimen was located in the test frame, the orientation of the No.5&6 boundary element was opposite for the case of RWC). The global displacement string pots were attached to the No.5&6 boundary element for RWN and RWS and attached to the No.9 boundary element for

RWC. This is an important detail when considering the effects of lateral expansion from splitting cracks. The effects of the lateral expansion of the measured global displacement of the walls is covered in Chapter 12.

4.2.5: Test Setup String Pots

Additional string pots were used in the experimental tests to measure the out-of-plane displacements of the test specimens (displacements normal to the plane of the test specimen wall). These string pots were connected to the ends of the test structures (boundary elements) at various heights. The first test, specimen RWN, had these string pots only at the top of the wall. The subsequent tests of RWC and RWS had these sensors present at the mid height of the wall as well. These string pots are shown in Figure 4.2. The naming convention used for these string pots is “SP(height of attachment) (attachment to the north or south side of the test specimen)”. The height identifier of “M” referred to the mid height of the wall (122”), “T” corresponded to a height of 230”, and “C” referred to the mid height of the loading channels (240”). For example, SPMN designated that the string pot was attached to the wall at a height of 122” at the north end of the wall. The north and south attachments were anchored to the boundary element on the north or south side of the test specimen. This convention is affected by the orientation of the specimens on the test floor. The No.5&6 boundary element was on the south end of the test specimen for RWN and RWS. The No.5&6 boundary element was on the north end of the test specimen for RWC.

4.3.0: Krypton-6000 3D Coordinate Measuring Machine (CMM)

The Krypton-6000 3D Coordinate Measuring Machine (abbreviated as Krypton) is a device that records the coordinates of LED sensors in three-dimensional space that are attached to any surface. The global coordinates are measured relative to three additional LEDs, which are attached to a reference frame that remains stationary throughout the test. The Krypton LEDs were attached to the test structure at various locations, with greater

density in the boundary element regions. The general locations of the Krypton LEDs is shown in Figure 4.3. The grid density available from these sensors allows for great detail when investigating wall behavior. Grids of the Krypton LEDs were transformed into a series of isoperimetric quadrilateral elements to compute axial and shear strains along the wall length and height throughout the test. Development of the isoperimetric quadrilateral elements is discussed in Appendix 5. In addition to strains, the recorded displacements of the individual Krypton LEDs were used to measure the global displacement of the walls and the total rotation from flexure and strain penetration.

This instrument has limitations. Cracking and damage to the wall, partially compromise the connection of the LEDs to the test structure which are hot glued to the wall face. The wall damage caused some LEDs to become detached from the test specimen. Krypton data was found to be effective until drift levels of 1.5% in the No. 5&6 boundary element in tension direction. Krypton data used to determine flexural and shear deformation was discarded after buckling of the test specimen, as the planar assumptions used in the data analysis no longer applied. Global out-of-plane deformations were still used to measure the buckled shape of the wall as this did not require the plane assumptions used to calculate flexural and shear deformation. The locations of the LEDs for each test specimen are reported in Table 4.4.

4.4.0: Strain Gages

Strain gages were attached to longitudinal reinforcement, transverse reinforcement, and confinement hoops. Concrete embedment strain gages were placed vertically and horizontally in the boundary element regions to measure the axial compression and lateral expansion of the concrete. Refer to Figure 4.4a through 4.4c for the layout of the different types of strain gages.

The naming convention for the strain gages was as follows:

- Longitudinal bar strain gages: SG(bar#)L(nominal gage height)(A for bottom splice or B for top splice while inside the splice length for RWS)
- Transverse bar strain gages: SG(x-position of the closest longitudinal bar#)T(nominal gage height)
- Hoop strain gages: SH(location on hoop)H(nominal gage height)
- Concrete strain gages: SG(x-position of the closest longitudinal bar#)C(nominal gage height)(V for vertical orientation or H for horizontal orientation)

The nominal positions of the strain gages was used for analysis. This was done when the resulting calculation represented a single height, such as curvature and rotation. The heights of all gages were averaged to give the height of the curvature calculations. The average height was taken to be the nominal height of the instruments due to a height variation of less than one half inch for each strain gage. Using an averaged height of the strain gages instead of the nominal locations had a negligible effect on the results from this instrument (less than .2% different on average). Nominal locations were used for simplicity of analysis.

4.5: Effects of Out-of-Plane Displacements on Sensor Measurements

Out-of plane displacements were measured with the string pot and Krypton sensors. Out-of-plane displacements were first observed at drift levels of 1% for each test specimen. The out-of-plane displacements measured are discussed in Chapter 13. Assumptions used to compute lateral deformation from the effects of flexure and shear become partially compromised when the test specimens begin to experience out-of-plane displacements. Calculations of deformation from the effects of flexure and shear are partially compromised from the assumption that measured displacements occurred only in the plane of the wall. This assumption was no longer completely true when the walls experienced out-of-plane displacements. A portion of the displacements recorded by the

string pots and Krypton sensors thought to be in the plane of the walls was due to out-of-plane displacements. This caused the results of the calculation of deformation from the effects of flexure and shear to become less precise at drift levels of 1% and larger. The increasingly larger effects of out-of-plane deformations on the perceived in-plane displacements made the calculation of lateral deformation from the effects of flexure and shear invalid at larger drift levels. The effects of out-of-plane displacements on in-plane sensor measurements is the reason why results for flexure and shear deformation at drift levels larger than 1.5% was not used in the determination of the effects of anchorage details on shear wall behavior.

4.6: Behaviors of Interest

The following sections cover the wall behaviors of interest for investigating the effects of anchorage details. These sections include abbreviated explanations of the methods used to calculate the behaviors of interest and chapters and appendices where the complete discussion of the behaviors of interest can be found in this thesis. The wall behaviors of interest for determining the effects of anchorage details are the deformation resulting from the effects of flexure, deformation from the effects of strain penetration, deformation from the effects of shear, and wall instability. The justifications for the instrumentation chosen to calculate each behavior of interest is also included in the following sections.

4.6.1: Determination of Flexural Deformation

Flexural deformation is defined in this thesis as a lateral deformation of the test specimen that is the result from curvature due to applied moment. Flexural deformation (i.e., curvature) was calculated from axial strain/deformation distributions along the test specimen length and height. The flexural deformation of the test specimens was computed by first determining axial strain from string pots, Krypton, and strain gages on longitudinal reinforcement. Refer to Chapter 7 and Appendix 1 for the methods used to

calculate axial strain from the effects of flexure. Curvature was then calculated from the distribution of axial strain over the wall length for heights instrumentation was present. Calculation of curvature is discussed in Chapter 8 and Appendix 2.

The lateral deformation resulting from flexure was then computed for each sensor type by integrating the curvature over height (from the calculated values of curvature at various heights where instrumentation was present), determining the total rotation and centroid of the curvature distribution over height. Resulting lateral deformation from the effects of flexure is the product of the total rotation and the center of rotation for the height the lateral deformation from flexure is being calculated. These results were compared to predicted BIAX results, where the same integration methods of the experimental data were applied to predicted curvature distributions over wall height for various reasonable loads. Refer to Chapter 9 for the flexural response of each wall and Appendix 3 for the complete explanation of the methods used to calculate the lateral deformation from the effects of flexure.

4.6.2: Determination of Strain Penetration Deformation

Strain penetration deformation is defined in this thesis as the lateral deformation of the test specimens from the effects of longitudinal reinforcement in the foundation undergoing elongation and shortening from flexural strains. Flexural strains were present in the anchored longitudinal reinforcement until the concrete bonds could transfer all of the force out of the bar and into the foundation block. The presence of axial strain in the anchored reinforcement caused a rotation to be imposed on the wall structure at the wall/foundation interface. This displacement mode can be considered as another type of flexural deformation (i.e., lateral deformation resulting from curvature & rotation caused from applied moment). The main difference between the flexural deformation mode discussed in the previous section and lateral displacements resulting from the effects of strain penetration is the cumulative effect of curvature creating rotation in the wall section for flexural deformation, versus the entirety of rotation from strain penetration

occurring at a single wall height location. Lateral displacements resulting from the effects of strain penetration were treated as a separate displacement mode from flexural displacement from the difference in the way rotations were imposed on the walls.

Deformation resulting from the effects of strain penetration was determined from Bar LVDTs. Bar LVDTs were the instruments chosen to calculate the rotations at the wall/foundation interface from the effects of strain penetration because bar LVDTs are the only instrument that is influenced solely by the elongation of the anchored reinforcement (excluding the 0.5" above the wall/foundation interface required for attachment of the bar LVDTs). The Krypton sensor was also able to measure the rotation of the specimens at the bottom of the wall. This could have been done with the vertical displacement readings of the bottom row of Krypton LEDs (the bottom row was typically 3" above the wall/foundation interface). These measurements are also affected by the elongation and shortening of the test specimens from the effects of flexure over the bottom three inches of the wall. The use of the bottom row of Krypton LEDs would have led to an overestimation of rotation at the wall/foundation interface from the effects of curvature over the bottom 3" of the wall. For this reason, the rotation measured by the bottom row of Krypton LEDs was only used to verify the results of the bar LVDTs.

Deformation from strain penetration was modeled as a rigid body of rotation. The resulting lateral displacement was taken as the height at which lateral displacement was being calculated, multiplied with the rotation of the wall at the wall/foundation interface from the effects of strain penetration. The rotation at the wall/foundation interface was determined from a linear trend line calculation through the elongations/shortenings recorded by the Bar LVDTs. Refer to Chapter 10 for the deformations resulting from strain penetration in each test specimen and further explanation of the methods used.

4.6.3: Determination of Shear Deformation

The lateral deformation due to the effects of shear is referred to in this thesis as “shear deformation”. Shear deformation was calculated with the string pot and Krypton sensors. Shear deformation calculated from string pot data by first calculating the total deformation of each wall height segment spanned by diagonal string pots. Shear deformation was calculated by subtracting the flexural deformation discussed in Section 4.6.2 (the only other mode of deflection present in the section of wall height spanned by the diagonal string pots) from the total deformation. The resulting displacement is the lateral displacement due to the effects of shear. Shear deformation was calculated from Krypton data by determining the shear strain distribution over the height of the Krypton LED grid. The shear deformation was calculated by integrating the shear strain over the height of the Krypton LED grid. Refer to Chapter 11 for the resulting deformations of the test specimens from the effects of shear and Appendix 4 for the complete explanation of the methods used to calculate shear deformation.

4.6.4: Instability Comparisons

Instability of the No.5&6 boundary element was observed for each test specimen. The magnitudes of the out-of-plane displacements and the distribution of the out-of-plane displacements over the height of instability varied for each specimen. The buckled shape of the walls was determined from the displacement measurements of the Krypton sensor and string pots in the direction normal to the plane of the test specimens. These results were used to determine the effects of anchorage detailing on wall stability. Parameters affecting the stability of ductile walls proposed by Paulay and Priestly (1993) were used to investigate the reasons for the differences observed in the buckled shapes of the test specimens.

RWN			RWC			RWS		
LVDT	Wall Attachment Location		LVDT	Wall Attachment Location		LVDT	Wall Attachment Location	
Name	Xposition [in]	Zposition [in]	Name	Xposition [in]	Zposition [in]	Name	Xposition [in]	Zposition [in]
LV90L	90.00	11.50	LV90L	90.00	12.50	LV90L	90.00	11.75
LV90S	90.00	5.75	LV90S	90.00	6.00	LV90S	90.00	5.88
LV69S	70.50	5.25	LV69S	69.81	6.19	LV69S	69.81	6.25
LV53S	52.25	5.00	LV53S	52.88	6.31	LV53S	52.88	4.81
LV37L	35.50	11.00	LV37L	35.50	12.13	LV37L	35.50	6.06
LV37S	37.50	5.25	LV37S	37.63	6.38	LV37S	37.63	12.38
LV21L	19.50	10.50	LV21L	19.50	11.63	LV21L	19.50	11.63
LV21S	21.25	5.25	LV21S	12.00	6.31	LV21S	12.00	6.19
LV0L	0.00	11.25	LV0L	0.00	12.00	LV0L	0.00	11.75
LV0S	0.00	5.50	LV0S	0.00	6.19	LV0S	0.00	6.38
BAR1	1.18	0.50	BAR1	2.25	0.50	BAR1	2.25	0.50
BAR2	4.56	0.50	BAR3	5.19	0.50	BAR3	4.94	0.50
BAR3	88.25	0.50	BAR7	15.88	0.50	BAR22	88.00	0.50
BAR4	67.31	0.50	BAR13	69.00	0.50			
			BAR22	88.00	0.50			

Table 4.1: LVDT wall attachment coordinates

RWN			RWC			RWS		
Attach-ment	Wall Attachment Location		Attach-ment	Wall Attachment Location		Attach-ment	Wall Attachment Location	
Name	Xposition [in]	Zposition [in]	Name	Xposition [in]	Zposition [in]	Name	Xposition [in]	Zposition [in]
1	2.75	2.88	1	3.00	2.75	1	3.13	2.75
2	45.00	2.88	2	46.00	2.75	2	44.50	2.75
3	87.00	3.13	3	87.00	2.75	3	86.00	3.50
4	2.63	20.50	4	3.00	19.25	4	3.41	19.13
5	87.25	20.25	5	87.00	19.50	5	86.00	20.00
6	2.63	36.75	6	3.00	36.50	6	3.28	35.38
7	45.00	36.00	7	45.00	36.50	7	44.50	35.50
8	87.25	35.25	8	86.00	36.50	8	86.00	36.13
9	3.13	53.69	9	3.00	53.00	9	3.25	53.00
10	86.875	52.875	10	87.00	53.00	10	86.00	53.00
11	3.00	69.00	11	3.00	69.00	11	3.00	67.50
12	45.00	69.00	12	45.00	69.00	12	45.00	67.50
13	86.00	69.00	13	87.00	69.00	13	86.00	68.50
14	3.00	122.00	14	3.00	122.00	14	3.00	122.00
15	86.00	122.00	15	86.00	122.00	15	86.00	122.00
16	3.00	176.00	16	3.00	176.00	16	3.00	176.00
17	86.00	176.00	17	3.00	176.00	17	86.00	176.00
18	3.00	230.00	18	3.00	230.00	18	3.00	230.00
19	86.00	230.00	19	3.00	230.00	19	86.00	230.00

Table 4.2: String pot attachment coordinates

RWN Krypton Locations

Krypton LEDs			Wall Attachment Location			Krypton LEDs			Wall Attachment Location		
Name	Xposition [in]	Zposition [in]	Name	Xposition [in]	Zposition [in]	Name	Xposition [in]	Zposition [in]	Name	Xposition [in]	Zposition [in]
1	87.49	67.50	24	66.22	10.70	47	24.19	19.35			
2	87.53	59.33	25	66.16	2.06	48	24.17	10.52			
3	87.51	51.29	26	55.43	1.92	49	24.27	1.91			
4	87.53	43.11	27	55.47	10.66	50	14.86	10.68			
5	87.42	35.15	28	55.40	19.44	51	14.02	1.89			
6	87.55	27.24	29	55.39	27.12	52	13.89	19.37			
7	87.68	19.44	30	55.37	34.88	53	13.92	27.07			
8	87.72	10.70	31	44.32	67.43	54	13.79	34.63			
9	87.70	2.05	32	44.56	51.11	55	13.76	42.77			
10	76.95	1.98	33	44.64	34.73	56	13.78	50.94			
11	76.89	10.72	34	44.63	27.16	57	13.79	59.13			
12	76.87	19.56	35	44.80	19.52	58	13.70	67.39			
13	76.83	27.12	36	44.83	10.72	59	3.53	66.62			
14	76.82	35.05	37	45.13	1.89	60	3.50	59.10			
15	76.78	43.05	38	34.60	1.95	61	6.26	6.52			
16	76.78	51.35	39	35.13	10.95	62	3.46	42.85			
17	76.76	59.41	40	34.40	19.43	63	3.67	34.77			
18	76.74	67.57	41	34.36	27.04	64	3.64	27.02			
19	66.05	67.53	42	34.35	34.76	65	3.84	18.96			
20	66.10	51.21	43	24.01	67.52	66	3.65	11.64			
21	66.08	34.93	44	24.11	51.01	67	2.53	15.41			
22	66.12	27.19	45	24.14	34.71	68	3.54	50.86			
23	66.15	19.49	46	24.16	27.07						

Table 4.4a: Krypton LED locations for RWN

RWC Krypton Locations

Krypton LEDs			Wall Attachment Location			Krypton LEDs			Wall Attachment Location		
Name	Xposition [in]	Zposition [in]	Name	Xposition [in]	Zposition [in]	Name	Xposition [in]	Zposition [in]	Name	Xposition [in]	Zposition [in]
1	2.50	2.58	26	23.64	33.33	48	86.51	41.90			
2	2.53	5.22	27	23.68	41.64	49	76.63	58.62			
3	2.58	8.50	28	34.11	4.98	50	77.03	66.70			
4	2.65	16.76	29	34.04	8.40	51	86.40	50.00			
5	2.69	25.29	30	34.10	2.49	52	86.70	16.86			
7	2.76	58.20	31	54.86	41.76	53	86.41	58.60			
8	2.74	66.85	32	44.59	41.77	54	86.37	25.01			
9	2.75	50.13	33	44.66	58.59	55	86.41	33.32			
10	2.76	41.81	34	44.46	25.06	56	76.16	49.94			
12	12.92	5.15	35	44.43	33.48	57	76.02	41.81			
13	12.92	8.47	36	44.48	16.59	58	75.85	33.30			
14	13.00	16.74	37	44.49	4.83	59	65.41	33.38			
15	13.01	25.25	38	34.22	41.71	60	65.34	58.52			
16	13.33	41.79	39	34.13	33.44	61	54.85	33.35			
17	12.96	66.76	40	34.17	25.01	62	65.28	4.94			
18	12.99	50.13	41	75.90	5.04	63	54.93	25.02			
19	13.09	33.50	42	76.02	8.45	64	55.31	2.26			
20	13.04	58.51	43	65.38	25.03	65	54.87	16.51			
22	23.66	5.12	44	65.37	41.80	66	86.57	4.88			
23	23.63	16.59	45	75.69	16.70	67	75.92	2.48			
24	23.62	25.11	46	75.89	24.96	68	86.39	8.49			
25	23.56	58.53	47	86.63	66.63	69	65.44	16.61			

Table 4.4b: Krypton LED locations for RWC

RWS Krypton Locations

Krypton LEDs			Wall Attachment Location			Krypton LEDs			Wall Attachment Location		
Name	Xposition [in]	Zposition [in]	Name	Xposition [in]	Zposition [in]	Name	Xposition [in]	Zposition [in]	Name	Xposition [in]	Zposition [in]
1	65.87	46.34	24	66.03	21.43	47	34.60	38.14			
2	87.25	1.95	25	55.69	21.38	48	24.18	38.00			
3	87.35	7.01	26	55.35	37.92	49	24.07	54.59			
4	87.16	13.37	27	44.88	1.79	50	13.67	46.25			
5	87.17	21.57	28	44.76	12.86	51	3.18	21.52			
6	87.12	29.83	29	44.84	54.94	52	3.20	29.69			
7	87.20	54.92	30	55.81	1.88	53	3.15	37.96			
8	87.12	63.09	31	44.83	29.58	54	3.12	46.28			
9	87.22	38.31	32	44.80	37.83	55	3.18	54.53			
10	87.03	46.61	33	44.68	46.67	56	3.27	62.75			
11	76.45	63.09	34	55.83	6.94	57	13.77	21.50			
12	76.49	29.97	35	44.69	21.32	58	24.08	21.57			
13	65.84	54.72	36	55.67	29.67	59	34.67	29.76			
14	76.52	38.25	37	55.43	46.29	60	24.12	29.63			
15	76.65	21.56	38	55.74	13.03	61	13.63	1.76			
16	76.36	46.56	39	65.93	38.07	62	34.00	2.10			
17	76.64	54.79	40	66.01	29.82	63	34.58	13.77			
18	76.53	13.31	41	34.60	46.39	65	24.10	13.23			
19	75.63	1.92	42	13.71	38.00	66	24.05	1.86			
20	76.44	7.02	43	23.97	46.20	67	24.06	6.88			
21	66.12	6.99	44	13.73	62.88	68	13.74	13.18			
22	66.13	1.93	45	13.70	54.59	69	34.62	22.03			
23	66.14	13.24	46	13.73	29.75	70	3.32	14.56			

Table 4.4c: Krypton LED locations for RWS

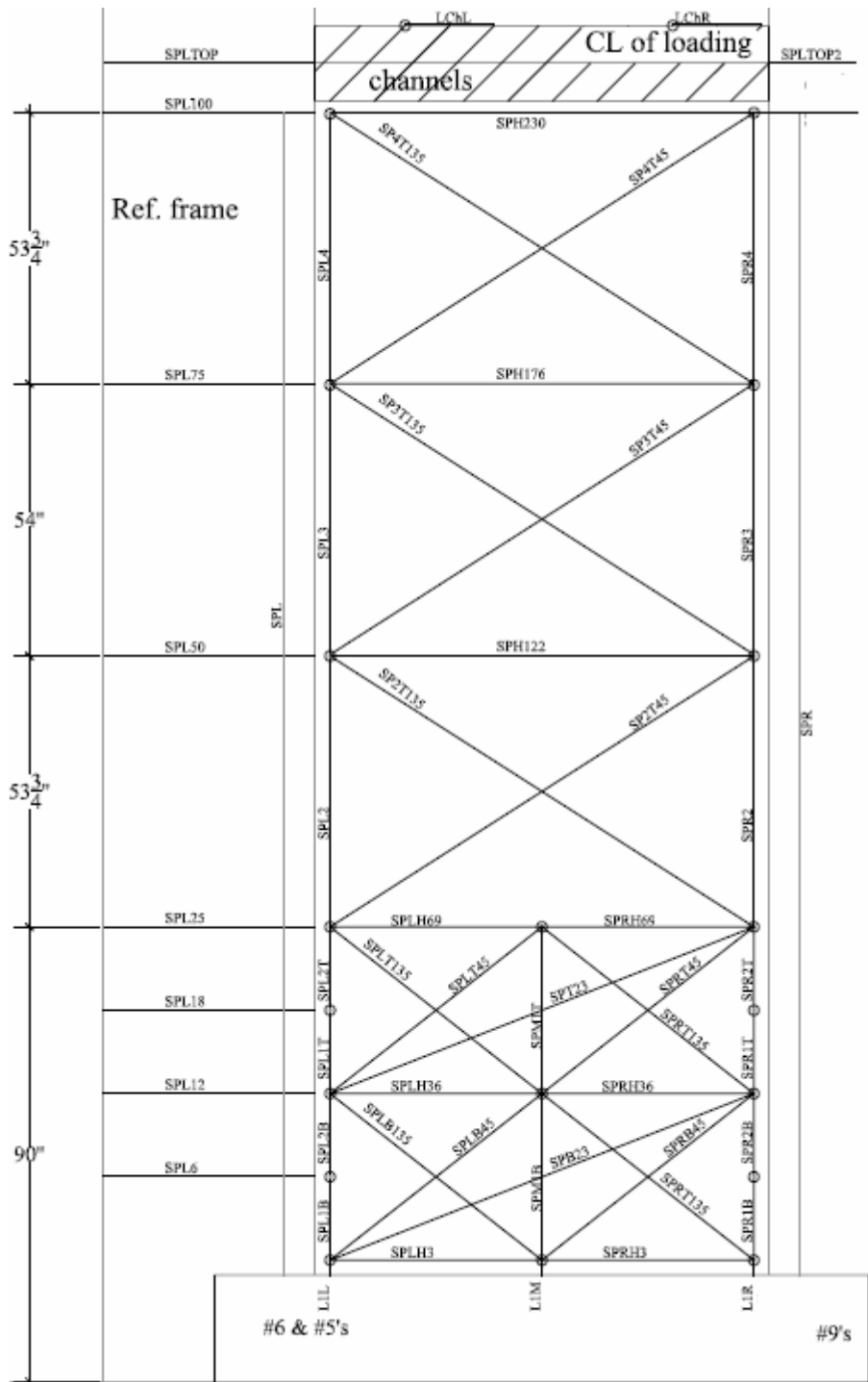


Figure 4.1: String Pot Layout on the east side of the test specimen

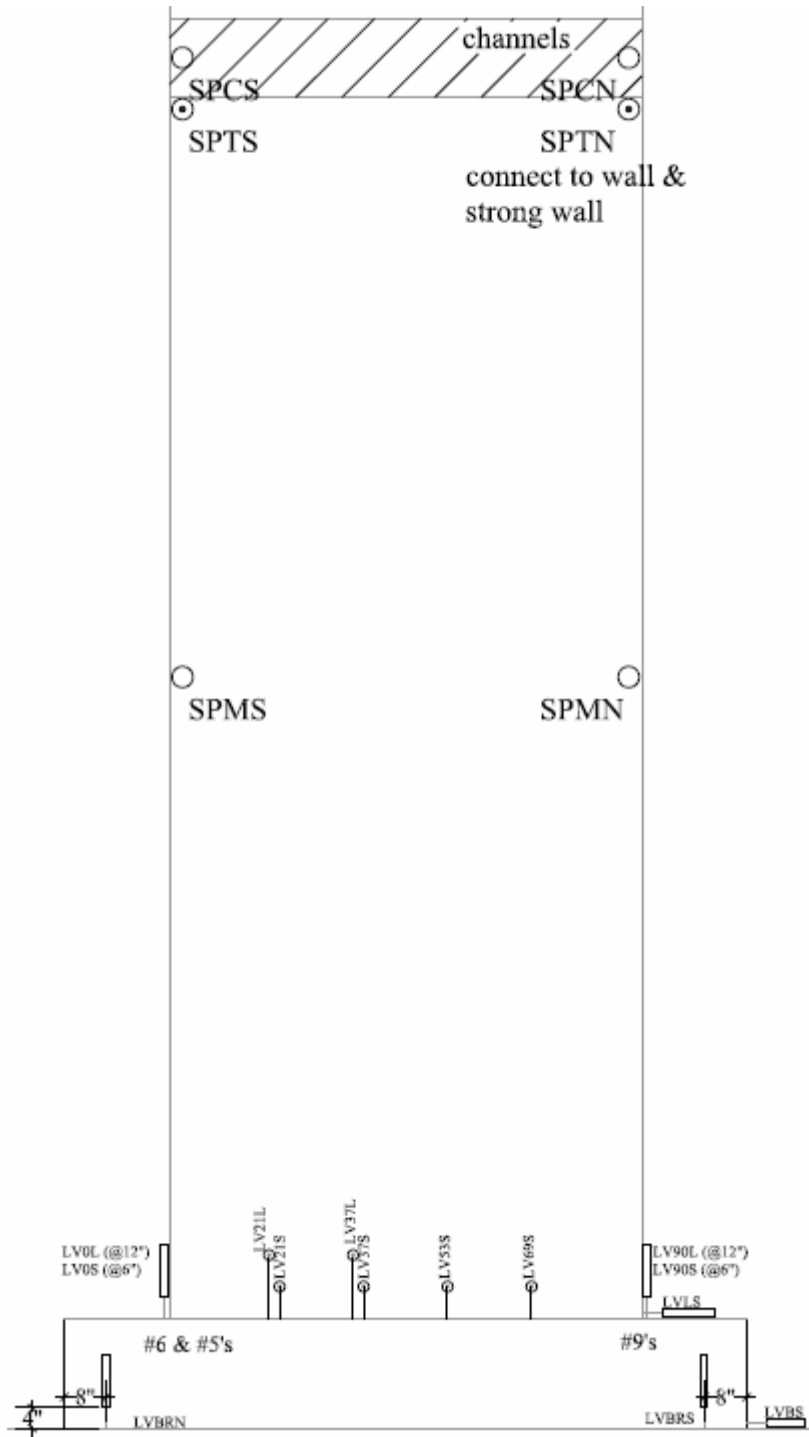


Figure 4.2: String pot and LVDT layout on the west side of the test specimen

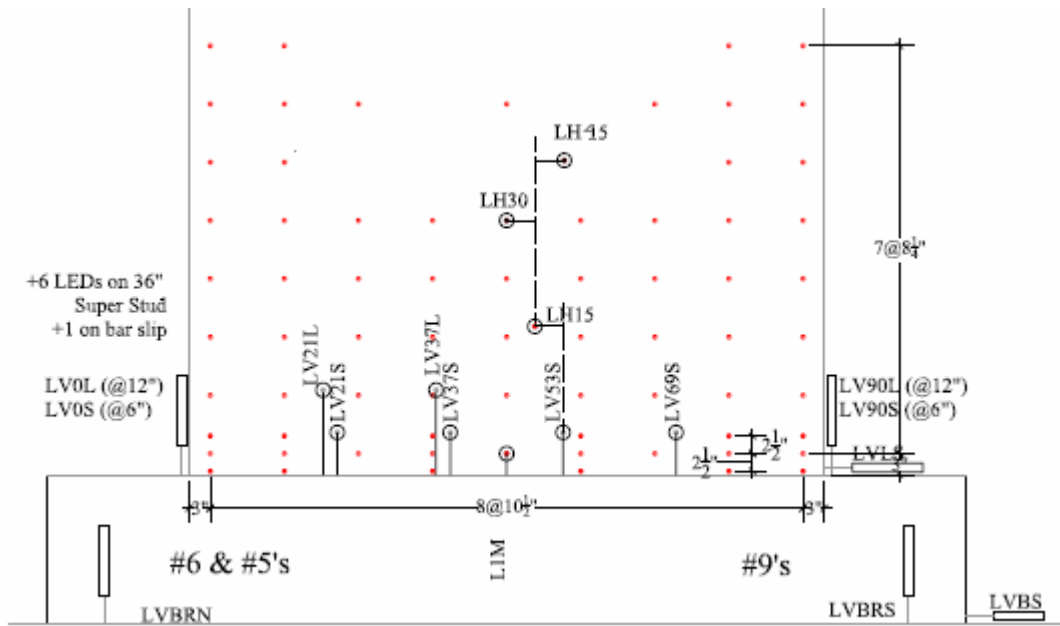


Figure 4.3a: Krypton (red dots) and LVDT instrumentation layout

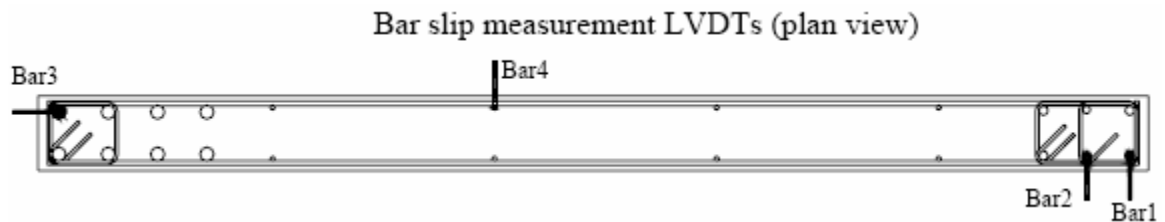


Figure 4.3b: Bar slip naming convention for RWN

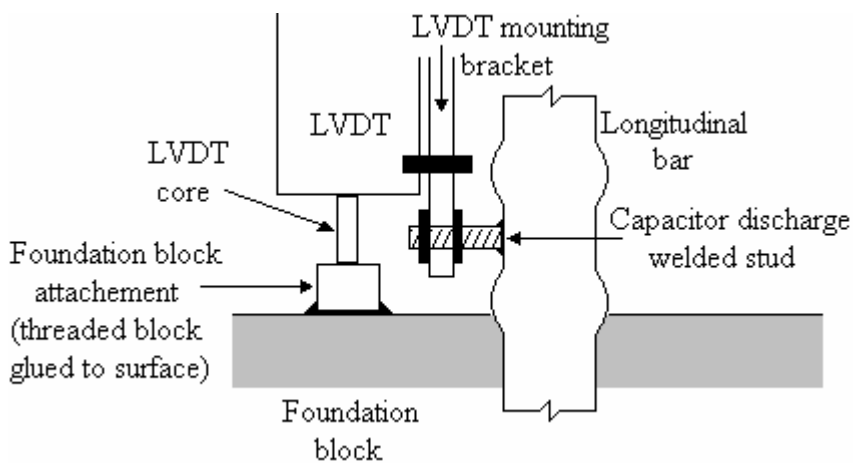


Figure 4.3c: Bar slip LVDT attachment schematic

Strain Gages on Longitudinal Reinforcement

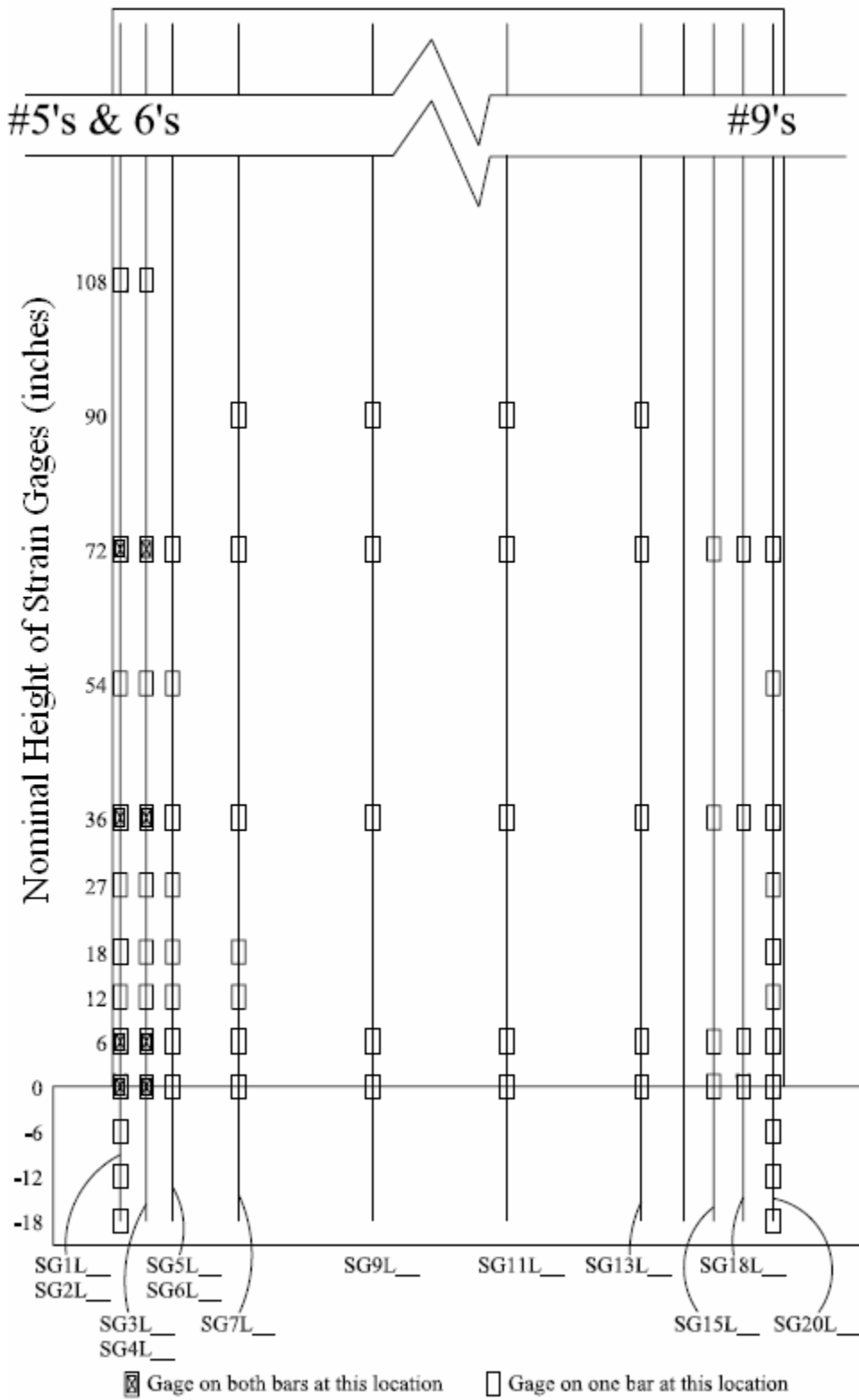


Figure 4.4a: Longitudinal strain gage setup

Strain Gages on Transverse Bars and Confinement Hoops

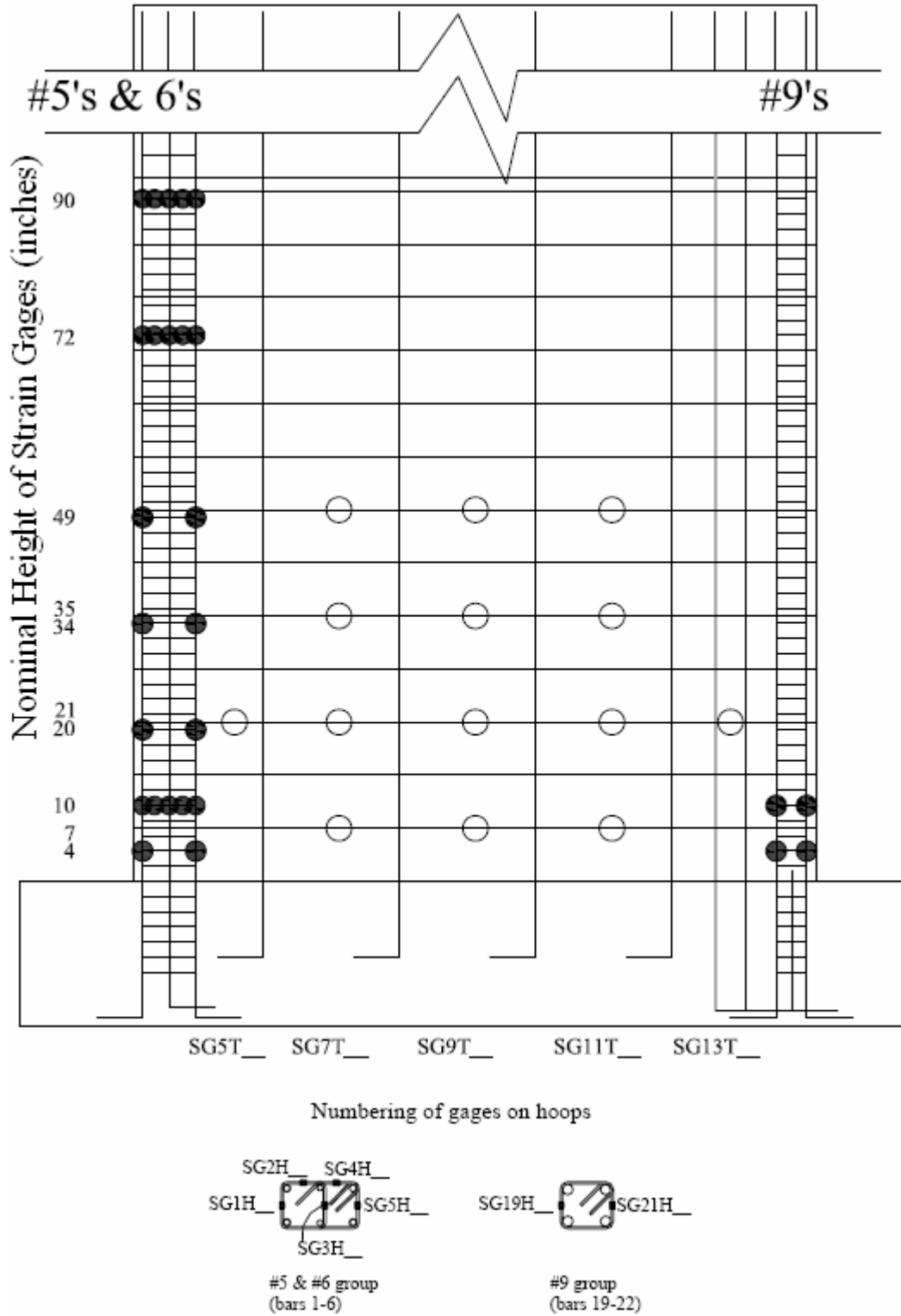
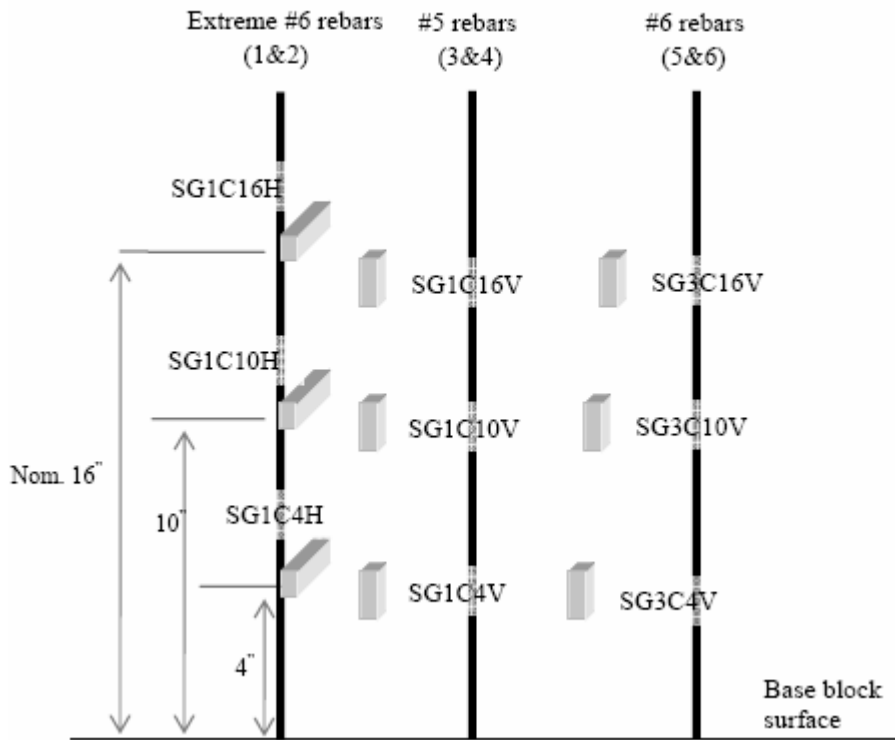
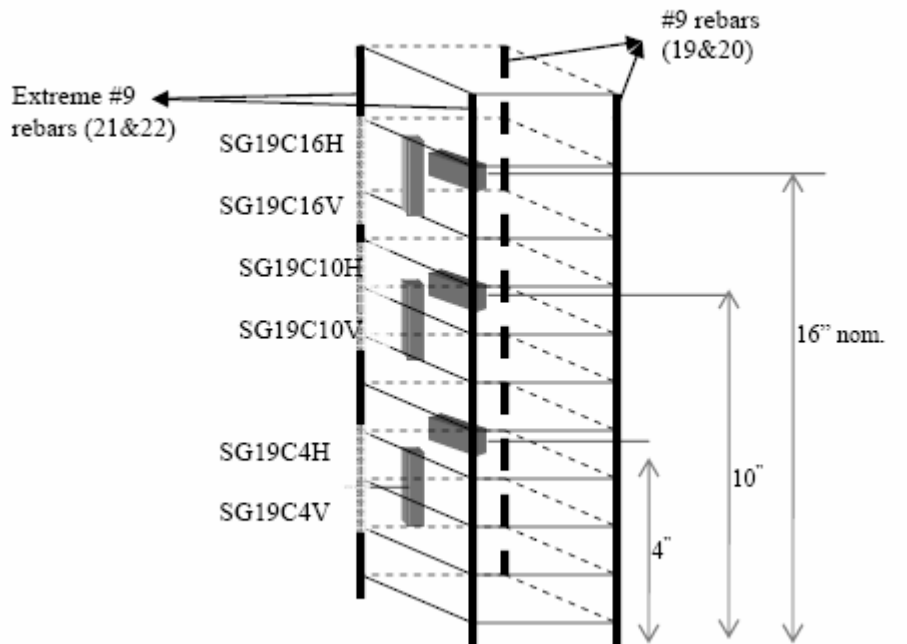


Figure 4.4b: Transverse bar and hoop strain gage setup

Concrete Gage Locations



No. 5&6 Boundary Element



No. 9 Boundary Element

Figure 4.4c: Concrete strain gage setup

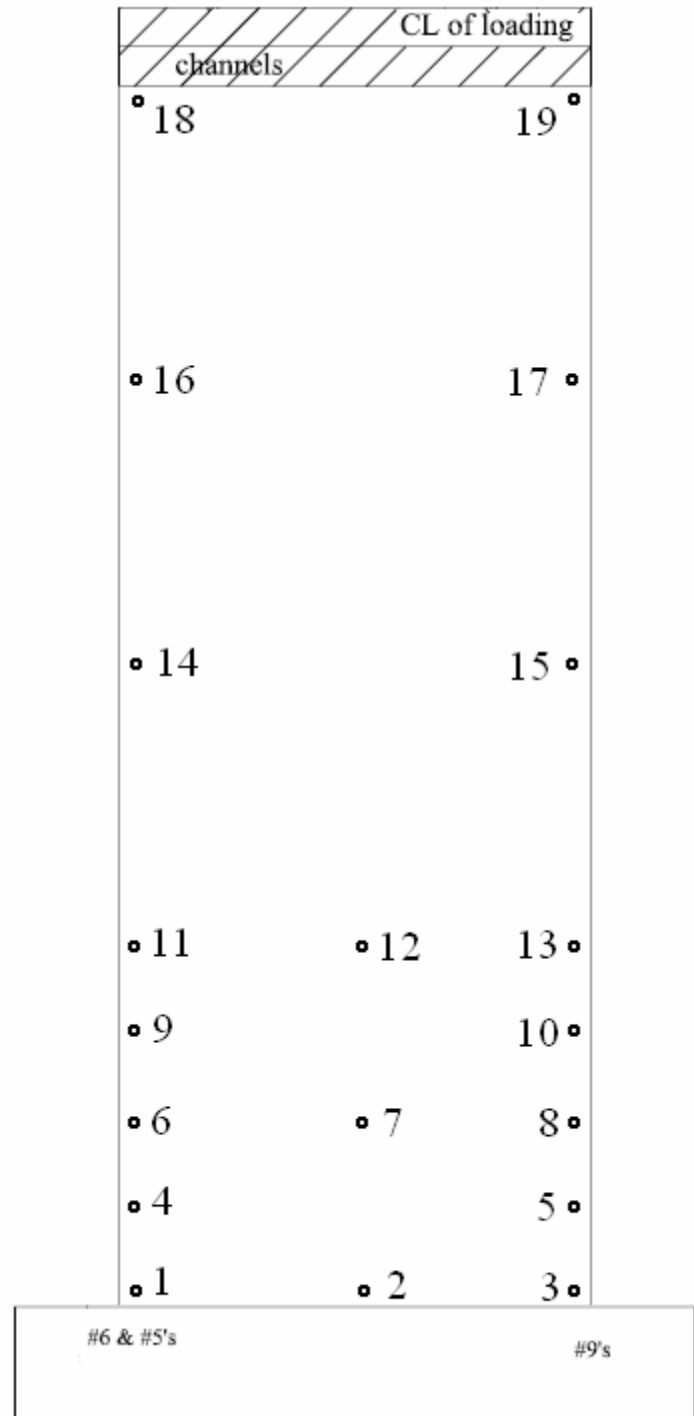


Figure 4.5: String Pot attachment naming convention

Chapter 5: Test Setup & Procedures

5.0: Introduction

This chapter covers the test setup, test frame and other testing structures, and the loading protocol of the experimental tests discussed in this report. The test setup for this experiment is designed to create a fully constrained boundary condition at the foundation of the wall, a rigid laterally braced condition of the wall in the direction normal to the plane of the wall, and a lateral load applied to a single height at the top of the wall which is distributed along the length of the wall. This is achieved with three test structures. The performance of these test structures is monitored with several instruments. In addition to this setup, a loading protocol is created to determine the effectiveness of the test structures to seismic loading. This entails a reversed cyclic loading function of target displacements. These target displacements were chosen to collect a great deal of information prior to yielding, well into the inelastic range, and ultimate strength. The target displacements are reached three times, in order to determine if the structure was stable at that drift level.

5.1: Foundation Setup

The foundation of the test structures were designed to create a fully restrained boundary condition, as well as be effectively rigid during the experimental test. The reinforcement details of the foundation block and photographs can be seen in figures 5.1a and 5.1b. Reinforcement was selected such that the foundation block would remain elastic and effectively rigid during the maximum predicted loading of the test, along with a conservative safety factor.

The interface of the foundation block and strong floor was intended to be a uniform surface. This was created by a grout bath, which was cast with the foundation block 0.25” off of the strong floor. The foundation block was attached to the strong floor of the

laboratory by means of ten, 1.5” diameter high strength steel rods. Note that more anchor rods are present on the No.9 boundary element side of the wall, where larger tensile forces can be developed from the larger area of cross sectional steel. These rods were prestressed to a load level such that slipping between the foundation and strong floor would not occur. This pretension also keeps the foundation block in compression, regardless of the load applied to the structure. The pretension in these anchor rods prevents any rotation of the foundation block in the plane of the wall. Refer to figures 5.2a and 5.2b for illustrations of the anchor rod/strong floor connection and photographs of the this test setup. Refer to chapter 4 for the instruments used to determine if slip or rotation of the foundation block occurred.

5.2: Actuator Loading Setup

Load was applied to the test structures by means of a single hydraulic actuator. This actuator was located approximately 20 feet above the wall/foundation interface. The load was applied to the test structure with two steel channels, located on either side of the wall. The opposing side of the actuator was connected to the laboratory strong wall perpendicular to the test wall plane. These channels “clamped” the wall with pretensioned, 1” diameter rods through the wall at five points. The rods through the loading channels were staggered with respect to the height of the wall, in order to deliver the maximum amount of friction between the walls and channels. Grout was placed between the channels and the test specimens in order to achieve a uniform friction surface. Refer to figures 5.3a through 5.3c for illustrations and photographs of this setup.

Slip between the loading channels and the test specimens was observed during each test. Slip occurred until the steel rods passing through the wall were bearing on the internal wall surface and loading channels. The slip was monitored by LVDTs that were attached with one point on the loading channels and one point on the test structure. The displacement recorded by the actuator and external string pots attached directly to the specimens differ by the amount of slip occurring. The total lateral displacement used is

always based on the global string pots instead of the internal LVDT of the actuator in order to neglect the effects of loading channel slip.

PVC ducts were placed through the top of the wall for the steel rods that were to pass through the wall and tension the loading channels in order to clamp the test structure. Possible interference with the lateral bracing was noticed prior to testing of RWN, requiring one the location of one of the loading channels to move. This was done by drilling through the wall after construction. Splitting cracks were observed to propagate from the top of the test specimens at large load levels. These splitting cracks are thought to be the product of the voids present in the wall from the loading channel tension rod ducts. This is illustrated in figure 5.3d.

5.3: Lateral Bracing Setup

Lateral bracing was designed to resist the maximum out of plane forces that could be generated during the test, while not contributing to the resistance of the test specimens. The maximum forces predicted were amplified by a generous safety factor. The bracing was then designed to resist these maximum forces and deflect less than 0.1” in the direction normal to the wall plane. This was achieved by a series of HSS and angle sections. These sections are located above the highest part of the wall and have W-section arms that extend down and connect to the test structure. The bracing setup can be seen in figures 5.4a and 5.4b.

The connection of the bracing to the wall is achieved by structural wheels. These wheels roll in the direction of the applied load and roll inside the loading channels. The location of the wheels and loading channel rods were chosen such that they would not interfere with each other, regardless of the displacement the wall would undergo during the test. Problems with this connection occurred during the test of RWN, where the loading channels were not deep enough to prevent the structural wheels from touching the bottom flange at displacement levels larger than 5 inches. This was due to the vertical elongation

of the tension boundary element at the large load levels. The wheels were replaced by shims for the loading ramps larger than 5 inches, in order to prevent the contribution of the lateral bracing to resistance of the walls. The depth of the loading channels was increased for the tests of RWC and RWS. Wheel interference was not a concern following this setup improvement. Refer to figure 5.5, which shows a picture of the interference of the bracing wheels and loading channels.

Insufficient clearance was observed when the bracing was initially installed. The W10x12 sections were extended with channels to increase the clearance between the top of the test specimens and the bottom of the HSS12x12x1/2" sections to 12 inches.

5.4: Testing Protocol

The test structures were loaded in reversed cyclic order. The test structures were loaded in displacement controlled mode, targeting displacement levels of predicted significance. Each loading cycle reached the target displacement three times for each boundary element (a total of six loading ramp peaks), except the first set of cycles.

The first set of loading ramps, or 'pre-cracking/verification' cycles had a single or two loading ramps, depending on the wall. RWN was loaded to a small displacement, requiring 500lbs of force in the direction of the No.5&6 boundary element in tension direction. RWN followed the predetermined loading plan following this 'pre-cracking/verification' ramp. RWC and RWS had considerably larger 'pre-cracking/verification' cycles. These two specimens also had a test loading ramp in the direction of the No.9 boundary element in tension. This is noted for the comparison of the load-displacement response of the walls, where the walls do not follow the same load-displacement response initially.

The loading history of the walls are shown in figure 5.6 Note that the loading histories beyond the possible buckling load are different for each wall. The differences are due to

the damage state of each wall at the time and the limitations of the test setup. RWN was unable to achieve displacements as large as RWC from interference with the test setup. RWS experienced bar fracture in the No.5&6 boundary element. The No.5&6 boundary element could no longer be loaded in tension. Additional loading cycles were then done in the No.9 boundary element in tension direction.

The load direction placing the No.5&6 boundary element was of the most interest to researchers. The No.9 in tension direction was cycled repeatedly at 1% (9 total load events) in order to limit additional damage to the structure, such that more information could be collected for the No.5&6 boundary element in tension.

5.5: Wall Orientation

RWN and RWS are oriented in the same direction in the testing bay. The No.5&6 boundary element is on the south side of the test setup. The loading actuator is attached on the north side of the specimen, the No.9 boundary element side. The global external string pots are attached to the south side of the specimen and the rigid reference frame. The orientation of RWC is reversed from the other two specimens. This orientation change was unintentional. The orientation of RWC was reversed when moving the constructed foundation block from the strong floor to the prep area for completion of the construction. The problem was not considered until construction had been completed. The orientation was chosen to remain as it was during construction to avoid damage to the specimen that could occur from rotating. The implication of this orientation change creates differences in the way the total displacement is measured.

The effects of cracking create a lateral expansion of the wall. This lateral expansion is not observed when the total displacement is taken from the tension side of the wall (when the No.5&6 boundary element is in tension for RWN and RWS and when the No.9 boundary element is in tension for RWC). The difference between the measurements of the total lateral displacement of the tension boundary element and compression boundary element

can be as large as 10%. The discrepancy between the difference in the total displacement can be resolved with the measurements of lateral expansion from the horizontal string pots discussed in chapter I. The effects of lateral expansion are discussed further in chapter 12, when all calculated components of deflection are compared to the total measured deflection.

Foundation Block Reinforcement Details

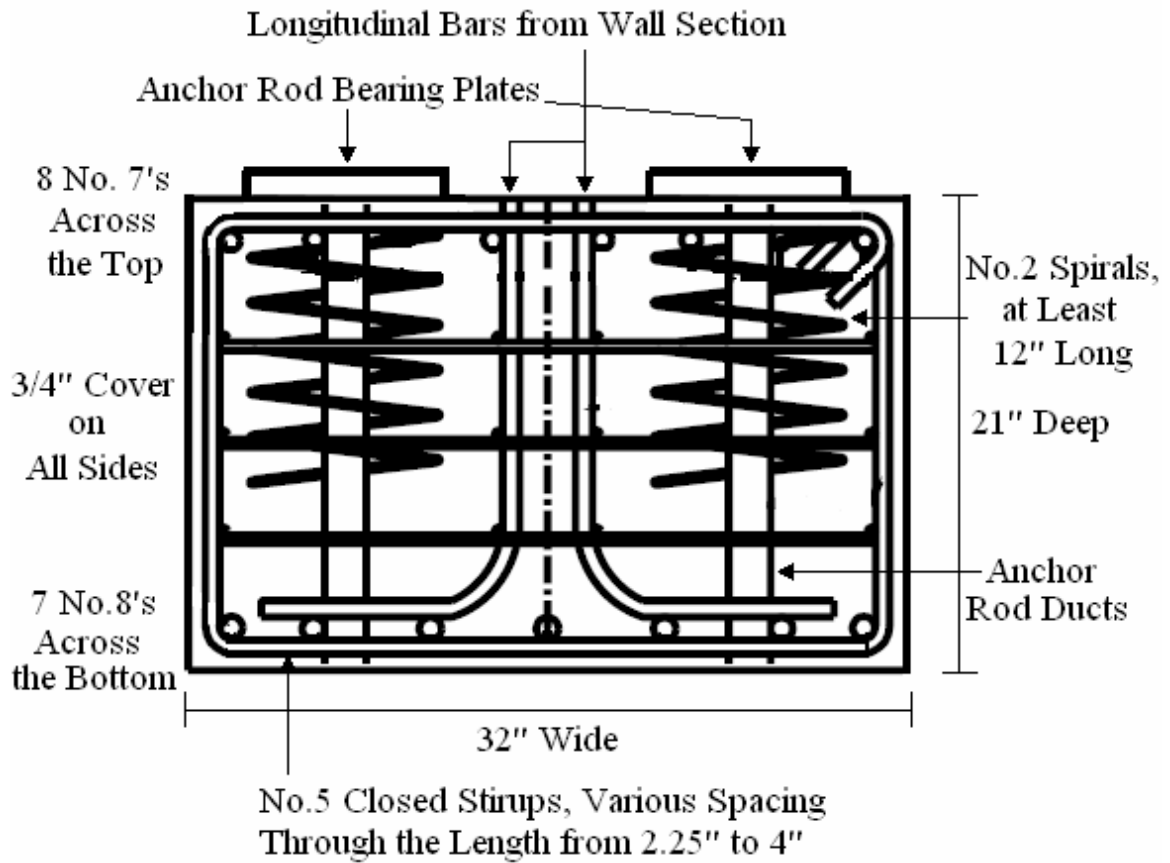


Figure 5.1a: Foundation block reinforcement details.

Reinforcement in the foundation of RWS



Figure 5.1b: Reinforcement cage in the foundation block of RWS.

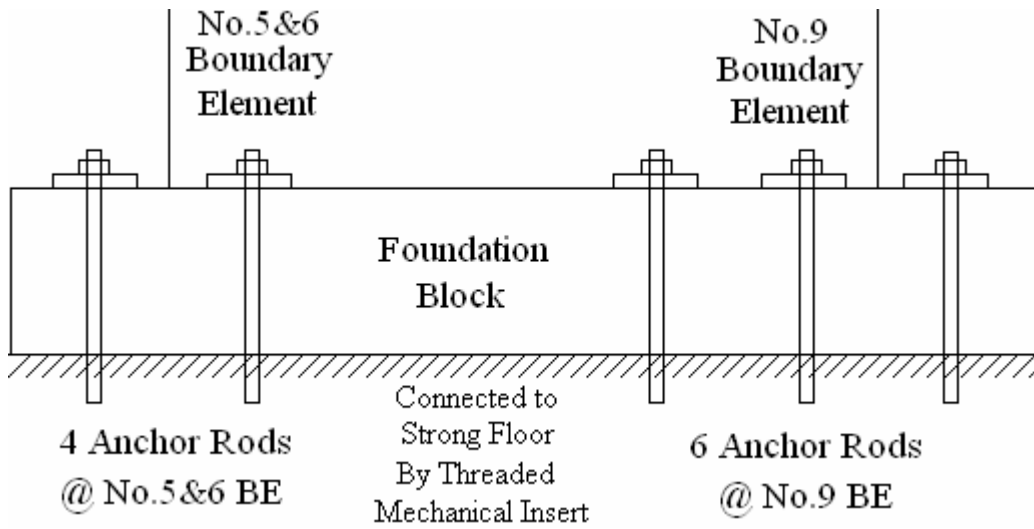


Figure 5.2a: Anchor rod layout across the length of the foundation block.

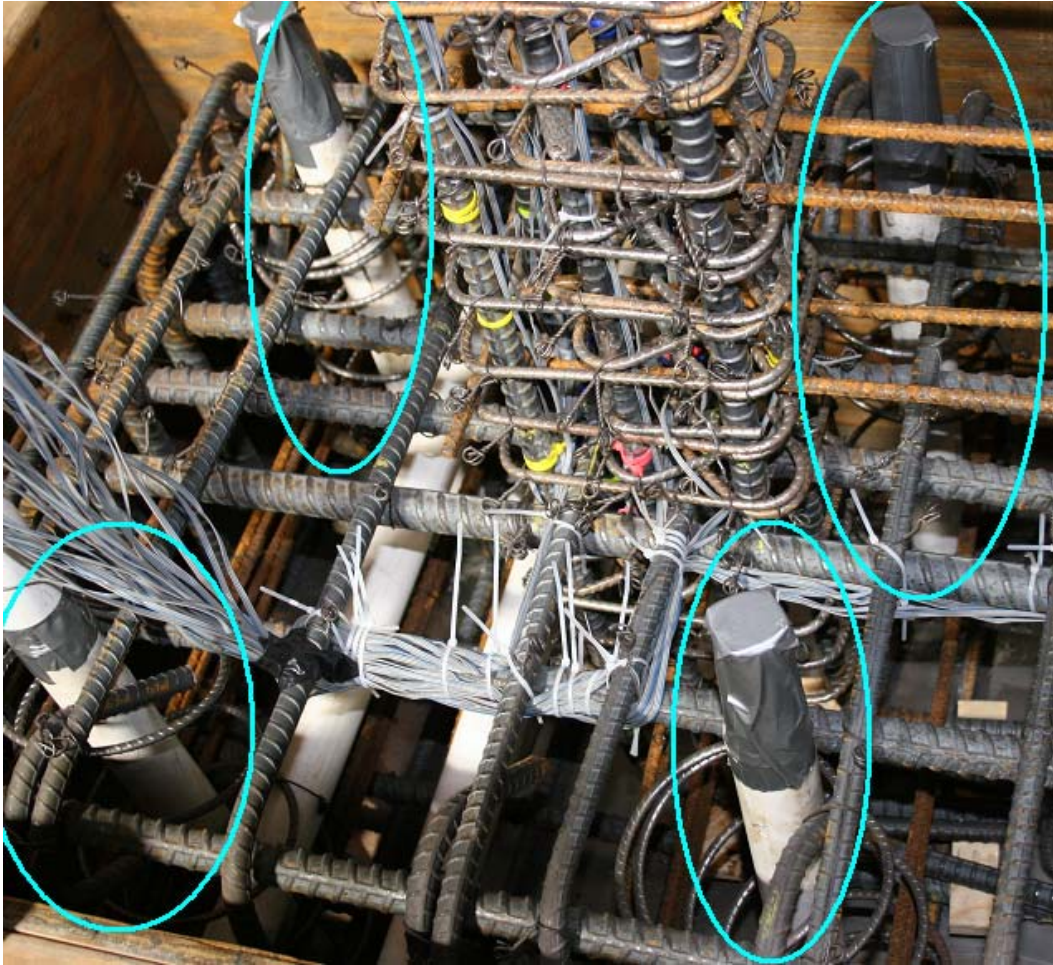


Figure 5.2b: Photograph of anchor rods in RWN at the No.5&6 boundary element.

Specimen / Loading Channel Connection

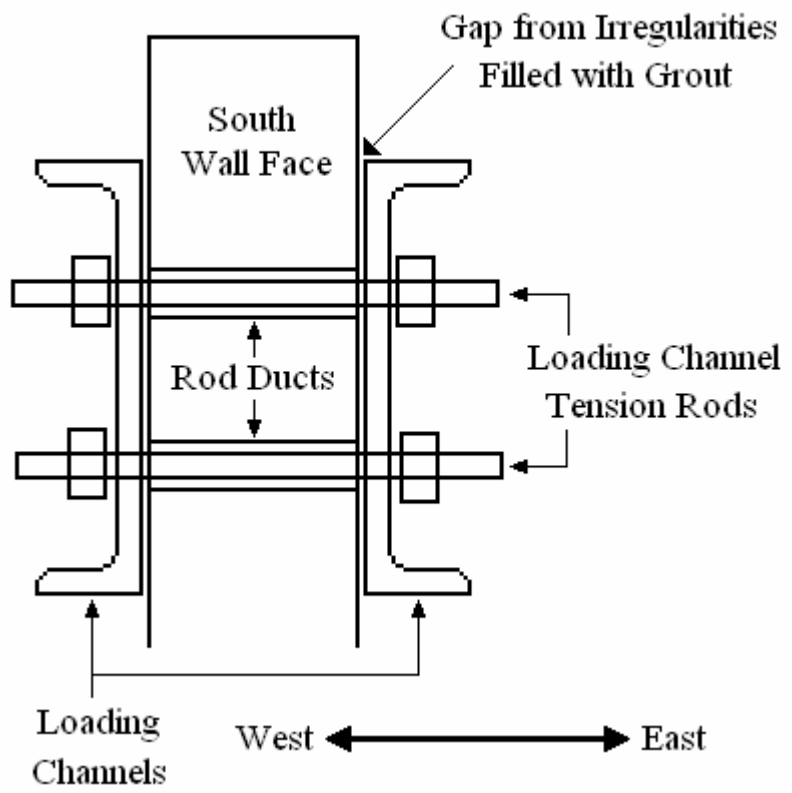


Figure 5.3a: Elevation view of specimen/loading channel connection, facing north.



Figure 5.3b: Picture of specimen/loading channel connection, facing north.

Elevation View of Loading Channel Connection

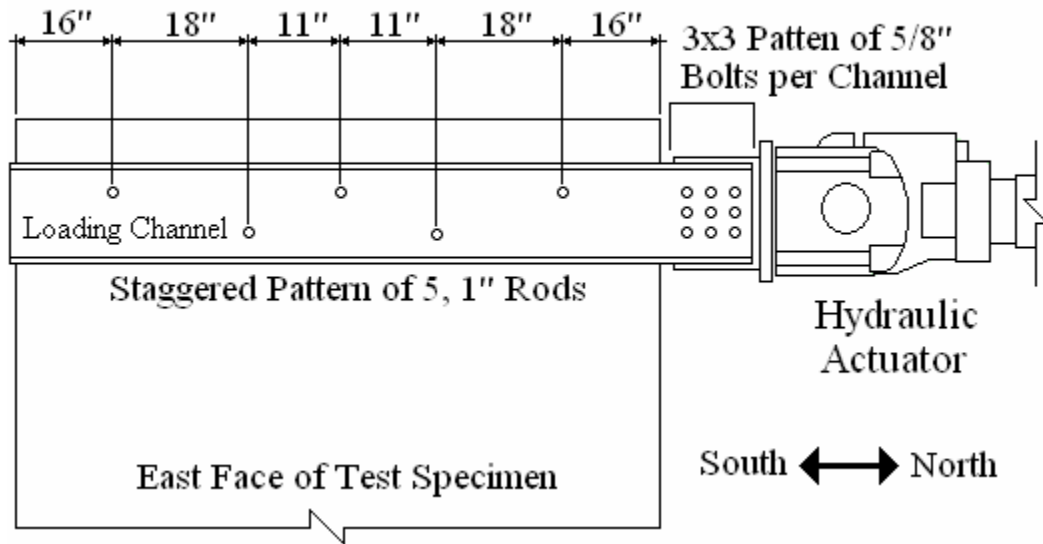


Figure 5.3c: Elevation view of specimen/loading channel/actuator connection.

RWN: Loading channel/specimen/actuator connection.



Figure 5.4d: Channel tension rod duct relocation for RWN. Splitting cracks can be seen to originate from the tension rod duct locations.

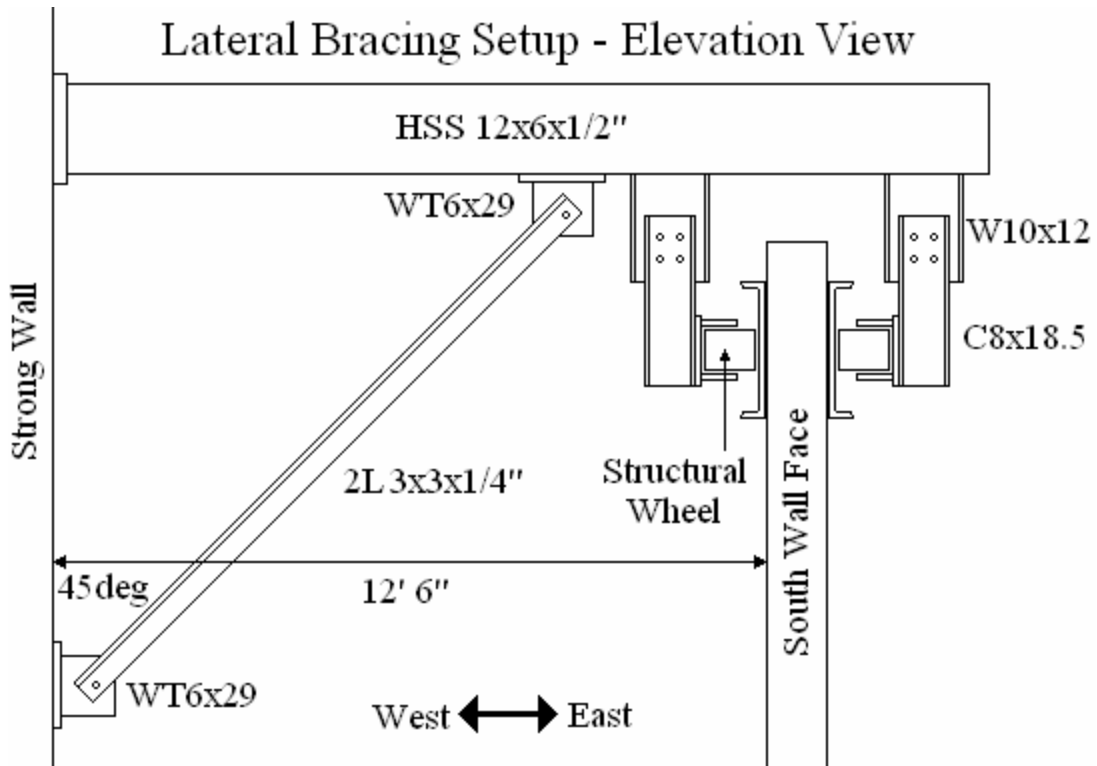


Figure 5.4a: Lateral bracing setup, elevation view facing north.

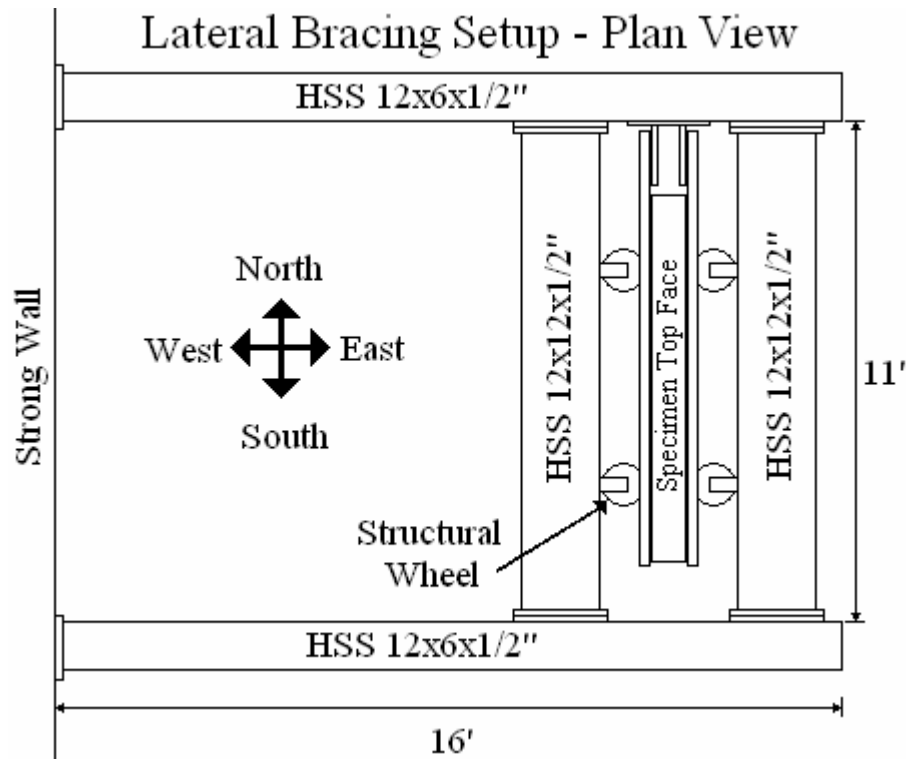


Figure 5.4b: Lateral bracing setup, plan view.

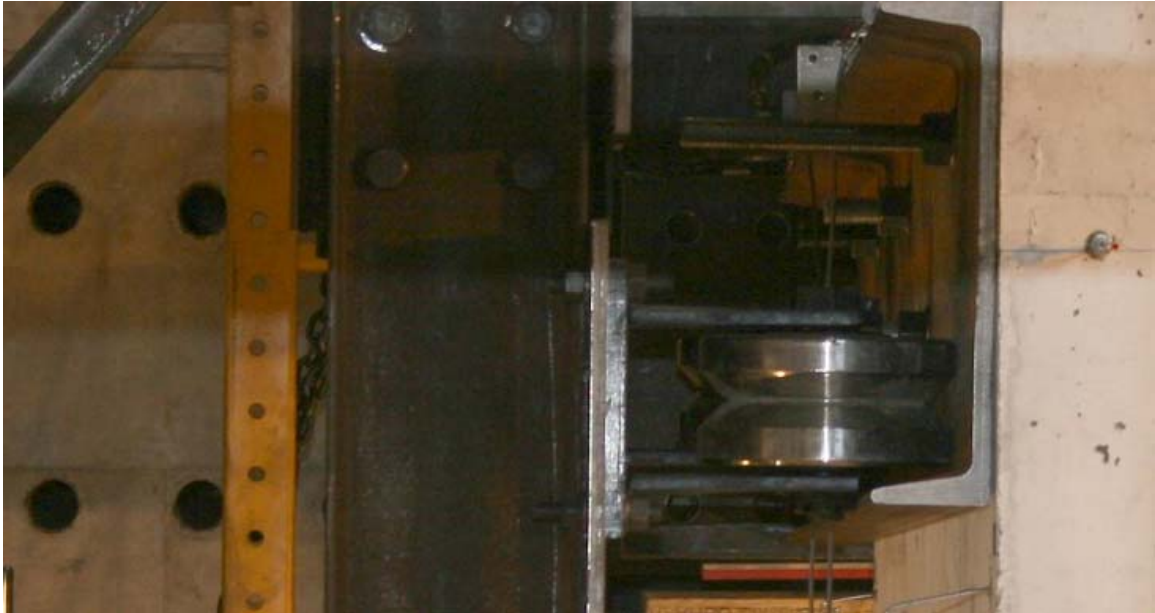


Figure 5.5: Structural wheel interference with the bottom flange of loading channels.

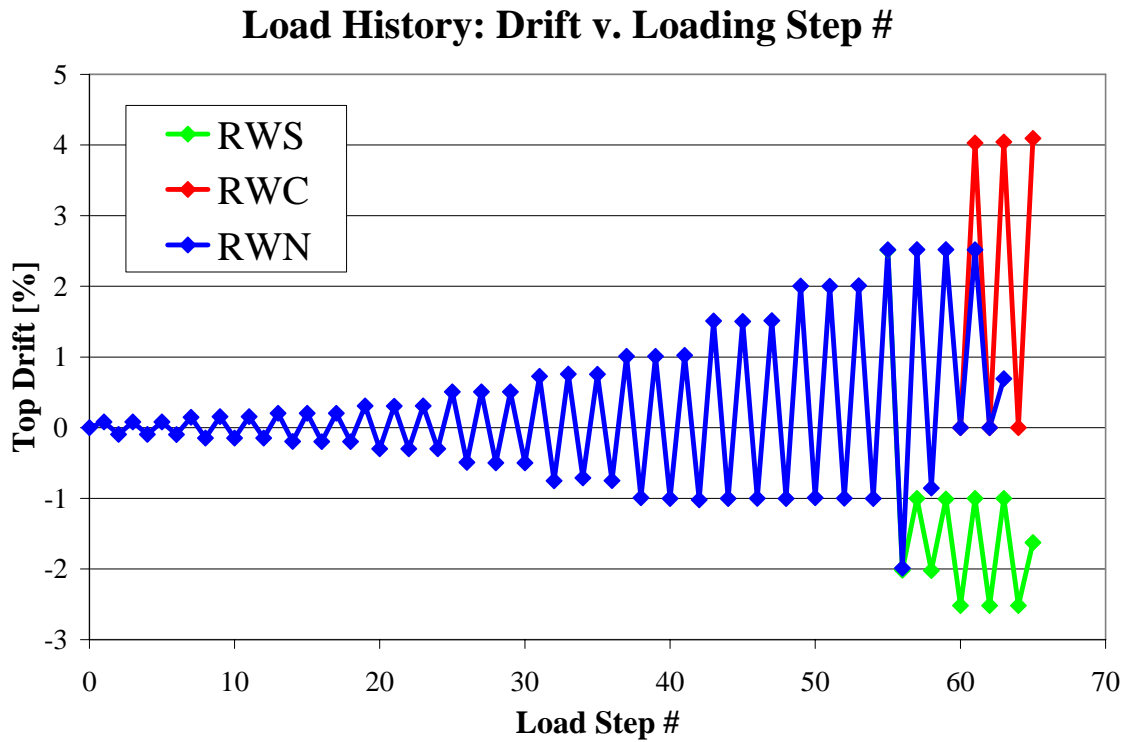


Figure 5.6: Load history for each wall. Note that positive drift refers to the No.5&6 boundary element in tension.

Chapter 6: Load v. Deflection Relationships

6.0: Introduction

This chapter covers the load deflection responses of the three test specimens. This was done in order to determine the preliminary differences in overall test specimen behavior. The reasons for the similarities and differences in wall behavior discussed in this chapter were discovered by investigating the individual deflection components and other test data. The similarities and differences in the load deflection responses of the three test specimens are contained in this chapter. The reasons for the differences documented in this chapter are examined in the chapters following the load deflection relationships.

6.1: Load v. Deflection Measurement

Load applied to the test structures was measured from the hydraulic actuator used to displace the test specimens. The lateral displacement used in the load v. displacement relationships is the measured global displacement of the test specimens. This displacement was measured as the change in distance from the south end of the test structure and a rigid reference frame.

The effects of splitting cracks that propagated from the top of the test specimens had a noticeable affect on the total measured displacement, depending on the side of the wall displacement is measured from. These effects were able to be neglected by using the lateral expansion of the walls from cracking, measured by horizontal string pots mounted on the test specimens. These measurements were then used to calculate the global displacement of the end of the wall in tension, the boundary element in tension. Global displacements of the boundary element in tension were then used in the load v. deflection relationships of the test specimens. This was done at multiple heights of the walls.

6.2: Load v. Deflection Relationships

The load v. deflection relationships of the three test specimens for every loading event applied during the experimental test are shown in figures 6.1 through 6.3. Positive load and displacement in these figures refer to the boundary element containing No.5 and No.6 longitudinal reinforcement in tension. This boundary element is often referred to and abbreviated as the No.5&6 BE. This sign convention remains constant throughout this report. Positive values, such as curvature and rotation, always correspond to the No.5&6 boundary element in tension. Conversely, negative parameters relate to the boundary element containing No.9 longitudinal reinforcement in tension.

The first similarity noticed when observing these figures is that the stiffness of the test specimens is much smaller when the No.5&6 boundary element is in tension. This is due to a smaller amount of longitudinal reinforcement in tension. This decreased cross sectional area of steel in tension reduces the cross sectional moment of inertia. This cross sectional property along the wall height creates decreased rotational stiffness for the No.5&6 boundary element in tension when compared to the stiffness of the wall when the No.9 boundary element is in tension. The different directional stiffness of the walls can be assumed to be completely flexural, as the shear reinforcement and properties are the same in each direction. This is expected, as the longitudinal reinforcement was selected to achieve these types of directional effects to mimic the response of a shear wall having a ‘T’ shaped cross section.

The load v. deflection response at the largest displacements shown is different for each wall. This is caused by test setup limitations and different wall failures. RWC has the largest lateral deflections when the No.5&6 boundary element is in tension. RWN was unable to achieve the same displacement levels from interference with the out-of-plane bracing at the top of the wall. Interference with the test setup would have created a false representation of wall behavior, as the bracing would have contributed to resistance to the actuator load. This reason, along with safety, was the cause for not displacing RWN to

the same drifts as RWC. It is assumed that RWN would have been able to reach displacements larger than what it was subjected to during the test. RWS did not achieve the same displacements as RWC as well. This was the product of wall failure. Longitudinal reinforcement in the No.5&6 boundary element fractured when displaced past a drift of 2%. This fracture is highlighted in figure 6.3. RWS was instead loaded with the No.9 boundary element in tension, post No.5&6 boundary element fractures. The issues discussed in this passage are the reasons for the glaring differences observed in the load v. deflections responses of the test specimens.

6.3: Load v. Deflection Comparisons

The effects of the various anchorage details: continuous bars, mechanically spliced couplers, and lapped splices can be seen when comparing the load v. deflection backbone curve responses of the test specimens. The term 'backbone' means that only the loading event peaks are shown for the first time the displacement in question has been reached. This makes the comparison of specimen response much easier, without the distraction of many loading loops. The comparisons of the three walls are shown in figures 6.4 and 6.5. These comparisons are for the No.5&6 boundary element in tension, as it is of greater interest to researchers. The elastic response and a portion of the inelastic behavior are only shown to magnify the differences of the walls by 'zooming in' on a section. Two different wall height locations are shown in these figures, the top of the wall and the mid-height of the wall.

RWN and RWC have nearly identical load v. deflection responses. RWS, however, is noticeably stiffer than the other two specimens. The load v. deflection relationship at the top of the wall is approximately the same for each wall in the elastic portion of the response. RWS does not experience a larger stiffness than the other two walls until yielding of the longitudinal reinforcement occurs and the walls begin to behave plastically. This is not the case when comparing the same relationships at the mid height of the wall, exactly half of the total height. Again, the load v. deflection relationships of

RWN and RWC are very similar in magnitudes and trends. The difference with these two curves, when compared to those at the top of the wall, is the magnitude of the displacements at the mid height of the walls. The total displacement at the walls mid height is smaller than that at the top of the wall, as expected. The decrease in total displacement from the top of the wall to the mid height of the wall is also observed for RWS. This change is much larger than RWN and RWC. The load v. deflection curve for RWS is now entirely above RWN and RWC for all displacements, not just in inelastic response of the wall.

These figures show that lapped splices increase wall stiffness, decreasing the overall lateral displacement. The reduction in lateral displacement, when compared to the other two specimens, is larger at lower wall heights. RWS clearly has a different deflected shape than the other two specimens. Little variation was observed in the load v. deflection response of the walls containing continuous bars and mechanically spliced longitudinal bars.

6.4: Lateral Stiffness

Lateral stiffness was calculated for each loading event peak. This stiffness is the straight line tangent stiffness from the origin to the loading event peak coordinate of load and displacement. The lateral stiffness calculated for each loading event peak and test specimens is shown in figure 6.6. RWS has larger, or the same stiffness as the other two walls. This is true for each boundary element in tension direction. Additional differences are observed when considering the return loading events to previously achieved displacements within a single cycle of loading events.

All loading events up to the point of observed wall buckling are shown in figure 6.6. Wall stiffness for return loading events was typically close to the stiffness for the specimen the first time the drift level in question had been reached. Return event wall stiffness was usually within 5% below the first loading event of the cycle group. A larger decrease was

observed in the case of the returns to 1% drift with the No.9 boundary element in tension for RWS. 1% drift was achieved a total of nine times. Lateral stiffness at this level continuously decreases for each return, unlike RWN and RWC. Lapped splices have an effect on the ability of the wall to sustain the same resistance for return to a drift level of 1%. The effects of lapped splices creating an unstable solution for RWS at 1% drift with the No.9 boundary element in tension were found to be a contributing factor to the fracture of the No.5&6 longitudinal bars as well.

6.5: Energy Dissipation

Dissipated energy was computed for each loading event for each test for the three test specimens. Dissipated energy was calculated by subtracting the area under the unloading load v. deflection curve from the area under the load v. deflection loading curve. The energy dissipation backbone, the amount of energy dissipated for each new drift level, is shown in figure 6.7.

It can be seen that very similar amounts of energy are dissipated for each specimen. RWS falls between RWN and RWC, showing that lapped splices do not have an effect on the amount of energy dissipated. The amount of energy that has been dissipated is approximately the same for each specimen; however, this does not ensure that energy was dissipated through the exact same means for each specimen. Different amounts of energy can be dissipated through flexure and shear to achieve the same dissipated energy total. The differences in the way the specimens dissipate energy is discussed in later chapters.

A negligible amount of energy is dissipated until drift levels of 0.5% for each test specimen. It is clear that the test specimens remain completely elastic at drift levels of 0.3%, were all dissipated energy can be attributed to cracking of the walls. No yielding of longitudinal reinforcement has occurred at 0.3% drift. This is not necessarily true for the next loading event peak of 0.5% drift. The drift peak of 0.3% referred to as the “elastic limit” of the load v. deflection response of the walls. This is done not because yielding

occurs at a drift of 0.3%, but because it is the last load peak prior to yielding occurring in the longitudinal reinforcement of any specimen.

6.6: Summary of Findings

The load v. deformation relationships of the test specimens were observed to find if any differences in wall behavior are created from various anchorage details. Lapped spliced at the base of the wall seem to have affected the deflected shape of test specimens and the lateral stiffness. Wall stiffness was increased. Lateral displacements were decreased. The decrease in lateral displacement, when compared to the other two test specimens, is larger at lower wall height locations in RWS. No significant differences were observed between continuous bars and mechanically spliced (couplers) bars at the wall/foundation interface.

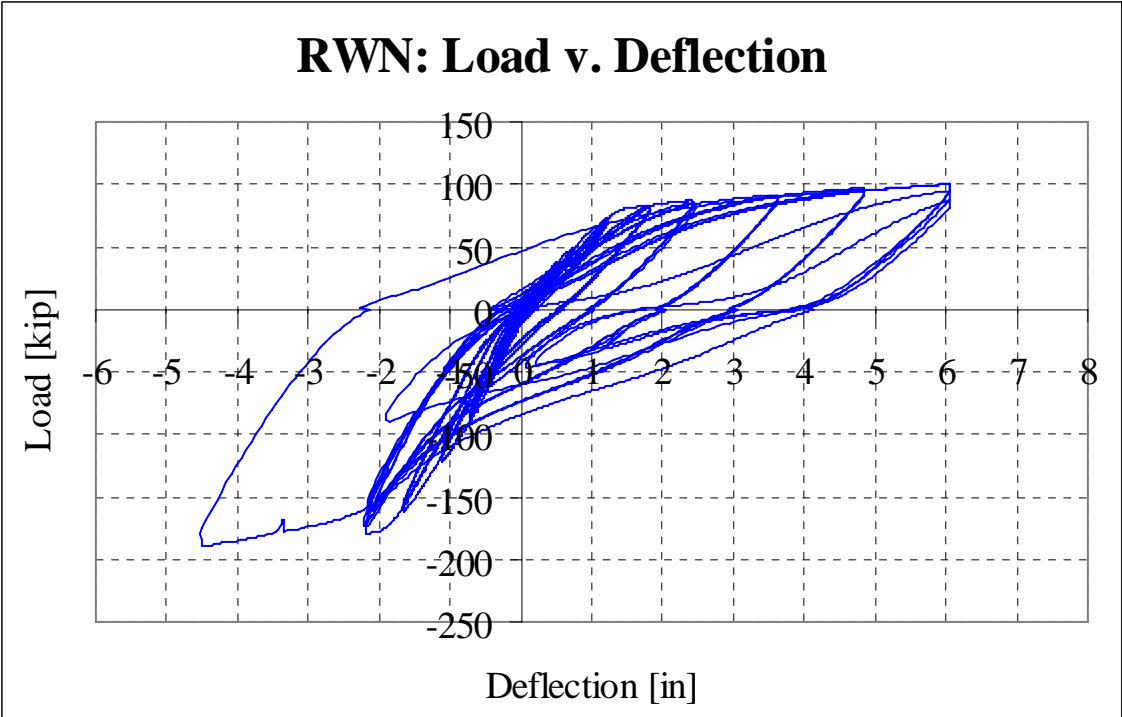


Figure 6.1: Load v. Deflection Relationship of RWN

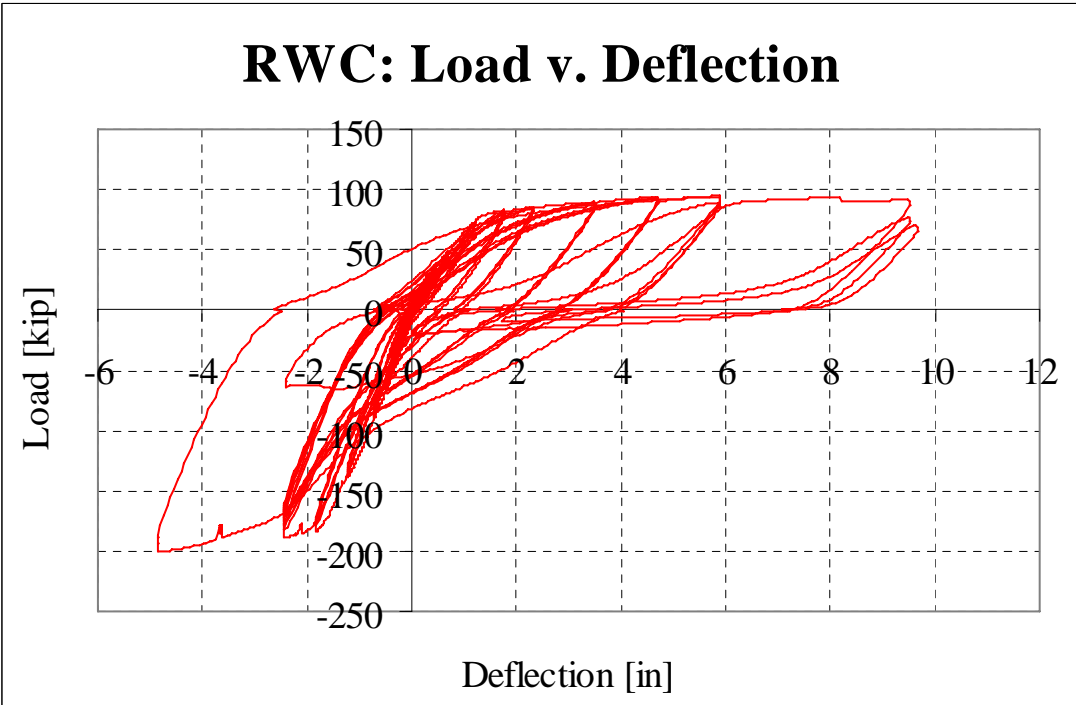


Figure 6.2: Load v. Deflection Relationship of RWC

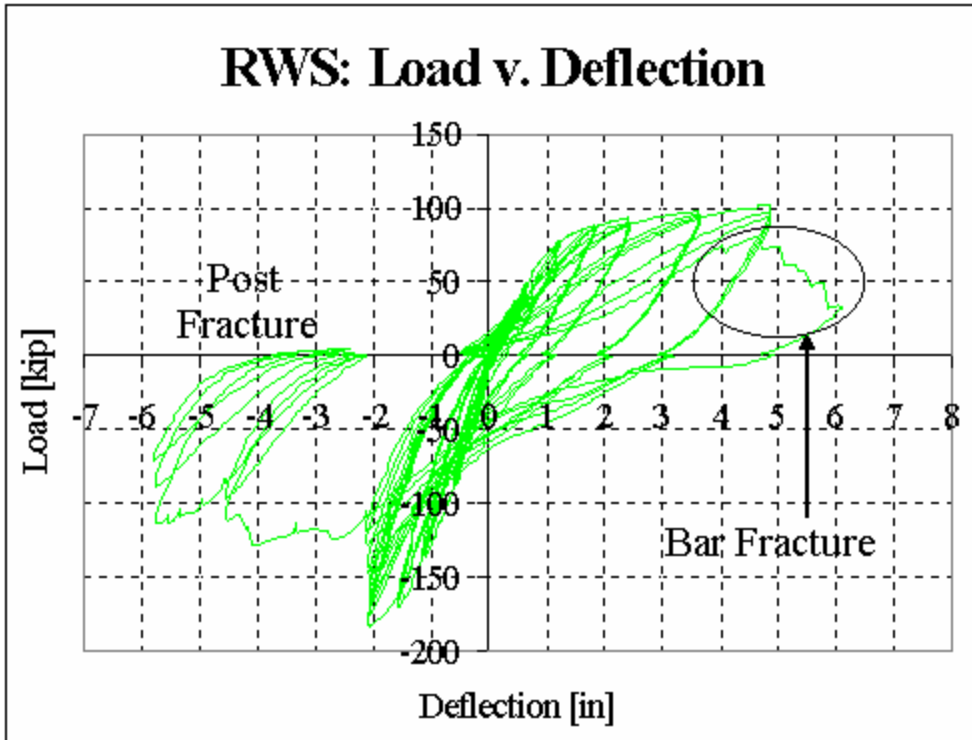


Figure 6.3: Load v. Deflection Relationship of RWS

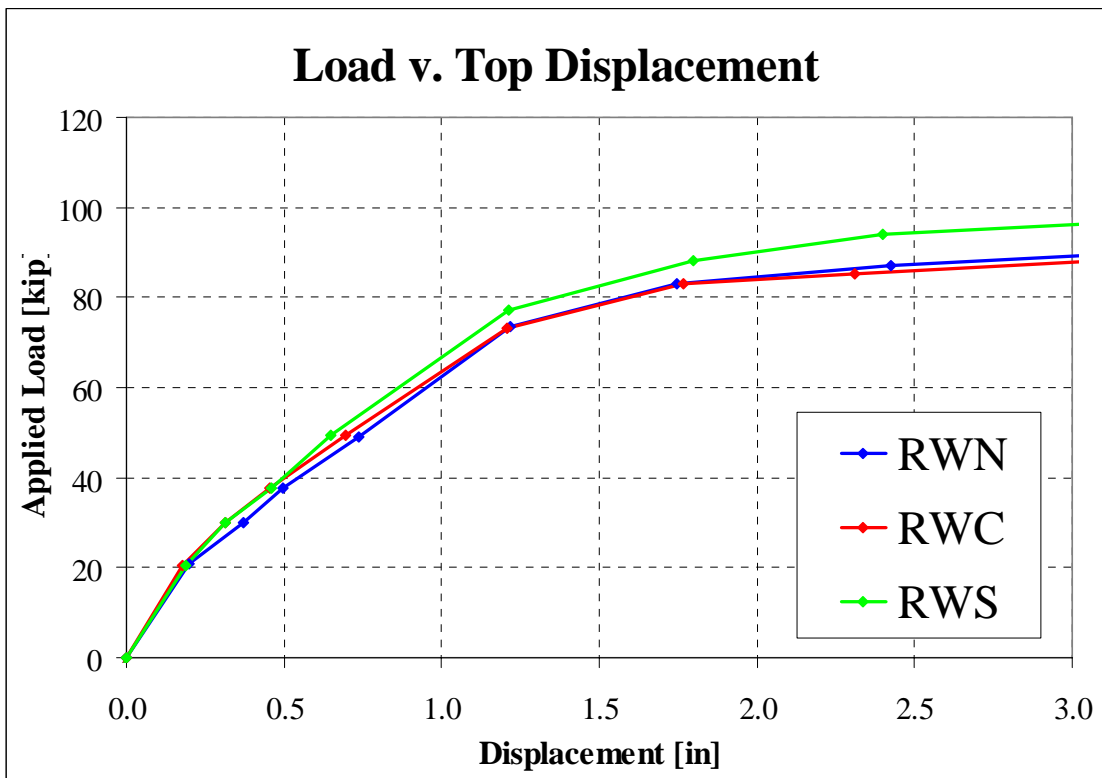


Figure 6.4: Load v. Deflection backbone, No.5&6 boundary element in tension

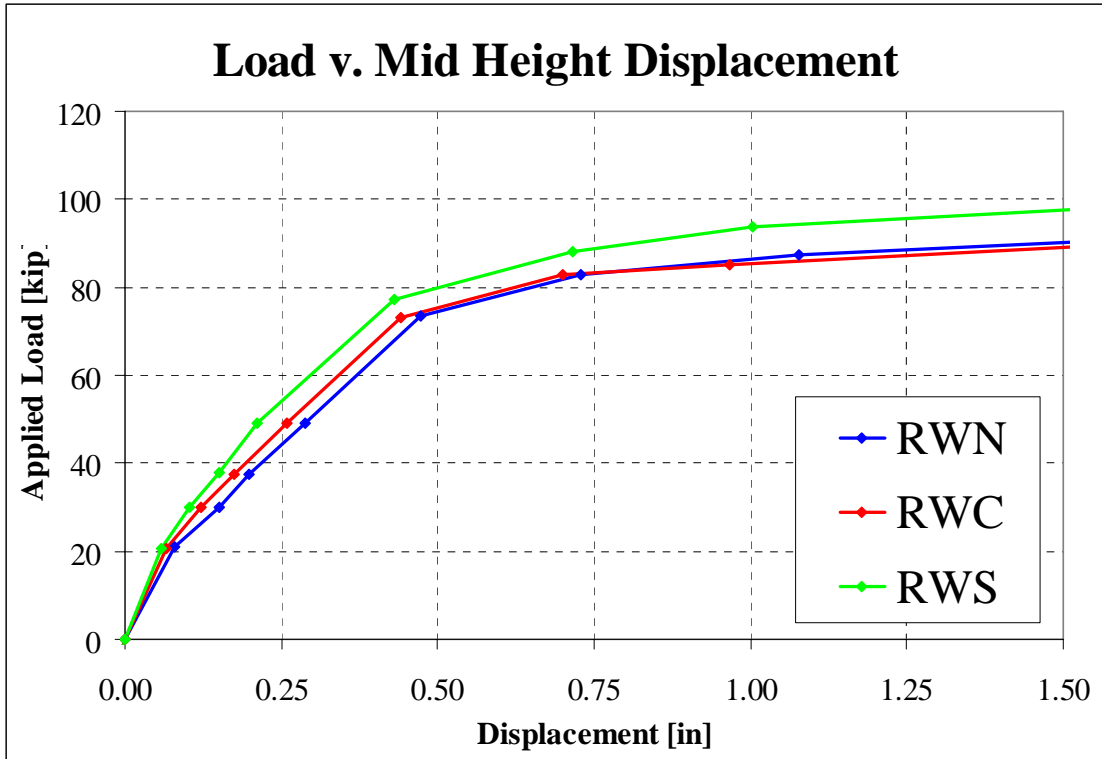


Figure 6.5: Load v. Deflection backbone, No.5&6 boundary element in tension

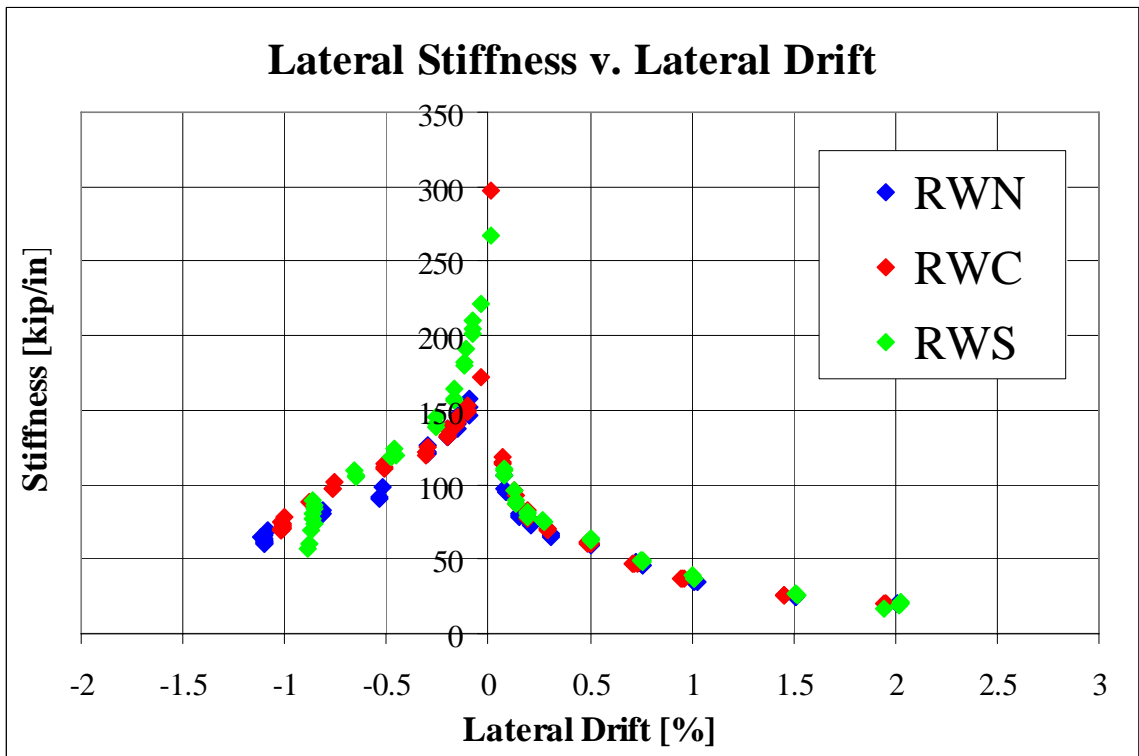


Figure 6.6: Stiffness calculations from tests data.

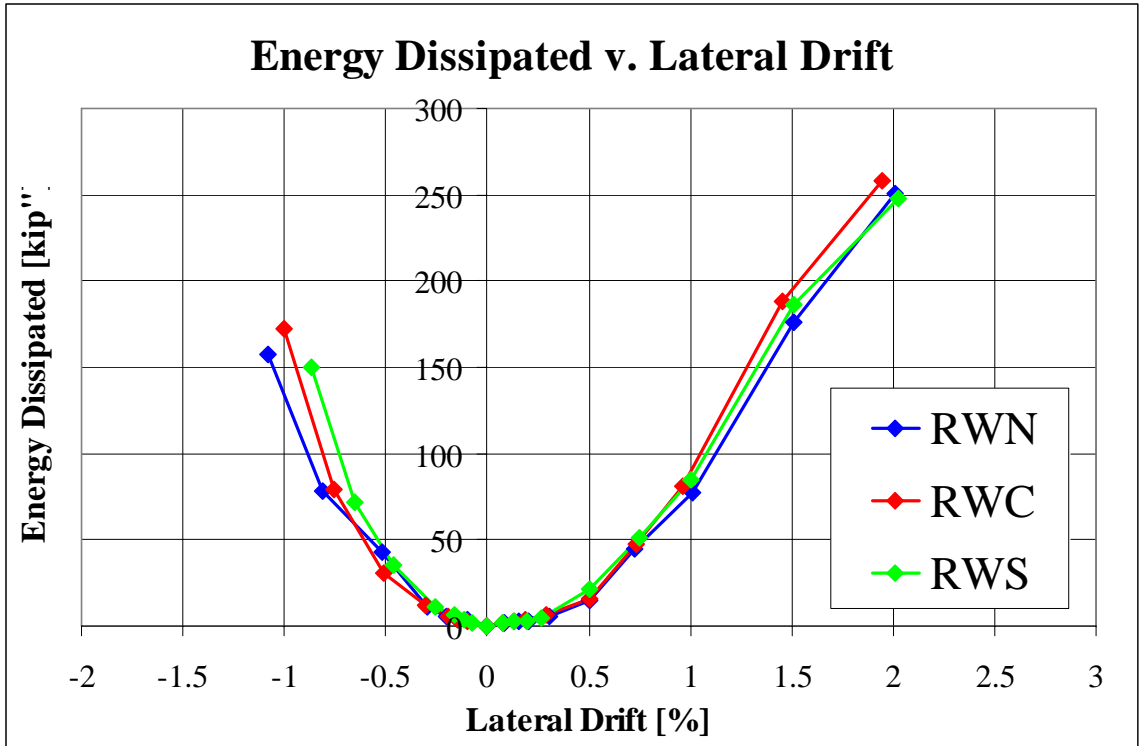


Figure 6.7: Dissipated energy backbone curve.

Chapter 7: Axial Strain from Flexure:

7.0: Introduction

The purpose of this chapter is to determine the validity of the experimental axial strain data. This is done by comparing recorded axial strain distributions along the length and height of the test specimens with predicted values from analysis. The axial strain distributions along the wall length will also be used to compute internal forces and moments with known material properties. These values will be compared with loads and moments recorded from the ancillary actuator used to load the test structure. The strain distributions along the length and heights of each wall will also be used to compare the effects of the various anchorage details. It was found that strain distributions along the wall length are non-linear in the boundary element regions, even in the elastic range of reinforcement. This non-linear distribution was similar for each test specimen and is consistent with deep-beam behavior. Axial strain is reduced along the wall length for heights below the termination of the lapped splices. The percent error of the calculation of internal moments was typically between -13% and 28%.

7.1: Computation of Axial Strains

The axial strain distributions were computed using all four types of sensors used on the test structure. The manners in which the distributions are computed were found to have an effect on the final result. For this reason, several approaches were used in computing the strain distributions. The assumptions and approaches for each method are discussed in detail in Appendix 1. The appendix also covers the reason for some outliers presented in this chapter.

7.2 Axial Strain v. Wall Length

The heights selected to compare strain distributions were based on several factors. It is important to have many sensors at each height of interest to show any variations from a linear curvature. Too few sensors lack the resolution to pick up any deviations from the linear assumption. The heights selected for comparison typically had many sensors of each type. This creates a wealth of information to compare and qualify sensors against each other, compare each wall to analysis, and easily show differences between each test specimen. The heights chosen are 6", 18", 36", and 54" above the foundation. These heights correspond to locations in RWS which all bars are lapped spliced, No. 4's are outside the splice and No.5's are close to the end of the lapped splice, and only the No 9's still spliced. The height of 6" is also chosen to compare the effects of the mechanical splices just outside the connection. Each height is compared at the loading ramp peak just prior to first yielding of each wall. These distributions can be seen in figures 7.1-7.3 and will be referenced specifically in the following sections.

Note that two loading ramps are shown on each plot, one for No.5&6's in tension and one for No.9's in tension. The No.5/6's in tension is shown with diamond point markers and the No.9's in tension is shown with triangle point markers. Also, the No.5&6 BE exists between 0-9" of the wall length and the No.9 BE exists between 78-90" of the wall length coordinates.

7.2.0: BIAX Analysis for Comparison

BIAX, (Wallace, 1989), was used to calculate the moment-curvature response of the general cross-section with known material properties from laboratory tests. The general cross-section is setup as the nominal longitudinal bar locations, confinement locations, and disregards lap splices and mechanical couplers. The results were then used to back-calculate the heights at which the moments would exist in the walls for known load data from the actuator and simple statics. The strain distribution along the wall length, or

curvature, was then plotted against calculated strain data for various heights. The purpose of the BIAX analysis is to simply check that the data for unrealistic values and as a benchmark that can be placed in each plot for comparison. In general, it is useful to see if data is either inside or outside the BIAX envelope in each plot. Axial strain values outside the BIAX envelope suggest a larger internal moment than measured, where values inside the envelope suggest the opposite. A more detailed discussion on the analysis performed with BIAX is covered in appendix AV.

7.2.1 Comparison of Strains v. Sensor Type

The general trends in sensor data was consistent for each wall. In general, strain gages and Krypton LEDs returned values of axial strain that were larger than BIAX predicted strains. The string pots were typically lower than the BIAX predicted strains. This is clear for RWN and RWC. However, RWS varies with height. Below the lapped splices, RWS has significantly lower axial strains. The values of axial strain for RWS are consistent with RWN and RWC outside the splice length. This shows that the data collected with each instrument is valid for further analysis. The only instruments to show significant deviation from other sensors are the LVDTs. This is thought to be caused by strain penetration of the longitudinal reinforcement into the foundation block. This increased larger cracking at the foundation interface from strain penetration is reflected in the displacements recorded by the LVDTs. The strain calculations for the LVDTs used an undeformed length equal to the distance from the top of the foundation block attachment to the wall attachment. The displacement recorded is not entirely the result of strain over the first 12 inches of height. For this reason, the LVDTs can only be used for strain penetration calculations, and not strain and subsequent curvature calculations.

7.2.2 Non-linear Strain Distributions

The assumption of plane sections remaining plane was not necessarily satisfied by the test specimens. This was first noticed with the cracking patterns of each wall. Cracks occurring in the boundary element in tension were typically smaller in width than crack widths directly outside the boundary element. These crack widths then decreased in size as the distance from the boundary element in tension increased. Strain calculation data supports this observation in many instances. The most prevalent examples are the string pot data and Krypton LED data. A plateau of strain from the boundary element in tension is sustained as far as 35 inches into the wall cross section for Krypton LED measurements. The poor resolution of the string pots makes does not allow for verification of this plateau length. However, the same general shape forms with only 3 points. Some cases of a very linear strain distribution are also observed. These cases may not be accurate from few sensors at the height in question, lacking the necessary number of sensors to capture a strain plateau. This non-linear strain distribution will be taken into account in further chapters when calculating curvatures and resulting flexural rotations.

The final figure to take into account is 7.8. This figure shows the lateral deflection measured by each Krypton LED, versus the location of the LED across the length of the RWN. This shows that the lateral deflection increases as the location of the sensor gets further away from the extreme tension face. This change over length is related to the cracking of the section. The largest measured crack from the test notes was given as between 0.016" and 0.02". This happens to be approximately the total change in lateral deflection across the entire section for 19" and 35" high. Also note that the largest incremental change in lateral deflection happens just outside the No.5&6 BE for 19" and 35". This is not the case for 51". The reason it does not occur at 51" is that the crack diagrams show only flexural cracking in the boundary element for this height and load. No cracks were open at this time for 51" to register larger cracking outside the boundary element. As a final verification to show this follows the crack data, the compression block is considered. According to neutral axis estimations from all sensors, the cracks

should be closed around 12” to 15” from the extreme compression face. Figure 7.8 does not show any increase in lateral deflection over this span as the cracks are closed from compression.

7.2.2 Comparison of Anchorage Details

Lapped splices double the amount of steel area in the wall at heights below the splice termination. This doubled steel decreases the necessary axial strain to achieve similar load levels as walls without lapped splices. This is evident when comparing the magnitudes of axial strain at 18” above the foundation for each wall in figures V2.a-c. RWS has each of the longitudinal bars spliced at this height. Comparing the relative magnitudes of strain in the boundary elements while in tension, it is clear that RWS has about half of the strain calculated by RWN and RWC. Using the ‘BIAX’ line as a rule, which denotes the analysis curvature calculated from the measured applied load; a similar trend is noticed when comparing the walls at 36” above the foundation. RWS has lower values of axial strain compared to RWN and RWC. The difference with this height is that the No.4’s in the web have terminated their splices. RWS experiences a slightly larger amount of axial tension strain when the splices terminate. The difference between 18” and 36” is not that significant. This is not the case when examining a height of 54” above the foundation. The tension strain in the No.5&6 BE is drastically increased. This is directly caused by the now complete termination of all lapped splices in the wall with the exception of the No.9’s. Note that the tensile strain in the No.9 BE is still well below that of RWN and RWS. The No.9’s have not terminated at this height and RWS still experiences the benefits of this doubled steel, as seen in figure V.4c. The evidence of the increasing tensile strain in the No.5&6 BE when lap splices terminate, along with the continued small tensile strains in the No.9 BE show that the lapped splices play a considerable role in the strain distributions of RWS. This decrease in axial strain plays a role subsequent curvature and rotation calculations.

7.3 Axial Strain v. Wall Height

The purpose of this section is to examine the changing strain values of the walls with height. The same load levels are used for this section as the figures for section 7.2. Sensors toward the extreme compression and tension fibers were chosen to plot over height. This was a simple matter of comparing the ‘largest’ magnitudes of tension and compression at the same time. The axial strain versus wall height reinforces the conclusions from section 7.2.2. RWS has a reduced strain magnitude while at heights of a lapped splice. This can be seen in figures 7.5a-c and figures 7.6a-c. RWN and RWC are outside the BIAX envelope for tension in the boundary elements. RWS is clearly bounded by the BIAX envelop for tension in the splice lengths. This first termination occurs at 21” above the foundation interface. It is not surprising to see the tensile stress increase as the height increases. More splices terminate until 45”, at which all bars in tension are outside their respective lapped splices. Shortly after the termination, at 63” of height, the strain is no longer increasing and begins to decrease with height. The height at which the strain stops increasing with height may be misleading from the analysis technique used for top and bottom row of the LED fields. This value is most likely smaller than shown, as no LEDs are present to balance with the elements bellow the top sensor. Knowing this, it is quite clear that the behavior of RWS is consistent with RWN and RWC outside the splice lengths. Each wall records approximately 0.002 for the maximum tensile strain at 60”.

The plots of the No.9 BE in tension further validate the strain profile for wall heights inside and outside the lapped splices. The Krypton LEDs do not go high enough to measure displacement outside the No.9 splice length. There is no abrupt change in the strain profile from the LEDs, as expected. The string pots above the splice length do record an increase in strain. This strain outside the splice length is again very close to RWN and RWC.

There is an exception for RWC with No.9's in tension. In this case, the Krypton returns smaller values at lower heights and the string pots are very close to the BIAX result. Note that this is not the undisputed maximum tensile stress. Figure 7.2b shows that a larger tensile strain reading is calculated just inside the points used for plotting. The bottom portion of this plot is somewhat misleading in that respect; but still possesses value in describing the wall response. This lower strain may be the residual effect of the mechanical couplers of RWC, which are high as 7" in the wall before the discontinuity ends. Also, the compressive strain measured by the Krypton for RWN is quite high for the top of the LED field. This is due in large to the analysis technique of over-predicting strains at the top of the LED field and some poor data sources. This is discussed further in appendix 1.

7.4 Internal Moments and Forces

The internal moment at each height was computed in order to compare with what should exist from known top load data. This was done for each sensor at select heights and loads. The internal moment was computed by first determining the strain at each bar location. This strain was then converted to stresses and forces from known material properties. The difference between the total tension in the steel and total compression in the steel was assumed to be carried by the concrete. Once the force distribution was known, the centroid of the tension and compression forces was computed. This required additional assumptions about the concrete force centroid. The load levels selected to do this comparison were chosen to be in the elastic range of both the steel reinforcement and concrete. Knowing this, the centroid of the concrete force was chosen to be the centroid of the strain distribution of the concrete. The moment was computed as simply the difference between the coordinates of the compression and tension force centroid and the total tension force. All strains were assumed to be linear between measured strain values. The moment calculated was then used to determine what the applied top load should be. A percent error between the calculated and measured top load is presented in figures 7.7a-c.

General trends emerged when doing such a calculation. First, the strain gages seem to give a larger calculation of top load than any other sensor. The exception to this is RWS, where the large number of strain gages on both bars provided excellent insight to the strains actually experienced in the walls. The Krypton LEDs seem to be the most consistent data source ranging between 0 and 60% error with a few outliers. Lastly, the string pots seem to have difficulty registering tensile strain as large as the other two sensors. This is seen in a consistent negative percent error. The string pots had the closest values to the measured load more often, but also returned large discrepancies from the No.9's in tension to the No.5&6's in tension directions. The reasons for which are unclear, but may have something to do with cracking occurring and the attachment giving way slightly.

7.5 Summary of Findings

This chapter covered the axial strain distributions along the wall height and length. These distributions seem to show prevalence of deep beam action from a non-linear strain gradient in certain cases and observed cracking patterns. This has ramifications on the calculation of curvatures and consequent rotations. The sensors were in close agreement about magnitudes of strains along both the height and length. This was observed between each test specimen as well, when no discontinuities are present in the reinforcement. Most importantly, the decreased axial strains from lapped splices was well documented through multiple sources. This decrease in axial strain decreases the curvature at the base of RWS and ultimately, flexural rotation of the base. These effects will be further explored in the following chapter.

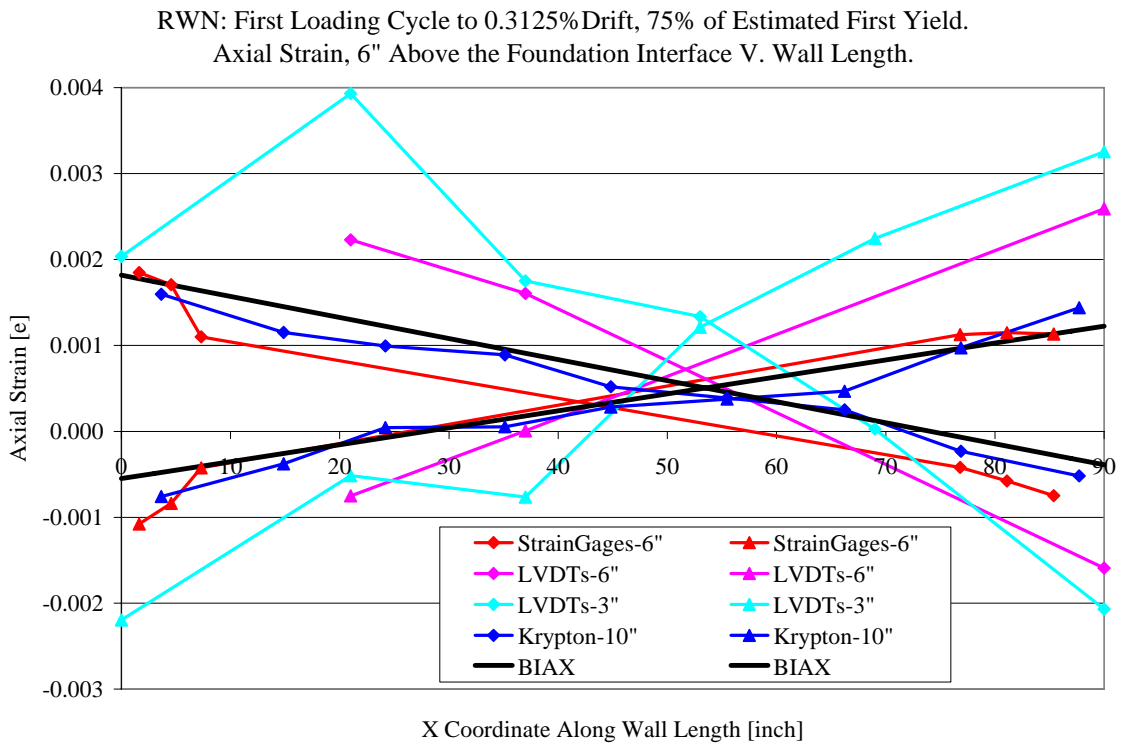


Figure 7.1a: RWN: Axial strain along wall length, 6" above the foundation

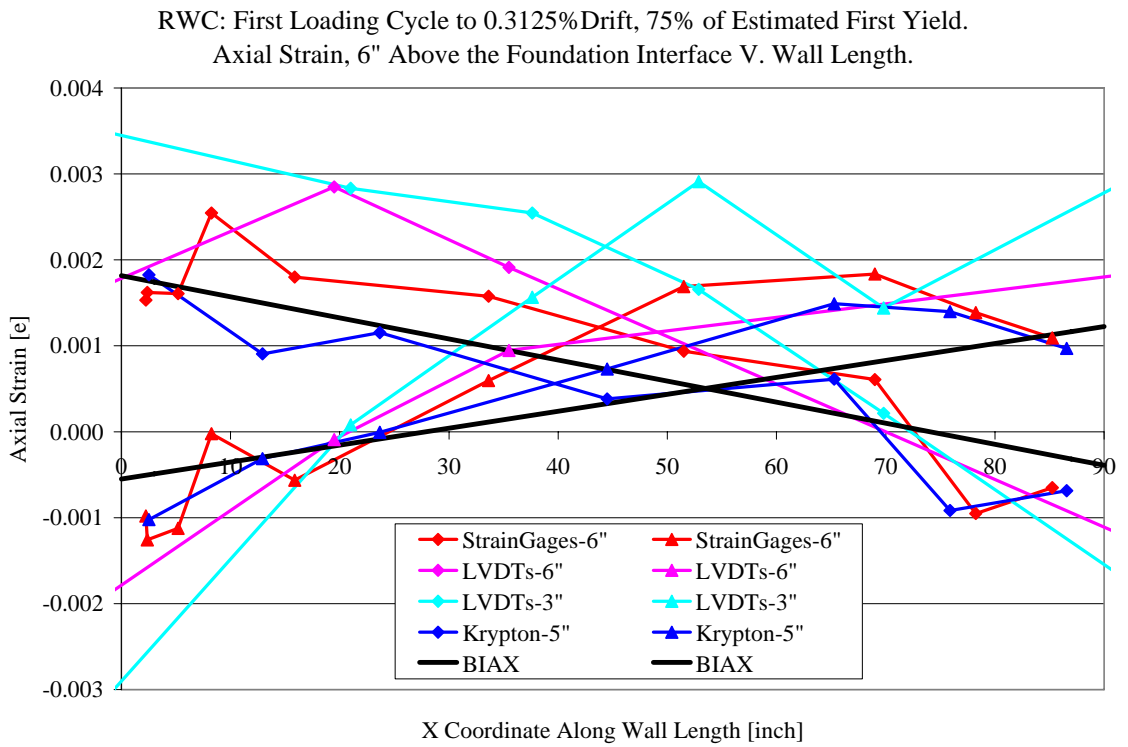


Figure 7.1b: RWC: Axial strain along wall length, 6" above the foundation

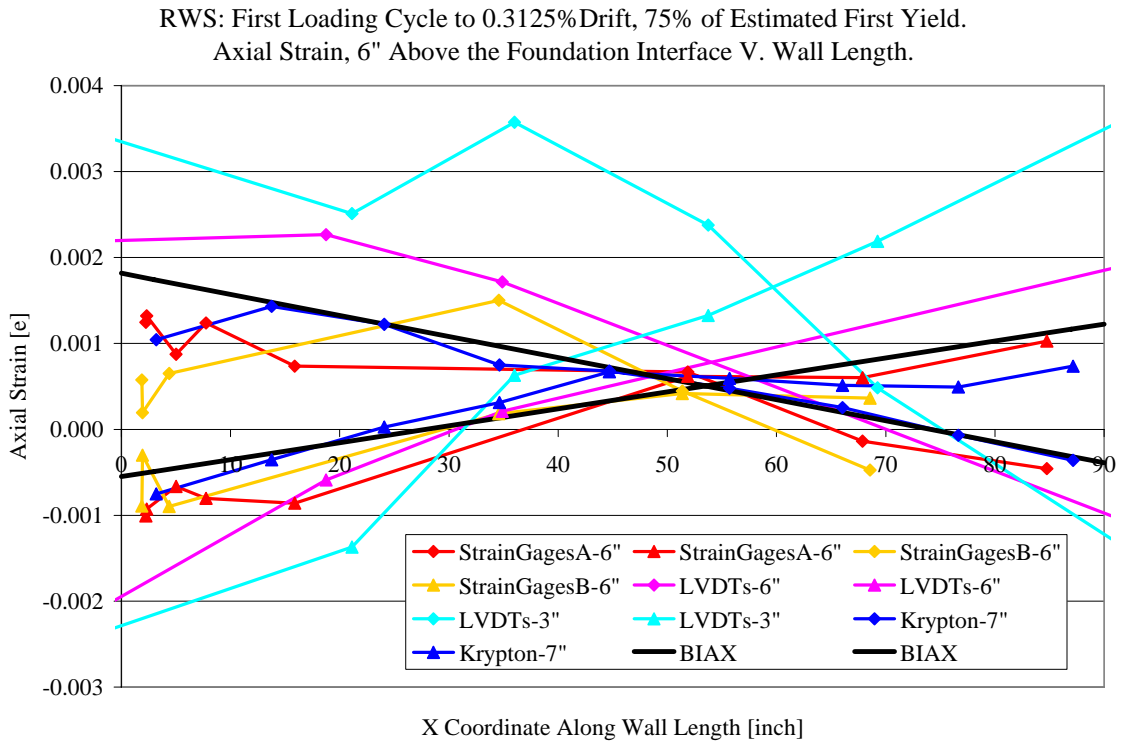


Figure 7.1c: RWS: Axial strain along wall length, 6" above the foundation

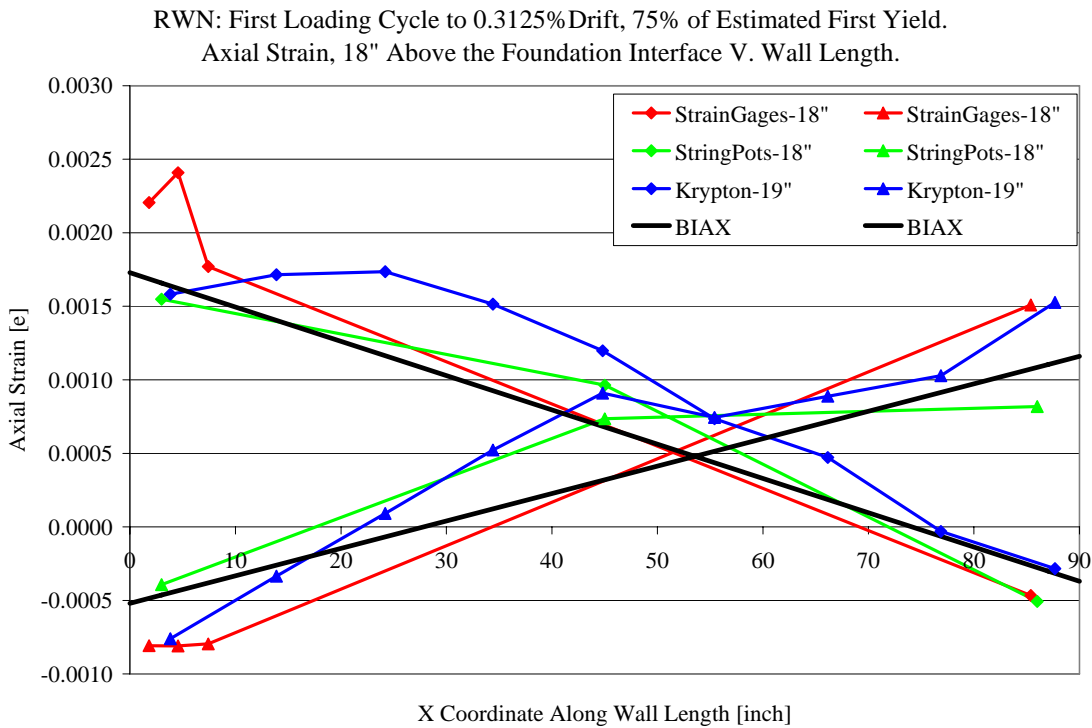


Figure 7.2a: RWN: Axial strain along wall length, 18" above the foundation

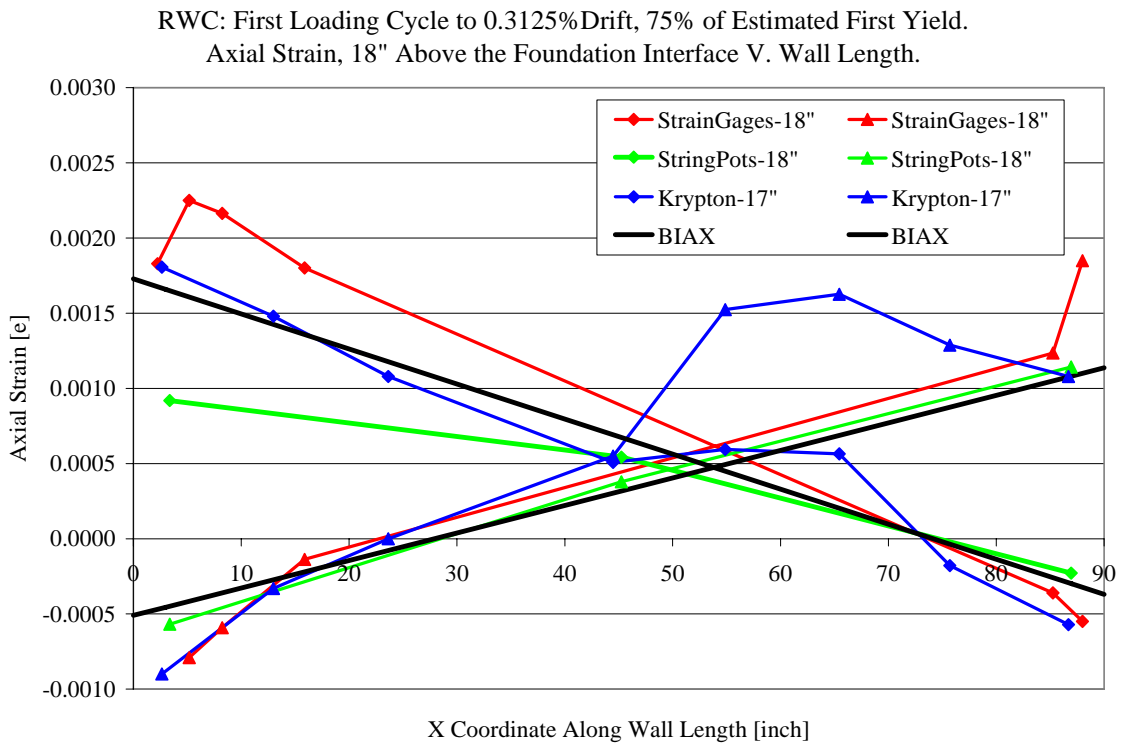


Figure 7.2b: RWC: Axial strain along wall length, 18" above the foundation

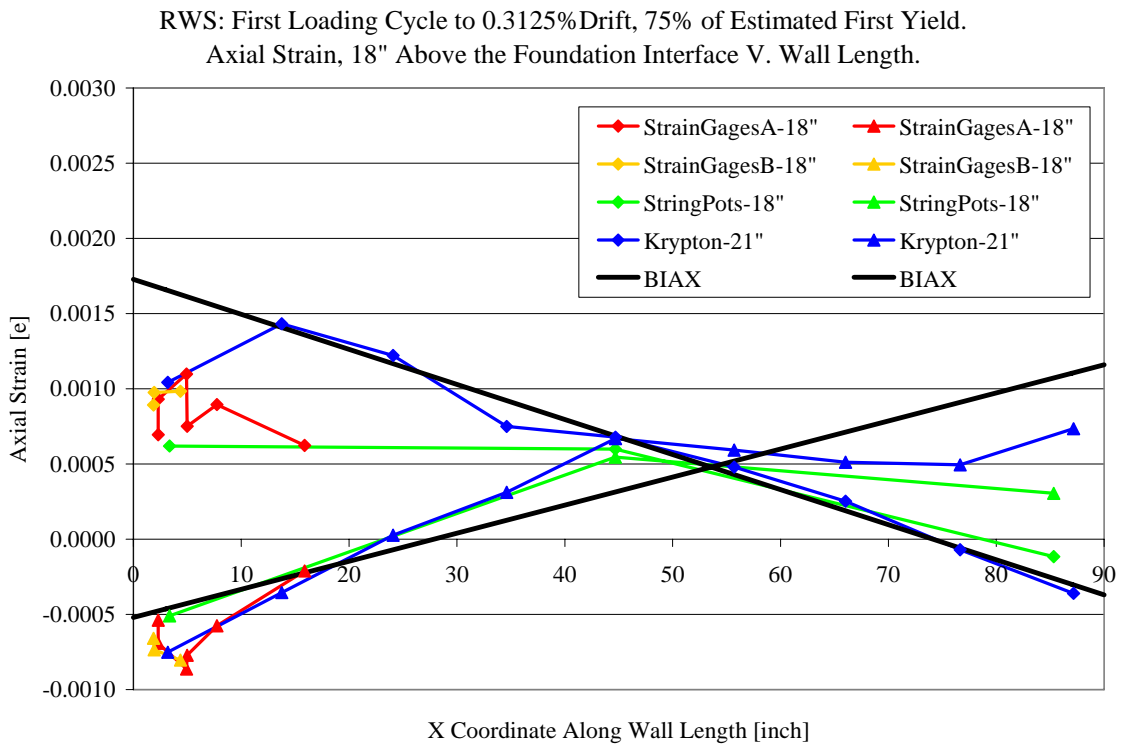


Figure 7.2c: RWS: Axial strain along wall length, 18" above the foundation

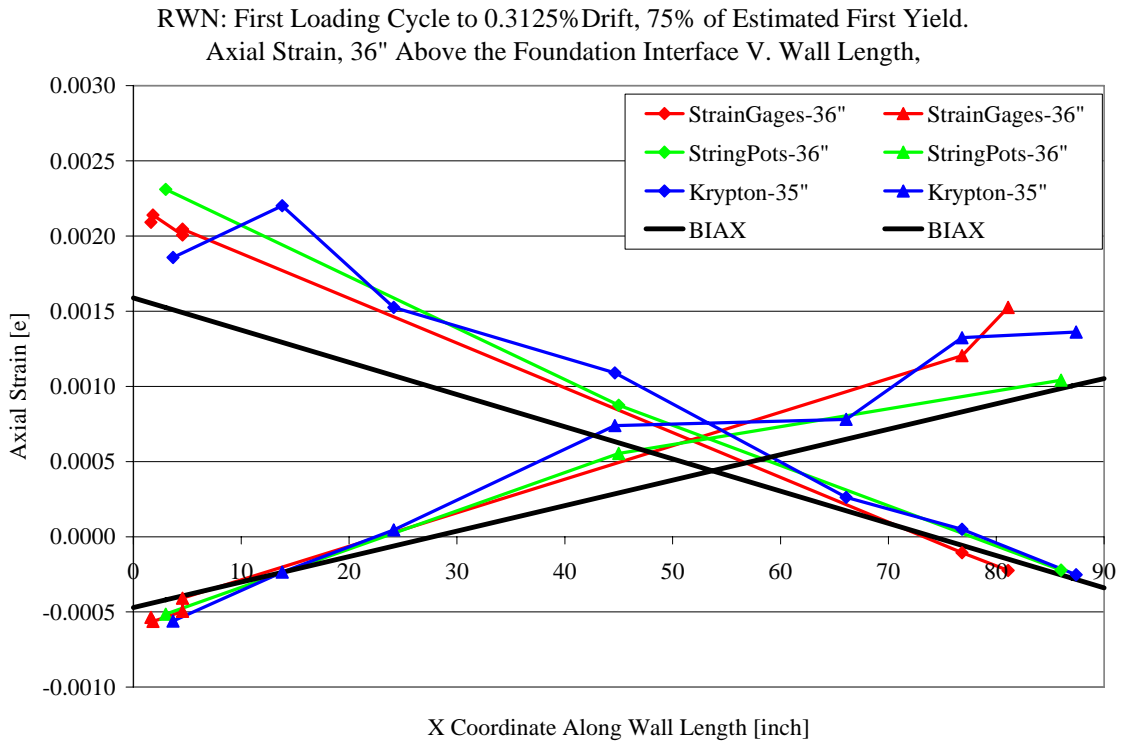


Figure 7.3a: RWN: Axial strain along wall length, 36" above the foundation

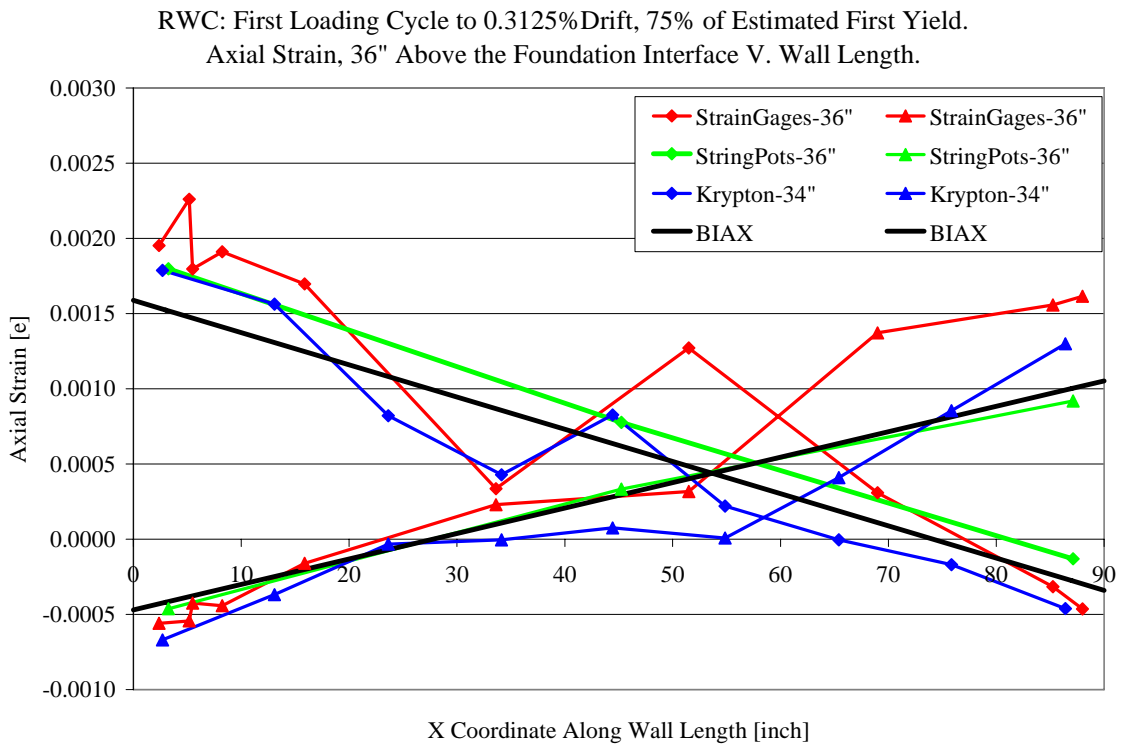


Figure 7.3b: RWC: Axial strain along wall length, 36" above the foundation

RWS: First Loading Cycle to 0.3125% Drift, 75% of Estimated First Yield.
 Axial Strain, 36" Above the Foundation Interface V. Wall Length.

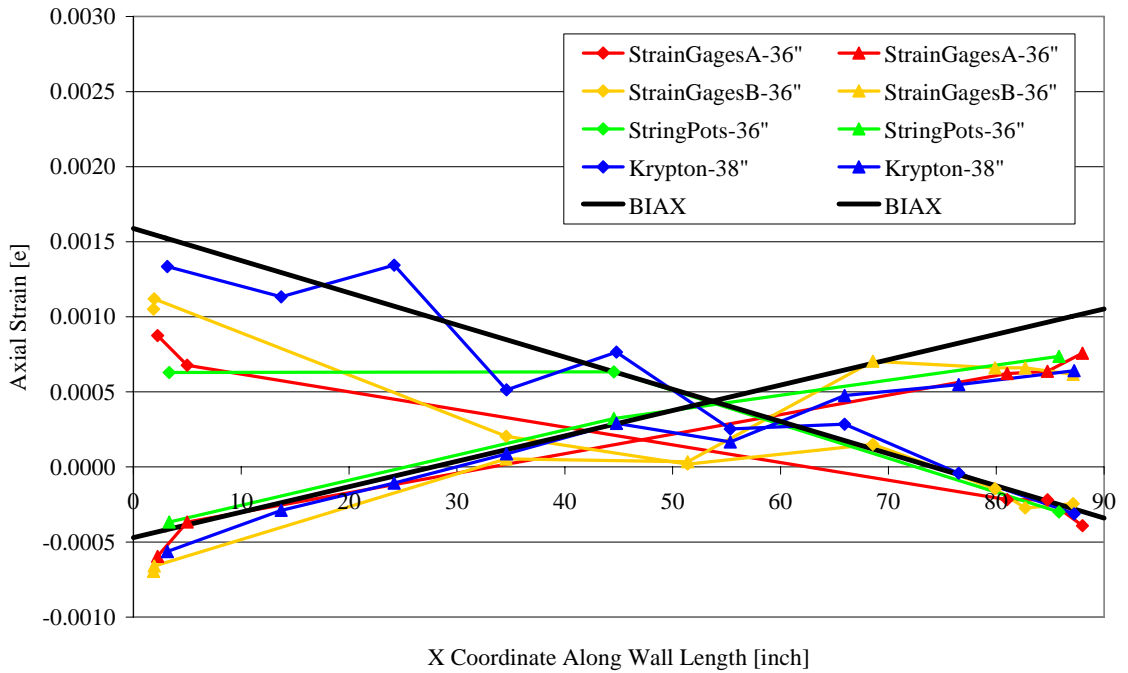


Figure 7.3c: RWS: Axial strain along wall length, 36" above the foundation

RWN: First Loading Cycle to 0.3125% Drift, 75% of Estimated First Yield.
 Axial Strain, 54" Above the Foundation Interface V. Wall Length,

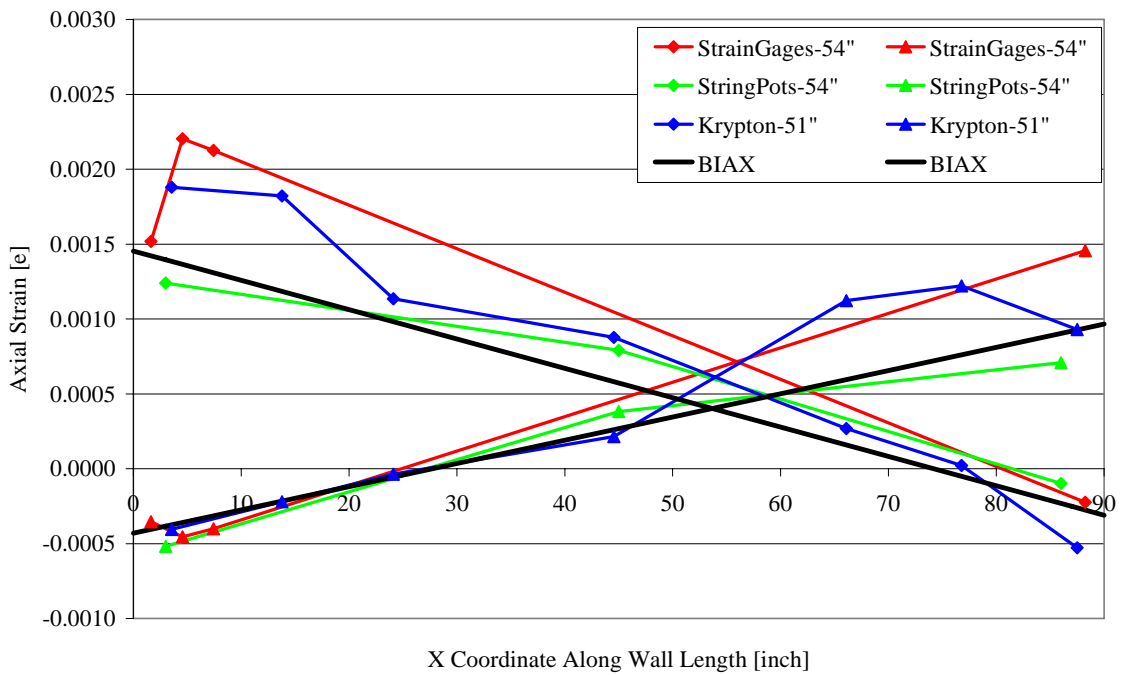


Figure 7.4a: RWN: Axial strain along wall length, 54" above the foundation

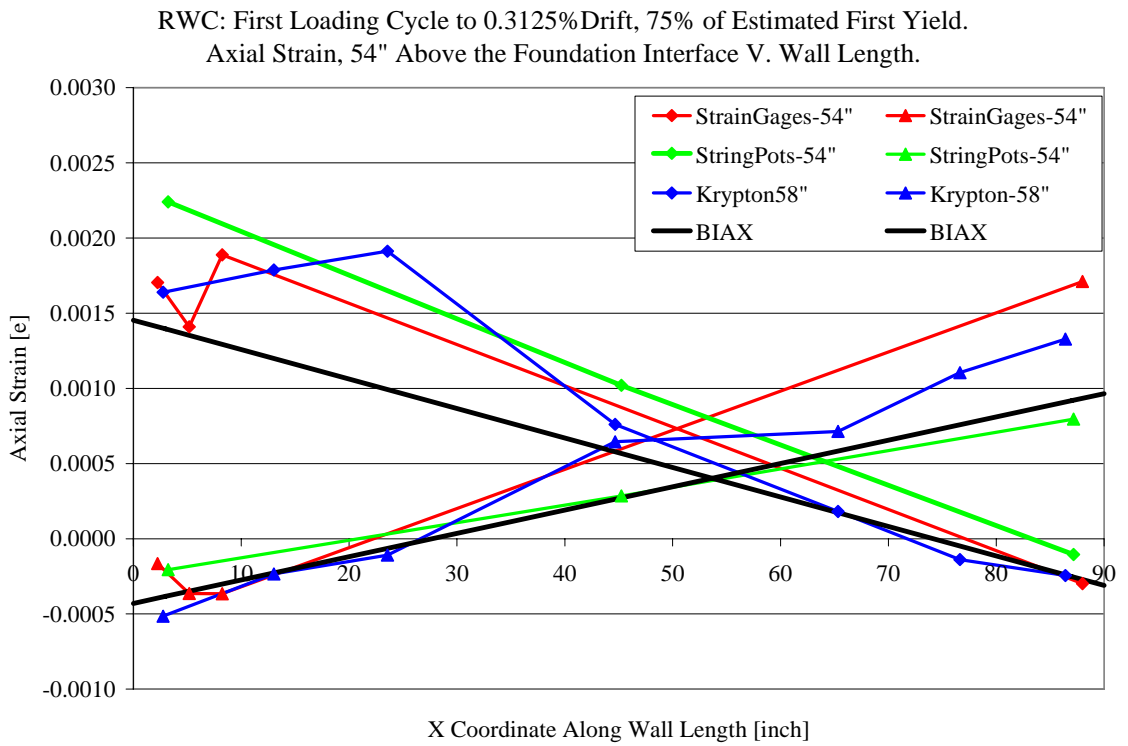


Figure 7.4b: RWC: Axial strain along wall length, 54" above the foundation

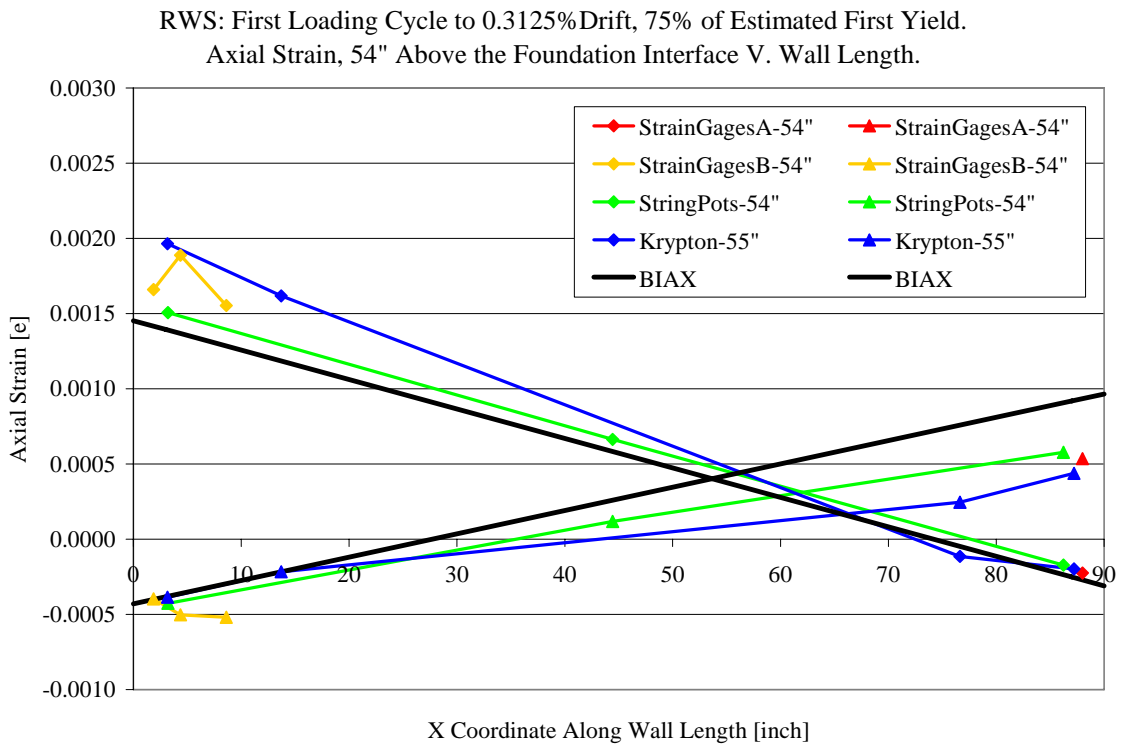


Figure 7.4c: RWS: Axial strain along wall length, 54" above the foundation

RWN: First Cycle to 0.3125% Drift, 75% of Estimated Yield. Axial Strain V. Wall Height, Sensors Closest to Extreme C/T Faces. No. 5/6 BE in Tension.

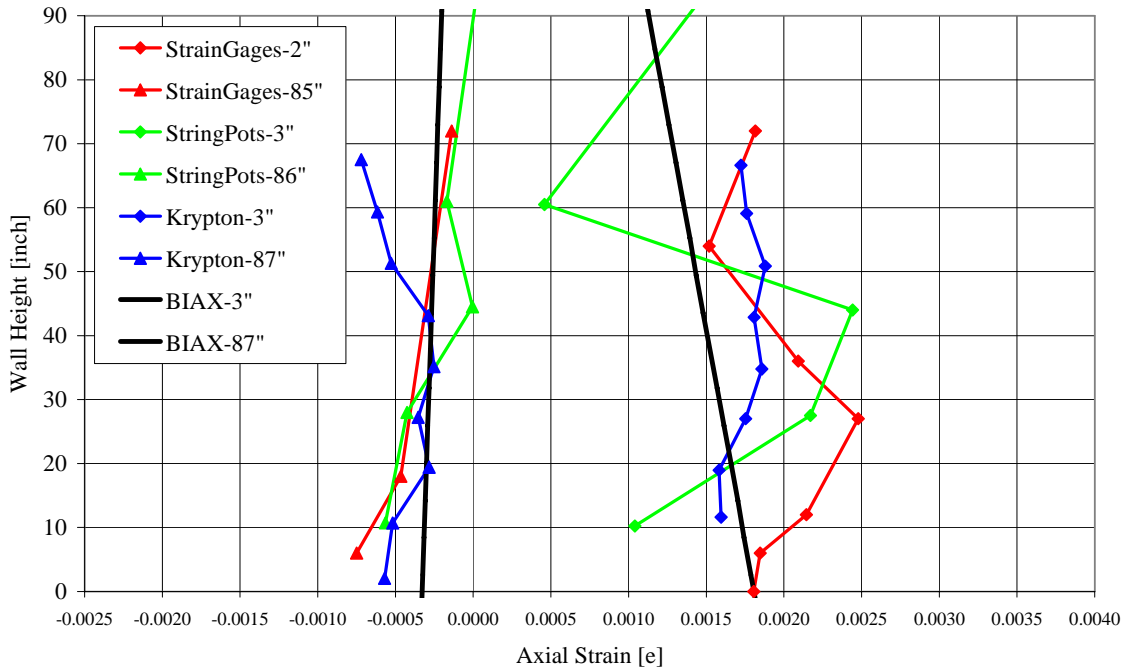


Figure 7.5a: RWN: Axial strain along wall height

RWC: First Cycle to 0.3125% Drift, 75% of Estimated Yield. Axial Strain V. Wall Height, Sensors Closest to Extreme C/T Faces. No. 5/6 BE in Tension.

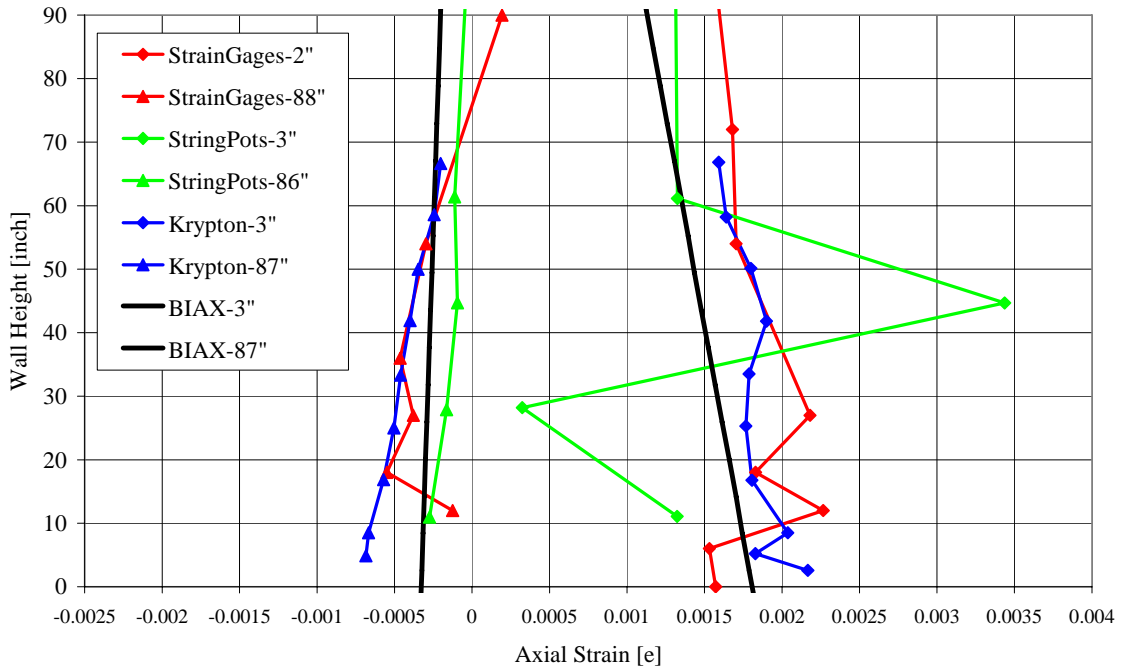


Figure 7.5b: RWC: Axial strain along wall height

RWS: First Cycle to 0.3125% Drift, 75% of Estimated Yield. Axial Strain V. Wall Height, Sensors Closest to Extreme C/T Faces. No. 5/6 BE in Tension.

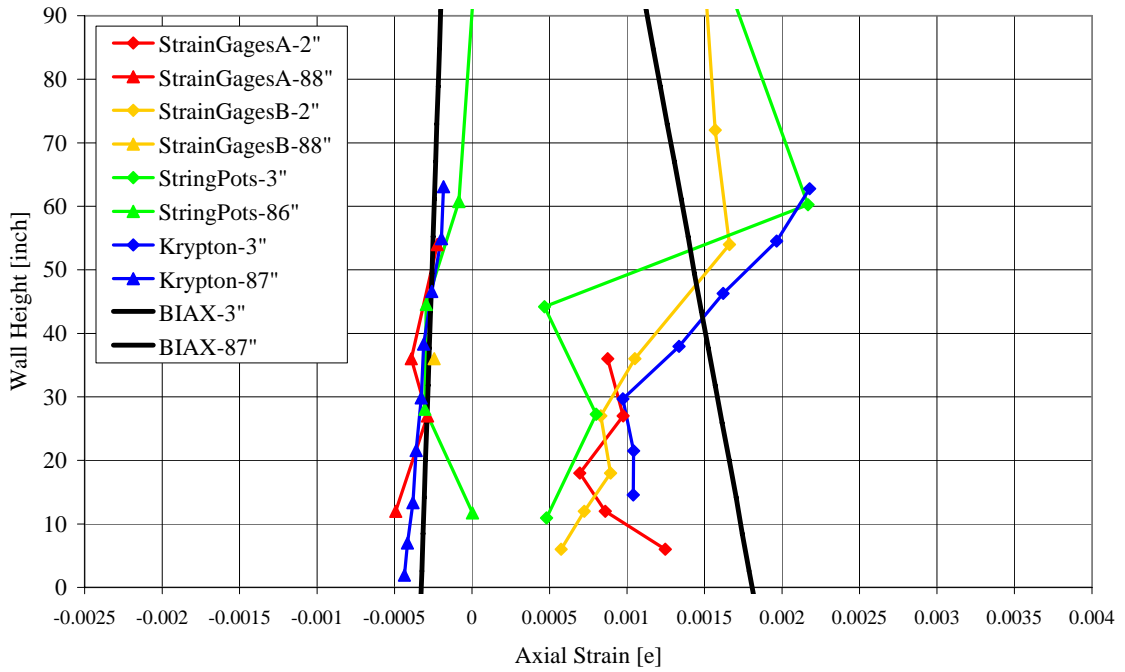


Figure 7.5c: RWS: Axial strain along wall height

RWN: First Cycle to 0.3125% Drift, 75% of Estimated Yield. Axial Strain V. Wall Height, Sensors Closest to Extreme C/T Faces. No. 9 BE in Tension.

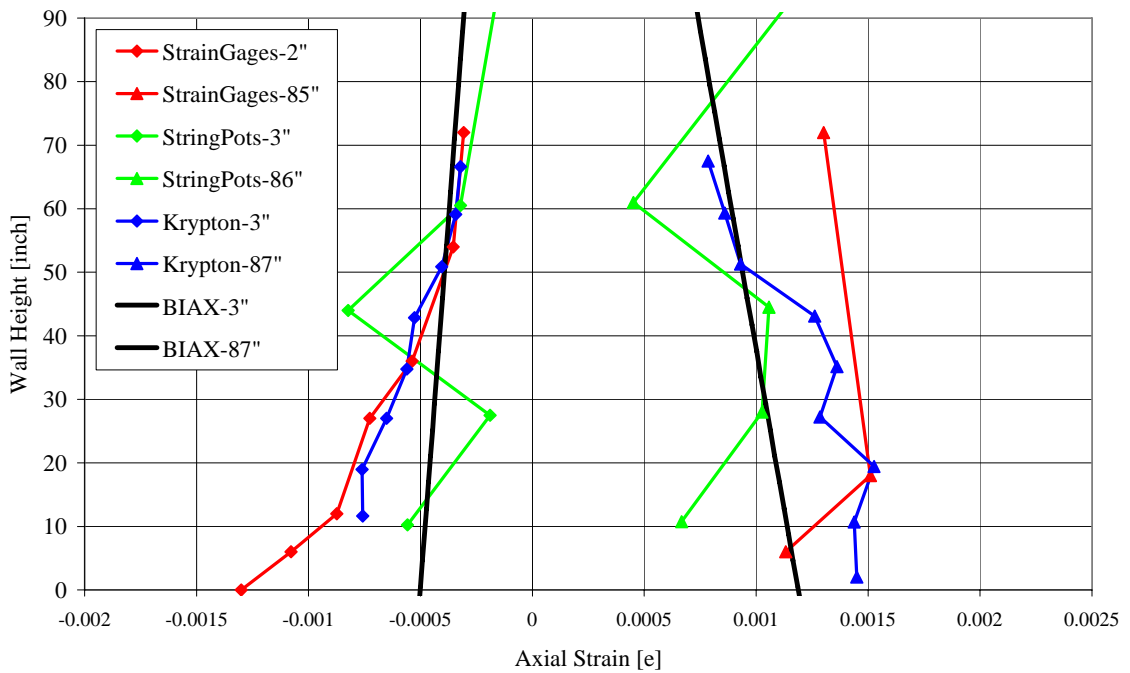


Figure 7.6a: RWN: Axial strain along wall height

RWC: First Cycle to 0.3125% Drift, 75% of Estimated Yield. Axial Strain V. Wall Height, Sensors Closest to Extreme C/T Faces. No. 9 BE in Tension.

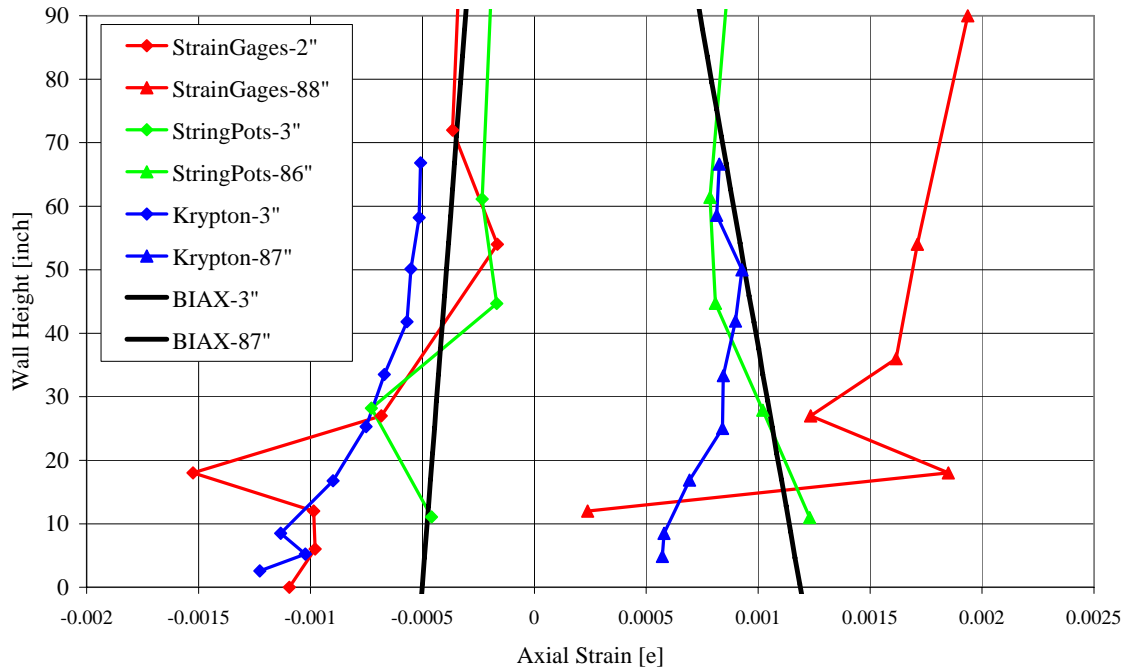


Figure 7.6b: RWC: Axial strain along wall height

RWS: First Cycle to 0.3125% Drift, 75% of Estimated Yield. Axial Strain V. Wall Height, Sensors Closest to Extreme C/T Faces. No. 9 BE in Tension.

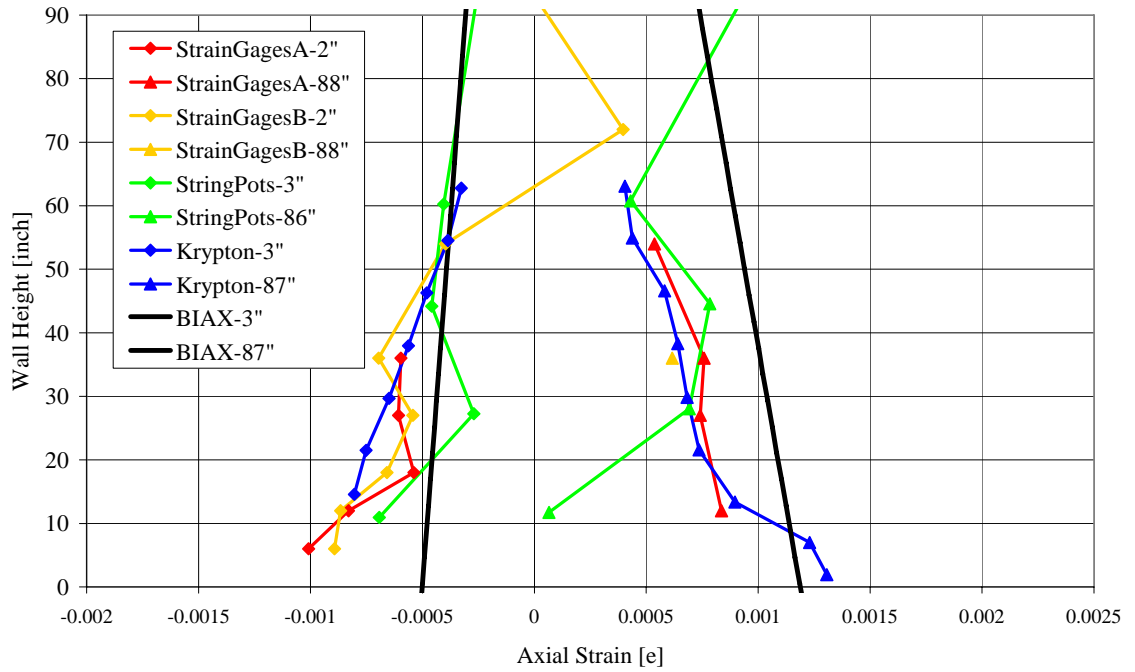


Figure 7.6c: RWS: Axial strain along wall height

RWN: %Error of Calculated & Measured Top Load V. Top Drift

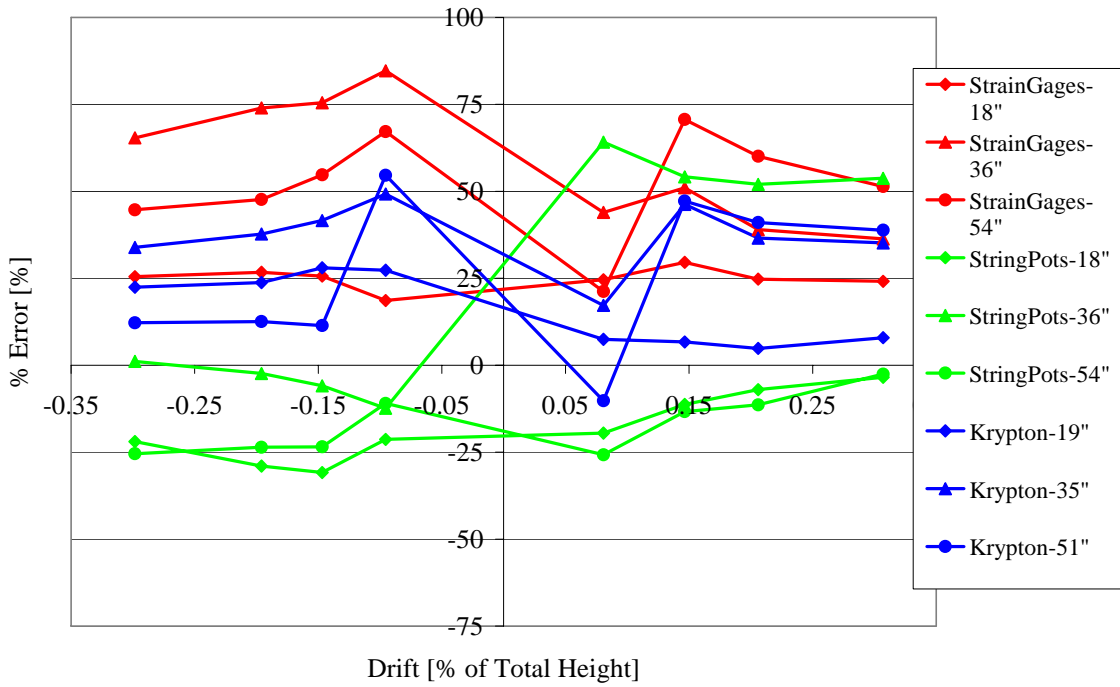


Figure 7.7a: RWN: % Error of internal forces compared to actuator data.

RWC: %Error of Calculated & Measured Top Load V. Top Drift

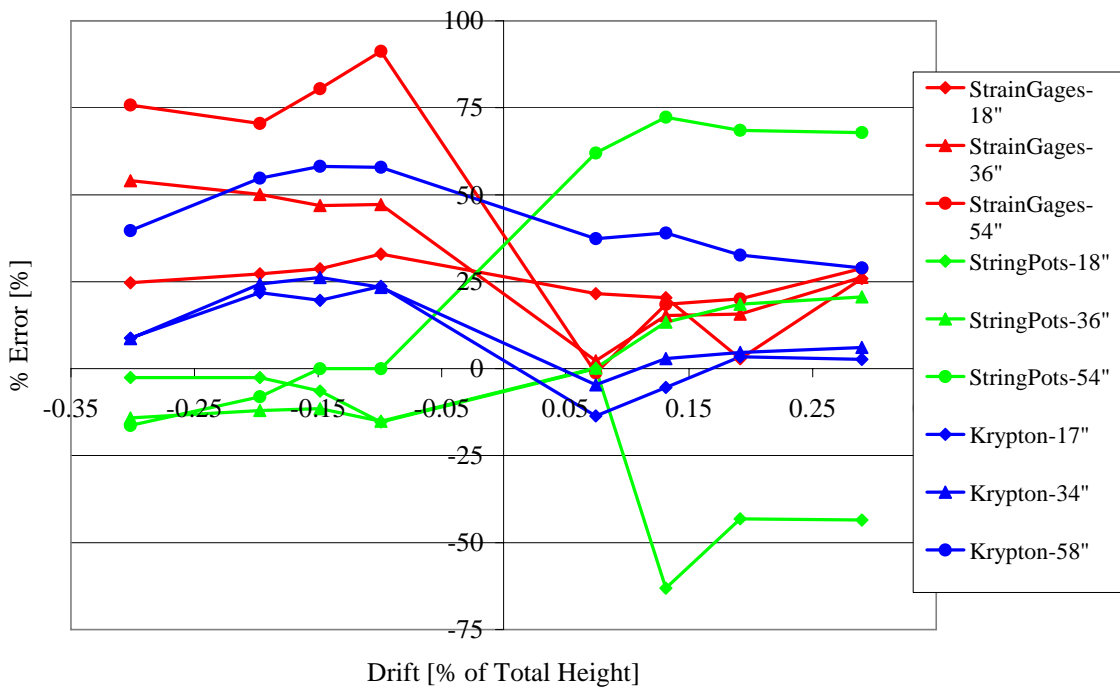


Figure 7.7b: RWC: % Error of internal forces compared to actuator data.

RWS: %Error of Calculated & Measured Top Load V. Top Drift

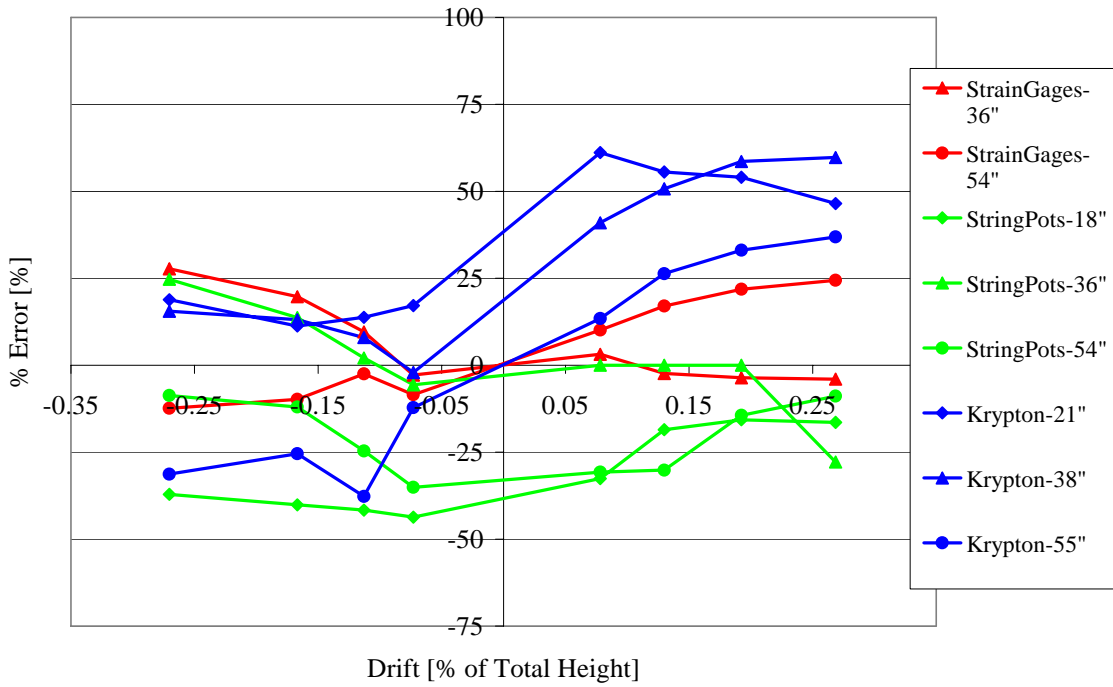


Figure 7.7c: RWS: % Error of internal forces compared to actuator data.

RWN: Lateral Deflection vs Length Along the Wall

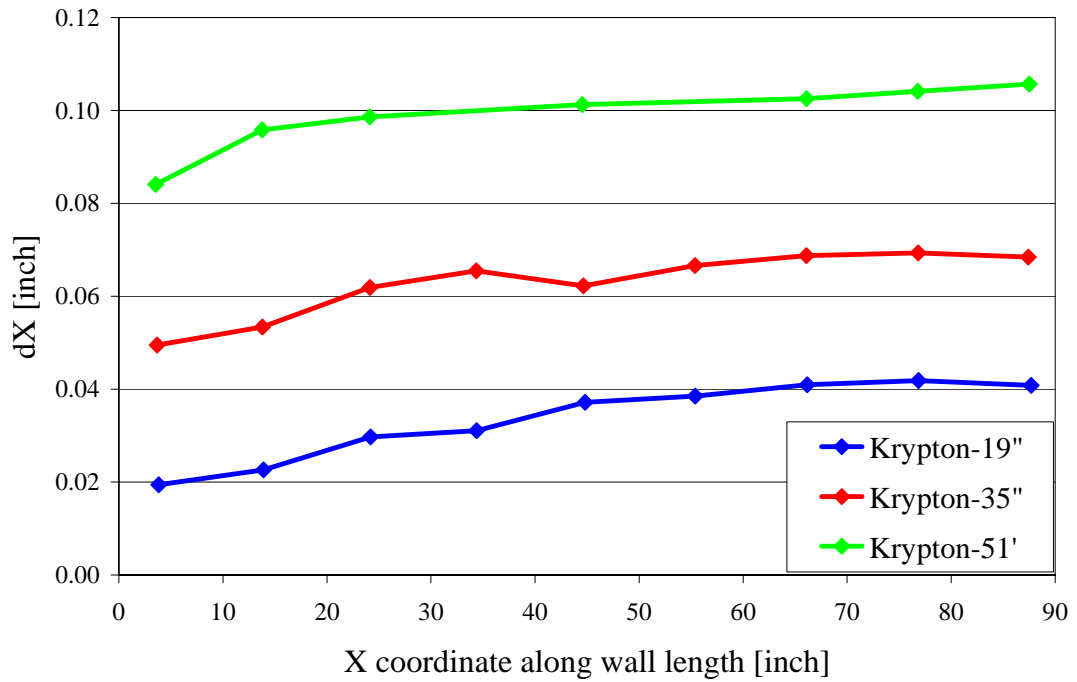


Figure 7.8: RWN, crack pattern verification & deep beam action.

Chapter 8: Moment v. Curvature Relationships

8.0: Introduction

Experimental test data was used to determine the curvature resulting from flexural loads. This was done in an effort to determine the effect of mechanical and lapped splices on cross-section behavior through longitudinal bar discontinuities. The resulting effects have a significant impact on the total flexural rotation undergone by each specimen, as well as the centroid of rotation with respect to height of interest. The curvature relationships are examined in this chapter as a means to discover the differences in observed load v. displacement responses of each wall. The curvatures reported in this chapter are verified through multiple sensors, using various rational methods of calculation. In general, it was determined that curvature is significantly reduced within the height of the lapped splices. In addition, the resulting stress/strain concentrations outside the lapped splices lead to a slightly increased curvature. The result of such behavior leads to a reduced total flexural rotation and a center of rotation higher than that of continuous bars. This change in response creates a reduced flexural deformation, discussed in future chapters.

8.1: Calculation of Curvature

Axial strain was computed for each sensor with a range of methods. This is discussed in detail in chapter and appendix 1. The gradient of the calculated axial strains (curvature) was then computed for each height where enough sensors were present to perform a reliable calculation. Three methods were used to create an envelope of possible results. The assumptions and resulting impacts of these methods are discussed in great detail in appendix 2.

Examination of these methods lead to the selection of two which represent the wall behavior most accurately. The first method is based on fitting a linear trend line through the strain data, using the all strain data through the cross section. This method is referred

to as the “whole cross section”, or “WC” method. This method is thought to have underestimated the true curvature at the base of the wall, where a non-linear gradient was often observed over the bottom three feet of height. This situation called for another method that would give an upper bound to the resulting curvature. The second method fit a linear trend line through the portion of the strain gradient which was larger for the compression zone. This was extended to the centerline of the wall for uniformity of approach. The second method is referred to as the “compression half cross section”, or “CH” method. The “CH” method is also prone to overestimating curvature in RWS to a far greater extent than RWN and RWC. This is due to the fact that the compressive strains observed in RWS did not differ a great deal from RWN and RWC. This is discussed in great detail in chapter 7. Secondly, the CH method incorporates the effects of increased axial strain from the termination of the longitudinal reinforcement in web, but misses the still decreased axial strain in the tension boundary element from the lapped splices. This leads to additional increases of curvature for RWS.

Both methods are unable to detect the true value of strain below the bottom row of instruments for Krypton data and string pot data. This can lead to an underestimation of the curvature at the base. The effect of this issue is a reduced total curvature and a higher center of rotation than the “true” behavior. In such a situation, it is useful to compare the calculations to that of the strain gages, which record the axial strain directly at the base of the walls. In general, the Krypton and string pots returned a curvature value lower than that of the strain gages. This discrepancy is however, within reasonable tolerances.

8.2.0: Comparison of Curvature From Various Sensors

The goal of this section was to verify the curvature calculated for each wall at select drift levels by comparing the curvature calculated by different sensors. Agreement between sensors for each individual wall indicates that the results are indeed reliable for comparisons between walls. Three significant loading ramp maximums have been selected for this comparison. The loading ramps of interest are 0.3% top drift, where the

walls were at their elastic limit; 0.75% drift, where the walls were well into their inelastic range; and 1.5% drift in the No.5&6 boundary element in tension and 1% drift in the No.9 boundary element in tension, where the walls were highly inelastic and most sensors were still giving reliable readings. The % drift reported is the approximate drift, but varies slightly between each wall. Also, the increased stiffness in RWS lead to slightly larger top loads at these target drift levels. All drifts shown are within 1% of each other and top load is within 4% of each other. All results are compared to a BIAX analysis using known material properties from the test specimens.

Comparisons of curvature calculated by different sensors are plotted against the height of the sensors used. The curvatures calculated are again compared to BIAX, where the moment v. curvature used to back-calculate the corresponding height v. curvature relationship from the known top load and statics. The top load used for each calculation was the top load recorded for each wall at the designated drift level. The height v. curvature relationships can be seen in figures 8.1 through 8.3.

8.2.1: Comparison of Curvature From Various Sensors

The calculations of curvature from various sensors follow a very similar trend in the elastic range for each wall. It is clear that each sensor is returning curvature values with consistent trends and magnitude over height. Some outliers do exist, but this is to be expected with a large volume of experimental data. This is most noted for the Krypton data, “CH” method, where much fewer sensors are used when compared to the “WC” method. Note that there are many instances where the Krypton “WC” method has the same value as the “CH” method. This is due to heights where too few sensors existed through the web of the wall and a “CH” calculation could not be done.

8.2.2: Comparison of Curvature at the Wall Interface

The limitations of the instrumentation did not allow for an accurate calculation of curvature at the foundation/wall interface. More specifically, the curvature at the bottom row of LEDs and string pot attachments underestimate the curvature. This is best illustrated when comparing the elastic limit of RWN and RWS. According to the Krypton data, the curvature is approximately 0.00002 radians per inch. The same calculation with the strain gages is 0.000028 radians per inch. This is an increase of 40%. The Krypton is unable to measure the larger curvature at the interface, where the strain gages give a direct reading, absent of user bias. This can be seen again with RWS, to a much larger magnitude. The strain gages return a curvature more than twice that of the Krypton. The error created with the instrumentation is amplified for RWS, due to the stress/strain concentration at the foundation interface from the termination of the lapped splices. This stress/strain concentration is being completely missed by the Krypton and string pot sensors that exist above the beginning of the lapped splices. Note that similar behavior to RWN is observed in RWC to a smaller extent.

The final qualifying comparison is the sensors and predicted BIAX curvature. The sensors in RWN and RWC were typically close to the predicted values. Sensors returned curvatures larger than BIAX in the elastic range. This was expected from inspection of the axial strain distributions discussed in the previous chapter. The inelastic range is also very similar to BIAX, especially at the point of first yielding toward the base. Nearly all sensors follow the same trend as BIAX. This is not true for RWS, where the discontinuity changes the cross sectional properties and consequently does not follow the BIAX trend as expected.

Good agreement in curvature calculations exists between all sensors used. The calculations are also confirmed to be reasonable when considering the ideal response of BIAX. The sensors are indeed trustworthy for comparisons between the test specimens.

8.3.0: Height v. Curvature Trends

The curvatures calculated for each wall meet expectations of a triangular distribution in the elastic range. This is evident when using the three top string pot readings to visualize a strain line over height. This is illustrated in figure 8.4a,b,&c. RWN is very close throughout the entire height. RWC has curvature values outside the trend line, but the same gradient is still apparent. Curvatures for RWS is clearly inside the trend line from the lapped splices. This is simply an illustration of elastic behavior. A similar comparison is made later to evaluate the height of plastic action.

The curvatures calculated in the highly inelastic range show counter intuitive behavior at the base of the wall. The curvatures “hook in” toward the base, becoming smaller in magnitude than those curvatures directly above them. This is the opposite of what one would expect, as larger moments and inelastic behavior would have significantly larger curvatures at the base. This can be seen in figures 8.1c and 8.2c, along with what is expected from BIAX. The No.5&6 boundary element in tension direction has decreasing curvatures at the base. This is seen with multiple heights above the interface, showing that this is not a result of the instrumentation limitations. Moreover, the same behavior is seen with both the Krypton and string pots for RWN and RWC. The sensors follow the same trend and have very similar magnitudes. The reasons for this behavior are not exactly known, but thought to be a product of excessive damage creating shear-flexure interaction.

Unfortunately, many sensors have failed at the highly inelastic range used as an example in this section. Specifically, strain gages are the most unbiased data, but often times do not last that far into the inelastic range. Figure 8.5 shows height v. curvature at the last reliable strain gage drift level for RWN. Note that the strain gages at the interface have failed at this point. However, the other gages were responding appropriately. The strain gages at 6” and 18” follow the rest of the instruments very well, suggesting that this behavior is indeed the true response of the wall and not an oversight in the analysis or

failure of string pots and Krypton LEDs from damage to the wall at the base. Again, shear-flexure interaction from the damage at the base is most likely the cause of this phenomena.

8.4.0: Effect of Anchorage Detailing on Curvature

The anchorage detailing of the longitudinal reinforcement has a significant impact on the resulting moment-curvature/height v. curvature response. Lapped splices double the amount of longitudinal reinforcement through the lapped splice length. This doubled steel results in significantly reduced axial strains and curvature. This was discussed previously in section 8.3.0, fist paragraph. Again, RWS has curvatures below its “elastic trend line” created from the top three string pot readings. The other two walls followed the elastic trend line almost completely or were slightly larger. This is seen in figures 8.4a,b,&c. The curvature in RWS increases as lapped splices terminate over the height. This is shown best by the No.5&6 boundary element in tension, where curvature begins increasing at the termination of the web steel at 29” and continues to increase until 72”, where all splices have been terminated. This is shown again with the No.9 boundary element in tension, but to a much lesser extent.

The curvature outside the terminations follows the same trend as the other two walls. The height above the final lap splice termination has curvatures larger than that of RWN and RWC at the same height. This is thought to be a result of a minimum energy response of RWS, where the top half of RWS will undergo more flexural deformation than the top half of RWN and RWC (the difference between top load applied at this point is less than 0.5% between walls, a negligible difference). Again, this can be seen as a stress/strain increase from the discontinuity of longitudinal steel.

These trends are continued throughout the test of each wall. RWS consistently has lower curvatures than RWN and RWC. This can be seen with a direct plots of string pot data comparison in figures C.6a&b. Note that RWC has an extreme oscillation of curvature

data at 36". It is unknown why this is occurring. Possibilities include a loose connection from cracking, causing the bottom string pot to have pulled down more. This would cause the bottom to error towards more negative, compressive strain and the top to error toward more positive, tensile strain. Additional possibilities are that the strings are rubbing on other attachments when the No.5&6 boundary element is in tension, as this problem is not seen when the No.9 boundary element is in tension.

The stress/strain concentration from the lapped splice termination is also very prevalent when viewing figures 8.6a&b. The final termination of the No.5&6 boundary element occurs at 45" high. This point is the height at which RWS records curvatures larger than RWN and RWC. Again, RWS has larger curvatures than RWN and RWC for the resulting height of the wall outside the splice termination.

8.5.0: Total Rotation Comparison

The curvature relationships over height have shown that RWS experiences significantly reduced curvature within the lapped splice length. In addition, RWS experiences slightly increased curvatures outside lapped splice lengths, when compared to RWN and RWC. It is of interest to compare the total rotation each wall undergoes at select drift levels. Comparisons of the three walls can be seen in figures 8.7a,b,c for the same load levels discussed throughout this chapter.

These figures show that RWS always has a reduced total rotation than RWN and RWC. It is clear at this point that RWS is experiencing less flexural deformation than RWN and RWC. In addition to the reduced rotation, far less is occurring at the base. This shows a center of rotation higher in the wall than RWN and RWC. This is most apparent in figure 8.7c, where RWN and RWC have a great deal of plastic hinging and approximately half of their total rotation is occurring at a height of 54".

8.6.0: Summary of Findings

This chapter has documented the curvature and rotation relationships of the three test specimens for drift levels of particular interest. In general, the curvature distribution over the height was very similar for RWN and RWC. However, RWS experienced significantly decreased curvature within its lapped splice lengths and slightly increased curvature outside its lapped splice length. This leads to a decreased total rotation of the wall and a center of rotation that will be higher in the wall when compared to RWN and RWC. This is the cause for the difference in flexural deformation discussed in the next chapter.

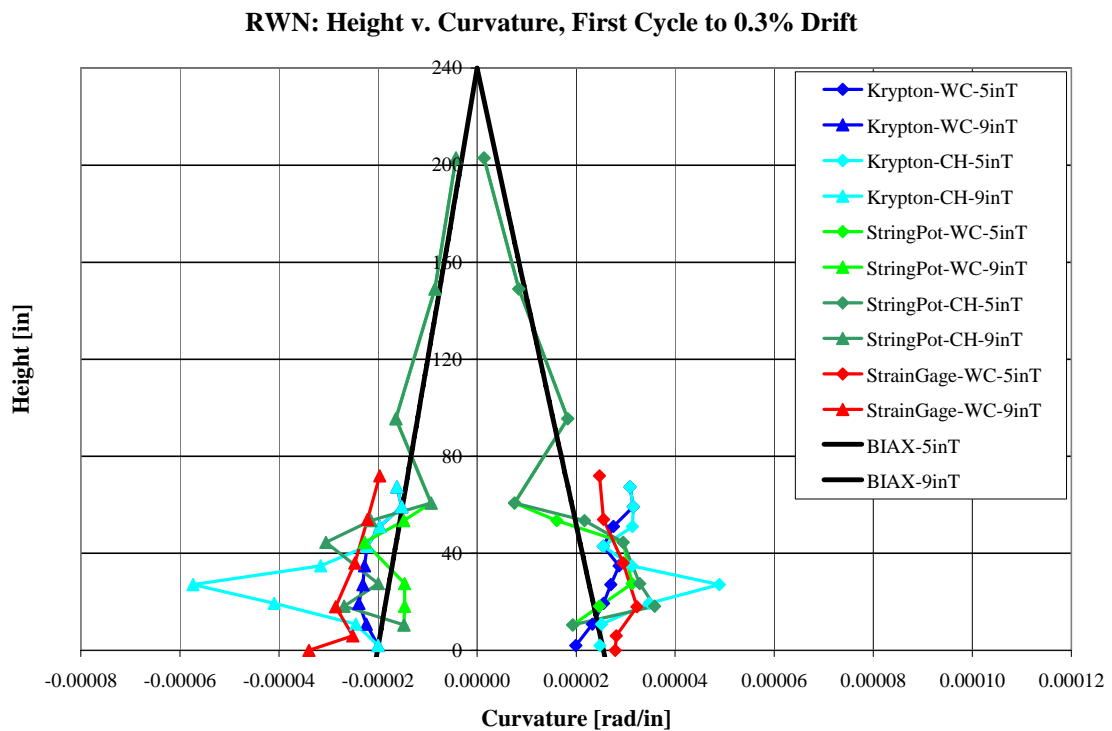


Figure 8.1a: Height v. Curvature for RWN at the elastic limit

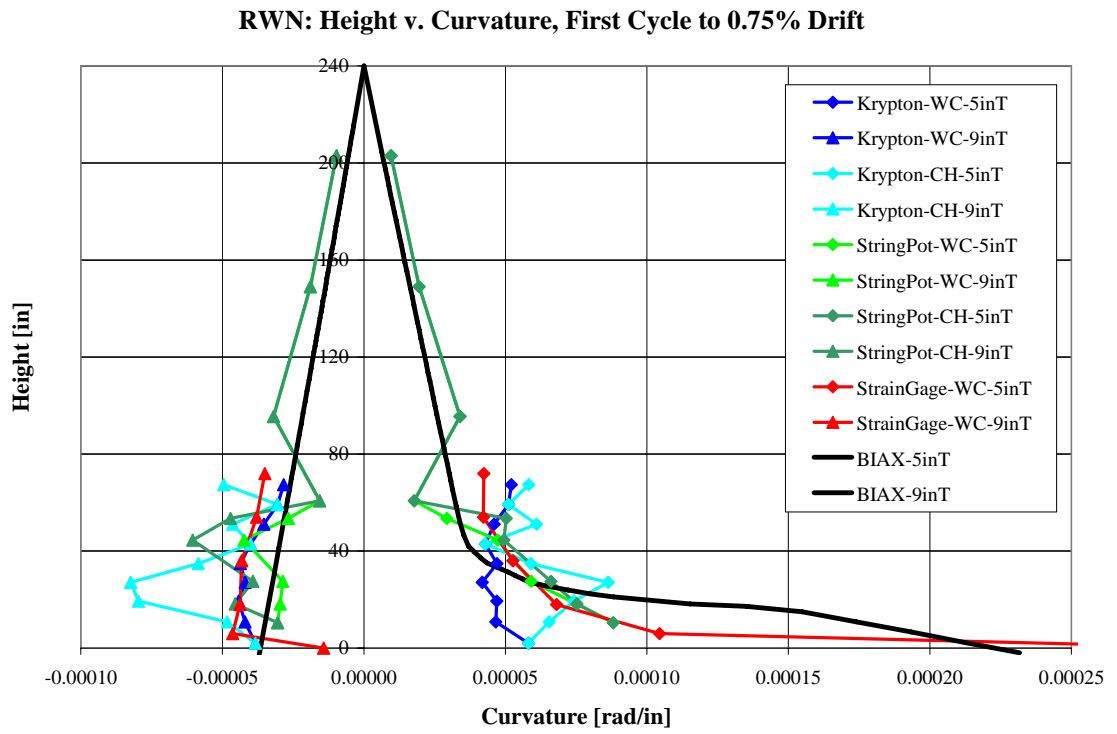


Figure 8.1b: Height v. Curvature for RWN well into the inelastic range

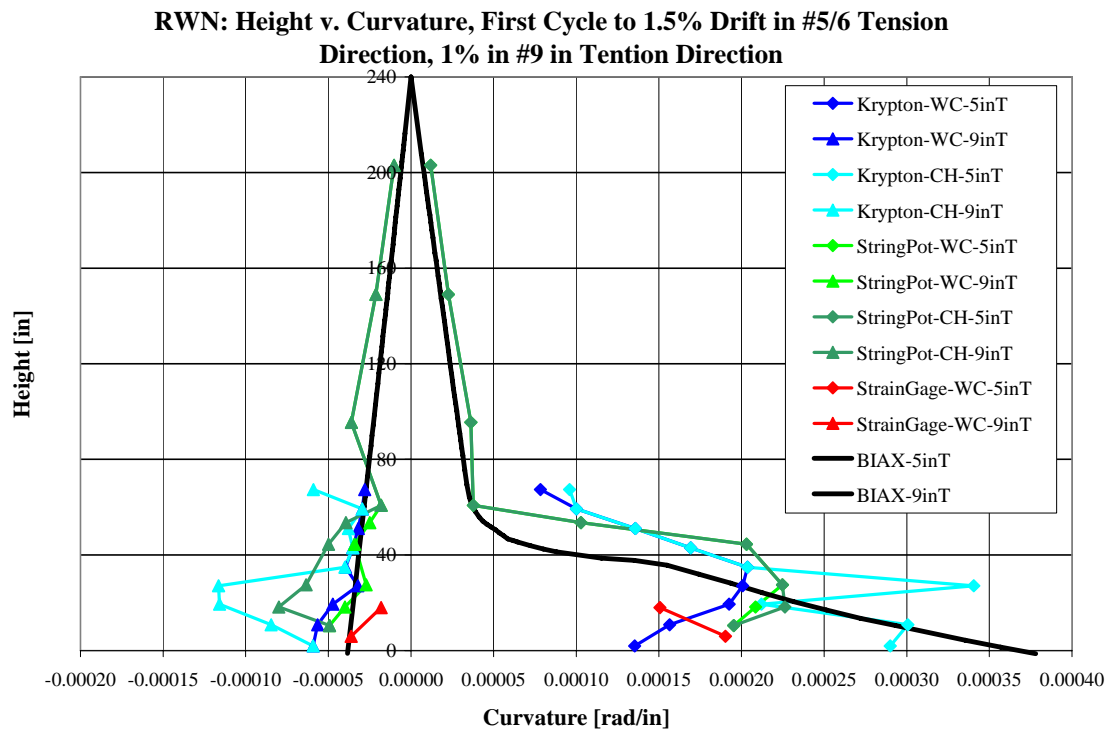


Figure 8.1c: Height v. Curvature for RWN at the last reliable sensor drift level

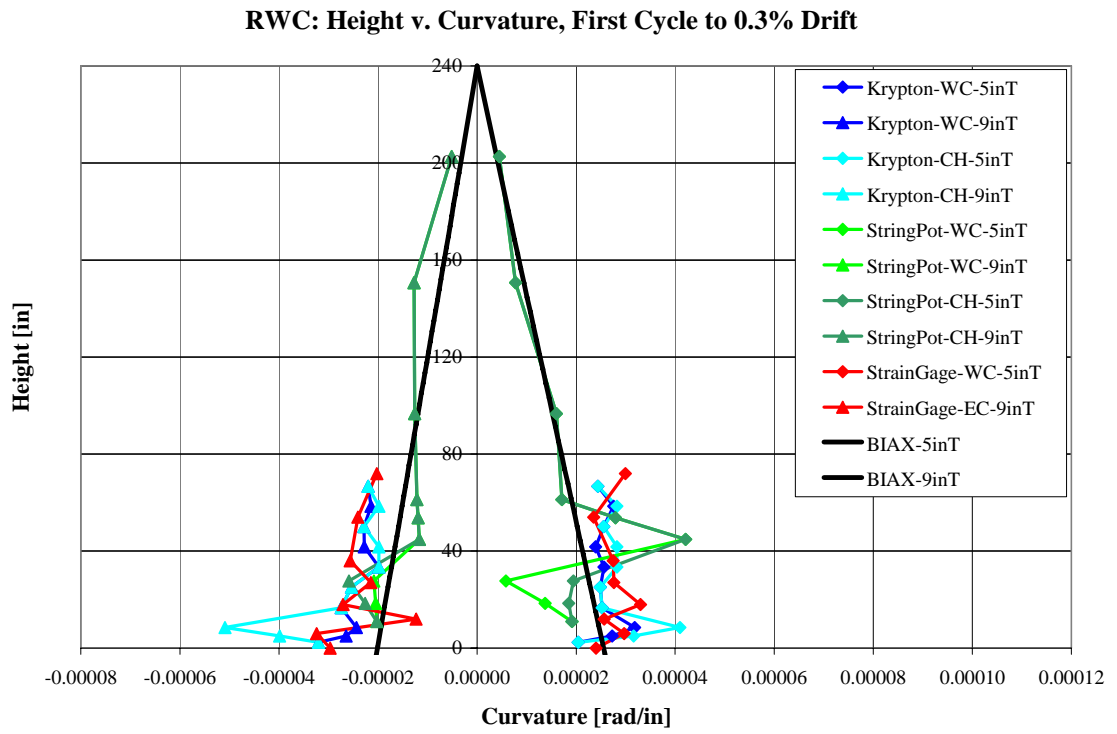


Figure 8.2a: Height v. Curvature for RWC at the elastic limit

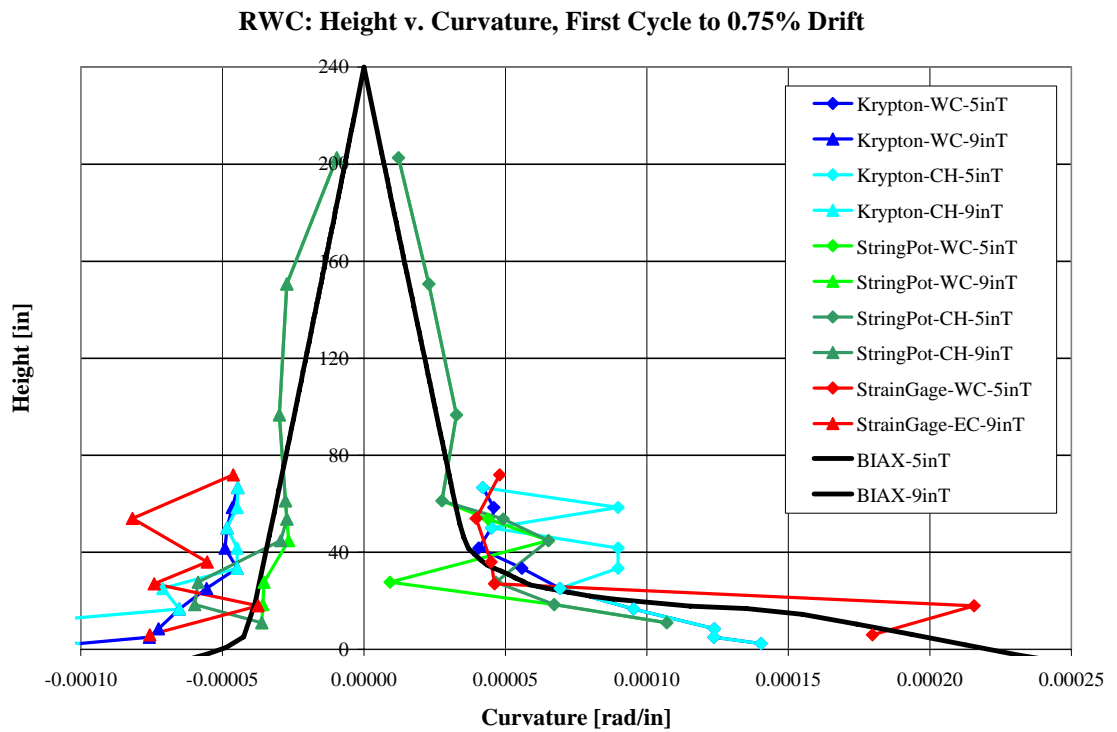


Figure 8.2b: Height v. Curvature for RWC well into the inelastic range

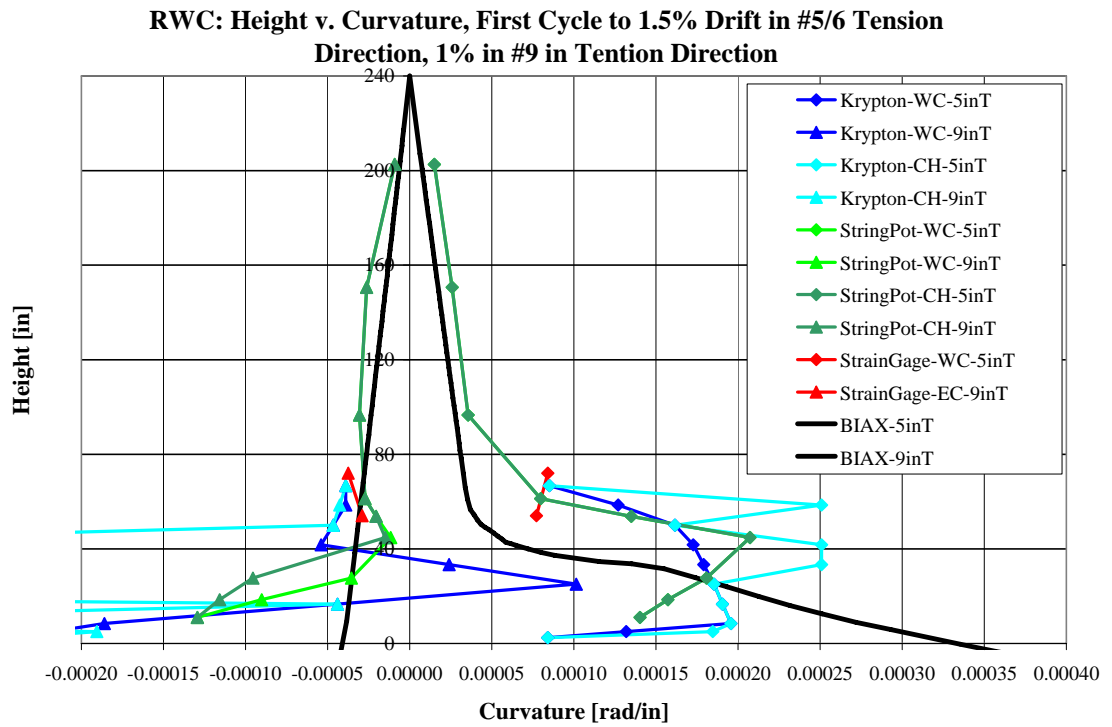


Figure 8.2c: Height v. Curvature for RWC at the last reliable sensor drift level

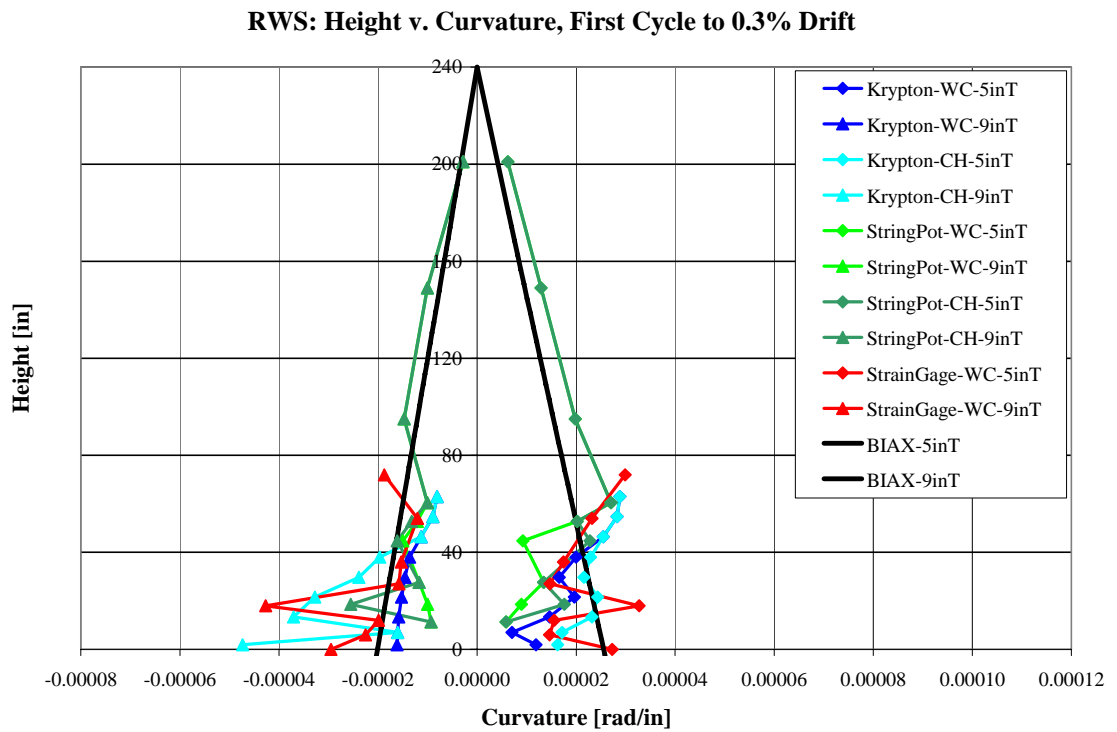


Figure 8.3a: Height v. Curvature for RWS at the elastic limit

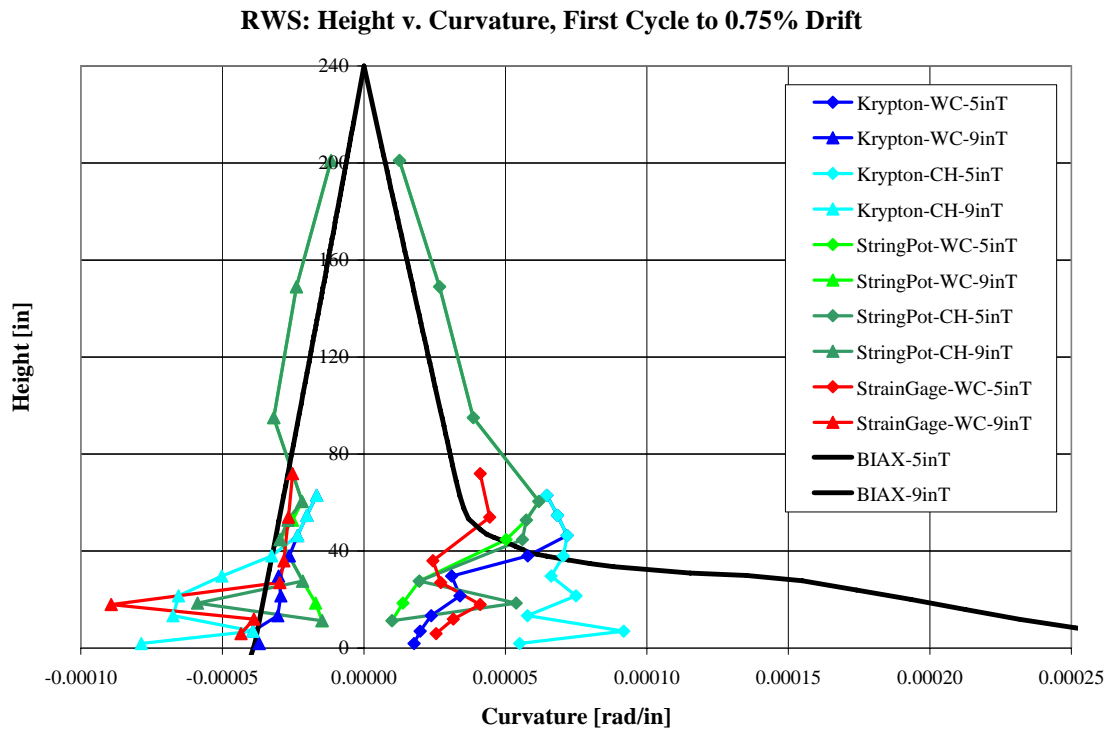


Figure 8.3b: Height v. Curvature for RWS well into the inelastic range

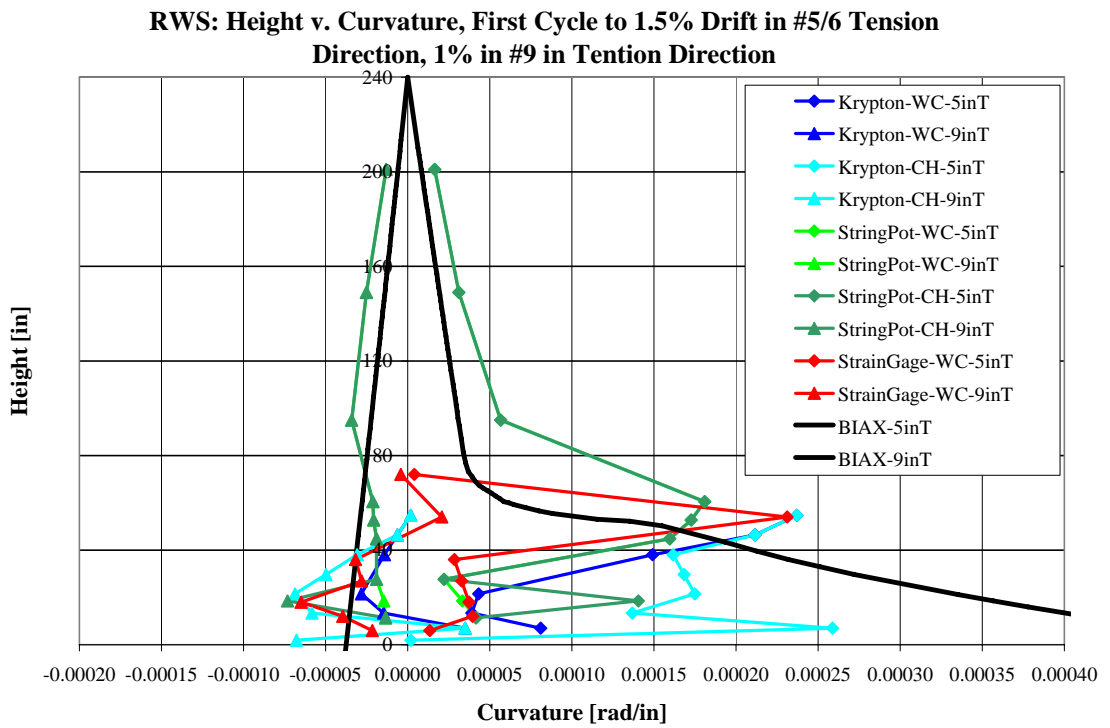


Figure 8.3c: Height v. Curvature for RWS at the last reliable sensor drift level

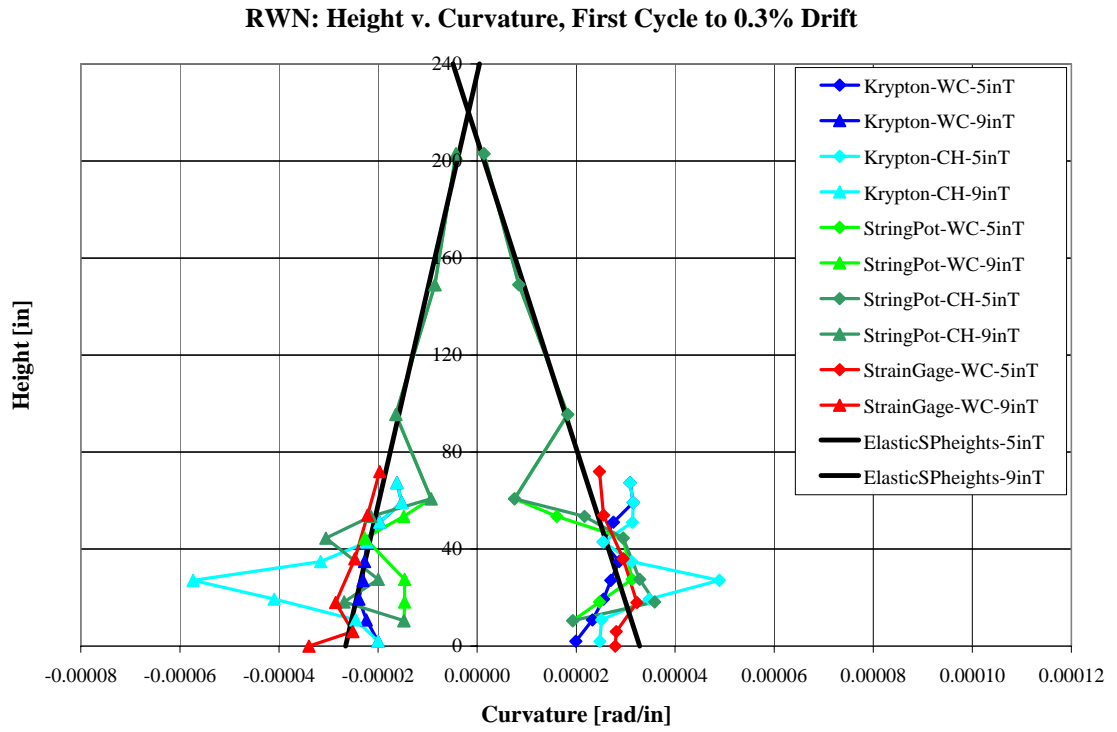


Figure 8.4a: Elastic trend line for RWN at elastic limit.

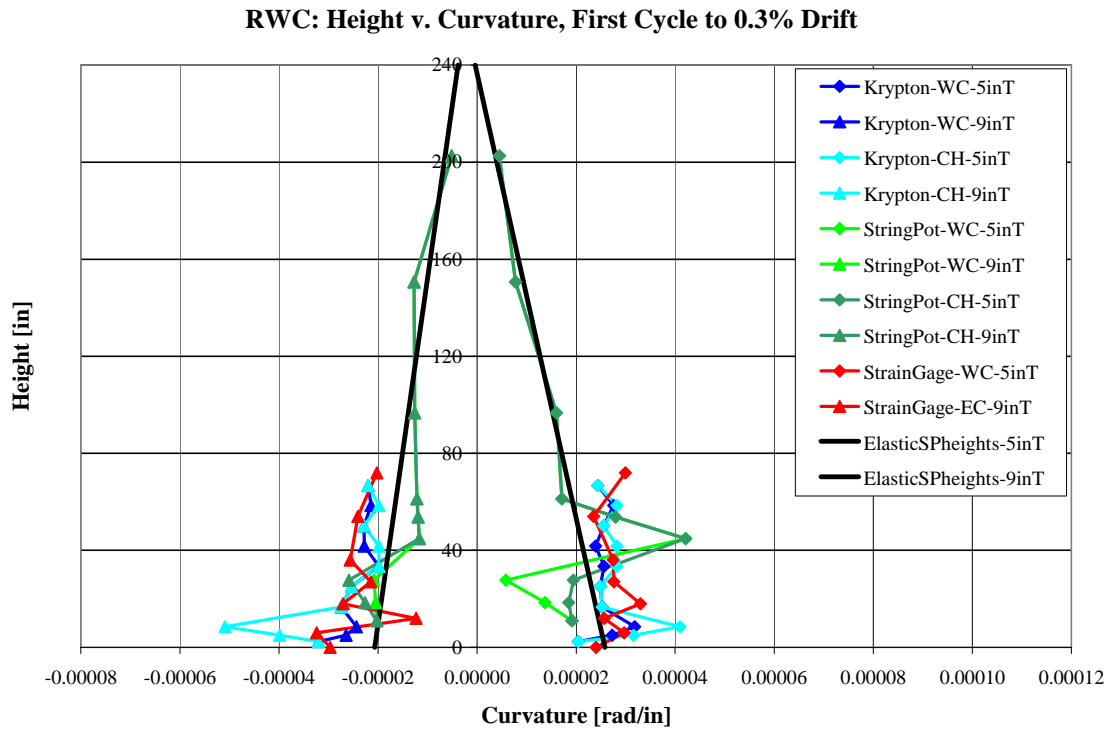


Figure 8.4b: Elastic trend line for RWC at elastic limit

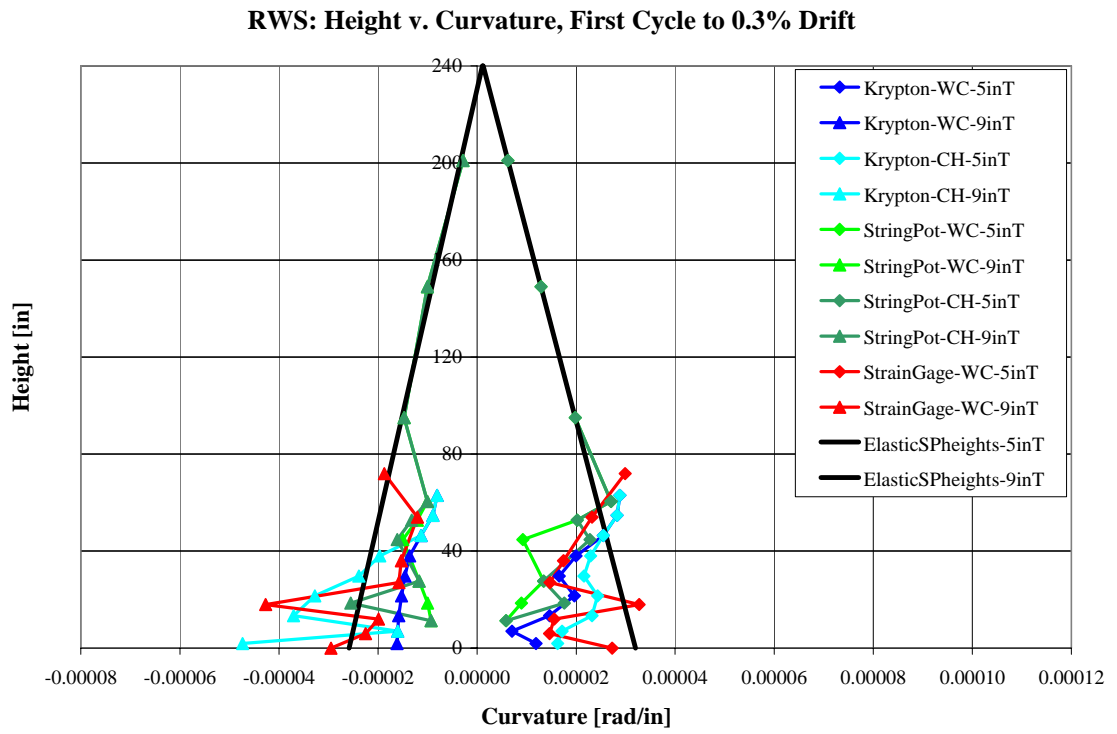


Figure 8.4c: Elastic trend line for RWS at elastic limit

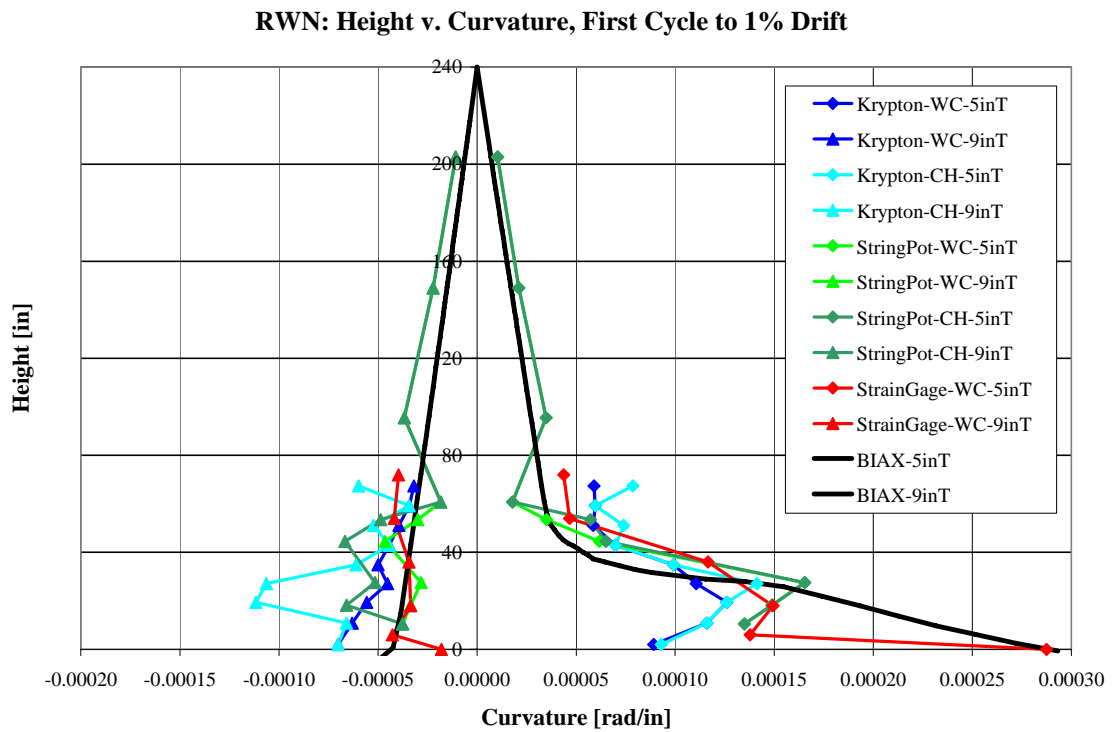


Figure 8.5: Reduction in curvature at the base for RWN.

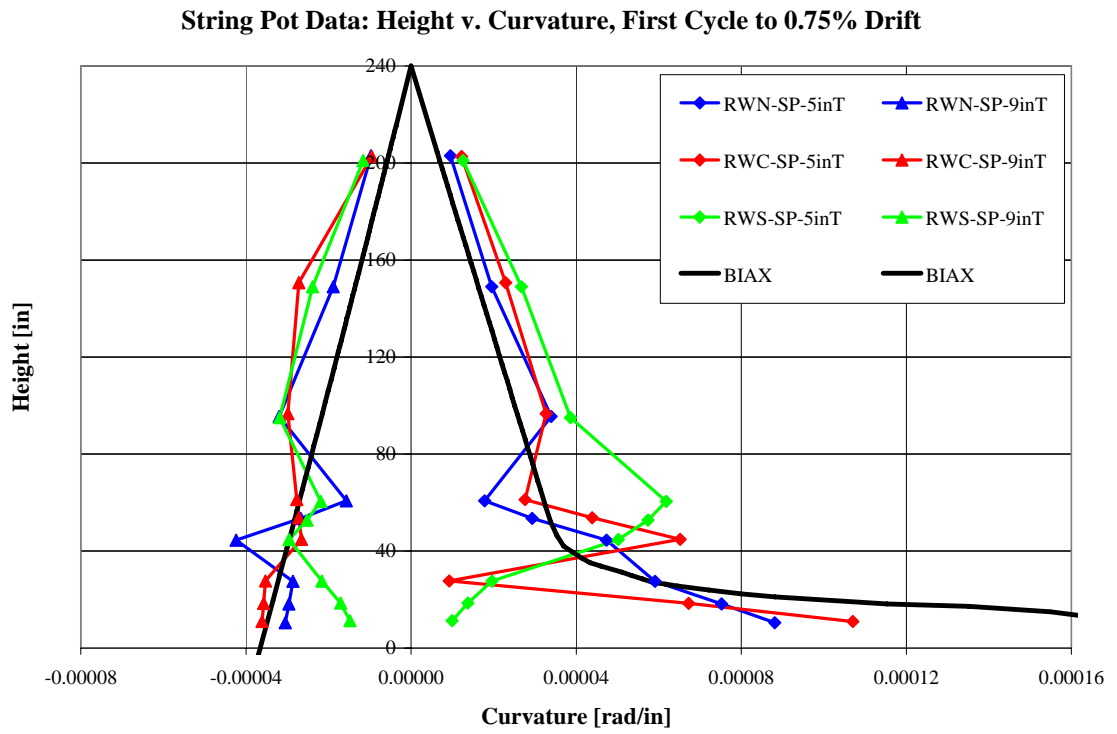


Figure 8.6a: Height v. Curvature comparison of all walls with string pot data

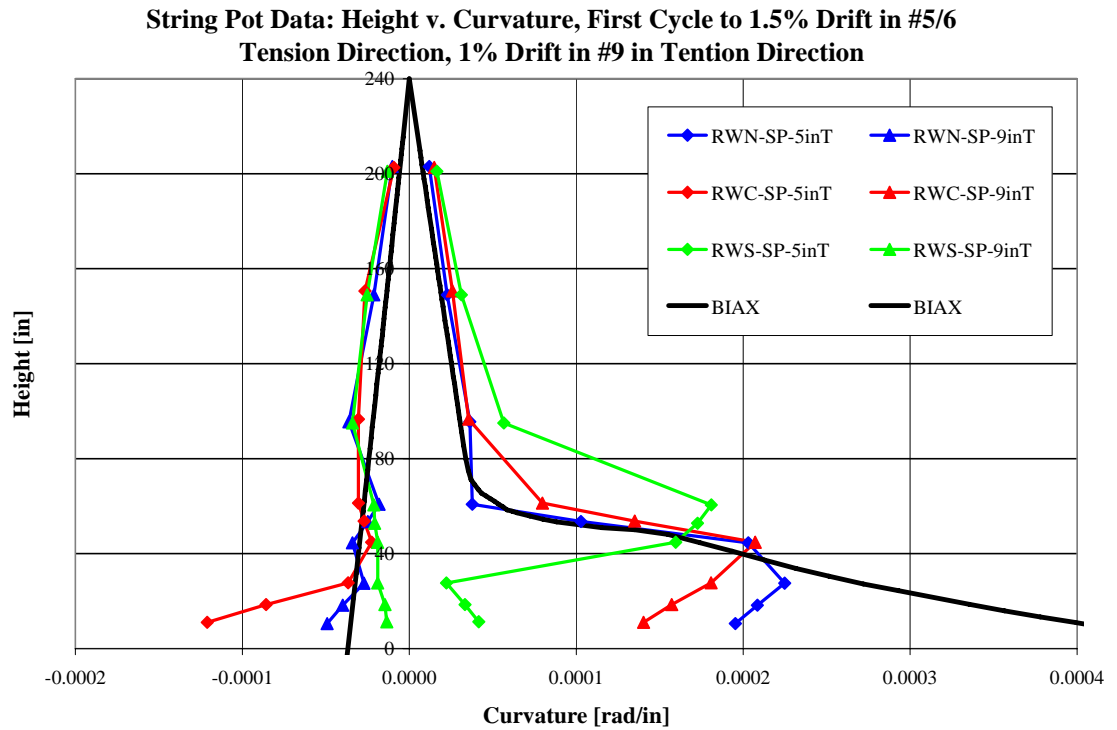


Figure 8.6a: Height v. Curvature comparison of all walls with string pot data

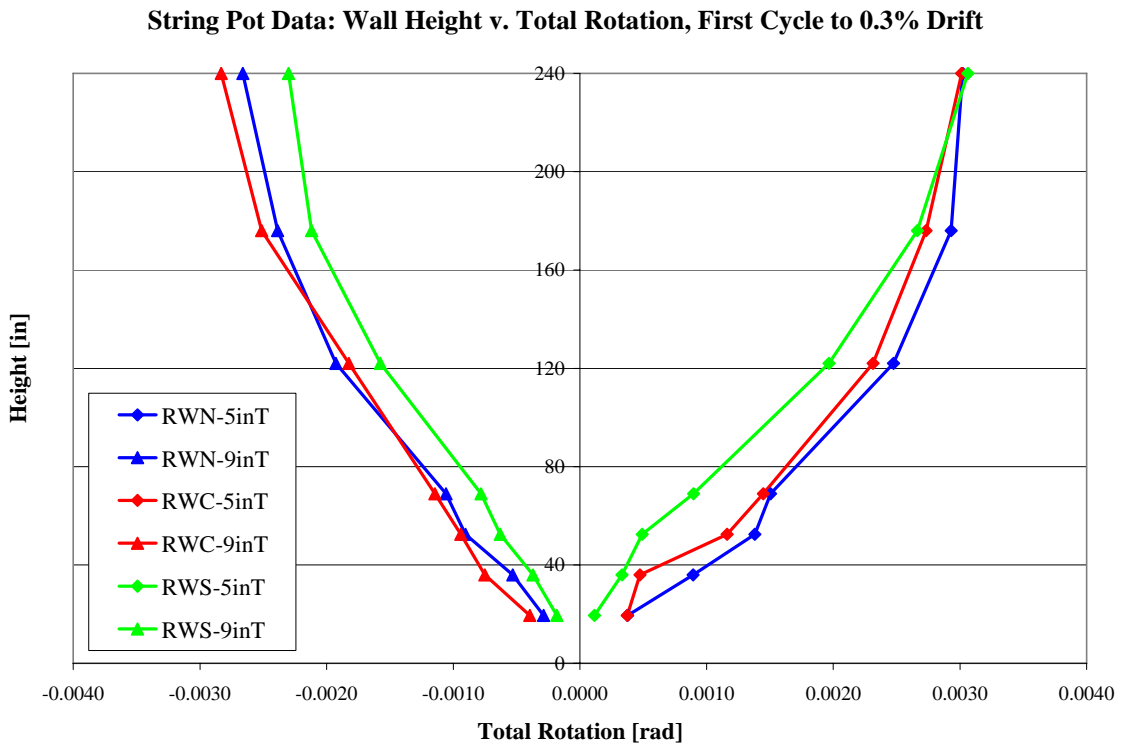


Figure 8.7a: Height v. Total Rotation comparison of all walls with string pot data

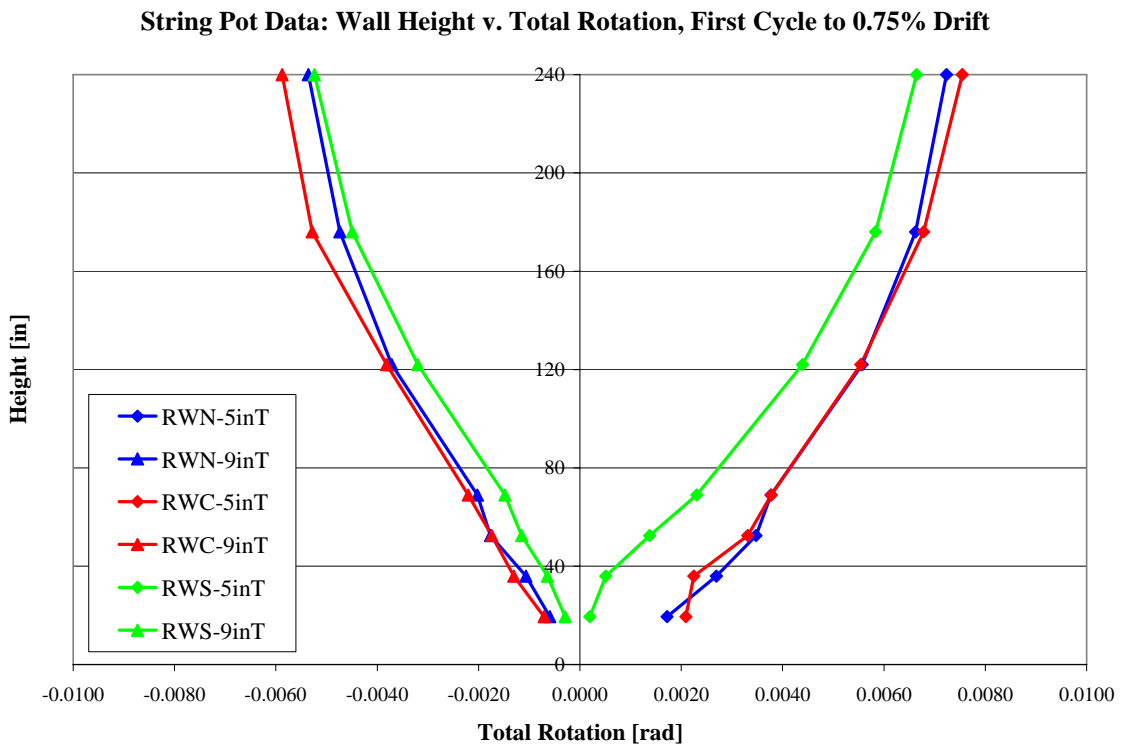


Figure 8.7b: Height v. Total Rotation comparison of all walls with string pot data

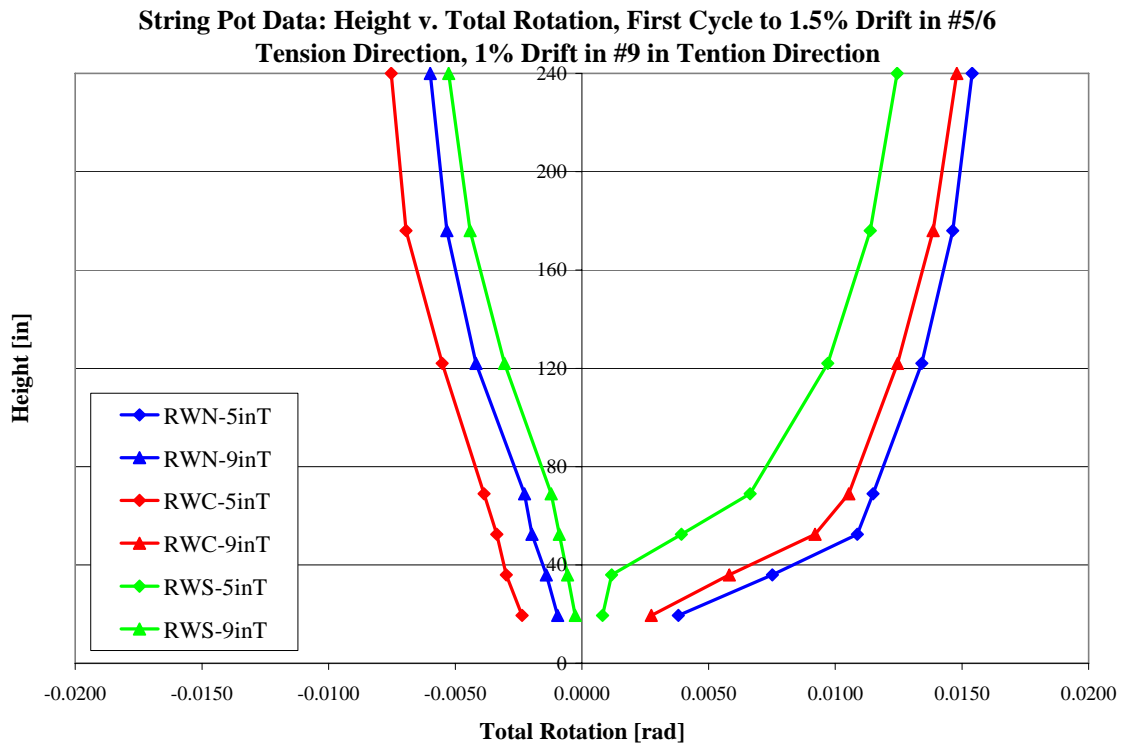


Figure 8.7c: Height v. Total Rotation comparison of all walls with string pot data

Chapter 9: Flexural Component of Lateral Deformation

9.0: Introduction

This chapter covers the methods of calculating the flexural component of lateral deformation and the results of the experimental data analysis. Each wall is evaluated individually first, qualifying the results of each different sensor type. The results will be compared with each other in order to determine which sensors and methods capture the behavior of the wall with the highest degree of precision and accuracy. Following the instrumental comparison, the individual test structures are compared in order to determine the effects of longitudinal bar anchorage details on the flexural deformation response. In general, lapped splices were found to decrease the total contribution from flexural deformation with varying magnitudes depending on the wall height in question. Lapped splices were found to decrease the total contribution of flexural deformation by approximately 40% at one quarter of the wall's total height and 15% at the top of the wall. The doubled longitudinal steel in the region of expected plastic hinging does indeed decrease the contribution of flexural deformation by increasing flexural stiffness.

9.1.0: Calculation of Flexural Deformation

The methods used to calculate flexural deformation are based upon classical beam theory and previous shear wall tests. This topic is covered in great depth in appendix F. Flexural deformation is calculated by integrating the calculated curvature distribution to determine the total rotation of the wall along the wall height. The curvature distribution is also used to determine the center of rotation, by determining the centroid of the curvature distribution. Different sensors required separate methods in determining this center of rotation.

The strain gages and Krypton data were assumed to report curvatures to be representative of a single height. The centroid of the curvature distribution was then found by

calculating a weighted average of each basic geometric sections of curvature along the wall height (rectangles and triangles of curvature-height area). The distance from the wall interface to the centroid for each geometric section was weighted by the portion of the total rotation they represented. The sum of the weighted centroids was divided by the total rotation for all sections below the point of interest.

The second sensor technique used was that for the string pots, where the rotation of each height segment was an average. This situation was unable to be broken down into accurate geometric sections. For this reason, the centroid of each segment was assumed based on an elastic curvature distribution. These assumptions were compared with ideal BIAX curvature distributions for various load levels, including a highly inelastic distribution that could have been achieved with the largest loads resisted during the experimental test. The maximum difference between the BIAX center of rotation (using the first method) and the ideal string pot centroids was 0.4%. The string pot data may under predict the total flexural deformation by this amount at very inelastic load levels.

9.1.1: Equation for Flexural Deformation (*From Appendix 3*)

Flexural deformation is calculated using classical beam theory. The mechanics of flexural deformation is well known and documented; however, nomenclature used by Massone & Wallace [R.A3.1] will be used in order for a uniform appearance with other experimental tests and reports on reinforced concrete shear walls. Flexural deformation is computed using the following equation:

$$\Delta_{\text{Flexure}} = \alpha h \theta \quad (\text{Eq. 3.1})$$

Where ' $\Delta_{Flexure}$ ' is the lateral deformation from flexure, 'h' is the height of the wall section in question, and ' θ ' is the total rotation of the height segment in question. Lastly ' α ' is a non-dimensional factor equal to:

$$\alpha = (h_{Center\ Of\ Rotation} - h) / (h)$$

Refer to figure A3.1 for a figure illustrating these terms and equations.

9.2.0: Comparison of Different Sensors

The three sensors used to determine the flexural component of deformation are the Krypton, strain gages, and string pots. The reasons for variation between these sensors are the same for the differences in calculated curvature. Refer to chapter 8 for a complete analysis of the methods, assumptions, and impacts of these techniques.

Two main methods were used to determine the curvature from each instrument: the "WC" and "CH" method. The "WC" or "whole cross section" method calculated curvature by fitting a linear trend line through all axial strain data at the height of interest. The axial strain distribution (curvature) was found to not be necessarily linear at the base of the wall, up to a height of approximately three feet. This observed difference required a second method, the "CH" or "compression half cross section" method. Curvature was calculated by fitting a linear trend line through the axial strain data from the centerline of the wall to the extreme compression face, where the axial strain gradient was observed to be larger than the rest of the cross section. This method seems to have over predicted the total flexural deformation of the wall when considering the Krypton data. This is discussed in greater detail when the results are compared to the ideal response of BIAx.

As seen in previous chapters, the "CH" method typically returned curvature values larger than the "WC" method. The result of this can be seen in figures 9.1.1a, b, &c. These plots show the flexural deformation calculated by the sensors discussed in this section for the

elastic limit for each wall. The Krypton “CH” method is almost always showing the largest flexural deformation of each wall at this load level. The difference is as much as twice that of the Krypton “WC” method and string pot results. The few available data points of the string pots at most heights (only two attachment points for all heights, except two) cause very little variability between the two methods for the string pot sensor. It is assumed that the string pot “CH” method would return the same result as the Krypton “CH” method if the appropriate number of sensors were available.

The string pot “WC” method returns a flexural deformation that would account for 70% of the total deformation at the top. If the “CH” method for the Krypton gave consistent results along the wall height, the total top deformation would be less than the flexural. This is incorrect, as the effects of shear and strain penetration also make up a considerable amount of the total top deflection. For these reasons, the “CH” method is thought to give an unreasonable result for flexural deformation and is discounted from the final conclusion, except in the case of comparison between the different test specimens.

With the exception of the Krypton “CH” method, the different sensors give values of flexural deformation that are quite close to each other. The Krypton and strain gages typically give larger values of flexural deformation when compared to the string pots. This difference is usually within 10 to 20% of each other, with the Krypton and strain gages giving consistently larger values. This creates a good envelop of possible results to be compared with the total deformation. This relationship can be seen for various load and ductility levels in figures 9.2a through 9.2i.

9.2.0: Comparison of Results to BIAX

Flexural deformation was computed with BIAX as a means to determine the validity of the experimental results. In addition to this, it was of interest to determine if the response of the real structures could be predicted by a simple analysis.

The flexural deformation calculated by BIAX was done using the same method as that for the Krypton and strain gage data. The moment v. curvature of the walls was predicted by BIAX with the known material properties. Knowing the moment v. curvature relationship, a top load of the wall was assumed for various levels. The curvature distribution was created by back-calculating the height of the curvature from the corresponding moment using statics. With this completed, solved was used to fine tune the load such that one of the curvature points would have a height equal to zero, the foundation interface. The curvature was then numerically integrated and the center of rotation found. The resulting flexural deformation could then be found from equation A3.1. The backbone load versus displacement, along with the calculated flexural deformation from experimental data and predicted BIAX values can be found in figures 9.3a, b, &c for each test wall.

The predicted BIAX load v. flexural displacement matches RWN and RWC very closely. This result suggests that the “WC” method is indeed giving the true response of the wall. Close agreement between the string pots and the Krypton “WC” method, along with the verification with BIAX show that these methods are indeed an accurate means to determine the flexural component of deformation.

9.3: Comparison of Flexural Deformation Profiles

Figures 9.2a through 9.2i depict the flexural deformation profiles of each wall at three representative loading ramp maximums. Each group of plots for each wall depict the elastic limit, the last loading ramp maximum prior to first yield; the inelastic range, where the wall is well into its inelastic properties and all instruments are functioning correctly; and the highly inelastic range, where the walls have well developed plastic hinges and instruments are at close the time at which failure was observed. The total displacements shown for string pot data in these figures represent the average lateral displacement of the wall at that height. This displacement is the average of the tension and compression sides, which differ by the width of the cracks which develop across the wall length.

Two distinct features are noticed when examining these profiles. The first is that RWS has a noticeable decrease in the total flexural deformation throughout the wall height. This is noticed more at the quarter height of the wall, where the lapped splices have just terminated and the total flexural deformation is significantly reduced (in terms percent of total lateral deformation). This is still noticed at the top of the wall, but to a much lesser extent. Very little difference was observed between RWN and RWC. Flexural deformation was typically reduced by 40% at the quarter height of the wall and reduced by 15% at the top of the wall.

The second feature is the development of plastic hinges. This was addressed previously in chapter 8, where plastic hinging was observed by the total amount of rotation at the base when compared to the rest of the wall. Plastic hinging is evident in figures 9.2c & f. The top flexural and total deformation profiles are essentially straight above 120 inches. This is not the case in the No.9 in tension direction, where the bars did not come close to achieving the same amount of plasticization as the No.5&6 boundary element. The same loading ramp for RWS is shown in figure 9.2i. It is not evident that a full plastic hinge has developed in this figure. Increasing rotation is observed throughout the wall, in both directions of loading. It is evident that the lapped splices have prevented the base of the wall from forming a full plastic hinge. Consequently, the flexural deformation is greatly reduced from this load level on.

9.4: Comparison of Load v. Flexural Deformation Backbone

Figures 9.3a, b, & c show the load v. flexural and total displacement backbones. These plots only include the first loading ramp maximum in each cycle. RWN and RWC follow the BIAx predicted values quite well. However, the effect of the lapped splices create additional rotational stiffness. This is evident when examining the load v. flexural displacement backbone for RWS, where the flexural line is clearly outside the BIAx envelope. This is true to a larger extent for No.5&6 boundary element in tension direction.

It can be seen from these figures that the lapped splices create additional rotational stiffness, decreasing the flexural component of deformation.

9.5: Comparison of Load v. Flexural Deformation Plots

The load v. flexural deformation plots for each wall were superimposed on the same plot in order to visually compare the reduced flexural deformation. The load v. flexural deformation plots can be seen in figures 9.4a through 9.4g. These plots clearly illustrate the reduction in flexural deformation again. More interesting, a large degree of variability is noticed with RWC. This is especially true for the No.9 in tension direction in the inelastic range. Yielding was clearly observed for the No.9 boundary element. This is confirmed by both the Krypton and string pot data, ensuring that it is not a sensor malfunction. The yielding observed is clearly due to the mechanical couplers. The couplers in the No.9 boundary element may be creating a strain concentration outside the connecting coupler welds. This strain concentration may have caused yielding prior to the continuous bar wall. The same should be evident for RWS. However, the instruments may not have picked up this strain concentration in RWS from limitations discussed in chapter 8.

9.6: Flexural Contribution to Total Deformation

Lapped splices in the region of expected plastic hinging clearly reduce the total flexural deformation a wall will undergo. However, it is of interest to determine the flexural deformation percentage of each wall with respect the total displacement it was subjected to. Refer to figures 9.5.a through 9.5f for plots of the percentage of total deformation resulting from flexure.

The contribution to total lateral deformation is typically 50% at 25% of the walls total height and 70% at the top of the wall for RWN and RWC. This is again reduced for RWS. A general trend appears when examining these figures. The flexural contribution

decreases as total displacement increases in the elastic range. This is not due to a change in the flexural stiffness, but a change in the mechanisms which the shear load is carried. Additional cracking as load and displacement are increased changes the shear stiffness properties of the wall. More emphasis is placed on aggregate interlock and shear steel as cracking increases. The flexural deformation may be increasing proportionately with load and displacement, but shear deformation is increasing at a larger rate from cracking. This total increase is responsible for the decreasing contribution of flexural deformation. Note the contribution of flexural deformation increases again after yielding occurs, where the flexural stiffness then decreases much more than the shear stiffness. The large decrease in flexural stiffness makes flexural deformation an increasing portion of total deformation in the inelastic range. Note that this is not observed for RWS, where plastic hinging was not able to form and the portion of total deformation comprised of flexural deformation never recovers.

9.7: Summary of Results

This chapter covered the methods used to calculate flexural deformation, as well as a comparison of the effects of longitudinal bars anchorage on the flexural deformation. Each sensor used to compare flexural deformation was compared to each other and predicted BIAX values. The compression half cross section method of determining curvature was found to over estimate flexural deformation by an unreasonable amount. Good agreement between other sensors and methods was found for flexural deformation.

The flexural deformation for each structure was compared to determine the effects of lapped and mechanical splices on flexural deformation. The continuous longitudinal bars and mechanically spliced bars were found to have approximately the same response, with the exception of the No.9 in tension direction. The mechanical splices appear to have created a stress concentration, creating larger flexural deformations at the 25% height level, but a negligible difference at the top of the wall. The largest difference was seen in the lapped splice wall. Flexural deformation is reduced by approximately 40% at 25% of

the wall's total height and approximately 15% at the top. This is reiterated in figure 9.6a&b. Lapped splices indeed decrease the flexural deformation experienced by the shear wall. However, the total deformation was not seen to be as large at the difference in flexural deformation. The lapped splices also affect other displacement modes. Specifically, the lapped splices create a strain concentration at the interface from the termination of the lapped splices. This strain concentration creates additional strain into the foundation, creating larger lateral deformations from strain penetration. This deflection mode is covered in depth in the next chapter.

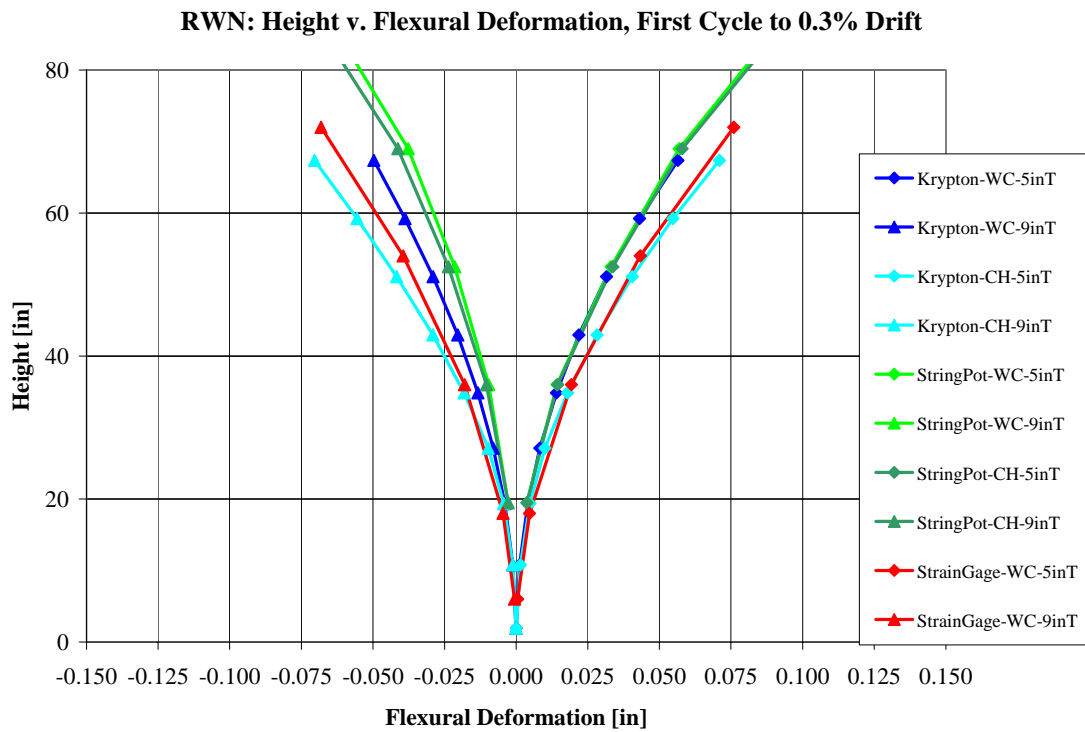


Figure 9.1a: Sensor comparison of elastic flexural deformation – RWN

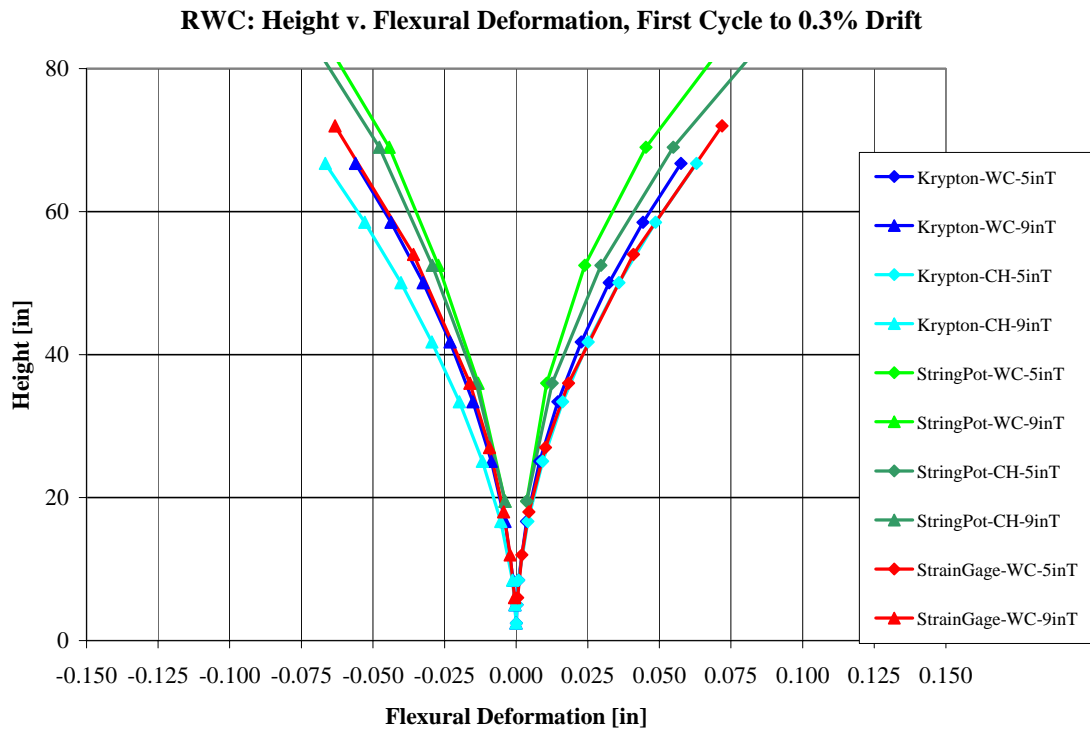


Figure 9.1b: Sensor comparison of elastic flexural deformation – RWC

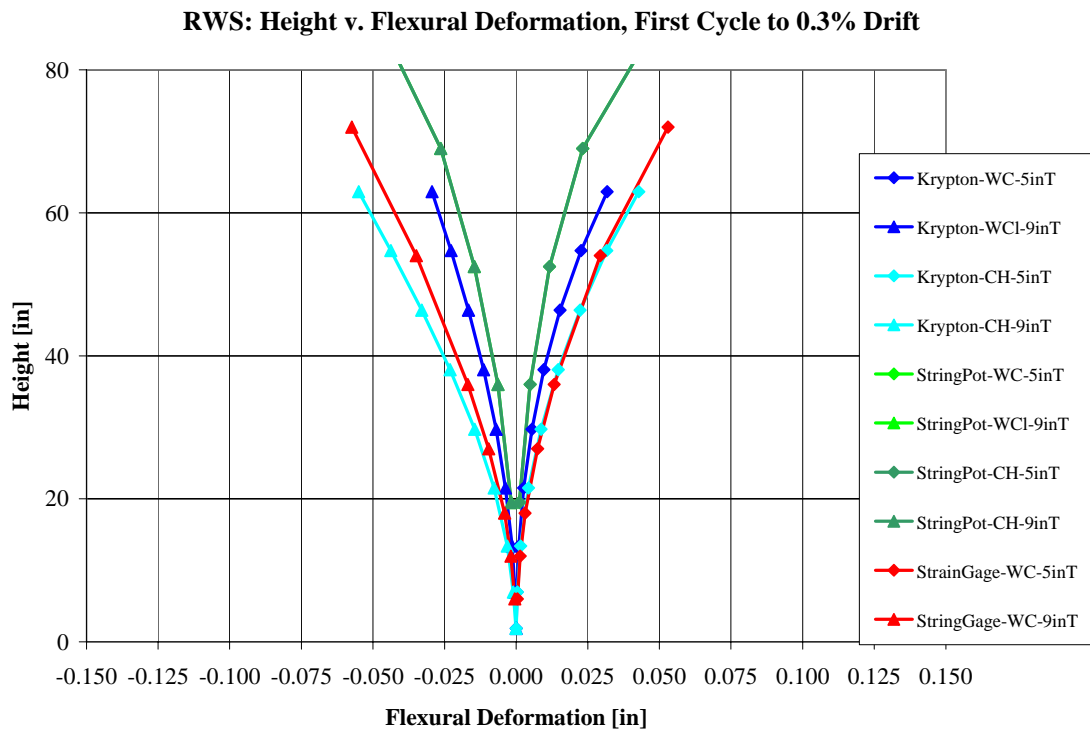


Figure 9.1c: Sensor comparison of elastic flexural deformation – RWS

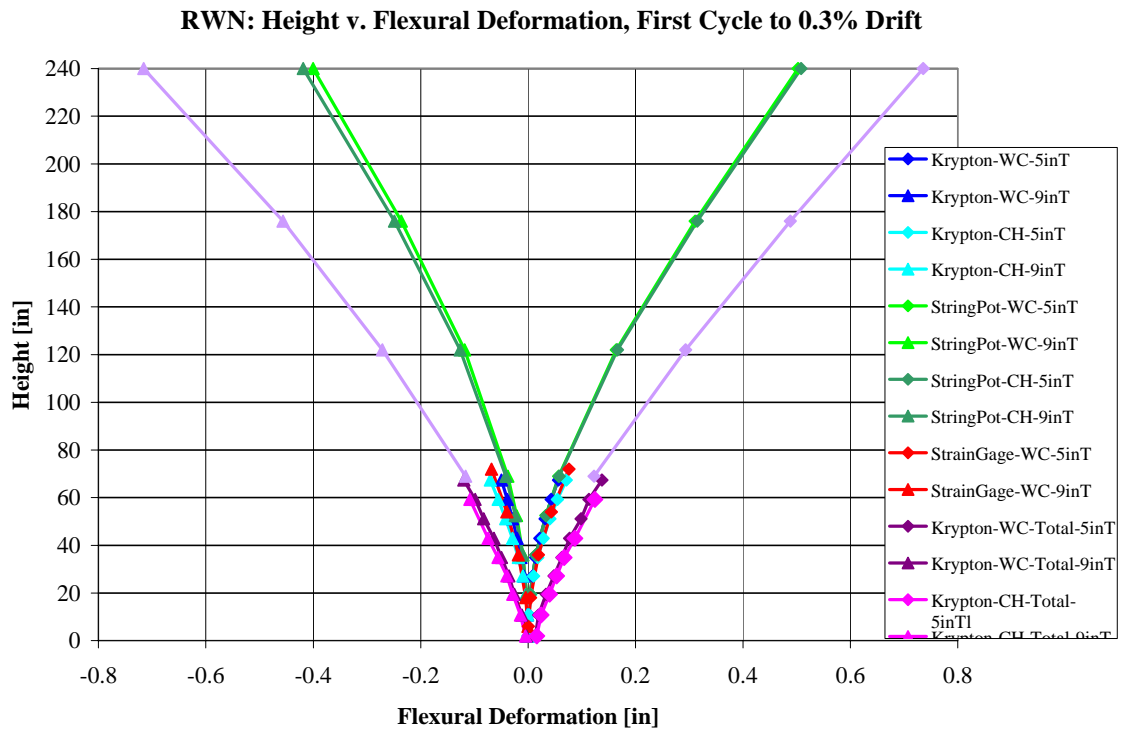


Figure 9.2a: RWN – Flexural deformation of various sensors – elastic limit

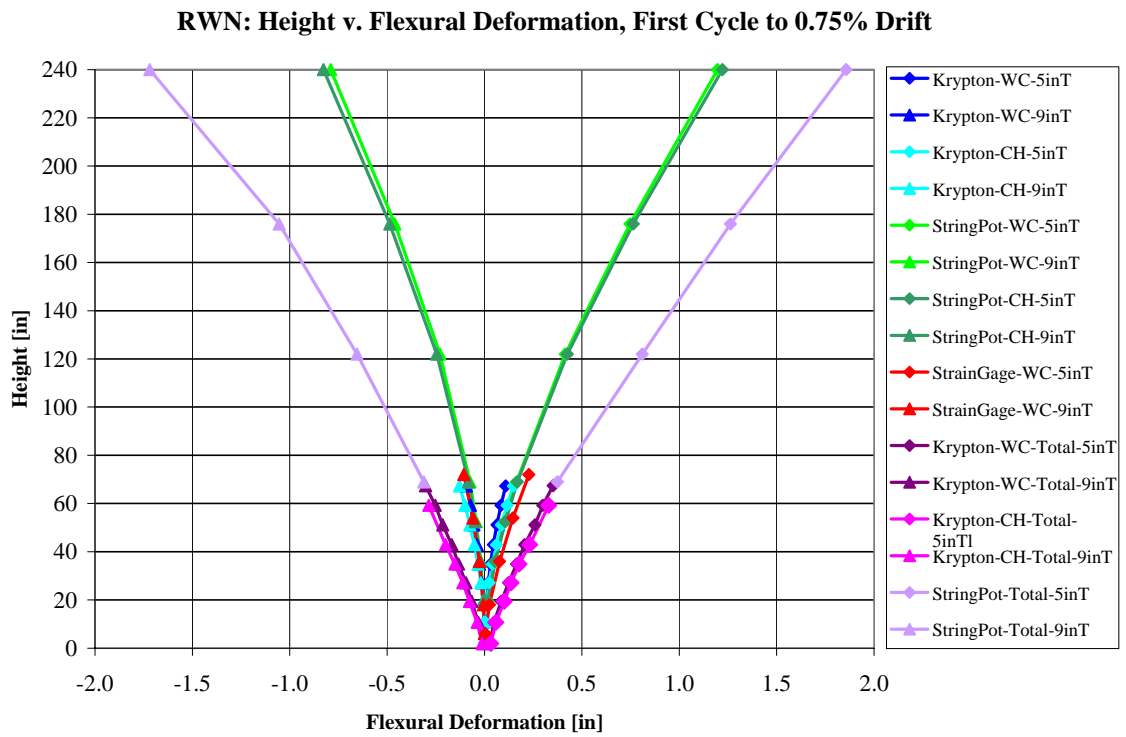


Figure 9.2b: RWN – Flexural deformation of various sensors – inelastic range

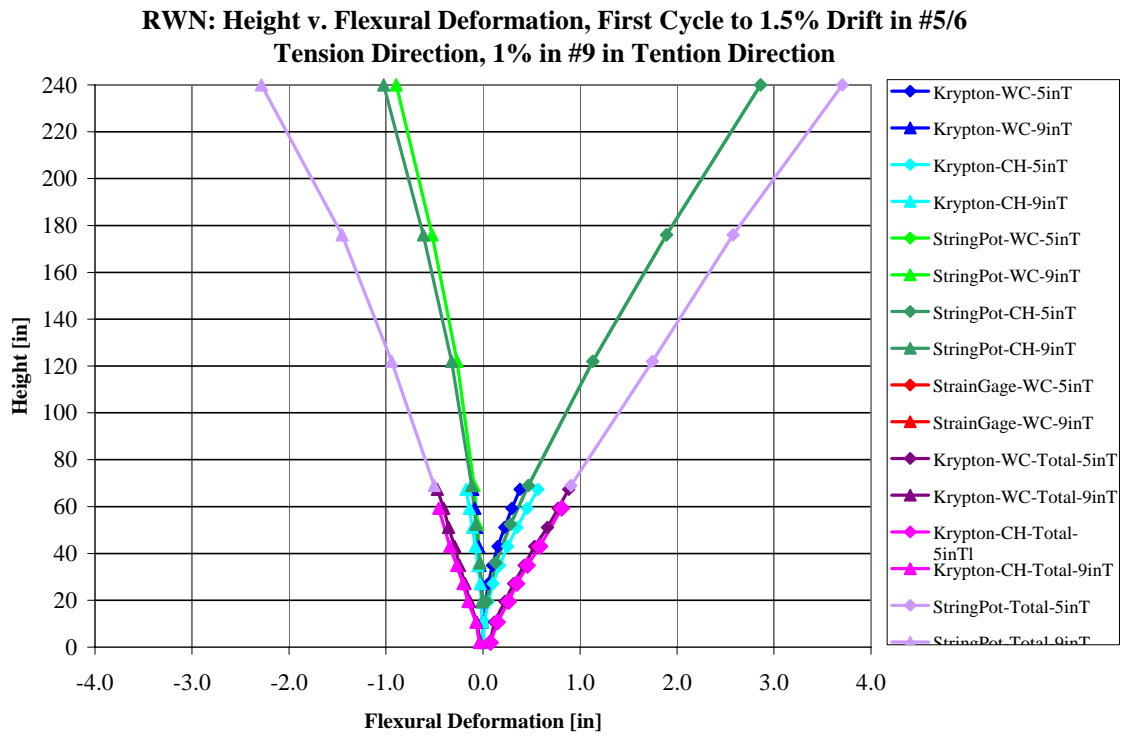


Figure 9.2c: RWN – Flexural deformation of various sensors – highly inelastic range

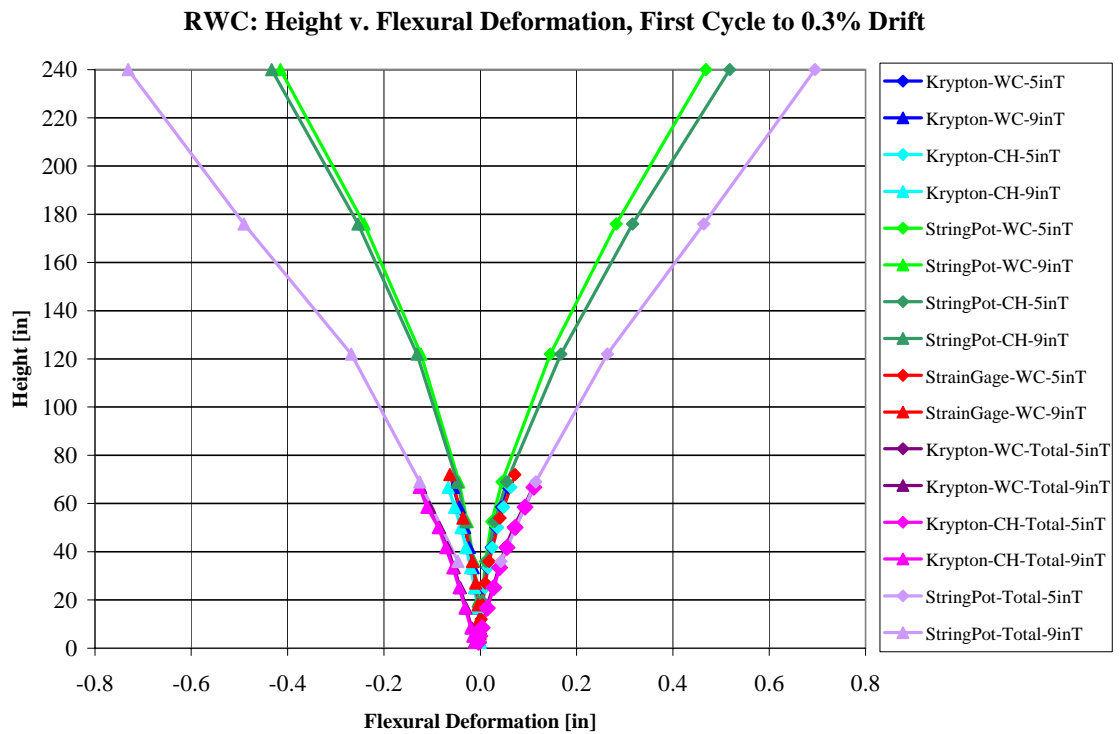


Figure 9.2d: RWC – Flexural deformation of various sensors – elastic limit

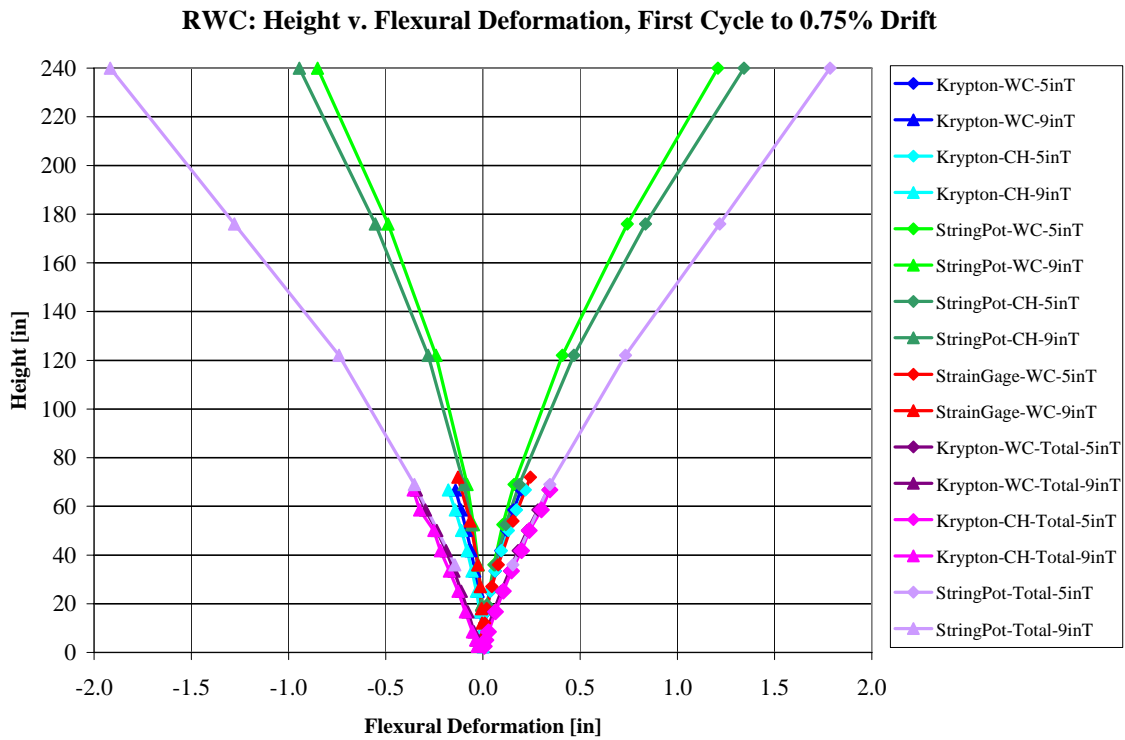


Figure 9.2e: RWC – Flexural deformation of various sensors – inelastic range

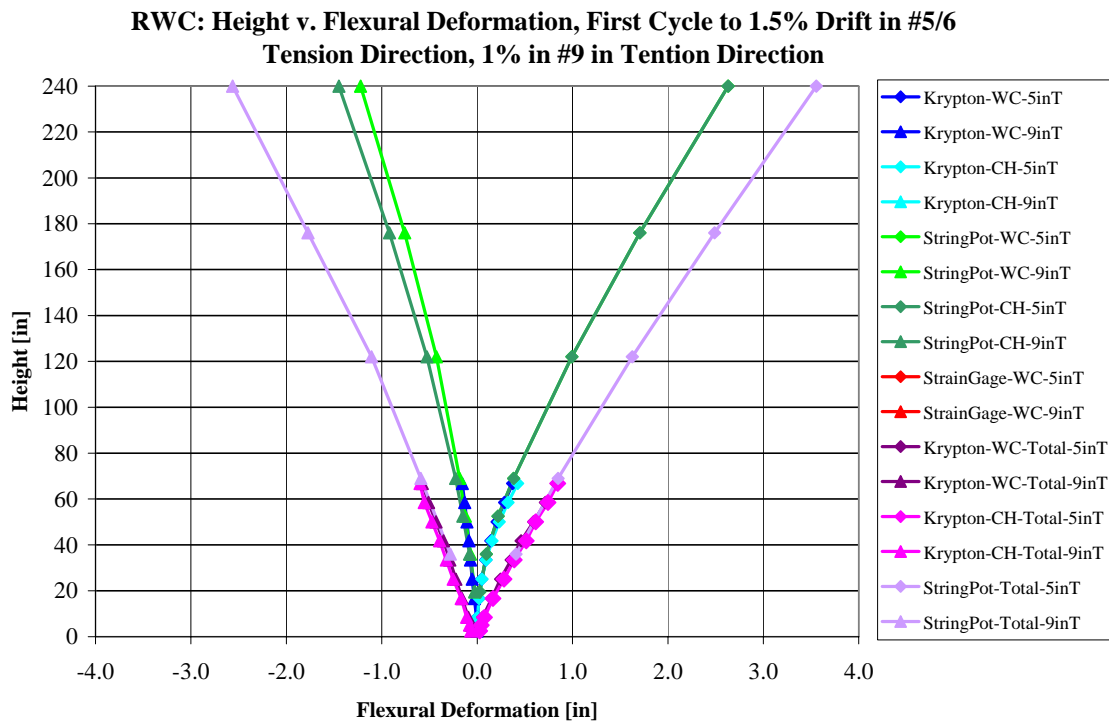


Figure 9.2f: RWC – Flexural deformation of various sensors – highly inelastic

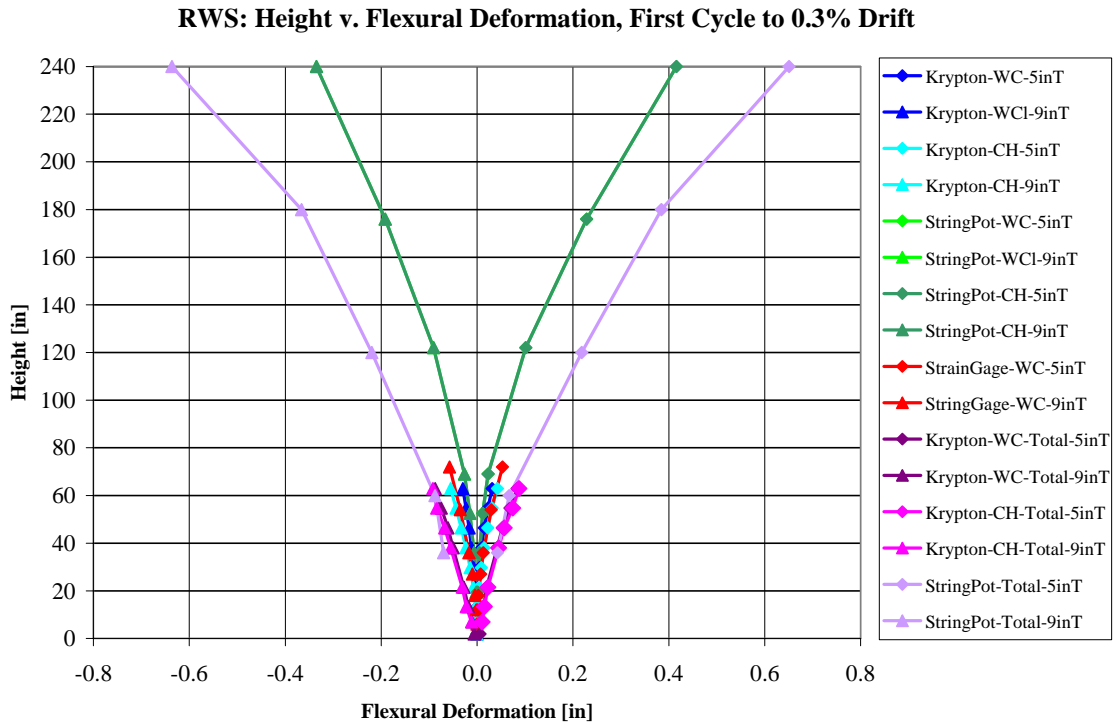


Figure 9.2g: RWS – Flexural deformation of various sensors – elastic limit

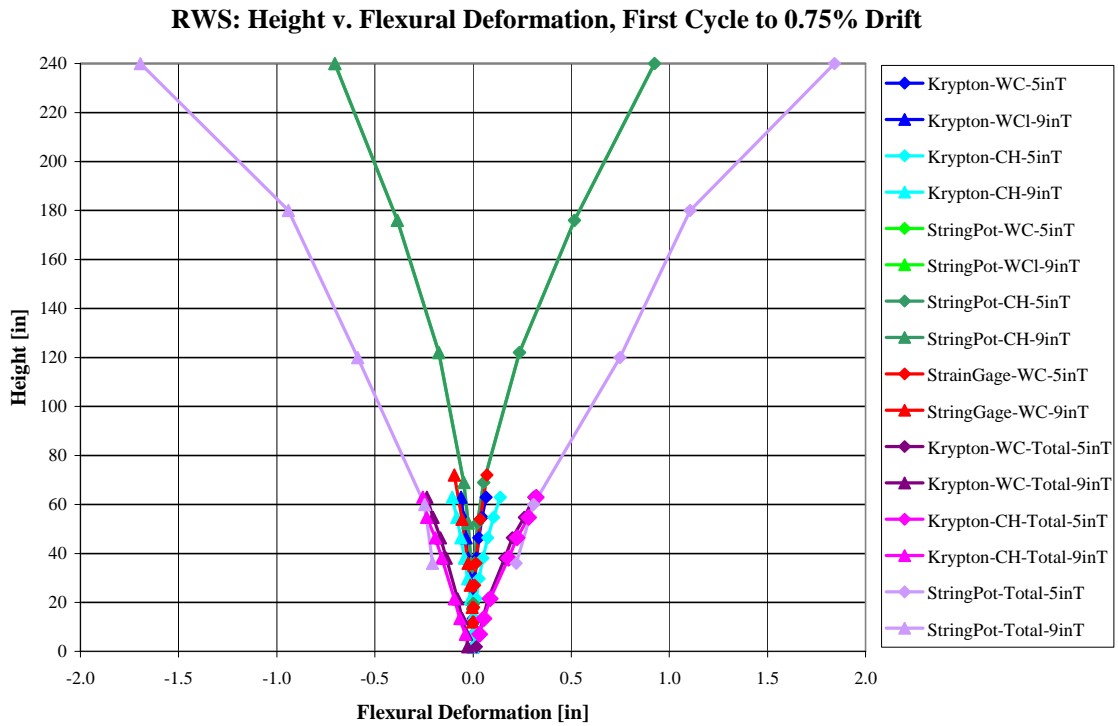


Figure 9.2h: RWS – Flexural deformation of various sensors – inelastic range

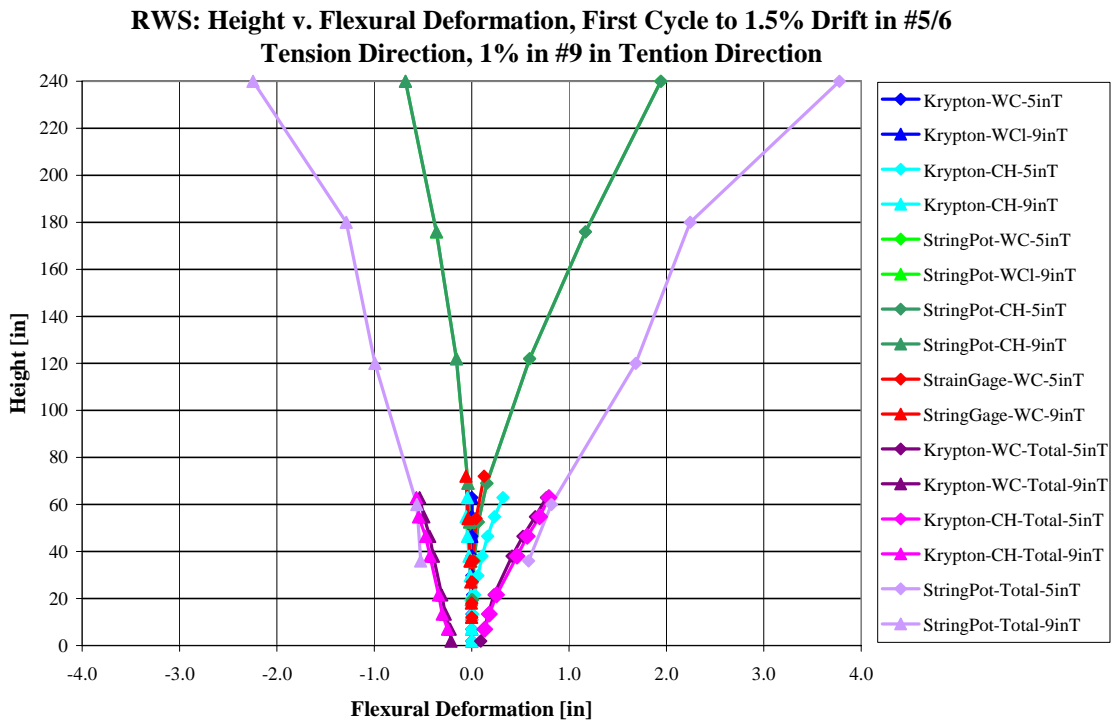


Figure 9.2i: RWS – Flexural deformation of various sensors – highly inelastic

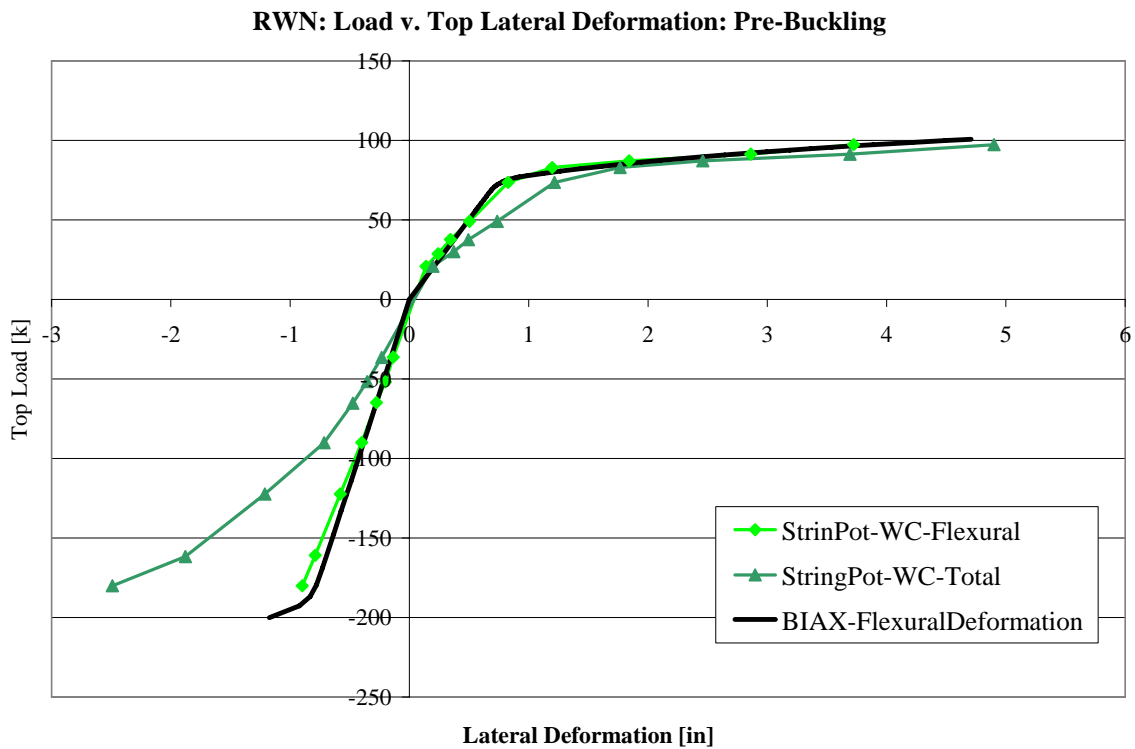


Figure 9.3.a: RWN – Predicted and calculated load v. deflection backbone

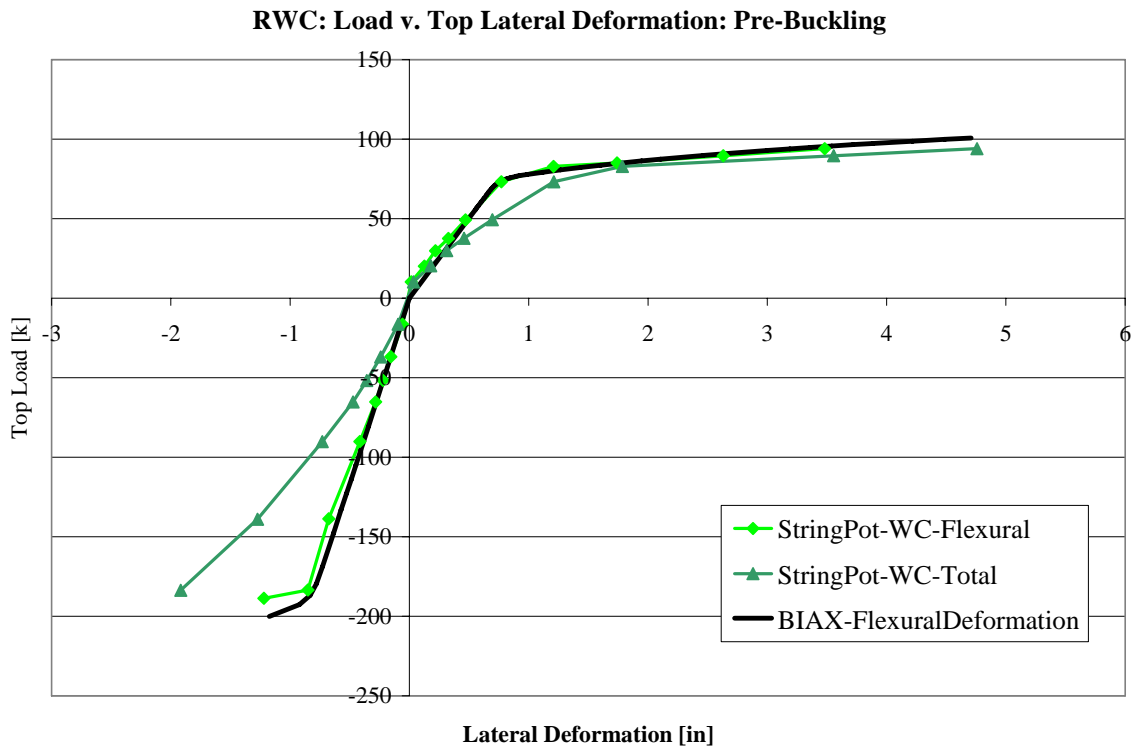


Figure 9.3.b: RWC – Predicted and calculated load v. deflection backbone

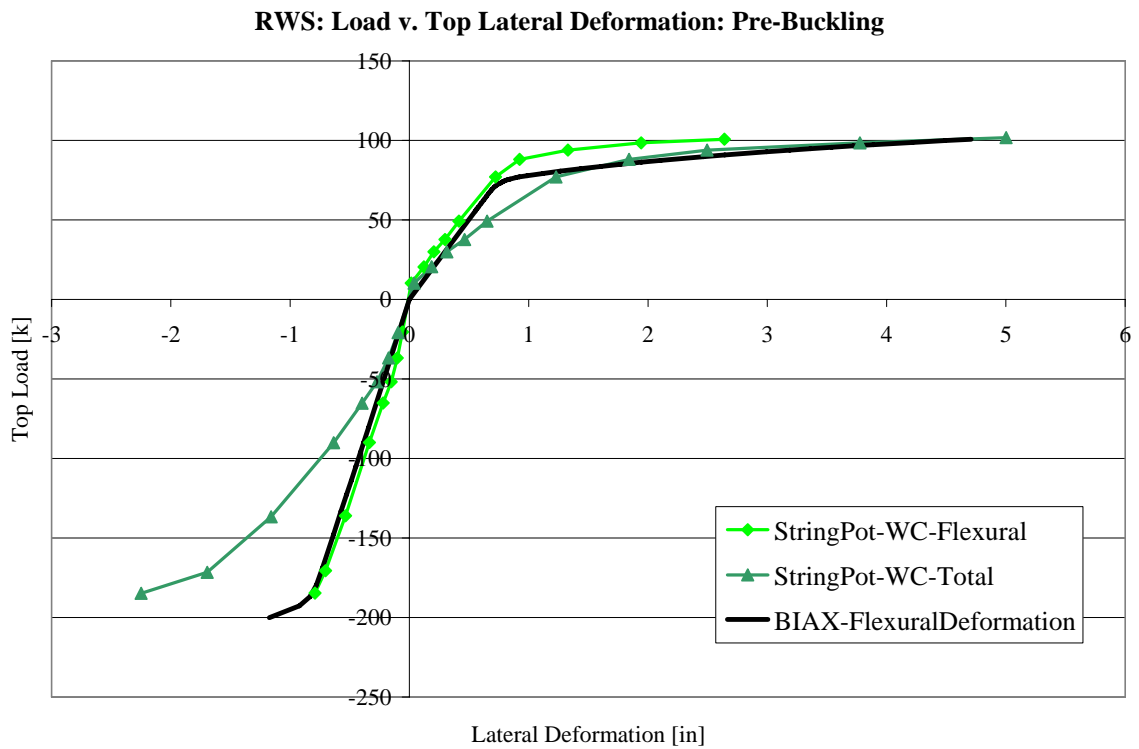


Figure 9.3.c: RWS – Predicted and calculated load v. deflection backbone

Load v. Flexural Deflection of 25% of Total Wall Height, Krypton-WC Data: Elastic Cycles

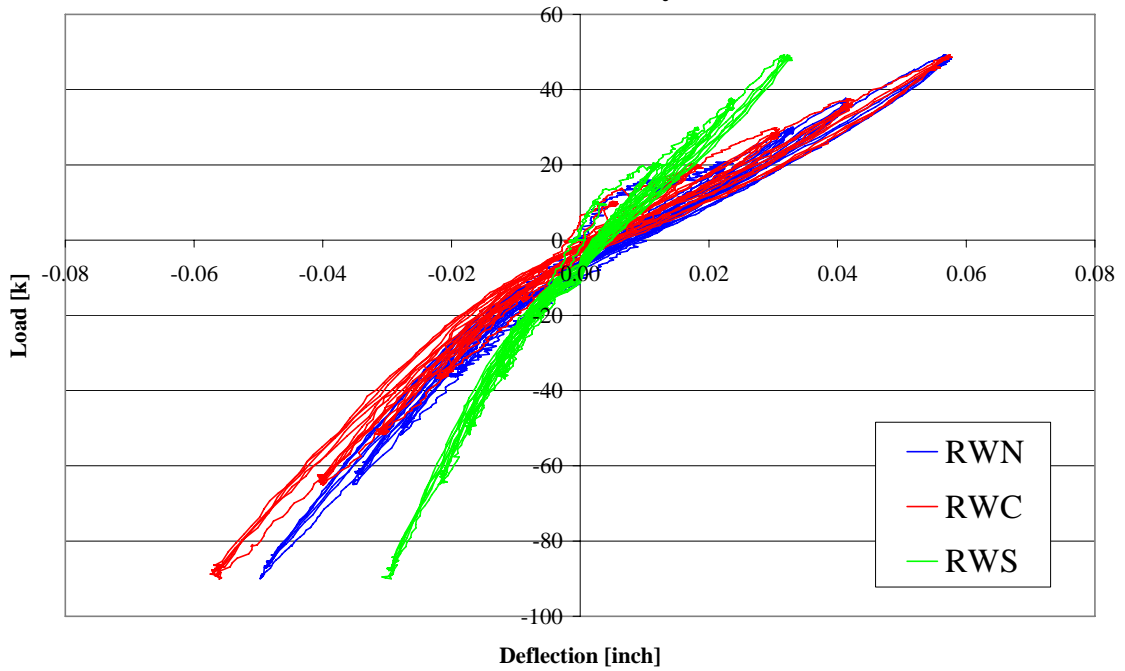


Figure 9.4a: Krypton comparison of load v. flexure – 25% wall height – elastic range

Load v. Flexural Deflection of 25% of Total Wall Height, Krypton-CH Data: Elastic Cycles

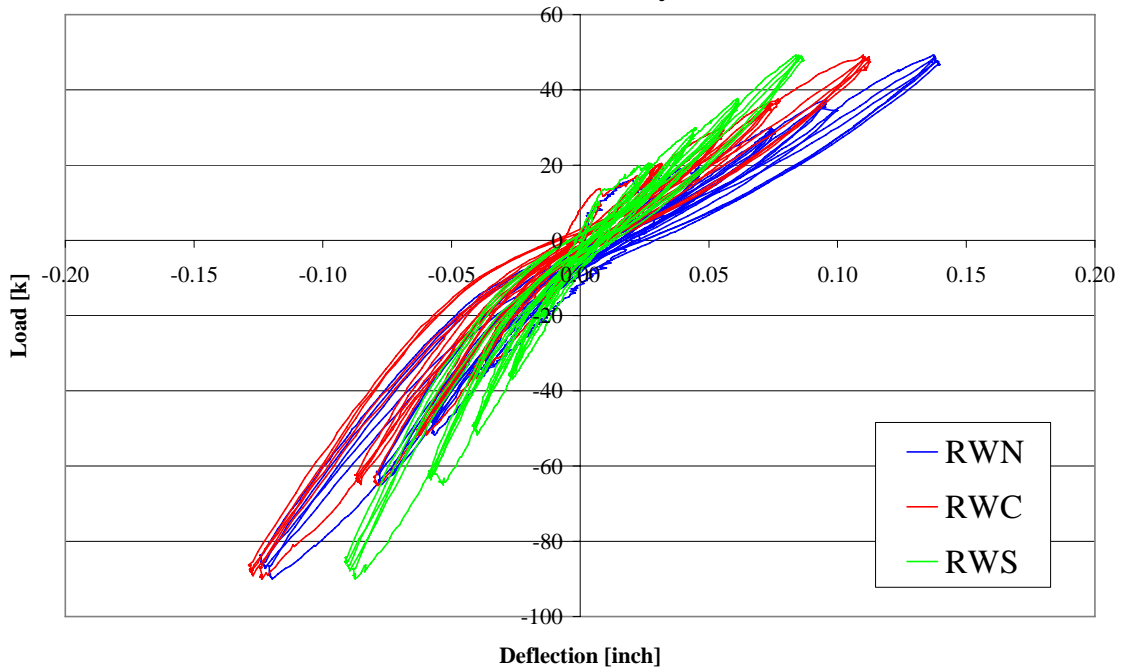


Figure 9.4b: Krypton comparison of load v. flexure – 25% wall height – elastic range

**Load v. Flexural Deflection of 25% of Total Wall Height, Krypton-
WC Data: Pre-Buckling**

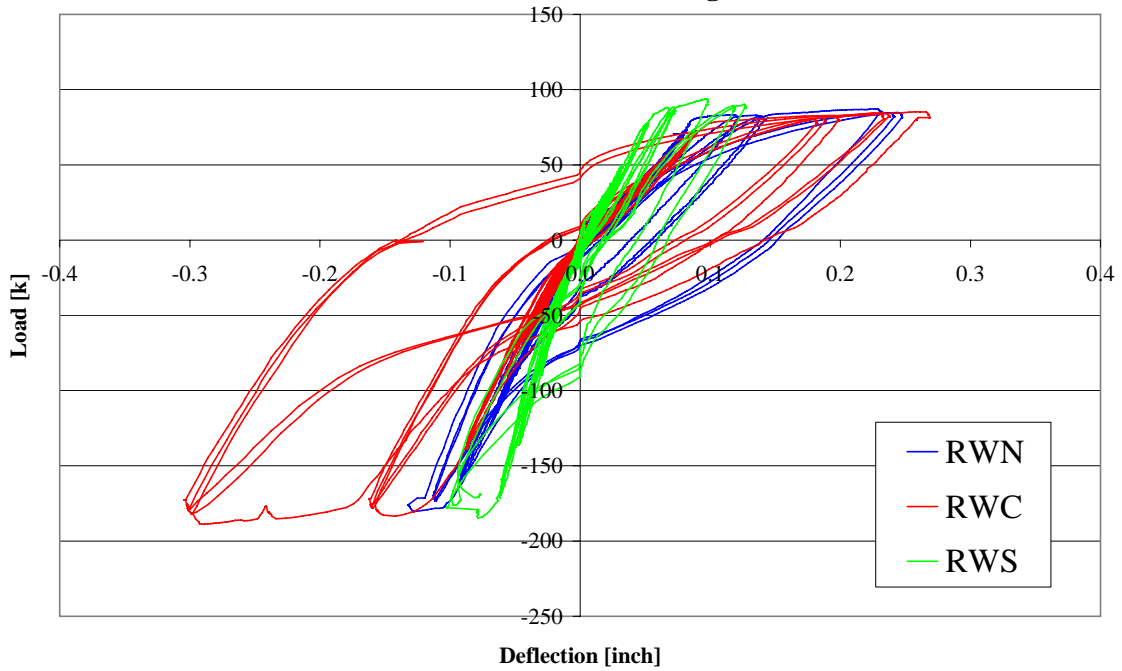


Figure 9.4c: Krypton comparison of load v. flexure – 25% wall height – inelastic range

**Load v. Flexural Deflection of 25% of Total Wall Height,
String Pot-WC Data: Elastic Cycles**

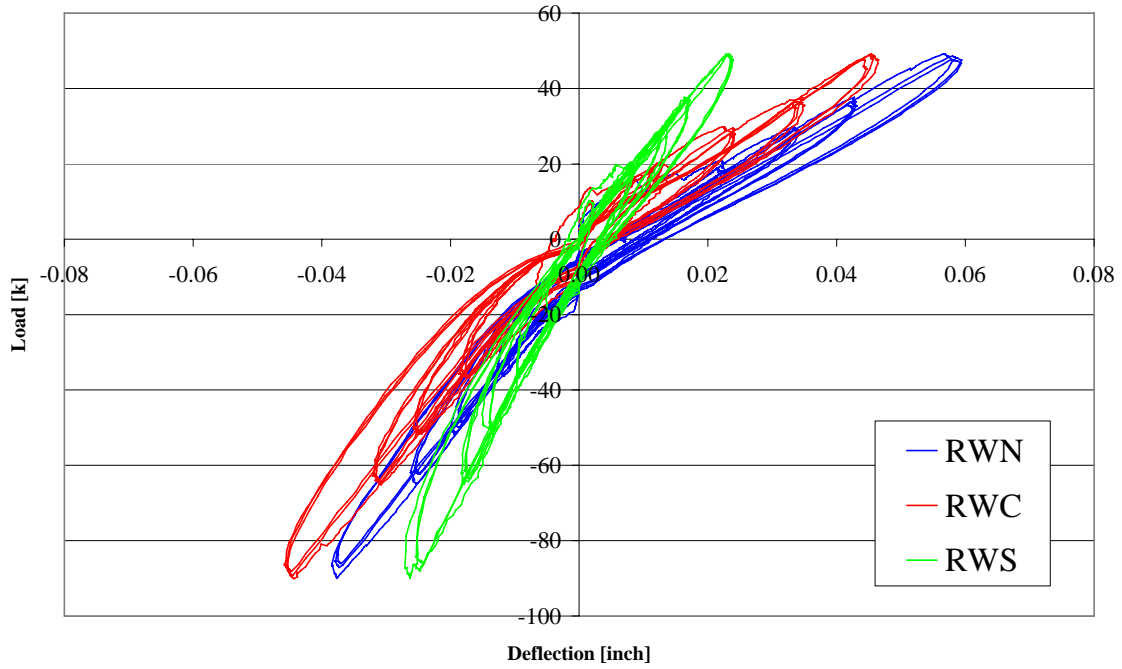


Figure 9.4d: String Pot comparison of load v. flexure – 25% wall height – elastic range

**Load v. Flexural Deflection of 25% of Total Wall Height,
String Pot-WC Data: Pre-Buckling**

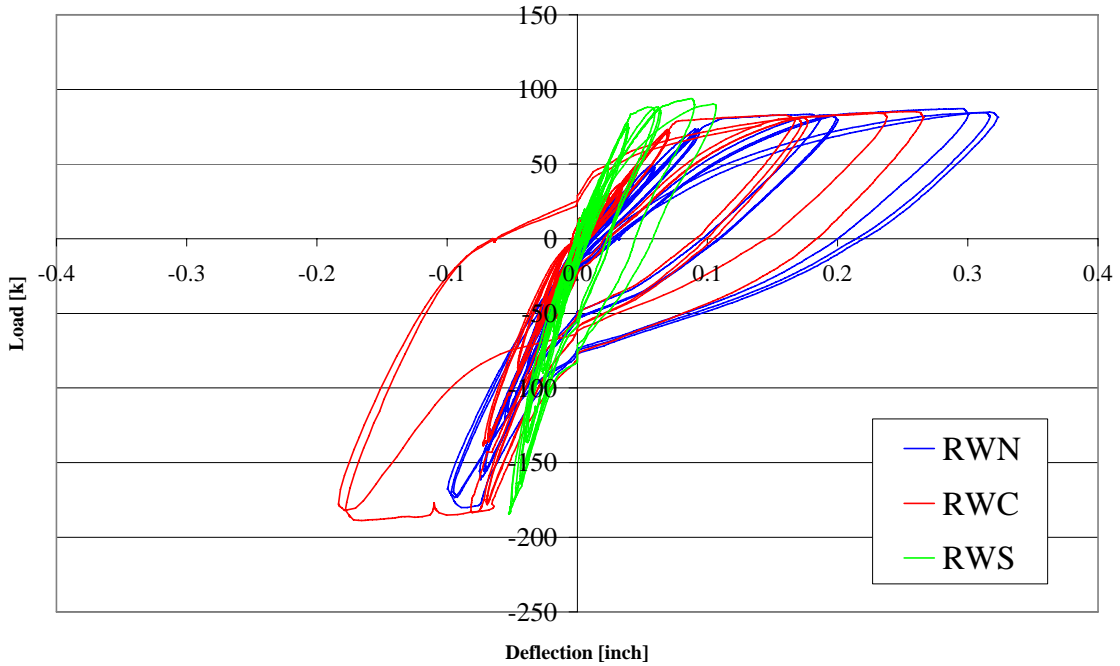


Figure 9.4e: String Pot comparison of load v. flexure – 25% wall height – inelastic range

Load v. Top Flexural Deflection, String Pot-WC Data: Elastic Cycles

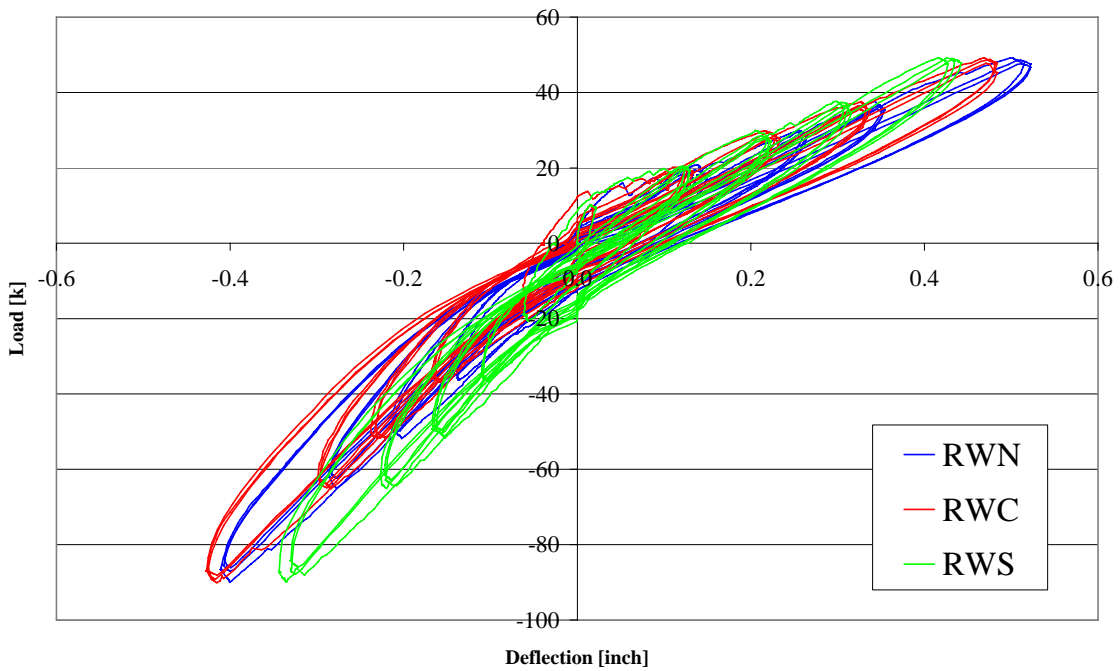


Figure 9.4f: String Pot comparison of load v. flexure – top wall height – elastic range

Load v. Top Flexural Deflection, String Pot-WC Data: Pre-Buckling

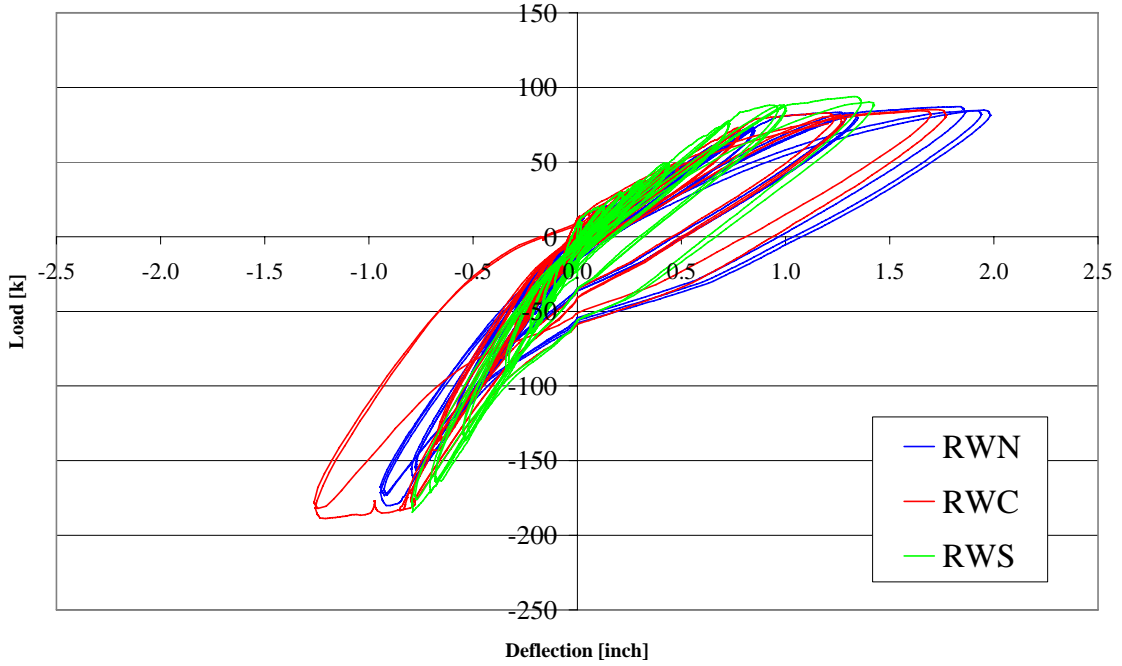


Figure 9.4g: String Pot comparison of load v. flexure – top wall height – inelastic range

RWN: Whole Cross Section: % Flexural Deformation v. Total Deformation at 25% of Total Height: Pre-Buckling

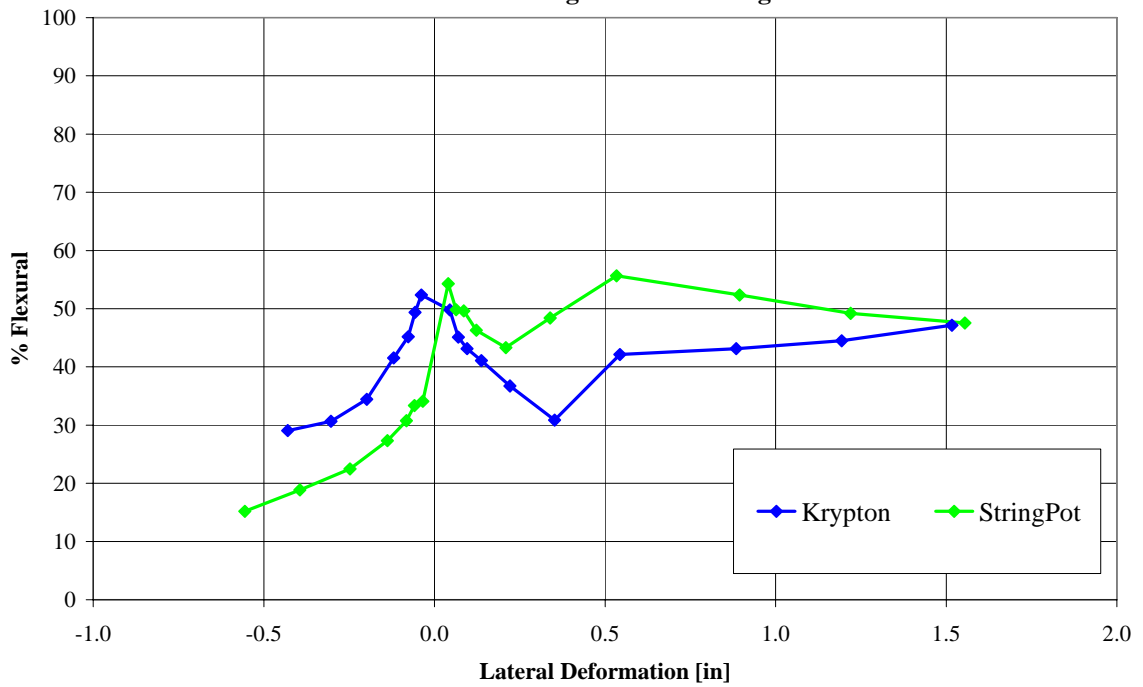


Figure 9.5a: Flexural percentage of total deformation v. total deformation – 25% height

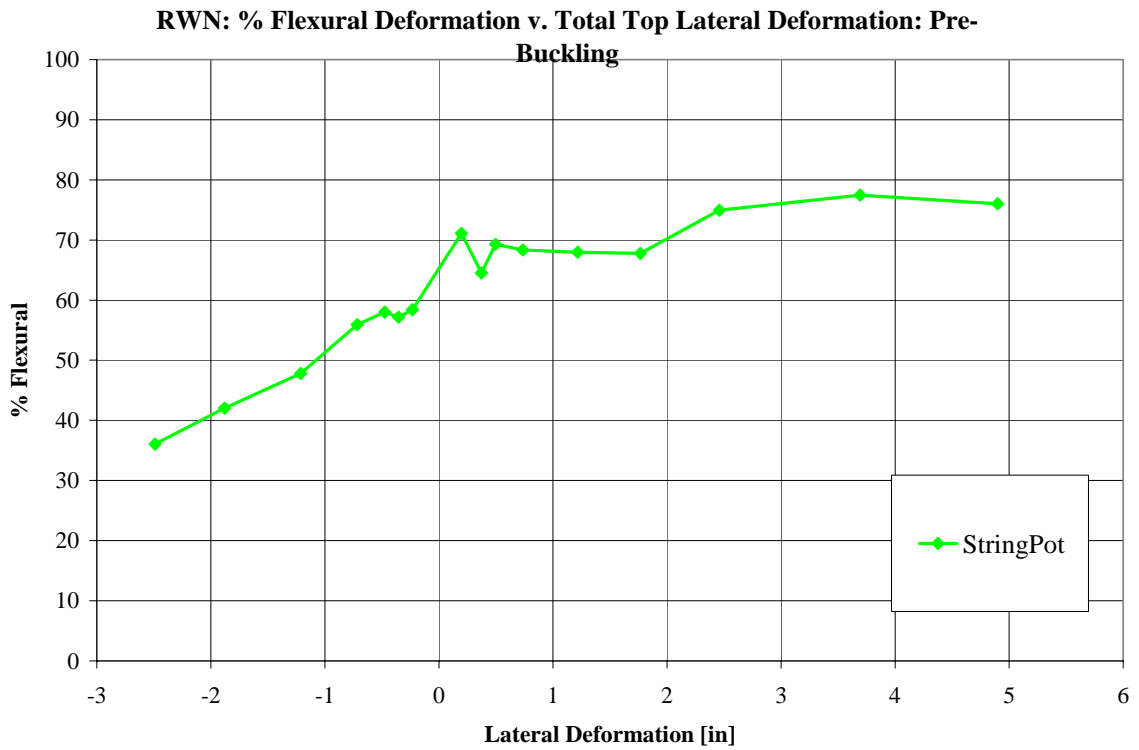


Figure 9.5b: Flexural percentage of total deformation v. total deformation – top height

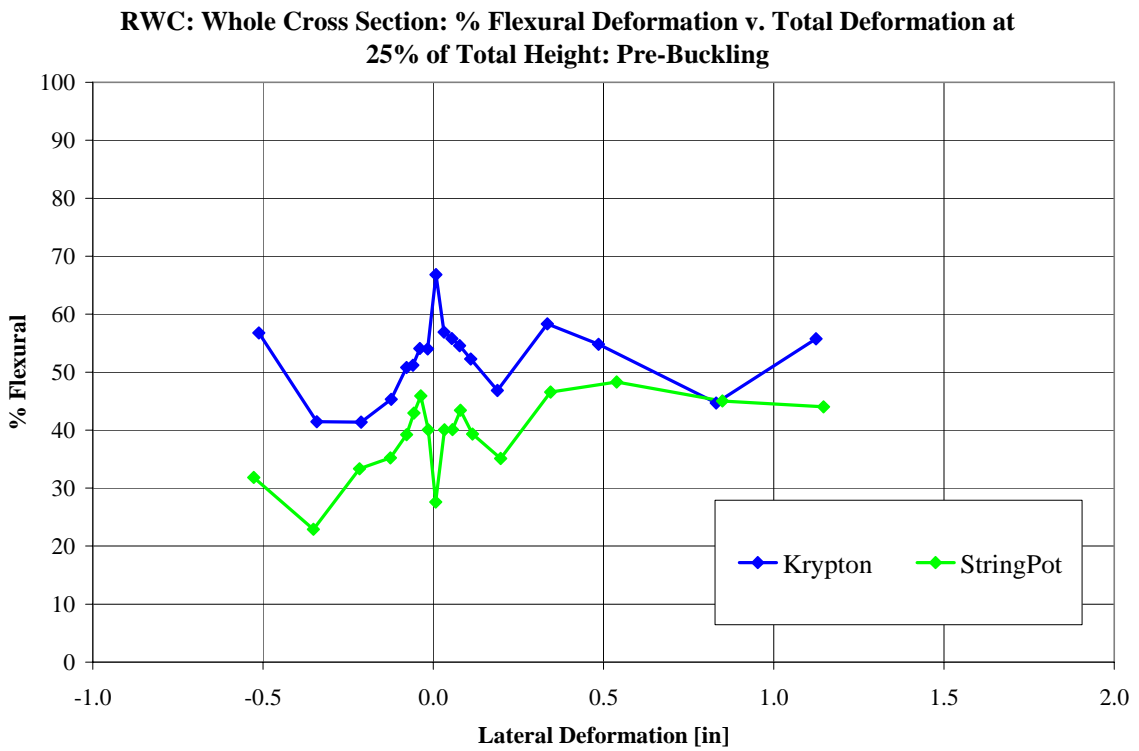


Figure 9.5c: Flexural percentage of total deformation v. total deformation – 25% height

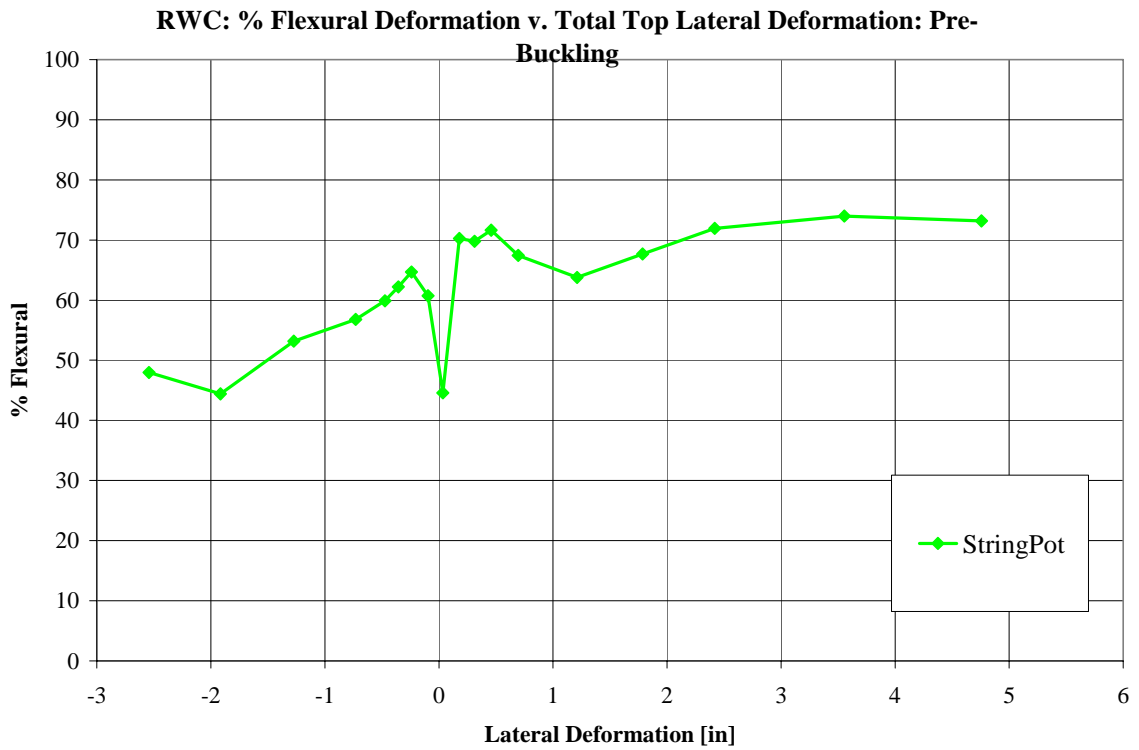


Figure 9.5d: Flexural percentage of total deformation v. total deformation – top height

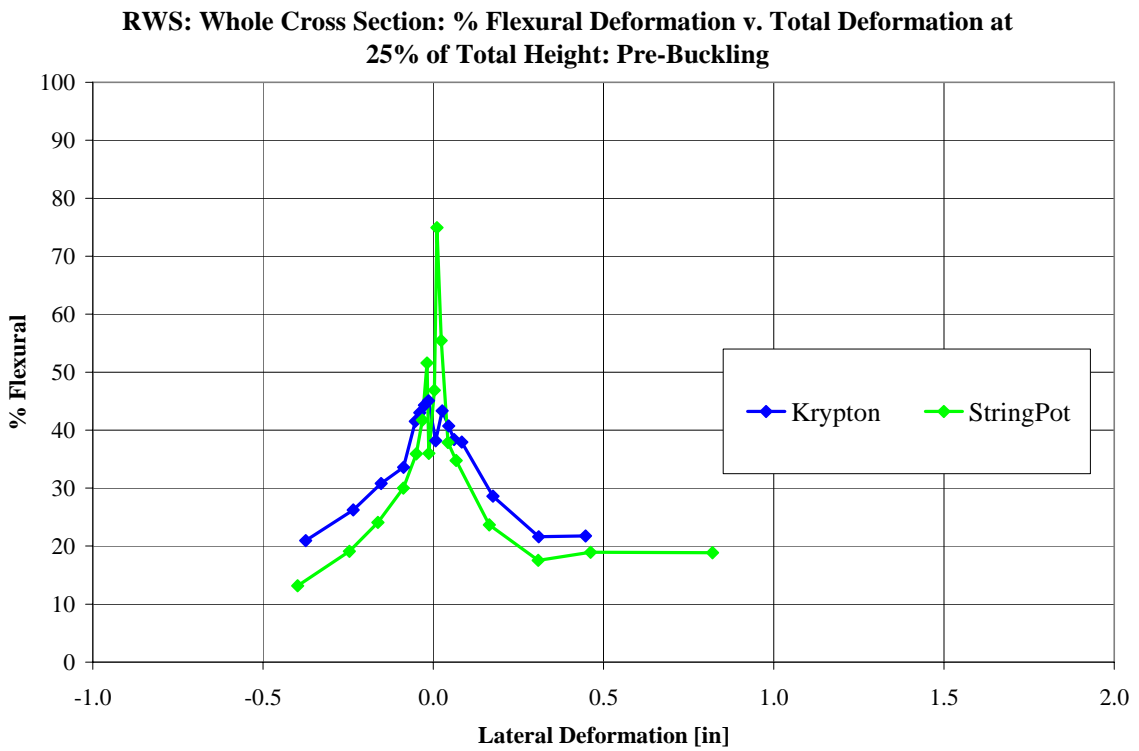


Figure 9.5c: Flexural percentage of total deformation v. total deformation – 25% height

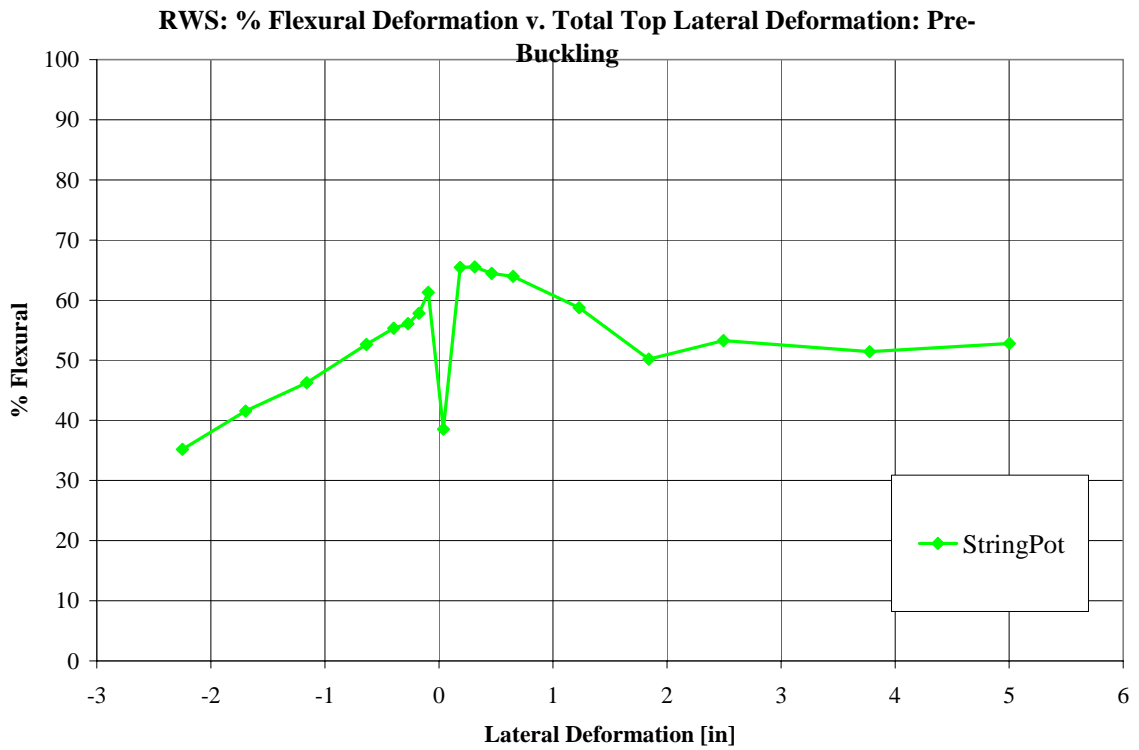


Figure 9.5d: Flexural percentage of total deformation v. total deformation – top height

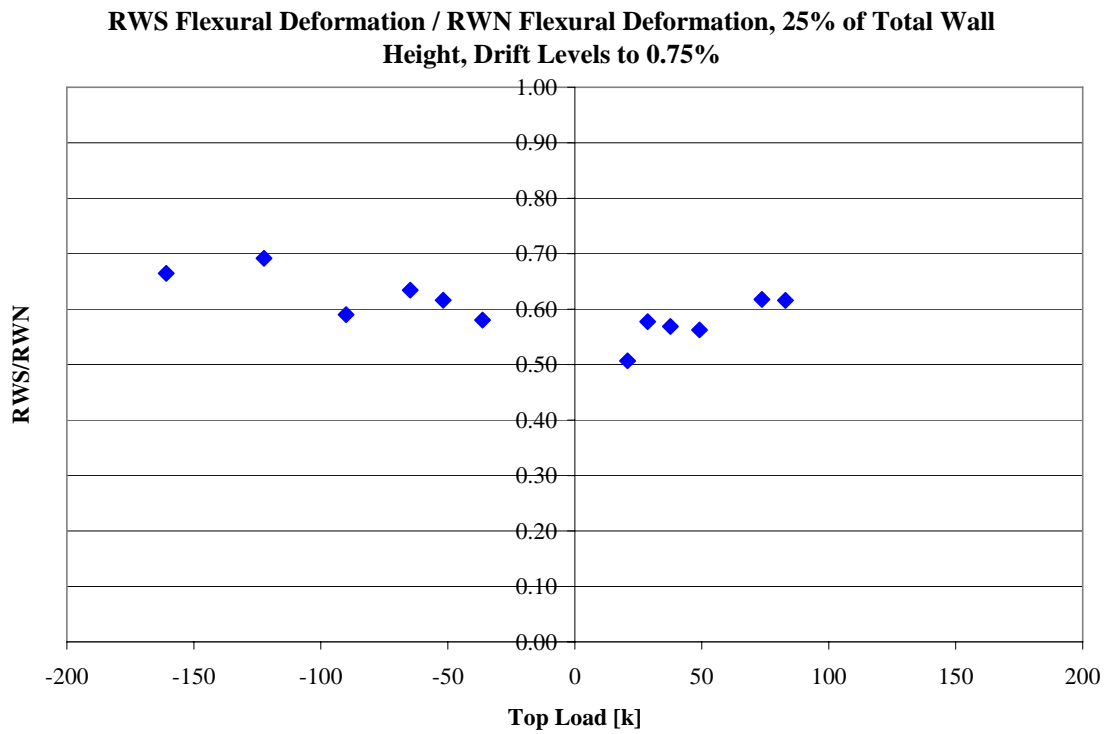


Figure 9.6a: Ratio of flexural deformation of RWS to RWN at similar displacements

**RWS Flexural Deformation / RWN Flexural Deformation, Top Height, String
 Pot Data, Drift Levels up to 1.5% in the No.5/6 in T Direction,
 1% in the No.9 in T Direction**

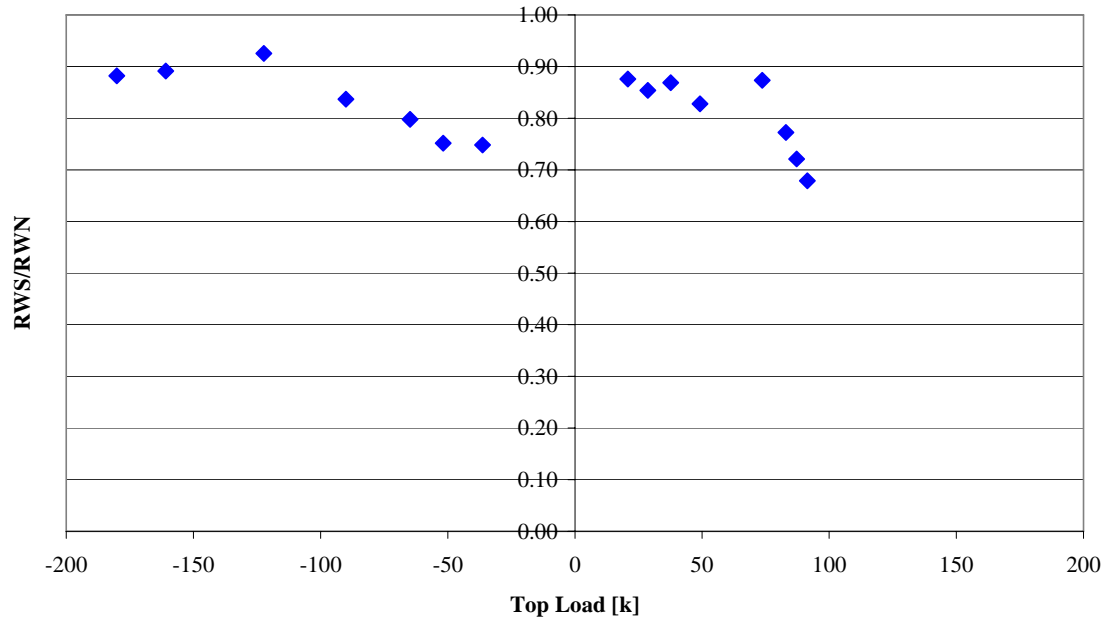


Figure 9.6b: Ratio of flexural deformation of RWS to RWN at similar displacements

Chapter 10: Steel to Concrete Bond Slip

10.0: Introduction

This chapter covers the methods used to determine the effects of strain penetration into the foundation of the test specimens, as well as the observed lapped splice bond slip. These two types of bond slip create a rotation at the foundation interface of the wall. Lateral deformation due to bond slip is then computed by modeling the deformation as a rigid body rotation. Strain penetration was found to be approximately 10% of the total top displacement undergone by RWN and RWC. This value was considerably larger for RWS, specifically in the inelastic range. Strain concentrations at the foundation interface created larger effects of strain penetration. This increase was as much as 20% of the total top displacement. In addition, lapped splice slip also contributed to additional top displacement in the inelastic range.

10.1: Calculation of Strain Penetration

Strain penetration is created by axial strain of the longitudinal reinforcement penetrating into the foundation of the test specimens. The gradient at which the axial strain is removed from the longitudinal reinforcement depends on the steel to concrete bond. Additional load creates larger strains in the longitudinal reinforcement, as well as a larger depth of penetration into the block. The elongation of the longitudinal reinforcement is equal to the area under the plot of axial strain versus length of penetration. This can be seen and measured with axial strain gages on the extreme longitudinal reinforcement in the foundation block. Unfortunately, not enough strain gages are present to make a precise calculation of longitudinal bar elongation for each test specimen. For this reason, the strain gages will be used as a means of comparison and not calculation.

The instrument used to calculate the rotation created by strain penetration is the bar LVDTs. These LVDTs are attached to the longitudinal reinforcement by means of a

capacitor discharge welded stud. This attachment is approximately one half inch above the foundation interface. This height was necessary for space to attach the LVDT, as well as clearance in between rib spacing. The opposite end is attached to the foundation block. The displacements measured by these LVDTs are the elongation from strain penetration, as well as the axial strain from the bottom one half inch of the wall. The rotation of this half inch is thought to be negligible, considering that strain penetration usually reaches depths of 14 to 20 inches.

Rotation from strain penetration is calculated by fitting a linear trend line through the displacements recorded by the bar LVDTs. The availability of these sensors is different for each wall, due to interference with other sensors deemed more important. For this reason, only the sensors available in common between each wall are used in the strain penetration calculations. This was done, such that the strain penetration calculations are done in the exact same manor for each wall, reducing the uncertainty from the calculations when comparing the walls. Fortunately, the extreme most LVDTs are common to each wall. This includes LVDTs attached to the most extreme No.6, No.5, and No.9 bars. The lateral displacement for each wall is then computed by multiplying the rotation at the interface by the height in question. Refer to figure 10.1 for an illustration of this model.

10.2: Calculation of Lapped Splice Bond Slip

The calculation of rotation from lapped splice bond slip is found by calculating the remainder of base rotation when all other rotation effects are subtracted. The total rotation at the base of the wall was calculated by fitting a linear trend line through the Krypton LEDs at a height of two inches. The rotation from strain penetration discussed in the previous section is then subtracted. Finally, the rotation from axial strain and resulting integrated curvature is subtracted. The rotation from flexure is lower than what is really occurring from the limitations in instrumentation discussed in previous chapters. For this reason, the rotation from flexure is also calculated with strain gages at the interface in

order to determine possible bounds of lapped splice slip. Unfortunately, the strain gages at the interface fail before the wall reached the highly inelastic range, where lapped splice slip is at its maximum.

This calculation is performed for the other two walls as well. These calculations are done in order to verify the results of RWS. The lapped splice bond slip calculations for RWN and RWC should return a negligible rotation when compared to RWS. Rotations calculated for RWN and RWC that are not negligible show that the analysis technique does not accurately capture the effects of flexural deformation when the No.9 boundary element is in tension.

10.3: Comparison of Axial Strain in the Foundation

Axial strain gages were placed on longitudinal reinforcement in the foundation at depths of 6", 12", 18", and the foundation interface. Some strain gages were damaged in the construction of the test walls, prior to the test of each wall. All available strain gages in each wall were shown in four select loading ramp maximums of interest. The significance of these four ramps are half of the elastic load limit, the elastic load limit, well into the inelastic range, and a highly inelastic ramp where many instruments were on the verge of failure. See figures 10.2a through 10.2d and figure 10.3a through 10.3c.

These figures show close agreement between the magnitudes of axial strain along the anchored reinforcement in the elastic range. This is expected, as the axial strain concentration above the lapped splice terminations is very close to RWN and RWC in the elastic cycles. This is depicted in figure 7.5a, b, & c in chapter 7. The strain concentration at the foundation interface can be assumed to be similar to that above. This suggests that the top displacements of each wall should be very close in the elastic range.

Axial strain at the foundation interface for RWS increases a great deal more than RWN and RWC in the inelastic range. This is not necessarily observed with the strain gages,

due to the interface strain gages of RWS failing shortly into the inelastic range. This failure is thought to be due to higher strains than RWN and RWC, which caused the failure. This is shown in greater detail with figures 10.4a through 10.4d. Note that figure 10.3d shows that the No.5&6 boundary element does not even register a compressive strain when that boundary element is clearly in compression. These plots are not exactly conclusive, which is expected from the highly localized readings of the strain gages.

The axial strain gages on the longitudinal reinforcement in the foundation suggest that the effects of strain penetration will be similar for each wall in the inelastic range, but larger for the lapped splice wall in the inelastic range from an additional strain concentration. This can be seen in figure 8.6a, depicting the height v. curvature relationship. RWS has a greatly increased curvature outside the lapped splice length at 1% drift, a highly inelastic loading ramp maximum.

10.4: Top Displacement Resulting from Strain Penetration

Rotations generated from strain penetration were computed for each time step of test data. These calculations have been consolidated into load v. top deflection resulting from strain penetration backbones. In addition to this plot, a top deflection resulting from strain penetration v. total top lateral deformation backbone has been generated. These plots include each loading ramp maximum, up to the ramps just prior to out of plane or local bar buckling. Refer to figures 10.5a, & b.

The strain penetration backbone curves show the same result as the axial strain penetration plots. Top displacement from strain penetration is very similar for each wall in the elastic range. This changes a considerable amount for RWS in the inelastic range. Each wall experiences a larger increase in top displacement from strain penetration in the inelastic range when compared to that in the elastic range. This increase is considerably larger for RWS, on the magnitude of twice that of RWN and RWC. The axial strain

concentration at the interface plays a large role in the total top displacement undergone by a wall with lapped splices in the region of expected plastic hinging.

10.5: Contribution of Strain Penetration to Total Displacement

Quantifying the contribution of strain penetration to the total top displacement is of interest for design purposes. Plots of the percentage of the total top displacement from strain penetration versus top load a total top displacement can be seen in figures 10.6a & b. These figures show that strain penetration accounts for approximately 10% of the total top displacement in continuous and mechanically spliced bar walls. Top displacement from strain penetration varies for lapped splices. Strain penetration typically accounted for 10% of the total top displacement in the elastic range and 20% in the inelastic range. Top displacement is again reported as the average displacement across the wall length.

10.6: Slip from Lapped Splice Bond Failure

The rotation at the interface for RWS from lapped splice bond failure is verified in figure 10.7. This figure shows no difference between the three walls at the displacement levels shown. The method used overestimates the contribution of displacement due to lapped splice slip from an underestimation of the rotation contribution from flexural rotation. This shows that no lapped splice slip occurs at these displacements levels. The Krypton data is at the verge of failure and some LEDs are questionable at the displacement levels shown from cracking at the sensor attachment. This is a possible cause for the registered displacement for RWN when considering the lapped splice slip calculations. This is confirmed when examining the flexural response of RWN and RWC. The difference between the two at the larger drift levels with the No.9 boundary element in tension is approximately 10% of the total deformation. This difference is the same percentage of deformation that is responsible from the residual base rotation. Excluding this portion of the plot, the result from lapped splice slip (or the missing part contribution of flexural deformation for RWN and RWC) is negligible, within 1% of the total contribution. This

method is unable to quantify the top displacement from lapped splice slip from failure of instruments at the observed load levels where slip was observed.

The possible contribution of lapped splice slip will be quantified later in this report when all displacement modes are summed. In addition to the possible lapped splice slip, the perceived lower flexural deformation for RWN will be quantified. The rotation that is not accounted for when considering all rotation effects is named the 'residual base rotation'. This rotation is partially due to a lower strain penetration and larger flexural rotation that the instruments failed to record. The residual base rotation is assumed to be solely the result of a smaller flexural rotation at the base from the similar strain penetration results of the walls and the variation of RWN in the No.9 boundary element when considering the flexural response. The residual base rotation is used in chapter T, as a means to place bounds on the possible contributions of flexural deformation.

Lastly, the discrepancies in the total calculated RWS response when compared to RWN and RWC can be attributed to lapped splice slip in lieu of being unable to calculate it directly. These calculations do however, verify that the methods used to calculate flexural deformation do not underestimate the total response a great deal from the underestimation of flexural rotation at the base.

10.7: Summary of Findings

Strain penetration was found to account for approximately 10% of the total displacement of the test specimens. This varied to as much as 20% for RWS in the inelastic region from strain concentrations at the foundation interface created from the lapped splices. Lapped splice bond slip was also quantified. This displacement causing mechanism was found to be negligible to a drift level of 1.5% in the No.5&6 boundary element in tension direction. Limitations of the sensors at larger drift levels does not allow lapped splice bond slip to be quantified past this drift level. Instead, the possible bounds of the displacement resulting from lapped splice bond slip will be quantified when all displacement modes are summed in chapter 12.

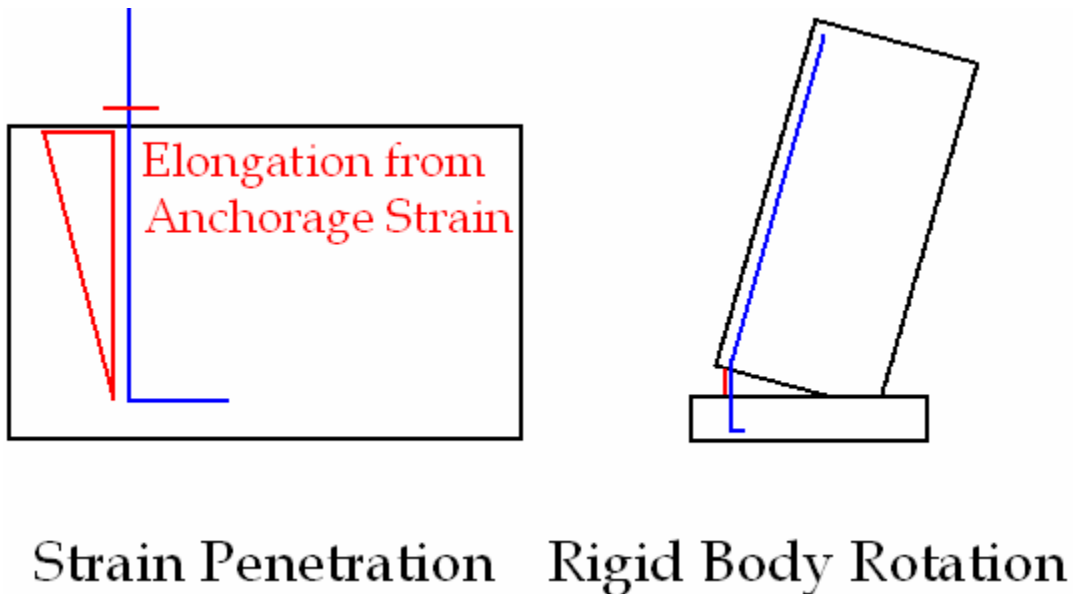


Figure 10.1: Rigid body rotation model for calculating lateral deformation

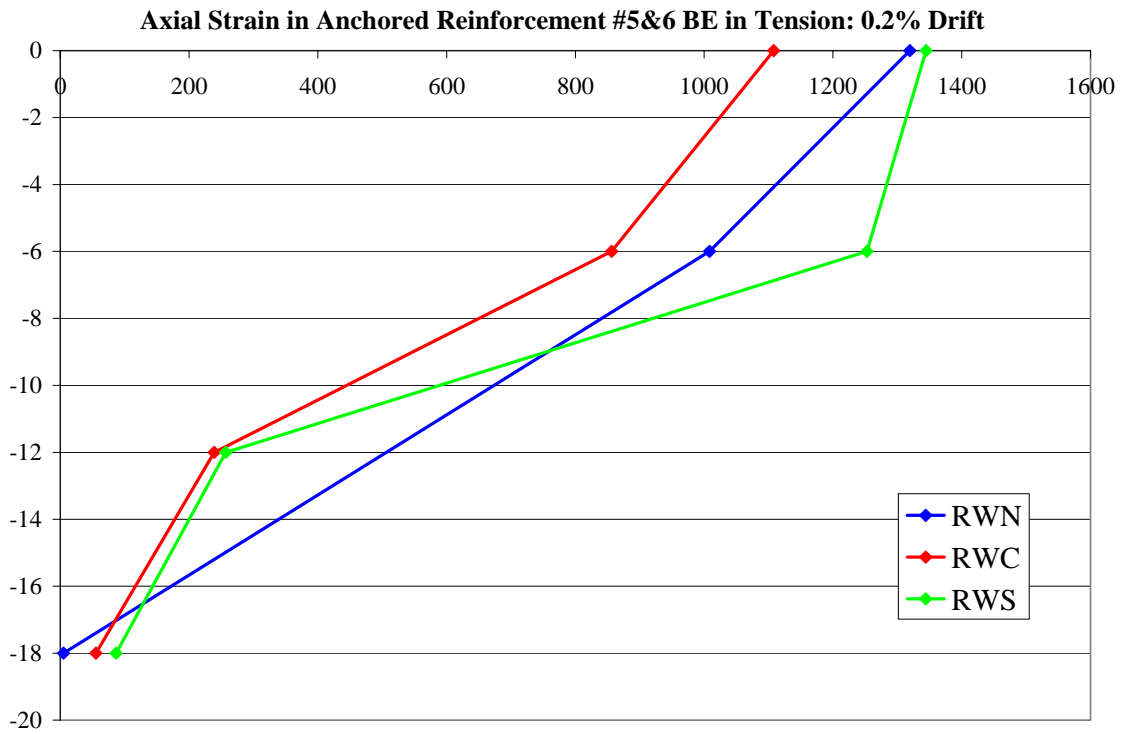


Figure 10.2a: Axial strain in extreme anchored reinforcement, well before elastic limit

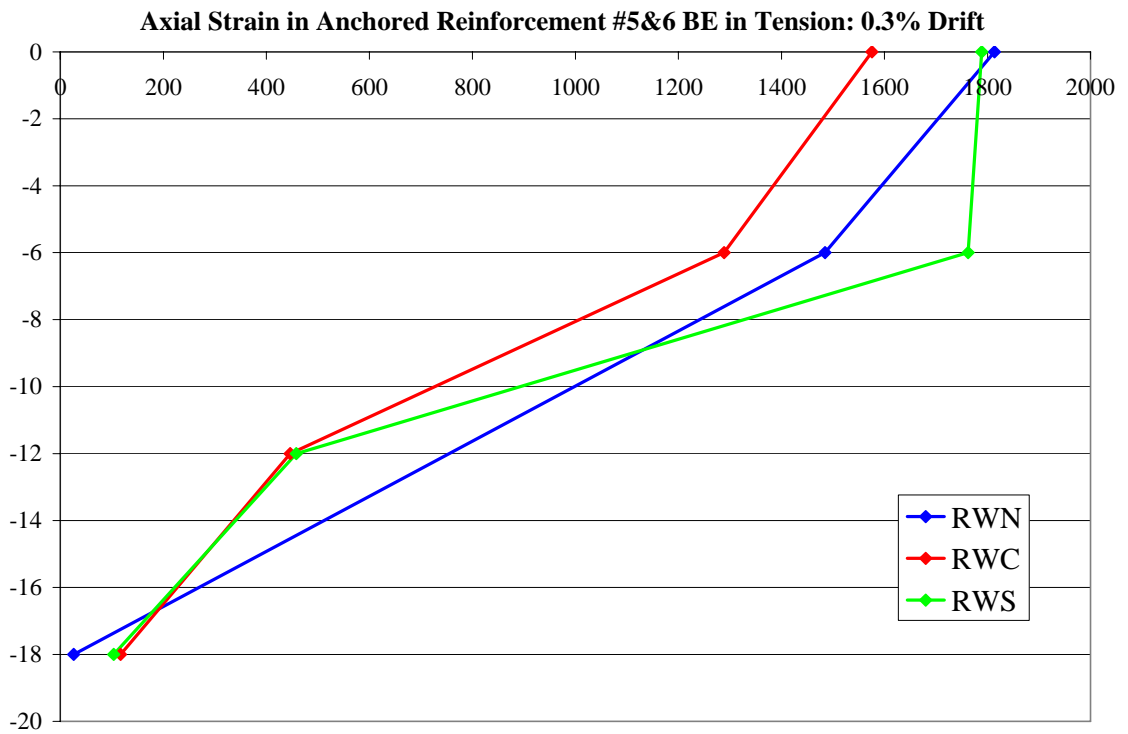


Figure 10.2b: Axial strain in extreme anchored reinforcement, at the elastic limit

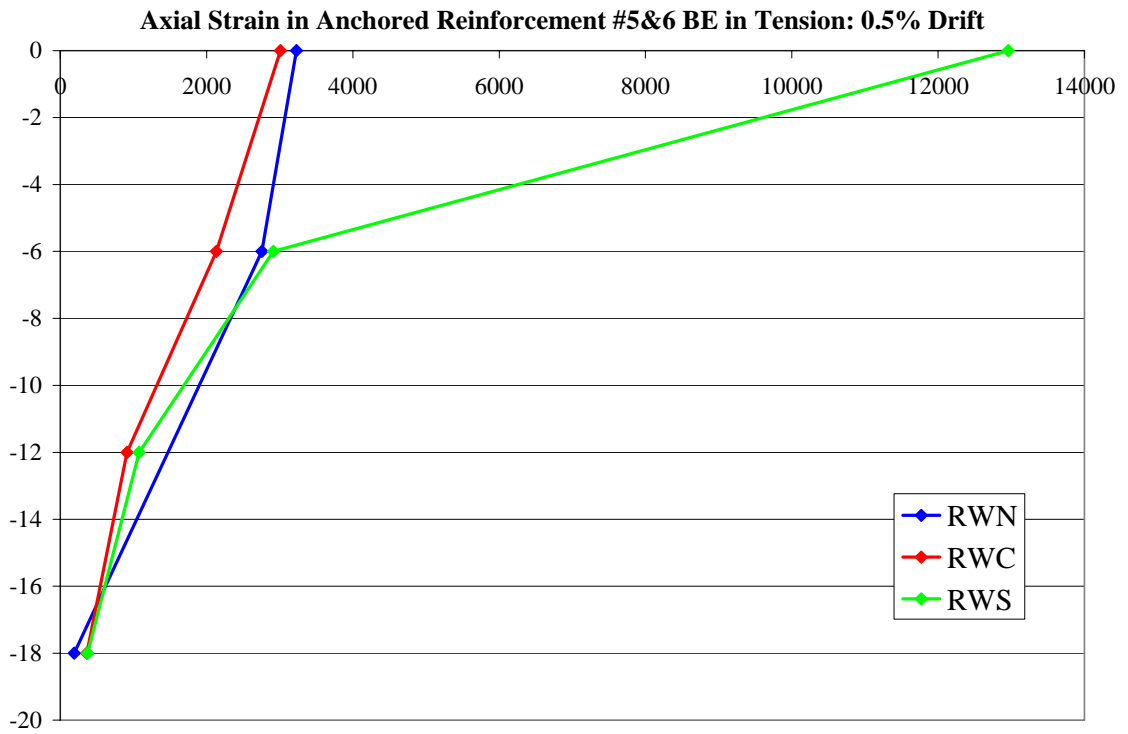


Figure 10.2b: Failure of RWS interface strain gage soon into the inelastic range

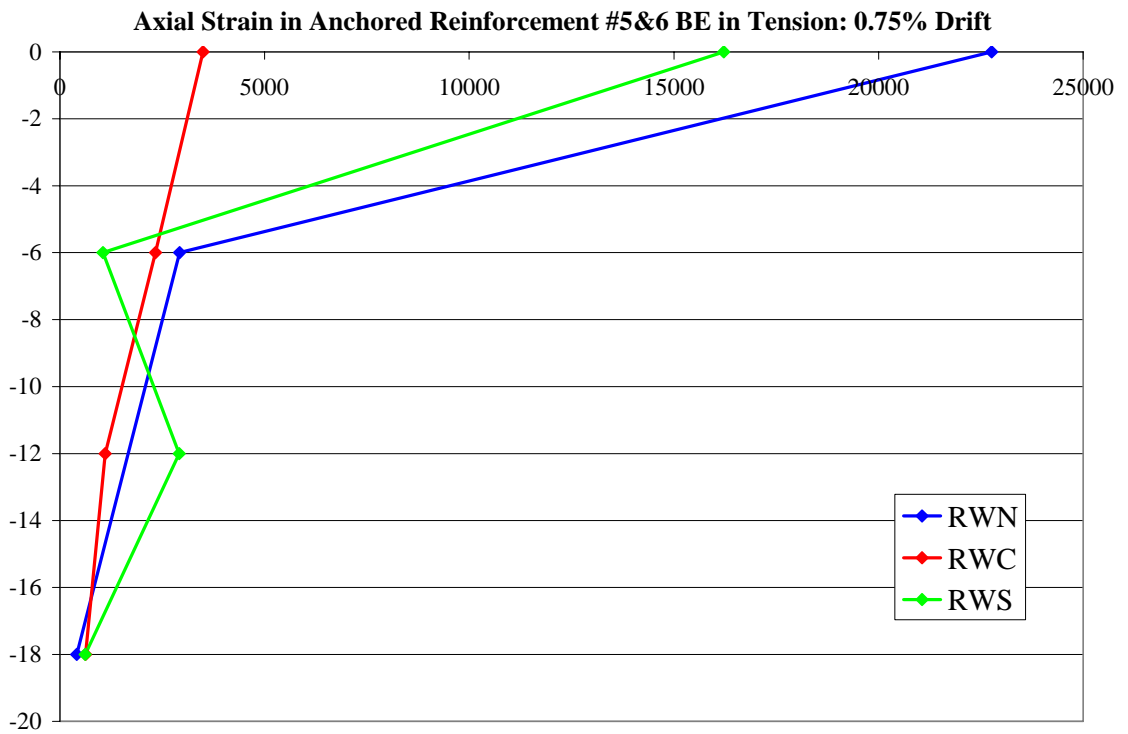


Figure 10.2b: Axial strain of extreme anchored reinforcement, just into the inelastic range

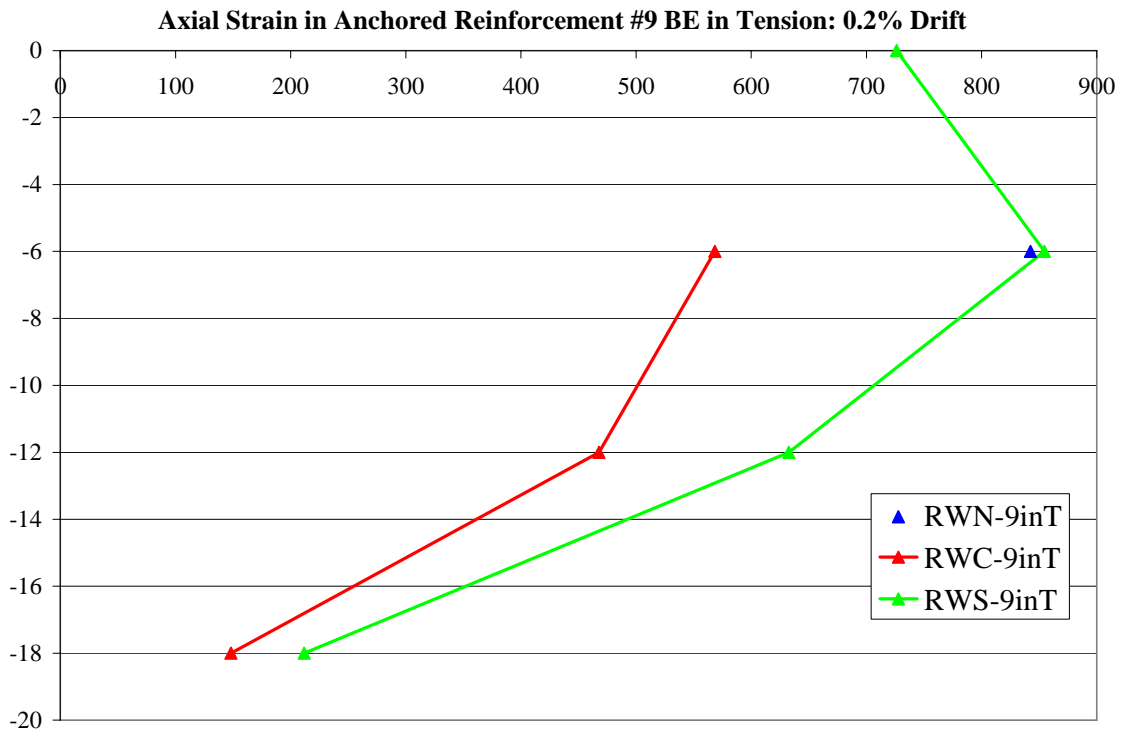


Figure 10.3a: Axial strain in extreme anchored reinforcement, well before elastic limit

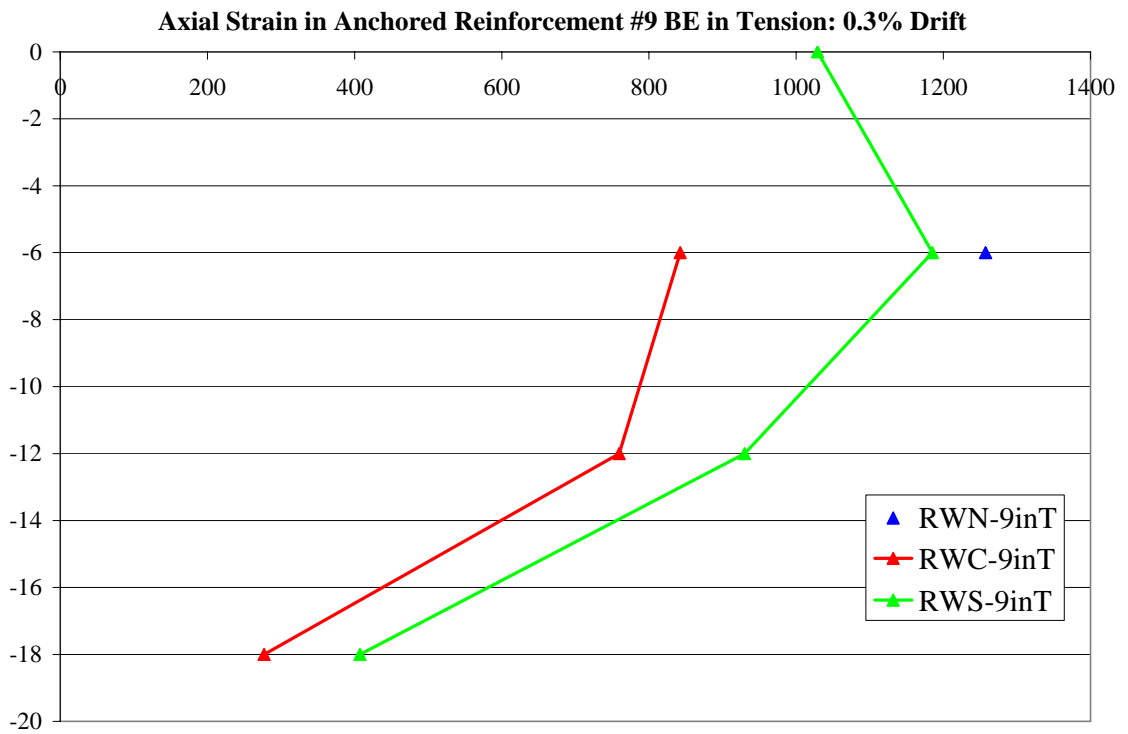


Figure 10.3b: Axial strain in extreme anchored reinforcement, at the elastic limit

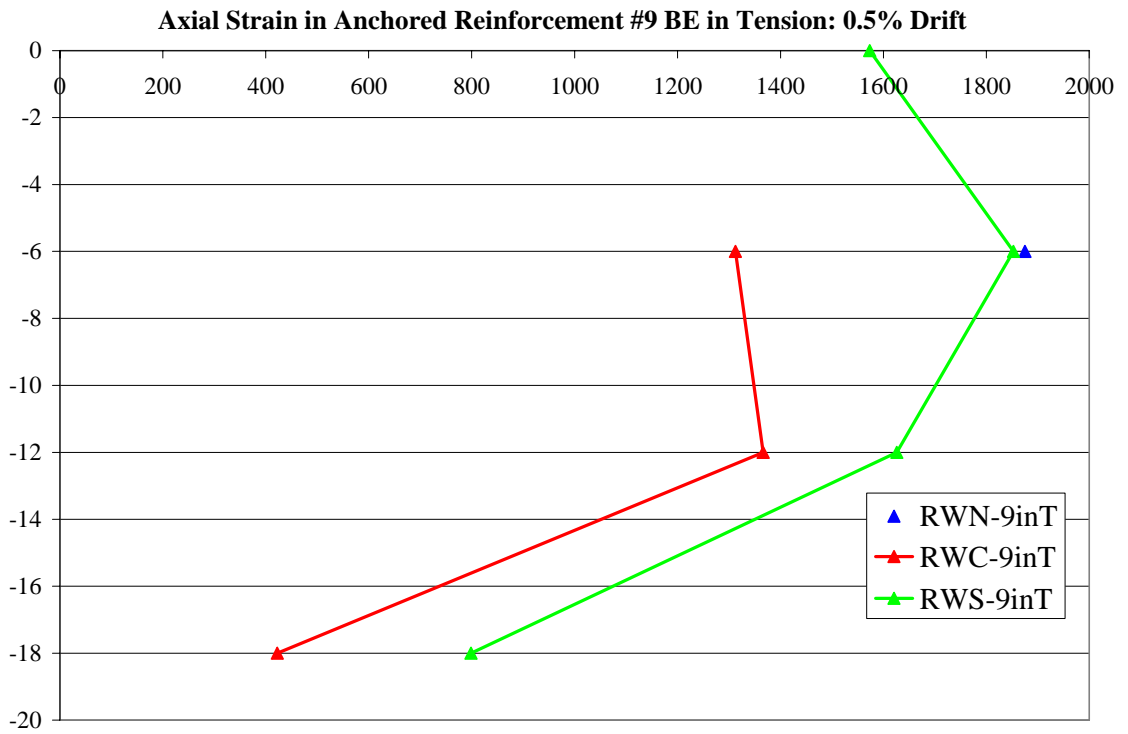


Figure 10.3c: Axial strain in extreme anchored reinforcement, just into the inelastic limit

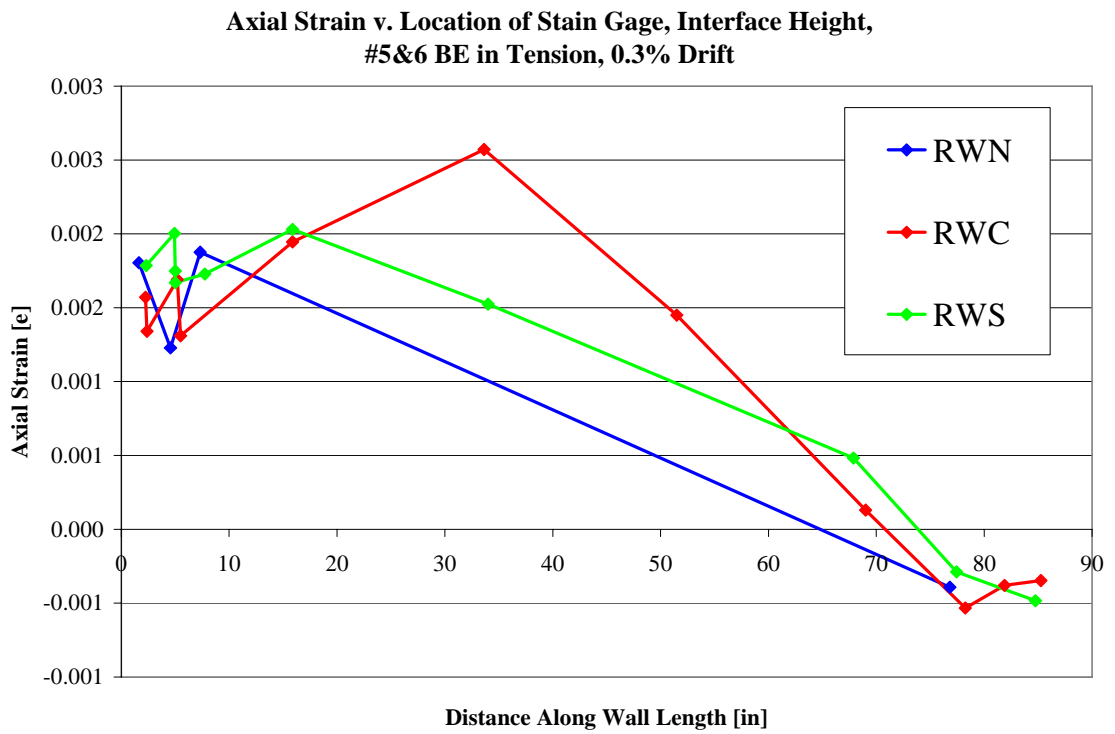


Figure 10.4a: Elastic comparison of axial strain at the foundation interface, No.5/6 in T

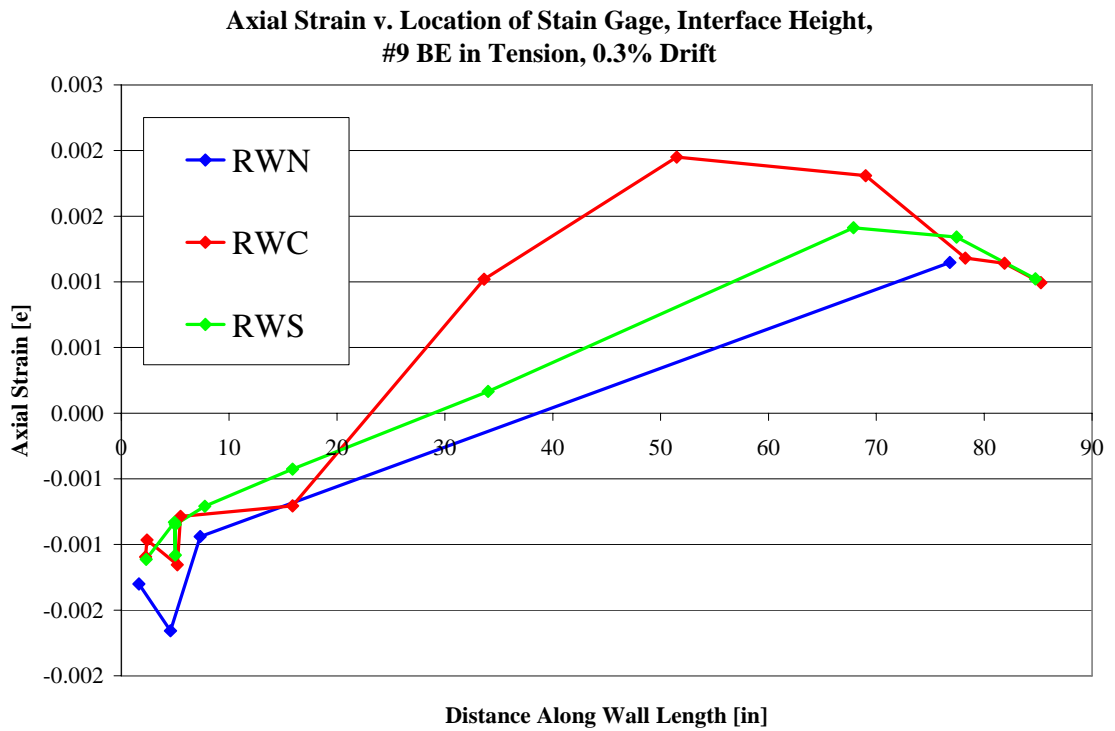


Figure 10.4b: Elastic comparison of axial strain at the foundation interface, No.9 in T

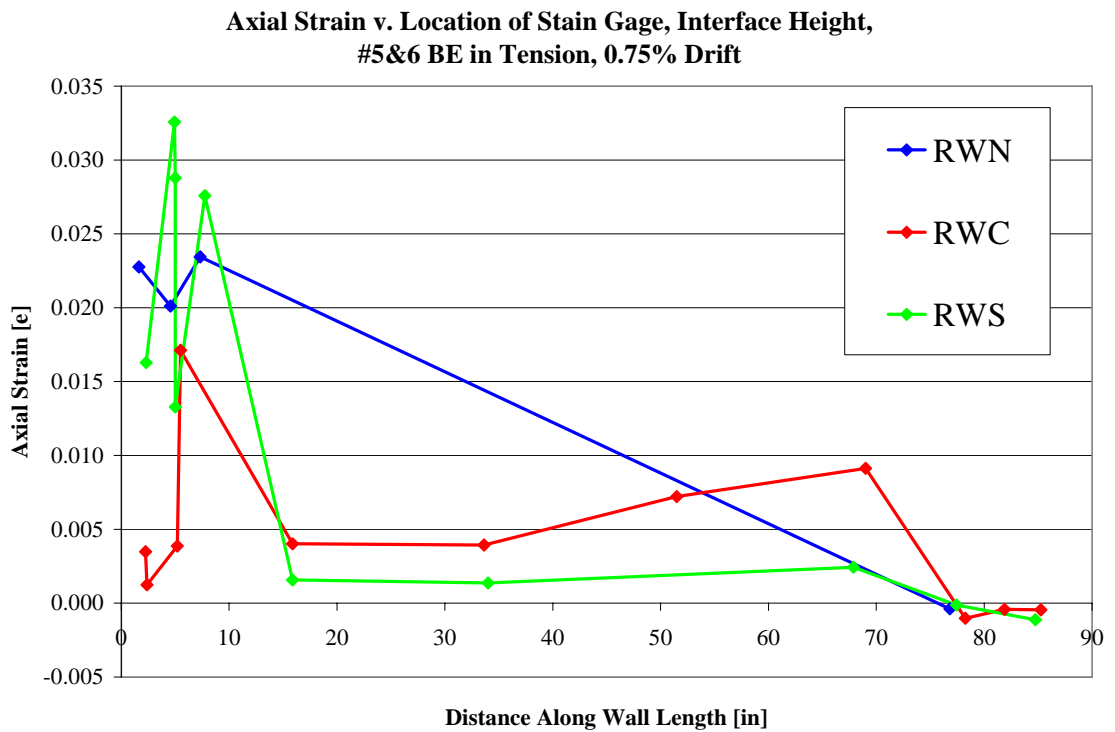


Figure 10.4c: Inelastic comparison of axial strain at the foundation interface, No.5/6 in T

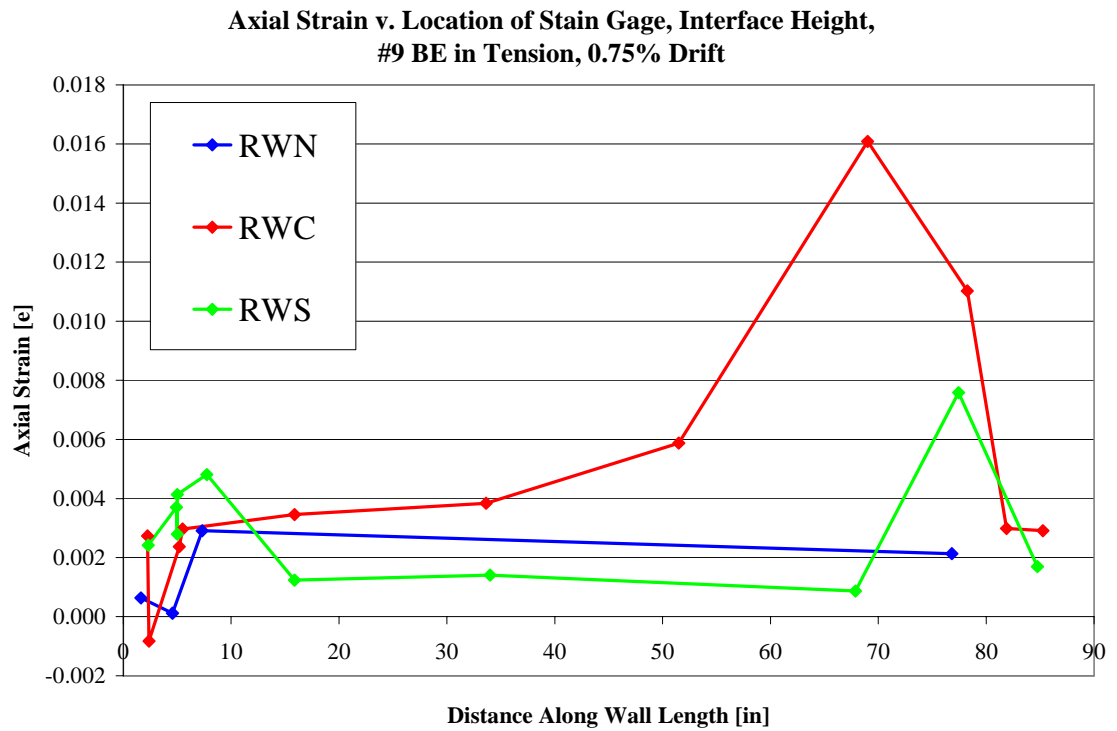


Figure 10.4d: Inelastic comparison of axial strain at the foundation interface, No.9 in T

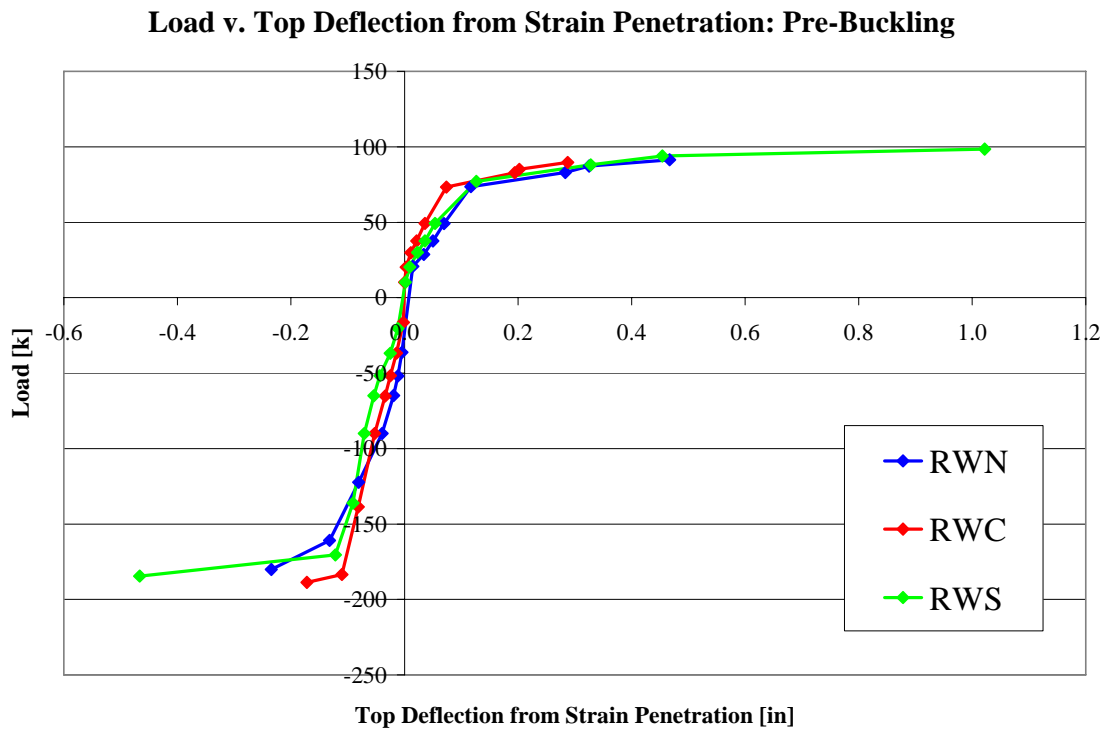


Figure 10.5a: Load v. Top deflection backbone resulting from strain penetration

**Top Deflection from Strain Penetration v. Total Top Deflection:
Pre-Buckling**

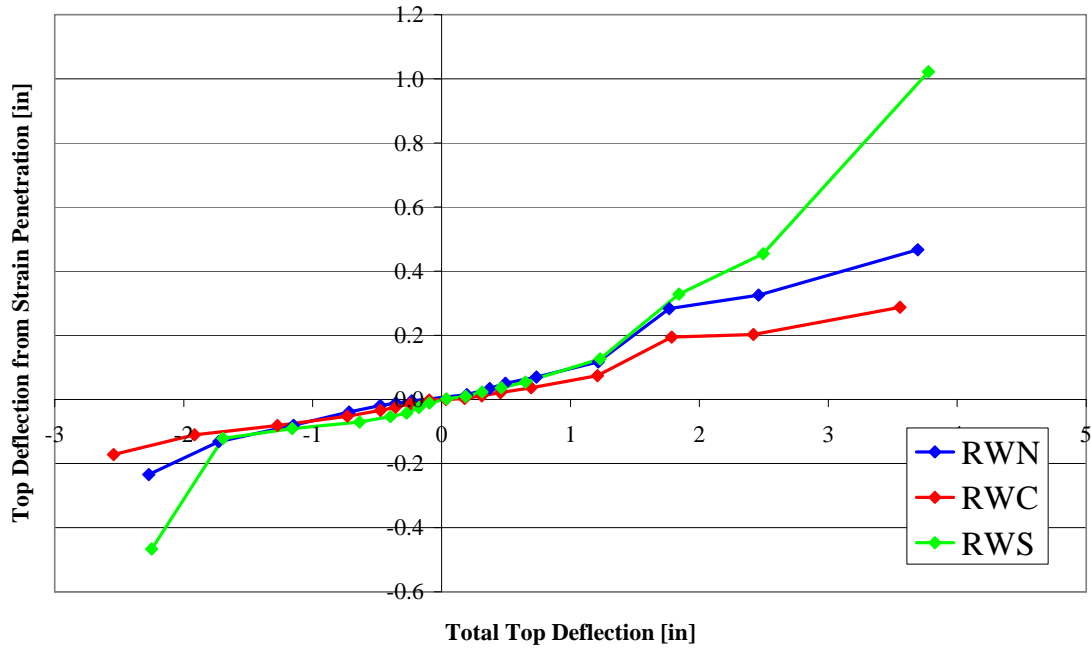


Figure 10.5b: Top deflection from strain penetration v. Total deflection backbone

**% of Top Deflection from Strain Penetration v. Total Top Deflection:
Pre-Buckling**

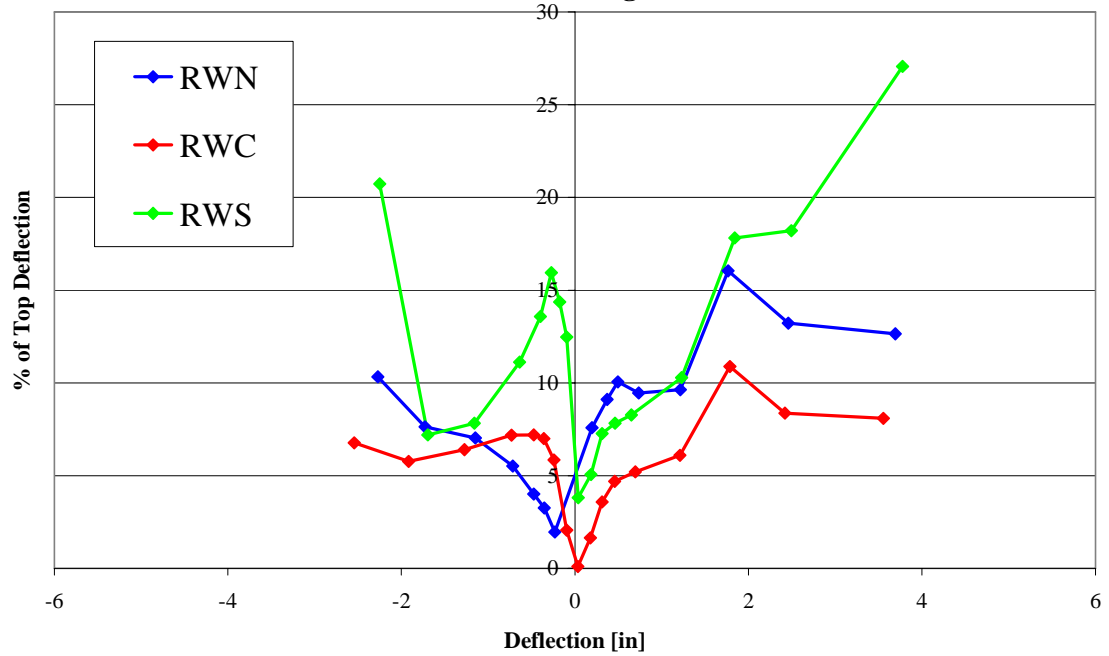


Figure 10.6a: Percentage of total displacement resulting from strain penetration

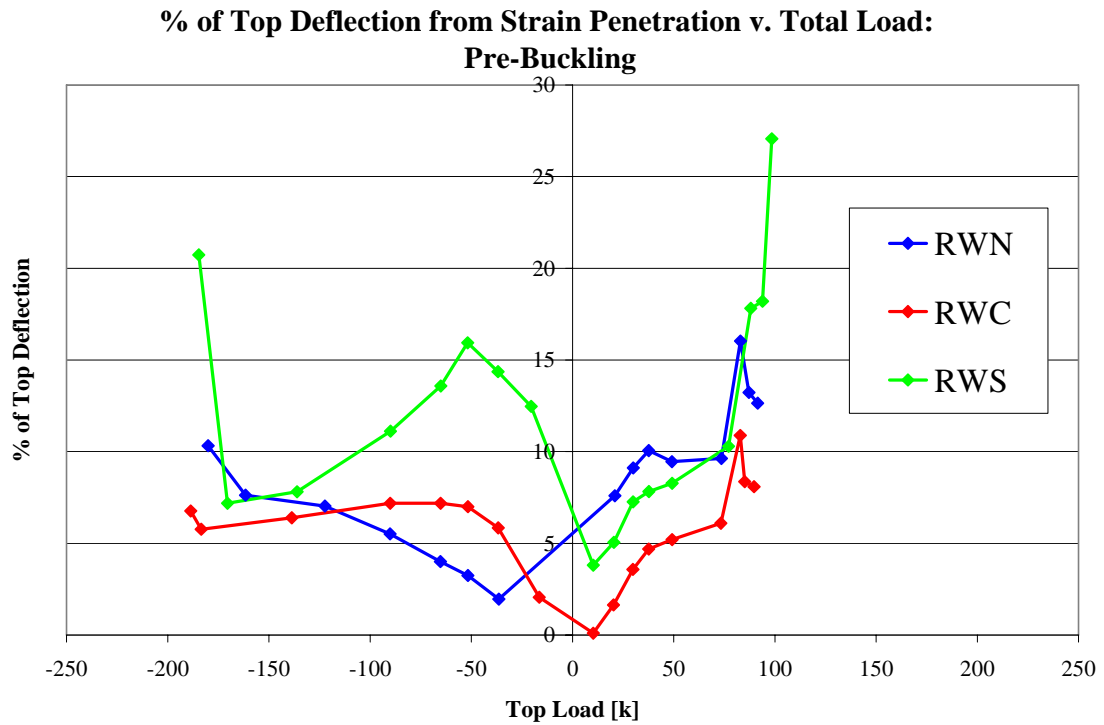


Figure 10.6b: Percentage of total displacement resulting from strain penetration

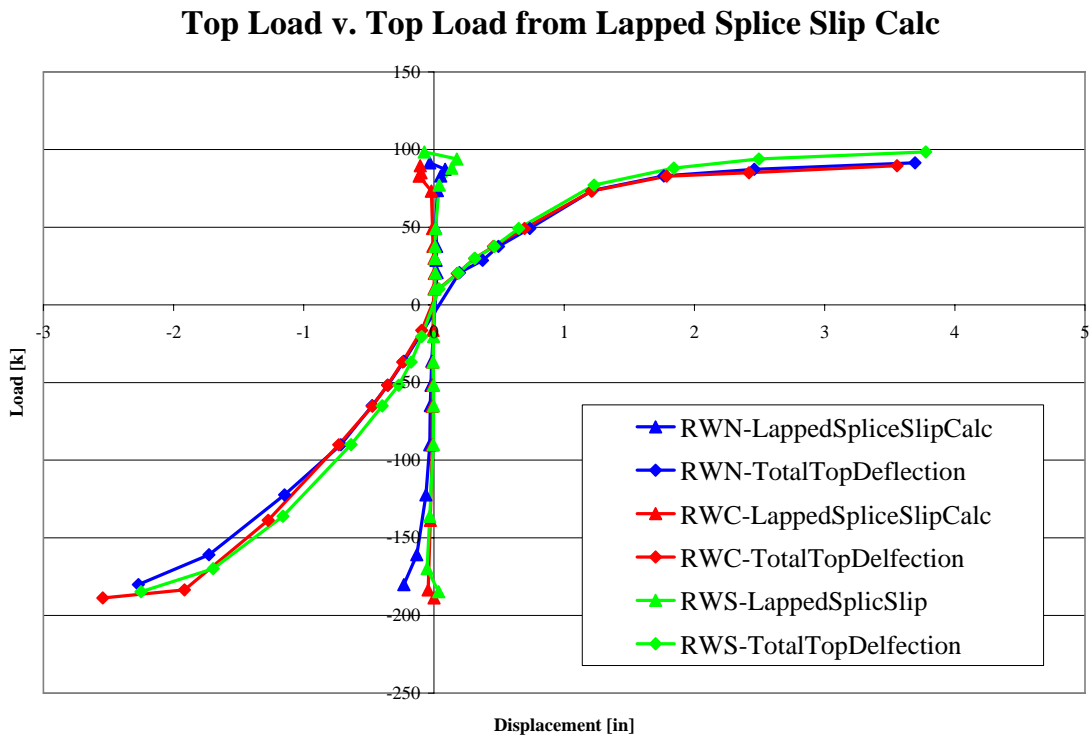


Figure 10.7: Top Displacement from lapped splice slip calculations

Chapter 11: Shear Component of Lateral Deformation

11.0: Introduction

This chapter covers the methods used to determine the shear component of lateral deformation and the results of these calculations. The resulting shear components calculated with various instruments are compared for each wall in order to determine if the results are reliable when determining the effects of the anchorage detailing. The effects of the anchorage detailing on the shear behavior of the walls is then examined. In general, it was found that the inability of RWS to develop full plastic hinges in the lapped splice lengths causes the wall to deform more in shear than the other test specimens in order to achieve the same top global displacement. The difference in shear deformation is proportional to the additional load necessary to achieve the target top global displacements.

11.1.0: Calculation of Shear Deformation

Shear deformation was calculated using the string pot and Krypton sensors. Different calculation methods were used for each sensor. The string pot sensors were used to calculate shear deformation by first computing the total average deformation from an 'x' configuration of sensors. This method calculates the total deformation by measuring the elongation of diagonal string pots that span the length of the wall over various segments of height. This was done for the entire averaged length of the wall, as well as over the half of the wall in tension. This was done to compare the effects of shear deformation that occurs in the section of wall length where shear cracking is present. Shear deformation calculated as an average of the entire wall length is referred to as the 'whole cross section' or WC method.

Shear deformation is then computed as the remainder of lateral deformation when the flexural component is subtracted from the total lateral deformation. Shear deformation

calculated as an average of the half of the wall length with the extreme tension face is referred to as the ‘tension half’ or TH method. Shear deformation calculated for the wall half with the extreme compression face is referred to as the ‘compression half’ or CH method. The calculation of shear deformation with the string pot data is covered in great detail in appendix 4.

Shear deformation was calculated with the Krypton data by integrating the calculated shear strains over the height of the sensors. The shear strain was computed using an isoperimetric quadrilateral element. The element coordinates used and the integration techniques are discussed in appendix 4. The shear strain and deformation was again computed using the WC, TH, and CH methods.

11.1.1: Verification of Shear Strains

Shear strain was computed directly with the Krypton data, knowing the displacements of the element nodes throughout the test of the specimens. Average shear strain over the span of the string pot sensor setup was computed by dividing the change in shear deformation over the height of the string pot ‘x’ configuration by the change in height of the sensor setup. These strains were compared to strains recorded by strain gages attached to the transverse reinforcement of the walls through the web of the test specimens at the base of the wall. This was done for the last elastic cycles for each wall. This sensor comparison showed good agreement between the string pots and Krypton data. The shear strains recorded for the transverse reinforcement was considerably lower for the transverse reinforcement but still within reasonable magnitudes. This discrepancy is caused by the mechanisms with which shear is resisted by the walls. The shear reinforcement is not solely responsible for resisting the entire shear load through the cross section. The loads carried by the transverse reinforcement are lower than the entire shear load of the cross section. This reduced load creates lower strains in the shear reinforcement when compared to the string pots and Krypton. Agreement between the

string pots and Krypton shows that the methods used are acceptable for evaluating the shear component of lateral deformation.

11.2: Shear Deformation Profiles

The shear deformation profile was computed for each wall for select loading cycles. This was done to compare the results of instruments for each wall, as well as a comparison of total shear deformation undergone by the walls. The loading cycles chosen are the same featured in chapter 9. The loading cycles chosen are 0.3% top drift, the last cycle which the walls were still elastic; 0.75% drift, when the walls display inelastic behavior and all instruments are functioning well; and 1.5% drift in the No.5&6 boundary element in tension direction and 1% drift in the No.9 boundary element in tension direction, when the walls are highly inelastic and instruments are on the verge of failure. All results shown are prior to buckling of the No.5&6 boundary element in compression. The shear deformation profiles are shown in figures 11.1a through 11.1i.

The shear deformation calculated with the string pot and Krypton data has good agreement when comparing the averaged 'whole cross section' shear deformation. This is not necessarily the case with the other methods. The reduced resolution of the string pot instruments may have missed some of the effects of the complex cracking patterns. In addition, the shear deformation was larger for the half of the wall in tension. This half of the wall always includes the effects of shear cracking. The compression half method may include some shear cracks that propagate across the centerline of the wall but will still have far less than the tension half. Note that this not observed for the No.9 in tension for RWS when using string pot data. This is thought to be a problem with instrumentation, as behavior consistent with the other walls is still observed with the Krypton results.

The shear deformation profiles for the walls when the No.5&6 boundary elements are in tension typically follow a different curve than the No.9 boundary elements are in tension. This is caused by the extent of shear cracking along the wall height. The No.9 boundary

element in tension requires a much greater top load to achieve the same deformations as the No.5&6 boundary element in tension. In addition, the shear resistance is not increased when the No.9 boundary element is in tension, unlike the flexural resistance (dowel action is assumed to be negligible for these specimens and boundary conditions). The increased loads create more shear deformation when the No.9 boundary element is in tension. The increased loads also cause additional shear cracking to occur, reducing the shear stiffness of the walls further away from the base of the wall. This reduced shear stiffness is more uniform than when the No.5&6 boundary element is in tension. The more uniform reduced shear stiffness creates a linear trend along the wall height. Shear cracking occurs much lower in the wall for the No.5&6 boundary element in tension. The height of the wall above the shear cracking has increased shear stiffness, creating a piecewise linear shear deformation profile. The top half of the wall has a much smaller shear deformation gradient than the base of the wall where shear cracking is prevalent. This hypothesis is confirmed when comparing the difference in the shear deformation profiles at the last elastic cycle (0.3% drift) and the inelastic range (0.75% drift). The shear deformation profile once again becomes piecewise at the highly inelastic profile shown. This is due to shear sliding observed at the base. Sliding deformations were observed from offsets on a grid drawn on the undeformed wall. These offsets were observed to be approximately 0.03” for the largest diagonal cracks at 1.5% drift for the No.5&6 boundary element in tension. Cracking patterns, along with shear sliding measurements from undeformed grid offsets can be accessed in appendix P.

11.3: Load v. Shear Deformation Backbone Plots

The calculated shear deformation was plotted against the applied top load for the first loading ramp of each cycle before buckling of the No5&6 boundary element. This was done for the shear deformation at the top of the wall and 25% of the wall where string pot and Krypton data was available. These backbone curves can be seen in figures 11.2a through 11.2f. The backbone curves at 25% of the total wall height again show good agreement between the Krypton and string pot data when the No.5&6 boundary element

is in tension. The sensors return different values for the No.9 boundary element in tension but are still within reason.

The results of the shear deformation calculations are compared to predicted values. The elastic prediction was calculated by determining the shear modulus from the elastic modulus of the concrete and an assumed Poisson ration of 0.3. The effective area from cracking was assumed to be half of the gross concrete area. This prediction is considerably less than what is calculated. The elastic prediction is only close when the No.9 boundary element is in tension. The elastic prediction deviates from the measured shear deformation well below half of the yield load. The second prediction was made from methods suggested by Park and Paulay (1975), [R.11.1]. This method is based on the shear stiffness of a section with 45 degree shear cracks:

$$K_{V,45} = \rho_v E_s b_w d / (1 + 4n\rho) \quad (\text{Eq 11.1})$$

Where $K_{V,45}$ is the shear stiffness of a section with 45 degree shear cracks, ρ_v is the reinforcement ratio of the longitudinal bars, E_s is the elastic modulus of steel, b_w is the width of the web, d is the depth of the tension steel, and n is the modular ratio of steel to concrete.

The prediction with Park and Paulay's method gives a much better estimate of deformation from shear. These estimates are simplified a great deal when considering the complex mechanism of shear resistance. In addition, the flexure-shear interaction is difficult to quantify. The damage occurring from internal flexural loads and consequent deflection reduce the shear stiffness considerably in the inelastic range of the walls. Inelastic coupling of the shear and flexural components of deformation is seen to take its greatest effect past 0.75% of top drift. This inability to predict the shear deformation of these test specimens at large drift levels poses a serious problem when attempting to predict the total deformation of structures in the field. Alternatives to these predictions are covered in the following section.

11.4: Total Deformation v. Shear Deformation

The contribution of shear to the total deformation is quantified in this section. The percentage of the total lateral deformation comprised of shear was calculated for each wall. The total lateral deformation used in these calculations is the average total lateral deformation described in appendix 4, where the lateral expansion of the walls from shear splitting cracks is taken into account. The percentage of total lateral deformation resulting from shear can be seen in figures 11.3a through 11.3f. The results for three walls are quite similar. The contribution of shear increases in the elastic range as cracking increases. The increased cracking reduces the shear stiffness of the wall while the flexural stiffness remains almost constant (assuming the tensile capacity of concrete is zero). This is not observed for RWS in the No.5&6 boundary element in tension for the string pot data. This is due to the external string pot possibly rubbing on the reference frame. The shear deformation computed for the string pot and Krypton data is very close, the variation in this plot is caused from the poor external measurement of displacement.

The second trend noticed is the drop in the shear contribution past 1 inch of deflection with the No.5&6 boundary element in tension. Displacement larger than 1 inch is in the inelastic behavior range of the walls. The longitudinal reinforcement yields, creating very large flexural deformations. This flexural increase decreases the percentage of total deformation comprised of shear. Lastly, the contribution of shear increases at the largest drift levels shown. This is due to the inelastic coupling of shear and flexural deformation. The shear stiffness is decreased greatly at these displacement levels. Shear sliding was also evident at displacement levels greater than 3 inches.

Lastly, the larger shear deformations observed for RWS can be seen when comparing the contribution of shear deformation at the top of the wall. Shear deformation for RWN and RWC accounted for approximately 15% of the total top deformation when the No.5&6 boundary element is in tension. The contribution of shear deformation in RWS is slightly larger than the other two walls. Shear accounted for approximately 20% of the total

deformation at the top of the wall. The same is observed when the No.9 boundary element is in tension to a lesser extent. Each wall experienced approximately 30% of its top deformation from shear. RWS had the largest contribution of shear. This difference was less than 5%, however.

11.5: Predicting Shear Deformations

The contribution of shear in the inelastic range does not seem to change a great deal from the elastic limit. The percentage of total deformation from shear at the top of the wall never deviates more than 5% from the contribution of shear at the elastic limit. This change is typically a decrease in the contribution of shear. The percentage of flexural deformation typically increased by 10% in the inelastic range. A useful estimate of shear deformation at highly inelastic levels can be made by keeping the ratio of shear deformation to flexural deformation at the elastic limit the same for all displacements greater than the yield displacement. This estimate is encouraging when considering the very good estimated of flexural deformation with BIAx, no matter the drift level of the walls. This estimate is shown in the following:

$$\begin{aligned}
 \Delta_{\text{total,elastic}} &= \Delta_{\text{shear,elastic}} / S_{\text{elastic}} \\
 \Delta_{\text{total,elastic}} &= \Delta_{\text{flexure,elastic}} / F_{\text{elastic}} \\
 S_{\text{elastic}} &= S_{\text{inelastic}} \\
 F_{\text{elastic}} &= F_{\text{inelastic}} \\
 \Delta_{\text{shear,inelastic}} &= \Delta_{\text{flexure,inelastic}} S_{\text{inelastic}} / F_{\text{inelastic}} \quad (\text{Eq.11.2})
 \end{aligned}$$

Where $\Delta_{\text{total,elastic}}$ is the total top deformation at the elastic limit, $\Delta_{\text{shear,elastic}}$ is the predicted shear deformation at the elastic limit from any reasonable approach, $\Delta_{\text{flexure,elastic}}$ is the predicted flexural deformation from any reasonable approach, S is the ratio of shear deformation to total deformation, F is the ratio of flexural deformation to total deformation, $\Delta_{\text{flexure,inelastic}}$ is the deformation at any inelastic displacement from any reasonable approach, and $\Delta_{\text{shear,inelastic}}$ is the predicted shear deformation at any inelastic

displacement. The ratios of shear and flexural displacement to the total displacement are kept the same from the elastic limit. This is done in order to achieve a conservative result. The inelastic flexural ratio will be larger than the elastic from increasing flexural deformations from plastic hinging. The shear ratio will decrease from flexural deformation increasing at a greater rate than shear deformation. Discounting the changes in these ratios will give a conservative estimate of shear deformation at inelastic drift levels. The result of this method, compared to the result of RWN is shown in figure 11.4. The predicted flexural deformation was done using the BIAX results from the flexural chapter. The details of this prediction can be found in appendix and chapter F.

This method is highly dependant on accurately predicting the shear deformation at the elastic range. As shown earlier, the predictions used are smaller than the experimental result. This creates a smaller ratio of shear and a smaller prediction. The same method is used if the shear deformation was predicted with 100% accuracy. The prediction of shear deformation is indeed good if the 'real' shear deformation can be predicted. The portion of the plot at yield is significantly smaller than the response of RWN. This is due to the inability to know shear deformation accurately at the true first yield moment. Yielding occurred during the loading of the wall and not at the peak. The shear at this point is the largest, but unknown and was not predicted well. This problem requires further investigation that will not be covered in this report.

11.6: Summary of Results

This chapter covered the contribution of shear to the total deformation. The results of different sensors were compared within each wall and it was determined that the results were reliable for comparisons of the effects of anchorage detailing. No considerable difference was observed between walls with continuous bars and mechanical splices. Increased shear deformation was observed for the lapped splice walls. This is due to the inability of the wall to deform as much of the other walls in flexure from the termination of the plastic hinge mechanism in the lapped splice length. The wall was pushed to the

same target displacements as the other walls. The target displacement could only be reached by creating larger deformations from the modes other than flexure. This increase in shear deformation was approximately 5% of the walls total top displacement.

The predictions of shear deformation were unable to predict the response of the walls. This is true for the elastic and inelastic behavior of the walls. The inelastic shear deformation increased by a considerable degree from inelastic damage and reduced shear stiffness, as well as shear sliding. A simple prediction method was proposed to account for the inelastic response of the walls, based on the ratio of the components of deformation. An accurate prediction of shear deformation in the inelastic range can be achieved if the elastic shear deformation and inelastic flexural deformation can be predicted precisely.

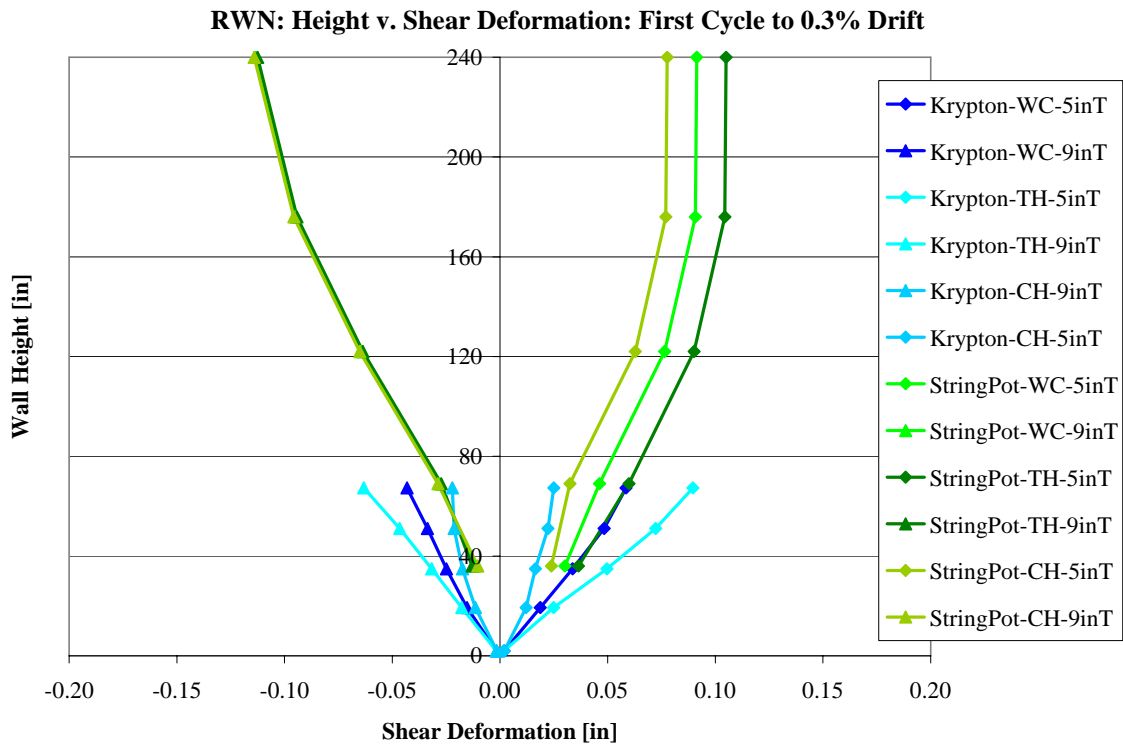


Figure 11.1a: Shear deformation profile of RWN at the last elastic cycle

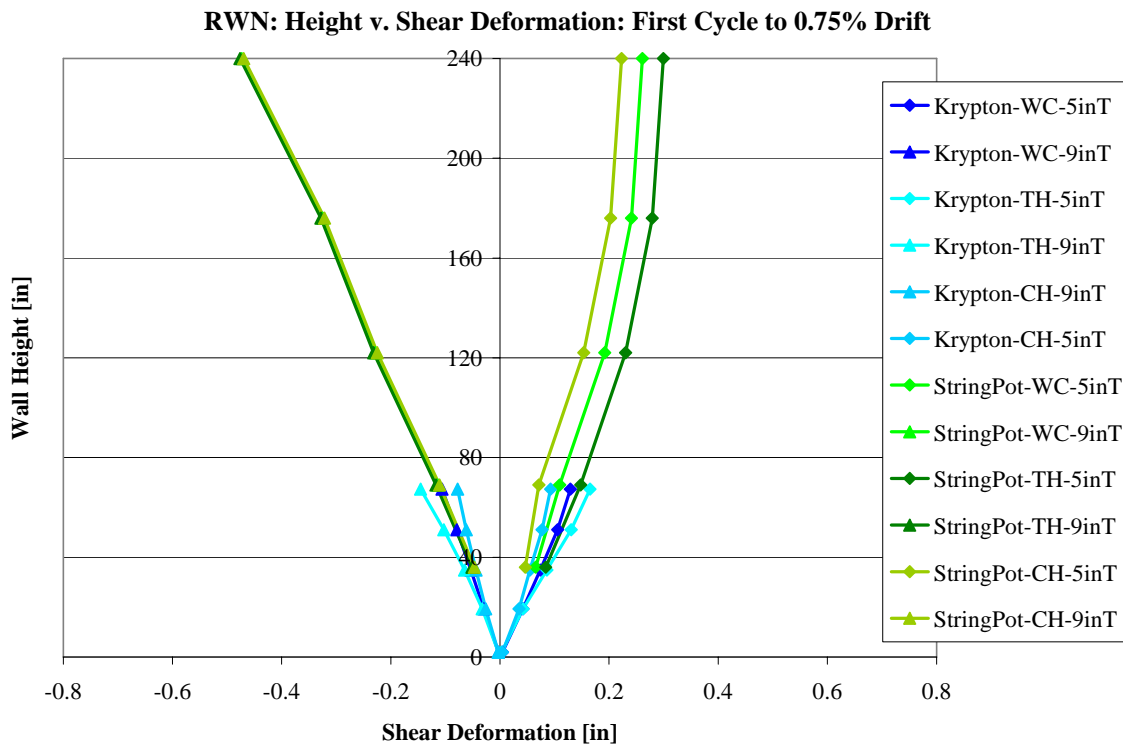


Figure 11.1b: Shear deformation profile of RWN well into the inelastic range

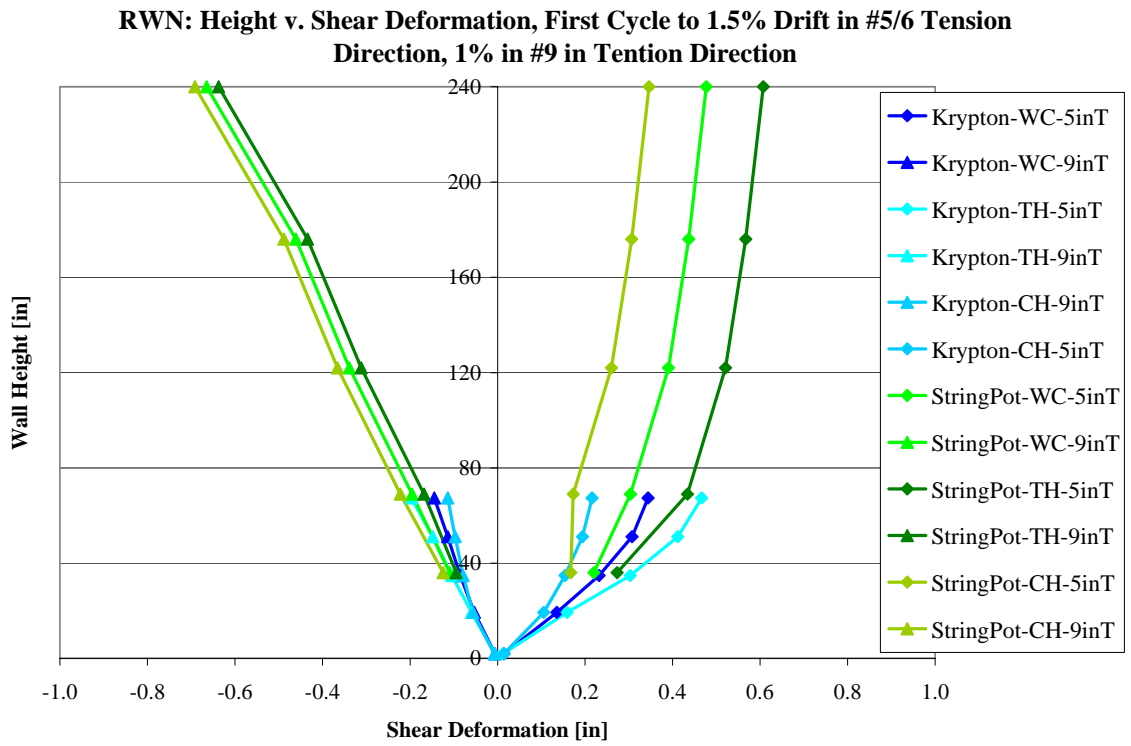


Figure 11.1c: Shear deformation profile of RWN at the last reliable inelastic cycle

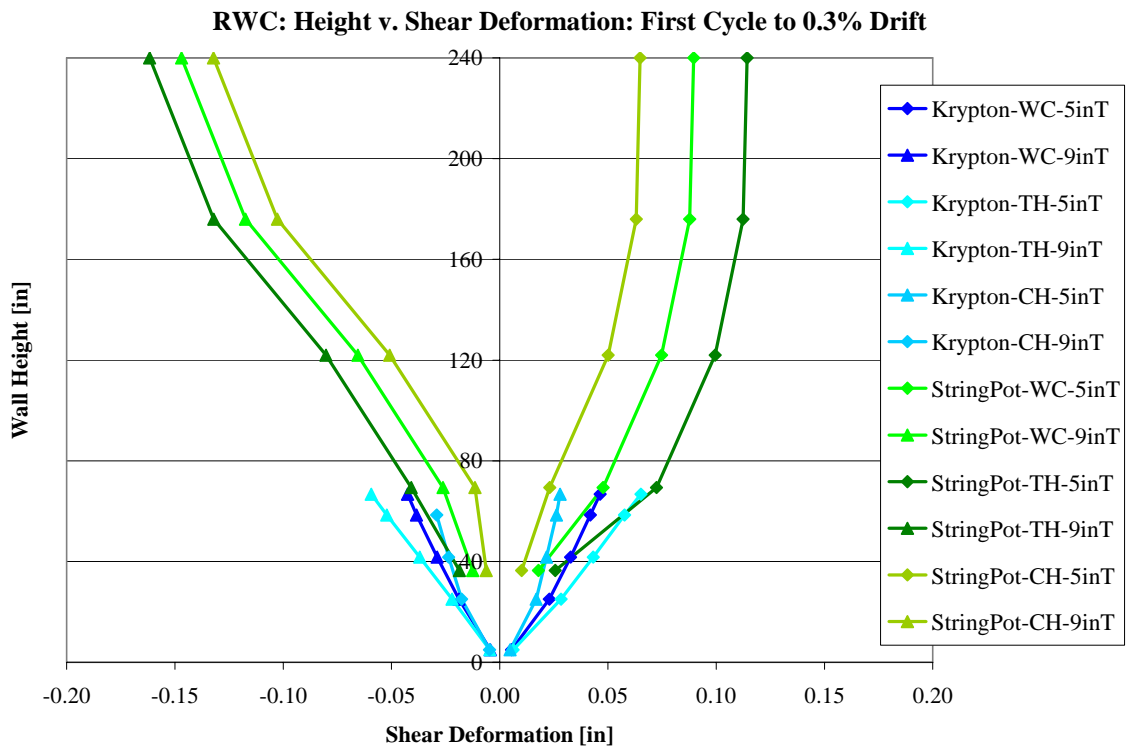


Figure 11.1d: Shear deformation profile of RWC at the last elastic cycle

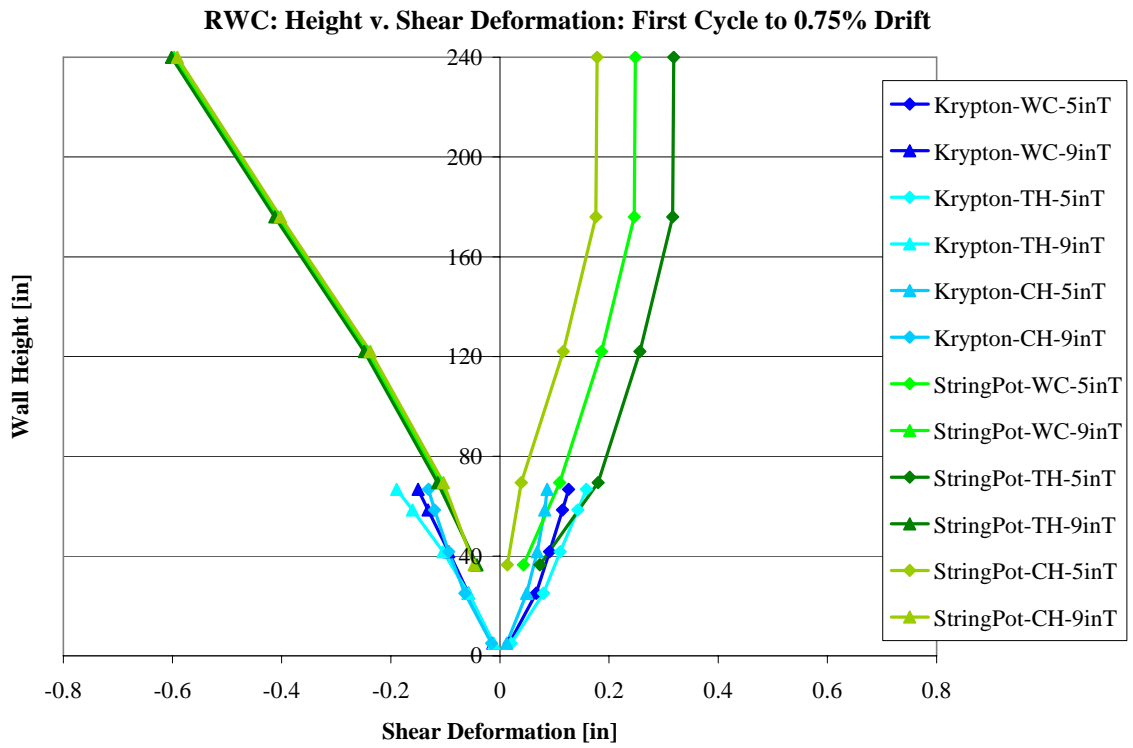


Figure 11.1e: Shear deformation profile of RWC well into the inelastic range

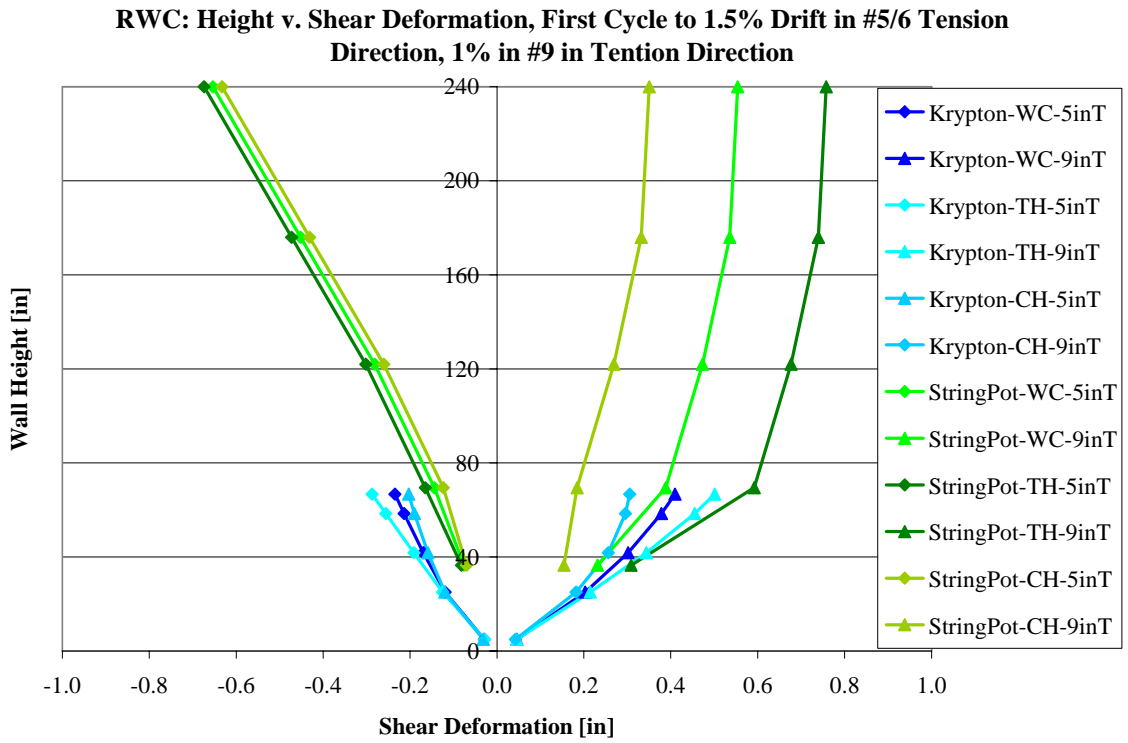


Figure 11.1f: Shear deformation profile of RWC at the last reliable inelastic cycle

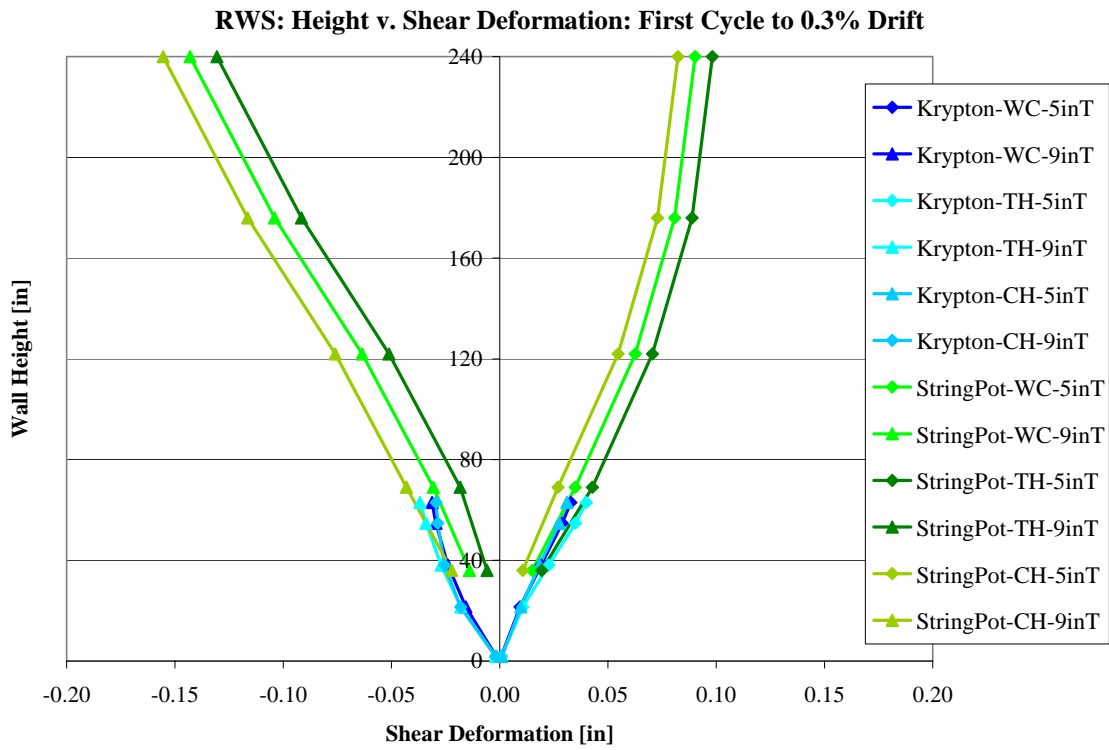


Figure 11.1g: Shear deformation profile of RWS at the last elastic cycle

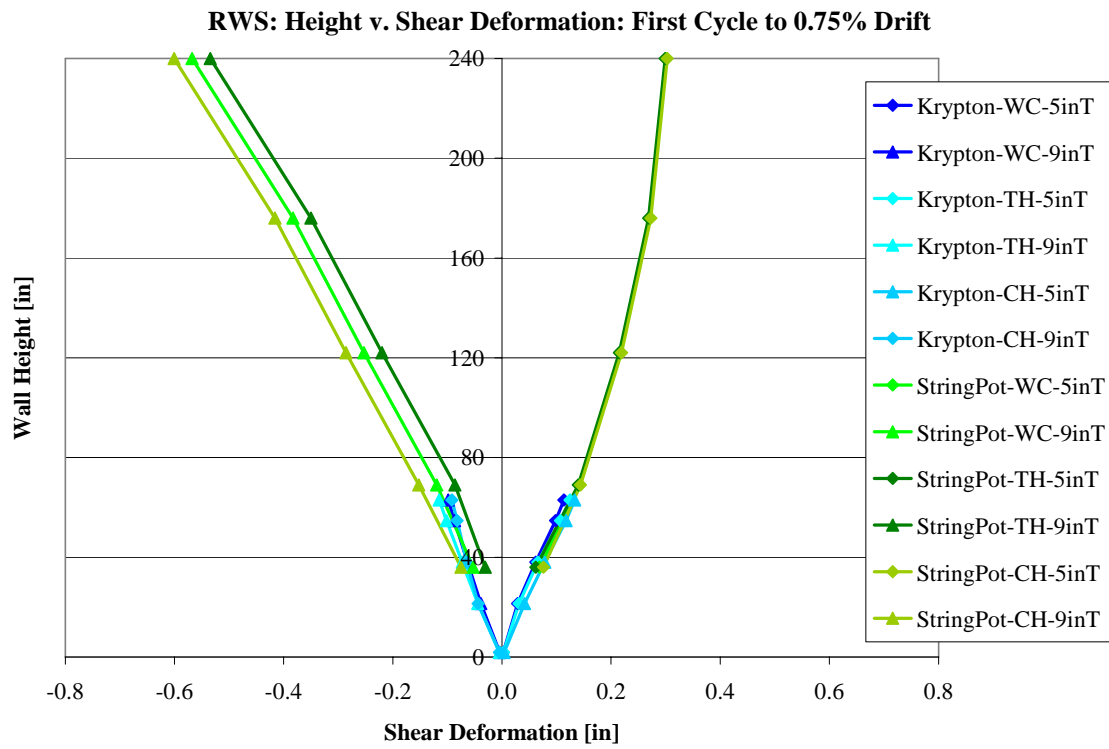


Figure 11.1h: Shear deformation profile of RWS well into the inelastic range

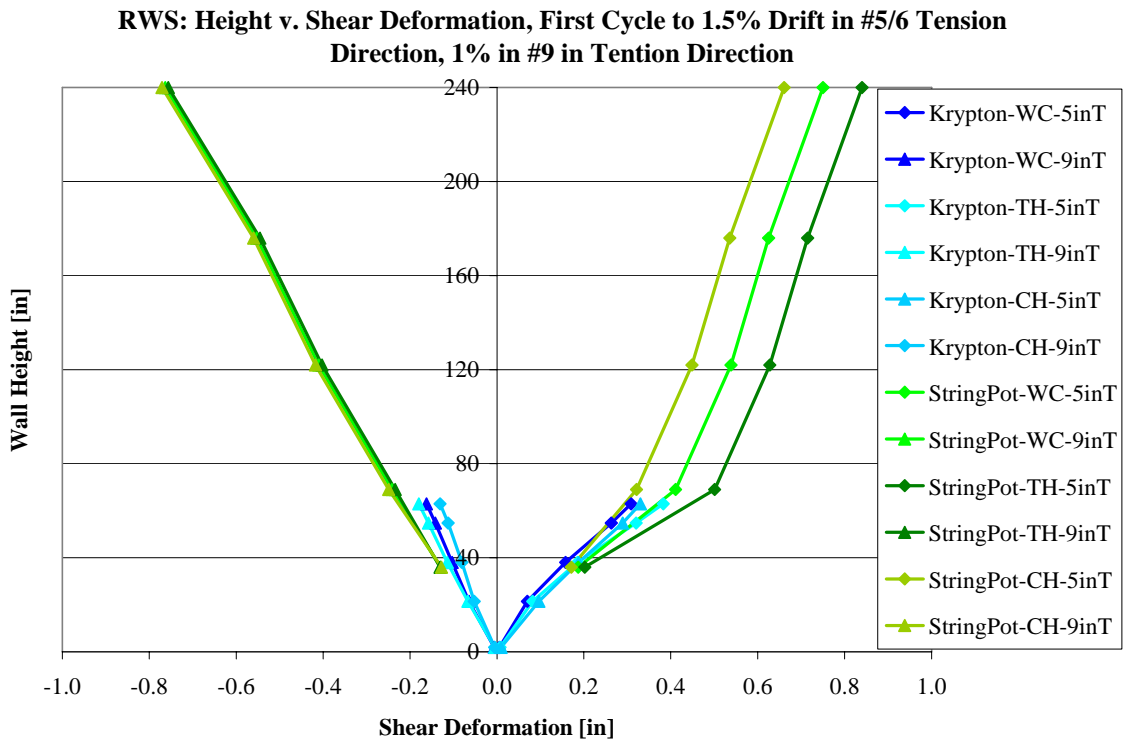


Figure 11.1i: Shear deformation profile of RWS at the last reliable inelastic cycle

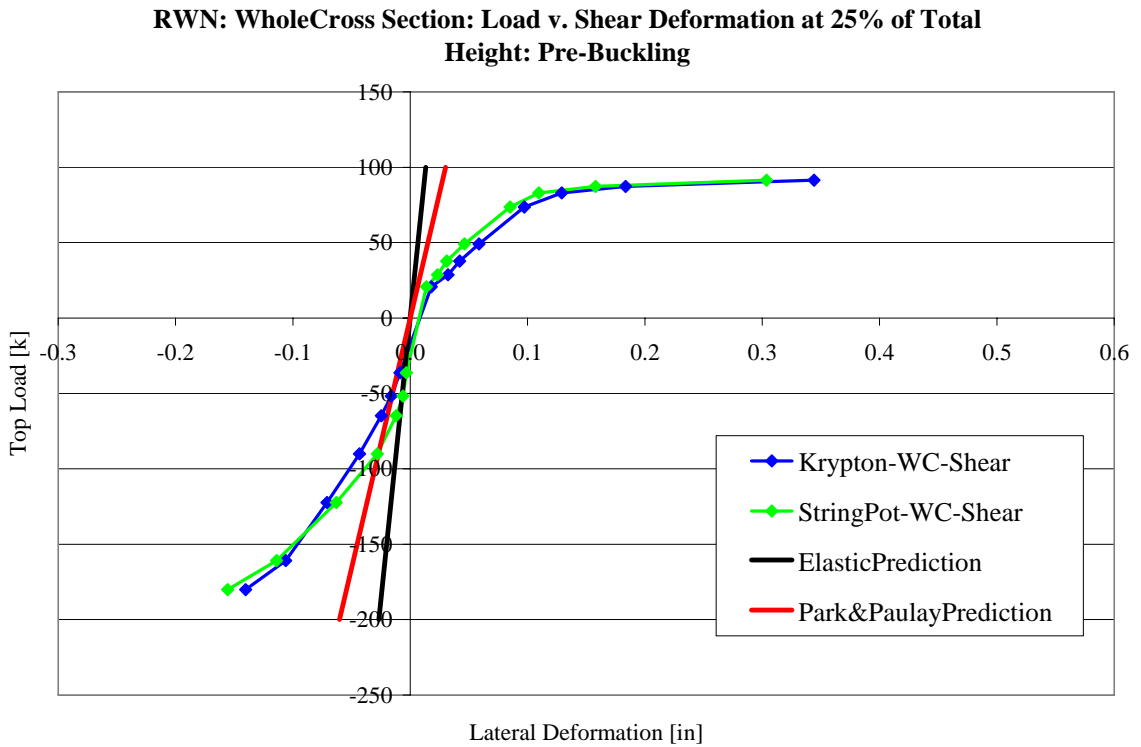


Figure 11.2a: Shear deformation backbone of RWN at 25% of total wall height

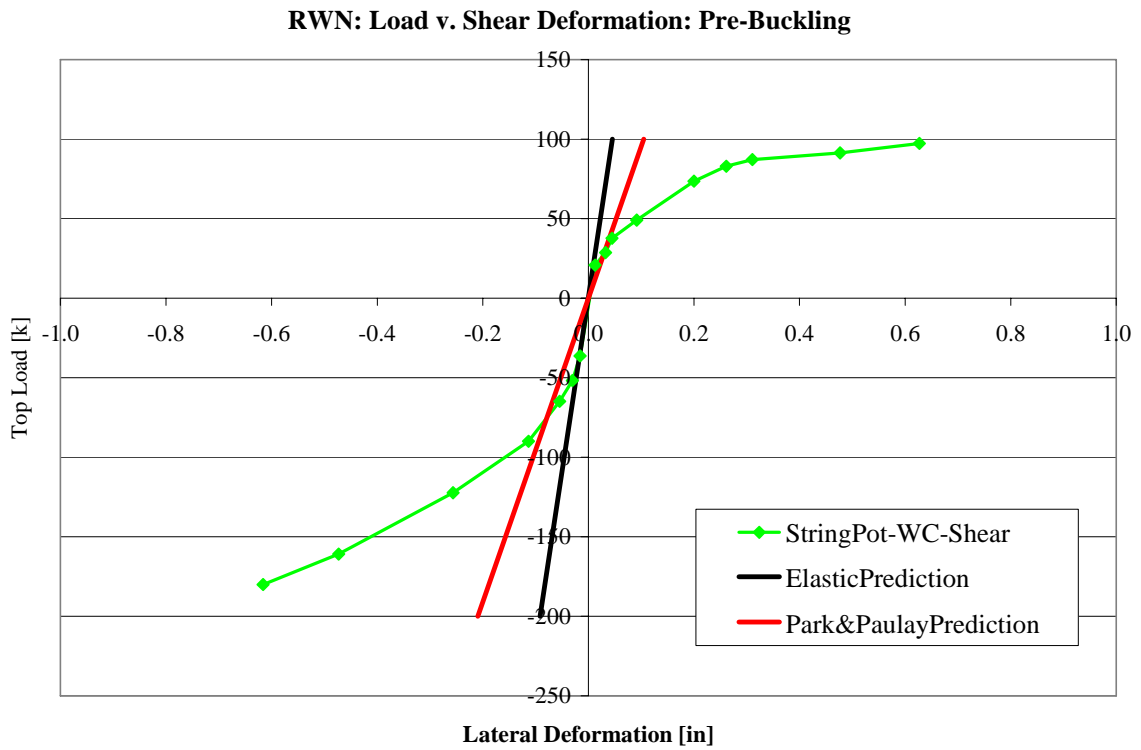


Figure 11.2b: Shear deformation backbone of RWN at the top of the wall

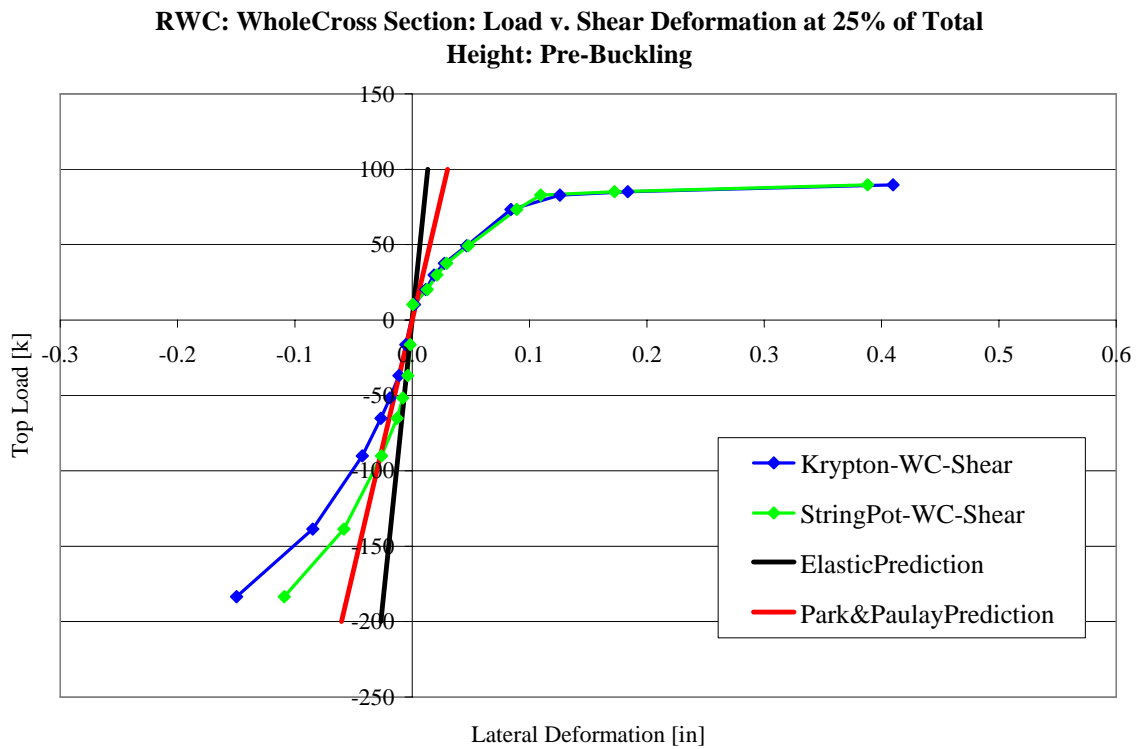


Figure 11.2c: Shear deformation backbone of RWC at 25% of total wall height

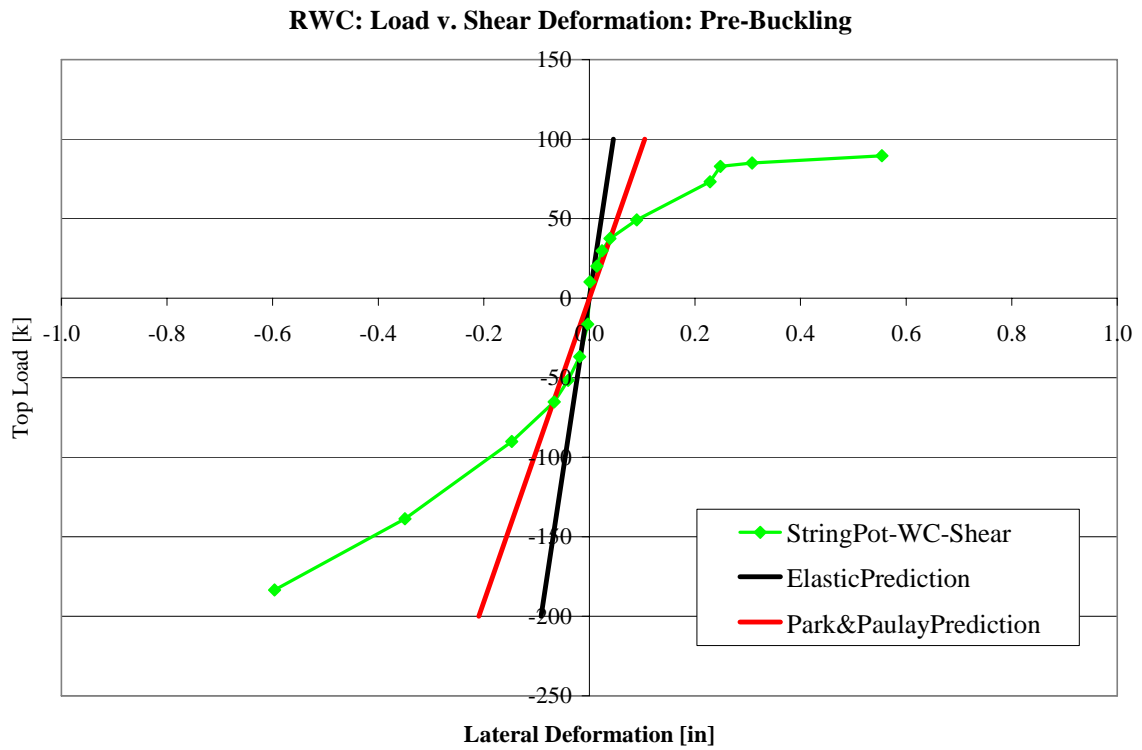


Figure 11.2d: Shear deformation backbone of RWC at the top of the wall

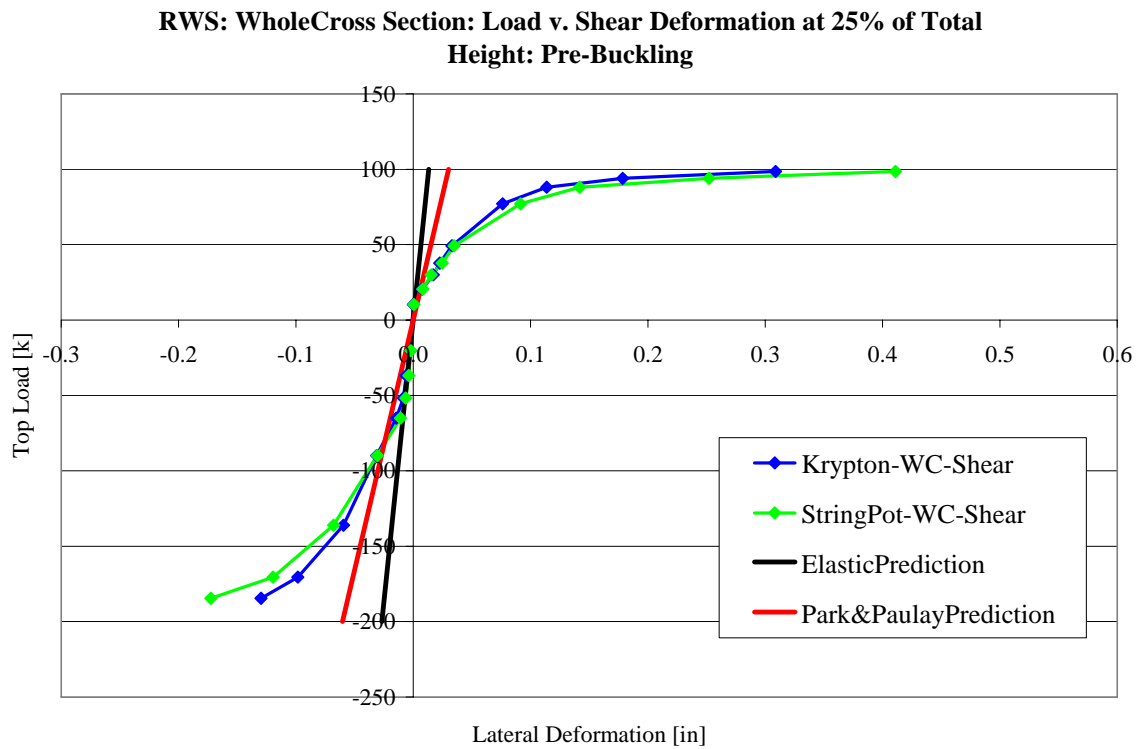


Figure 11.2e: Shear deformation backbone of RWS at 25% of total wall height

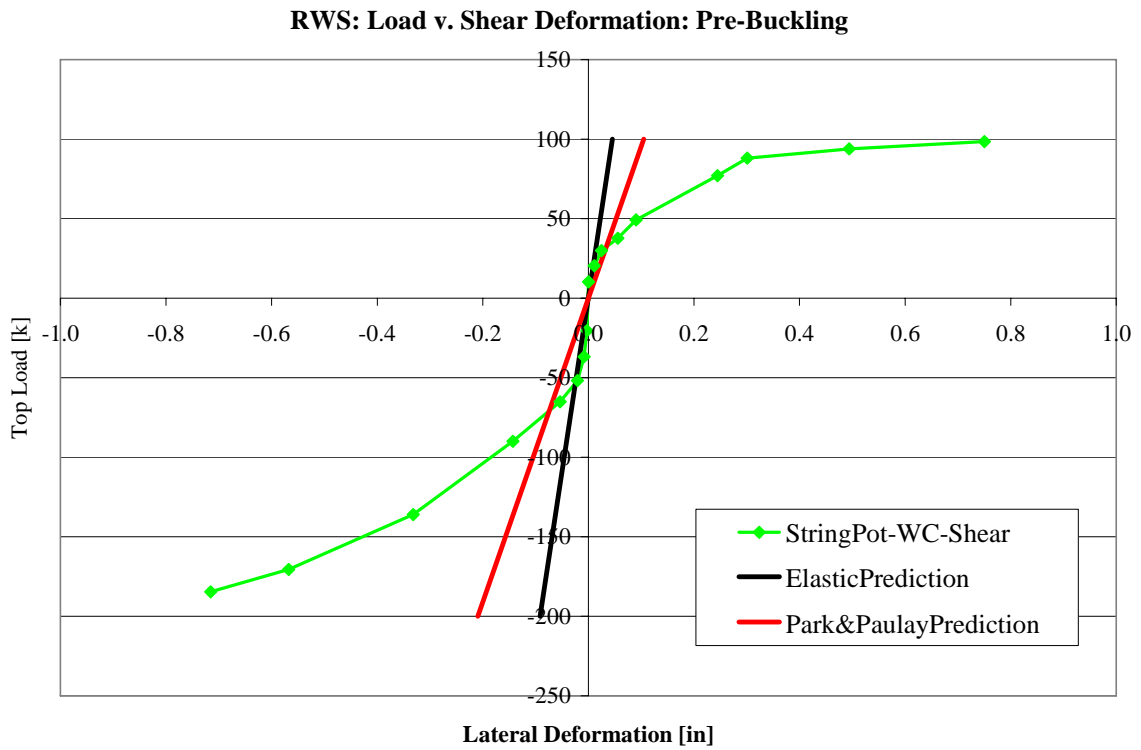


Figure 11.2f: Shear deformation backbone of RWS at the top of the wall

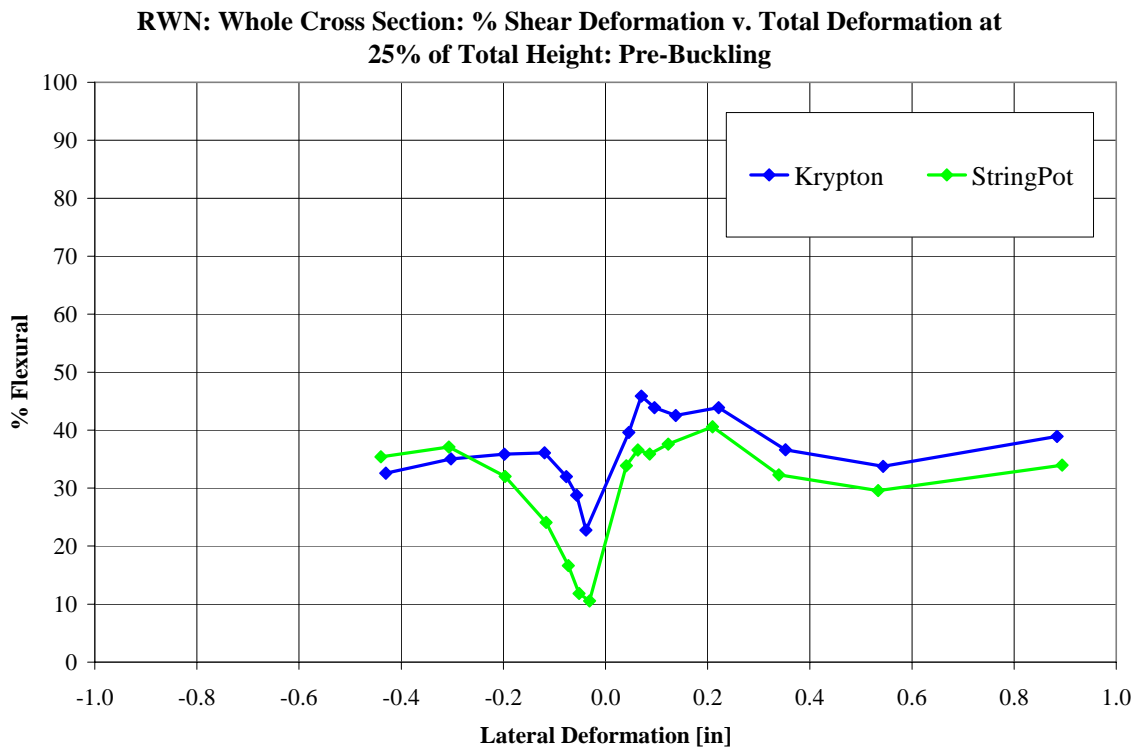


Figure 11.3a: Percentage of total deformation from shear, 25% of the total height: RWN

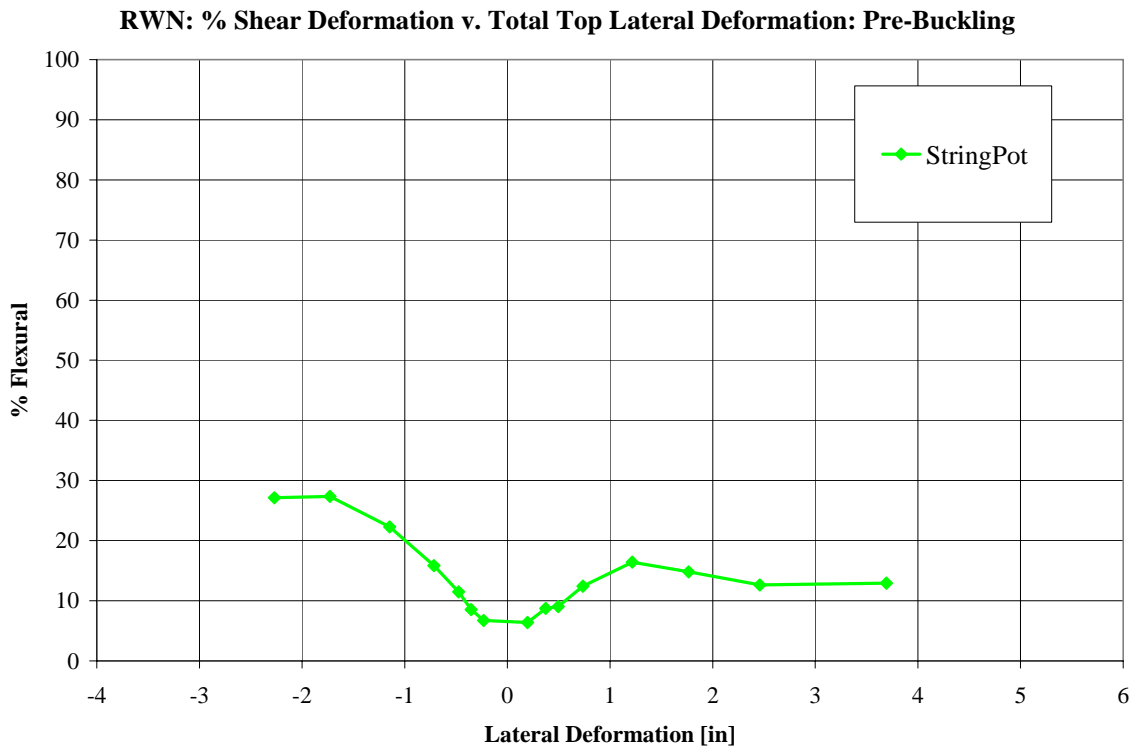


Figure 11.3b: Percentage of total deformation from shear at the top of the wall: RWN

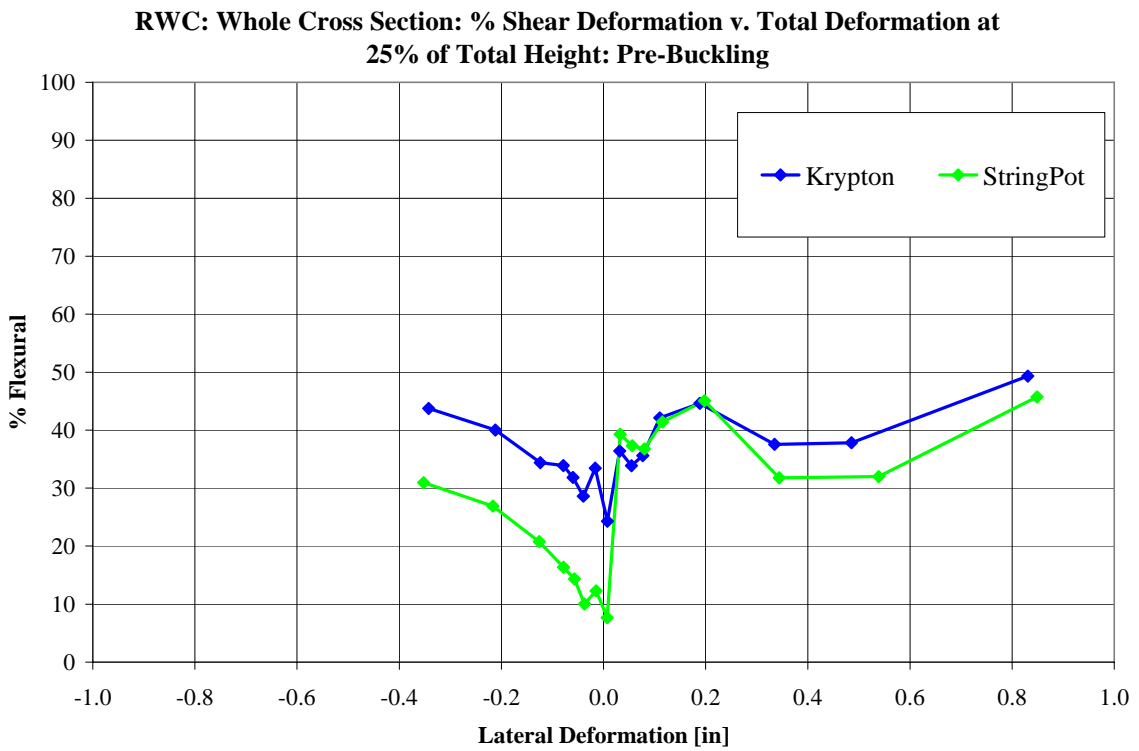


Figure 11.3c: Percentage of total deformation from shear at 25% of the total height: RWC

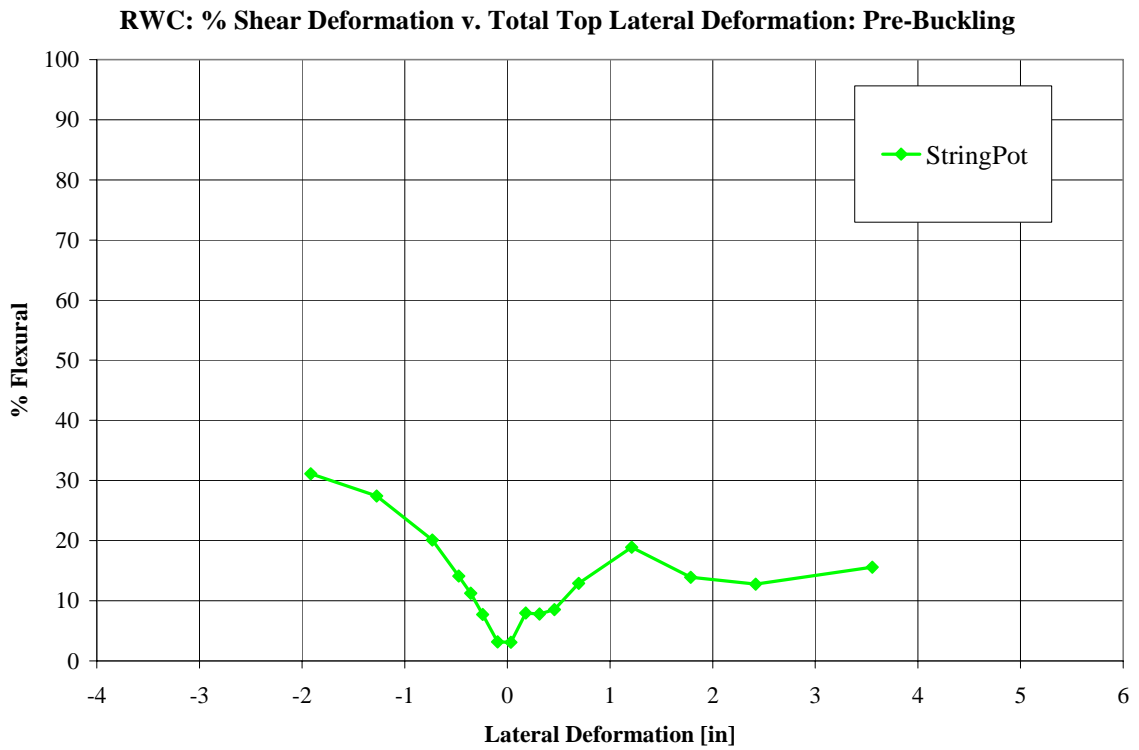


Figure 11.3d: Percentage of total deformation from shear at the top of the wall: RWC

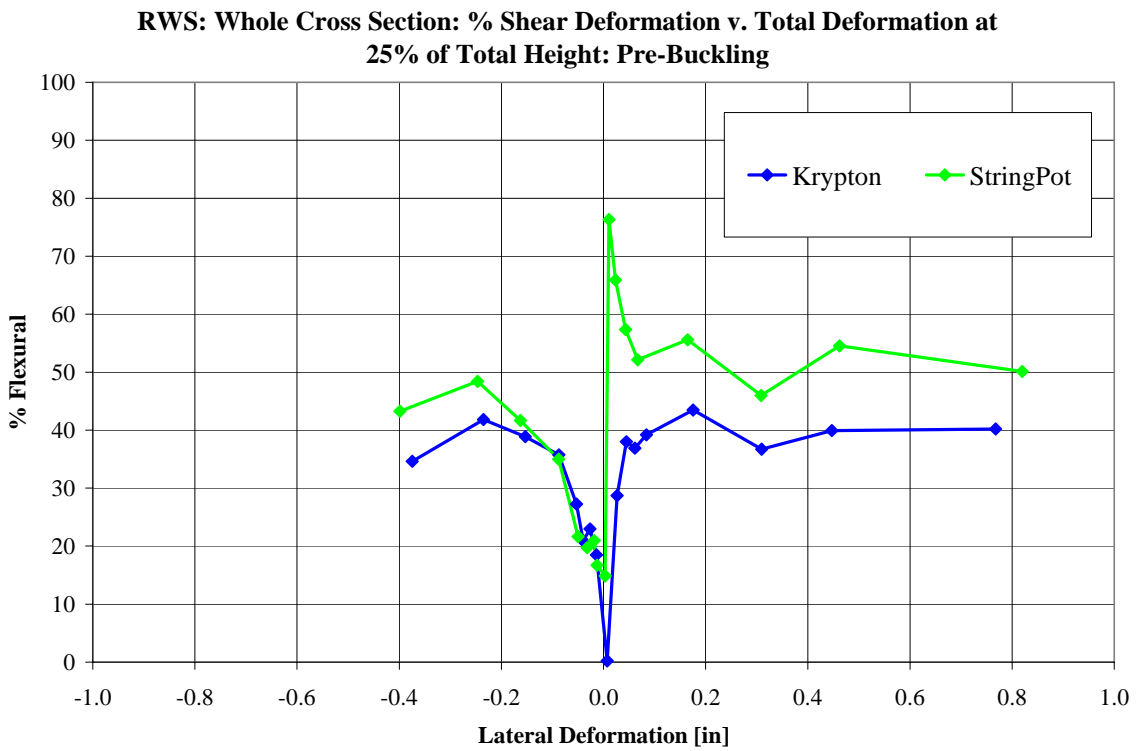


Figure 11.3e: Percentage of total deformation from shear at 25% of the total height: RWS

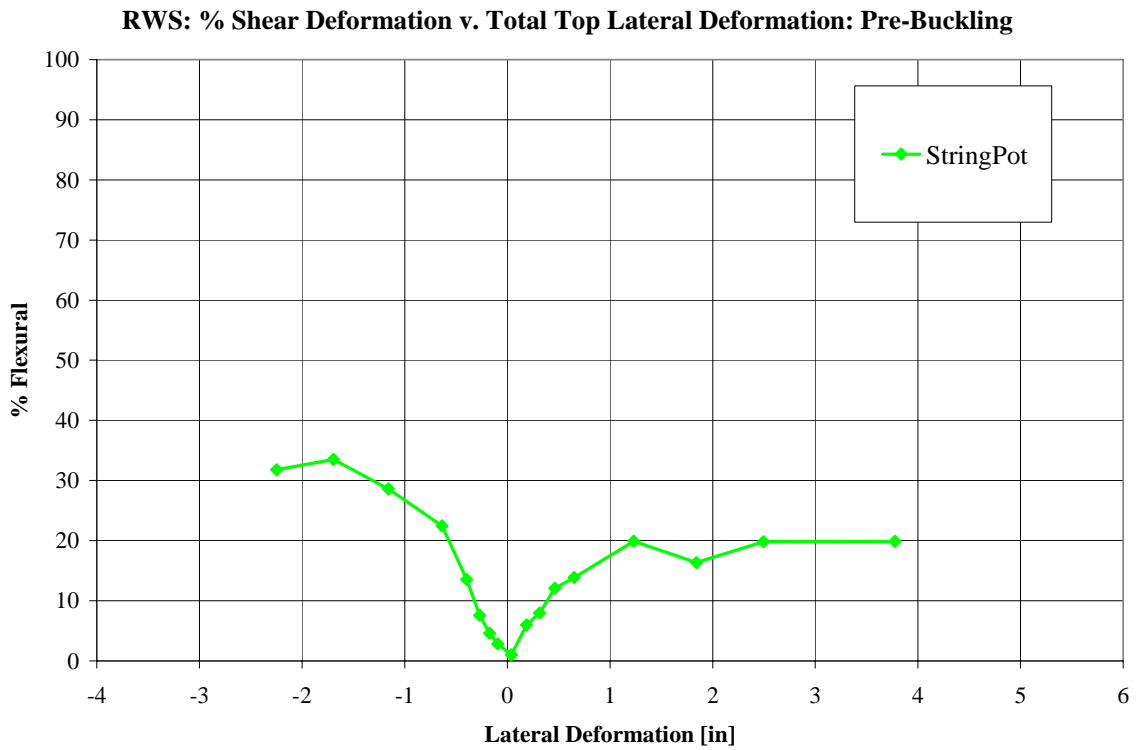


Figure 11.3f: Percentage of total deformation from shear at the top of the wall: RWS

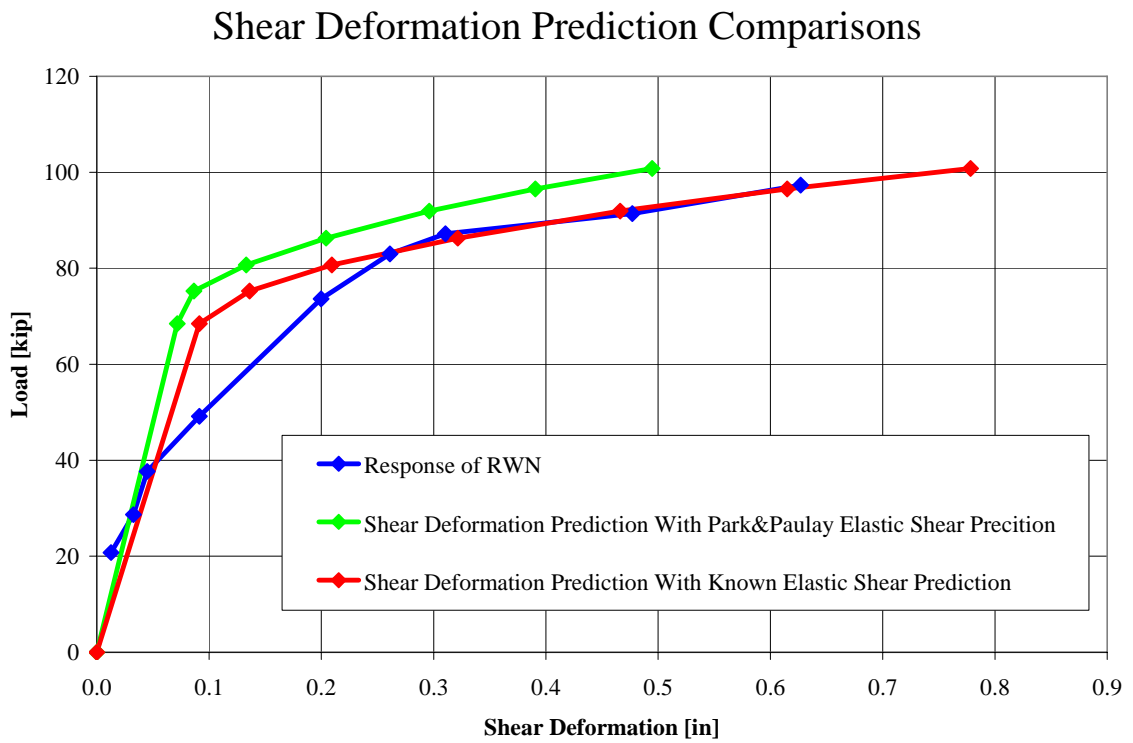


Figure 11.4: Shear deformation predictions discussed in section S.5.

[R.11.1] Park, R., and Paulay, T., 1975, "Reinforced Concrete Structures," John Wiley & Sons, Inc. USA., pp. 315-317.

Chapter 12: Total Calculated v. Measured Deformations

12.0: Introduction

This chapter covers the verification and summarization of the calculated components of lateral deformation. Results of the experimental tests are verified by comparing the summation of all deformation components to the global deformations measured externally. The correlation between the calculated and measured total deformation is calculated to show that all deformation modes have been accounted for. Total calculated deformation was typically within +/- 10% of the measured deformation. The results of the calculated deformation components are within the expected variation that can arise from experimental testing. The components of deflection for each wall are deemed accurate for comparison. The final results are compared and summarized to compare the effects of anchorage detailing and give guidance for performance based designs.

12.1.0: Summation of Deflection Components

The summation of the all contributing deformations was done for each wall and sensor at two select heights, 25% of the total wall height and 100% of the total wall height. Termination of the lapped splices in the No.5&6 boundary element occurs just below the 25% height. Both the Krypton and string pot sensors are available at this height and are used to verify the results when computed by two separate methods. These sensors are used for the flexure and shear components of deformation. Flexure and shear are discussed in great deal in chapters 9 and 11, respectively. Strain penetration is the last main contributor to total deformation. Strain penetration was computed with LVDTs attached to the longitudinal reinforcement at the foundation/wall interface. Strain penetration is discussed in chapter 10.

Additional deformation can occur from deformation of the test setup structures. These deformations include rotation of the foundation block, lateral slip of the foundation block,

and lateral sliding of the wall in the foundation measured at the foundation/wall interface. The rotation of the foundation block was calculated with LVDTs on opposite sides of the block. This deformation resulting from rotation was modeled as a rigid body rotation. The deformations from foundation block rotation and slip were found to be less than 1% of the total deformation of the walls.

The total calculated deformation was plotted versus the total measured deformation. String pots attached to the wall and an external rigid reference frame were used as the total measured deformation for the string pot data. The average global lateral deformation calculated from the top row of Krypton LEDs is used to compare the results of the deformation components calculated with the Krypton data. Note that the string pot at 25% of the wall height for RWS was malfunctioning. This is noted in chapter 9. The measured lateral deformations from the top row of Krypton LEDs are used to verify the results of the string pots instead. The displacement of the top row of Krypton LEDs was linearly interpolated to estimate the displacement at the height of the string pots (heights vary by 5 inches). The displacements plotted are the maximum displacements of all loading ramps when instruments were functioning correctly, before buckling of the No.5&6 boundary element. Lastly, a linear trend line was fit through the calculated v. measured displacement points with a zero intercept. The slope of this linear trend line is the correlation between the calculated and measured deformations.

12.1.1: Splitting Crack Effects

Large splitting cracks were observed during the test of each specimen. The lateral expansion of the walls caused by these cracks is measured with horizontal string pots spanning between the two boundary elements. The measured displacement is greatly influenced by this expansion, as much as 0.25" at the top of the wall. In the interest of consistency, the measured lateral deformation was taken as the deformation of the boundary element in tension. This was chosen to be consistent with shear walls in the field. Shear walls in the field would not experience such splitting cracks from a much

more distributed applied load from multiple floor diaphragms over the height of the wall. The string pots used to measure global displacement were attached to only one of the boundary elements. For this reason, the displacement of the string pots is used when the boundary element they are attached to is in tension. The expansion from cracking is subtracted from the global string pot displacements when the boundary element they are attached to is in compression. This applies only to the string pot calculated deformation components.

The effects of cracking must also be subtracted from the shear components calculated for the string pots. This is done with the following equation:

$$U_{\text{shear uncracked}} = U_{\text{shear average}} + \frac{\Delta_L^{\text{bottom}} - \Delta_L^{\text{top}}}{2} \quad \text{Eq (12.2)}$$

Where $U_{\text{shear uncracked}}$ is the displacement of the tension boundary element, $U_{\text{shear average}}$ is the shear deformation calculated in chapter S, and DL is the lateral crack expansion at the top and bottom of the string pot ‘x’ configuration. The difference in expansion is divided by 4 in the bottom segments where two configurations were averaged over the wall length. The derivation of this equation is shown in figure 12.1. This adjustment was made for each ‘x’ configuration section over the wall height, such that the cumulative effect was addressed.

Examination of this equation reveals some important aspects of the average shear deformation. The bottom cracks are typically larger than the top at the base of the wall where more moment creates more damage and larger cracking (with the exception of the bottom, where shear cracks do not span the entire length). The average shear deformation is actually smaller than the shear deformation of the tension boundary element, which has the smallest displacement of any point along the wall length. The effects of splitting cracks propagating from holes from the loading channel connection rods at the top of the wall leads to larger expansions at the top of the ‘x’ configuration when compared to the bottom. The shear deformation at the top is overestimated, while the shear deformation at the base is being underestimated. The magnitude of this change is typically less than 2%

of the average shear deformation. As an example, Refer to figure 12.2 for a plot of the expansion from cracking over wall height for RWN at a highly inelastic load level.

The effects of splitting cracks are ignored for the Krypton. This is due to the Krypton's ability to measure the lateral displacement along the wall length, giving no bias to one boundary element or the other. The results of the Krypton are not adjusted for the comparison of total calculated versus measured displacement.

12.1.2: Residual Base Rotations

Calculations were performed in order to determine if lapped splice slip was occurring. This was done by computing base rotations that are unaccounted for when subtracting the flexural and strain penetration rotation from the total rotation calculated with the Krypton LEDs 2 inches above the base of the wall. This rotation is referred to as the residual base rotation. While the results of these calculations showed no lapped splice slipping at the load levels used to determine the components of deformation, a discrepancy was observed for RWN when the No.9 BE was in tension. Discrepancies were noticed for RWC and RWS as well, but to a much lesser extent, typically less than 5% of the total deformation of the wall.

The residual rotation is thought to be the result of two problems. First, the flexural rotation is underestimated at the base. This is discussed in chapters 8 and 9. The reason for RWN having such a large residual rotation and consequent displacement is thought to be due to this problem when considering the similar strain penetration responses and smaller flexural responses. Possible reasons for this include an incomplete full row of LEDs at the base and the large amount of cracking that occurred at the base that may have compromised some the axial strain and consequent flexural deformation calculations. The reasons for this problem are unknown, however, this additional rotation must be accounted for. This is done by again modeling the displacement as a rigid body rotation, assuming the center of rotation is half way between the bottom row of LEDs and

the foundation/wall interface. The residual rotation is taken into account for each wall, regardless of magnitude. The residual rotation is assumed to be the result of missing flexural response only.

12.2: Comparison of Total Calculated and Measured Deformations

The comparisons of total versus measured deformations can be seen in figures 12.3, 4, and 5. The computed deformation components used for the Krypton data were the ‘whole cross section’ data which accounted for all sensors along the wall length. This was deemed to be the most reasonable from previous chapters. The drift levels included are all ramp maximums to 1% drift in the No.9 boundary element in tension and 1.5% drift in the No.5&6 boundary element direction where all instruments were functioning correctly. Each figure has two sets of data. The first is all components of deformation and deformations from compliance in the foundation block. The second data set is the same as the first, with the addition of the residual base rotation. The difference between the two is negligible for RWC and RWS. As expected, the residual base rotations observed from chapter B had a large effect on the total calculated deformation of RWN when the No.9 boundary element was in tension.

Most results were within +/- 10% of the total measured displacement. The average correlation was 100.6% using the residual rotation results of each wall in both boundary element in tension directions. The standard deviation is 6.1%. The calculated total displacement correlation with the total measured displacement suggests that all modes of displacement have been accounted for and the results are reliable to draw conclusions about the effects of longitudinal bar anchorage detailing.

12.3.0: Contribution of Deflection Components

The percentage of total deformation from each deflection component was computed over the reliable load range of the tests. An envelope of results was created at 25% of the wall.

This envelope was created by taking the maximum and minimum results from the Krypton calculations and String Pot calculations. The string pot percentages are for the average displacement in order to be consistent with the Krypton results. No envelope could be created for strain penetration, as only a single instrument was used to determine strain penetration. An envelope cannot be created with only a single value at each drift level. For this reason, the strain penetration is given as a single value and not an envelope. The residual rotation is assumed to be the missing flexural deformation only. A portion of the residual rotation is likely strain penetration, but assumed to be far less than the missed contribution of flexural deformation. No envelope could be created for the shear and strain penetration deflections at the top of the wall due to a single sensor being able to calculate the top deformations. Flexural deformation at the top of the wall is reported as an envelope, consisting of the flexural deformation with and without the effects of the residual base rotation. Refer to figures 12.6a through 12.6f for the contributions of flexure shear and strain penetration.

12.3.1: Performance Based Design Information

The results of RWN and RWC have very little difference. The effect of mechanically spliced longitudinal reinforcement is effectively negligible to shear wall behavior. For this reason, these specimens are used for comparison of deflection mode contribution at various damage levels. The results of the No.5&6 boundary element in tension direction were much more consistent than the No.9 boundary element in tension direction. In addition, the design is more reasonable to walls in the field. For these reasons, the results of the No.5&6 boundary element in tension for RWN and RWC have been chosen for consideration with performance based design issues. The contribution of each component is reported at the mean contribution percent, plus and minus half of one standard deviation, rounded to the nearest percent. Refer to table 12.1 for the approximate contribution of each deflection component at various damage levels. Refer to table 12.2a through 12.2c for the cracking information for these damage levels.

The contributions of flexure and shear are comparable at 25% of the wall height in the elastic range. The contribution of flexure decreases from the undamaged state to the elastic limit. This is caused by the increase in shear deformation from cracking and the reduction of shear stiffness. Flexure is much greater than shear at the top of the wall, but the same increase in shear and reduction in the contribution of flexure is observed. This is confirmed with the cracking patterns, where the number of shear cracks increased more than the increased number of flexural cracks. In addition, the length of the wall over which shear cracking occurred increased from 55% to 75% of the wall length. This increased length of cracking creates a larger portion of the wall that resists shear with the decreased cracked shear stiffness properties.

Following yielding, the flexural contribution increases. This is observed for both wall heights in question. Yielding of the longitudinal reinforcement allows the wall deform in bending more from the large decrease in flexural stiffness. Some yielding penetrates into the foundation block, increasing the effects of strain penetration as well. This is again confirmed with the cracking patterns. The number of shear cracks and their span over the wall length increased slightly. In addition, a slight grid offset was observed from shear sliding. However, the shear stiffness properties are not reduced as much as the flexural stiffness properties from yielding of the longitudinal reinforcement.

The ratio of each component of deflection at the full plasticization level is similar to the previous damage level for the top of the wall. This is thought to be from decreasing shear stiffness from increased damage and sliding at this level. This is not true for the 25% of the wall height. The shear component increases. The flexural deformation cannot increase as much as the top of the wall from the much smaller height over which the increased curvature and rotations are increasing. The decreased shear stiffness and sliding increase the shear deformation at a greater rate than the flexural stiffness change. This creates the increase in shear component contribution at 25% of the wall height. The observed cracking at this point confirms this result. An increase in shear cracking was observed from the last damage level. However, the flexural cracking did not change much.

Increased cracking and shear sliding decreases the shear stiffness more than the change in flexural stiffness, increasing the contribution of shear deformation.

The flexural deformation was well predicted throughout the elastic and inelastic range by BIAX in chapter 9. The shear deformation was under predicted by two different methods. This was especially true in the inelastic range from damage coupling the response of flexure and shear. The contributions shown in this report were used to perform a simple calculation of shear. This method was based on the percentage of shear in the elastic and inelastic range at the top of the wall. This method predicted the shear component of deformation in the inelastic range with improved accuracy. Understanding the contributions of each displacement mode is indeed valuable for predicting displacements at various damage levels.

12.4: Anchorage Detailing Effects

Two different methods of longitudinal bar splicing were used at the base of the test structures. The mechanically spliced wall did not have a significant variation in behavior from the control specimen with continuous bars through the wall and into the foundation. The test specimen using lapped splices at the base of the wall had noticeable differences in behavior. The first reason for the difference in behavior was the doubled longitudinal bar effect in the elastic range, increasing the flexural stiffness. The second reason for the difference in behavior was the inability to form a full plastic hinge in the lapped splice length, forcing the wall to deform more in other modes when loaded to the same displacement levels as the other walls.

RWS experienced reduced axial strains from the increase in longitudinal steel area. This created a reduced flexural deformation when compared to RWN and RWC. This reduction was approximately 40% at 25% of the walls height and 15% at the top of the wall. Strain concentrations were also observed above and below the lapped splice lengths just outside their termination. In addition, the inability to form a full, continuous plastic

hinge forced the wall to have larger plastic deformations than RWN and RWC at the termination of the lapped splices. This strain concentration lead to a considerably larger strain penetration contribution in the inelastic range.

The total deformation at the top of the walls was the same for each wall when pushed to a target displacement. The load required to achieve this top displacement was slightly larger for RWS from the increased stiffness from flexure, approximately 1 to 6% larger. RWS compensated to achieve the same top displacement by having slightly larger shear deformations, approximately 5 to 10% larger. This is confirmed with the cracking data where RWS experienced more shear cracking in the base panel. These shear cracks spanned further than the shear cracks in RWN and RWC.

The top displacement was the same for each wall at the loading ramp maximums, however, this is not true at the height of 25% of the total. The reduction in total displacement was approximately 40% in the elastic range and 20% in the inelastic range.

Lapped splices in the base of the test specimen clearly change the behavior of the wall. The contributions of flexure are decreased. As a result, the contributions of strain penetration and shear are increased. In addition to the increased strain penetration, lapped splice slip was also observed. This lead to an interface crack as large as large as 1". The lapped splices also had an effect on the ultimate failure mechanisms of the wall. Anchorage detailing effects on wall instability and ultimate failures are covered in the following chapter.

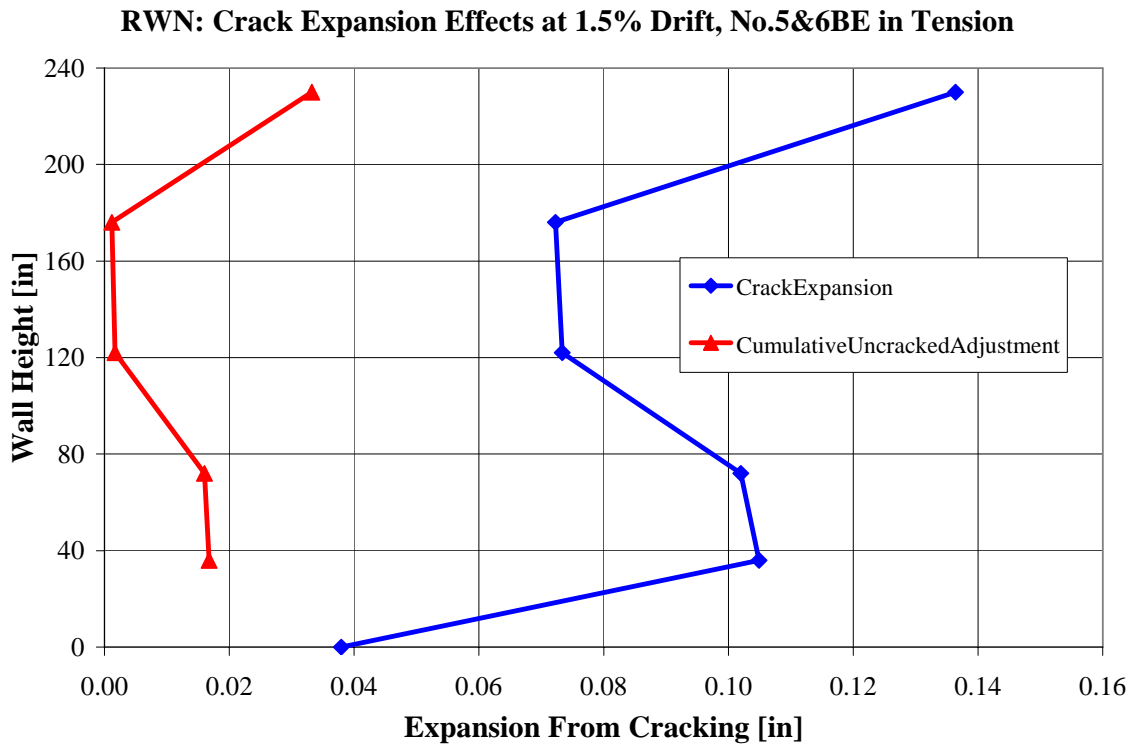


Figure 12.2: Example of the effect of expansion from cracking

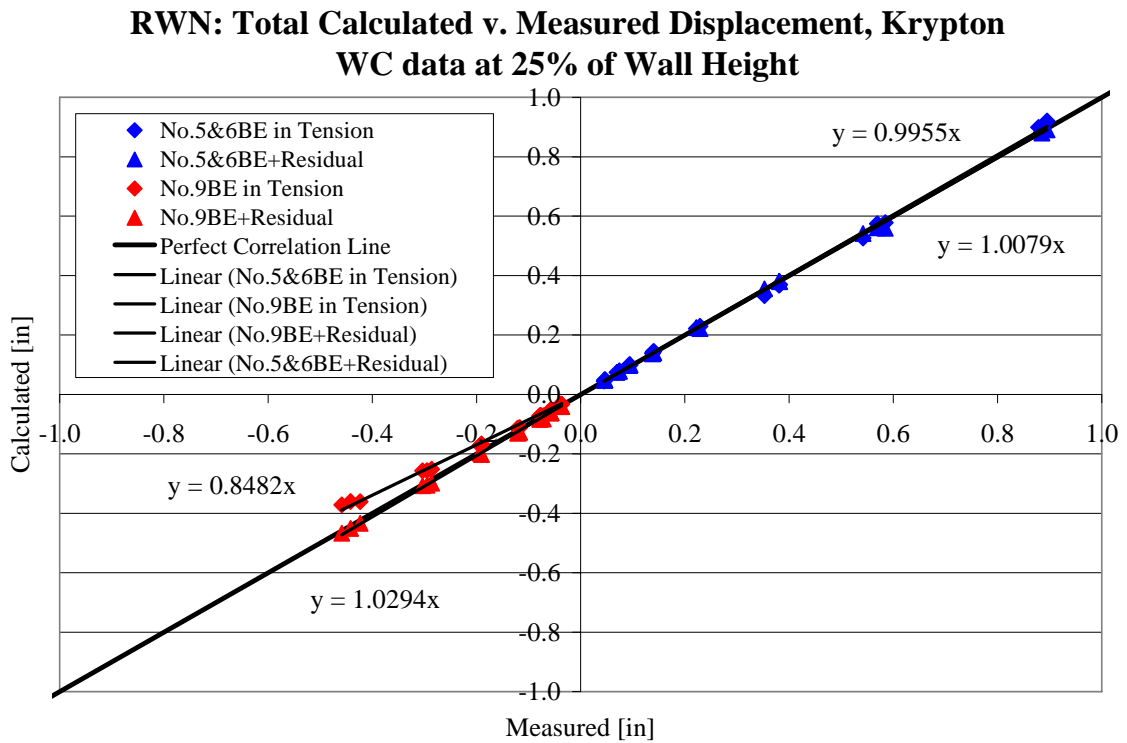


Figure 12.3a: Calculated v. Measured Deformation for RWN: Krypton Data

**RWN: Total Calculated v. Measured Displacement, String Pot
Data at 25% of Wall Height**

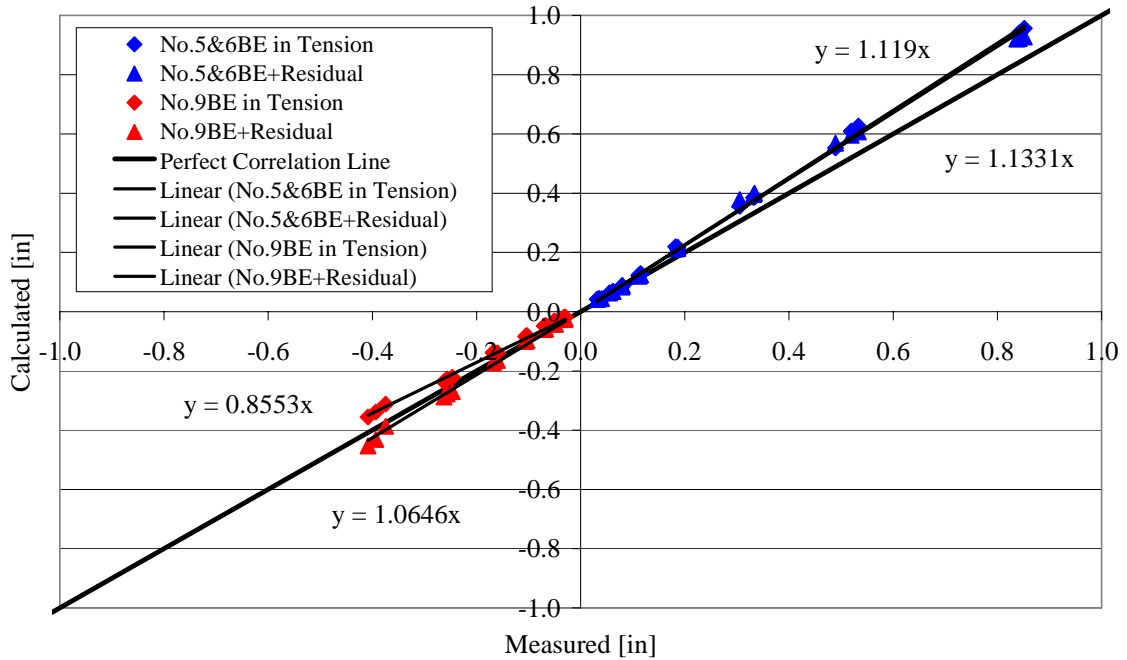


Figure 12.3b: Calculated v. Measured Deformation for RWN: String Pot Data

**RWN: Total Calculated v. Measured Displacement, String Pot
Data at 100% of Wall Height**

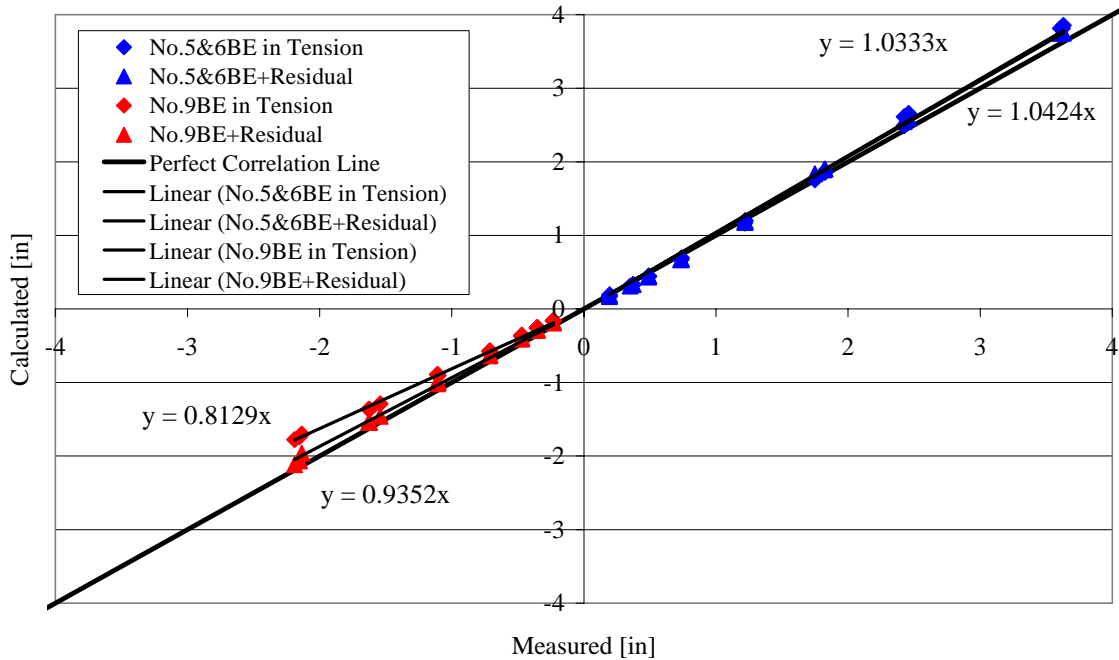


Figure 12.3c: Calculated v. Measured Deformation for RWN: String Pot Data

**RWC: Total Calculated v. Measured Displacement, Krypton
WC data at 25% of Wall Height**

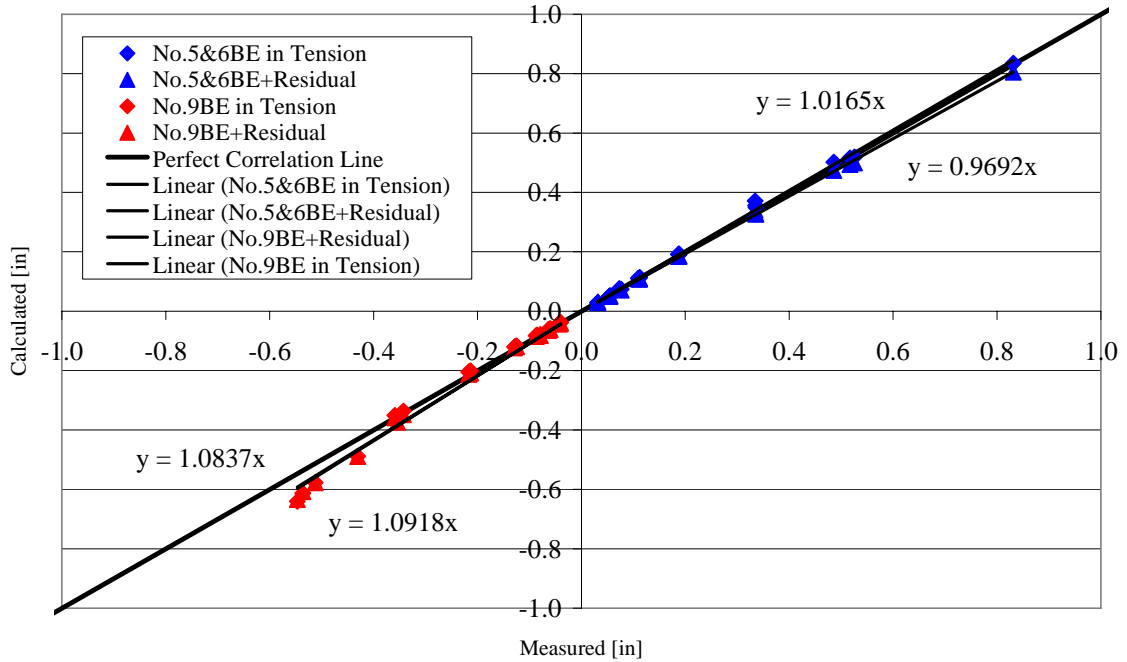


Figure 12.4a: Calculated v. Measured Deformation for RWC: Krypton Data

**RWC: Total Calculated v. Measured Displacement, String Pot
Data at 25% of Wall Height**

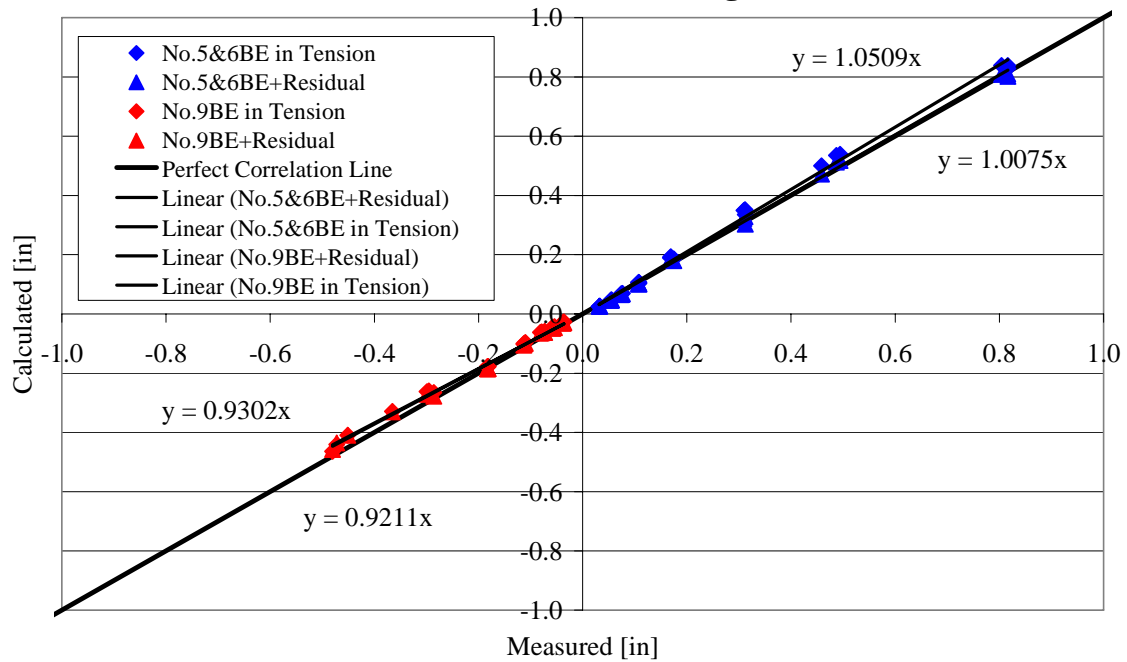


Figure 12.4b: Calculated v. Measured Deformation for RWC: String Pot Data

**RWC: Total Calculated v. Measured Displacement, String Pot
Data at 100% of Wall Height**

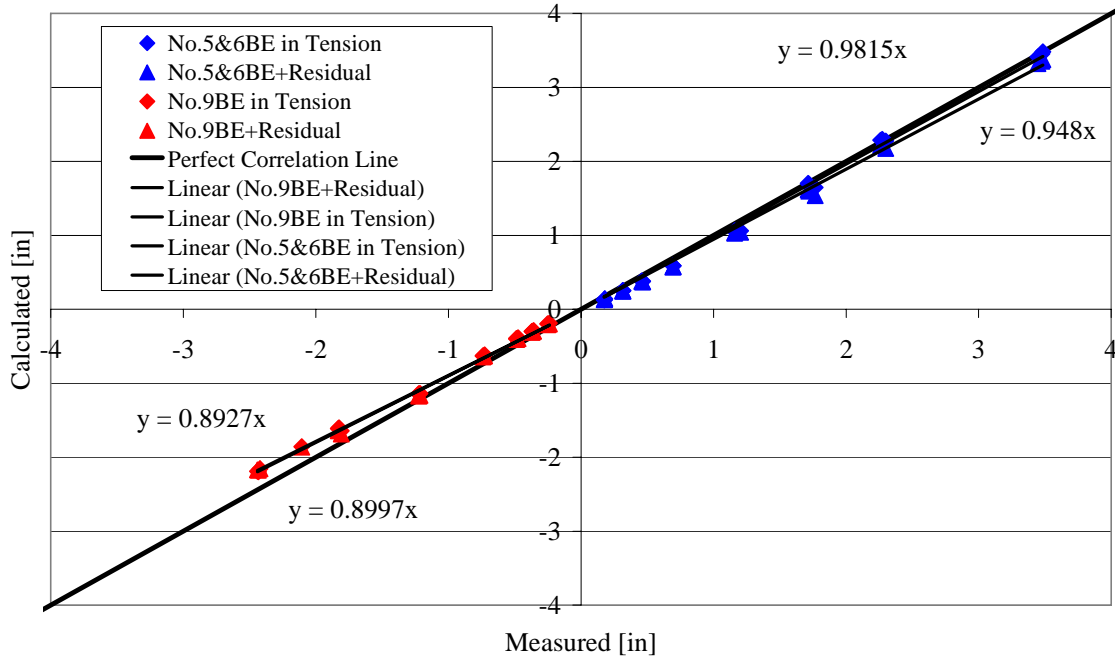


Figure 12.4c: Calculated v. Measured Deformation for RWC: String Pot Data

**RWS: Total Calculated v. Measured Displacement, Krypton
WC data at 25% of Wall Height**

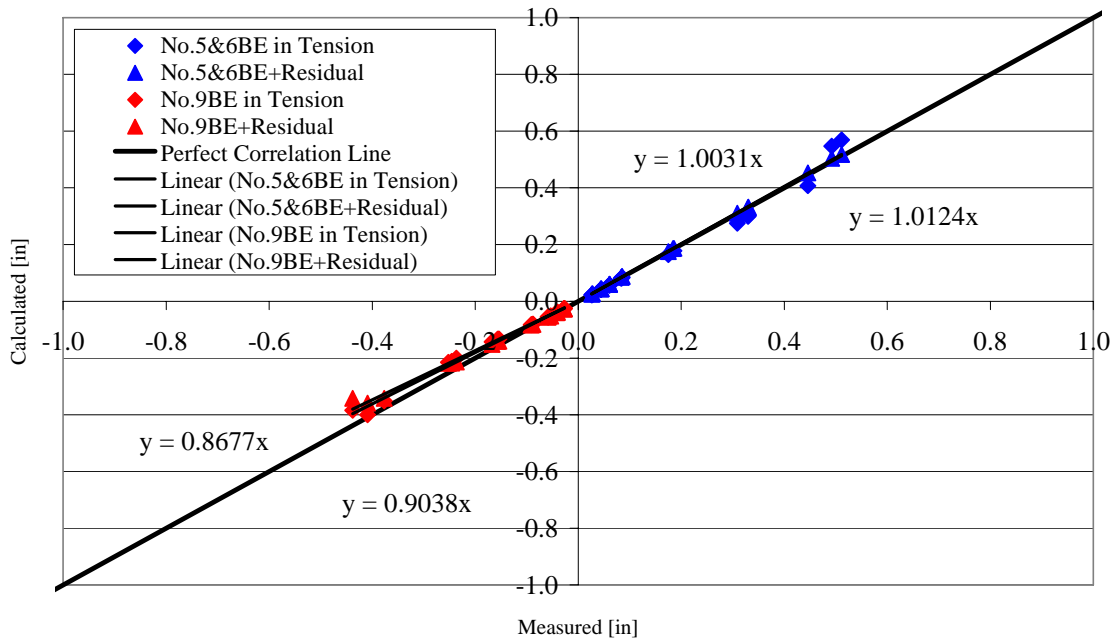


Figure 12.5a: Calculated v. Measured Deformation for RWS: Krypton Data

**RWS: Total Calculated v. Measured Displacement, String Pot
Data at 25% of Wall Height**

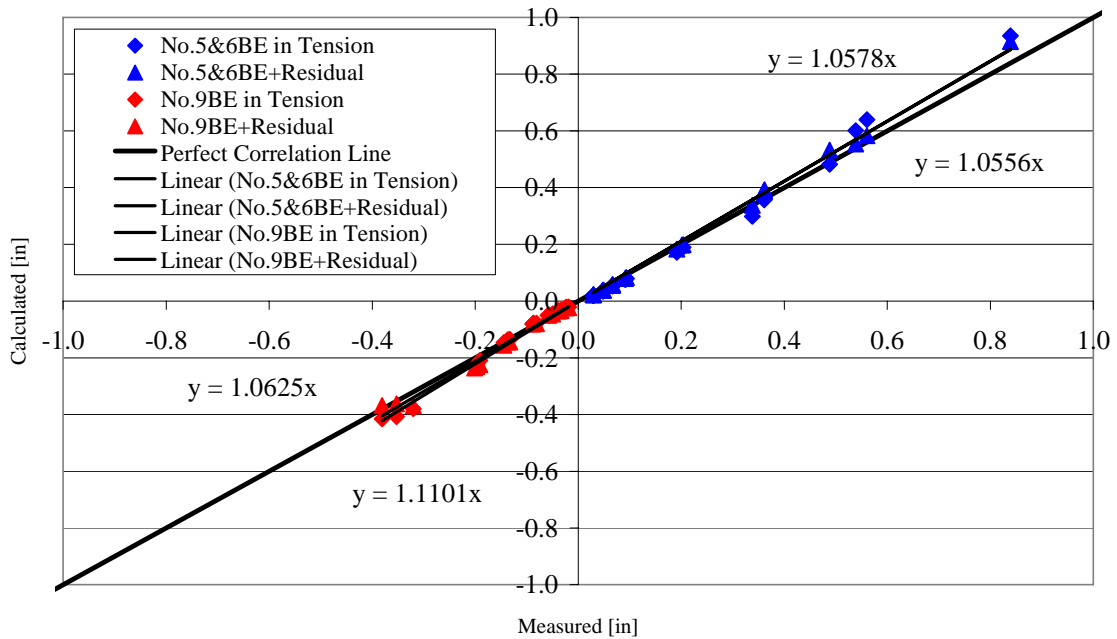


Figure 12.5b: Calculated v. Measured Deformation for RWS: String Pot Data

**RWS: Total Calculated v. Measured Displacement, String Pot
Data at 100% of Wall Height**

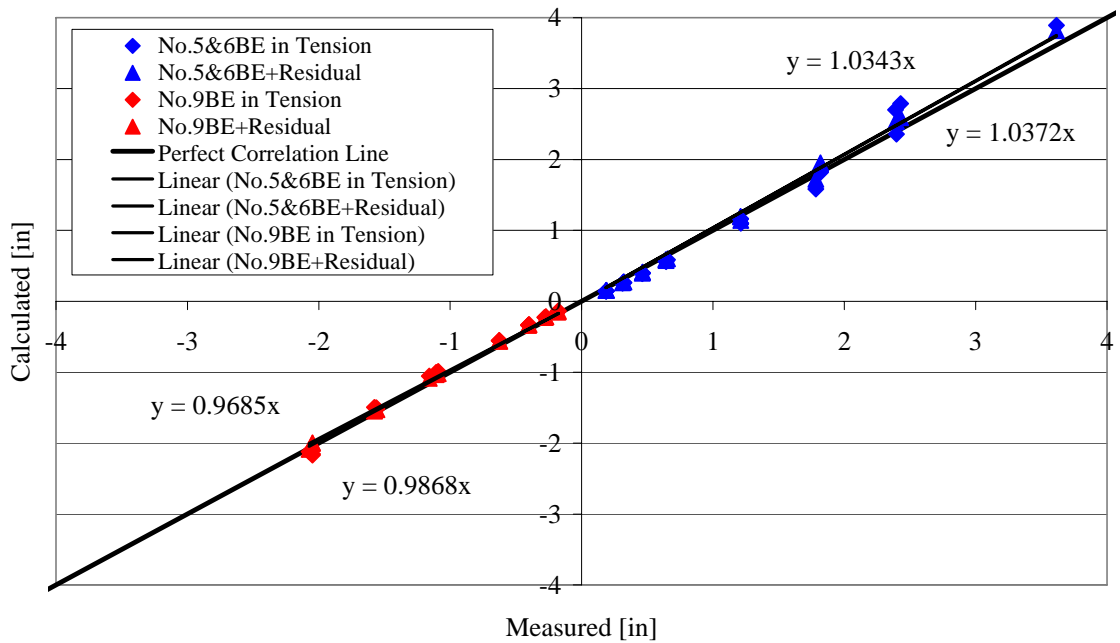


Figure 12.5c: Calculated v. Measured Deformation for RWS: String Pot Data

RWN: Component Contribution v. Total Measured Displacement at 25% of Wall Height

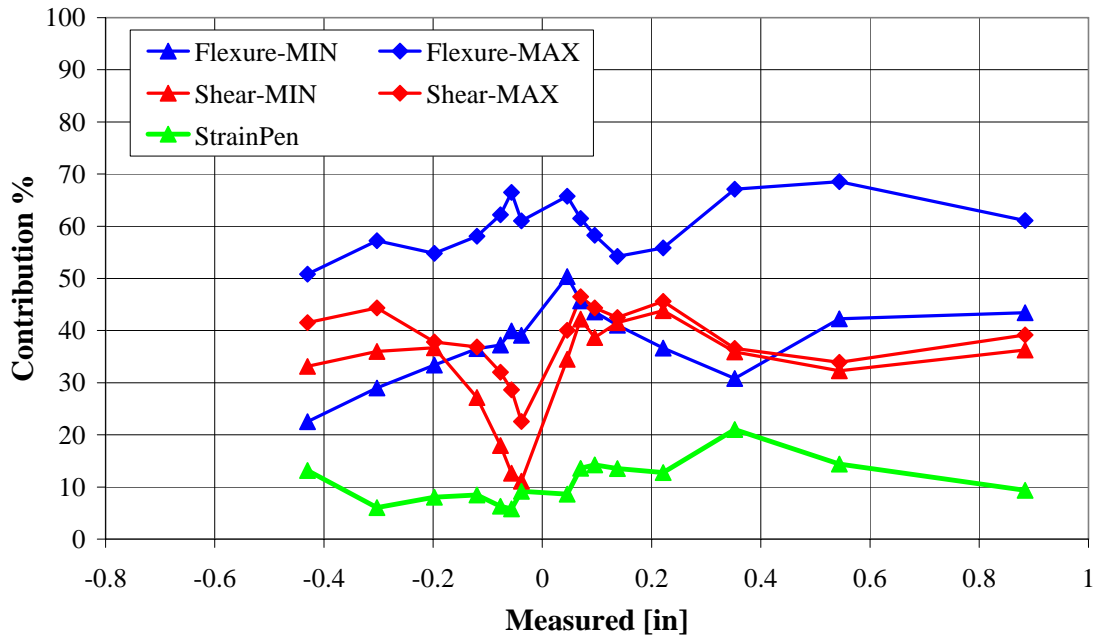


Figure 12.6a: Deflection component contributions at 25% of wall height: RWN

RWN: Component Contribution v. Total Measured Displacement at 100% of Wall Height

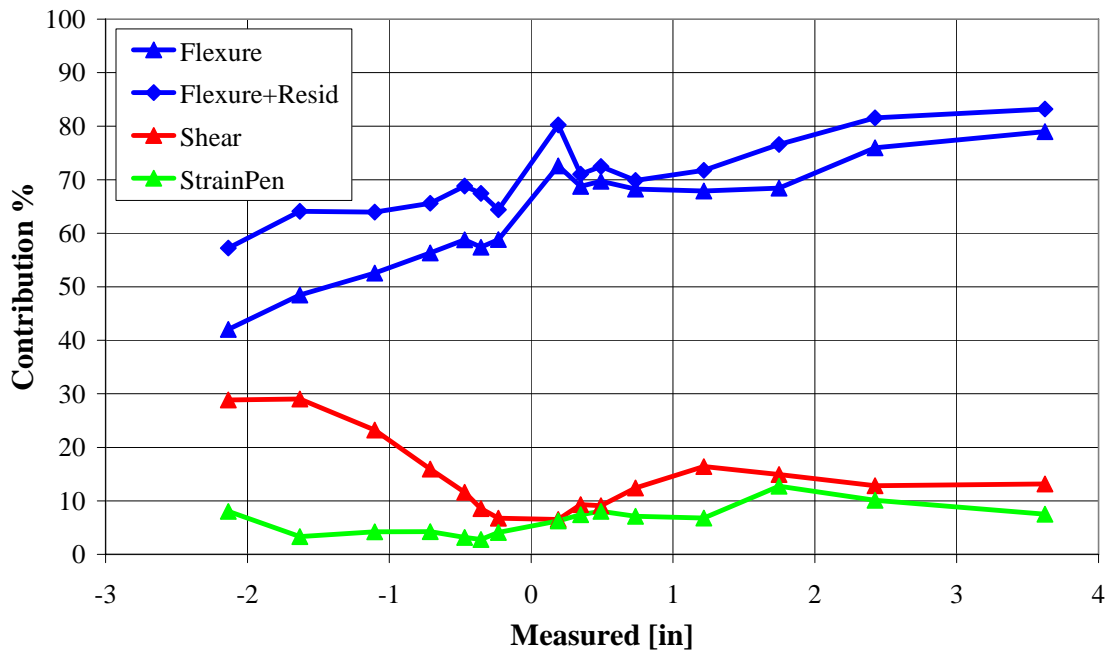


Figure 12.6b: Deflection component contributions at 100% of wall height: RWN

**RWC: Component Contribution v. Total Measured
Displacement at 25% of Wall Height**

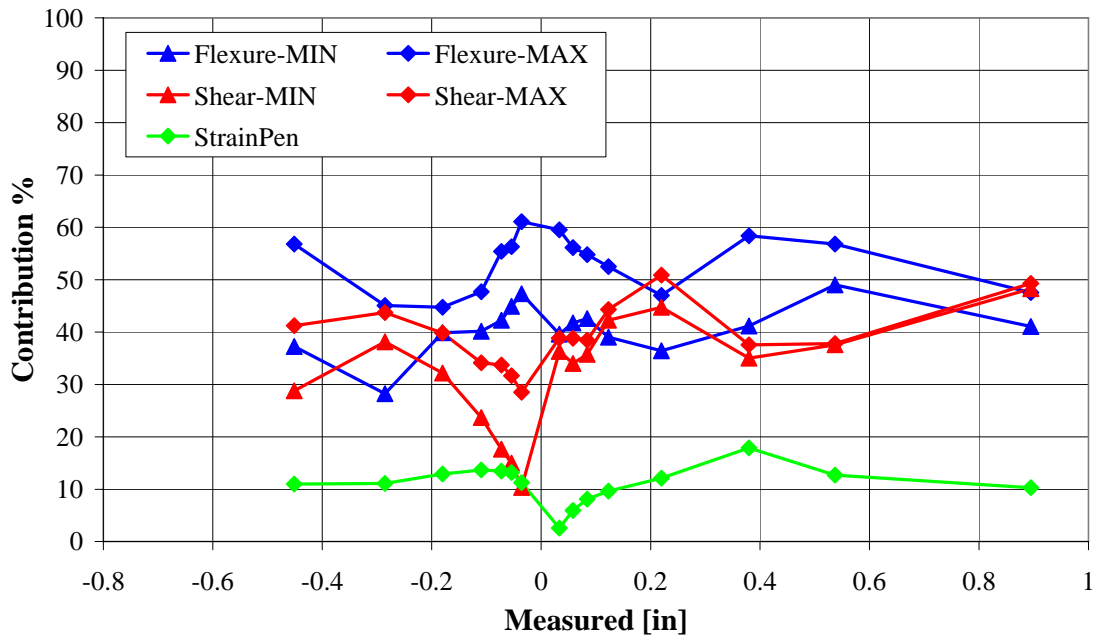


Figure 12.6c: Deflection component contributions at 25% of wall height: RWC

**RWC: Component Contribution v. Total Measured
Displacement at 100% of Wall Height**

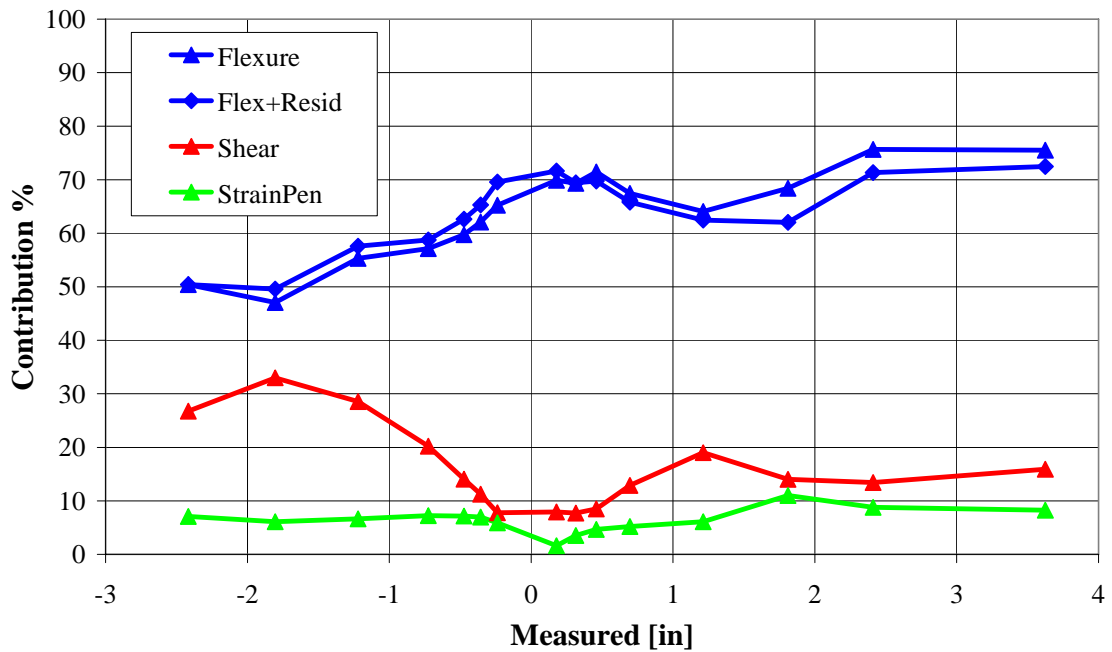


Figure 12.6d: Deflection component contributions at 100% of wall height: RWC

**RWS: Component Contribution v. Total Measured
Displacement at 25% of Wall Height**

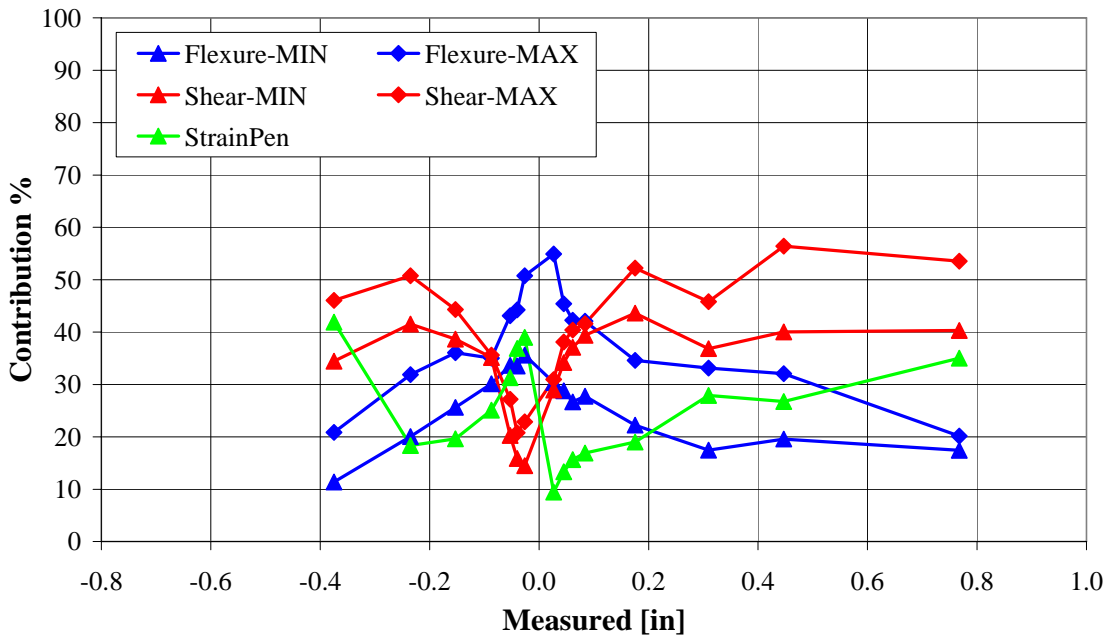


Figure 12.6e: Deflection component contributions at 25% of wall height: RWS

**RWS: Component Contribution v. Total Measured
Displacement at 100% of Wall Height**

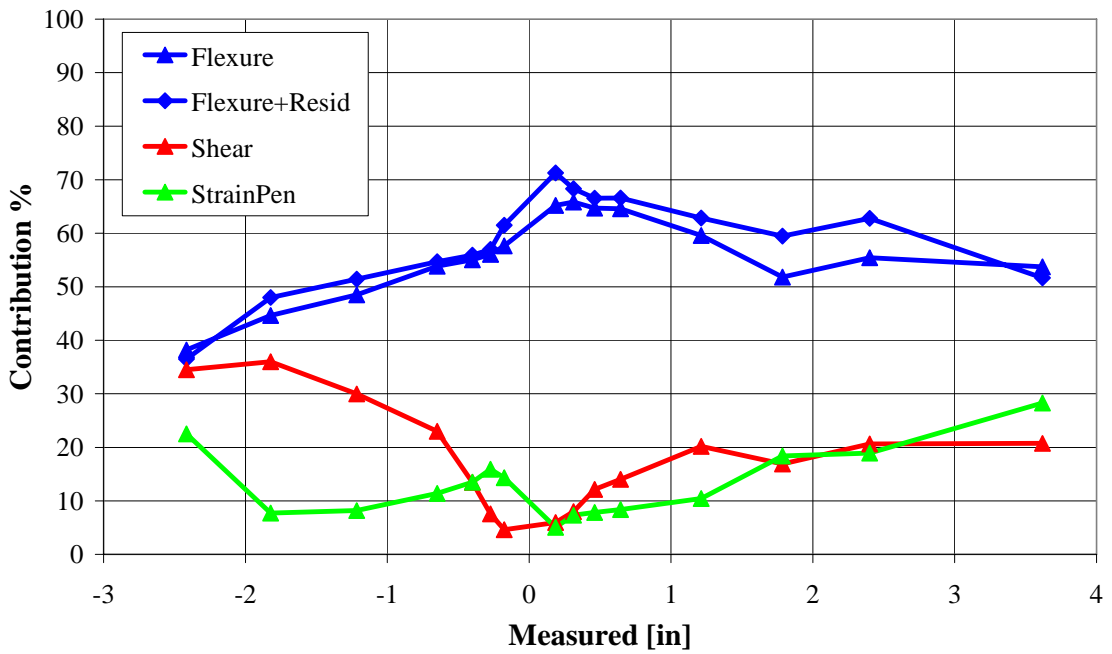


Figure 12.6f: Deflection component contributions at 100% of wall height: RWS

25% of Total Height			Deflection Contribution	
Damage Level	Drift Level	Flexure	Shear	Strain Penetration
Undamaged	0.10%	49-58%	36-39%	4-8%
Elastic Limit	0.30%	44-50%	42-43%	10-13%
Some Plasticization	1.00%	50-58%	34-37%	13-14%
Full Plasticization	1.50%	45-52%	40-47%	9-10%

Top of Wall			Deflection Contribution	
Damage Level	Drift Level	Flexure	Shear	Strain Penetration
Undamaged	0.10%	71-76%	7-8%	2-6%
Elastic Limit	0.30%	67-69%	12-13%	6-7%
Some Plasticization	1.00%	74-78%	12-13%	9-10%
Full Plasticization	1.50%	75-80%	14-16%	8-9%

Table 12.1: Deflection Contributions v. Damage Level

RWN-Crack Data

Damage Level	Drift Level	Max Crack Width [inch]	Max Grid Offset From Shear Sliding [inch]	Height of Top Crack [% of Total]
Undamaged	0.10%	0.007	N/A	20
Elastic Limit	0.30%	0.02	N/A	40
Some Plasticization	1.00%	0.125	0.05	100
Full Plasticization	1.50%	0.25	0.01	100

Damage Level	Drift Level	Length of Cracking [% of Wall Length]	Base Panel Shear Crack Distribution [# Cracks / 25% of Wall Height]	Base Panel Flexural Crack Distribution [# Cracks / 25% of Wall Height]
Undamaged	0.10%	55	12	10
Elastic Limit	0.30%	75	18	14
Some Plasticization	1.00%	85	23	16
Full Plasticization	1.50%	85	26	19

Table 12.2a: Crack information from final loading cycle at each drift level.
RWC-Crack Data

Damage Level	Drift Level	Max Crack Width [inch]	Max Grid Offset From Shear Sliding [inch]	Height of Top Crack [% of Total]
Undamaged	0.10%	0.004	N/A	20
Elastic Limit	0.30%	0.028	N/A	60
Some Plasticization	1.00%	0.125	0.053	100
Full Plasticization	1.50%	0.234	0.098	100

Damage Level	Drift Level	Length of Cracking [% of Wall Length]	Base Panel Shear Crack Distribution [# Cracks / 25% of Wall Height]	Base Panel Flexural Crack Distribution [# Cracks / 25% of Wall Height]
Undamaged	0.10%	55	11	13
Elastic Limit	0.30%	75	14	18
Some Plasticization	1.00%	85	23	20
Full Plasticization	1.50%	85	31	26

Table 12.2b: Crack information from final loading cycle at each drift level.

RWS-Crack Data

Damage Level	Drift Level	Max Crack Width [inch]	Max Grid Offset From Shear Sliding [inch]	Height of Top Crack [% of Total]
Undamaged	0.10%	0.009	N/A	70
Elastic Limit	0.30%	0.025	N/A	70
Some Plasticization	1.00%	0.073	0.040	100
Full Plasticization	1.50%	0.087	0.050	100

Damage Level	Drift Level	Length of Cracking [% of Wall Length]	Base Panel Shear Crack Distribution [# Cracks / 25% of Wall Height]	Base Panel Flexural Crack Distribution [# Cracks / 25% of Wall Height]
Undamaged	0.10%	60	11	9
Elastic Limit	0.30%	85	21	17
Some Plasticization	1.00%	85	34	23
Full Plasticization	1.50%	90	39	26

Table 12.2c: Crack information from final loading cycle at each drift level.

Chapter 13: Instability & Bar Fracture

13.0: Introduction

This chapter covers the observed buckling of the test specimens and fracture of the longitudinal reinforcement in the test specimens. Each test specimen underwent buckling of the No.5&6 boundary element. The magnitude of out of plane deflection was observed to be a function of the axial strain in the buckled boundary element from the previous loading ramp in which the buckled boundary element was in tension. The buckled shape of the No.5&6 boundary element varied for each test specimen. In general, RWN and RWC experienced a global buckling mechanism where RWS experienced more of a localized buckling mechanism of the longitudinal reinforcement at the wall/foundation interface. Instability of the test specimens is then compared to idealized methods of predicting buckling by Paulay and Priestley [R.13.1]. The consequence of buckling of the No.5&6 boundary element is then discussed for the test specimens.

13.1: Observed Instability

Buckling of each test specimen was apparent from visual inspection of the No.5&6 boundary element. Instability of the No.5&6 boundary element was not noticed in the case of RWN and RWC until loading of the No.9 boundary element in tension following top drift levels of 2.5% with the No.5&6 boundary element in tension. The buckling observed by researcher can be seen in figures 13.1a through 13.1g. The global versus local buckling is also illustrated in these photographs where the wall/foundation interface of RWN and RWC does not have a noticeable out of plane deflection and out of plane rotation is apparent visually. This is not the case for RWS, where the buckled shape is much more of a shift at the base without out rotation in the wall section in the plane normal to the plane of the wall above the foundation/wall interface.

Measured out of plane deflections of RWN and RWC reveal that out of plane deflections occurred prior to the loading level at which it was noticed visually by researchers. These measured out of plane deflections were apparent during the return loading ramps of the No.9 boundary element in tension with a top drift of 1%. A total of nine load events were applied to the test structures which achieved a top drift of 1% when the No.9 boundary element was in tension. The applied load to the test structures decreases very little during these return loading ramps for RWN and RWC, showing that the out of plane deflections at these drift levels are stable. The opposite was observed for RWS. Buckling of RWS was observed during the test during the return loading ramps of the No.9 boundary element in tension to 1%. This observed buckling was more of a local effect where the longitudinal reinforcement at the wall/foundation interface was observed to buckle in the direction normal to the plane of the wall, pushing the concrete cover away from the test structure. This is illustrated well by figure 13.2. This figure shows the load required to return the No.9 boundary element in tension with a top drift of 1%.

It can be seen in figure 13.2 that these return loading events appear to be stable for RWN and RWC. The load decreases as wearing along cracking occurs and the stiffness of the wall is reduced. RWC appears to converge to a decreased load of 20kips. This is not the case for RWS, which does not appear to be converging to a stable load when returning to 1% drift of the No.9 boundary element in tension. This relationship appears to be decreasing linearly with each return to 1% drift, showing that buckling of the longitudinal reinforcement is occurring and unable to achieve a stable response.

Lastly, the top drift of the wall when the No.5&6 boundary element is in tension was increased for every three returns to 1% drift in the No.9s in tension direction (1%, 1.5%, and 2%). The load for RWN drops significantly at the final return to 1% drift of the No.9 boundary element in tension. This is due to the increasing tensile strains that are being developed in the No.5&6 boundary element and consequent larger cracking contributing to instability. This is not observed for RWC, again to the effects of the opposite orientation in the test frame. RWC was loaded to slightly smaller drift levels in the

No.5&6 boundary element in tension from the effects of splitting cracks being unaccounted for when pausing at the target drift level. The tensile strain in the No.5&6 boundary element was slightly smaller for RWC when compared to RWN, creating the more stable result of applied load during the returns to 1% drift in the No.9 boundary element in tension direction. The effects of the previous load level and tensile strains in the boundary element of possible buckling are covered in the following section.

13.2: Previous Axial Stain & Buckling

Buckling of boundary elements in rectangular shaped walls is discussed in great detail in the paper “Stability of Ductile Structural Walls” by Paulay and Priestley [R.13.1]. This resource presents an idealized situation in which instability of boundary elements can be quantified. The main contention of this paper is that instability is a product of the cracking of the boundary element which buckles. This is the driving force of wall instability of very ductile systems that undergo very large inelastic tensile strains and have large crack widths. The cracks that form from previous loading of the boundary element in tension must close before the concrete can participate in the resistance of the compressive forces. Inherent eccentricities of the longitudinal reinforcement and applied loading will cause differential stresses in reinforcement at the same position along the wall length. In the case of two curtains of longitudinal reinforcement, the eccentricity will cause one curtain of reinforcement to yield prior to its counterpart. This yielding will create an out of plane displacement as one side of the wall will have effectively zero stiffness. Out of plane displacements will continue until the cracks in the concrete have closed and the concrete can participate in the resistance of out of plane moments. In short, large previous axial tensile strains that developed in the boundary element of possible buckling will create larger cracks and increase the possibility of instability. This hypothesis was confirmed when examining the buckled shape of the walls with the applied loading history, where the compression force in the buckled boundary element does not increase while out of plane displacements increase.

13.3: Loading History & Observed Buckling

Instability of the No.5&6 boundary element for each test specimen occurred during the loading history of the walls where the No.9 boundary element was in tension at drift levels of 1%. The No.9 boundary element was loaded to 1% drift for a total of 9 load steps following increasing drift levels of the No.5&6 boundary element in tension. The loading history is key when validating the assumptions of Paulay and Priestley. Out of plane deflections in the No.5&6 boundary element increased in magnitude during the returns to 1% drift. The out of plane deformations measured by the Krypton and string pots is shown in figures 13.3a through figure 13.3c. These figures show a significant increase in the out of plane deformations of the walls each time the top drift is increased for the No.5&6 boundary element from the previous loading event. The axial tensile strain and consequent crack size in the boundary element is the only variable that changes when considering the increase in the out of plane deflections. The compressive load applied to the buckled boundary element is in fact decreasing each time the out of plane deformations are increased (refer to figure 13.2). The driving factor in the out of plane deformations experienced by the No.5&6 boundary element is indeed the previous axial strain in the boundary element and not the applied compressive load resisted by the boundary element. The last deflected shape shown in figure 13.3a through 13.3b corresponds to the photographs shown in figure 13.1a through 13.1g.

13.4: Local v. Global Buckling Mechanisms

Figures 13.3a through 13.3b show the difference in the buckling mechanism observed for RWS. The photographs show very little out of plane rotation of RWS. Indeed the out of plane deflections are mostly the cause of the local buckling of the longitudinal reinforcement at the wall/foundation interface. The out of plane deflection measured by the bottom Krypton LED for RWN and RWC was typically less than 10% of the maximum out of plane deflection measured. The out of plane deflection measured by the bottom Krypton LED for RWS was as much as 70% of the maximum out of plane

deflection measured by the other sensors. This indicates that the buckling is a localized lateral shift at the base of the wall. This hypothesis is further supported by the reasons for instability discussed by Paulay and Priestley. Their contention is that instability is the product of the crack widths that developed in the boundary element of possible buckling from previous loading. The interface crack measured during the test of RWS was as large as 1". Refer to appendix 7 for photographs of the interface crack of RWS. Such a significant crack would require a great deal of deformation of the longitudinal bars before the crack could close and the concrete could participate the resistance of out of plane moments. The large interface crack observed in the test of RWS is thought to be the largest contributing factor of instability of the No.5&6 boundary element.

The buckled shape resembling more of a typical buckled shape for RWN and RWC is again explained with the crack distribution over the height of buckling. A much more uniform crack width was observed over the height of buckling during the previous loading event of the buckled boundary element in tension. The interface crack for these walls was much smaller than RWS, preventing a single height at which out of plane moments can be developed faster than the rest of the wall at locations above the interface. The more uniform cracking widths create equal contributions of out of plane deformation along the wall height, creating the typical curved shape of the wall when buckling. Indeed, crack sizes from the previous loading event are the cause of instability.

13.5.0: Critical Buckling Width of Rectangular Walls

The proposed methods for determining the width of a rectangular shear wall at which buckling will not occur (critical width) proposed by Paulay and Priestley is evaluated with the test data. The specimen chose to make this evaluation is RWC. RWC was chosen because of the additional string pot measuring out of plane deflections at mid height of the wall, as well as displaying a typical global deformed shape that would occur for walls without lapped splices in the region of possible plastic hinging. The critical width of a rectangular wall is given as:

$$b_c = l_0 (\varepsilon_{sm} / 8 \beta \xi)^{1/2} \quad (\text{Eq. 13.1})$$

$$b_c = 0.019 l_p (\mu_\phi / \xi)^{1/2} \quad (\text{Eq. 13.2})$$

These two equations differ only from substitution of equivalent expressions. The term ‘ b_c ’ refers to the critical buckling width of a rectangular shear wall. ‘ l_0 ’ is the height of the wall over which out of plane deflections exist from buckling. ‘ l_p ’ is the length of plastic hinging. Note that the length of the buckled shape and the length of plastic hinging are assumed to be the same value in the method. ‘ ε_{sm} ’ is the average tensile strain in the boundary element prior to buckling. ‘ μ_ϕ ’ is the curvature ductility, the ratio of ultimate to yield curvature of the cross section. ‘ β ’ is the distance between the side concrete face and the longitudinal reinforcement furthest away (in the direction normal to the plane of the wall), divided by the width of the wall section. ‘ ξ ’ is an eccentricity ratio, equal to the out of plane deformation of the section to the width of the section. In absence of knowing the out of plane deformations during design, the eccentricity ratio can also be calculated with the following equation:

$$\xi = 0.5 [1 + 2.35m - (5.53m^2 + 4.70m)^{1/2}] \quad (\text{Eq. 13.3})$$

Where ‘ m ’ is the mechanical reinforcement ratio: $m = \rho f_y / f'_c$. Refer to [R.13.1] for a full derivation of all equations presented in this chapter. The critical buckling width can be estimated with either of equation 13.1 or 13.2.

13.5.1: Paulay & Priestley Prediction

The proposed method was used to predict the critical buckling width of the test specimens. The prediction was first made with equation 13.1, as the test specimens were not designed for a particular drift ductility. The plastic hinge length, or length of out of plane deformation, was computed with the given estimation from [R.13.1]. ‘ ε_{sm} ’ was

estimated from BIAX results at the load level prior to buckling observed in the experimental tests. ' β ' was calculated from the nominal longitudinal reinforcement locations. ' ξ ' was calculated from equation 13.3. The critical buckling width was predicted to be 4.3", suggesting that no buckling should occur for this wall at the loads it was subjected to. As a check, equation 13.2 was rearranged to predict the drift ductility of the walls at which the actual width of the wall would become the critical buckling width. This returned a drift ductility of nearly 40, unreasonable for any structural wall system. This prediction was made only with equations provided in the paper, removing any doubt that the BIAX prediction of tensile strain in the boundary element is the cause of the poor estimation of critical buckling width.

The method proposed by Paulay and Priestly is clearly missing an aspect of instability for these test specimens. The problem is thought to be that the length of out of plane buckling is equal to the length of plastic hinging. This can be seen when inspecting figures 13.3a and 13.3b, the buckled shape of RWN and RWC. These test specimens displayed buckled shapes that are consistent with the assumptions of the paper, an idealized circular shape. The height of the maximum out of plane deflection is between 60 and 70" for both specimens. The height of the maximum out of plane deflection, not even the entire length of out of plane deformation, is much greater than the predicted length of 29". The length of buckling appears correlate well with the height of first yield. Using this estimation of the length of buckling instead of the length of plastic hinging returns a critical buckling width of 9.5", suggesting that buckling would occur at the top drift that buckling was observed in the test specimens. The estimation of the length of the buckled shape is clearly the largest factor in the poor prediction of the critical width of these test specimens.

Crack width is assumed to be the lead cause of instability from section 13.3 and 13.4. Eccentricity of the applied compressive load in the boundary element of predicted buckling is also thought to be a large contributing factor in wall instability. A larger eccentricity of the compression force will create one curtain of longitudinal

reinforcement to yield in compression much sooner than the same compression force at a smaller eccentricity. The larger length of buckling than assumed is thought to be caused from increasing eccentricity of the applied compressive force from buckling below the height in question. Buckling below a height in question increases the eccentricity of the applied compressive load at the height in question without any changes to the height in question itself. This increased eccentricity would propagate up the wall height, causing heights that have cracks smaller than what would cause buckling alone to begin displacing out of plane. This may only be a problem with these test specimens, as floor diaphragms would exist between the wall/foundation interface and the total applied lateral force. These diaphragms would likely stop such propagation of buckling due to increasing eccentricity.

13.5.2: Verification With Test Data

Paulay and Priestley's method for determining the critical width of rectangular shear walls was further explored with the test data. The data from RWC at the observed buckling load was chosen for the reasons discussed in section 13.5.0. A variation of equation 13.1 was used to calculate the critical width of the test specimens. The substitution of the eccentricity ratio, ' ξ ', with δ/b is made to again remove any possible error associated with equation 13.3. The critical width of the test specimens can be computed as:

$$b_c = l_0 (\epsilon_{sm} b / 8 \beta \delta)^{1/2} \quad (\text{Eq. 13.1})$$

All terms are those discussed in section 13.5.0, except 'b' and ' δ '. 'b' is the actual width of the test specimen and ' δ ' is the maximum out of plane deformation. ' ϵ_{sm} ' was calculated with the vertical string pots attached to the No.5&6 boundary element. 'b' was taken as the nominal width of the wall. ' β ' was calculated from the nominal longitudinal reinforcement locations. ' δ ' was taken as the maximum measured out of plane deformation from the Krypton LEDs. ' l_0 ' was taken as the length of plastic hinging. The plastic hinge length was computed by finding the centroid of plastic curvature from string

pot data. The critical buckling width was determined to be 9.4” from the test data, suggesting that buckling should occur. The critical buckling width calculation is thought to work well for the test data because it is based entirely on pure mechanics and well accepted assumptions.

The method proposed by Paulay and Priestley seems to work when using the experimental test data, but is unable to predict the critical buckling width with the equations proposed in the paper. This is thought to be a product of the nature of the test specimen. The absence of floor diaphragms is thought to allow buckling at lower heights to influence the behavior of the wall above the height of initial buckling. The critical width of the test specimens was not predicted well because it does not behave like the idealized buckled geometry. Structural walls in the field would likely follow the idealized buckled geometry much closer from the interaction of the floor diaphragms constraining lateral deformation at the height of the diaphragm. The methods used to calculate critical buckling width for shear walls in [R.13.1] is thought to adequately estimate buckling width for walls constrained laterally by floor diaphragms or other means of lateral bracing or restraint.

13.6: Longitudinal Bar Fracture

Ultimate failure can be defined by a wide range of criteria. Ultimate failures include lateral instability, post-peak decreasing load resistance, and fracture of longitudinal reinforcement. The more significant difference between the three test specimens when considering the ultimate failure mode was the fracture of longitudinal bars. RWN did not experience any fracture and RWC only experienced fracture of a single longitudinal bar in the web. While any fracture is significant, the fracture experienced by RWC is insignificant when compared to that of RWS.

RWS experienced fracture of all bars in the No.5&6 boundary element during the loading event to 2.5% top drift with the No.5&6 boundary element in tension. The fracture

happened following the largest observed local buckling of longitudinal bars at the wall/foundation interface. The extreme strain demands on the longitudinal bars from a local buckling mechanism left the No.5&6 boundary element with little capacity for load reversal. Consequently, RWS could not even achieve the previously attained drift level with the No.5&6 boundary element in tension before fractures occurred. Refer to figure 13.4 for the load v. deformation response of RWS during bar fracture. Refer to appendix P for photographs of the fractured longitudinal reinforcement.

13.7: Summary of Results

Instability of the No.5&6 boundary element was observed for each test specimen. Out of plane deformations increased as the tensile axial strain and crack widths were increased from the previous loading cycle where the buckled boundary element was previously in tension. This was verified from the many return loading ramps where the compressive force applied to the No.5&6 boundary element was decreased, while out of plane deformations increased. This is consistent with the assumptions about wall instability in [R.13.1].

The importance of crack width is highlighted with the different buckled shapes of the three test specimens. RWN and RWC experienced more ‘global’ buckled shapes that are typically expected. RWS experienced more of a ‘local’ buckling mechanism of the longitudinal reinforcement at the wall/foundation interface. This is thought to be the product of the very large interface crack that developed during the test from increased effects of strain penetration and lapped splice bond slip. Local buckling of the No.5&6 boundary element was also observed by the unstable response of the return ramps of 1% top drift when the No.9 boundary element in tension. RWS could not sustain the same load resistance when returning to the same top drift. RWN and RWC were able to achieve a stable response during this same load history. Lapped splices in the base of the wall contribute to the possibility of instability of the wall by means of localized longitudinal bar buckling.

Methods of predicting the critical width were also explored. The prediction of the width at which buckling would not occur was underestimated. The critical buckling width was however, consistent when comparing the calculation of critical width with test data. This seems to suggest that the equation used to calculate the critical width is indeed correct. However, the behavior of these specimens is different from the expected behavior of similar walls in the field from the additional lateral constraint from floor diaphragms. It is thought that this prediction would have been adequate had the test specimens been laterally braced at multiple points along the wall height.

The localized demand from buckling in RWS contributed to the fracture of the longitudinal reinforcement of the No.5&6 boundary element when the load was reversed. Fracture of the No.5&6 longitudinal reinforcement did not occur for RWN or RWC, even at displacements twice as large as that when RWS experienced fracture. Lapped splices in the region of plastic hinging increase the chances of lateral instability and fracture of longitudinal reinforcement.



Figure 13.1a: Buckled shape of the No.5&6 boundary element of RWN following a drift of 2.5% of the No5&6 boundary element in tension. No.9 boundary element in tension with a top drift of 2%.

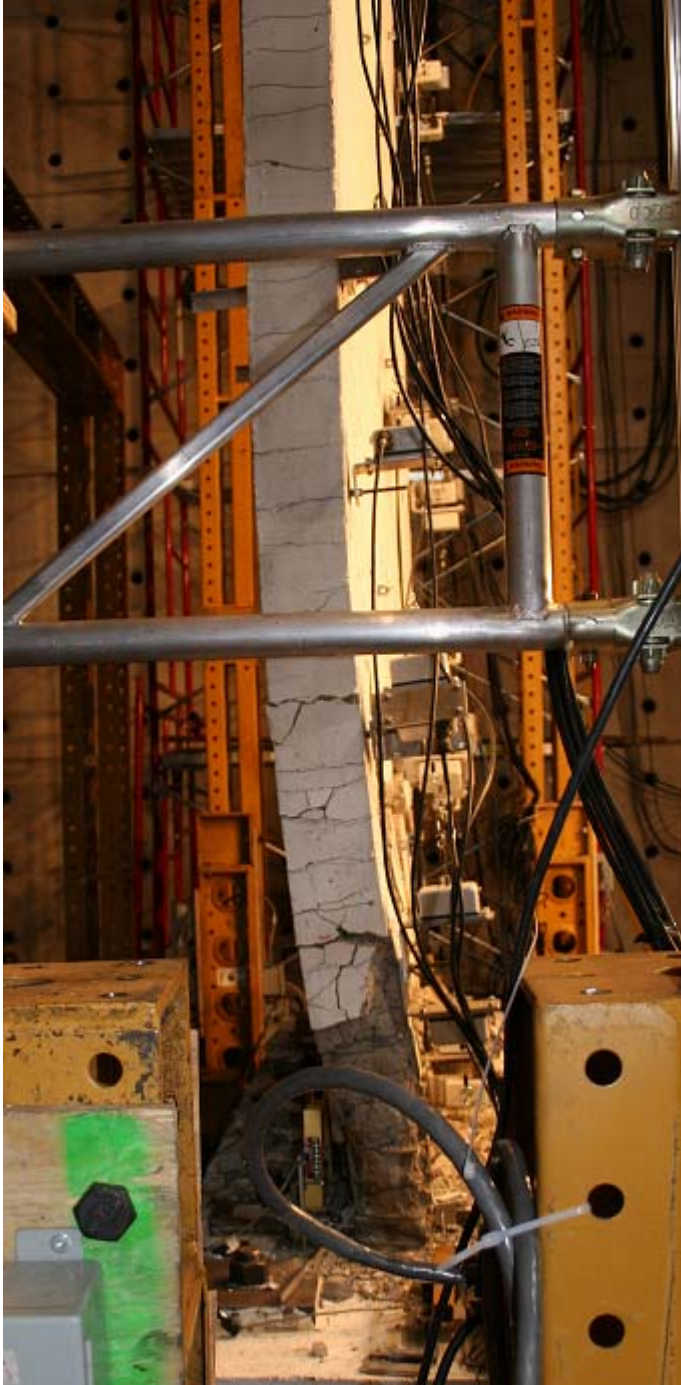


Figure 13.1b: Larger view of the buckled shape of the No.5&6 boundary element of RWN following a drift of 2.5% of the No5&6 boundary element in tension. No.9 boundary element in tension with a top drift of 2%.



Figure 13.1c: Buckled shape of the No.5&6 boundary element of RWC following a drift of 2.5% of the No5&6 boundary element in tension. No.9 boundary element in tension with a top drift of 2%.



Figure 13.1d: Larger view of the buckled shape of the No.5&6 boundary element of RWN following a drift of 2.5% of the No5&6 boundary element in tension. No.9 boundary element in tension with a top drift of 2%.



Figure 13.1e: Bucking of the longitudinal reinforcement of RWS in the No.5&6 boundary element following 2% drift of the No.5&6 in tension, 9th return to 1% of the No.9 boundary element in tension.



Figure 13.1f: Bucking of the longitudinal reinforcement of RWS in the No.5&6 boundary element following 2% drift of the No.5&6 in tension, 9th return to 1% of the No.9 boundary element in tension.



Figure 13.1g: Larger view of buckling of RWS in the No.5&6 boundary element following 2% drift of the No.5&6 in tension, 9th return to 1% of the No.9 boundary element in tension. No apparent global out of plan rotations.

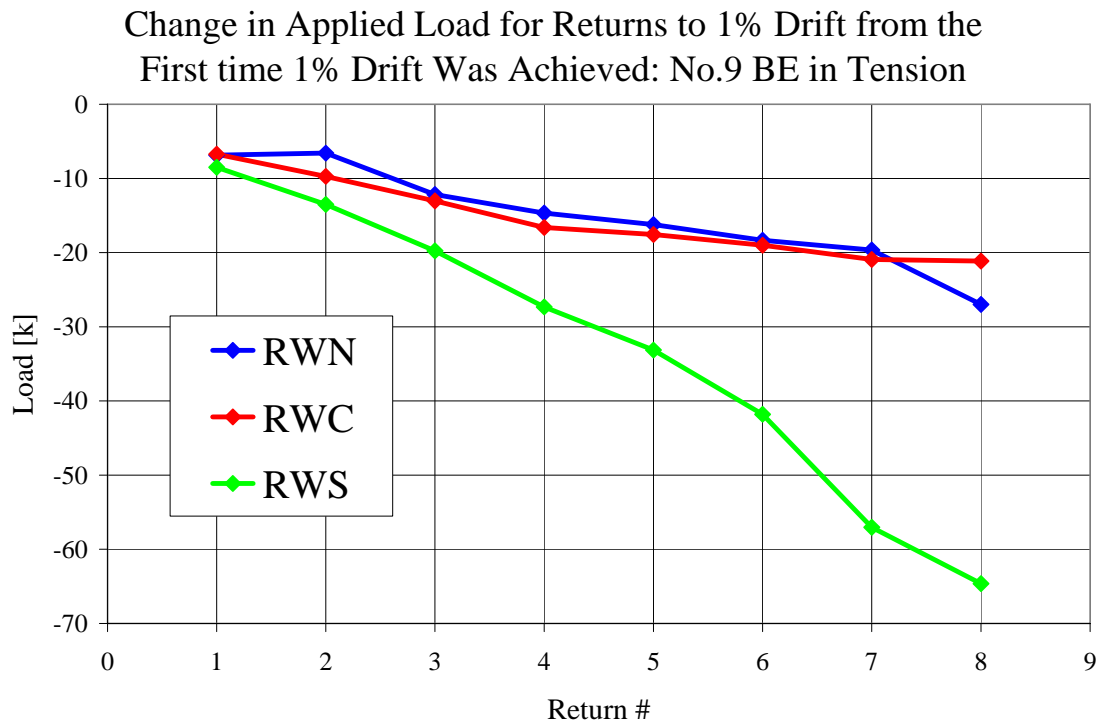


Figure 13.2: Change in applied load for returns to 1% drift from the first time 1% drift was achieved: No.9 boundary element is in tension. Note that the sign convention is not consistent with other figures, a negative change denotes a decrease in applied load.

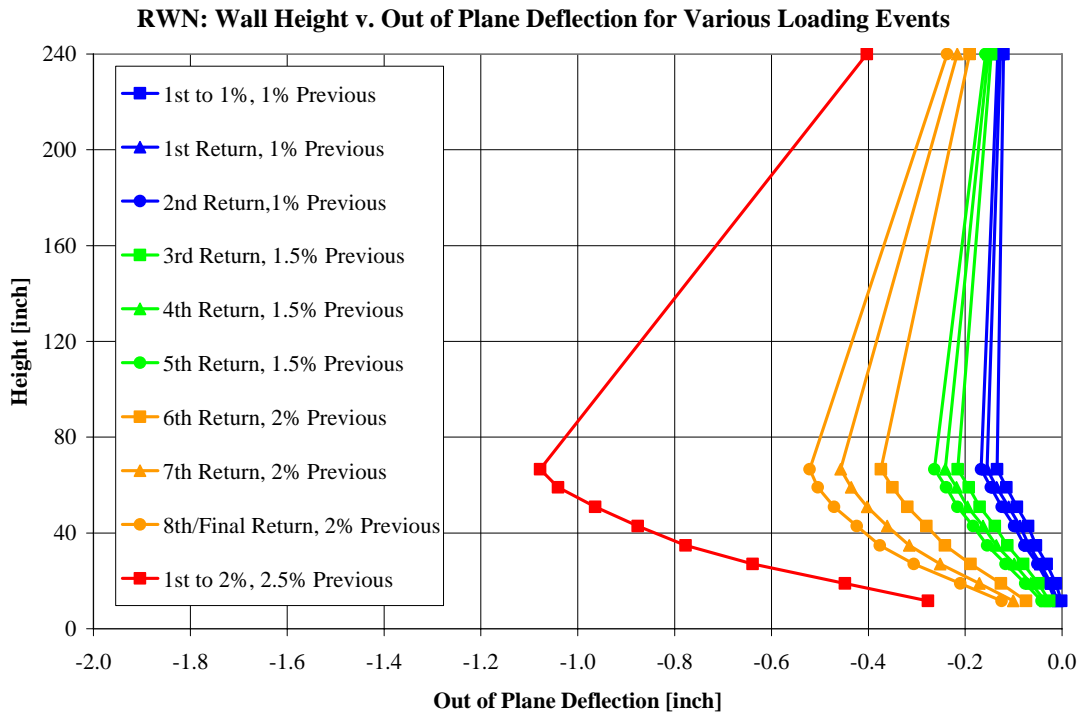


Figure 13.3a: Out of plane deflections of RWN, Legend refers to [No.9 BE in tension drift, previous drift level when the No.5&6 BE was in tension]

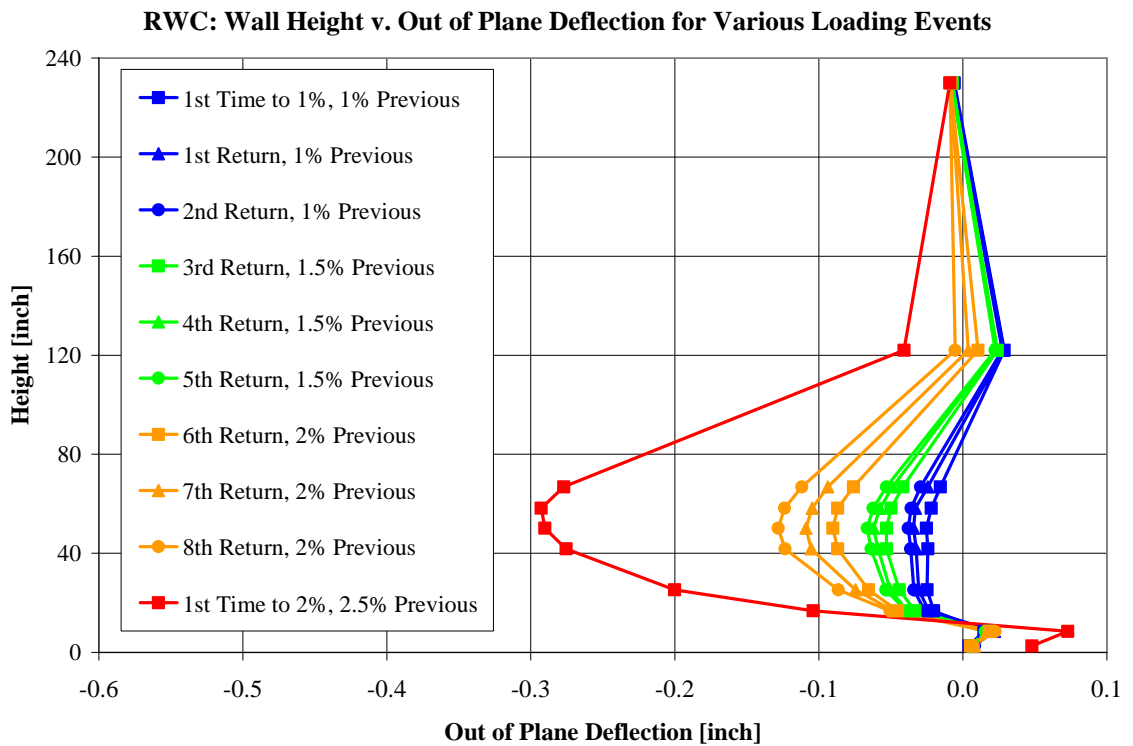


Figure 13.3b: Out of plane deflections of RWC, same legend scheme

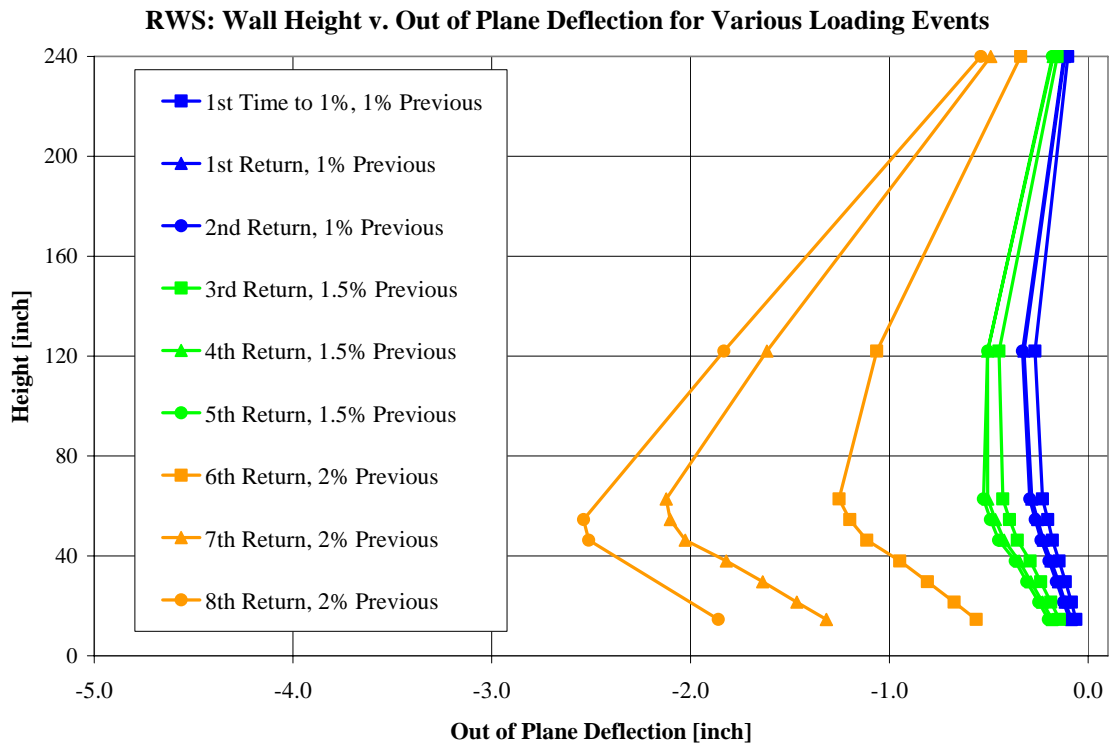


Figure 13.3c: Out of plane deflections of RWS, same legend scheme. 2% drift for the No.9 boundary element in tension following 2.5% drift in the No.5&6 in tension direction is not shown due to the fracture of the longitudinal reinforcement of the No.5&6 boundary element at 2.5% drift.

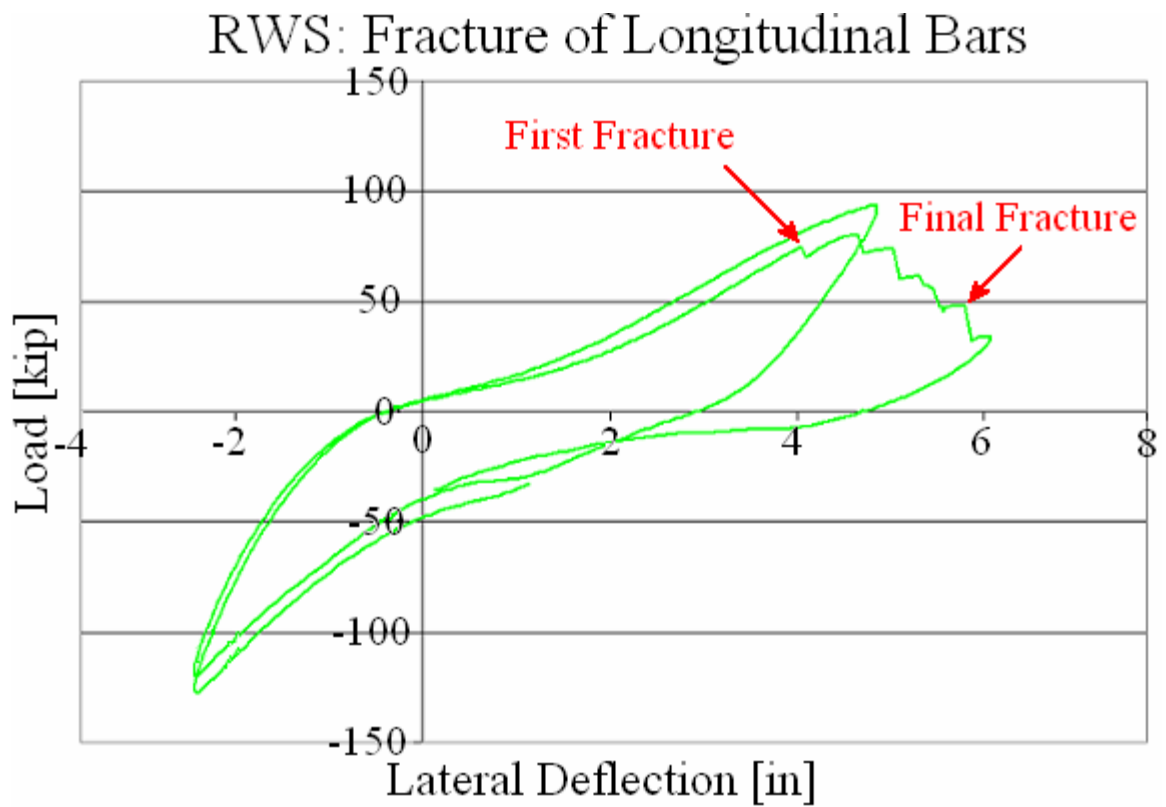


Figure U.5: Load drop during the fracture of the No.5&6 longitudinal bars

[R.U.1] Paulay, T. and Priestley, M.J.N., 1993 “Stability of Ductile Structural Walls,”
ACI Structural Journal, V.90, No.4, July-August, pp. 385-392

Chapter 14: Conclusions & Recommendations

14.1: Summary of Presented Material

This report documents the results of experimental tests performed on structural walls. The first objective of these tests was to determine the individual components of lateral deformation, which are responsible for the total lateral displacement of the structural wall. Secondly, relationships were developed between the lateral deflection components and the damaged state of the wall. Lastly, the impact of anchorage detailing on wall behavior was determined. The anchorage detailing considered for these experiments was mechanically spliced longitudinal reinforcement at the wall/foundation interface, and lapped spliced longitudinal reinforcement at the base of the wall/plastic hinge region.

These research goals were achieved with three test specimens. Specimens were approximately 1/2 scale and had an aspect ratio of 2.67. Test structures were cantilevered, un-perforated, and had a rectangular cross section with specially confined boundary elements. Boundary elements had non-symmetric reinforcement details to help determine how these anchorage details would perform in wall having a ‘T-shaped’ cross section. Each wall was loaded with a single lateral load, distributed across the length of the wall at the top of the structure. Loading protocol for these tests was reversed cyclic lateral loading of target displacements of increasing amplitude. Target displacements were chosen to collect data at various damage levels of the test structure.

Instrumentation was attached to the test structure to measure displacements and strains. The data from these sensors was used to compute the components of lateral deformation. The results of the lateral deflection component calculations were verified in multiple ways. Each calculation made to determine the deflection components was first verified by comparing the results from different sensors. Agreement of results obtained by separate instruments suggests that the calculated parameters in question are indeed the ‘true’ response of the test structure. The second verification technique used was to change the

analysis method used to calculate deflection components or filter the data. Small variations between completely separate analysis techniques suggest that the true structural response is within reason to the calculated parameters. Lastly, the calculated results were compared to theoretical predictions. Results that were consistent with all three verification tools are deemed most trustworthy when drawing conclusions about structural response and the effects of anchorage detailing.

Deflection components were related to lateral drift levels and the damaged state of the test structure. This was done to help develop guiding information for performance based designs. The reported correlations for performance based design information were created from the test data for RWN and RWC. RWN was chosen for the lack of additional influence from longitudinal bar anchorage detailing. RWC was also chosen to develop the reported performance based design information due to the negligible observed difference in wall performance when compared to RWN. The test data suggests that mechanically spliced couplers in the base of shear walls do not have a significant impact on the behavior of the structure. RWC is then treated as an additional specimen with continuous reinforcement for the performance based design information in order to increase the sample set of information.

Lastly, lapped splices in the base of the wall were observed to have a significant impact on the behavior of the test specimen. Lapped splices affected all components of lateral deformation. The flexural component of lateral deformation was directly changed by the lapped splices. Other components were affected indirectly by the change in the structural response. The components of shear and strain penetration were increased to compensate for the decreased flexural deformation.

The results of these experimental tests are used to draw the final conclusions about lateral deflection components and anchorage detailing effects in the following sections of this chapter. These conclusions are used in conjunction with existing literature to make

recommendations about the future use of longitudinal splices in the region of potential plastic hinging of reinforced concrete structural walls.

14.2.0: Lateral Deformation Components

Lateral deformation components were computed for the three test specimens. The three deflections components that account for effectively all of the lateral deformation are flexural deformation from in plane rotations, shear distortion over the wall height, and strain penetration from elongation of vertical reinforcement in the foundation and consequent bond slip at the wall/foundation interface. These deflection components were computed with all sensors that could capture the behavior in question. Other sensors were also used to verify the computed results. This section chronicles the methods used to solve the components of deflection, the verification of the results, and the summarized findings. This section focuses on RWN and RWC, with the No.5&6 boundary element in tension, as the reinforcement scheme was more reasonable than the No.9 boundary element and the results were much more consistent to make accurate judgments about wall behavior. Negligible differences were observed in the behavior of these specimens. RWC behaves very closely to a continuous bar wall and is treated as such when developing the performance based design information presented in this chapter, in order to widen the sample set. The behavior of RWS was significantly different from the other two specimens. For this reason, the deflection components of RWS are discussed in a separate section that aims to show how lapped splices in the critical section affect the behavior of structural walls.

14.2.1: Flexural Deformation

Flexural deformation is documented fully in appendix 3, and chapter 9. Flexural deformation was computed with three instruments, the Krypton, string potentiometers, and strain gages attached to the longitudinal reinforcement. Lateral deformation from

flexural was first computed by calculating axial strains from the test data of the three instruments. This was done for location across the wall length, at various wall heights.

Next, a best fit line was applied to the axial strain across the wall length at each height to compute curvature (average slope of the axial strain along the wall length). Some patterns arose when viewing the axial strain data. The strain gradient (curvature) seemed to be larger for the portion of the wall in compression, or simply through the half of the wall on the compression side. For this reason, two analysis techniques were used to determine curvature and give an envelope of possible flexural deformations. These two analysis techniques were entitled the 'whole cross section' and 'compression half cross section' method. These methods refer to the section of wall length used to calculate curvature. This was performed for each of the three sensors. A small number of sensors at select wall heights made this computation impossible. This is reflected in the small variation of the two methods when considering the string pot results.

Lastly, the total cumulative rotation was calculated and the center of rotation was solved. This again required various analysis techniques. Two numerical integration techniques were used for Krypton and strain gage data. The center of rotation, or centroid of the curvature distribution over wall height could be then be calculated by simple weighted averages of basic geometric shapes created from the curvature distribution. This could not be done with the string pot data. These sensors recorded the total rotation over a specific height segment directly. The center of rotation from these segments could not be calculated and had to be assumed. This was done with an elastic analysis and geometric relation of curvature and height. Errors from the ideal prediction and using the string pot methods lead to an underestimation of flexural deformation of less than 0.5%, well within tolerances for inherent noise in typical test data.

Flexural deformation could then be calculated as the product of the total rotation at the height in question and the distance from that height to the location of the center of rotation. Good agreement was found when comparing the results of the Krypton and

string pot, using the entire cross section length for curvature calculation. These results are further supported when comparing the string pot results at the top of the wall to BIAX predicted values. Test data values and BIAX predictions were quite close, even well into the inelastic range. It is for these reasons that the flexural deformation results from data using the entire length of the wall is considered most trustworthy and is used when developing the performance based design information.

The results of the flexural deformation calculations are consistent with previous experimental research, literature, and theory. Flexural deformation increases exponentially over wall height in the elastic range, due to the cumulative effect of the deformed rotations. In addition, the base is fully constrained from rotation, neglecting strain penetration from the consideration of rotation. These conditions make flexural rotation an ever increasing contributor of total deformation when considering higher locations of the wall. Flexural deformation is observed to be a large contributor of total deformation at 25% of wall height, approximately half of the total lateral deformation. Flexural deformation is responsible for the majority of total deformation at the top of the wall, typically 70 to 80% of the total lateral deformation.

The contribution of flexural to the total deformation was observed to change with the various damage levels and conditions of the test structures. Initially, the flexural contribution of the 'undamaged state' is much higher than the elastic limit. This is thought to be the result of additional shear cracking and some wearing of existing cracks. The new cracking decreases the shear modulus of the wall when switching from the material properties of the concrete in shear to mechanisms of transverse steel carrying load and aggregate interlock. In addition, existing cracks have experienced some wearing, reducing the effectiveness of the aggregate interlock mechanism. These decreased shear stiffness make the shear component of deformation larger. This is the reason for the decrease in the contribution of flexure, and not a change in flexural properties. Secondly, the flexural deformation increases following yielding. The flexural properties have now changed, as flexural stiffness is greatly reduced from yielding of longitudinal

reinforcement. Decreased rotational stiffness causes the contribution of flexural to then increase. These observations were very consistent for all specimens, with varying magnitude for RWS.

14.2.2: Strain Penetration

Strain penetration is documented in chapter 10. Strain penetration, or bond slip is a mechanism that causes lateral deformation from rotation at the bottom of the wall, the wall/foundation interface. Rotation is caused from axial strain in the longitudinal reinforcement that penetrates into the foundation. This penetration is the result from the concrete bond mechanism's inability to transfer all force out of the reinforcement at the bottom of the wall. Concrete requires a certain length of the reinforcement to transfer load in and out of the bars, the development length of the bar. The strain present in the bars for a certain length will cause an elongation. The rotation at the bottom of the wall is the result of the total elongations of all bars at the bottom of the wall. Lateral deformation from this mechanism is modeled as a rigid body rotation.

Total elongation of anchored reinforcement can be found by integrating the axial strain over the length of the bar, or multiplying the average axial strain in the foundation reinforcement by the length of the reinforcement which the strain is present. This method of finding the total elongation of the bars can be done using strain gages attached to the anchored reinforcement. Unfortunately, many of these instruments were damaged during construction. The low number of anchored bars instrumented and number of surviving number of strain gages makes this method a poor one for calculating rotation from strain penetration and consequent deformation. Instead, the more reliable data from the bar bond LVDTs are used to calculate strain penetration rotations.

Bar bond LVDTs are attached to the longitudinal reinforcement at the bottom of the wall. The connection was made as close to the foundation/wall interface as possible, in order to isolate the elongation of anchorage reinforcement only. This connection was typically at

0.5” above the top face of the foundation block. The second connection was the top face of the foundation block. The displacement readings of these instruments is effectively the total elongation of the anchored reinforcement from the effects of strain penetration. The rotation from stain penetration was computed as a best fit line of the axial bar displacements at the wall/foundation interface, along the length of the wall.

Lateral displacement from the effects of strain penetration was then computed. This was done with a rigid body rotation model, where the lateral deformation is the product of the rotation at the wall/foundation interface and the height in question. The lateral displacement results of the walls were verified by comparing the axial strain readings of the anchored reinforcement. This was a comparison between specimens. The verification was done in a very simple way, similar calculated lateral displacements of the walls means that similar wall/foundation rotation happened. Similar rotations suggest that similar bar displacements at the wall/foundation interface had occurred. By inspection, the axial strain readings in the anchored reinforcement of the same bar location should be very close if calculated lateral deformations are also very close. Similar trends in changes between lateral deformation and recorded strains should also be apparent. This was the case for the strain penetration calculations and the results were deemed reasonable.

The contribution of strain penetration to the total lateral deformation was found to be approximately 10% at 25% of the wall height and approximately 8% at the top of the wall, increasing as flexural demand and yielding occurred. This is was observed during the testing of the specimens, as the crack at the wall/foundation interface typically became one of the largest cracks (width and length) observed at any location of the wall. Again, similar trends were observed with RWS, but with varying magnitude of changes and contributions.

14.2.3: Shear Deformation

Shear deformation is documented fully in appendix 4, and chapter 11. Shear deformation was computed with two instruments, the Krypton and string potentiometers. In the case of shear, strain gages could only be used as a verification tool and are not included in shear deformation calculations. Strain deformation was calculated through completely unrelated methods for each instrument, due to the nature in which the instruments measured displacements. Shear deformation was again computed for various heights of the wall and verified through the usual techniques.

The different nature of the Krypton and string pot instruments required very different analysis techniques to estimate the shear component of deformation. The string pot instrument measures the relative displacement of certain locations of the test structure. This allows researchers to calculate incremental displacements of particular wall height segments. These incremental segments only displace from the modes present in the wall height segment. In this case, only shear and flexure. Strain penetration does not influence incremental displacement calculations from the 'x' configuration of string pots, due to the relative relationships of the string pots attached to the test structure. This makes the calculation of shear deformation very simple. The total incremental deformation of the wall height segment is calculated first. The previously calculated flexural deformation is then subtracted, leaving only the deformation responsible from the effects of shear.

Krypton data cannot be treated as the string pot data, due to the previously discussed global versus local effects. The LEDs of the Krypton track the global displacement, they are influenced by all modes of deformation. The previously discussed method for the string pot data could have been used, if the strain penetration displacements are also subtracted. However, this adds uncertainty to the analysis, where derived results of shear for the Krypton are contingent on LVDT measurements at the bottom of the wall. Instead, a completely independent method was used. A simple finite element method was used to calculate shear strains from the undeformed geometry of the Krypton grid and the known

global displacements. The result is then contingent on the relative displacements of the nodes selected to make the quadrilateral finite element. The shear strains are then relative, helping negate the effects from other displacement modes. Shear deformation was then calculated by averaging shear strain across the wall length at a single height and then integrating the result over the height of the LED field.

Shear deformation was first verified by comparing calculated shear strains from the Krypton and string pots to the strain readings on the shear reinforcement. Next, the results of the Krypton and string pots were compared. Good agreement exists for the walls, with much more consistency when the No.5&6 boundary element is in tension. The reasons for this are discussed in great detail in chapter T. Large splitting cracks were found to have a large influence on the lateral deformation results. This is the reason for worse results when the No.9 boundary element is in tension. The lateral displacements for this direction were much smaller than those when the No.5&6 boundary element were in tension. In addition, the effects of splitting cracks were again much larger when the No.9 boundary element was in tension from the much larger load required to achieve the same top displacement as the No.5&6 boundary element in tension. These combined factors make the results of shear much less consistent than the results for flexure. The final verification tool used to qualify the results was predictions of shear deformation. The methods used did not accurately predict the shear deformation of the wall. Predictions were within reason in the elastic region, but became poor following inelastic increases in shear deformation from inelastic coupling of the flexure and shear mechanisms.

Shear deformation follows expectations of contribution to total deformation over the wall height and at various damage levels. Total shear deformation increases over wall height, but is most influential at the base of the wall where flexural deformation is still small from the boundary condition. Shear typically accounted for 40% of the total deformation at 25% of the wall height and 12% at the top of the wall. Shear deformation was also observed to be larger at the base from the effects of shear cracking. This cracking

decreases the shear stiffness of the wall, allowing more shear deformation to occur in the base. The contribution of shear deformation increases from the ‘undamaged’ state to the elastic limit from the increasing amount of shear cracks and continuously decreasing shear stiffness. Increased cracking and wearing of existing cracks eventually lead to shear sliding in the plastic hinge region of the structure. This can be seen in the highly inelastic range of the wall, where the contribution of shear increases, even in the presence of a full plastic hinge from flexural deformation.

Lastly, a simplified method was proposed to help predict inelastic shear deformations from inelastic coupling and damage. The ratios of contribution of shear and flexure was observed to remain relatively constant following yielding of the longitudinal reinforcement. This ratio at the elastic range can be used to make a conservative estimate of inelastic shear deformations if the flexure-shear ratio is predicted well. Predictions of inelastic shear deformations are not the intent of this document. This point was only made to show a possibly worthwhile study on inelastic coupling of shear deformations.

14.3: Performance Based Design Information

The information contained in this section relates the components of deformation to drift levels and the damaged state of the test structures. This is done in order to give guidance to designers using similar dimensions and aspect ratios of structural walls in the field. It should be noted that performance of any structural member is completely dependent on the specific material properties, geometry, reinforcement details, and loading history of the member in question. However, similar structures to these test specimens can be assumed to perform in a similar fashion and the results of these test can be used as comparison for predicting the stiffness of the structure being designed.

The first step in determining the performance based design information was to verify that all deflection components had been accounted for. This was done by summing all measured/calculated deflections that occurred at loading ramp maximums, including

compliance in the test setup. Total deflection was taken as the sum of the deflections resulting from flexure, strain penetration, shear, foundation block slide, wall slide at the foundation/wall interface, in plane foundation block rotation, residual base rotation from flexure underestimation, and corrections to shear deformation to represent the displacement of the tension boundary element. Results of this summation were plotted against the total measured deformation of the tension boundary element, as measured by the global string pots attached to the external reference frame.

Comparison of the calculated total deformation and measured total deformation was made by means a best fit line through a plot of calculated v. measured total deformation. Data points included were the loading ramp maximums. The results of this comparison revealed a wide range of correlation coefficients (slope of the best fit line of calculated v. measured.) Correlation coefficients were typically within 10% of perfect correlation. The largest discrepancies were usually observed when the No.9 boundary element was in tension. This is thought to be caused from the large splitting cracks observed when the No.9 boundary element was in tension. For this reason, the performance based design information focuses on the No.5&6 boundary element. In this case, the variation did not seem to be consistently off for a single sensor, height location, or the specimen in question. This suggests that the variation is random noise and errors that are to be expected from experimental tests. Deflection components were then assumed to have accounted for all deflection modes and the performance based design information is related to damage and reported.

Deflection components are reported as a range of percentages for the various damage levels. These ranges were computed by first calculating the mean contribution of the component in question from all applicable sensors. As an example, the results at 25% height include the Krypton and string pot data calculated contributions for both RWN and RWC. Next, the standard deviation was calculated. The range of values was given as the mean, plus or minus one half standard deviation. The performance based design information from chapter 12 is given again in figure 14.1. Again, the changes in each

deflection component with additional damage to the wall that are discussed in previous sections can be seen in the changing ranges of possible component contributions.

The damaged state reported for each row of information refers to the damage from flexure, as it is the most influential component of deformation. Additional information on the amount of cracking, widths, and crack distributions are reported at the same drift levels in chapter T. The damage reports for these drift levels were taken from photographs, cracking patterns, and reported measured crack data during the load pauses.

14.4: Lapped Splice Effects on Deflection Components

The previous sections discuss the deflection component results for RWN and RWC. These sections also contained the manner in which the deflection components were calculated. The same methods were used for RWS and are not reproduced for this section of the chapter. Instead, this chapter reviews the reasons for the observed behavior variations between the lapped splice wall and the other two specimens.

Differences in wall behavior were noticeable during the test of RWS. It was clear that the wall was more stiff than the other two specimens, requiring larger loads to achieve the same target displacements at the top of the wall. Additional required load was typically between 1 and 6% of the load required for RWN and RWC. The top of the walls were displaced to the same drift level for the loading ramp maximums, however, this does not mean that the displacement profile along the wall height was the same for each wall. RWS was also observed to have a reduced total lateral deformation along the wall height until the top of the wall. This reduction is illustrated well by comparing the total displacements at 25% of the total wall height, where the lapped splices have just terminated. The reduction was typically 40% of the total lateral deformation of the other two specimens in the elastic range and 20% following yielding of longitudinal reinforcement in the inelastic range. The reasons for these differences are highlighted when the individual deflection components are studied.

The reason for the difference in wall behavior for RWS is the increased axial stiffness of the wall in the height section of the wall where lapped splices are present. Splices increase the cross sectional area of steel present in the length of the splice. In the case of lapped splices of the same bar diameter, the cross sectional area is doubled. The stiffness of this section is effectively doubled for axial tension/compression through the length of the splice. This increased stiffness of a localized area can still have a large impact on the total stiffness of the member.

Flexural deformation is dictated by cross sectional properties of the structure, which accumulate over wall height. Deflection from flexure comes from rotation, the elongation of one side of the structure and shortening of the opposite side of the structure. These deformations are axial deformations that can be influenced heavily from the aforementioned effects of using lapped splices. Flexural deformation is decreased for RWS in the elastic range from the increase in axial stiffness from the lapped splice effect. This reduction was typically 40% at 25% of the total wall height and 15% at the top of the wall. The change in axial stiffness explains the difference in flexural deformation when the wall is elastic, but requires additional consideration when the wall undergoes plastic deformations at the base of the wall.

Drift ductility of structural walls is achieved through the development of a plastic hinge at the base of the wall. This plastic hinge is a mechanism of large rotation at the base from the reduced flexural stiffness following yielding of the longitudinal reinforcement. It is known that lapped splice can terminate such plastic hinges. This is observed for the test of RWS. The increased axial stiffness through the lapped splices prevents yielding of longitudinal reinforcement. Prevention of yielding is a termination of plastic rotation. The wall rotates plastically above and below the splices, but reduced to elastic bending in the splice length. Inability to form a full plastic hinge prevents RWS from deforming as much in flexure as the other walls in the inelastic range. However, RWS was displaced to the same top drift as the other wall. The total deformation had to be made up through other sections of the wall and by other mechanisms. Additional flexural demand was placed on

the longitudinal reinforcement adjacent to the lapped splice terminations. This increased demand is the cause for other differences in wall behavior.

Increased flexural demand outside the lapped splices occurs at the bottom of the wall and at the end of the necessary splice development in the wall section. The increased demand at the bottom of the wall is responsible for larger axial strains in the longitudinal reinforcement. Larger axial strains in the longitudinal reinforcement continue to be more prevalent well into the anchored portion of the reinforcement, as the concrete bonds can only transfer a certain amount of force out of the bar per anchored length. Therefore, the increased flexural demand during inelastic behavior creates larger axial strains in anchored reinforcement, causing more elongation and shortening of anchored bars. Axial bar displacements at the bottom of the wall are amplified, creating additional lateral deformation from the effects of strain penetration when compared to walls without lapped splices in the base of the wall. The increased contribution of strain penetration to total deformation for RWS in the inelastic range when compared to the other two specimens was typically 15%.

Shear deformation was affected indirectly by the presence of lapped splices in the base of the test structure. Again, the same target displacements were achieved at the top of the wall. These displacements were achieved by means of larger applied loads. The larger applied top load creates larger internal shear forces that must be resisted. This fact alone would lead to expectations of larger shear forces. It was observed though, that increased loading lead to more cracking and decreases in shear stiffness. For this reason, load and shear deformation do not have a linear relationship. Applied load was usually 1 to 6% larger for RWS, and top displacement resulting from shear was typically 5 to 8% larger than RWN and RWC. This was confirmed with the observed cracking patterns of RWS at the base of the structure. Shear deformation is clearly affected by lapped splices. The effects of lapped splices are however, indirect when considering the influence lapped splices had on flexural deformation.

14.5: Wall Instability

Each test specimen underwent some type of buckling of the No.5&6 boundary element during the experimental tests. The buckled shape and out of plane buckling that occurred varied for the specimens. RWN and RWC experienced a typical global buckling mechanism with apparent out of plane rotations. RWS buckled in much more of a localized way, where the wall shifted laterally at the bottom of the wall. The concept that out of plane deformations of ductile structural walls being dependant on flexural crack widths and previous tensile axial strains proposed in previous literature has been confirmed. This concept also explains the reasons for the difference in the buckled shaped of the specimens. These reasons are again due to increased flexural demands on the structure at the base of the wall from lapped splices terminating plastic hinges, as well as bond failure from cyclic testing.

Paulay and Priestley's work on wall instability was used to help determine the causes of the wall stability. In short, instability in ductile systems can arise from the cracking widths that develop in the boundary element of potential buckling from the previous loading event where it was in tension. Refer to chapter 13 for this reasoning. This hypothesis was confirmed by the loading history of the walls, where the No.9 boundary element was continually loaded to the same drift level, while the No.5&6 boundary element was loaded to increasingly larger drift levels. The compressive load the No.5&6 boundary element was required to resist decreased for each return ramp to the No.9 boundary element in tension from stiffness degradation. However, the out of plane deformations increased for the return ramps. This is especially true when the previous drift level of the No.5&6 boundary element was increased, increasing the crack width and previous axial tension strain in the boundary element. Out of plane deformations are clearly a function of previous crack widths that must close to resist compression through the concrete. This explains the variation in the buckled shape of RWS.

RWN and RWC experienced a wide variety in crack widths over the height of the wall experiencing instability. However, all cracks were well an order of magnitude in width from each other. This was not the case for RWS, which had a single crack that was overwhelmingly larger than any other crack in the specimen. This crack occurred at the wall foundation interface. Again, this crack is caused by increased demands at the bottom of the wall in the inelastic range from lapped splices in the base of the wall. Slip was also observed between the lapped splices during the experimental tests.

Lapped splice bond slip, along with the increased demand on strain penetration lead to an interface crack that had a width of approximately one inch. Such a large crack creates a great amount of out of plane deformation to occur at a single location. This is a localized buckling event. The single large crack for RWS created a localized bucking event, where as RWN and RWC had much more uniform crack widths along the wall height. The consequence of such a localized demand in RWS was the eventual fracture of longitudinal bars in the No.5&6 boundary element upon load reversal.

14.6: Conclusions

Lapped splices in the base of a structural wall will decrease the flexural deformation of the wall in two ways. Increased axial stiffness increases flexural stiffness. More importantly, lapped splices terminate plastic hinges and prevent the structure from dissipating as much energy as possible in this ductile mode. Inability to deform uniformly in flexure through the base increases demand on longitudinal reinforcement outside the splice terminations. This increase demand could lead to fracture of longitudinal reinforcement at displacements smaller than expected. Premature fracture is a possibility, but increased deformation from strain penetration is certain. Penetrating strains are increased, causing the structure to deform more in this mode. Additional strain in the foundation also places more demand on the bar anchorage. This must be taken into consideration when detailing reinforcement with possible pull out failure. Shear deformation is indirectly increased from the structures inability to deform through flexure;

more demand is placed on a potentially more brittle failure mechanism. This should be considered when detailing shear reinforcement.

Finally, the increased rotational demand at the bottom of the wall and possible lapped splice slip may lead a structural wall to develop the large interface cracks observed during this experimental test. Such a crack can lead to large out of plane deformations over a short distance, a local buckling event. Local buckling places far more strain demand on longitudinal reinforcement than a global buckling from the drastically changing curvature. This buckling event can be extremely dangerous, as load reversal is very likely during a seismic event. Load reversals following a local buckling event can cause low cycle fatigue fracture of reinforcement far before a simple push over calculation would predict. Special attention to this problem is necessary when detailing structural walls.

Splicing longitudinal reinforcement is a necessary part of practical concrete structures. The way in which splices are placed and detailed can have a tremendous effect on the behavior and performance of the structural element. These effects can be adverse and may not be acceptable for elements of particular importance and vulnerability, such as structural walls. These elements are responsible resisting the forces generated during high winds and earthquakes. Structural walls are charged with preventing damage to buildings and keeping their occupants safe. Understanding of structural wall behavior is absolutely critical to the preservation of concrete structures and life safety. The ability to predict deformations is a large part of properly designing such an element. More importantly, detailing of reinforcement in effort to make construction of walls easier should in no way hinder the elements ability to resist loads, undergo plastic deformations, or fail in a ductile mode. Failure to do so may lead to a brittle failure and unacceptable performance by any measure. It is in the interest of ductile ultimate failures that lapped splices should not be used within the region of potential plastic hinging.

14.7: Recommendations

These tests have revealed important aspects about splicing longitudinal reinforcement in the region of potential plastic hinging. First, mechanical splices that can develop the ultimate strength of the reinforcement they are splicing do not have a significant effect on the behavior of the structure. Provisions that allow splicing in the plastic hinge region in ACI Committee 318 for type 2 mechanical splices are indeed good for design. No further experimental tests are recommended to show that wall behavior is not affected by mechanically spliced couplers in the base of the wall. However, tests should be performed on any type of mechanical splice planned for use in actual field structures. Such tests should reflect the loading expected in the design of the structure (cyclic tests if built for seismic areas), as recommended by Paulay and Priestley.

Secondly, new provisions are needed in ACI Committee 318 to limit the use of lapped splices in structural walls. It is suggested that no lapped splices be used in the region of potential plastic hinging, or height of plasticization to be conservative. This can be determined quite simply by calculating the nominal yield strength of the cross section and determining the height at which this moment occurs from statics, at the ultimate load condition. This is most likely a very conservative height limit for the start of splicing. However, conservative measures should be taken without more tests to confirm the impact of splices at various heights. It is the recommendation of this report that more tests be performed with walls containing lapped splices in the base of the wall.

Future tests on walls containing lapped splices should use test multiple specimens that start the splices at various heights in the base of the wall. Specimens may include another wall with splices starting at the wall/foundation interface to verify the results of this document, another wall which starts splicing at $1/3$ the height of yielding, and $2/3$ the height of yielding. These test would allow designers to be able to splice longitudinal reinforcement as low as possible and have confidence that the design detail does not negatively impact wall behavior.

Additional variables for consideration would be the aspect ratio of the wall. Increasing the aspect ratio would require more longitudinal reinforcement from the decreased moment arm to support the same magnitude of loads. This would likely be achieved through larger bars, increasing the necessary splice length. Such a change would increase the effects of the lapped splices discussed in this chapter, as well as increasing the deflection modes affected by the lapped splices.

Lastly, it may be of great worth to determine if increasing the required splice length could mitigate the observed lapped splice slip that occurred during this test. Such slip greatly increases crack widths and potential instability. Instrumentation should be placed on the structure to monitor the degree of slip. The same bar bond attachment techniques could be used to achieve this goal.

25% of Total Height		Deflection Contribution		
Damage Level	Drift Level	Flexure	Shear	Strain Penetration
Undamaged	0.10%	49-58%	36-39%	4-8%
Elastic Limit	0.30%	44-50%	42-43%	10-13%
Some Plasticization	1.00%	50-58%	34-37%	13-14%
Full Plasticization	1.50%	45-52%	40-47%	9-10%

Top of Wall		Deflection Contribution		
Damage Level	Drift Level	Flexure	Shear	Strain Penetration
Undamaged	0.10%	71-76%	7-8%	2-6%
Elastic Limit	0.30%	67-69%	12-13%	6-7%
Some Plasticization	1.00%	74-78%	12-13%	9-10%
Full Plasticization	1.50%	75-80%	14-16%	8-9%

Figure 14.1: Performance Based Design Information

Appendix 1: Calculation of Axial Strain

A1.0: Introduction

The purpose of this appendix is to show the methods used to calculate axial strains. The assumptions used effect the final strain values in different ways. The effects of the methods used and justifications for the final methods chosen are described in the following text.

A1.1: Assumptions

The major assumption used in all methods is that the axial strain gradient along the wall height is linear for each location along the wall length. This was based on a BIAX analysis of a cracked section with known material properties and a linear elastic finite element analysis. This assumption is quite good for all elastic loads. However, this assumption breaks down when a plastic response occurs at the base of the wall section. A large degree of non-linearity in the strain gradient is predicted at the height sections where first yielding occurs. The maximum span of heights over which a sensor is used to calculate strain must be limited to about 10” to preserve this assumption. It is also seen that a linear gradient is expected at heights above 54” at the maximum observed test loads. This allows string pots above the plastic region to use the linear assumption throughout the entire test without consequence. The plots of axial strain versus height calculated with BIAX can be seen in figures A1.1a, b, and c.

The second assumption used is directly related to the previous assumption. The height location at which the average curvature occurs is assumed to be the average height of the sensors used to calculate strain. This assumption is true for a linear axial strain gradient. The average height of the sensors used refers to the points at which string potentiometers are attached to the test structure, as well as height coordinates of Krypton LEDs. Again,

this assumption is not entirely accurate when yielding is occurring in the height section used for the calculation of strains.

A1.2.1: Longitudinal Strain Gages

Longitudinal strain gages were used at select locations on vertical reinforcement. Strain gages were placed in groups corresponding to various heights over the first 108" of the wall height. Few strain gages were present in the web section of the wall. This poor resolution of data points along the wall length creates problems in determining the linearity of strain distributions. In the absence of a direct strain reading at bar locations, a linear interpolation was employed from adjacent strain gages. This assumption leads to the appearance of a linear strain distribution along the wall length, which may not necessarily be the case.

A1.2.2: LVDTs

LVDTs were attached to the test structure at heights of 6 and 12 inches. These sensors were distributed along the wall length with greater resolution toward the No.5&6 BE. The LVDT displacement readings were divided by the height of their attachment to compute the average strain over the attachment height. This assumes that the base of the LVDT remains fixed to the wall foundation. The resulting strain reading was assigned the average height of the attachment height for the purposes of plotting and resulting computations (Z coordinate of average strain). Refer to equations A1.1 and A1.2 for the symbolic representation of this calculation. The axial strains calculated with the LVDTs may also be skewed by the effects of strain penetration of the longitudinal reinforcement into the foundation. This was typically noticed in the much larger values of strain calculated by the LVDTs when compared to other sensors.

$$\varepsilon_{\text{average}} = \frac{\Delta L}{Z_{\text{attachment height}}} \quad (\text{E.A1.1})$$

$$Z_{\varepsilon_{\text{ave}}} = \frac{Z_{\text{attachment height}}}{2} \quad (\text{E.A1.2})$$

Where ‘ ΔL ’ is the change in length recorded by the LVDT and ‘ $Z_{\text{attachment height}}$ ’ is the height coordinate which the instrument is connected to the wall. A graphic representation of the geometry used to calculate strains can be seen in figure A1.3.

A1.2.3: String/Wire Potentiometers

String/Wire Potentiometers (String Pots) were used to measure vertical displacement at the ends and midpoint length of the test structure. The same technique discussed in the previous section was used to determine the average strain and location of average strain from the string pots. The difference with the string pots and LVDTs is that the string pot displacement readings are recorded from two moving points on the test structure, where the LVDT base point is assumed to remain fixed to the base. This can lead to additional variability with strain pot measurements. The strain for String Pots is computed with the following equation:

$$\varepsilon_{\text{average}} = \frac{\Delta L}{L_{\text{undeformed}}} \quad (\text{E.A1.3})$$

$$Z_{\varepsilon_{\text{ave}}} = \frac{L_{\text{undeformed}}}{2} \quad (\text{E.A1.4})$$

$$L_{\text{undeformed}} = Z_2 - Z_1 \quad (\text{E.A1.5})$$

The variables ‘ Z_2 ’ & ‘ Z_1 ’ in these equations are the undeformed coordinates of the top and bottom string pot, respectively.

A1.2.4: Krypton LEDs

The displacement readings from the Krypton LEDs allowed for several strain calculation techniques to be used. The first of which is the technique discussed in previous sections of an average strain computed from the foundation to the height of the sensor. This calculation is given at the location of half the height used for computation for plotting. This technique was observed to give strain distributions with the least amount of variation over the wall length and height. However, this method tends to ‘smooth’ out changes in strain magnitude expected at discontinuities, such as the termination of a lap splice. This makes the ‘total average’ method undesirable for RWS.

The second technique used for the Krypton data was that used for the String Pots, where the change in length between adjacent sensors at the same wall length coordinate was used to compute strain. The difference between the String Pots and Krypton LEDs when doing this is the coordinate system each sensor is using. String pots measure displacement along the wall height axis at all times, where the Krypton LEDs measure displacement in the original undeformed Cartesian coordinate system. The additional axial strain along the wall height caused by lateral deflection is not accounted for with the Krypton. This second order effect was determined to have a negligible effect on the strain calculations. The last assumption used in these calculations is that Krypton LEDs form a perfect grid system. This is simply impossible to do. Instead, a more sophisticated computation of strains can be used to correct this problem. A large degree of variation was observed using this ‘incremental average’ technique. Oscillations of strain magnitude were noticed over the wall height. This is the result when an LED measures a much different displacement than what is expected from random data ‘noise’, a poor connection from the LED to the acquisition system, or a malfunctioning LED.

The next method for strain calculations used for the Krypton LEDs was an isoperimetric quadrilateral element which maps the non-square/rectangular elements into a square element of parametric coordinates. A depiction of the isoperimetric mapping used can be

seen in figure A1.4. The isoperimetric mapping equations and evaluation of strains were referenced from [R.A1. 1]. The equations used to determine the strains from the Krypton data are discussed in great detail in appendix 5. The change in perceived axial strain was negligible when comparing the change in vertical height only to the isoperimetric quadrilateral elements. The isoperimetric quadrilateral element was used to compute strains in a couple different ways. First, the ‘incremental average’ approach was used for adjacent LEDs. The parametric coordinates for the calculation of strain were solved to determine points of interest which coincide with other sensors. Again, an oscillation was observed with strain over the wall height. A more sophisticated averaging system was then used to cope with this problem.

The last method used for strain calculations used for the Krypton LEDs was again an isoperimetric quadrilateral element. However, the size of the element changes with location along the wall height. This was done following an investigation on the maximum variations observed during a load pause, where the wall was not moving. The maximum variations observed during a load pause, where the wall was not moving. The maximum variation in displacement readings were done for each LED, calculated as the difference from the average reading over the pause. This maximum error was then used to determine the grid size necessary to limit possible errors. The maximum deviation from the mean reading was seen to be as large as 0.001”. This would require a grid size of about 20” to limit axial strain errors to 5% of the yield strain if the top LED misread high and the bottom LED misread low. Both a 4X4 LED, 21” grid and a 3X3 LED, 14” were used to determine the effect. A 14” grid was chosen for the reduced oscillation, while remaining small enough to avoid ‘smoothing out’ changes in strain from discontinuities.

The next change for this method was the calculation of strains directly at the LED locations of the quadrilateral element instead of at heights of interest. Strains were calculated along each height, where one LED formed a corner of two quadrilateral elements, one above and below the LED in question. The two values of strain at each LED were then averaged and attributed to the location of the LED. This posed problems for LEDs at the top and bottom of the LED field, as well as LEDs at wall sections were

the LED field changed in grid size. For this reason, an inverse weighted average of strain readings was used. The equation for this averaging technique is shown in equation AV.6.

$$\varepsilon_{\text{average}} = \frac{\varepsilon_{\text{top}}(\mathbf{h}_{\text{bot}}) + \varepsilon_{\text{bot}}(\mathbf{h}_{\text{top}})}{(\mathbf{h}_{\text{top}}) + (\mathbf{h}_{\text{bot}})} \quad (\text{E.A1.6})$$

Where ‘top’ and ‘bot’ denote the values for the elements above and below the LED in question. The height of the element was calculated as the vertical distance between the LED in question and the LED directly above or below. This way of calculating strain is geometrically true for a perfectly linear strain distribution, regardless of magnitude in strain or difference in height of the elements above and below the LED. This method proved to give reasonable values of strain, without oscillations. An example of the elements used to calculate strains can be seen in figures AV.5a, b, and c. This method also has limitations. LEDs that do not have an adjacent LED above or below it do not have two elements to average strain. Also, the elements that can be used to estimate strain can only be above or below the LED, giving strain readings that are either larger or smaller than what really exists at the LED. For this reason, LEDs that do not have an element both above and below are disregarded in calculations for equilibrium and curvature for the cross sectional height in question.

Lastly, the axial strain is always being calculated on the edge of the quadrilateral element. This allows the top and bottom elements being used for an LED to be any width desired, since the LEDs directly above and below each other influence the strain along their edge entirely. This also allows the calculations for and LED to be done on either the right or left hand side of the element without consequence. This is very advantages when gaps occur in the LED field, such as figure AV5.c for RWS, where an LVDT blocked the view of an the LED from the Krypton camera. Element #32 can be used directly with element #32 in the calculation of strain in column #8 (8th column of LEDs from the left).

A1.3.1: Comparison of Krypton Techniques

The three methods discussed have distinct assumptions that effect the calculated strain. The method based on averaging strains at the location of the LED seems to represent the axial strains in the wall accurately, while taking a uniform and unbiased approach. This method reduces the effect of any single LED and reports an average based upon multiple readings. This point is illustrated best in figure A1.6. This plot shows the axial strain along the height of RWN at loading just prior to first yield. The location along the height was chosen to be 3" from the extreme compression face. This location was chosen for the comparison because it showed the greatest amount of variation in readings of any data for each wall. The oscillation in test data can be seen in the incremental average method. This is due to a poor reading by the LED at 36". This LED recorded a smaller downward displacement than the LED below it (figure A1.7). This caused a large decrease in compressive strain for the span from 27 to 36". This calculation actually returned a tensile strain, just 3" from the extreme compression face. In addition to this jump, the LED at 36" then influenced the span from 36" to 43" to return a much larger compression reading than expected. The influence of this bad LED can be seen again in the total average method, where the strain at 18" (half the height of 36") has a slight oscillation of decreased compression when compared to adjacent calculations. The weighted average method does the best job of preserving local effects and limiting vulnerability to a single poor data point.

A13.2: Associated Errors

The maximum percent error associated with the magnitude of average axial strain was determined to be approximately between -14 and 28%. This error was computed from the most non-linear strain gradient portions of the BIAX analysis, using typical element sizes and weighted average. The average strain for each element was computed as the average strain of the points between the shared point and the top and bottom points. Note that this calculation was a percent error from the values given directly from BIAX. The large percentage difference of 113% was due to a relatively small level of strain at that location

in the first place. A larger total error was calculated for the extreme tension face, but a lower percent error from already large levels of strain. This can be seen in figure A1.2, where the span of the elements used is depicted by black lines and the percent error calculated is at the point of interest. These variations may seem large, however, they are the maximum errors at the worst locations for the largest loading.

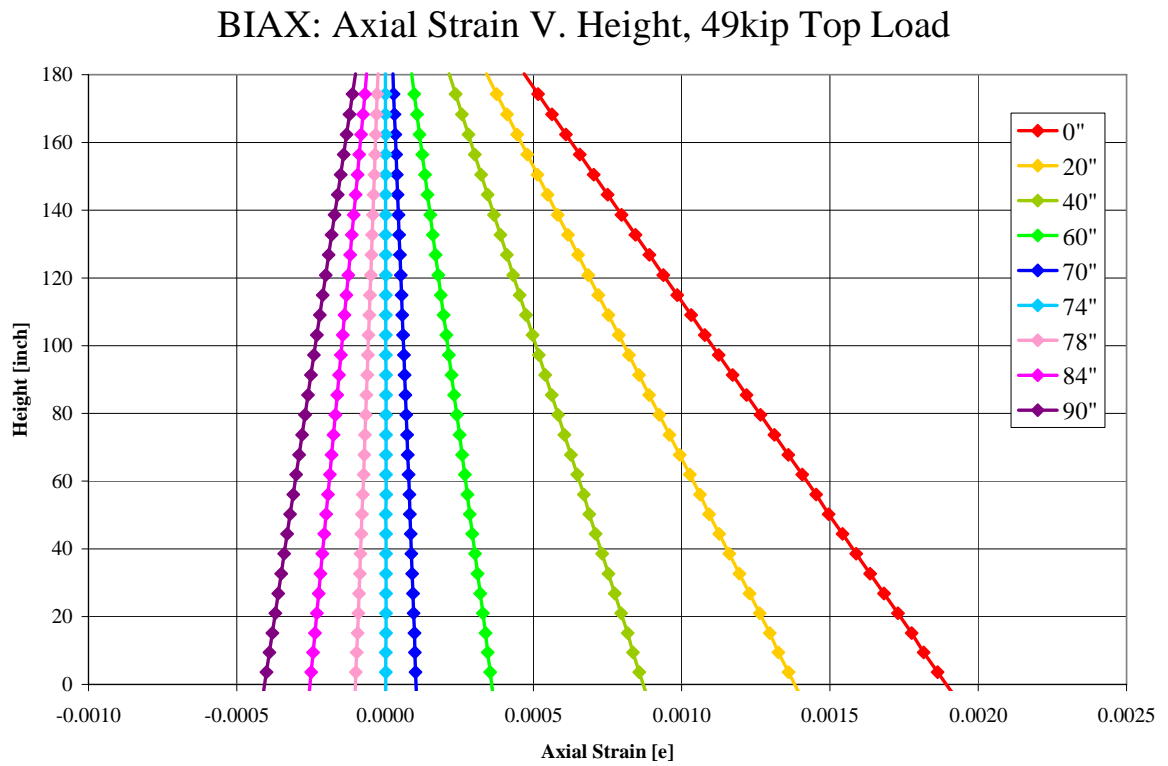


Figure A1.1a: BIAX calculated axial strains versus wall height.

BIAX: Axial Strain V. Height, 73kip Top Load

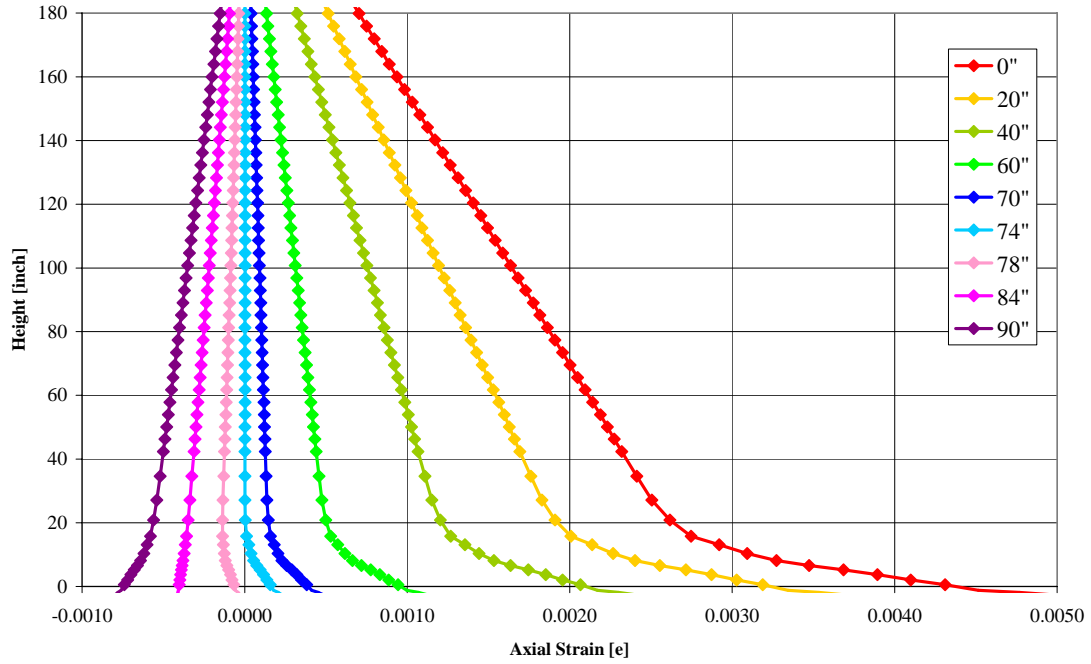


Figure A1.1.b: BIAx calculated axial strains versus wall height.

BIAX: Axial Strain V. Height, 90kip Top Load

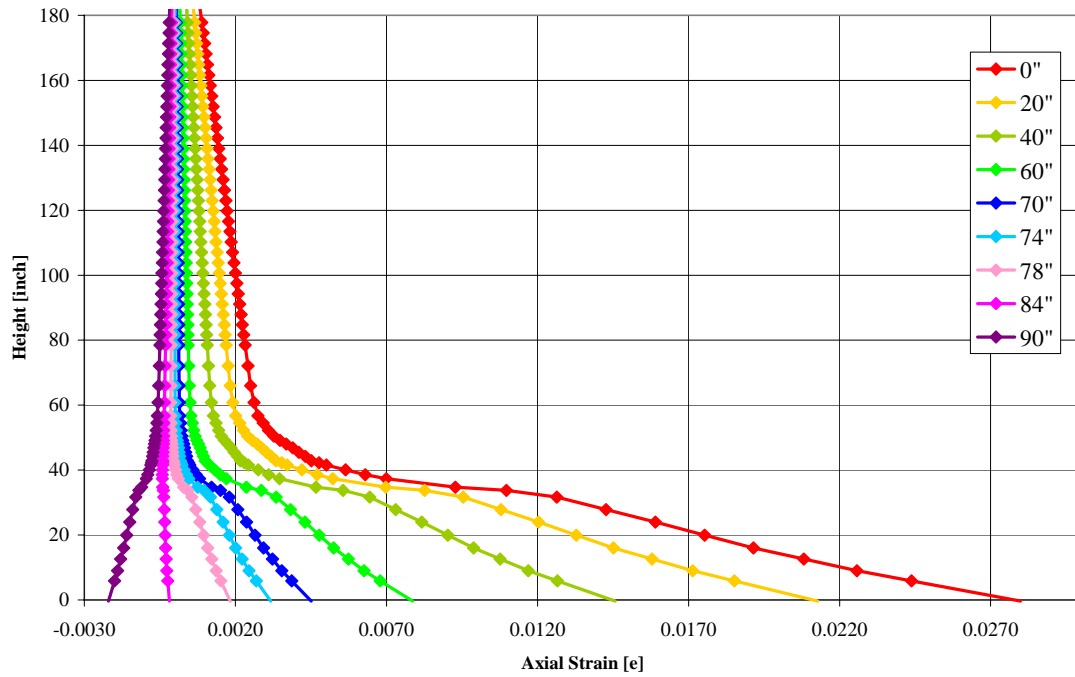


Figure A1.1.c: BIAx calculated axial strains versus wall height.

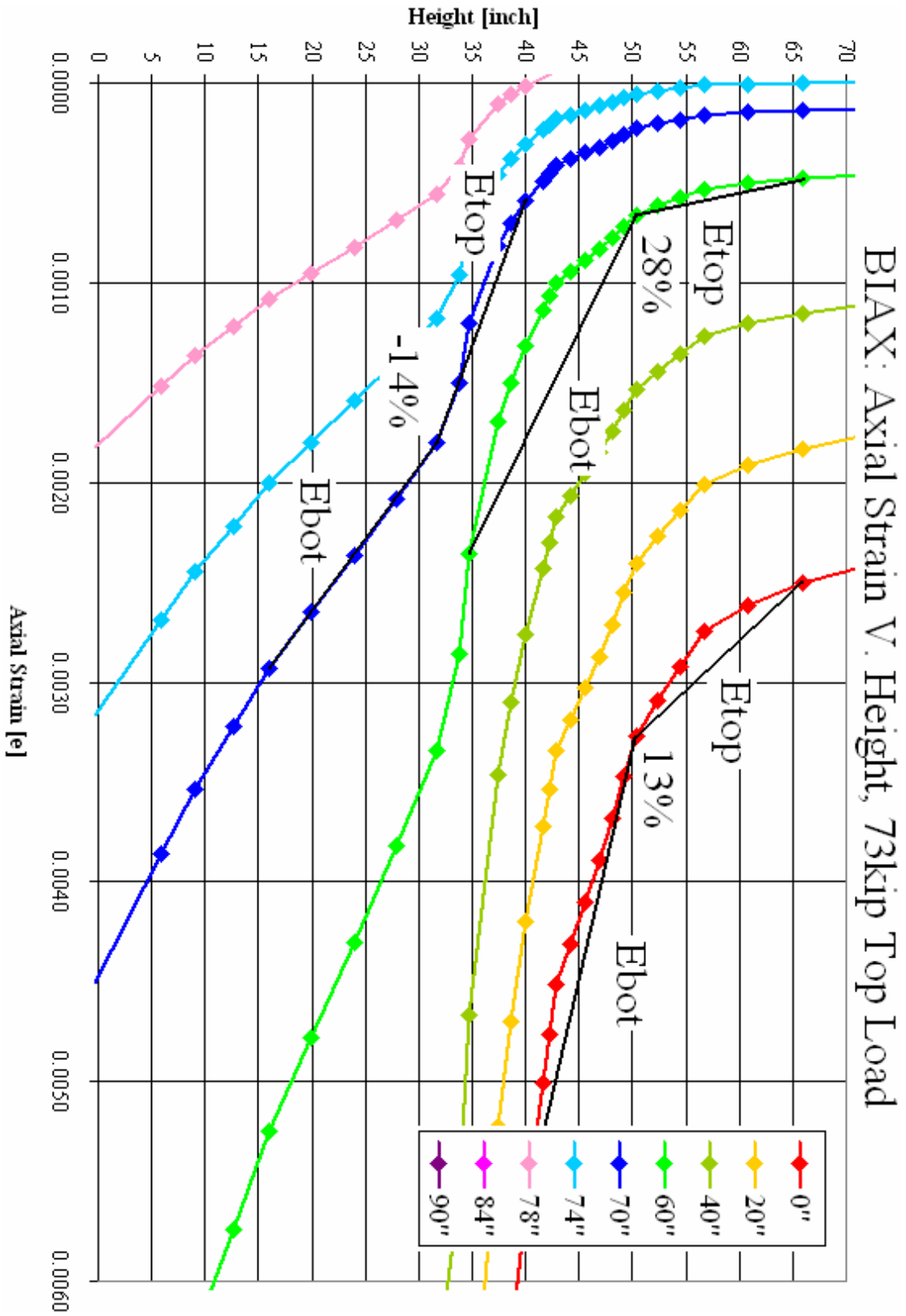


Figure A1.2: Maximum errors from assumptions on BIAX analysis, 90kip top Load

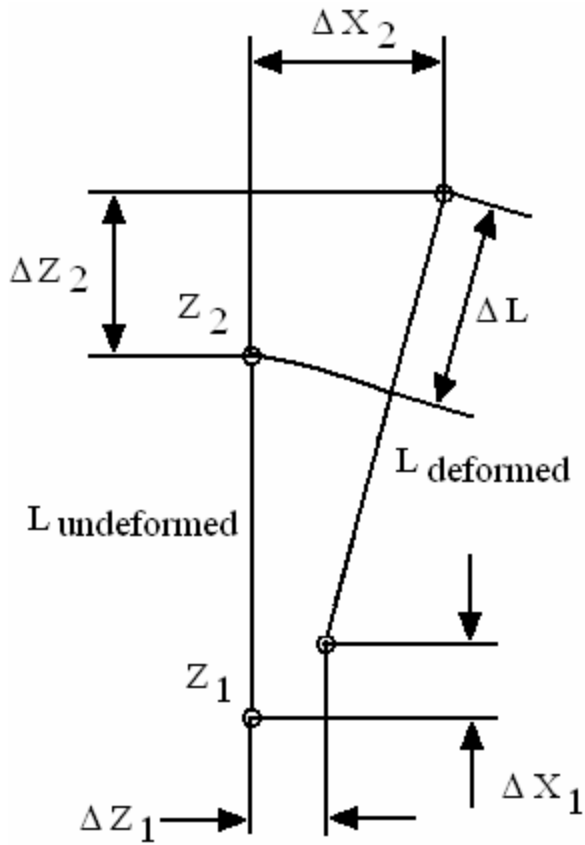


Figure A1.3: Average strain geometry used in calculations.

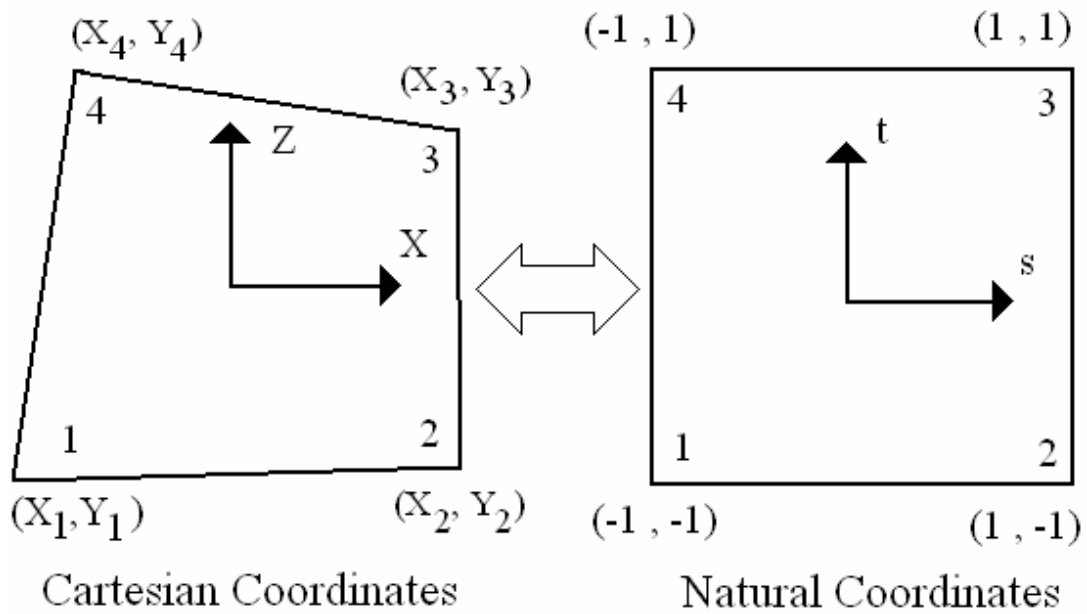


Figure A1.4: Isoperimetric mapping for Krypton LEDs

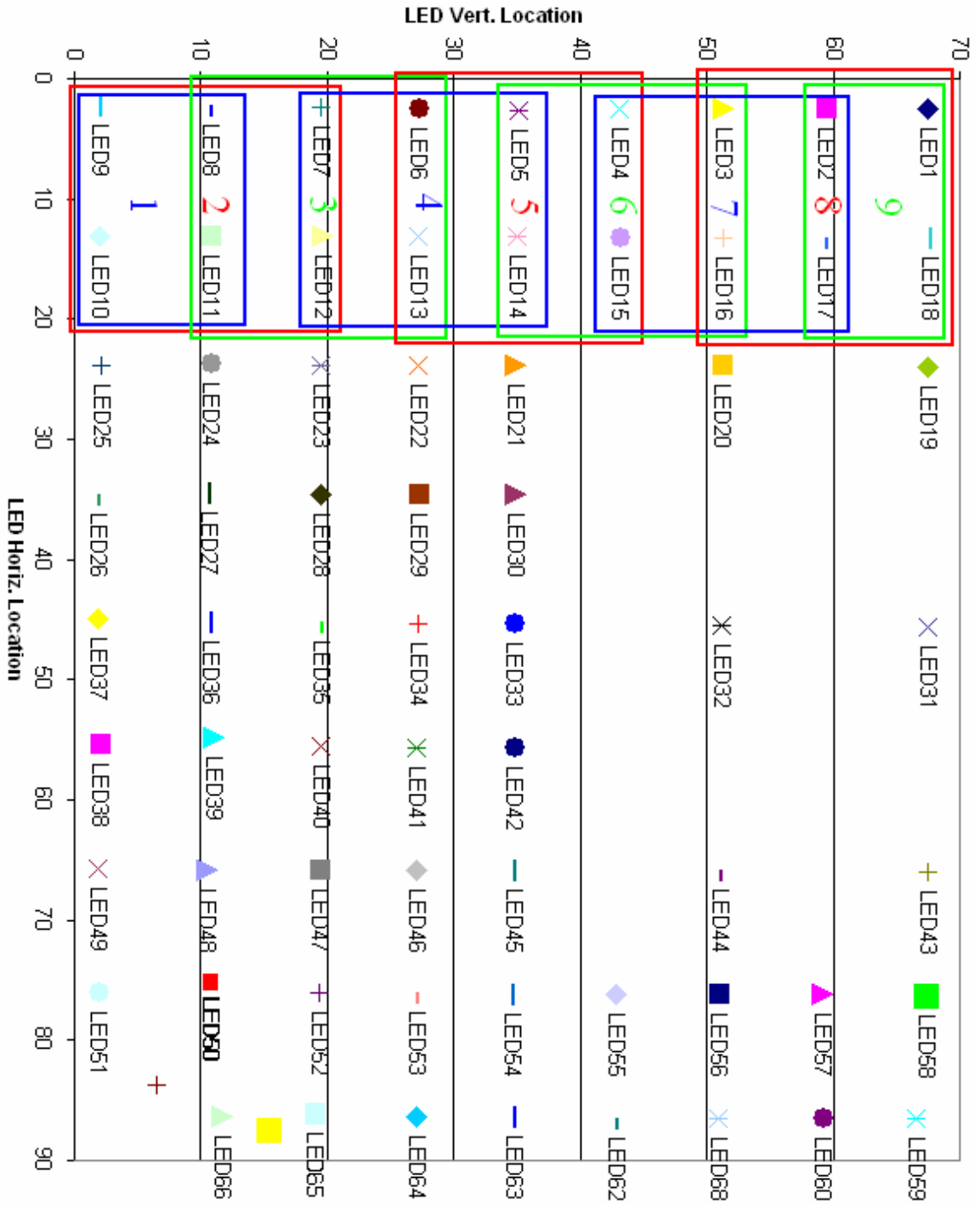


Figure A1.5a: LED elements for strain calculation of LEDs in columns 1&2 for RWN.

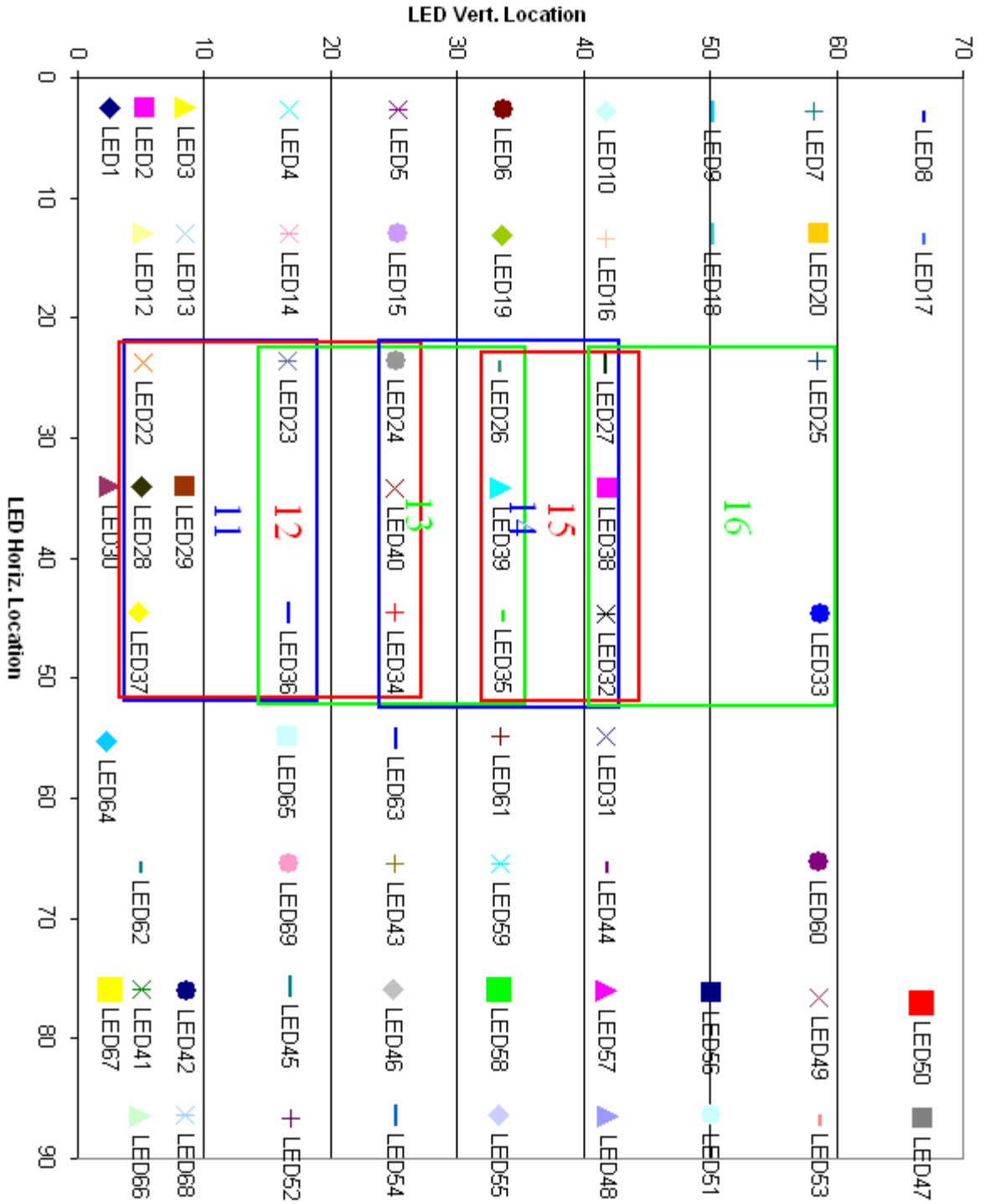


Figure A1.5b: LED elements for strain calculation of LEDs in columns 3&5 for RWC.

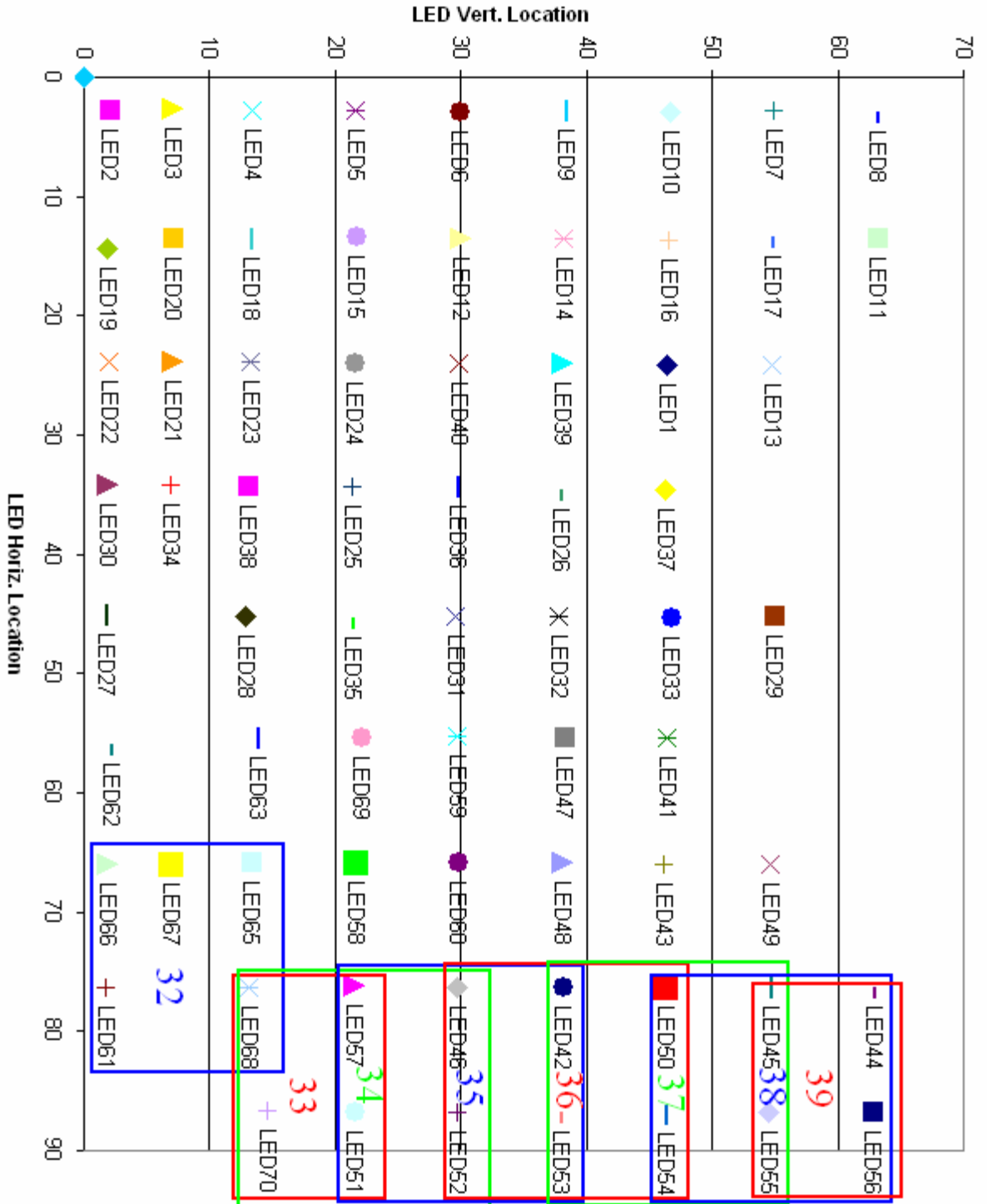


Figure A1.5c: LED elements for strain calculation of LEDs in columns 8&9 for RWS.

RWN: Comparison of Strain Calculation Methods, 0.3125% Drift, LEDs 3" From Extreme Compression Face.

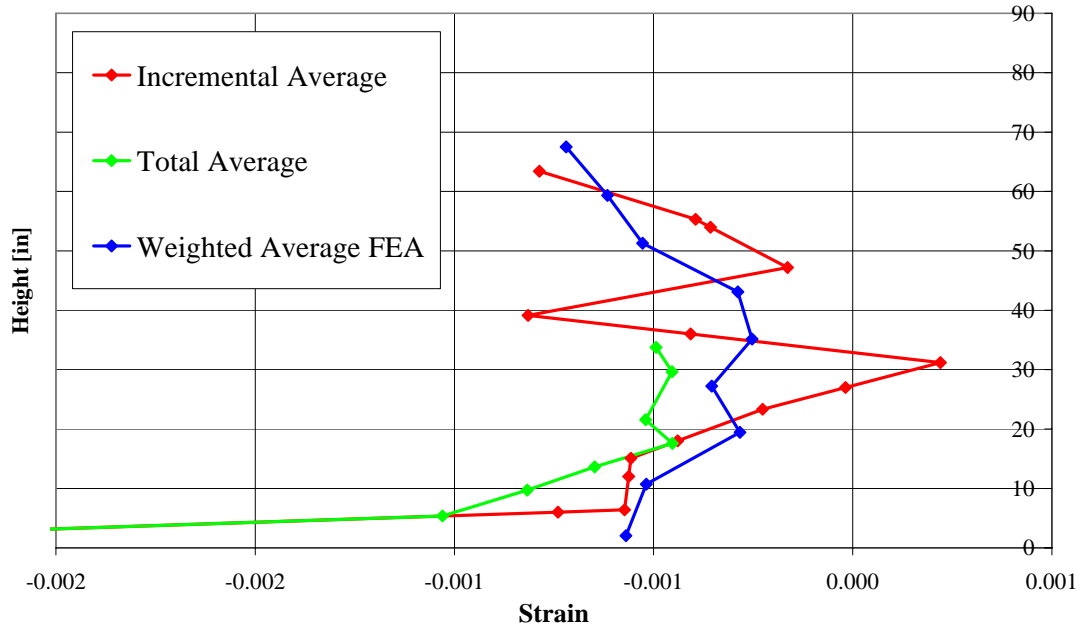


Figure A1.6: Comparison of strain calculation methods from Krypton data.

RWN: Total Vertical Displacement v Wall Height, 2.5" from Extreme Compression Fiber, No.5&6 BE in Tension

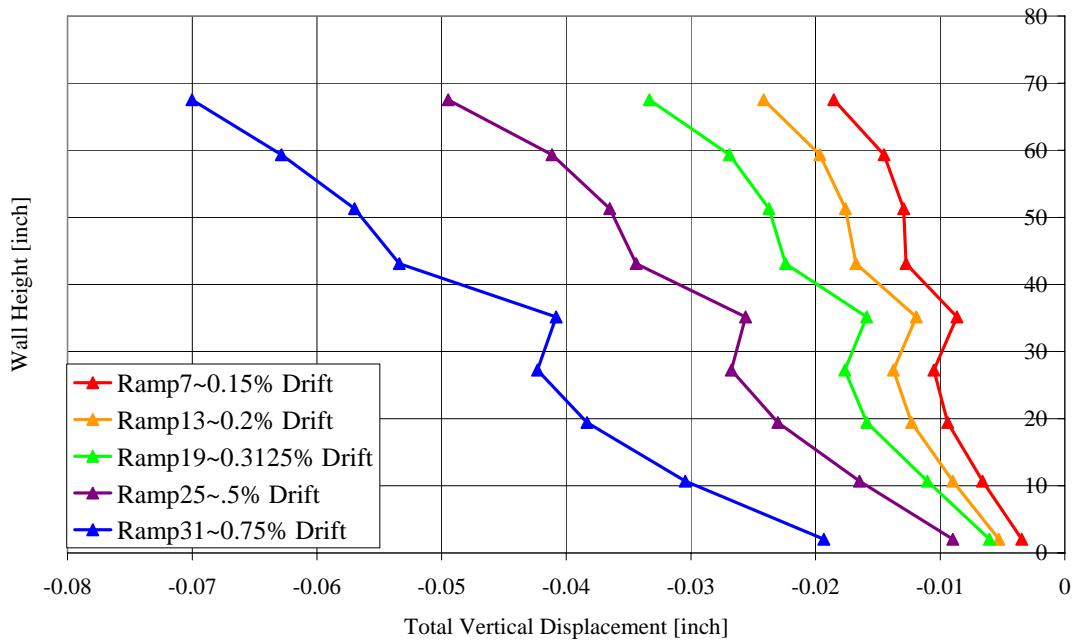


Figure A1.7: Total Vertical Displacement v. Wall Height.

Appendix 2: Calculation of Curvatures and Rotations

A2.0: Introduction

This appendix covers the methods used to calculate curvature and rotation from the experimental data. The assumptions used for the calculations of curvature and rotation have a significant impact on the resulting flexural deformation. The effects of these assumptions are examined and quantified in order to determine the best method for determining flexural deformation.

A2.1: Methodology

Examination of axial strain across the wall length in previous chapters revealed a non-linear distribution. The axial strain gradient (curvature) was observed to be larger over the section of the wall in compression. This non-linear distribution was typically noticed over the bottom three feet of the wall.

Flexural deformation is influenced by the base of the wall to a much larger degree than any other height section. This places a great deal of importance on accurately calculating the resulting curvature at the base of the wall. For this reason, three methods are used to calculate curvature. The three methods will be used to create an envelope of possible results, representing the three extreme possibilities.

A2.2.1: Calculation of Curvature

Curvature was calculated from the experimental data with a minimized error, linear trend line. This calculation was performed twice for each sensor and wall height. The first calculation included all data points along the entire wall length for the height in question. This first method is referred to as the “whole cross section” or “WC” method.

The second method was computed using sensors from the compression half of the wall length (extreme compression fiber to the centerline of the wall length). Increased curvature was not always seen to extend that far outside the compression block. However, the section was chosen for its unbiased and uniform approach. Namely, the method does not change to suit the instantaneous loading situation and availability of sensors. This second method is referred to as the “compression half cross section” or “CH” method. Examples of this method can be seen in figures A2.1. More strain profiles can be seen in appendix V.

The CH method has some limitations. The first problem is the availability of sensors at the proper locations. The number of sensors at certain heights was often insufficient to calculate a curvature over only half of the wall section. Specifically, string pots usually have only two points to calculate curvature. The same is true for strain gages, where sensors were only present in the boundary elements. The second problem with the CH method is defining the point when the side used for calculation switches. This is simple in the elastic range, but becomes more difficult when hysteretic damage has occurred. In general, the compression half method is used when the load and displacement signs agree (+, + or -, -). Often times, the signs do not agree during loading/unloading. In this case, the CH method defaults to the WC method.

The final method incorporated rotations calculated from strain penetration data. This method is referred to as the strain penetration hybrid, or “hybrid” method. The curvature at bottom row of Krypton LEDs was based upon displacements from the bottom and second to bottom row. This was done to eliminate the effect of strain penetration on the recorded displacements. However, this leads to an underestimation of strain and consequent curvature at the bottom row of LEDs. This location is the most influential on the resulting flexural deformation. In addition, this problem is increased for RWS, where a strain concentration from lapped splice termination exists. For these reasons, the curvature was again calculated at the bottom row based on the change in rotation. The rotation at the interface from strain penetration was subtracted from the rotation of the

bottom row of LEDs. The resulting rotation is from pure flexure. This rotation was then divided by the height of the instruments to determine the curvature for means of comparison to other instruments. In general, this method tends to overestimate curvature to a large degree. The result is far outside reasonable curvatures for known elastic behavior. This can be seen in figures A2.2a and A2.2b.

It can be seen from these plots that the hybrid method gives unreasonable results when compared to predicted BIAx analysis. The whole cross section and compression half cross section methods may under predict curvature at the base, but are much more reasonable than the strain penetration hybrid method. This can be seen with the close agreement between the Krypton and strain gage readings at the base, where the Krypton returns curvatures lower than the strain gages.

A2.2.2: Calculation of Moment

Load applied by the actuator was used to calculate the moments at various wall heights throughout the test from basic statics. This was done to create a moment versus curvature relationship that could be used to compare the experimental specimens, as well as verify a consistent moment-curvature relationship between cross sections at different heights. This can be seen in RWN and RWC but not in RWS, as discontinuities in longitudinal reinforcement change the cross sectional rotation properties.

A2.2.3: WC & CH Method Implications

Curvatures calculated with the WC method may be lower than the “true” behavior of the wall. This can be seen in figures A2.3a-e and A2.4a-e. These figures depict the “backbone” moment versus curvature relationships of RWN and RWC, considering only loading ramp maximums. These plots do not reflect the hysteretic response and include data until the failure of the instruments. A drop in stiffness in the No.9 boundary element

does not reflect a change in the No.9 reinforcement, but a larger target displacement ramp following several ramps returning to the same displacement.

The moment versus curvature relationship depends solely on cross-sectional properties. Without discontinuities, the moment versus curvature relationship should be independent of the height it was measured at. This is not the case. Larger curvatures are calculated higher in the wall, compared to curvatures lower in the wall at the same applied moment. This discrepancy is far less when considering the CH method. The result of the CH method makes more sense intuitively, as the moment versus curvature relationship should be independent of wall height. Again, this is not true for RWS, as discontinuities change cross sectional properties.

Curvatures calculated with the CH method may have misrepresented RWS. Specifically, the compressive strains in the boundary elements of RWS did not differ that greatly from those in RWN and RWC (refer to chapter V). In addition to this, the termination of the No.4 bars in the web occurs first and the strain concentrations resulting will always be used in curvature calculations with the CH method. The section of the wall left out of these calculations is the section affected most by the lapped splices, the tension boundary element. Ignoring the tension boundary element affects RWS far more than RWN and RWC. This is illustrated in figures A2.5a-e.

The difference between the WC and CH methods are not as apparent when considering string pot data. This is due to the reduced number of heights where string pots were available to make a compression half curvature calculation. The difference between the WC and CH methods between Krypton data and string pot data is due to instrumentation limitations and not a difference in observed behavior.

Note that all figures referred to in this section have the same scale, for means of comparison.

A2.3: Verification of Curvature Calculations

The ultimate goal of using instruments to calculate strain and subsequent curvature was to determine the center of rotation for flexural deformation. However, the data processing can lead to a “washed out” effect that does not give the rotation result already known from instrument displacement readings. The analysis techniques for curvature are verified by comparing the rotations calculated by integrating the calculated curvatures to the total rotations calculated from the displacement data.

Total calculated rotation was computed by numerically integrating the calculated curvatures over the wall height. Total rotation was then calculated again using vertical displacement data directly. This rotation calculation was done using the same WC and CH methods described earlier. Plots of this result can be found in figures A2.6a-f, where Krypton data is compared for each test specimen.

It can be seen that the total rotations at the top LED row differ by a considerable amount. However, the “total rotation” calculated from displacement data also includes the additional rotations resulting from strain penetration effects at the wall interface. The discrepancy is close to being resolved perfectly when the rotation from the bottom row is subtracted from the rotation of the top row. This result is the change in rotation from the bottom to top row of LEDs from flexure alone. This is true for each wall, far into the inelastic drift range. Note that the second to the top row is used for RWC and RWS, as not enough sensors were present at the top row to make a CH method comparison.

The comparison of total rotation to calculated rotation suggests that the analysis techniques used for axial strains and consequent curvatures are indeed good considering either of the two curvature calculation methods. The WC method is almost in perfect agreement with the total rotation and the CH method is well within an acceptable tolerance. The analysis techniques used are indeed unbiased and a good approach to determining curvatures and rotations in the test specimens.

**RWN: First Loading Cycle to 0.3125% Drift, 75% of Estimated First Yield.
Axial Strain, 36" Above the Foundation Interface V. Wall Length,**

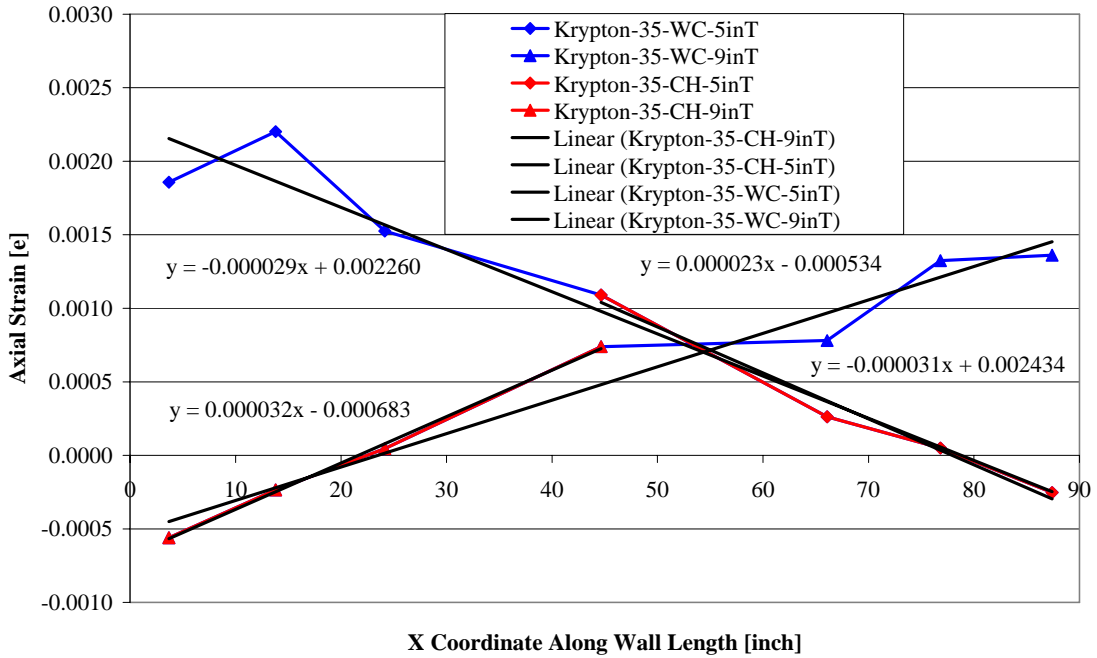


Figure A2.1: Example of curvature calculation methods using elastic RWN limit.

RWN: Height v. Curvature, First Cycle to 0.3% Drift: Final Elastic Cycle

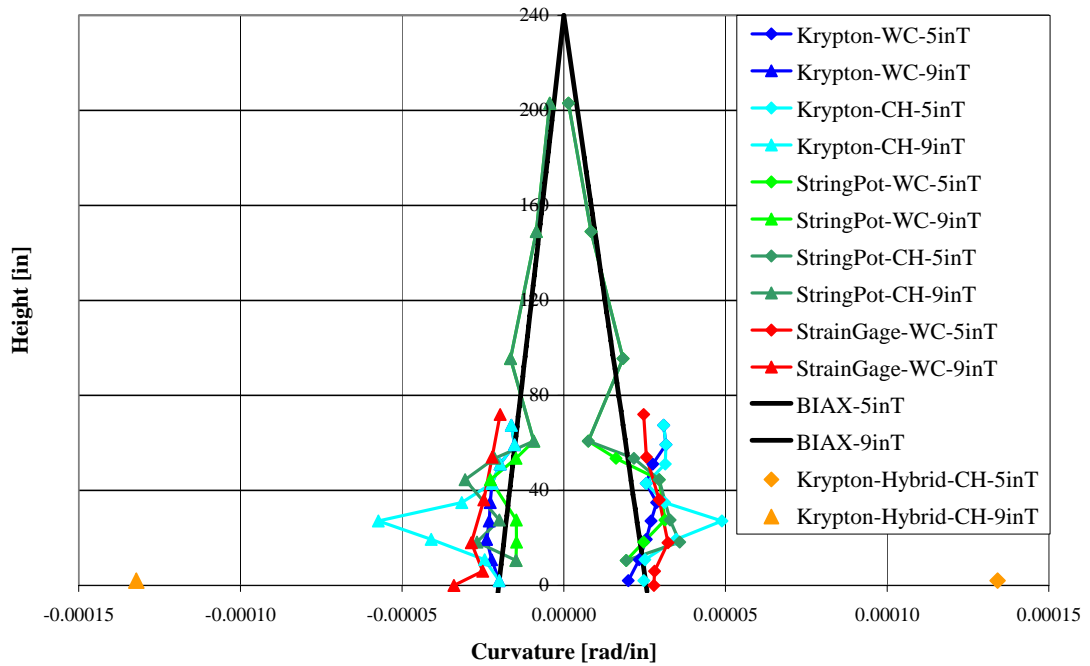


Figure A2.2a: Comparison of curvature methods over height.

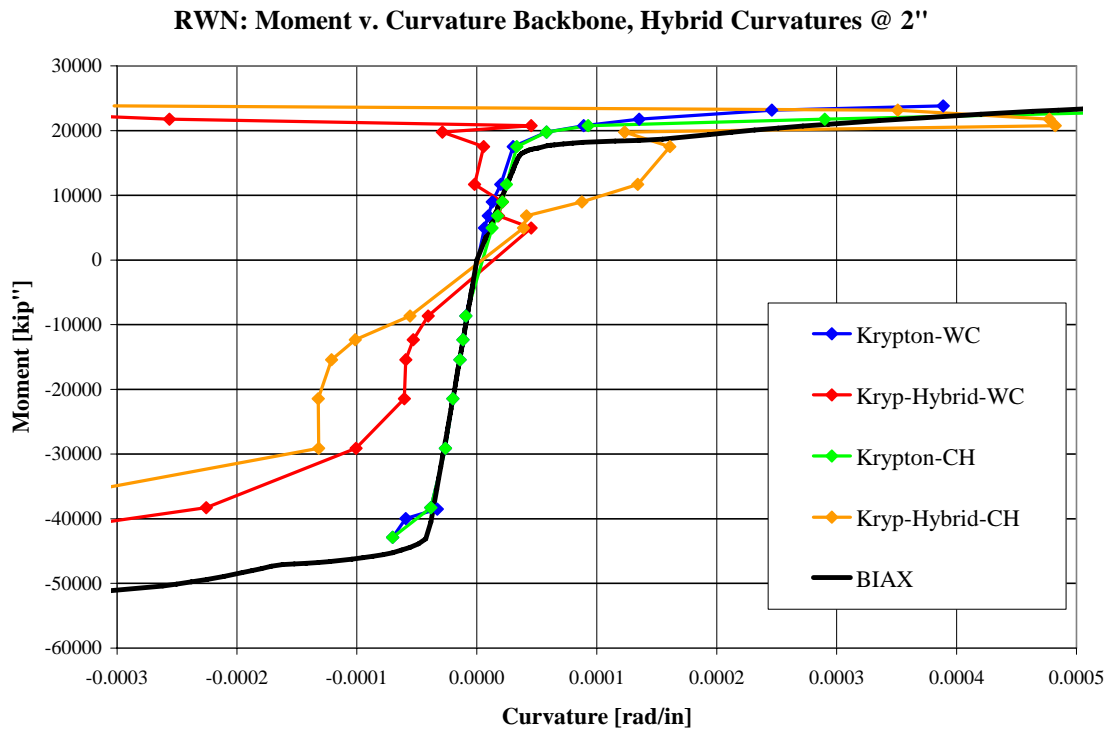


Figure A2.2.b: Moment v. Curvature backbone of RWN comparing WC, CH, and Hybrid

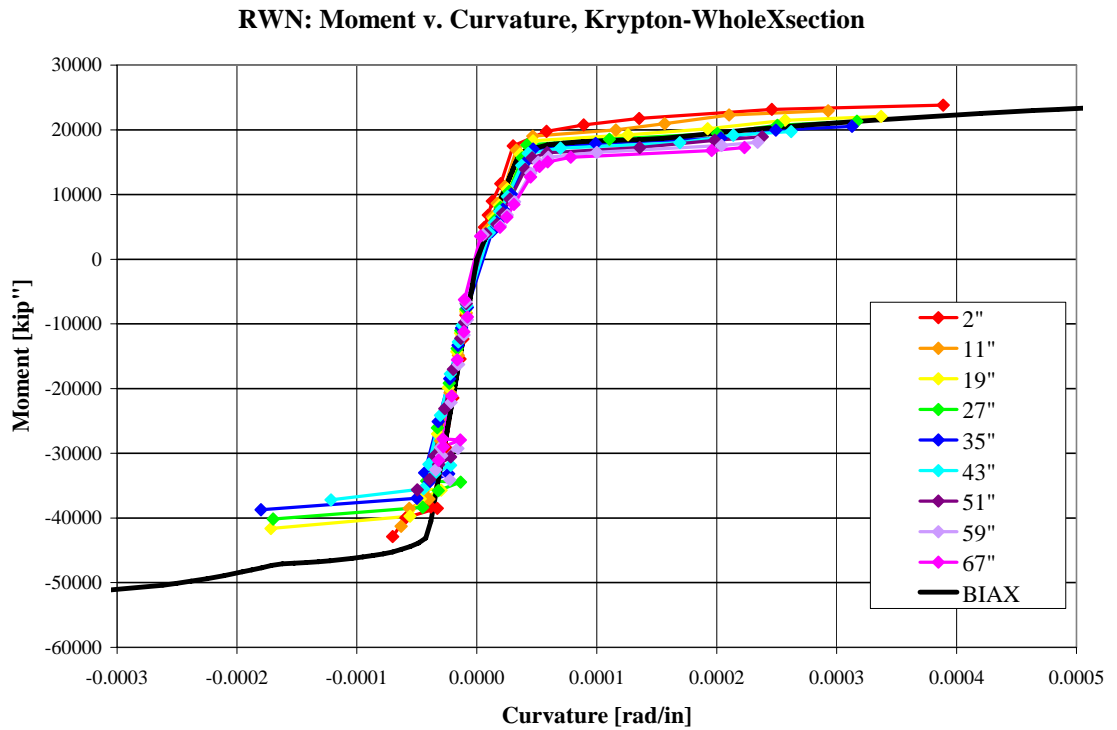
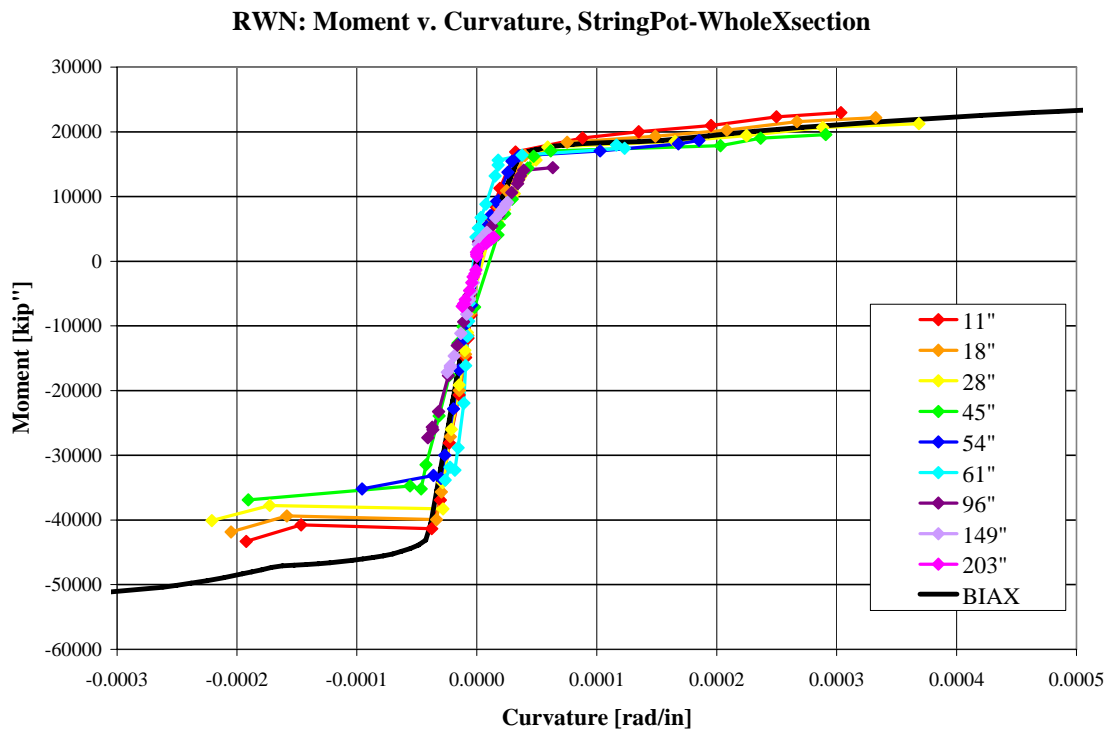
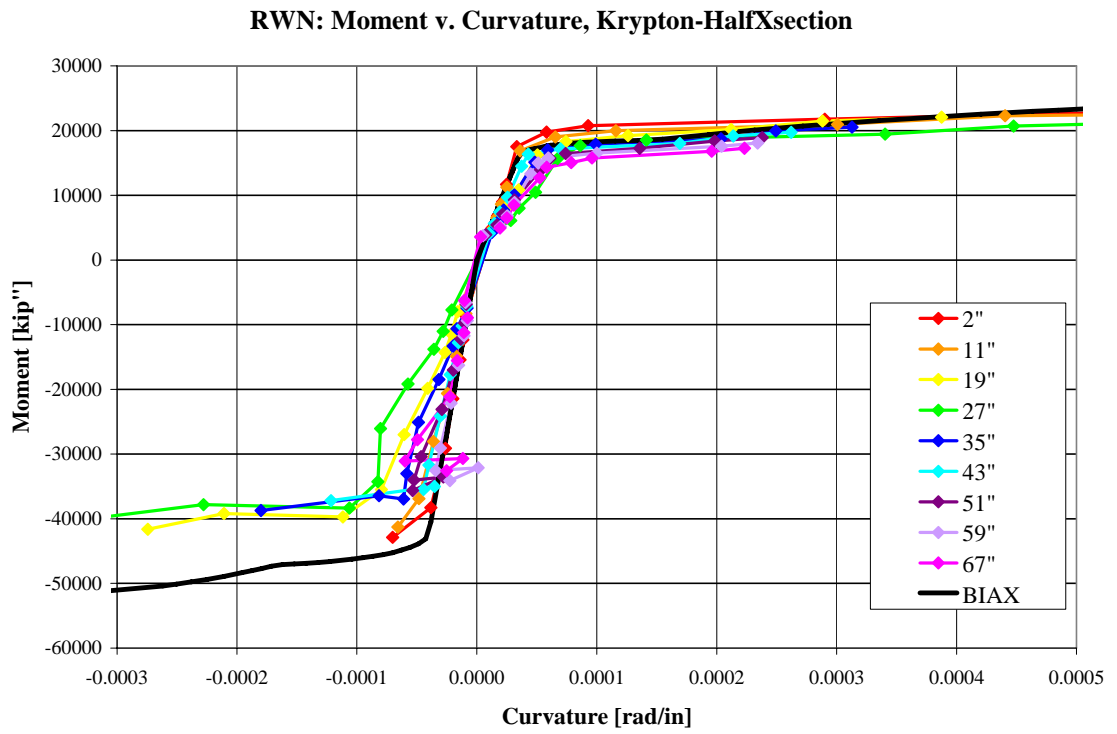


Figure A2.3a: Moment v. Curvature backbone of RWN using Krypton Data: WC



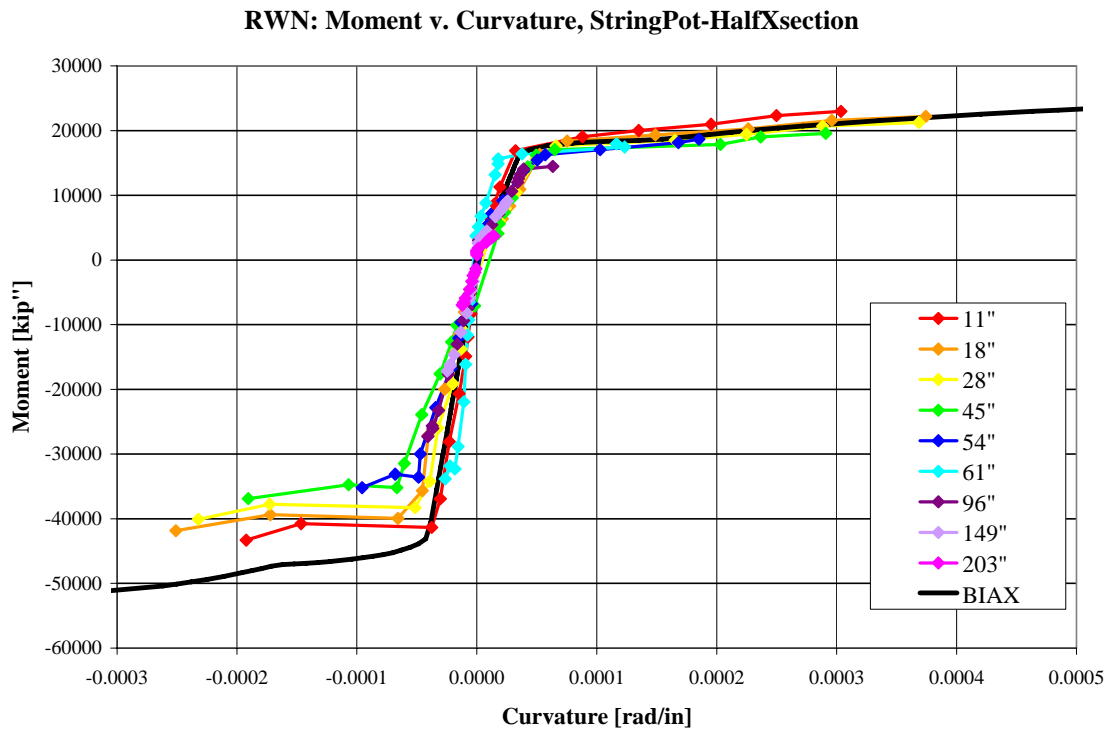


Figure A2.3d: Moment v. Curvature backbone of RWN using String Pot Data: CH

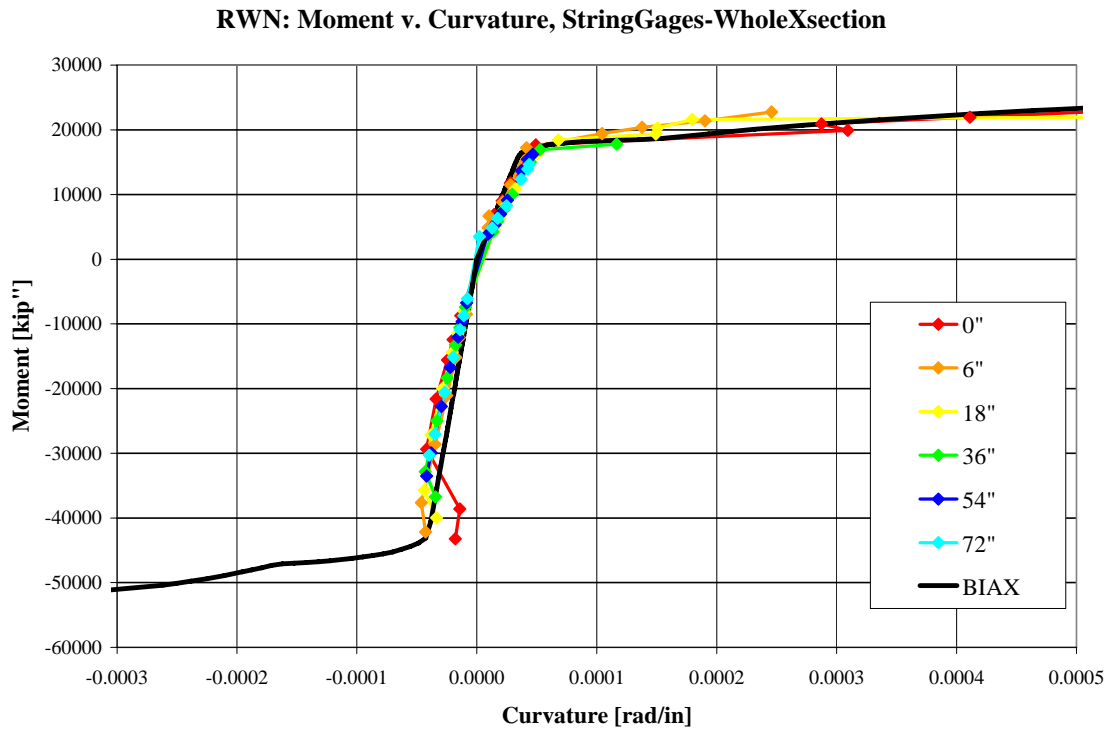


Figure A2.3e: Moment v. Curvature backbone of RWN using Strain Gage Data: WC

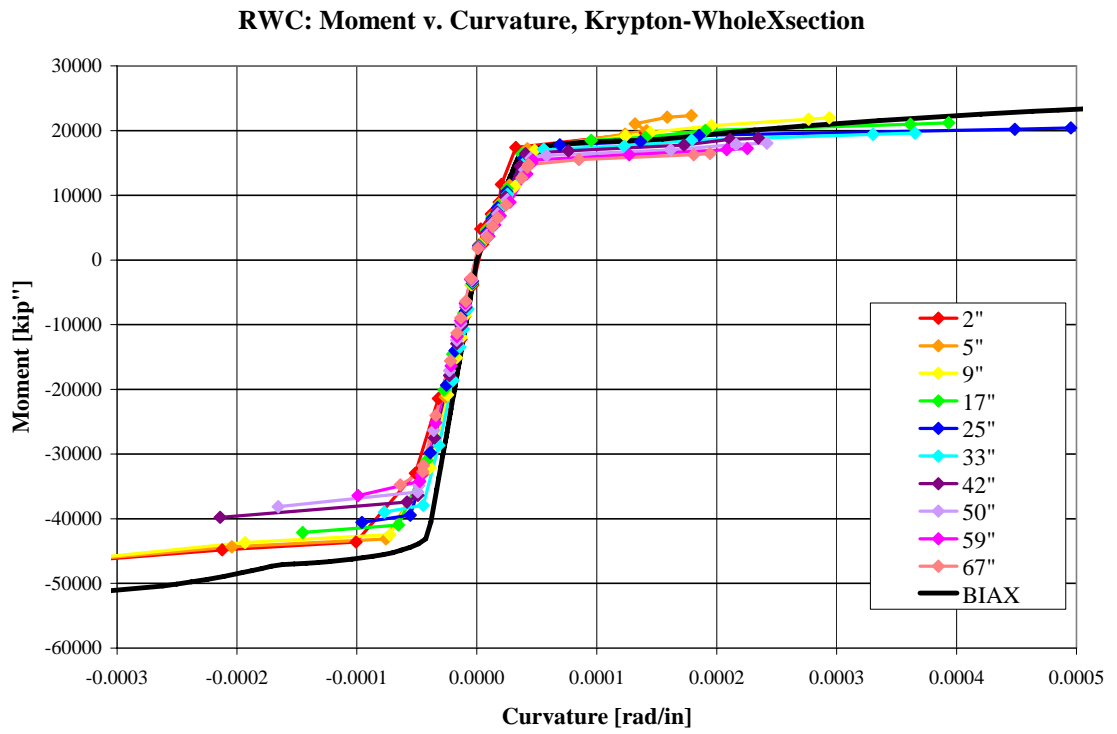


Figure A2.4a: Moment v. Curvature backbone of RWC using Krypton Data: WC

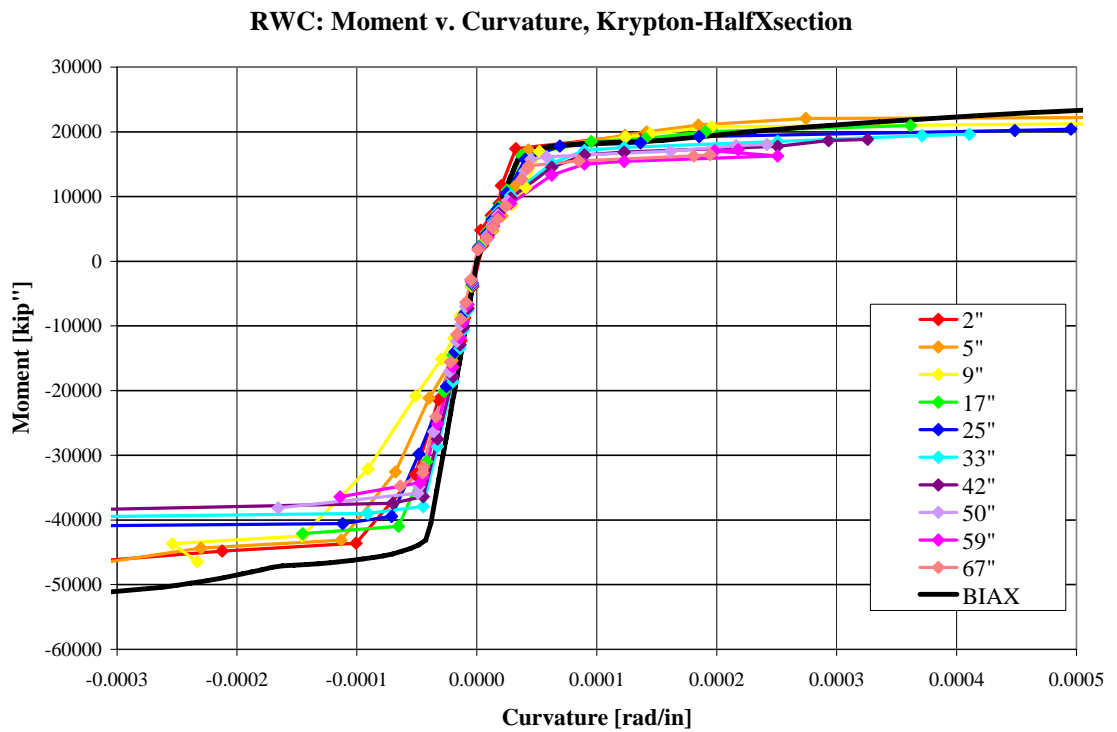


Figure A2.4b: Moment v. Curvature backbone of RWC using Krypton Data: CH

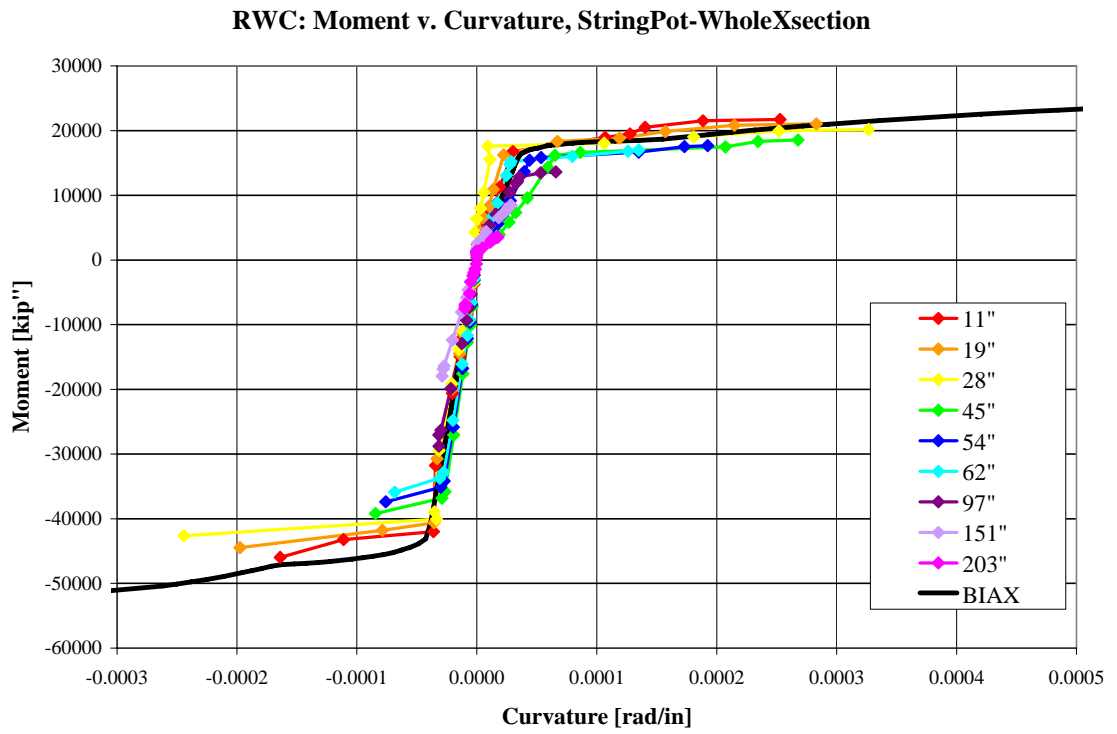


Figure A2.4c: Moment v. Curvature backbone of RWC using String Pot Data: WC

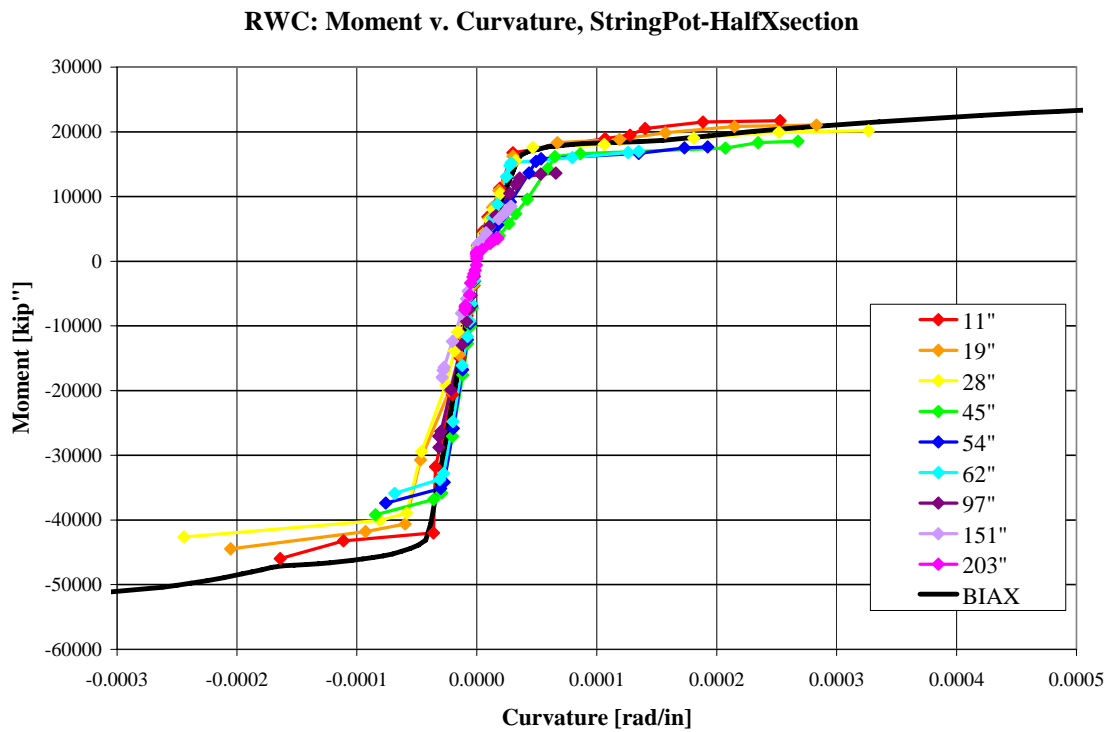


Figure A2.4d: Moment v. Curvature backbone of RWC using String Pot Data: CH

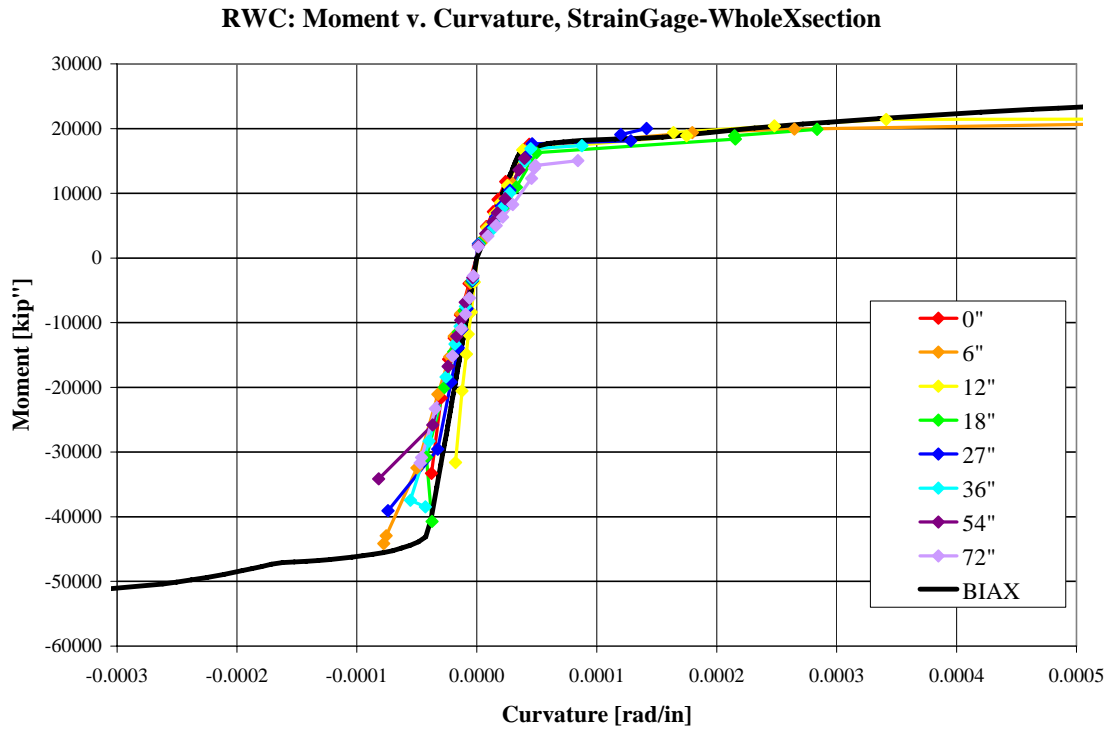


Figure A2.4e: Moment v. Curvature backbone of RWC using Strain Gage Data: WC

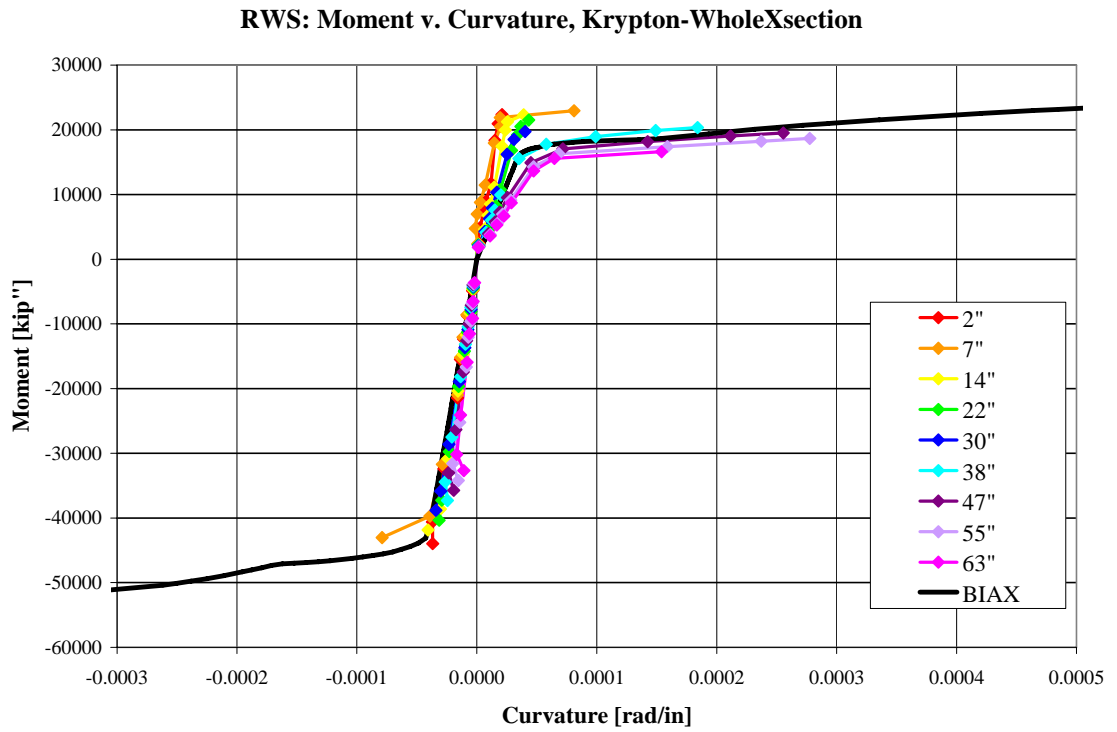


Figure A2.5a: Moment v. Curvature backbone of RWS using Krypton Data: WC

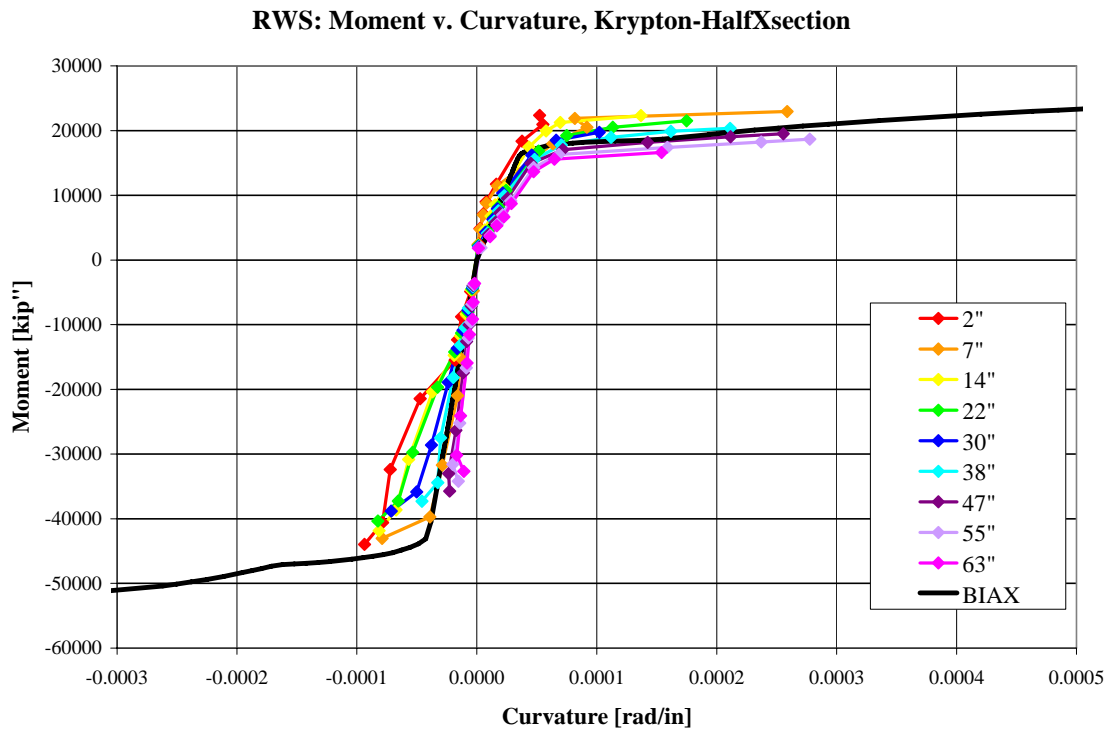


Figure A2.5b: Moment v. Curvature backbone of RWS using Krypton Data: CH

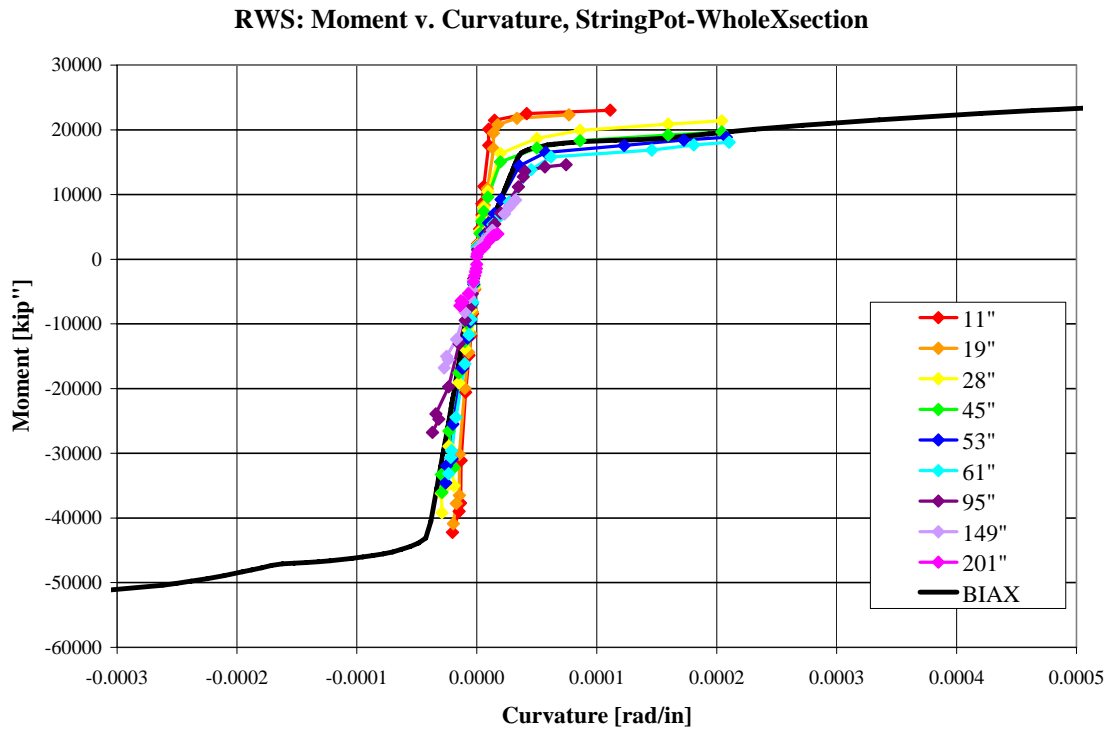


Figure A2.5c: Moment v. Curvature backbone of RWS using String Pot Data: WC

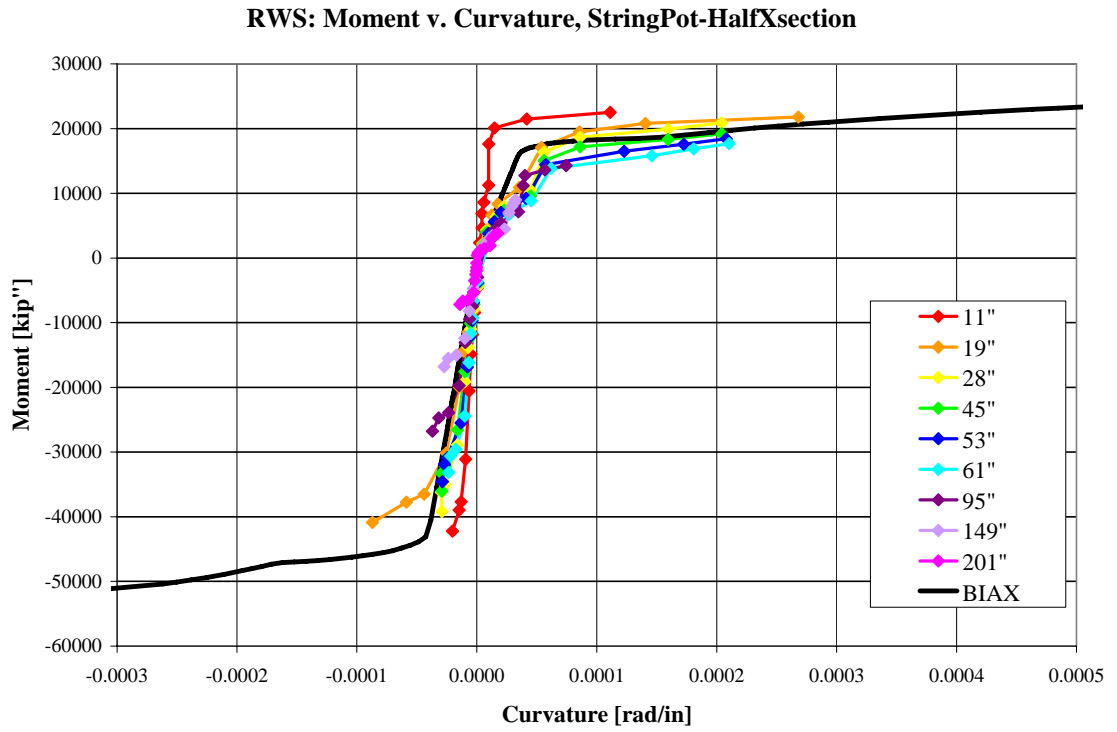


Figure A2.5d: Moment v. Curvature backbone of RWS using String Pot Data: CH

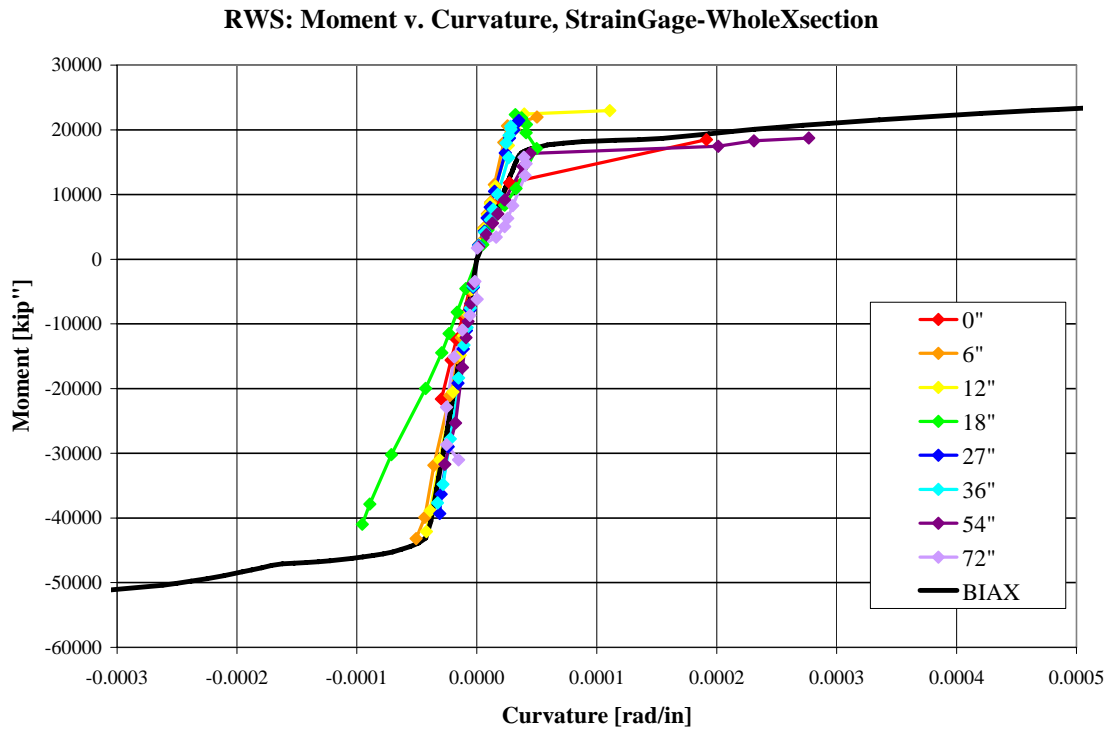


Figure A2.5d: Moment v. Curvature backbone of RWS using Strain Gage Data: WC

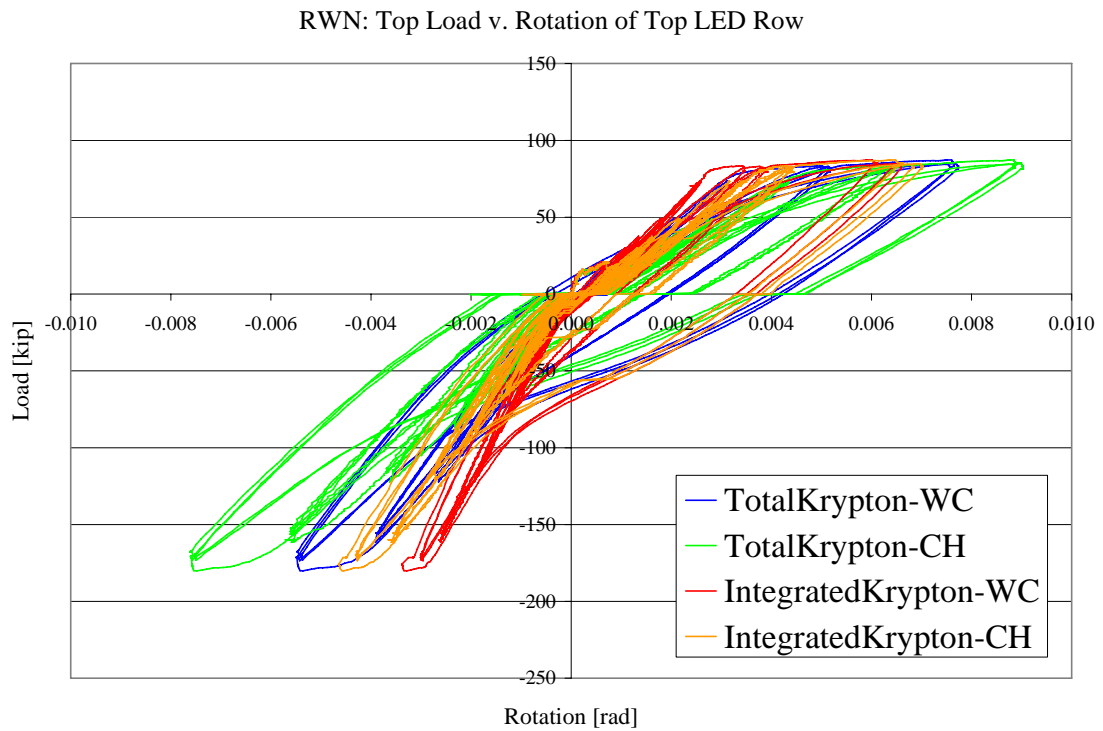


Figure A2.6a: Total rotation of RWN compared to integration rotation

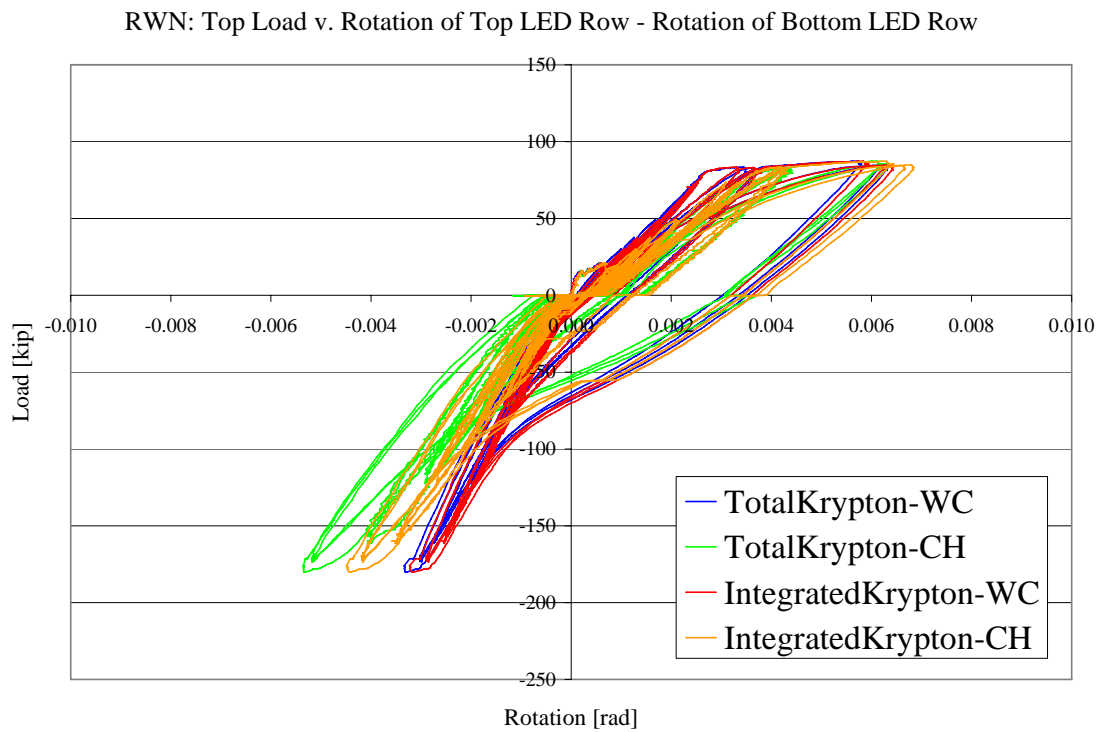


Figure A2.6b: Flexural rotation of RWN

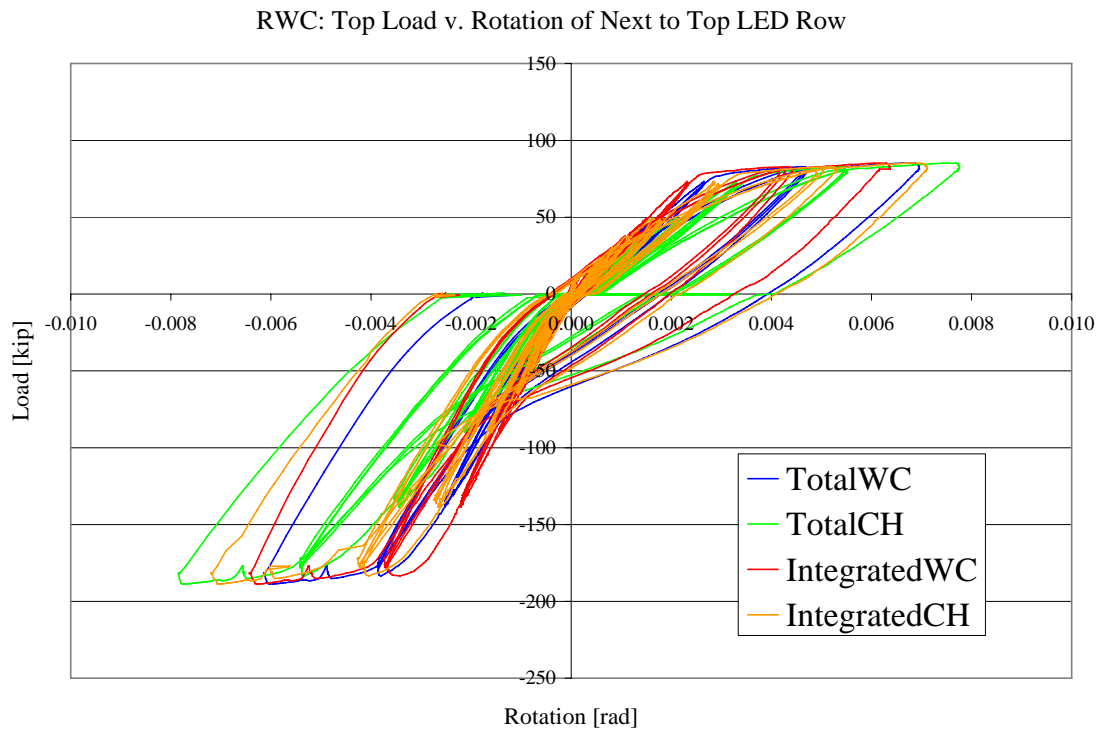


Figure A2.6c: Total rotation of RWC compared to integration rotation

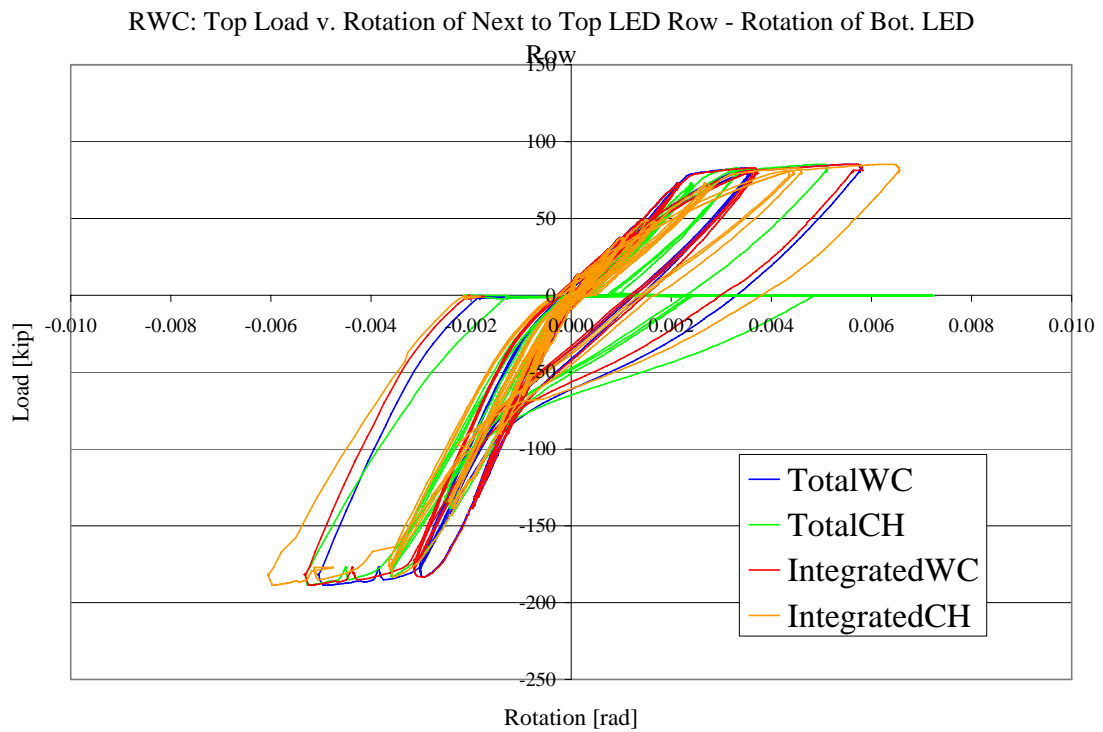


Figure A2.6d: Flexural rotation of RWC

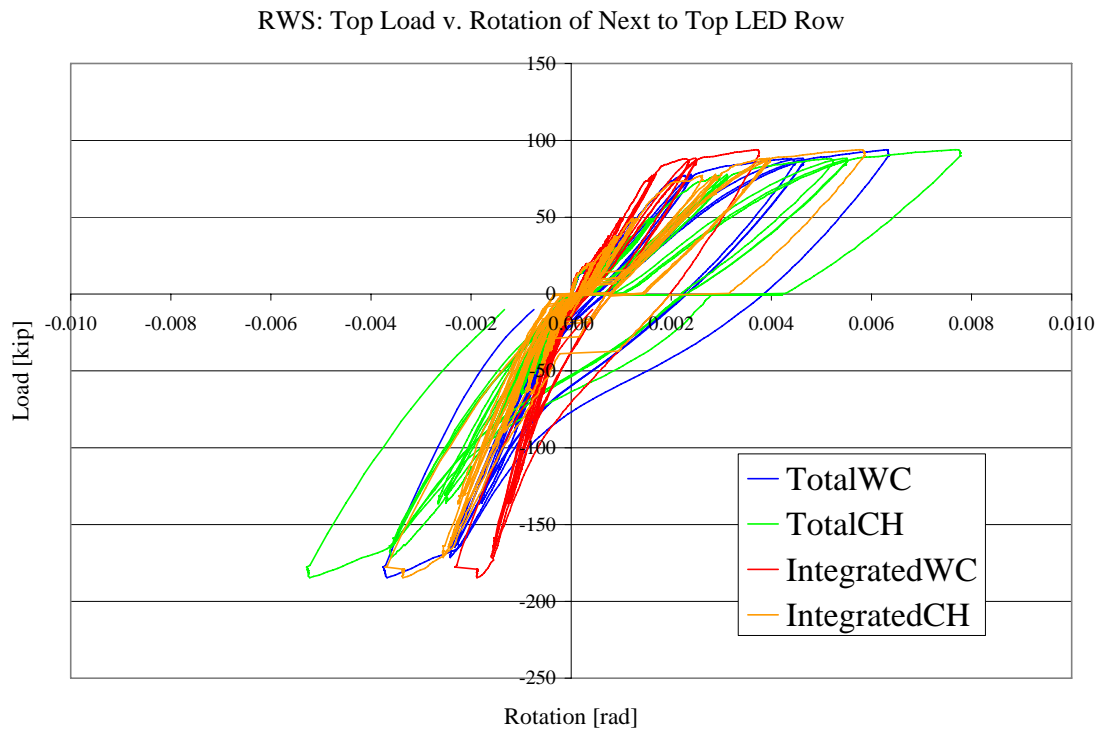


Figure A2.6e: Total rotation of RWS compared to integration rotation

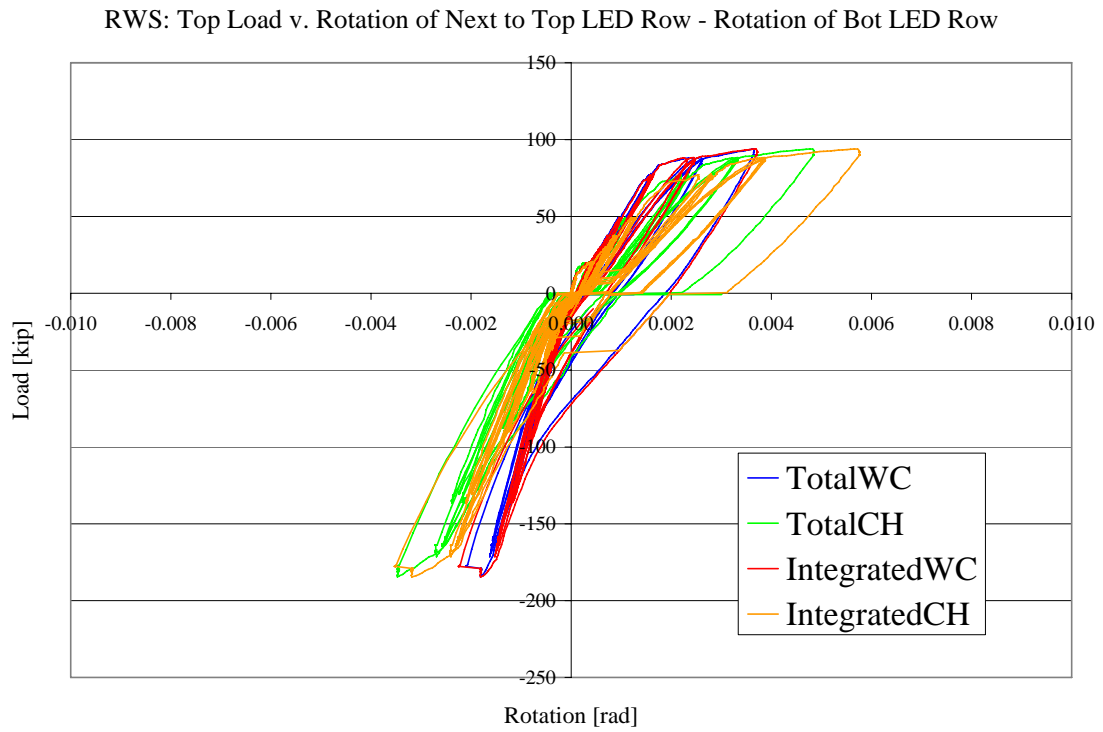


Figure A2.6e: Flexural rotation of RWS

Appendix 3: Calculation of Flexural Deformation

A3.0: Introduction

This appendix covers the methods and assumptions used to compute flexural deformation from the experimental test data. The methods used are based on traditional mechanics, where the lateral deformation is product of the total rotation and the distance from the point of interest to the center of rotation. Variations on the method used to examine the test data were focused on the way the center of rotation is found. The assumptions used for the center of rotation calculations and their associated problems are covered in the following sections.

A3.1: Calculation of Flexural Deformation

Flexural deformation is calculated using classical beam theory. The mechanics of flexural deformation is well known and documented; however, nomenclature used by Massone & Wallace [RA3.1] will be used in order for a uniform appearance with other experimental tests and reports on reinforced concrete shear walls. Flexural deformation is computed using the following equation:

$$\Delta_{\text{Flexure}} = \alpha h \theta \quad (\text{Eq. A3.1})$$

Where ' Δ_{Flexure} ' is the lateral deformation from flexure, 'h' is the height of the wall section in question, and ' θ ' is the total rotation of the height segment in question. Lastly ' α ' is a non-dimensional factor equal to:

$$\alpha = (h_{\text{Center Of Rotation}} - h) / (h)$$

Refer to figure A3.1 for a figure illustrating these terms and equations.

A3.2.1: Center of Rotation: Individual Sections of Wall Height

Axial strain was computed for each sensor type with a range of methods. Each method used to calculate axial strain can be placed into two separate categories: strain computed for a single height and strain computed over an average height specifically.

Strains computed for a single height include strain gages and the Krypton data. The strains computed with the Krypton were done so by averaging the average strains from above and below the LED in question. This is not necessarily the strain at a single point, but the strains calculated for that point represent that point alone. The length over which that strain would be a representative average is not known (especially true for LEDs bordering non-uniform sections of the LED field). For this reason, the Krypton data is grouped with the strain gages as sensors which report strain for a specific height.

The subsequent curvature calculated with these sensors is again representing a single height. The center of rotation for these types of sensors is based on the curvature geometry over the wall height by assuming a straight line between the known curvatures. The center of rotation at each height is calculated by finding the centroid of the curvature distribution of all geometric sections below the height of interest. This method is illustrated in figure A3.2. The significance of the triangular portions was found to be relatively negligible to the overall results. However, these sections were still included in the interest of being as precise as possible. Each geometric section, or wall height segment, is computed individually and then combined at the end to get the total center of rotation at all applicable wall heights.

The second type of sensor is the string pot. This sensor was used to calculate average strain over a known distance. Moreover, the total rotation from this sensor was already known from fitting a linear trend line through the recorded string pot displacements. The characteristics of the string pot instrument require an assumption to be made about the center of rotation between the points at which the string pot was attached to the wall.

A triangular curvature distribution was assumed to be true for the elastic range. Simple mechanics, along with the known total wall height, were used to solve the centroid of the curvature distribution between any two heights of interest. Refer to figure A3.3 for an illustration and proof of the equation used to calculate the centroid of the curvature distribution/ center of rotation. The center of rotation for each string pot segment was calculated with the α factors shown in plot A3.4.

The α factor is essentially 0.5 when the height segment used is less than 80", further reinforcing the reasons for which the triangular portion of the curvature distribution used for the Krypton and strain gage data was negligible.

A3.2.2: Center of Rotation: End Zones

The instrumentation used in this experiment has certain limitations. The curvature at the extreme bottom (foundation interface) and the curvature above the top string pot attachment (loading channels) cannot be determined with the Krypton or string pots. For this reason, the curvatures adjacent to these end zones are assumed to be the average curvature for the length over which it was calculated, as well as the remaining height to the end zone. This approach allows the calculated flexure to be closer to the 'true' behavior, but will still return flexural deformations slightly smaller than actual. This approach is conservative because the most influential height section, the wall interface, is underestimated. The contribution of the top of the wall will be slightly overestimated, but is also the least influential section in the entire wall.

The approach is conservative due to the fact that the curvature of the base is larger than the curvature bellow the loading channels by over one order of magnitude. Secondly, the distance to the center of rotation at the base is again larger than the distance to the center of rotation from the missing top segment by an order of magnitude. The top segment is

indeed negligible when compared to the base, but is included for uniformity of approach and the highest reasonable precision that can be achieved.

A3.2.3: Total Center of Rotation

Once the height of the center of rotation is known for each wall height section (segments between instruments), the total center of rotation can be found for each sensor height location. This is done by taking a weighted average of all segmental centers of rotation heights, weighted by the total rotation of the wall height segment. All segments below the height in question are included for the total center of rotation of the height in question.

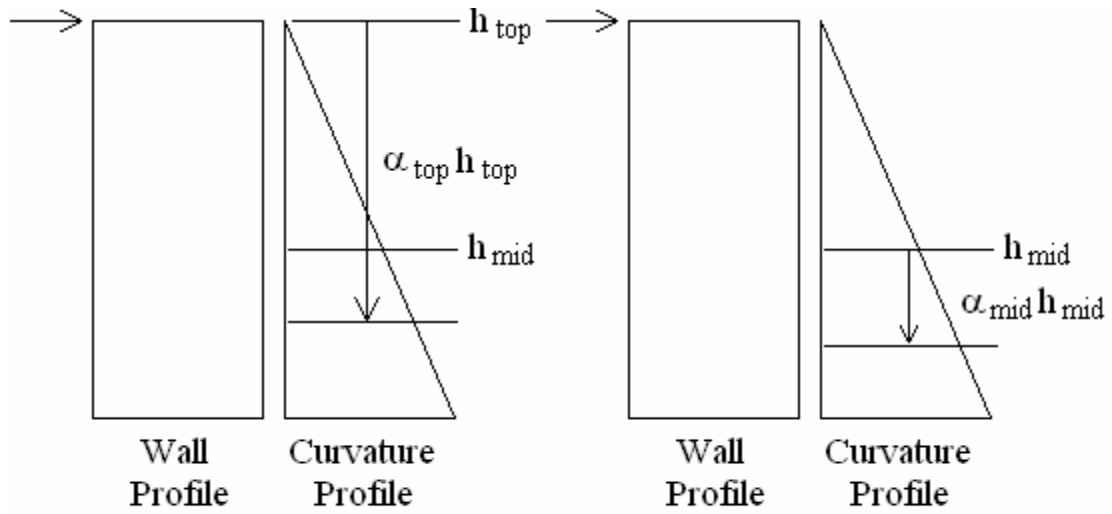
A3.3: Assumption Limitations

The main assumption made in this chapter was the center of rotation for the string pot data. The assumptions made for the string pot data were based on an elastic curvature profile. Inelastic behavior will create a curvature profile that is much more horizontal than it was in the elastic range. Inelastic behavior will lead to a center of rotation that is lower than the elastic assumption for any wall height segment undergoing yielding. This change in the segmental center of rotation is not accounted for with the assumptions used. Flexural deformation will be reduced from this limitation of the calculation method by means of a smaller distance from the center of rotation to the top height. However, this reduction is thought to be quite small when considering the relatively small wall height segments.

BIAX was used to quantify the maximum possible error for the center of rotation location. Alpha factors were calculated for three load levels with various degrees of yielding up the wall height. Alpha factors were computed for wall height segments approximately equal to the actual string pot attachment coordinates by numerically integrating the BIAX values. These BIAX alpha factors are compared to the idealized alpha factors used for the string pot analysis. Plots of these comparisons are found in figures A3.5a, b, & c. In

addition to these comparisons, the total alpha for the entire wall height was found for the three load levels. The maximum percent error between the BIAX values and the idealized assumed values was as large as -0.4%. Refer to figure A3.6 for a plot of applied top load v. expected % error.

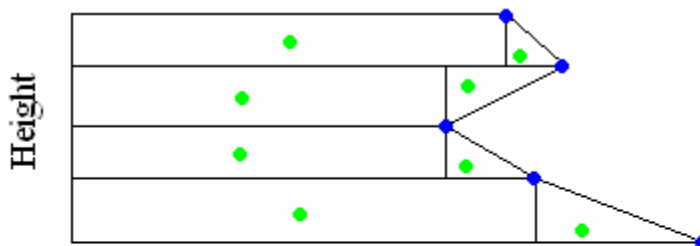
The assumptions used to calculate the center of rotation for the string pots can lead to an underestimation of flexural deformation by less than a half percent in the highly inelastic range. The assumptions made about the center of rotation for the string pot data does not create an unreasonable possible error. This is true far into the inelastic range. For these reasons, the assumptions are deemed acceptable and flexural deformation calculations can be trusted.



$$\Delta_{\text{flexure top}} = \alpha_{\text{top}} h_{\text{top}} \theta_{\text{top}}$$

$$\Delta_{\text{flexure mid}} = \alpha_{\text{mid}} h_{\text{mid}} \theta_{\text{mid}}$$

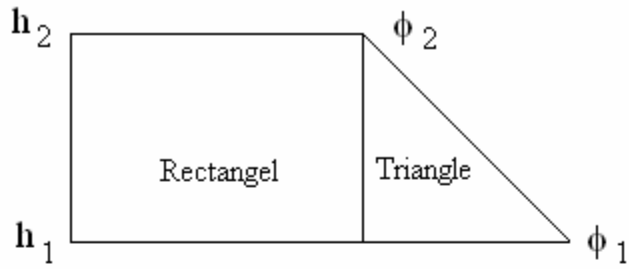
Figure A3.1: Illustration of terms used to compute flexural deformation



Fictitious Curvature Distribution

- Centroid of Basic Geometric Section
- Known Curvature at a Single Point

Figure A3.2: Illustration of Known Point Center of Rotation Method



$$\alpha_{\text{Rectangel}} = (1/2)$$

$$\alpha_{\text{Triangle}} = (2/3)$$

$$\theta_{\text{Rectangel}} = \phi_2 (h_2 - h_1)$$

$$\theta_{\text{Triangle}} = (1/2)(\phi_2 - \phi_1)(h_2 - h_1)$$

$$\alpha = \frac{\alpha_{\text{Rectangel}} \theta_{\text{Rectangel}} + \alpha_{\text{Triangle}} \theta_{\text{Triangle}}}{\theta_{\text{Rectangel}} + \theta_{\text{Triangle}}}$$

$$M_1 = P (h_{\text{top}} - h_1) \quad M_1 = EI \phi_1$$

$$M_2 = P (h_{\text{top}} - h_2) \quad M_2 = EI \phi_2$$

$$\phi_1 = \phi_2 \frac{(h_{\text{top}} - h_1)}{(h_{\text{top}} - h_2)}$$

$$h_{\text{top}} = 240 \text{ inches}$$

$$\alpha = 1 - (1/3) \frac{(720 - h_1 - 2 h_2)}{(480 - h_1 - h_2)}$$

Figure A3.3: Calculation of alpha for various heights

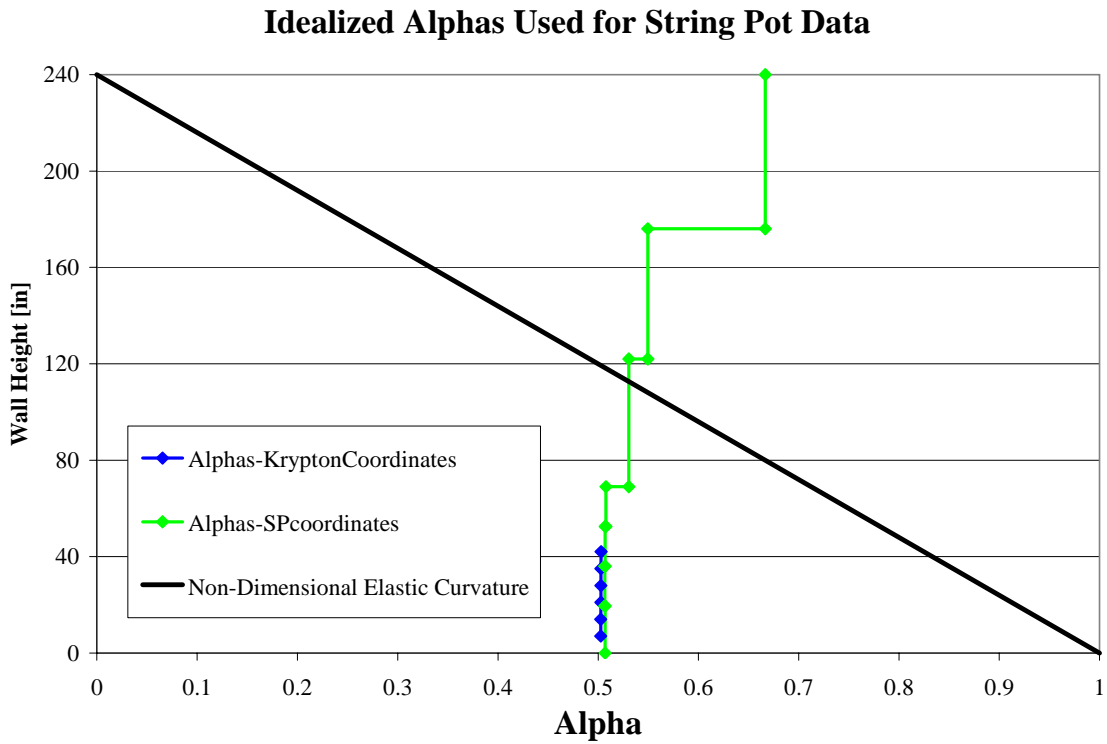


Figure A3.4: Alphas calculated for each known string pot segment.

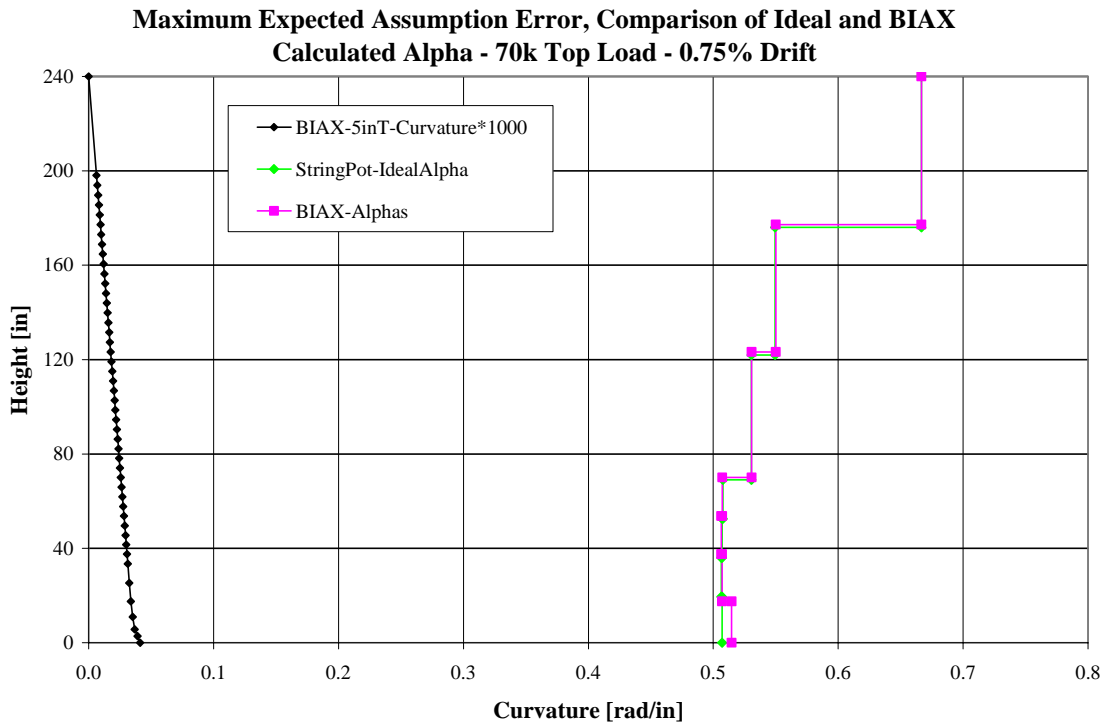


Figure A3.5a: Alphas calculation assumptions compared to BIAX calculated values

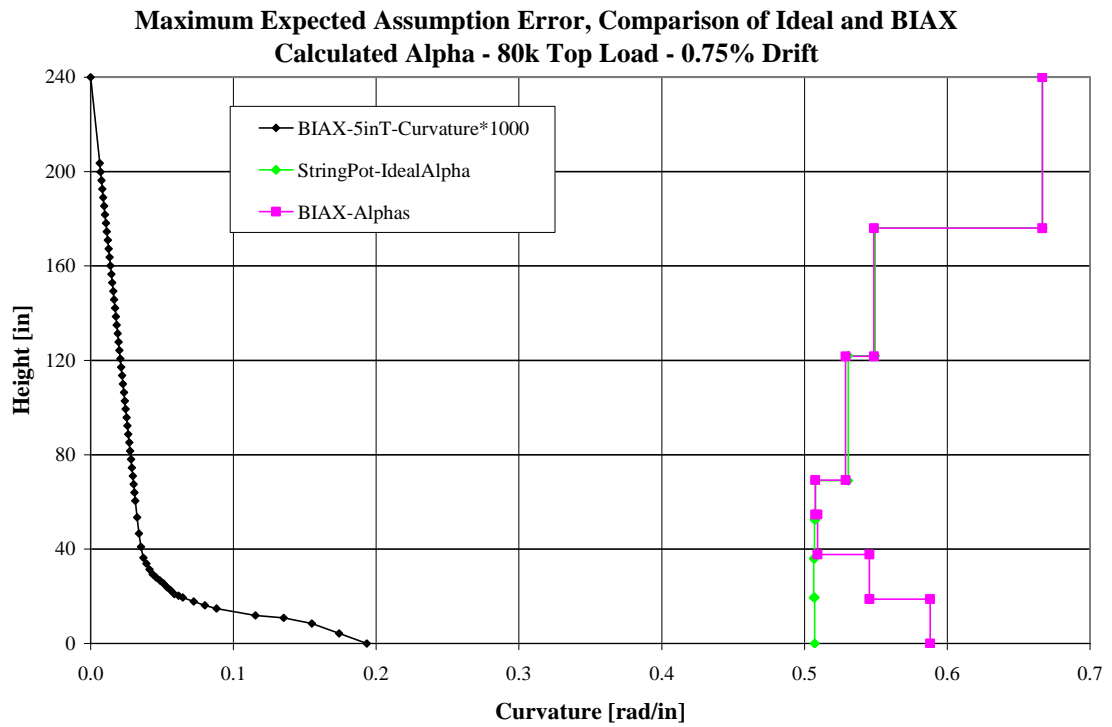


Figure A3.5b: Alphas calculation assumptions compared to BIAX calculated values

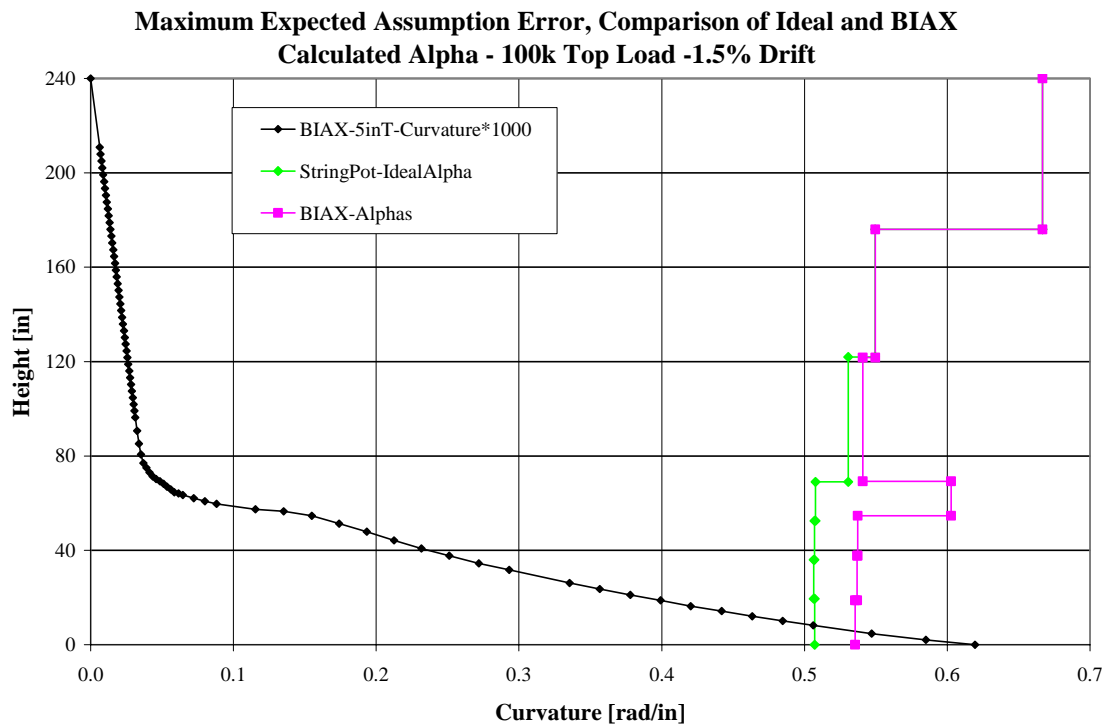


Figure A3.5c: Alphas calculation assumptions compared to BIAX calculated values

**Percent Error of Total Height Cumulative Alpha Error,
BIAX results versus Assumption Used**

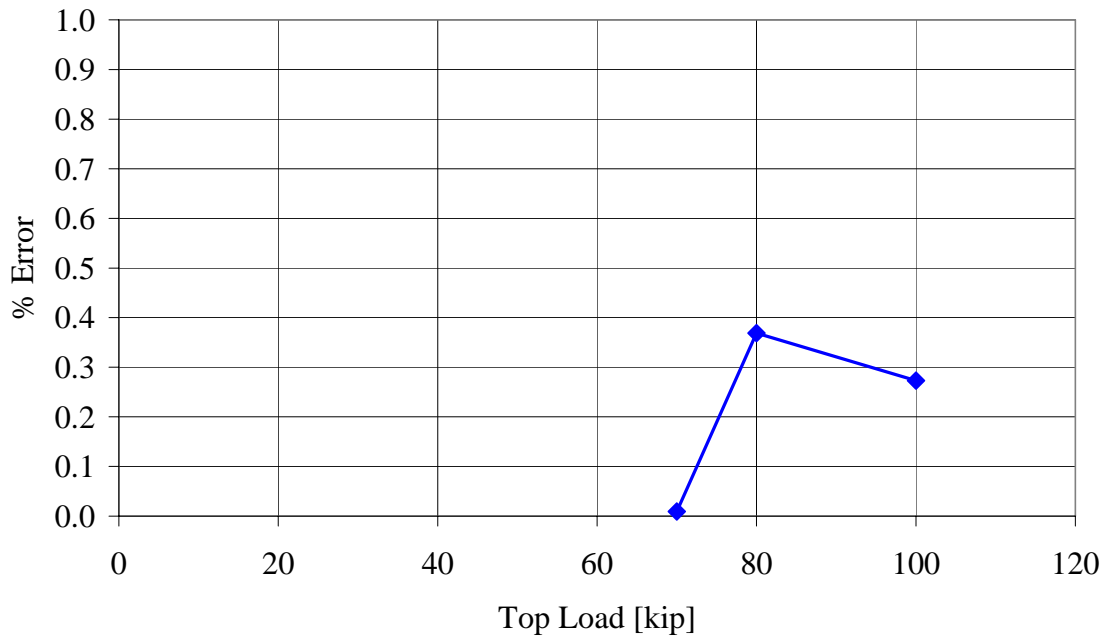


Figure A3.6: Alphas calculation assumptions compared to BIAX calculated values

[RA3.1] Massone, L. and Wallace, J., 2004 "Load-Deformation Responses of Slender Reinforced Concrete Walls," *ACI Structural Journal*, V.101, No.1, Jan-Feb, pp. 103-1

Appendix 4: Calculation of Shear Deformation

A4.0: Introduction

The goal of this appendix is to cover the methods used to compute the shear component of lateral deformation of the test specimens. The assumptions used and their impact on the final result are discussed and quantified. This is done with string pot, strain gage, and Krypton data. In general, the different methods and sensors used to compute the shear component of lateral deformation returned very similar results. Close agreement of all resulting shear calculations suggests that the methods used are precise and reliable for quantifying shear deformations.

A4.1.0: Calculation of Shear Deformation

Shear deformation was calculated in a different way for each sensor used. Shear deformation from string pot data was determined with similar methods used by Massone and Wallace [R.A4.1]. An isoperimetric quadrilateral finite element approach was used for the Krypton data. Finally, the shear strains calculated with the string pot and Krypton data are compared to strain readings from gages on transverse reinforcement through the web of the test structures.

A4.1.1: String Pot Calculations

Shear deformation from string pot data was found by using an instrumentation model from experiments performed by several researchers. The model used particularly by Massone and Wallace in reference [R.A4.1] was used for this experiment. This model is an 'x' configuration of string pots, spanning diagonally across certain segments of the wall height. The length over which the string pots spanned was changed over the wall height, in order to have higher resolution at the base of the wall. Illustrations of this instrumentation setup can be seen in figures A4.1a, b, & c.

Previous models used by various researchers only accounted for the change in length of the diagonal string pots in the computation of lateral deformation from shear. This is shown in figure A4.1a. Wallace discussed the need to incorporate changes in the undeformed geometry from flexure. Ignoring this change in geometry can lead to an overestimation of shear deformation. This overestimation problem is addressed with Massone and Wallace's method, shown in figure A4.1b. This model is used by first computing the total lateral deformation of each wall height segment spanned by the string pots. Shear deformation is then assumed to be the remaining lateral deformation when subtracting the flexural deformation from the total deformation. The methods used by Massone and Wallace are discussed in appendix and chapter 9. The total lateral deformation and resulting shear deformation are calculated with the following:

$$U_{\text{total}} = \frac{\sqrt{D_1^{\text{meas}^2} - (h + V_2)^2} - \sqrt{D_2^{\text{meas}^2} - (h + V_1)^2}}{2} \quad \text{Eq (A4.1)}$$

$$U_{\text{shear}} = U_{\text{total}} - U_{\text{flexure}} \quad \text{Eq (A4.2)}$$

Where U_{total} is the average total lateral deformation across the wall length of the wall height segment, h is the average height of the undeformed element, V is the change in vertical location between the top and bottom string pot attachments for each end of the wall height segment, and D^{meas} is the measured diagonal distance between string pot wall attachments.

Massone and Wallace's method accounts for the change in geometry from flexure by measuring the change in vertical locations of the diagonal string pot attachments. This change in vertical location is only the incremental change over the height segment in question, for both the side of the wall in tension and compression. This method is thought to only accurately capture the shear deformation of the bottom wall height segment,

where the change in vertical location of the bottom string pot attachments is negligible. Massone and Wallace’s method underestimates the total lateral deformation when the cumulative vertical displacement is no longer negligible. This creates an increasingly poor estimation of the correction from vertical displacement at higher sections of the wall. For this reason, a ‘cumulative vertical deformation’ method is used. This method uses the same principles as Wallace’s method, but accounts for the additional effects of the cumulative vertical displacements of each string pot attachment. This method is illustrated in figure AS.1c. The total deformation is determined with the following:

$$\begin{aligned}
 U_{\text{total}} = & \frac{\sqrt{(D_{\text{meas}_1})^2 - (h + V_{\text{top}_2} - V_{\text{bot}_1})^2}}{2} \\
 & - \frac{\sqrt{(D_{\text{meas}_2})^2 - (h + V_{\text{top}_1} - V_{\text{bot}_2})^2}}{2}
 \end{aligned}
 \tag{A4.3}$$

Where U_{total} is the average total lateral deformation across the wall length of the wall height segment, h is the average height of the undeformed element, V is the total vertical displacement of the string pot attachment in question, and D^{meas} is the measured diagonal distance between string pot wall attachments. The shear displacement is again the remaining displacement when subtracting the flexural component from the total calculated displacement. The total deformation calculated at the bottom and top of the wall are used to linearly interpolate what the displacement would be if the bottom 3” and top 10” were included in the spans of the string pot ‘x’ configurations.

The total deformation of the test structures was computed with both Massone and Wallace’s method and the ‘cumulative vertical displacement’ method. These two methods are compared in figures A4.2a, & b. These figures depict the total deformation calculated with the two methods for the elastic limit of RWN with each boundary element in tension. It can be seen from these figures that Massone and Wallace’s method performs worse over wall height. This is again due to increasingly larger cumulative

vertical displacements that are not being accounted for. The total deformation of the ‘cumulative vertical displacement’ method seems to be more consistent over the wall height. This is verified by the total external deformation measured from other string pots. The total external displacement is larger than the ‘x’ configuration methods from the effects of strain penetration. These figures show that the ‘cumulative vertical displacement’ method is indeed the best approach for determining the total lateral displacement and resulting shear component of lateral deformation.

A4.1.2: Cracking Effects

The total deformations calculated with the ‘x’ configuration of string pots include the effects of cracking. Cracks that develop across the length of the wall will cause the lateral displacement of the end of the wall in tension to be smaller than the end of the wall in compression. The end in compression is larger than the tension end by the sum of the crack widths across the wall length, referred to as the lateral expansion of the wall. The average lateral displacement of the wall at each height is the average of these two sides, or the tension side plus half of the expansion measured from cracking. This average displacement is what the ‘x’ configuration methods are measuring. The external string pot displacements are adjusted with the horizontal expansion string pot measurements to match this result. This is an important step when comparing each wall, as the orientation of RWC is the opposite of the other two walls in the test frame. Displacements of the wall when the No.5&6 boundary element are in tension will be smaller than the average for RWN and RWS. The opposite is true for RWC. This can lead to considerable errors when comparing the global string pot readings and not the average lateral displacements.

A4.1.3: Krypton Calculations

Shear deformation was calculated with the Krypton data by means of an isoperimetric quadrilateral finite element. The shear strain of the element can be calculated by knowing the undeformed coordinates of the element in question, along with the nodal

displacements of the element. The approach used to determine the axial and shear strains were based on the methods covered in appendix 5. The equations necessary to determine the axial shear strains are also given in appendix 5.

The element sizes used to determine the shear strain are based on the maximum noise levels observed for the Krypton data over a half hour period of time where no load was applied to the test structures. The minimum element size for calculating axial strain was determined to be 20" by 20" in order to limit the possible strain error to 5% of the yield strain. Axial strain is essentially a single degree of freedom problem with two sources of error, the vertical displacements of the top and bottom sensors. Shear strain is a much more complex problem. Shear strain is a two dimensional calculation, with eight possible sources of error (lateral and vertical displacements of the four element corners). For this reason, the element size is increased. The elements used to compute shear strain are shown in figures A4.3a, b, & c.

Shear strain calculated at a single LED, from multiple elements is averaged in the same manor as the axial strain. This is done in order to compare the strain results of the krypton to that of the string pots and strain gages. The resulting shear deformation is computed by first averaging the shear strains calculated across the wall length of the height in question. This is done by a weighted average of elements by their dimensions. The average shear strain over each height segment, defined by the finite element group height, is multiplied by the average height of the elements to determine the shear deformation. The total shear deformation is then found by summing the shear deformations from all heights below the height in question. Not enough LEDs were present at the top of the LED field for RWC and RWS. In this case, the strain at the top of the LED field was used to compute the additional total shear deformation at the top of the LED field. This was necessary for comparisons to flexural calculations with the Krypton, as well as returning a shear deformation at a height closer to the string pot attachments for comparison of sensors.

A4.1.4: Strain Gage Calculations

Strain gages were placed on the transverse reinforcement for each wall specimen. The locations of these instruments is covered in chapter 3. The axial strain of these reinforcing bars is not necessarily the shear strain of the entire wall section. The test specimens resist shear forces by several mechanisms, depending on the level of damage in the wall. A cracked section carries shear forces primarily through the axial forces in the transverse reinforcement, aggregate interlock, and compression zone friction of the concrete. The forces carried in the transverse reinforcement are smaller than the total shear forces carried by the entire wall cross section. This leads to smaller strains in the transverse reinforcement when compared to the wall as a whole. For this reason, the axial strains recorded for the transverse reinforcement will be used to verify the results of the other sensors and not for computation of shear deformation. The shear strains recorded by the transverse reinforcement are reported as negative for the No.9 boundary element in tension. This was done in order to match the sign conventions of the other two sensors and not because the reinforcement was in compression.

A4.1.5: Shear Strain Across Wall Length

Shear deformation was computed as an average across the entire wall length, across the half of the wall in tension, and the half of the wall with one end in compression. This was done to show that the effects of shear cracking creates larger deformations in the section of the wall which is spanned by shear cracks. Larger shear strains were always observed in the half of the wall in tension with the Krypton. This was generally true for the string pots but some data points do not follow this hypothesis. This is thought to be caused from complicated cracking patterns that may not necessarily be captured by the small resolution of data points used to calculate shear deformation. Good agreement between all sensors was almost always observed when averaging the whole length of the wall. This method is chosen for the calculation of shear deformations, as the behavior of the

wall as a whole is of interest. These local effects are still of interest in evaluating each wall individually and are shown in chapter 11.

A4.2: Sensor Comparison of Shear Strain Calculations

The shear strain computed by the three different sensors is compared over the wall height for select loading ramps of interest. The shear strain from the strain gages and Krypton is known from the direct calculations. The shear strain for the string pots is calculated by dividing the change in shear deformation over a wall height segment by the change in height of the wall height segment in question. Refer to figures A4.4a, b, & c for the sensor comparisons of shear strain for various loading ramps of interest.

These figures show good agreement between the instruments, with the Krypton typically returning slightly larger strains at the base of the wall. As expected, the strains recorded from the shear reinforcement is smaller than the results of the other sensors. The strains in the shear reinforcement are again used to simply show that the results of the string pots and Krypton are reasonable. The shear strains of the transverse reinforcement is smaller for several reasons. Other shear resisting mechanisms are present that take some of the shear load, reducing the strain in the transverse reinforcement. In addition, cracks that span over multiple transverse bars will distribute the loads in the bars which the crack spans, making it difficult to quantify the overall shear strain in the wall. Shear is indeed a complicated phenomena in concrete from the effects of cracking. The localized effects on the shear reinforcement create an unreasonable result for computing shear deformation but do allow the results of the string pots and Krypton to be qualified. The results of the independent shear calculation methods will be used to create an envelope of the possible 'true' responses of the walls.

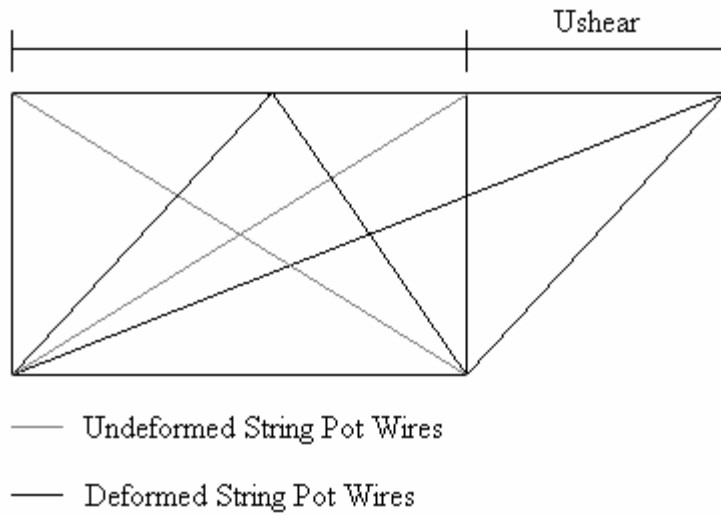


Figure A4.1a: Uncorrected String Pot Model for Shear Deformations

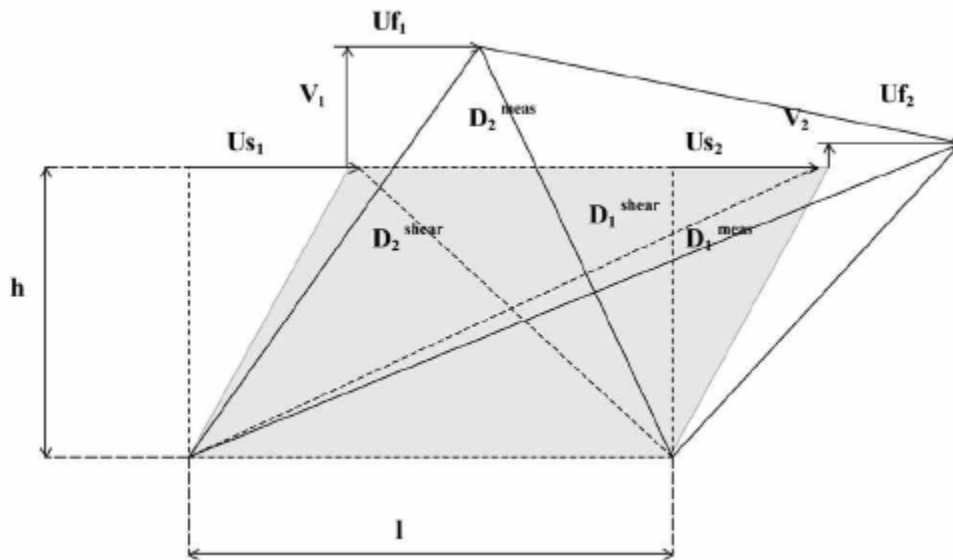


Figure A4.1b: Massone and Wallace's String Pot Model from [R.A4.1]

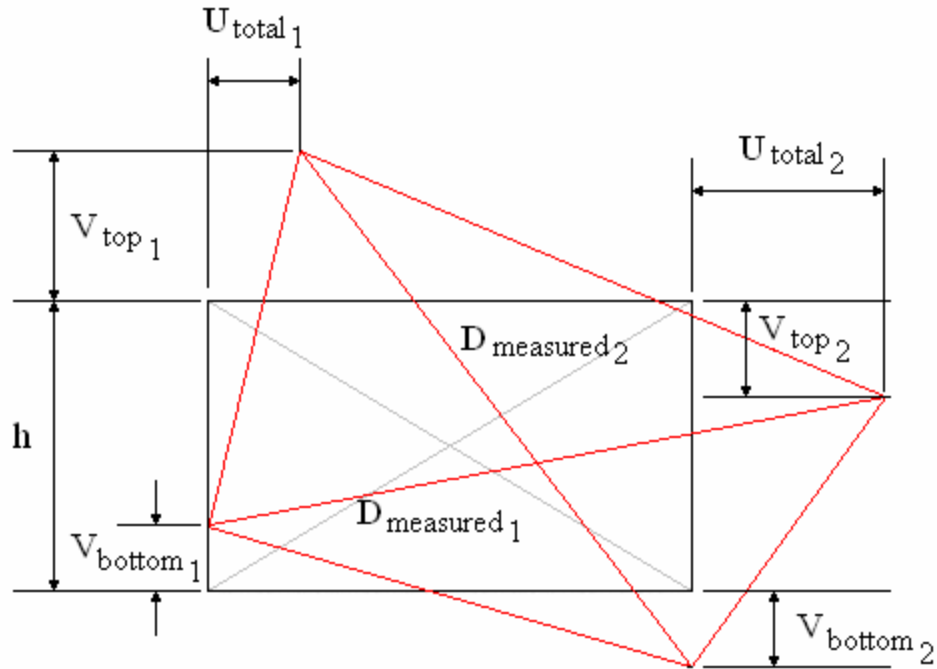


Figure A4.1c: Cumulative Vertical Displacement Method

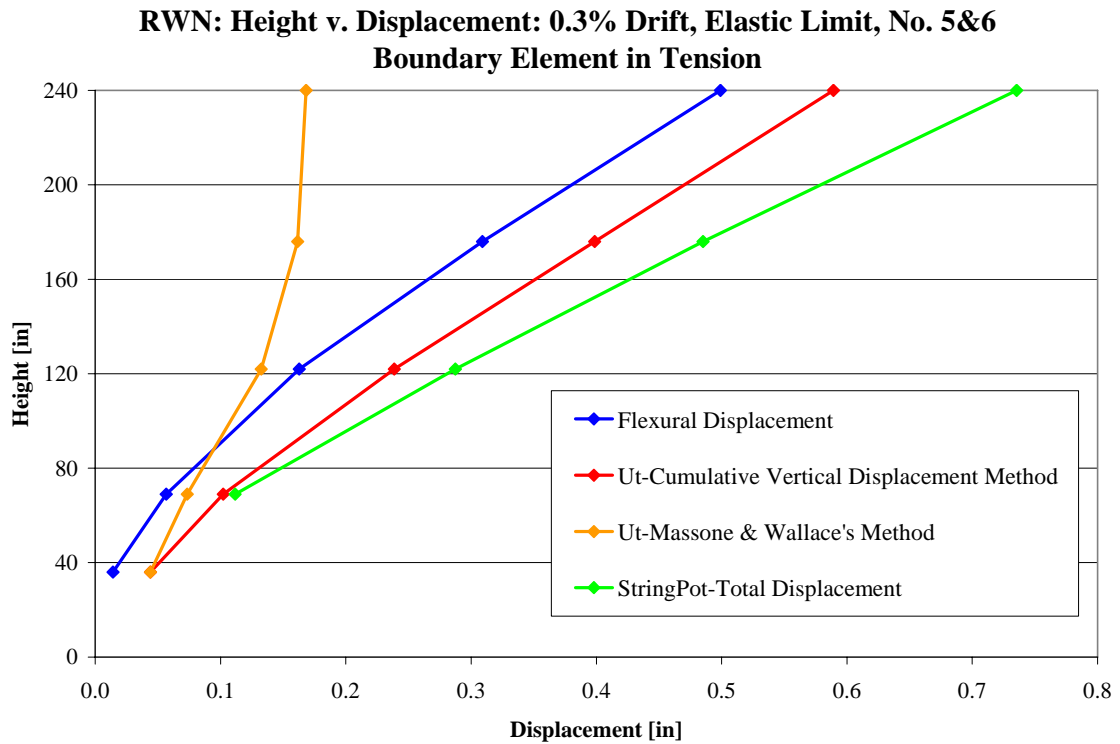


Figure A4.2a: Comparison of total deformation calculation methods.

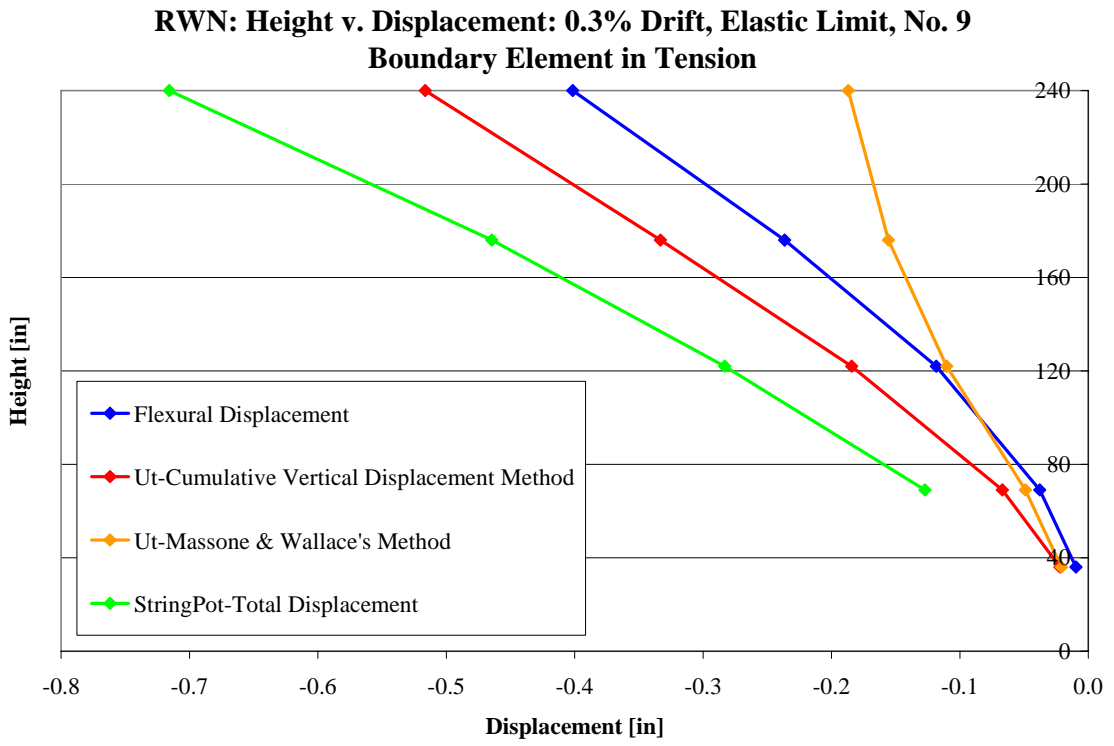


Figure A4.2b: Comparison of total deformation calculation methods.

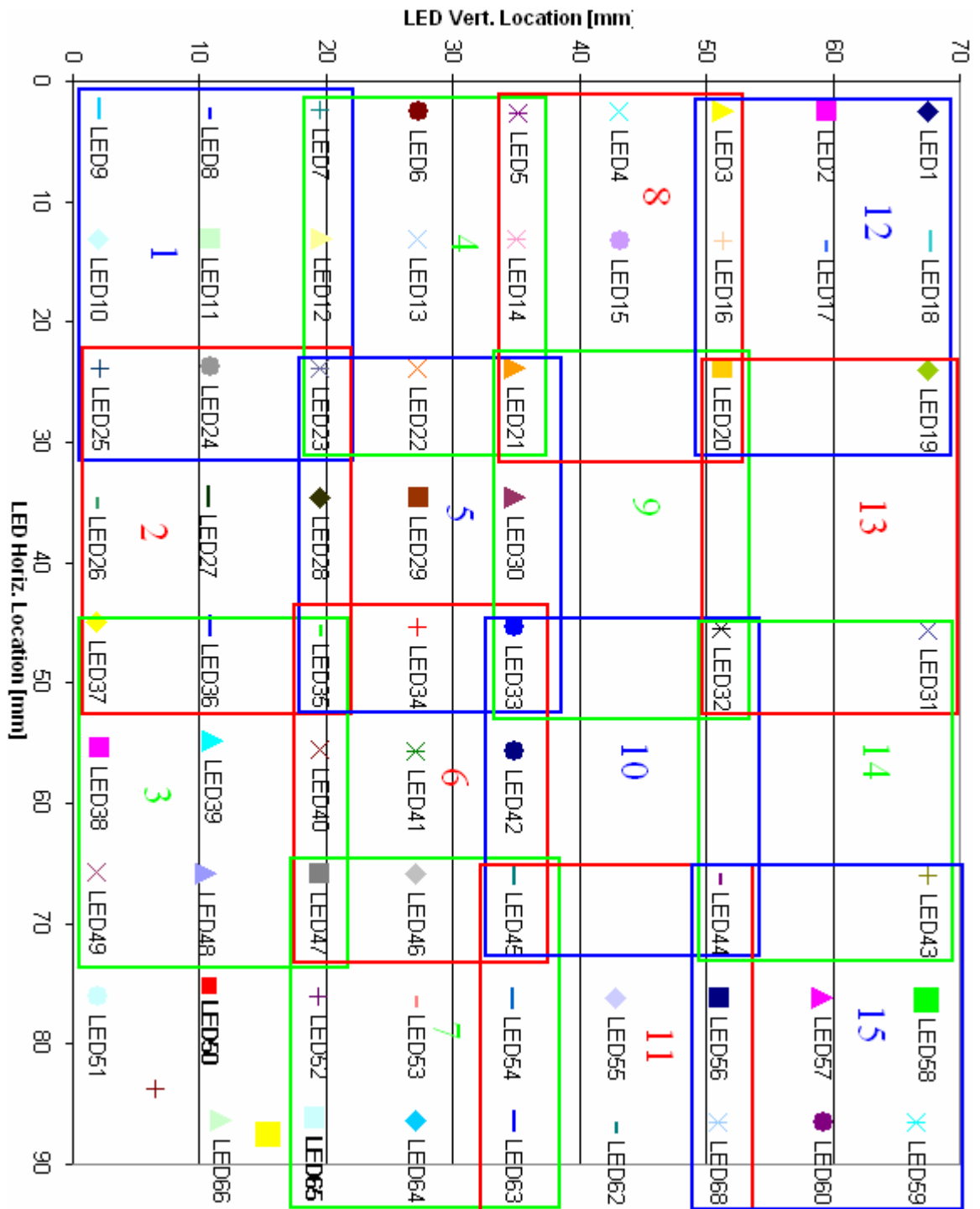


Figure A4.3a: Krypton Elements used for shear strain of RWN

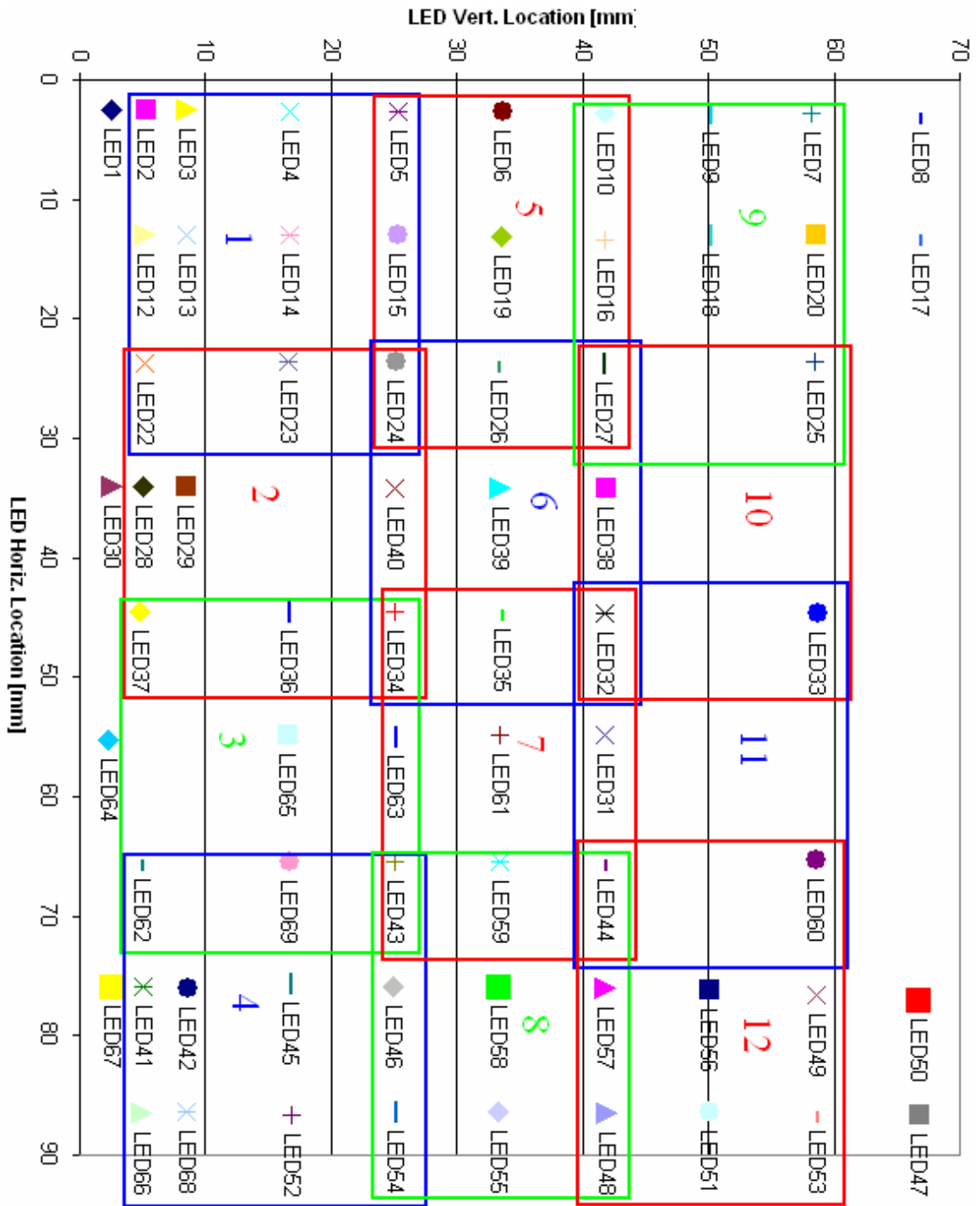


Figure A4.3b: Krypton Elements used for shear strain of RWC

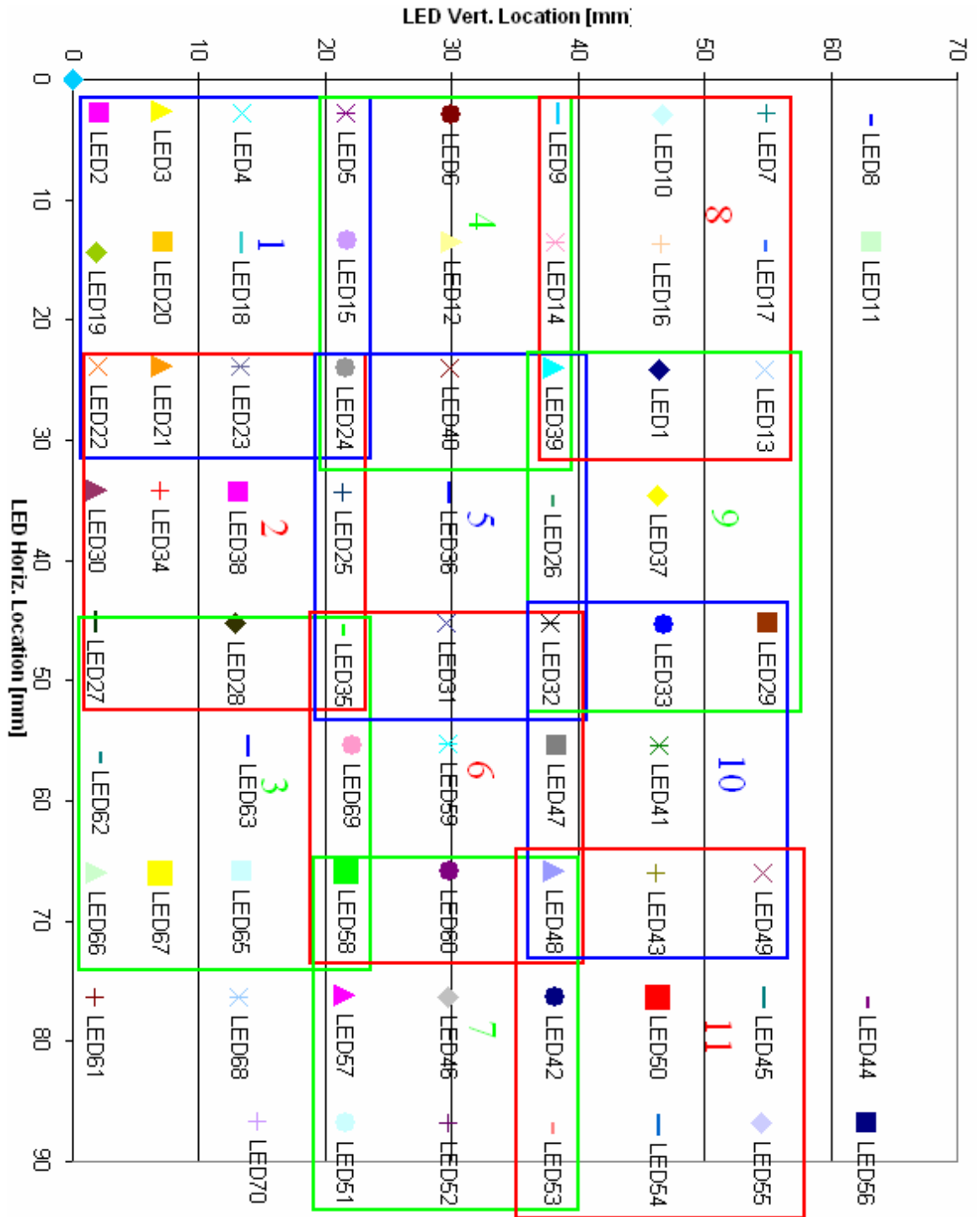


Figure A4.3c: Krypton Elements used for shear strain of RWS

**RWN: Height v. Shear Strain, First Cycle to 0.3% Drift:
Elastic Limit**

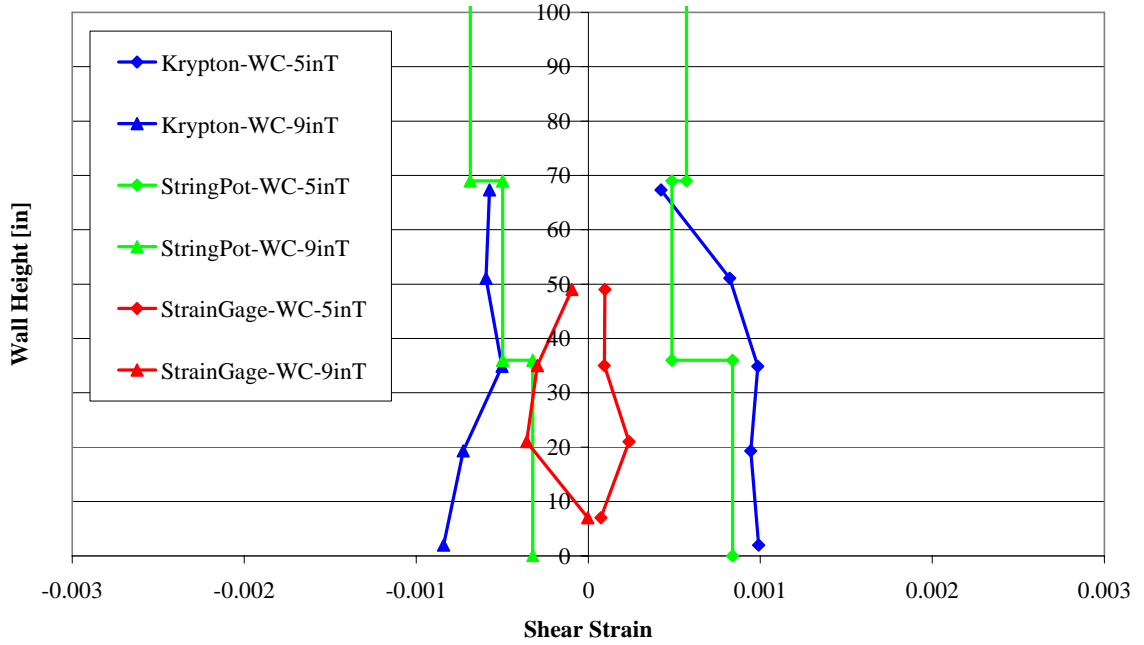


Figure A4.4a: Comparison of shear strains calculated from various sensors: RWN

**RWC: Height v. Shear Strain, First Cycle to 0.3% Drift:
Elastic Limit**

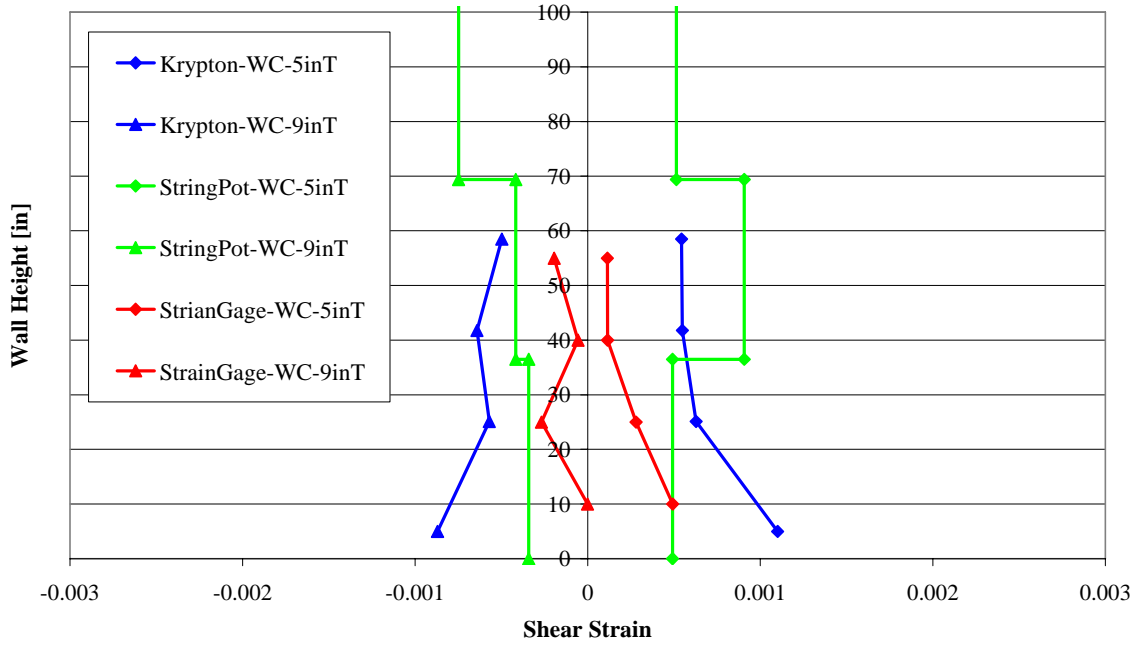


Figure A4.4b: Comparison of shear strains calculated from various sensors: RWC

**RWS: Height v. Shear Strain, First Cycle to 0.3% Drift:
Elastic Limit**

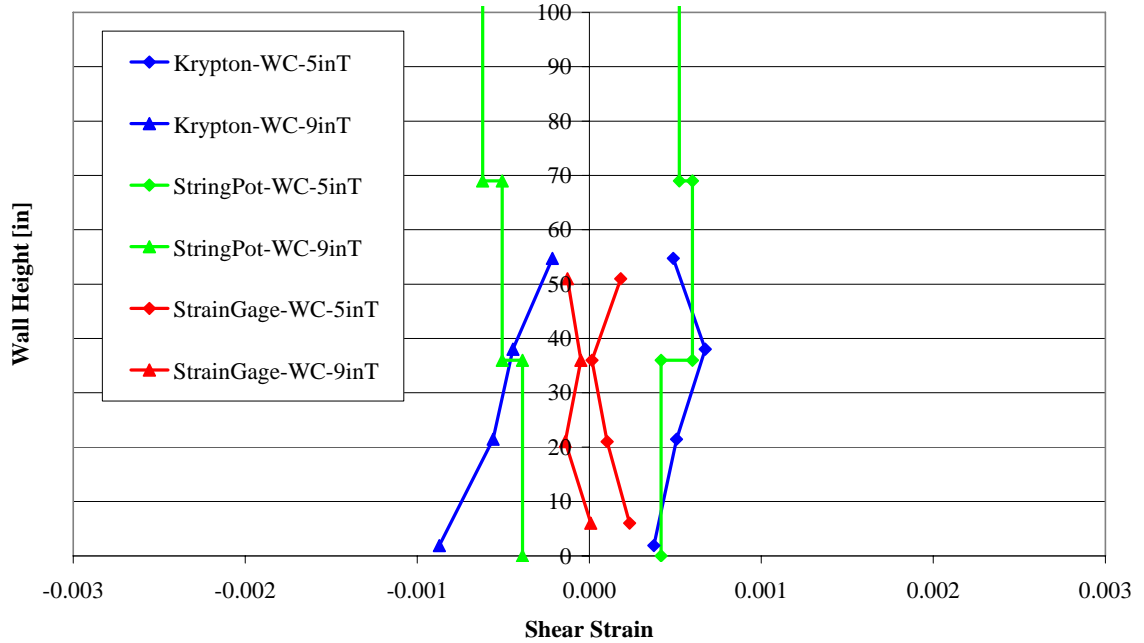


Figure A4.4c: Comparison of shear strains calculated from various sensors: RWS

[RA4.1] Massone, L. and Wallace, J., 2004 “Load-Deformation Responses of Slender Reinforced Concrete Walls,” *ACI Structural Journal*, V.101, No.1, Jan-Feb, pp. 103-113.

Appendix 5: Calculation of Strains With Krypton Data

A5.0: Introduction

This appendix covers the methods used to compute axial and shear strains with the Krypton sensor. A simple isoperimetric mapping procedure is used to develop the relationship between the nodal displacements in a four node quadrilateral element and the corresponding normal and shear strains. The procedure used to determine the relationship between nodal displacements and strains is that given by Logan [R.A5.1]. This text book on the finite element method discusses the theory used in great detail to develop the procedures used. This appendix simply covers the essential material in order to reproduce the results of this report. The reader is referred to [R.A5.1] for the comprehensive approach to the methods discussed in the following sections. The following procedure is entirely from [R.A5.1], the equations are changed only to reflect the naming convention of the global Cartesian coordinate system of the test structures.

A5.1: Strain Calculation Procedures

The following text describes the methods used to determine strains for a rectangular plane stress element. Strains are computed by first converting the global coordinate system of the Krypton data in to the ‘natural coordinate system’. The natural coordinate system is square element with each corner ‘node’ having coordinates of positive or negative unity. This conversion is shown in figure A5.1. This conversion eliminates problems that arise from starting with an imperfect square from LED attachment to the wall. Isoperimetric mapping is done with shape functions, defined as such:

$$N_1 = (1-s)(1-t)/4 \quad (\text{Eq A5.1})$$

$$N_2 = (1+s)(1-t)/4 \quad (\text{Eq A5.2})$$

$$N_3 = (1+s)(1+t)/4 \quad (\text{Eq A5.3})$$

$$N_4 = (1-s)(1+t)/4 \quad (\text{Eq A5.4})$$

Where s , and t are the natural coordinates of the isoperimetric quadrilateral. The variables s and t are set to the values shown in figure A5.1 in order to determine the shape functions for each quadrilateral node ($s=1$ and $t=1$ for node #3). The isoperimetric conversion between global Cartesian coordinates and natural coordinates can be achieved by multiplying the following matrix with the global Cartesian coordinate vector:

$$\mathbf{N} = \begin{bmatrix} \mathbf{N1} & 0 & \mathbf{N2} & 0 & \mathbf{N3} & 0 & \mathbf{N4} \\ 0 & \mathbf{N1} & 0 & \mathbf{N2} & 0 & \mathbf{N3} & 0 \end{bmatrix} \quad \text{Eq (A5.5)}$$

$$\{x \ z\}^T(s, t) = [\mathbf{N}]\{x_1 \ z_1 \ x_2 \ z_2 \ x_3 \ z_3 \ x_4 \ z_4\}^T \quad \text{(Eq A5.6)}$$

Where $\{x \ z\}^T(s, t)$ refers to the natural coordinates of the node in question and $\{x_1 \ z_1 \ x_2 \ z_2 \ x_3 \ z_3 \ x_4 \ z_4\}^T$ refers to the global Cartesian coordinate vector. The same conversion can be applied to the nodal displacements of the Cartesian coordinate system to the nodal displacements in the natural coordinate system. Once the nodal displacements are converted, the relationship between strain in the normal x direction, z direction, and shear strains can be computed. This process requires partial differentiation of the relationships between Cartesian coordinates and natural coordinates. The reader is referred to [R.A5.1] for this process due to its tedious nature and relative unimportance for reproducing the results of this report. The relationship between the primary strains and nodal displacements is given by the following equation:

$$\{\varepsilon_x \ \varepsilon_z \ \gamma_{xz}\}^T = [\mathbf{B}]\{u_1 \ v_1 \ u_2 \ v_2 \ u_3 \ v_3 \ u_4 \ v_4\}^T \quad \text{(Eq A5.7)}$$

Where $\{\varepsilon_x \ \varepsilon_z \ \gamma_{xz}\}^T$ is the vector containing the lateral strain: ε_x , vertical strain: ε_z , and shear strain: γ_{xz} . The terms u and v refer to the lateral and vertical displacements of the four nodes. The matrix \mathbf{B} , is the resulting relationship between the nodal displacements and strains when the partial derivatives for strain are applied and conversion between the coordinate systems with the Jacobian matrix. Reference [R.A5.1] gives simple ways to

determine the ‘B’ matrix from the undeformed nodal coordinates of Cartesian quadrilateral and the point of interest in the natural coordinate system. The ‘B’ matrix can be determined by performing the following computations:

$$[B] = (1/|J|)[[B_1] [B_2] [B_3] [B_4]] \quad (\text{Eq A5.8})$$

Where $|J|$ is the determinant of the Jacobian matrix. This determinant is computed with the following operation:

$$|J| = (1/8)\{X_c\}^T \begin{bmatrix} 0 & 1-t & t-s & s-1 \\ t-1 & 0 & s+1 & -s-t \\ s-t & -s-1 & 0 & t+1 \\ 1-s & s+t & -t-1 & 0 \end{bmatrix} \{Z_c\} \quad (\text{Eq A5.9})$$

Where $\{X_c\}$ and $\{Z_c\}$ refer to the nodal Cartesian coordinates in the x, and z direction, respectively. Next, the four components of the right hand side of the ‘B’ matrix (Eq AK.8) can be calculated with the following method:

$$[B_i] = \begin{bmatrix} a(N_{i,s}) - b(N_{i,t}) & 0 \\ 0 & c(N_{i,t}) - d(N_{i,s}) \\ c(N_{i,t}) - d(N_{i,s}) & a(N_{i,s}) - b(N_{i,t}) \end{bmatrix} \quad (\text{Eq A5.10})$$

Where ‘i’ refers to nodes 1, 2, 3, and 4. The terms $(N_{i,s})$ and $(N_{i,t})$ refer to the derivatives of equations AK.1 through AK.4 with respect to the natural coordinate variables s and t. The coefficients a, b, c, and d are defined as follows:

$$a = (1/4)[z_1(s-1) + z_2(-1-s) + z_3(1+s) + z_4(1-s)] \quad (\text{Eq A5.11})$$

$$b = (1/4)[z_1(t-1) + z_2(1-t) + z_3(1+t) + z_4(-1-t)] \quad (\text{Eq A5.12})$$

$$c = (1/4)[x_1(t-1) + x_2(1-t) + x_3(1+t) + x_4(-1-t)] \quad (\text{Eq A5.13})$$

$$d = (1/4)[x_1(s-1) + x_2(-1-s) + x_3(1+s) + x_4(1-s)] \quad (\text{Eq A5.14})$$

Where x and z are the undeformed coordinates of the four nodes in Cartesian coordinates. Strains are always computed at the element nodes for the data analysis described in this

report. This requires that these computations be performed four times for each Krypton element used in the data analysis.

A5.2: Summary

The principle strains of a four node quadrilateral element defined by Krypton LEDs were computed with procedures given by [R.A5.1]. The procedures given in section A5.1 are abbreviated in order to simply reproduce the results reported by researchers. The methods used are indeed more complicated than what is reported in section A5.1. The reader is referred to [R.A5.1] for a complete understanding of the theory used to determine the principle strains from the Krypton data.

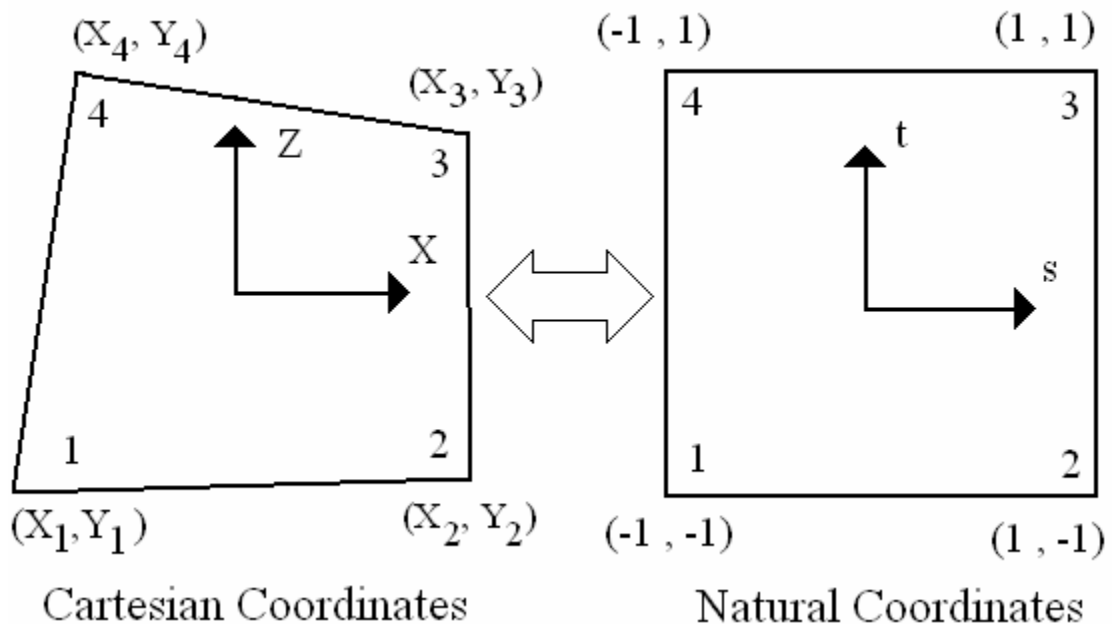


Figure A5.1: Isoperimetric mapping of global to natural coordinate system.

[R.A5.1] Logan, Daryl L. “A First Course in the Finite Element Method, 3rd Edition”. Chapter 10, section 10.3, pp 395-402, equations 10.3.4, 5, 11, 18, 19, 20, 22. Copyright 2002, Wadsworth Group. Brooks/Cole, a division of Thomson Learning, Inc; Pacific Grove CA, USA.

Appendix 6: Data Management & Reduction

A6.0: Introduction:

The data used in the analysis of the wall specimens was collected from several types of instruments. The way in which the data was acquired differs for each type of instrument. The way the data was managed and reduced was also contingent on the way the data was acquired. This appendix documents the way data was acquired and the reasons for different management and reduction techniques.

A6.1: Data Acquisition: MAST laboratory DAQ system versus Krypton:

Data from the experimental tests was recorded by the MAST laboratory data acquisition (DAQ) machines. The data from each instrument was recorded directly with the DAQ with the exception of the Krypton data. The DAQ machine continuously records data at a rate of 1 Hz. The record of the data has been filtered by the DAQ system at the time of collection. This filtration process eliminates erroneous data at a rate of 10 Hz for strain channels and 2 Hz for voltage channels. This ability greatly reduces the instantaneous variations seen in the test data. Data recorded from the Krypton machine is also recorded as a single value for each time step. However, this data point is the actual value at the time stamp and is not filtered for vibrations. This single data point record reflects the instantaneous variations inherent in the system. Consequently, a larger degree in variation of the data values is observed for the Krypton data when compared to the other instruments used in the test. This variation is addressed in the reduction scheme of the Krypton data.

A6.2: Data Management: File size breakdown:

The time required for each test was a considerable problem when managing the data output files from the DAQ. Loading ramp rates for a static load assumption and the time

required for marking cracks and making decisions greatly increased the time of each test. The number of time steps was on the order of 10^6 for each rectangular wall test. The time for each test, coupled with the number of sensors required researchers to break test files into multiple segments each day. These breaks in data files also gave researchers time to make changes to instrumentation on the wall as needed. The implications of the breaks of these data files and changes in the instrumentation on the test structures were also addressed in the reduction of data files.

A6.3: Data Management: Changes in Instrumentation:

Changes in the instrumentation scheme needed to be made during each test. Changes included the addition and removal of sensors, as well as resetting existing sensors. The addition of sensors was typically done when existing sensors failed or additional measurement of certain behaviors was desired. The removal of instrumentation was made for safety of the instrument itself as damage levels increased or when new damage levels no longer allowed accurate measurement of behavior. Lastly, some instruments needed to be reset during the test. This occurred when researchers bumped existing instrumentation during the marking of cracks or observing damage during load pauses. The changes in instrumentation were also addressed during the reduction of the data files.

A6.4: Data Reduction: Changes in Instrumentation:

Changes in instrumentation and the affect on recorded data were done during the test itself and during the post-processing of the data. The addition of a new instrument was typically dealt with the day of the test. DAQ offset files were manipulated prior to recording data with a new sensor. This was done in the same manor as existing instruments. Once a new instrument had been added and connected to the DAQ system, new offsets were recorded.

Offsets are the average data values recorded over a ten second period when no load is applied to the structure. The average values recorded in the offset files are then used to bias the data being recorded, “zeroing” out the instrument from initial readings that do not reflect a test structure at zero load and displacement. The offset value recorded for a new sensor, taken after it had been attached to the test structure was then spliced into the original offset file used for the rest of the instrumentation. This allows for an accurate representation of the changes in data values for all sensors when loading of the test structure resumes.

The data being recorded once an instrument has been removed from the test structure was dealt with in the post-processing of the data. The data for these sensors is simply deleted from the file to help eliminate the problems arising from working with such large data files. Data following a failure is included in the archived files for researchers to make their own judgments about questionable data. This is specifically for the Krypton when cracking at the LED attachment causes the results to be questionable. The degree of failure still allows for some useful information, such as the buckled shape of the walls. For this reason, the time at which the data is thought to be compromised by researchers is simply documented for viewing by other parties.

Researchers often blocked the view of the Krypton camera while marking cracks and inspecting the test structures during load pauses. This causes the Krypton LED readings to jump to an unreasonable value or return the response ‘#VALUE!’ in the Excel output. These points are removed from the corrected data files. A large number of instances exist when less than 10 seconds removed. These points are not documented due to the insignificance of the event.

Instruments that were bumped or adjusted during ramp pauses of testing were dealt with during the test itself and during the post-processing of the data. Instruments that were bumped were manually reset during the test to get as close as possible to the values they were reading prior to the accident. Next, the data was manually offset again during post-

processing of the data. The first step in doing this was to take an average of the data values being recorded prior to the problem. The data which was selected for the average was chosen to be after the values which were being recorded settled from structural response at the peak pause to seconds before the instrument was disturbed. Secondly, an average was computed from seconds after the instrument was reset to seconds before load was removed from the test structure. The difference in these averaged values was then subtracted from every data point following seconds after the instrument was reset.

In addition to bumping and resetting instruments, drift the instruments was sometimes observed during the night when no testing occurred. Instruments that had drifting readings were dealt with by first calculating the drift rate over night. The drift is assumed to be time dependant. The data following the observed drift was corrected by subtracting the drift rate multiplied by the change in time from the drift. Refer to section A6.7 for a list of instruments which were changed and the steps taken to alter the data which they recorded. Refer to figures A6.1 for an example of a correction to test data.

A6.5: Data Reduction: Reducing data file size

Once the data had become more manageable, a reduction in the volume of data was desired to make file size appropriate for analysis. The file size prior to reduction was simply too large to make computations with EXCEL time and space efficient. Several problems arose when attempting to perform the large amount of computations required for certain behaviors. Simply put, the size of the files became so large with embedded calculations that standard computers would not have adequate virtual memory to re-open them. This was still the case when data from only the necessary files was present in the file. For this reason, it was essential to remove portions of the data.

The first data points removed were sections of the ramp pauses that were unnecessary for computations. The sections that were removed began at least one minute into a ramp pause and at least 30 seconds before unloading began. These end points were chosen such

that settling of the structure at the ramp peak would not be eliminated. No data was removed for pauses shorter than two minutes long. The same end points were chosen for additional data at the beginning and end of each test file.

Once the unwanted pause data had been removed, a reduction macro was used to delete $\frac{3}{4}$ of the data points recorded in the data file. This macro was indiscriminant in the data which was removed. Problems such as resolution at ramp peaks were considered when reducing data in this way. Comparisons of the original and reduced data were made at ramp peaks to ensure that data removal did not adversely impact the perceived maximum values the structure was subjected to. It was concluded that the loading rate was slow enough that the reduced data still returned values very close the original data. The study in the variations between perceived ramp maximums for the reduced and original data can be seen in Figure A6.2. Values were typically between 0 and 0.2% of the maximums recorded for the original data.

The reduction of the Krypton data differed slightly from that of the data recorded directly from the DAQ machine. As discussed before, the data from the Krypton machine had a larger variation than that from the DAQ instruments. This was addressed with a floating average of the recorded data from the Krypton machine. Several ranges were selected for the floating average of the data. It was concluded that a seven-point floating average reduced the noise levels in the data appropriately and represented the changing data points well. The study on the effect of implementing such a technique is discussed in appendix 1 in determining grid sizes for calculating strains with the Krypton. Once the floating average had been implemented, the same data reduction technique used for the DAQ instruments was applied to the data from the Krypton machine. This was done such that the times that data was recorded for the remaining data points matched for both the DAQ instruments and the Krypton. Lastly, the coordinate system of the Krypton was converted to match the other instruments. The units were converted to inches and the positions of the LEDs were offset to the known undeformed location of the bottom LED on the north side of the walls from measurement in the field.

A6.6: Data Archiving

The test data for the rectangular walls adheres to the following naming scheme:

specimen name_intstrument_processing stage_data range_derived data

Where the ‘specimen name’ field is the specimen being tested. The ‘instrument’ field refers to the data from a specific type of instrument. The ‘processing stage’ refers to the level of post processing the data has undergone, such as raw or filtered. The ‘data range’ field refers to the contents of the file, such as the entire test data with load pauses removed or just the loading ramp maximum times. The ‘derived data’ field states the calculations performed with the data. These files were uploaded to the project site on NEES central for viewing. The project is titled: Experimental and analytical investigation of nonrectangular walls under multidirectional loads and is available at <https://central.nees.org/?projid=22>.

A6.7.0: Post Processing Decisions

This section covers the changes made to the experimental test data. Each wall and instrument required special treatment depending on the situations that arose during the experimental testing. This section is also included in the data archives at www.nees.org.

A6.7.1.1: RWN Krypton Data

The Krypton data for RWN was treated with the post processing techniques discussed previously in this chapter. The archived ‘converted’ file contains the Krypton data that has been filtered with the seven point floating average and the ramp pauses removed. The archived ‘corrected’ file contains the displacements recorded for each LED. The offset used for the undeformed position was the average position reading over one minute prior to load being applied to the test structure. The coordinate system has also been modified

from the camera coordinate system to match the sign conventions of the other instruments. The lateral displacement has been reversed such that a positive displacement refers to the No.5&6 boundary element in tension. In addition, the 'X' coordinate of the LEDs has been changed to match the other instruments where a position of zero is the extreme face of the No.5&6 boundary element. The specific changes and failure of the Krypton LEDs are as follows:

Krypton-LED Failure

1. LED #27 removed during the load pause between 5/2/06 12:35:32 PM and 5/2/06 1:07:03 PM due to excessive cracking and a failing connection to the concrete cover.
2. LED #37 was not in clear view of the camera between 4/28/2006 4:01:41 PM and 5/1/2006 11:10:13 AM. The reasons for this are unknown. Data in this region is excluded from analysis.

Krypton-LED data removed from blocked view of camera

1. 4/28/2006 4:40:32 PM to 4:41:20 PM
2. 4/28/2006 9:10:18 AM to 9:10:22 PM
3. 4/28/2006 9:10:46 AM to 9:10:50 PM
4. 5/2/2006 10:04:39 AM to 10:04:43 AM
5. 5/2/2006 11:06:48 AM to 11:07:28 AM
6. 5/2/2006 3:30:02 PM to 3:30:10 PM
7. 5/3/2006 8:41:10 AM to 8:41:18 AM

A6.7.1.2: RWN String Pot Data

The portion of the data prior to load being applied has been removed for analysis in the 'corrected' file. This file still contains ten minutes of data prior to load being applied to

the test structure. The following are the changes to the experimental data and disturbance/failure events to the string pot data in the 'corrected' data file:

String Pot-Failures and Disturbances

1. SPB23 is interfered with by researchers at 5/3/2006 at 5:06:44 PM. The disturbance occurred during inspection of the wall following the buckling cycle. The displacements seem to return to normal following the disturbance.
2. SPL75 has several unrealistic spikes in displacement readings at 5/2/2006 at 12:01:34 PM. This occurs later in the test at 4 other time steps. The data returns to a 'normal' reading quickly. The problem is not due to researchers, as the instrument was out of reach. The cause is unknown, but does not have an impact on the results of the test.
3. SPLB is interfered with by researchers at 5/3/2006 at 4:30:48 PM and 5:06:12 PM. The disturbance occurred during inspection of the wall following the buckling cycle. The displacements seem to return to normal following the disturbance.

String Pots-Data Corrections

1. SPLTOP2 is added at 4/27/2006 at 11:02:59 AM. The reading of SPLTOP2 was to be set equal to SPLTOP. The difference between the two when averaging the readings prior to loading was 0.00155". 0.00155" added to all SPLTOP2 readings

A6.7.1.3: RWN LVDT Data

The portion of LVDT data prior to testing has been removed in the 'corrected' data file in the same manor as the string pot data. Other changes made to this file were bumping of instrumentation, drifting, and +/- sign changes when LVDTs were installed upside down. The following are the changes made to the 'corrected' data file for LVDTs:

LVDTs-Instrument Failures

1. LV0L was observed to drift a great deal from the start of the test. The sensor was removed at 4/28/2006 at 11:06:15 AM. LV0L was replaced at a zero load pause with LV0Lnew. LV0Lnew was offset at the time of installation.
2. LV0Lnew fails at 5/3/2006 at 11:41:00 AM and is removed from the test structure.
3. LV0S fails due to spalling at 5/2/2006 at 2:24:01 PM and is removed.

LVDTs-Installation Sign Errors

1. BAR1, LV0S, LV53S, LV21L, and LV90L have been multiplied by -1 to correct the upside down installation.

LVDTs-Data Corrections

1. BAR1 and BAR2 are disturbed by researchers marking cracks at 4/27/2006 at 1:58:00 PM. BAR1 seems to have returned to the undisturbed position during unloading from the load maximum pause during which it was bumped. No data correction is made to adjust the offset during the load pause for BAR1. BAR2 did not seem to return to the undisturbed position during unloading and is offset accordingly in the 'corrected' data file. BAR2 is offset by the difference in the average reading before and after the disturbance, 0.000651". This correction is shown in figure AG.1.
2. LV0Lnew drifted from the end of testing on 4/28/2006, observed on 5/1/2006. Data corrected by the drift rate observed over the break in testing.
3. LVBR5 and LVBS were bumped during the load pause of loading ramp #25 at 4/28/2006 at 2:58 PM. These instruments were offset manually at the time to match their undisturbed positions prior to being interfered with. LVBS was disturbed again at 5/1/2006 at 2:10:00 PM. This disturbance was dealt with during the data post processing.

4. LVBRN drifted throughout the test. Drift was corrected in the 'corrected' data file.
5. LVBS drifted after the second day of testing. This drift was not apparent during any other breaks in testing. This drift was treated as an offset, and not a time dependant correction.
6. LVWA1 and LVWA2 are added to the test setup at 5/1/2006 at 11:09:33 AM. These LVDTs are attached to the concrete cover of the test structure and the loading channels to determine the amount of slip occurring between the test structure and loading channels. These instruments are offset prior to installation, no modification is made to their data files.

A6.7.1.4: RWN Strain Gages

This section covers the data modifications strain gage data. Strain gages are only used as a verification tool to compare with the results of the Krypton and String pot sensors. Virtually all strain gages fail at some point in the inelastic range of the tests. The small number of available gages at certain heights creates a great deal of difficulty in calculating accurate components of deformation. For this reason, the results of the strain gage data is only used in the elastic range of the walls. Due to the large number of strain gage failures in the inelastic range, only the strain gages that fail prior to the elastic limit of the walls are documented. These pre-elastic failures are discounted from analysis.

Strain Gages-Pre-elastic Failures

1. SG116 fails at 4/27/2006 at 2:46:06 PM
2. SG20L36 seems to give the poor results from the beginning of the test from poor installation or damage during construction
3. SG9L108 seems to give the poor results from the beginning of the test from poor installation or damage during construction

A6.7.2.1: RWC Krypton Data

The Krypton data for RWC was treated in the same fashion as RWN with the exception of the coordinate system change. Specimen RWC was oriented opposite of RWN and RWS in the test frame. The Krypton remained the same. The Krypton coordinate system is one in the same as the boundary element coordinate system convention.

The failure of LEDs is only noted for the portion of the experimental test prior to wall buckling. Assumptions used in calculating the components of deflection from the Krypton no longer apply after buckling. For this reason, only the LEDs which fail in the portion of the test which the data is used for analysis is noted. Virtually all LEDs fail after buckling of the wall. The following are the LEDs that failed prior to buckling:

Krypton-LED failure

1. LED 14 fails at 8/9/2006 at 3:24:30 PM
2. LED 18 fails at 8/10/2006 at 10:13:27 AM
3. LED 26 fails at 8/10/2006 at 12:13:54 PM
4. LED 36 fails at 8/10/2006 at 1:54:56 PM
5. LED 40 fails at 8/10/2006 at 10:13:27 AM

Krypton-LED data removed from blocked view of camera

1. 8/8/2006 at 1:41:15 PM
2. 8/8/2006 at 3:46:46 PM to 3:56:26 PM
3. 8/8/2006 at 4:13:06 PM
4. 8/8/2006 at 5:18:38 PM to 5:28:26 PM
5. 8/8/2006 at 5:49:54 PM
6. 8/8/2006 at 6:23:53 PM to 6:33:03 PM
7. 8/8/2006 at 6:37:51 PM to 6:39:23 PM

8. 8/9/2006 at 9:12:00 AM to 9:12:04 AM
9. 8/9/2006 at 9:51:00 AM to 9:53:08 AM
10. 8/9/2006 at 11:13:00 AM
11. 8/9/2006 at 11:16:19 AM to 11:16:27 AM
12. 8/9/2006 at 12:23:49 PM to 12:32:02 PM
13. 8/9/2006 at 12:39:06 PM to 12:46:14 PM
14. 8/9/2006 at 12:51:46 PM
15. 8/9/2006 at 12:53:30 PM to 12:55:42 PM
16. 8/9/2006 at 1:17:00 PM to 1:17:12 PM
17. 8/9/2006 at 2:21:56 PM to 2:34:01 PM
18. 8/9/2006 at 2:40:09 PM to 2:44:06 PM
19. 8/9/2006 at 3:48:53 PM to 3:49:37 PM
20. 8/9/2006 at 4:11:57 PM
21. 8/10/2006 at 9:07:02 AM to 9:19:18 AM
22. 8/10/2006 at 9:26:10 AM to 9:37:11 AM
23. 8/10/2006 at 9:41:31 AM to 9:45:32 AM
24. 8/10/2006 at 9:54:16 AM to 10:10:15 AM
25. 8/10/2006 at 11:33:00 AM to 11:33:40 AM
26. 8/10/2006 at 11:37:08 AM to 11:43:01 AM
27. 8/10/2006 at 11:44:25 AM to 11:44:37 AM
28. 8/10/2006 at 11:45:41 AM to 11:45:49 AM
29. 8/10/2006 at 12:16:22 PM to 12:16:34 PM
30. 8/10/2006 at 12:17:06 PM to 12:17:38 PM
31. 8/10/2006 at 12:45:14 PM to 12:56:01 PM
32. 8/10/2006 at 1:05:33 PM to 1:05:41 PM
33. 8/10/2006 at 1:14:09 PM
34. 8/10/2006 at 1:16:32 PM to 1:19:20 PM
35. 8/10/2006 at 2:03:08 PM to 2:17:08 PM
36. 8/10/2006 at 2:18:20 PM to 2:18:28 PM

A6.7.2.2: RWC String Pot Data

Corrections to string pot data are done in the same manor described for RWN. The following are the corrections to the string pot data and failures for RWC:

String Pots-Failures and Disturbances

1. SPB23 gives suspect results following the load peak at 8/10/2006 at 2:46:56 PM.
2. SPL12 fails at 8/10/2006 at 4:17:07 PM.
3. SPL1B, SPL2B, SPL6, SPL1B135, SPLB45, and SPM1B are disconnected from the test structure at 8/11/2006 at 9:46:53 AM.
4. SPL1T fails at 8/10/2006 at 2:00:48 PM.
5. SPL2T fails at 8/10/2006 at 2:00:48 PM.
6. SPL25 fails at 8/10/2006 at 4:17:07 PM.
7. SPLH3 fails at 8/10/2006 at 5:21:59 PM
8. SPR1B is unreliable after the peak at 8/10/2006 at 2:48:32 PM
9. SPR2B is unreliable after the peak at 8/10/2006 at 2:48:32 PM
10. SPRA is disturbed several times after 8/10/2006 at 1:02:49 PM. Displacement readings return to 'normal' following the disturbances.
11. SPRB135 records suspect data readings past 8/10/2006 at 4:55:43 PM. Data is assumed to be compromised.
12. SPRB45 records suspect data readings past 8/10/2006 at 1:59:52 PM. Data is assumed to be compromised.

String Pots-Data Corrections

1. SPRA and SPRB were touching scaffolding. This was noticed after the 'pre-cracking' loading ramp for the No.9 boundary element in tension. The values following this loading ramp are offset to be zero during the load pause after the 'pre-cracking' loading ramps when no load was applied to the test structure.

A6.7.2.3: RWC LVDT Data

Corrections to the LVDT data for RWC follow the same methods described for RWN. The following are the failures and changes made the LVDT data for RWC:

LVDTs-Instrument Failures

1. All BAR LVDTs, L1R, LV21L, LV37L, and LV69S are removed from the test structure at 8/11/2006 at 9:46:53 AM.
2. L1L fails at 8/10/2006 at 5:21:59 PM.
3. L1M fails at 8/10/2006 at 3:31:03 PM.
4. L1SR fails at 8/10/2006 at 11:33:00 AM.
5. LV0L and LV0S fail at 8/10/2006 at 9:19:02 AM.
6. LV90L and LV90S fail at 8/10/2006 at 5:21:19 PM.
7. LVLS fails at 8/10/2006 at 11:14:01 AM.

LVDTs-Installation Sign Errors

1. All BAR LVDTs were installed upside down. Multiplied by -1 in the corrected data file.
2. LV0L was installed upside down. Multiplied by -1 in the corrected data file.

LVDTs-Data Corrections

1. BAR7 disturbed by researchers at 8/9/2006 at 10:27:01 AM. Data corrected by offsetting data following this point by the change in displacement reading observed before and after the disturbance.
2. LH45 added at 8/10/2006 at 8:44:37 AM in order to measure crack widths.

3. LV0S disturbed by researchers at 8/9/2006 at 11:38:03 AM. Data offset to reflect the displacement prior to this interference.
4. LVBRS disturbed by researcher at 8/10/2006 at 11:33:00 AM. Data offset to correct this interference.
5. LVBS disturbed by researchers at 8/9/2006 at 10:27:01 AM. Data offset in the corrected file to reflect the displacement prior to the event.

A6.7.2.4: RWC Strain Gage Data

The corrections to strain gage data are done in the same manor described in section A6.7.1.4. The following are the strain gages that failed prior to the elastic limit of RWC:

Strain Gages-Pre-elastic failures:

1. SG15L_6 seems to give unrealistic results from the beginning of the test. Readings suggest compression yielding early in the test when the wall is still elastic.
2. SG1L18 experiences the same problem as SG15L_6.
3. SG21L90 fails at 8/8/2006 at 6:20:01 PM. No longer reads compressive strains and it is an extreme tension/compression face longitudinal bar.
4. SG2L90 seems to give unreliable data from the beginning of the test. Strain readings drift more positive between loading ramps #3&4, does not respond to load direction change.

A6.7.3.1: RWS Krypton Data

The Krypton data for RWS was treated in the same fashion as RWN and RWC. The LED failure reporting is again only for the portion of the experimental test prior to wall buckling. The following are the Krypton LED failures from concrete cover spalling and

cracking, as well as the displacement of the wall displacing LEDs out the view range of the Krypton camera.

Krypton-LED failure

1. LED 2 fails at 8/29/2006 at 3:40:00 PM
2. LED 22 fails at 8/29/2006 at 2:06:12 PM
3. LED 27 fails at 8/29/2006 at 12:38:07 PM
4. LED 31 fails at 8/29/2006 at 12:38:07 PM
5. LED 50 fails at 8/29/2006 at 12:21:14 PM (out of camera range)
6. LED 51 fails at 8/29/2006 at 3:28:41 PM (out of camera range)
7. LED 52 fails at 8/29/2006 at 3:28:41 PM (out of camera range)
8. LED 53 fails at 8/29/2006 at 3:28:41 PM (out of camera range)
9. LED 54 fails at 8/29/2006 at 3:28:41 PM (out of camera range)
10. LED 55 fails at 8/29/2006 at 4:48:41 PM
11. LED 61 fails at 8/29/2006 at 1:11:42 PM
12. LED 62 fails at 8/29/2006 at 3:02:10 PM
13. LED 66 fails at 8/29/2006 at 2:32:49 PM
14. LED 69 fails at 8/29/2006 at 4:49:17 PM
15. LED 70 fails at 8/29/2006 at 4:40:41 PM

Krypton-LED data removed from blocked view of camera

1. 8/28/2006 at 10:32:25 AM to 10:40:00 AM
2. 8/28/2006 at 10:45:12 AM
3. 8/28/2006 at 12:02:40 PM to 12:06:13 PM
4. 8/28/2006 at 1:02:56 PM to 1:06:33 PM
5. 8/28/2006 at 1:22:07 PM
6. 8/28/2006 at 1:23:33 PM to 1:24:05 PM

7. 8/28/2006 at 2:13:44 PM to 2:18:06 PM
8. 8/28/2006 at 2:33:47 PM
9. 8/28/2006 at 2:35:54 PM to 2:36:54 PM
10. 8/28/2006 at 3:49:05 PM
11. 8/28/2006 at 3:51:43 PM to 3:52:55 PM
12. 8/28/2006 at 4:00:15 PM to 4:14:35 PM
13. 8/28/2006 at 4:54:12 PM
14. 8/29/2006 at 8:56:00 AM to 8:56:28 AM
15. 8/29/2006 at 9:03:12 AM to 9:17:01 AM
16. 8/29/2006 at 9:53:21 AM to 10:05:02 AM
17. 8/29/2006 at 10:53:40 AM
18. 8/29/2006 at 10:55:35 AM to 10:56:31 AM
19. 8/29/2006 at 11:33:27 AM to 11:35:59 AM
20. 8/29/2006 at 12:00:31 PM to 12:07:23 PM
21. 8/29/2006 at 12:14:07 PM to 12:21:10 PM
22. 8/29/2006 at 12:26:31 PM to 12:28:23 PM
23. 8/29/2006 at 1:59:26 PM
24. 8/29/2006 at 2:02:00 PM to 2:03:32 PM
25. 8/29/2006 at 3:44:04 PM
26. 8/29/2006 at 3:46:28 PM to 3:47:24 PM
27. 8/29/2006 at 4:26:29 PM to 4:33:01 PM
28. 8/29/2006 at 4:57:53 PM to 5:10:17 PM

A6.7.3.2: RWS String Pot Data

Corrections to string pot data are done in the same manor described for RWN. The following are the corrections to the string pot data and failures for RWS:

String Pots-Failures and Disturbances

1. SPB23 disturbed at 8/29/2006 at 3:54:32 PM. Disturbance is thought to be interference with other instrument attachments and not researchers. Instrument disconnected from test structure at 8/29/2006 at 5:10:01 PM.
2. SPL1B data readings are suspect after 8/29/2006 at 2:36:05 PM.
3. SPL2B data reading are suspect after 8/29/2006 at 3:54:28 PM.
4. SPLB45 fails at 8/29/2006 at 3:54:28 PM.
5. SPR1B, SPR135, and SPRH3 are disconnected from test structure at 8/29/2006 at 2:46:02 PM.
6. SPL1B, SPLB45, SPLH3, SPM1B, SPRB45, and SPLB135 are disconnected from test structure at 8/30/2006 at 11:30:11 AM.

String Pots-Data Corrections

No corrections were made to the string pot data for RWS. However, note that the readings for SPL25 do not match the displacement readings of the Krypton in the No.5&6 boundary element in tension direction. It is thought that the instrument is being interfered with by the reference frame.

A6.7.3.3: RWS LVDT Data

Corrections to the LVDT data for RWC follow the same methods described for RWN. The following are the failures and changes made the LVDT data for RWC:

LVDTs-Instrument Failures

1. BAR1 fails at 8/29/2006 at 2:35:09 PM.
2. BAR3 fails at 8/29/2006 at 3:53:28 PM.
3. L1M, L1R, LH15, LH45, LV21L, LV37L, LV37S, LV53S, and LV90L are disconnected from test structure at 8/29/2006 at 11:30:11 AM.
4. L1SR disconnected from test structure at 8/29/2006 at 1:40:01 PM.

5. LV0L and LV0S removed from the test structure at 8/29/2006 at 2:28:01 PM due to spalling of the concrete cover.
6. LV90S fails at 8/29/2006 at 3:30:53 PM.
7. LVLS disconnected from the test structure at 8/29/2006 at 2:46:02 PM.

LVDTs-Installation Sign Errors

1. BAR LVDTs were installed upside down. Multiplied by -1 to correct the sign convention in the corrected data file.

LVDTs-Data Corrections

2. LH45 disturbed at 8/29/2006 at 9:41:01 AM. Data is offset in the corrected data file to match the undisturbed displacement reading.
3. LVBS disturbed at 8/29/2006 at 2:28:01 PM. Data is offset in the corrected data file to match the undisturbed displacement reading.

A6.7.3.4: RWS Strain Gage Data

The corrections to strain gage data are done in the same manor described in section A6.7.1.4. Several instruments were observed to give questionable results above the height of 72". The strains recorded are thought to be too large for the small drift levels at which they change rapidly. Some of these strain gages to not have increasing strains at larger drift levels, suggesting that the sensor has failed. These instruments are used in the determination of flexural deformation from the consistent trend and time at which this occurs. The instruments that show this behavior are documented for others viewing the archived data to make their own decisions on the validity of these readings. The following are the strain gages that failed prior to the elastic limit of RWS:

Strain Gages-Pre-elastic failures:

1. SG1L72 gives suspect results at 8/28/2006 at 11:00:30 AM. Strains become very large, but less than yield. These strains decrease at larger load levels, suggesting that the sensor is malfunctioning.
2. SG1T21 fails at the beginning of the test from either a poor installation or damage during construction.
3. SG5H4 fails at the beginning of the test from damage or improper connection to the reinforcement
4. SG7L90 gives suspect results at 8/28/2006 at 11:00:30 AM. Strains become very large, but less than yield. These strains do not decrease as SG1L72. Strains readings react to the changing loads much better than SG1L72.
5. SG9L90 gives suspect results at 8/28/2006 at 11:00:30 AM. This instrument behaves the same as SG1L72.

RWN: BAR2 Disturbance Correction

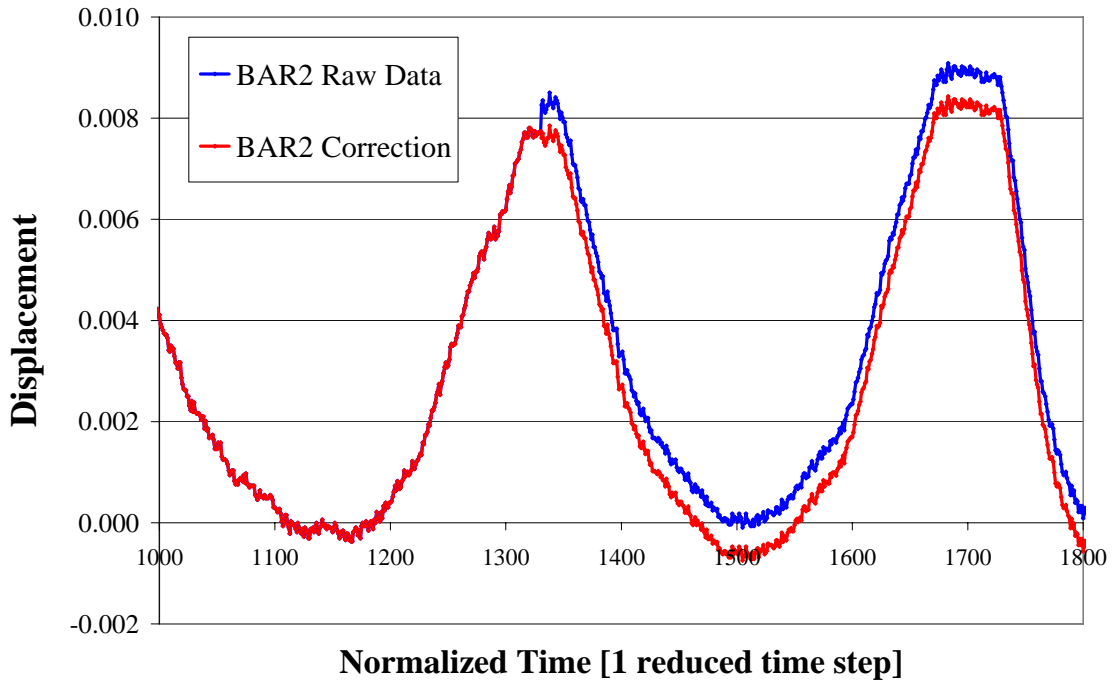


Figure A6.1: Correction to BAR2, Normalized time used for ease of viewing.

Data Reduction Comparison of RWN Load Displacement Data at 0.3% Drift Loading Ramp Maximum

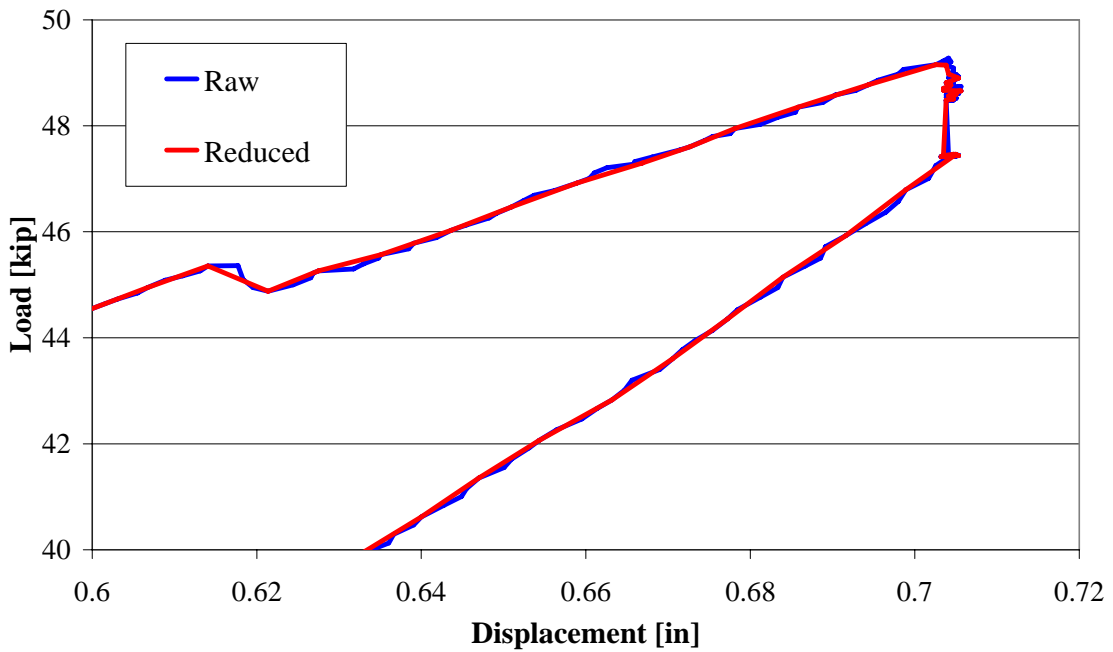


Figure A6.2: Raw v. Reduced data comparison. Load paused removed.

Appendix 7: Photographs and Crack Data

A7.0: Introduction

This appendix covers the photographs taken during the experimental tests and the observed crack widths and shear sliding. Large quantities of photographs were taken of the test specimens at each loading ramp maximum and zero load pauses. All photographs have been uploaded to www.nees.org, along with the test data. Far too many photographs exist to include them all in this report. Instead, select photographs were chosen to convey the key points of this thesis. The final state of the walls at the end of each group of loading ramps to a single drift level have been included for the base of the wall. These photographs are from a single camera position that showed the wall section base and as much of the height above the region a plastic hinging as possible. In addition to these photographs, additional figures show the splitting cracks that developed at the top of the wall and the ultimate state and failures of the walls. Information on the cracking width and observed shear sliding are also included in this appendix.

A7.1: Photographs

Photographs were taken from cameras mounted on telepresence towers at four locations on the laboratory floor: south east, south west, north east, and north west of the test specimen. All photographs at the base of the wall in this appendix come from the south east telepresence tower for RWN, the north east tower for RWC and RWS. This was done for two reasons. First, the camera positions gave the widest camera view of the test specimen at the base of the wall. This allows for more cracks to be seen with a smaller volume of photographs. Secondly, the instrumentation on the east side of the wall does not interfere with crack marking as much as the west side of the specimen. This allows for clearer viewing of the cracks marked by researchers.

The photographs chosen to show the cracking at the base of the wall are the final loading ramp maximum from the loading group at a single drift level. These photographs were chosen to show all of the cracking that had occurred at the drift level in question. The final loading ramp from the previous loading group is used as a comparison to determine the new cracking that occurred at the drift level in question. These photographs show the marked cracks from loading both boundary elements in tension, such that a single photograph can be used to determine the cracking that occurred for each boundary element in tension.

No significant differences in cracking were observed from the first to last time a boundary element was in tension within a single loading group. The only difference was typically small extensions of existing cracks. This difference is too small to notice with the size of photograph in this report. This is shown in figure A7.1. The cracking shown can be assumed to be entirely from reaching the drift level in question for the first time. The cracks at the base of the wall can be seen in figure A7.2 through A7.4, for the different test specimens.

The second type of photographs shown is that at the top of the wall. Researchers could not reach these heights to mark cracks. One photograph must be shown for each boundary element in tension in this case, as cracks can only be seen at the top at the point at which they are open. Cracks in these photographs have been marked in post processing. These photographs are included to show the extent of splitting cracks at the top of the wall and illustrate why they had such a large impact on the way the total measured displacement was reported. The drift levels at which the photographs represent are shown in the figure caption. The drift levels shown are the largest drift levels for each boundary element in tension, prior to the loading ramp where buckling was observed. This is done to show that more cracking occurs for the No.9 boundary element in tension, even when compared to the No.5&6 boundary element at much larger drift levels. The No.5&6 boundary element is shown for 2% drift, as fracture occurring on the way to 2.5% drift

created much smaller loads, showing far less shear cracking. These photographs can be seen in figures A7.5 through A7.7.

Lastly, many photographs of the ‘ultimate’ state of the walls are included in this appendix. These photographs were taken by researchers on the floor to achieve more detail. These photographs are not at the drift levels stated earlier. The details and time of these photographs are noted in the figure caption. In addition to the ultimate state photographs of the test specimens, photographs were taken of the specimens during a ‘post mortem’ investigation. These photographs were taken of the specimens following the removal of concrete and some transverse reinforcement. These photographs are included to show the fracture of the bars in RWC and RWS and also to confirm that no fracture occurred for RWN. These photographs are noted ‘post mortem’ in the figure caption. Note that the No.5&6 boundary element is on the south side of the lab (left) for RWN and RWS and the No.5&6 boundary element is on the north side of the lab (right) for RWC. Ultimate photographs are shown in figure A7.8 through A7.12.

A7.2: Cracking Patterns

Researchers recorded the locations of cracks that occurred during the experimental tests. These cracks were drawn to scale on “crack sheets”, showing the east and west face of the test specimen. These sheets also show the labels used by researchers to identify the major cracks in the test specimen. Crack label locations also note where the crack was measured when reporting crack widths and shear sliding from undeformed grid lateral offsets. All crack sheets have been uploaded to www.nees.org, along with photographs and test data.

A7.3: Crack Data

Information on cracks that occurred during the experimental tests was recorded at loading ramp maximums and zero load pauses. Not all loading ramp maximums were recorded, as the testing process was sped up for RWC and RWS. Crack data was sometimes not recorded at return ramps to the same drift level due to little to no change in the crack widths or amount of cracking.

Crack data recorded by researchers include crack widths and offsets in the undeformed grid drawn on the wall from shear sliding. Cracks were recorded in multiple locations: the boundary element in tension, the foundation/wall interface, and the major cracks that were observed in the walls. This information has been compiled for each loading ramp maximum in this report. See table A7.1 through A7.3 for the crack data. Only the crack widths for the boundary element in tension, the foundation/wall interface, gird offset from sliding, and the overall maximum crack width at the base of the wall have been compiled for this report in the interest of simplicity for the reader. The reported crack data is the average from all measured crack sized during the load group to a single drift level, from both faces of the wall. The range of possible crack sizes can be taken as the range from the crack widths in the boundary element to the maximum crack widths in the web of the section. Note that the term “N/A” appears in many columns at the beginning of the tables. This term simply means that the crack/type in question had not first opened at that ramp/drift level. The term “-“ means that the crack could not be measured or was not measured (interface crack was often obscured by test setup and could not be measured when very small).

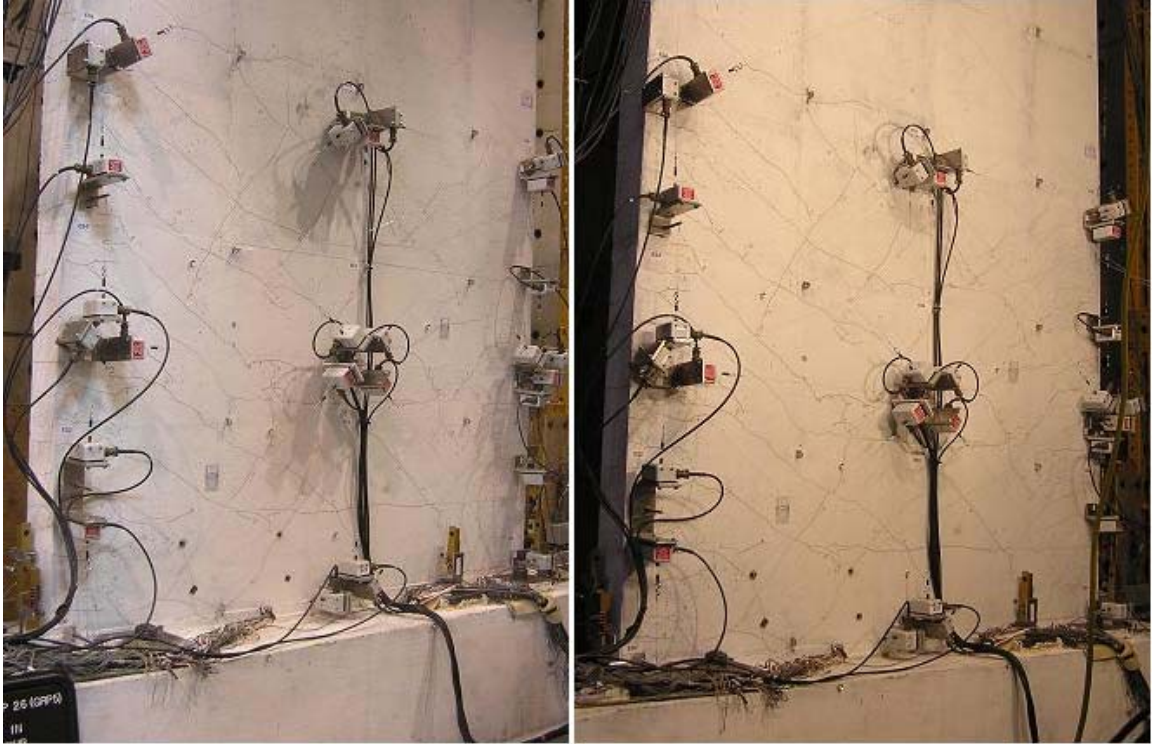


Figure A7.1: First and Third Loading Cycles at 0.5% Drift, No. 9BE in Tension, No visible difference in the cracking at the scale of the photograph.

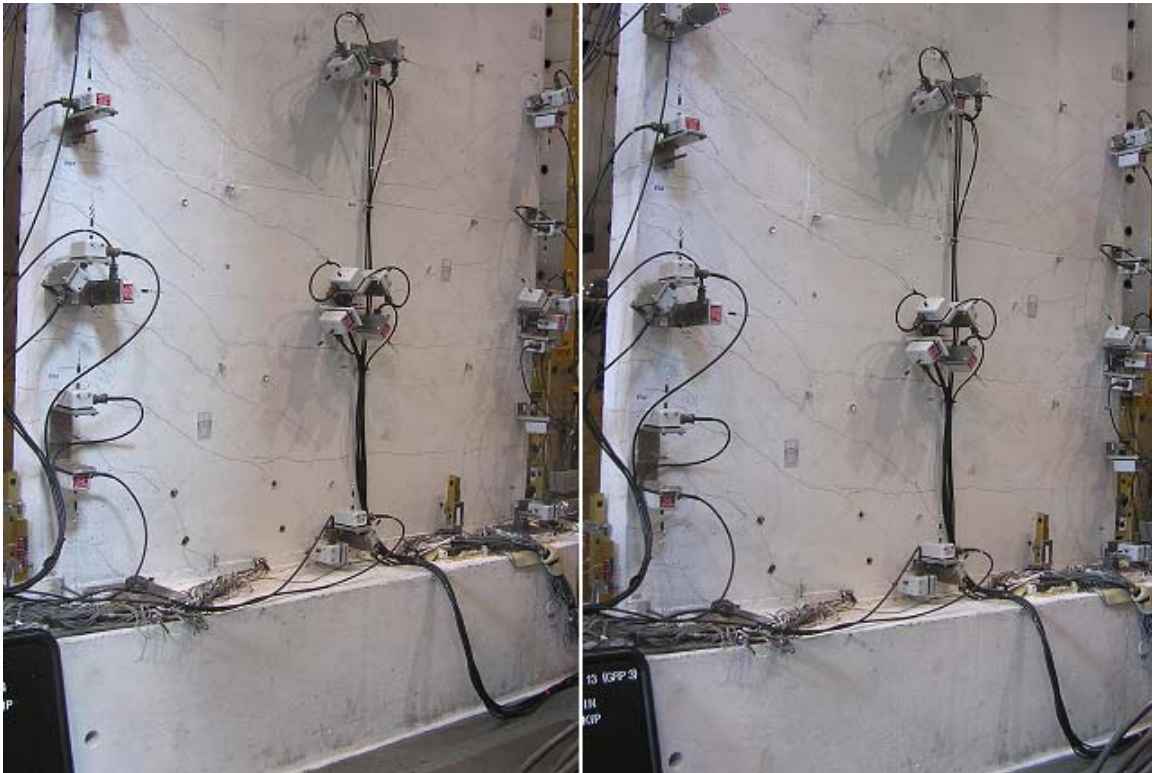


Figure A7.2a: RWN, drift levels of 0.1% (L) and 0.15% (R).

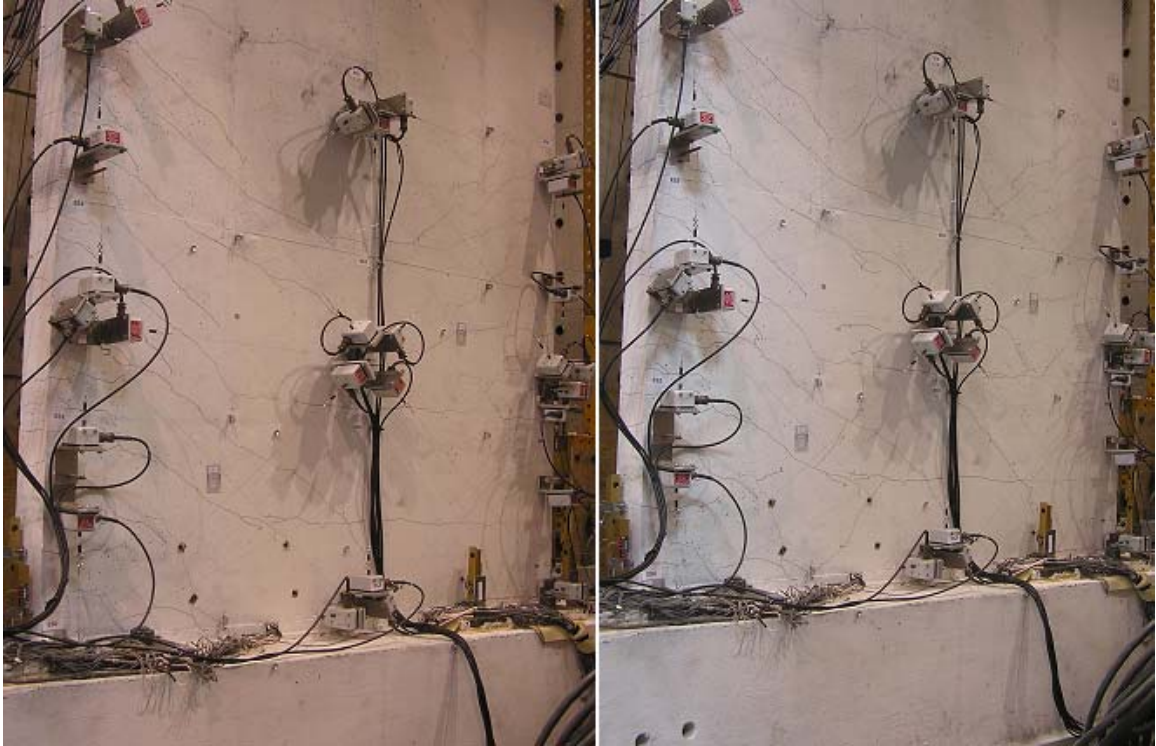


Figure A7.2b: RWN, drift levels of 0.2% (L) and 0.3% (R).

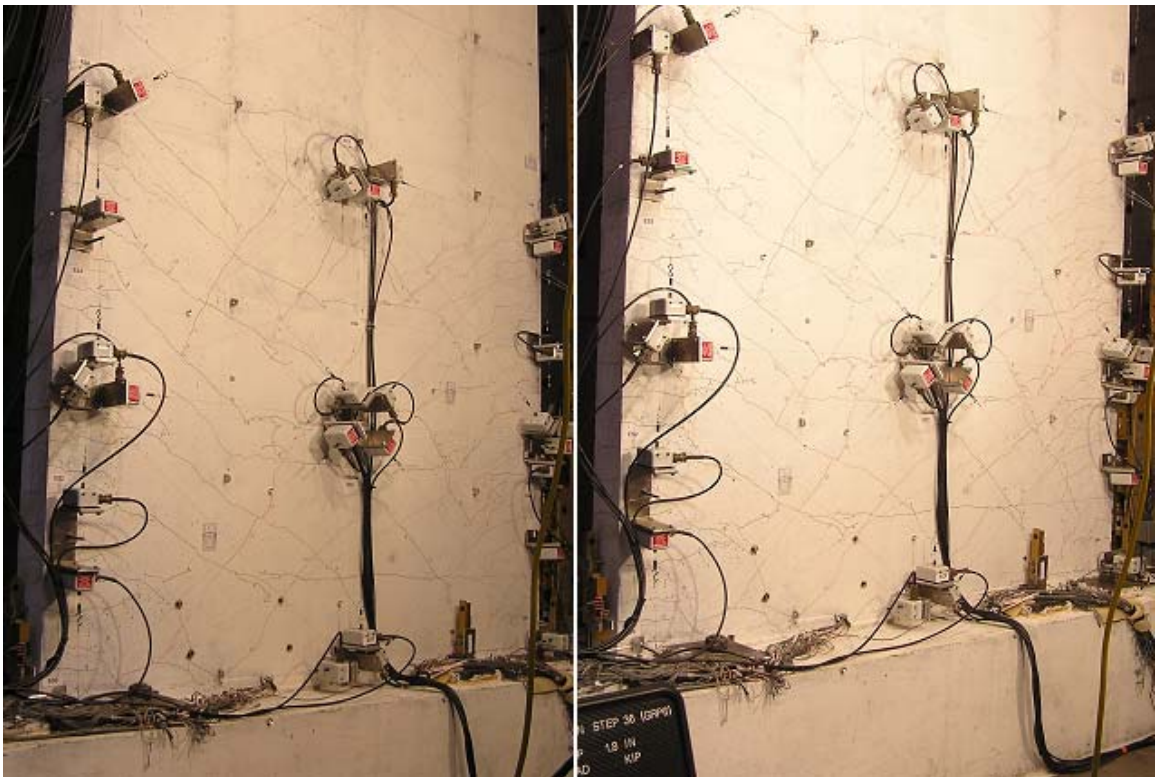


Figure A7.2c: RWN, drift levels of 0.5% (L) and 0.75% (R).

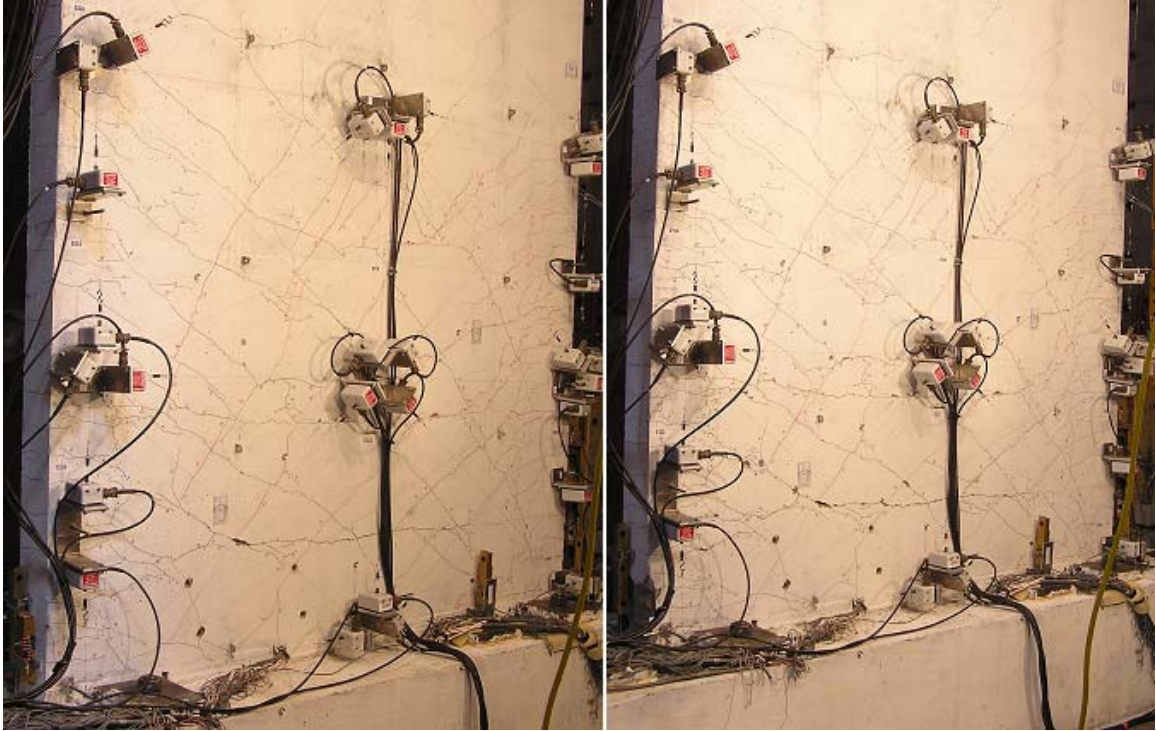


Figure A7.2d: RWN, drift levels of 1.0% (L) and 1.5% in the No.5&6 BE in tension direction w/ 1.0% in the No.9BE in tension direction (R).

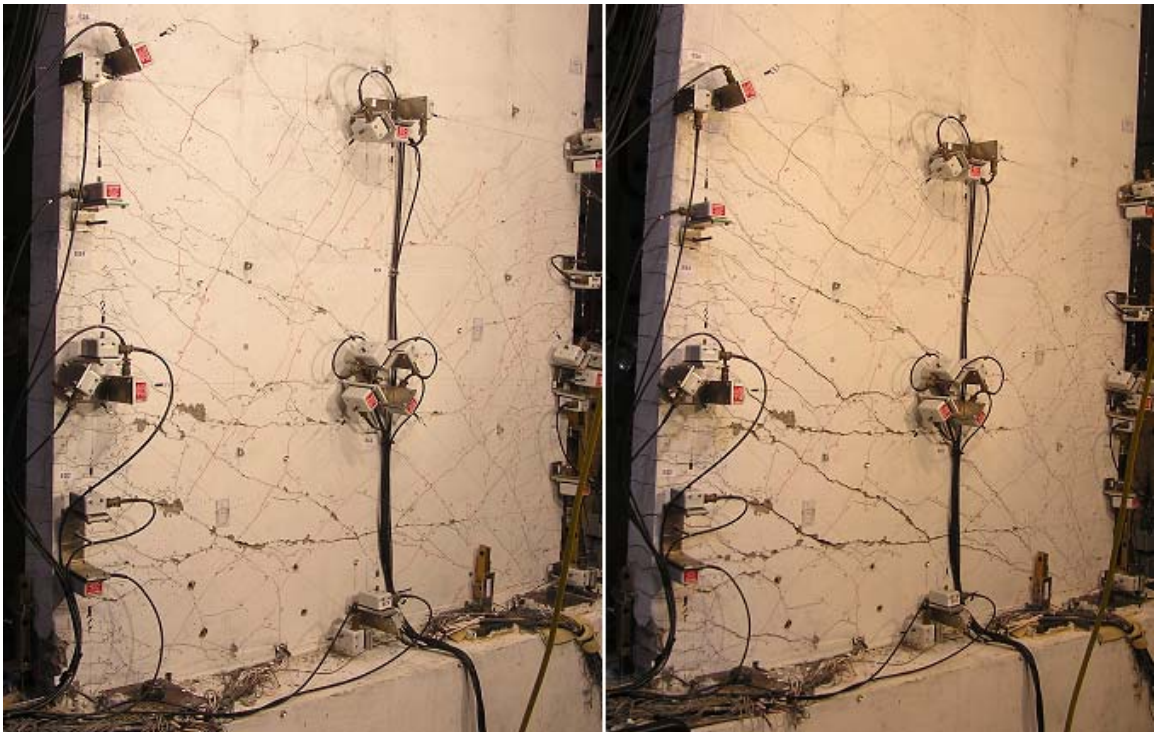


Figure A7.2e: RWN, drift levels of 2.0% in the No.5&6 BE in tension direction w/ 1.0% in the No.9BE in tension direction (L) and 2.5% in the No.5&6 BE in tension, loading ramp maximum prior to buckling (R).

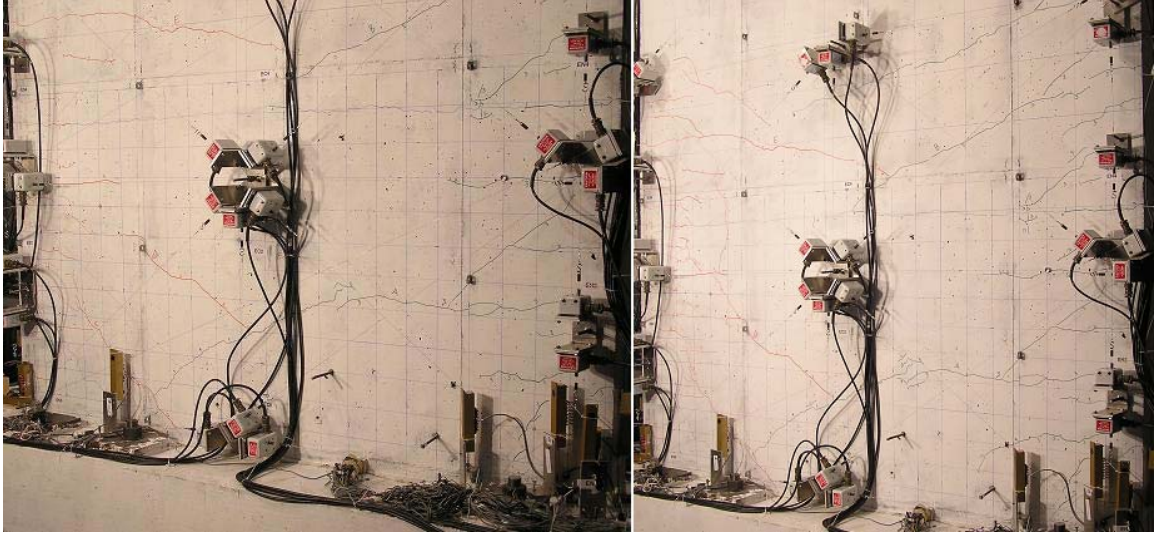


Figure A7.3a: RWC, drift levels of 0.1% (L) and 0.15% (R).

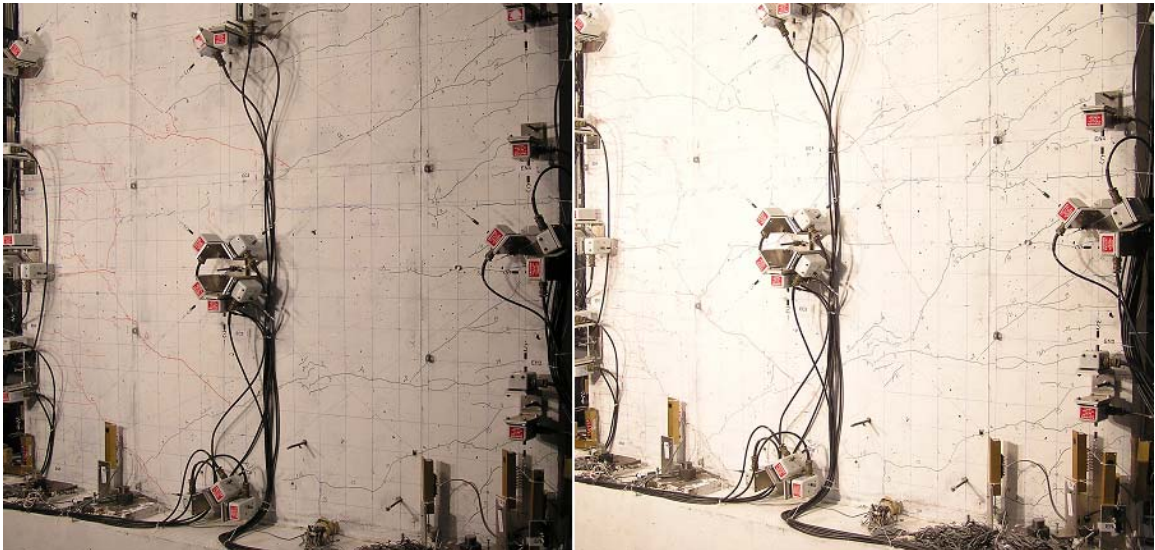


Figure A7.3b: RWC, drift levels of 0.2% (L) and 0.3% (R).

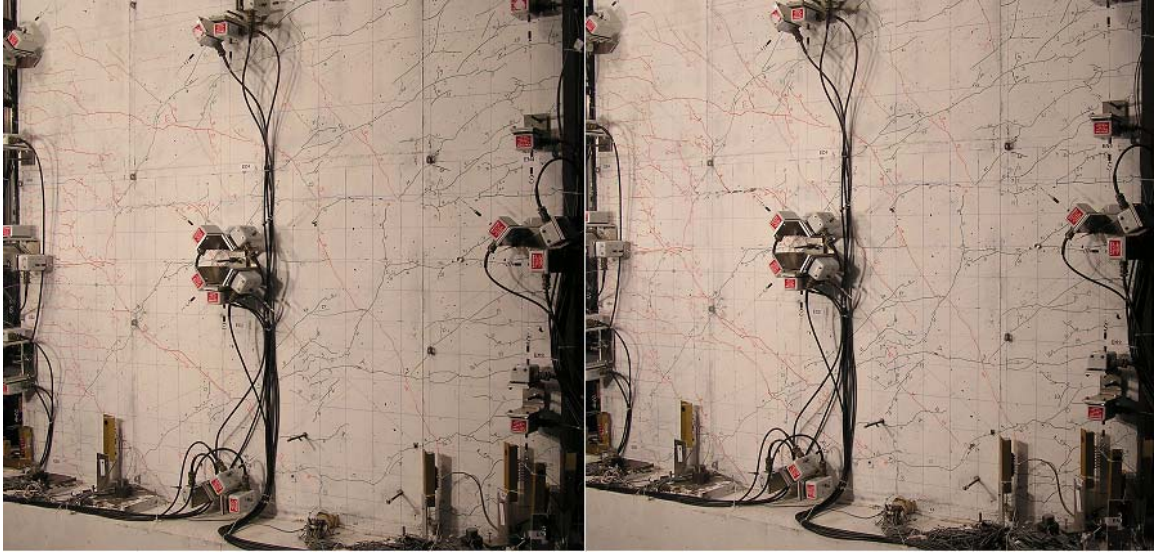


Figure A7.3c: RWC, drift levels of 0.5% (L) and 0.75% (R).

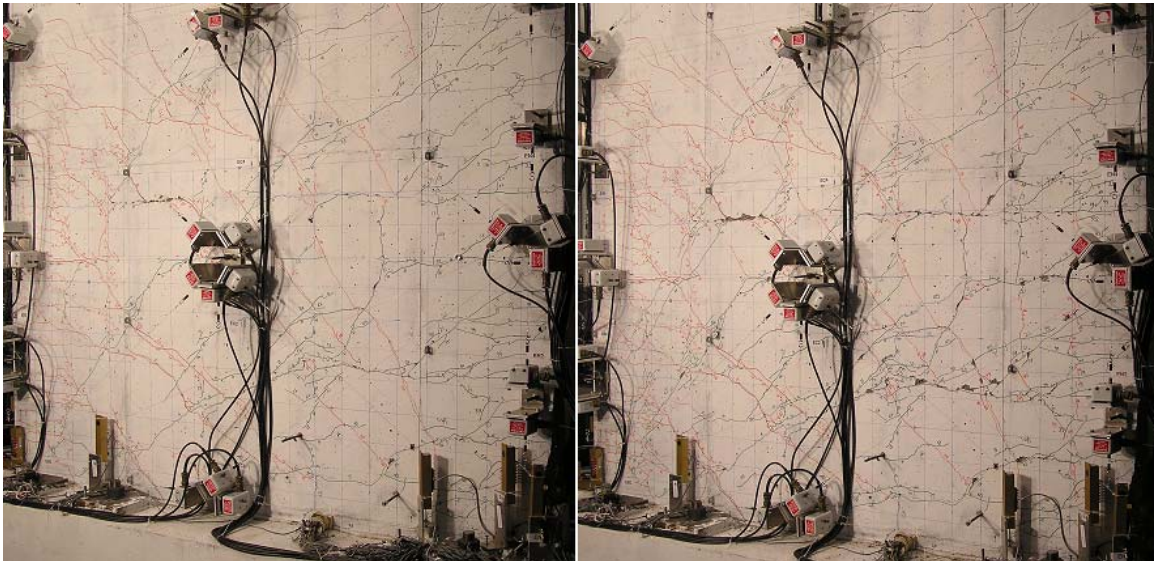


Figure A7.3d: RWC, drift levels of 1.0% (L) and 1.5% in the No.5&6 BE in tension direction w/ 1.0% in the No.9BE in tension direction (R).

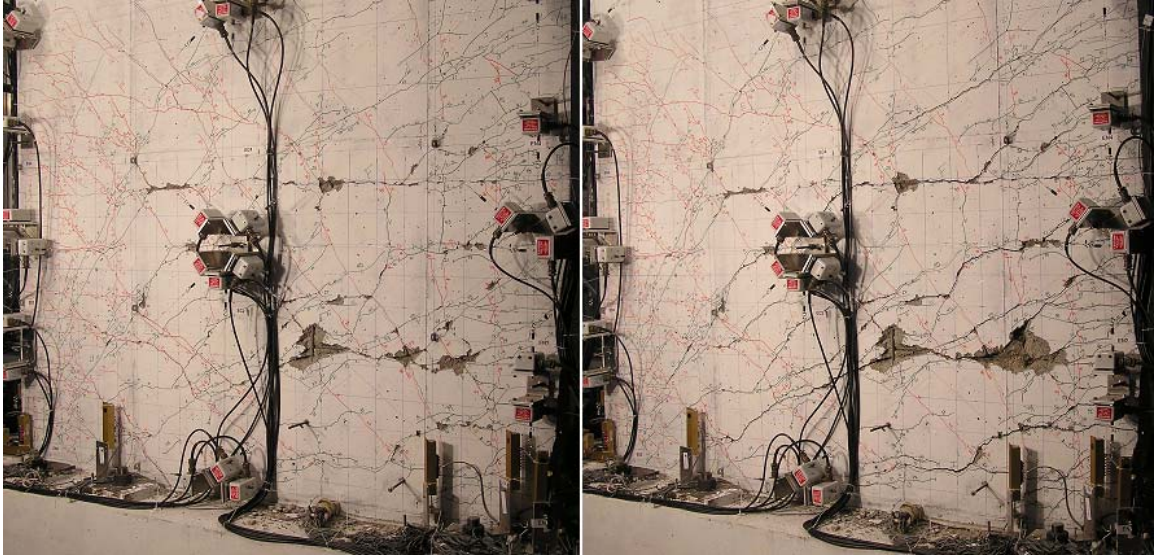


Figure A7.3e: RWC, drift levels of 2.0% in the No.5&6 BE in tension direction w/ 1.0% in the No.9BE in tension direction (L) and 2.5% in the No.5&6 BE in tension, loading ramp maximum prior to buckling (R).

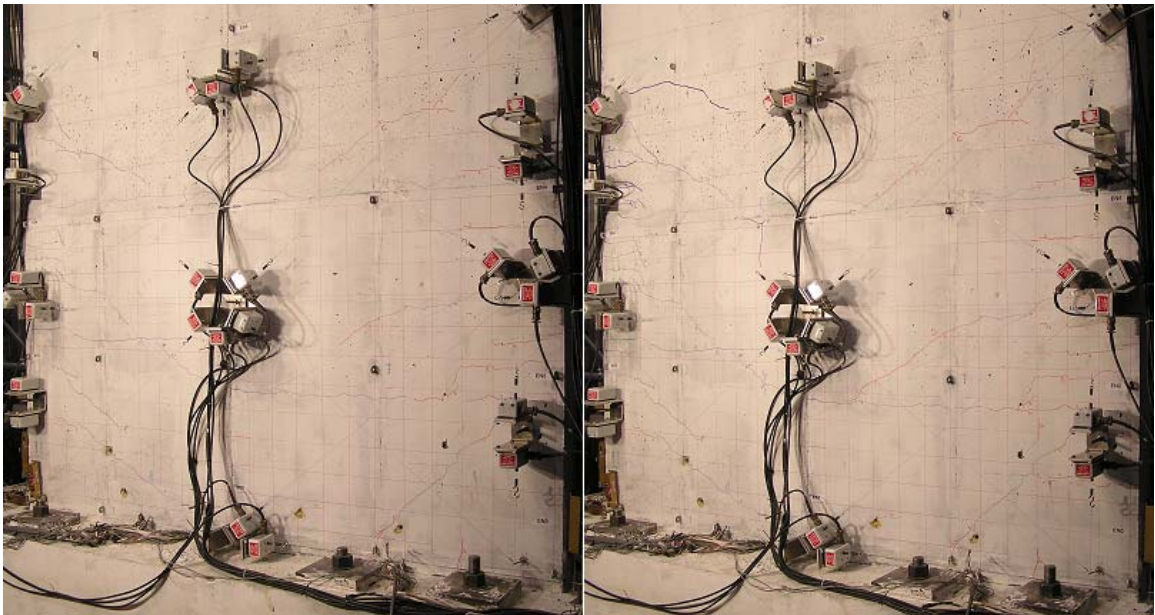


Figure A7.4a: RWS, drift levels of 0.1% (L) and 0.15% (R).

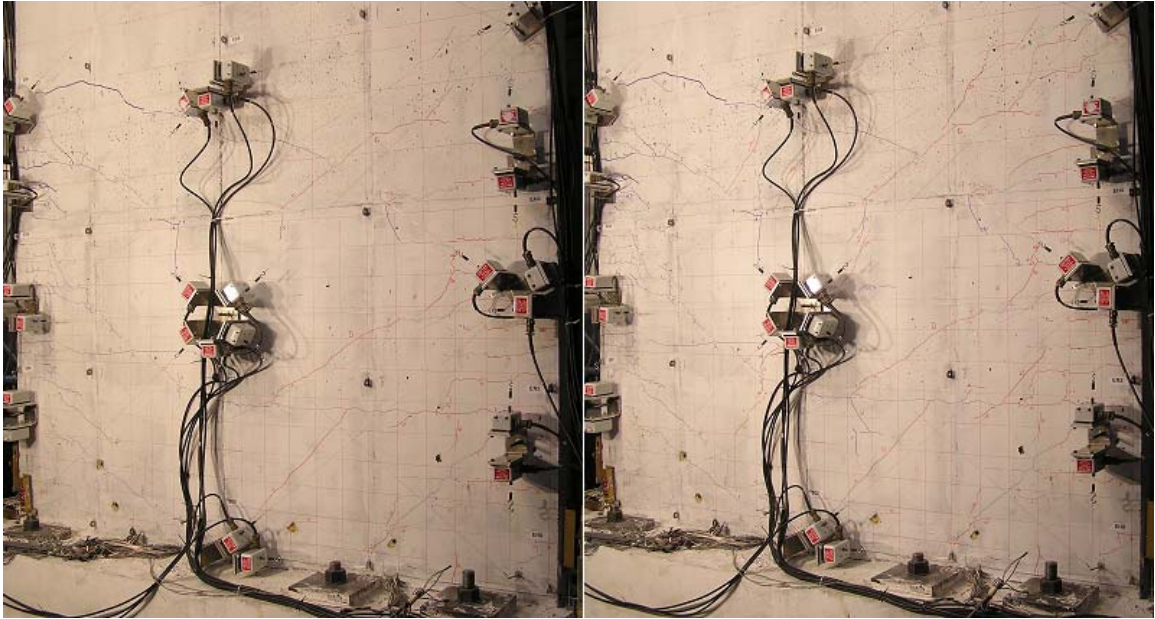


Figure A7.4b: RWS, drift levels of 0.2% (L) and 0.3% (R).

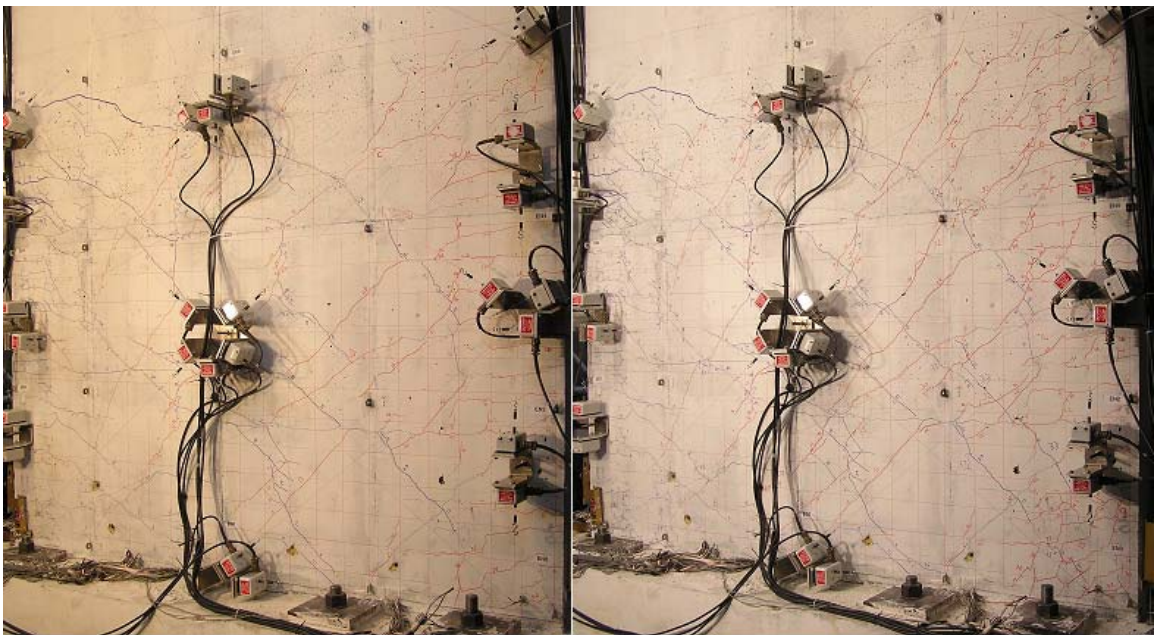


Figure A7.4c: RWS, drift levels of 0.5% (L) and 0.75% (R).

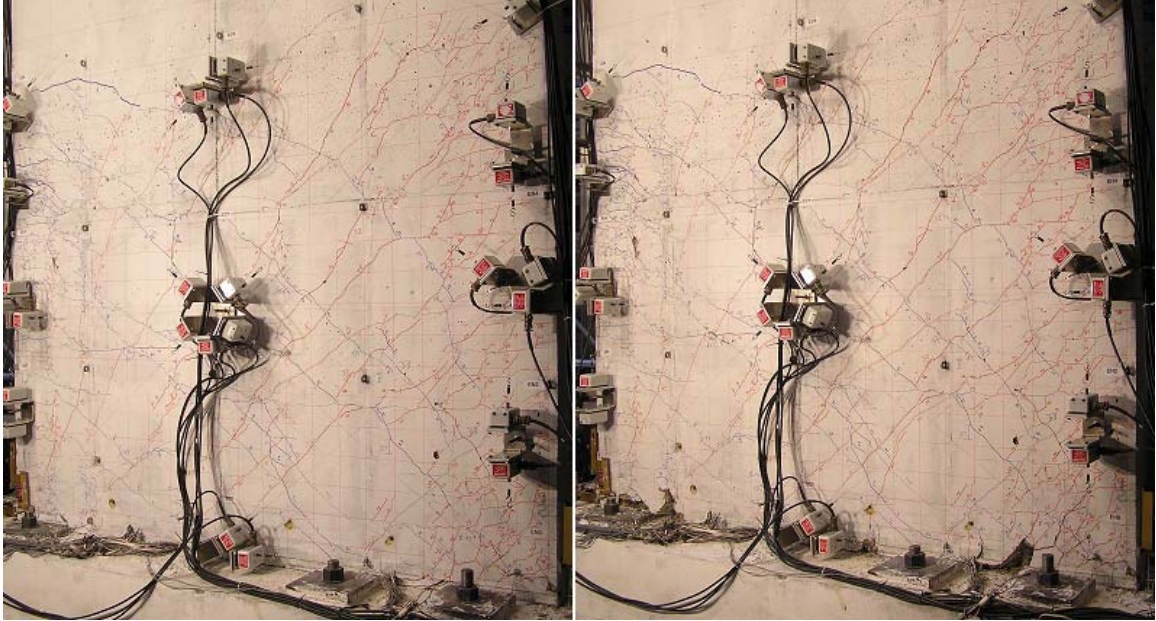


Figure A7.4d: RWS, drift levels of 1.0% (L) and 1.5% in the No.5&6 BE in tension direction w/ 1.0% in the No.9BE in tension direction (R).

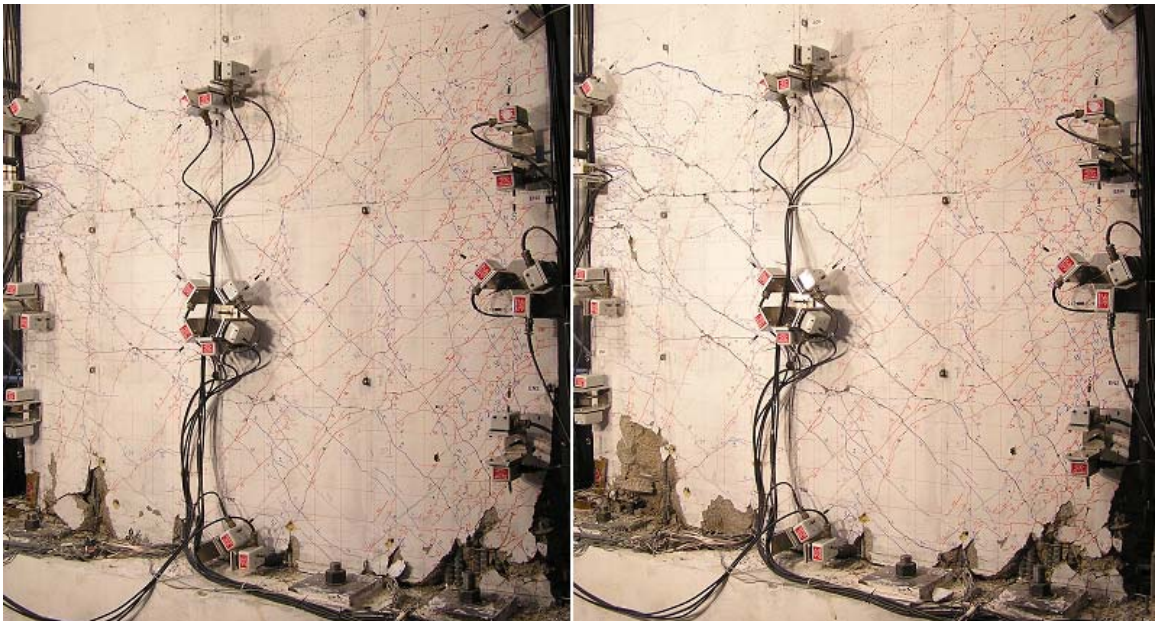


Figure A7.4e: RWS, drift levels of 2.0% in the No.5&6 BE in tension direction w/ 1.0% in the No.9BE in tension direction (L)-Note the local bar buckling at the No.5&6 boundary element at the base of the wall. 2.5% in the No.5&6 BE in tension, loading ramp at which fracture of the No.5&6 boundary element was observed.



Figure A7.5.a: RWN, Splitting cracks from No.5&6 BE in tension, 2.5% Drift

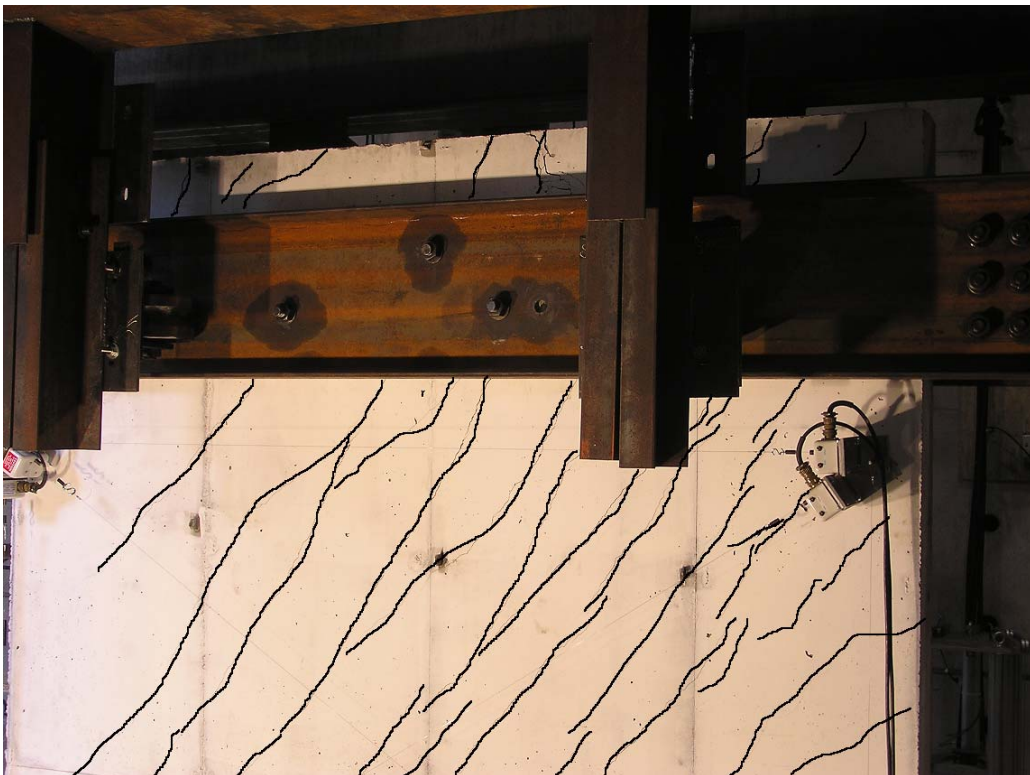


Figure A7.5.b: RWN, Splitting cracks from No.9 BE in tension, 1.0% Drift



Figure A7.6.a: RWC, Splitting cracks from No.5&6 BE in tension, 2.5% Drift



Figure A7.6.b: RWC, Splitting cracks from No.9 BE in tension, 1.0% Drift



Figure A7.7.a: RWS, Splitting cracks from No.5&6 BE in tension, 2.5% Drift

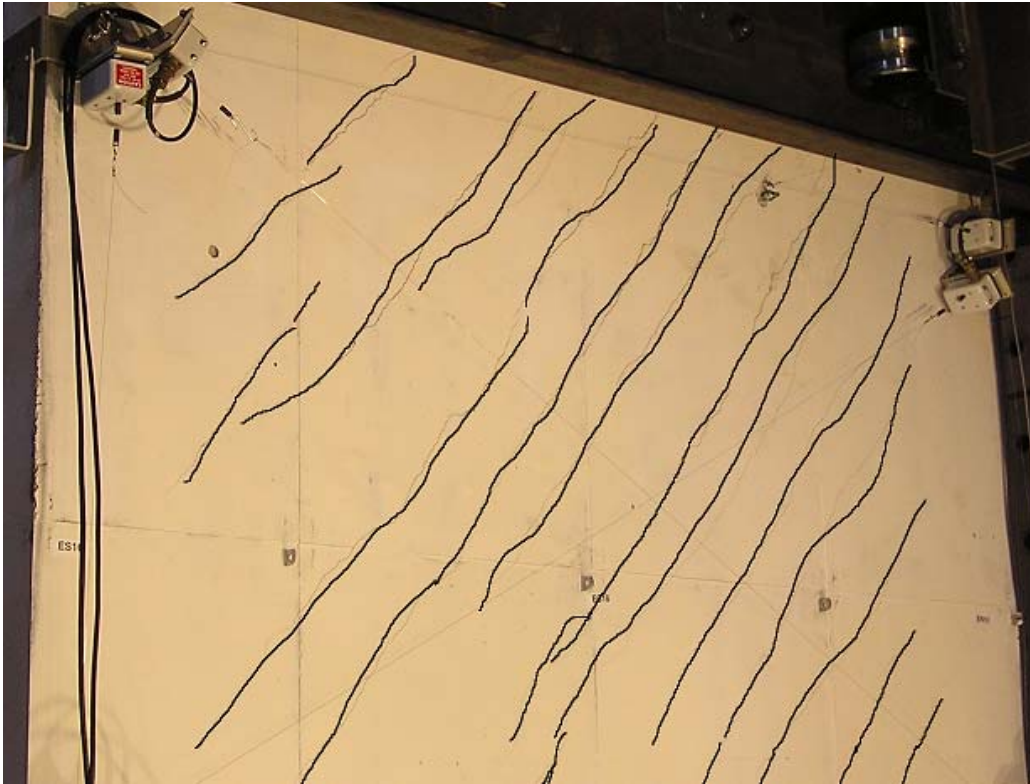


Figure A7.7.b: RWS, Splitting cracks from No.9 BE in tension, 1.0% Drift



Figure A7.8.a: RWN, interface crack at the No.5&6 BE, No. 5&6 BE in tension, 2% drift.



Figure A7.8.b: RWC, interface crack at the No.5&6 BE, No. 5&6 BE in tension, 2% drift.



Figure A7.8.c: RWS, interface crack at the No.5&6 BE, No. 5&6 BE in tension, 2% drift.



Figure A7.8.c: RWS, interface crack at the No.5&6 BE, No. 5&6 BE in tension, 2% drift, west side of the test specimen.



Figure A7.8.d: RWS, interface crack at the No.5&6 BE, No. 5&6 BE in tension, 2% drift, east side of the test specimen. Bar slip shown for No.4 web reinforcement. The bottom pen mark on the bottom splice shows the location of the bottom of the top splice bar before the current loading ramp maximum.



Figure A7.9.a: RWN, transverse 90 degree bend popping out at a height of 21 inches. Located at the No.9 BE face. 2.5% Drift for the No.5&6 boundary element and 1% Drift for the No.9 boundary element.



Figure A7.10.a: RWN, buckling of the No.5&6 boundary element following 2.5% drift in the No.5&6 BE in tension direction, 2% drift in the No.9 BE in tension direction.



Figure A7.10.b: RWC, buckling of the No.5&6 boundary element following 2.5% drift in the No.5&6 BE in tension direction, 2% drift in the No.9 BE in tension direction.



Figure A7.10.c: RWS, local buckling of the bars at the No.5&6 boundary element. Final loading ramp of the No.9 boundary element in tension at 1.0% drift following the No.5&6 boundary element in tension at a drift of 2.0%.

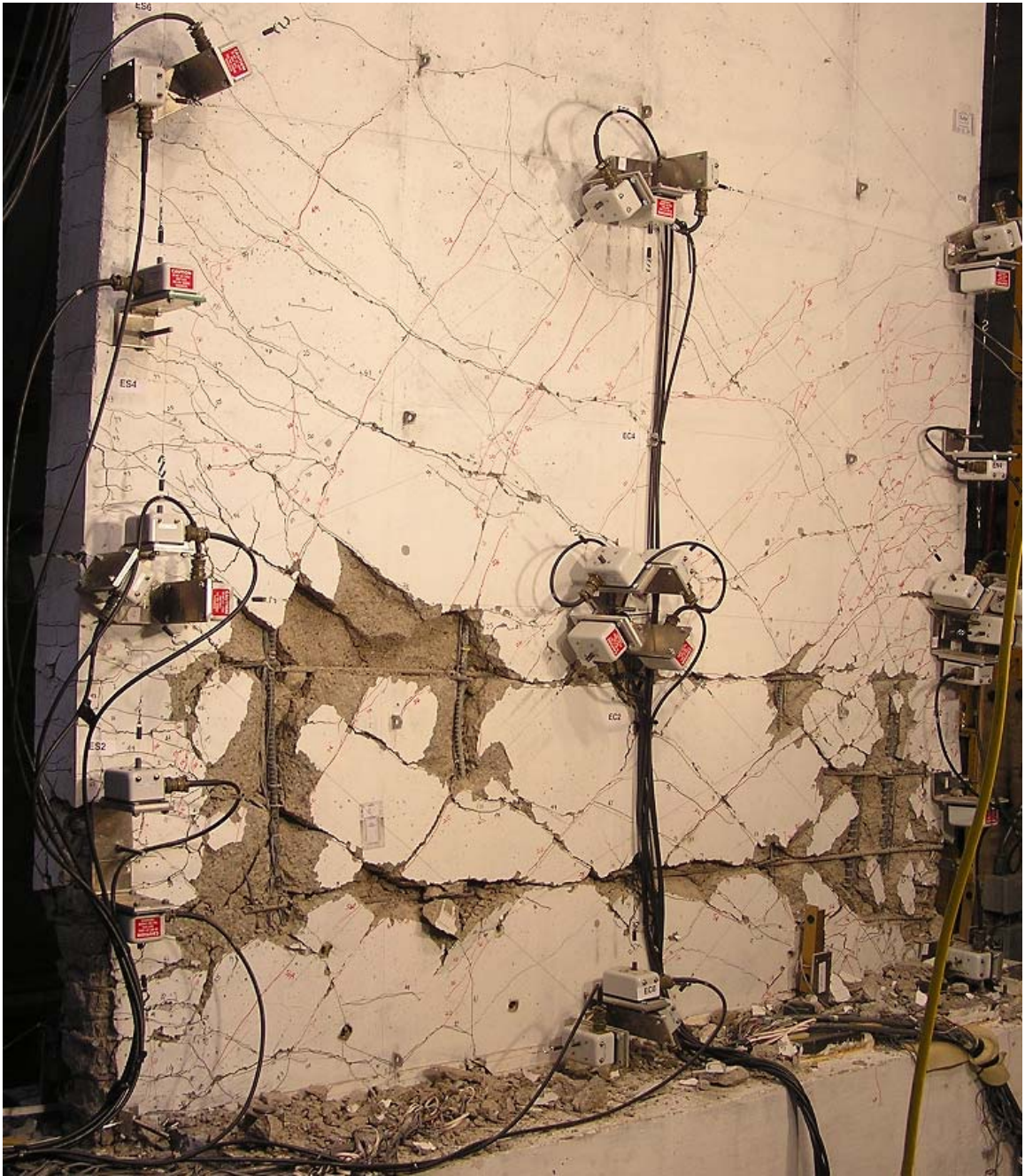


Figure A7.11.a: RWN following all loading applied to the test structure.



Figure A7.11.b: RWC following all loading applied to the test structure.

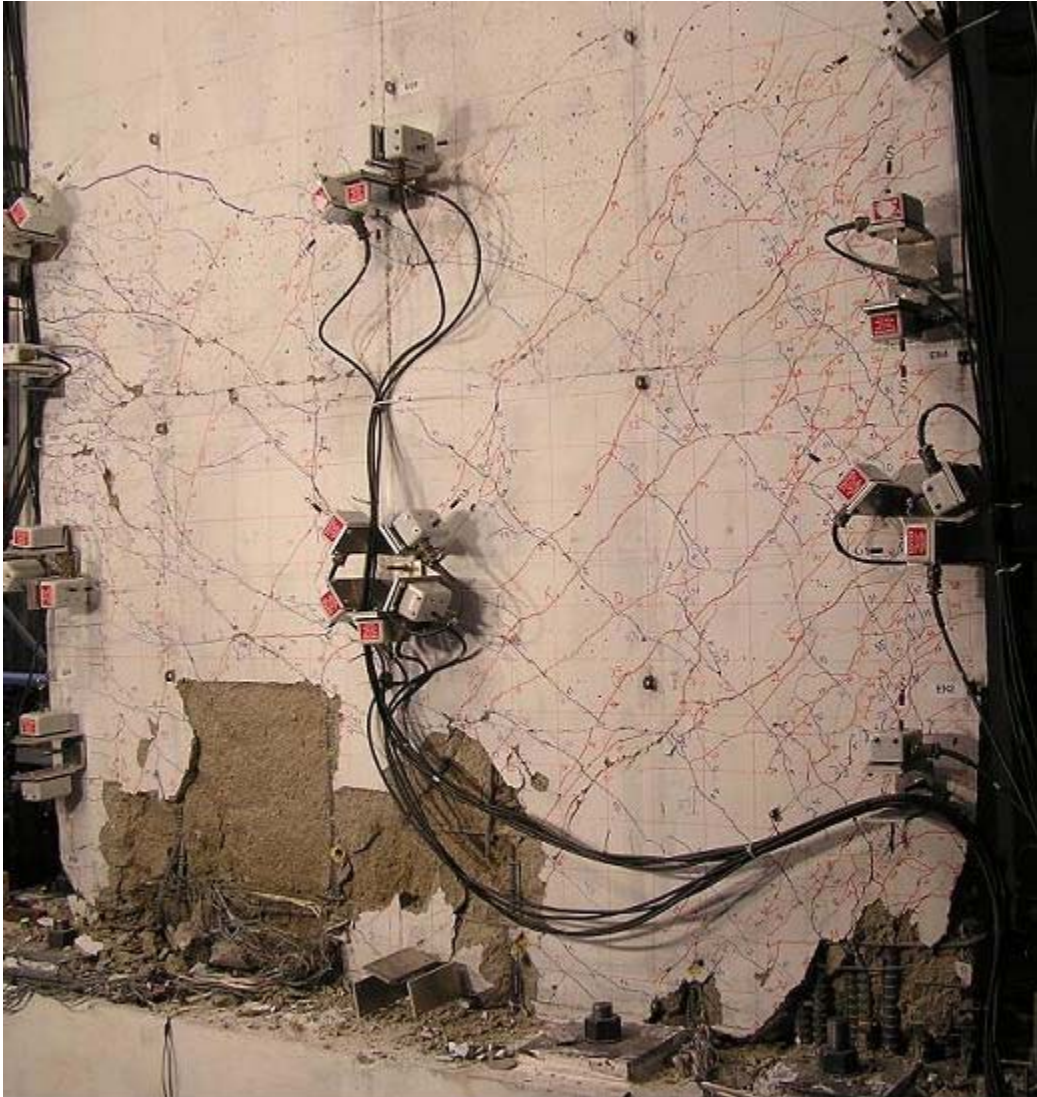


Figure A7.11.c: RWS following all loading applied to the test structure.



Figure A7.12.a: RWN 'post mortem', No.5&6 BE. No fracture of No.5&6 bars.



Figure A7.12.b: RWC 'post mortem', No.5&6 BE. No fracture of No.5&6 bars.



Figure A7.12.c: RWC 'post mortem', fracture of above the coupler of bar #8 (No.4 web)



Figure 12.d: RWC 'post mortem', necking above the coupler of bar #10 (No.4 web)



Figure A7.12.e: RWS 'post mortem', No 5&6 boundary element, visible fractures of No.5&6 bars in the boundary element. Local buckling evident in longitudinal bars.



Figure A7.12.f: RWS 'post mortem', No 5&6 boundary element, , visible fractures of No.5&6 bars in the boundary element. Local buckling evident in longitudinal bars.

RWN: Cracks When the No.5&6 BE is in Tension

Drift [%]	BE in Tension [in]	Max in Web [in]	Shear in Web [in]	Shear Slide [in]
0.100	0.005	-	0.007	N/A
0.150	0.005	-	0.009	N/A
0.200	0.007	-	0.012	N/A
0.300	0.007	-	0.020	N/A
0.500	0.010	-	0.028	N/A
0.750	0.013	0.035	0.048	0.005
1.000	0.033	0.060	0.125	-
1.500	0.047	0.219	0.258	-
2.000	0.068	0.250	0.235	0.010
2.500	0.086	0.292	0.250	0.125

Table A7.1a: RWN crack data

RWN: Cracks When the No.9 BE is in Tension

Drift [%]	BE in Tension [in]	Max in Web [in]	Shear in Web [in]	Shear Slide [in]
0.100	0.002	-	0.007	N/A
0.150	0.005	-	0.013	N/A
0.200	0.005	-	0.018	N/A
0.300	0.007	-	0.025	N/A
0.500	0.009	-	0.040	N/A
0.750	0.009	0.003	0.040	-
1.000	0.060	0.060	0.125	-
1.000	0.025	-	0.060	-
1.000	0.064	0.250	0.135	0.125

Table A7.1b: RWN crack data

RWC: Cracks When the No.5&6 BE is in Tension

Drift	BE in Tension	Max in Web	Shear in Web	Shear Slide
[%]	[in]	[in]	[in]	[in]
0.100	0.002	-	0.004	N/A
0.150	0.005	-	0.016	N/A
0.200	0.005	-	0.023	N/A
0.300	0.009	-	0.028	N/A
0.500	0.014	-	0.039	N/A
0.750	0.025	0.060	0.048	0.030
1.000	0.025	0.114	0.125	0.053
1.500	0.035	0.375	0.234	0.098
2.000	0.045	0.375	0.225	0.146
2.500	0.125	0.313	0.250	0.188

Table A7.2a: RWC crack data

RWC: Cracks When the No.9 BE is in Tension

Drift	BE in Tension	Max in Web	Shear in Web	Shear Slide
[%]	[in]	[in]	[in]	[in]
0.100	0.005	-	0.005	N/A
0.150	0.002	-	0.013	N/A
0.200	0.005	-	0.021	N/A
0.300	0.008	-	0.028	N/A
0.500	0.012	0.016	0.036	0.035
0.750	0.010	-	0.050	0.040
1.000	0.025	0.098	0.058	0.039
1.000	0.030	0.188	0.084	0.085
1.000	0.040	0.500	0.156	0.109

Table A7.2b: RWC crack data

RWS: Cracks When the No.5&6 BE is in Tension

Drift	BE in Tension	BE above Splice	Max in Web	Shear in Web	Shear Slide
[%]	[in]	[in]	[in]	[in]	[in]
0.100	0.002	-	-	0.009	N/A
0.150	0.002	-	-	0.014	N/A
0.200	0.002	-	-	0.018	N/A
0.300	0.002	-	-	0.025	N/A
0.500	0.004	0.023	-	0.034	0.010
0.750	0.009	0.060	-	0.055	0.025
1.000	0.009	0.025	0.035	0.073	0.040
1.500	0.010	0.050	0.375	0.087	0.050
2.000	-	0.250	0.833	0.093	0.060

Table A7.3a: RWS crack data

RWS: Cracks When the No.9 BE is in Tension

Drift	BE in Tension	BE above Splice	Max in Web	Shear in Web	Shear Slide
[%]	[in]	[in]	[in]	[in]	[in]
0.100	0.002	-	-	0.009	N/A
0.150	0.002	-	-	0.010	N/A
0.200	0.002	-	-	0.012	N/A
0.300	-	-	-	0.017	N/A
0.500	0.002	0.025	-	0.028	0.010
0.750	-	-	0.025	0.027	0.016
1.000	0.009	0.125	0.125	0.037	0.023
1.000	-	-	-	-	-
1.000	-	-	-	-	-

Table A7.3b: RWS crack data